NASA Conference Publication 2152

Fifth Annual Flight Mechanics/Estimation Theory Symposium October 1980

Jerome Teles, *Editor*
Goddard Space Flight Center

Proceedings of a symposium
held at Goddard Space Flight Center
Greenbelt, Maryland
October 21-22, 1980

NASA

NASA Conference Publication 2152

Fifth Annual Flight Mechanics/Estimation Theory Symposium October 1980

Proceedings of a symposium
held at Goddard Space Flight Center
Greenbelt, Maryland
October 21-22, 1980

NASA

National Aeronautics and
Space Administration

Scientific and Technical
Information Branch

1980

FOREWORD

The papers presented herein have been derived primarily from speakers' summaries of talks presented at the Fifth Annual Flight Mechanics/Estimation Theory Symposium held October 21 and 22, 1980, at Goddard Space Flight Center. For the sake of completeness, abstracts are included of those talks for which summaries were unavailable at press time. Papers included in this document are presented as received from the authors with little or no editing.

CONTENTS

Paper No.

Forword

SESSION I

Feasibility Study of Using a Two-Plate Model to Approximate the TDRSS Solar Pressure Effects
F. K. Chan (SASC) 1

Improved Chebyshev Series Ephemeris Generation Capability of GTDS
S. Liu and J. Rogers (CSC) and J. Jacintho (GSFC) 2

An Economical Semi-Analytical Orbit Theory for Retarded Satellite Motion About an Oblate Planet
R. A. Gordon (GSFC) 3

Another Semi-Analytic Orbit Theory
K. T. Alfriend (NRL). 4

Semi-Analytical Orbit Determination
P. J. Cefola (CSDL) 5

Semi-Analytical Satellite Theory and Sequential Estimation
P. J. Cefola and S. P. Taylor (CSDL). 6

SESSION II

Estimation of Kalman Filter Model Parameters From an Ensemble of Tests
B. Gibbs, D. Haley, W. Levine, D. Porter, and C. Vahlberg (BTS) 7

Analysis of Estimation Algorithms for Autonomous Navigation with TDRSS Data
J. Dunham, A. Long, P. Gural, K. Preiss, and H. Sielski (CSC) 8

Precision Orbit Computations for Satellite Altimetry
J. G. Marsh (GSFC) and R. G. Williamson (EG&G WASC) 9

CONTENTS (Continued)

Paper No.

Autonomous Navigation Accuracy Using Simulated Horizon Sensor and Sun Sensor Observations
H. T. Hendrickson and G. E. Pease (Aerospace Corporation) 10

Accurate Mars Flyby of Galileo Using Viking Lander
F. B. Winn, E. W. Walsh, M. P. Ananda, and F. T. Nicholson (JPL) 11

SESSION III

An Analysis of GDOP in Global Positioning System Navigation
B. T. Fang (CSC). 12

A Quadrilateralized Spherical Cube Earth Data Base
F. K. Chan (SASC) 13

Adaptive Guidance and Control for Future Remote Sensing Systems
J. W. Lowrie and J. E. Myers (Martin Marietta) 15

The Resurrection of LANDSAT-2 Attitude Control System
P. S. Hui (GSFC). 16

Doubly-Periodic Orbits in the Sun-Earth-Moon System
R. Farquhar and D. Muhonen (GSFC) and D. Dunham (CSC) 18

SESSION IV

Attitude Ground Support System for the SMM
G. Nair (CSC) 19

Inflight Calibration and Performance Evaluation of the Fixed Head Star Tracker for SMM
P. Gambardella and R. Thompson (CSC). 20

Inflight Calibration of the Fine Pointing Sun Sensor on SMM
P. Gambardella and R. Thompson (CSC). 21

CONTENTS (Continued)

Paper No.

SESSION IV

MAGSAT Attitude Dynamics Control: Some Observations and Explanations
T. H. Stengle (GSFC) 22

The Response of the SEASAT and MAGSAT Infrared Horizon Scanners to Cold Clouds
S. Bilanow and M. Phenneger (CSC) 23

Spacecraft Momentum Management Procedures
L. C. Chen (General Software Corporation), P. B. Davenport (GSFC), and C. R. Sturch (CSC) 24

SESSION I

J. Teles, Chairman

FEASIBILITY STUDY OF USING A TWO-PLATE MODEL TO APPROXIMATE THE TDRSS SOLAR PRESSURE EFFECTS

F. K. Chan
Systems and Applied Sciences Corporation
6811 Kenilworth Avenue Suite 500
Riverdale, Maryland 20840

ABSTRACT

An investigation was performed to determine the feasibility of using a two plate model to approximate the Tracking and Data Relay Satellite (TDRS) in orbit propagation, taking into account the effects of solar radiation pressure. The two-plate model comprises one plate which always points to the earth, and the other which is hinged to an axis normal to the orbital pland and is always rotated so that its normal makes a minimum angle with the direction of the sun.

The results indicate that it is sufficient to take three parameters (i.e., the areas of the two plates and the reflectivity of the earth-pointing plate) to achieve an accuracy of one meter during a 24-hout orbit propagation.

This work was supported by NASA Contract No. NAS5-25139. The authors wish to acknowledge the programming assistance provided by Michael Toporek.

SECTION 1 - INTRODUCTION

Most of the work involving solar radiation pressure on orbiting satellites has so far been limited to those which are spherical and which have circular nominal orbits. The comparatively few studies which are less restrictive are still based on very simplified models. For example, the work of Eliasberg[1] deals with an elliptically orbiting spherical satellite and is concerned with the first order perturbation effects expressed in terms of Keplerian elements. The work of Fang[2] deals with a circularly orbiting spherical satellite with a perfectly reflecting earth-pointing disk. It is concerned with the first order effects expressed in terms of along-track, cross-track and radial components. Moreover, it also deals with the physical insights into the modeling errors connected with tracking and orbit determination of the Tracking and Data Relay Satellites (TDRS). On the other hand, the work of Georgevic[3] deals only with the computation of solar radiation force on a cylinder and on a parabolic reflector, but does not deal with an orbiting satellite. (Even then, the computation for the parabolic reflector is further simplified by assuming that the ratio of the force on the illuminated area of the reflector and the force on the whole area of the reflector is the same as the ratio of the corresponding projected areas. It is obvious that this assumption, introduced to eliminate the cumbersome self-shadowing effects, is not really correct.)

The present work is concerned with the solar radiation effects on the TDRS illustrated in Figure 1.1, and modeled as comprised of the 69 components listed in Table 1.1. (In the course of the present study, a novel method, simple in comparison to other existing methods, for computing self-shadowing was formulated but this consideration was not included in computing the net solar radiation force on the satellite). The orbit of the TDRS is taken to be representative of a realistic one in that it is not nominally perfectly circular. The study also considers the question of how accurately the 69-component TDRS can be

approximated by a two-plate model, i.e., one plate is hinged to an axis normal to the orbital plane and is always rotated to make a maximum angle with the sun, while the other plate is always earth-pointing. This two-plate model has the capability of handling up to four solve-for parameters, i.e., the area and reflectivity of each of the two plates.

Section 2 is concerned with the analysis of a differential correction procedure to obtain the values of these four solve-for parameters. A reference orbit for the 69-component TDRS is first generated. Its orbital position at regular intervals of one hour is then used as epoch elements of the two-plate model to obtain the values of the parameters which yield the best approximating orbit over the next 24 hours.

Section 3 summarizes the numerical results obtained in this feasibility study, and presents tabulated and graphical results for rapid comparisons.

Section 4 discusses the quality of the results, and the applicability of the two-plate model for use in orbit determination purposes.

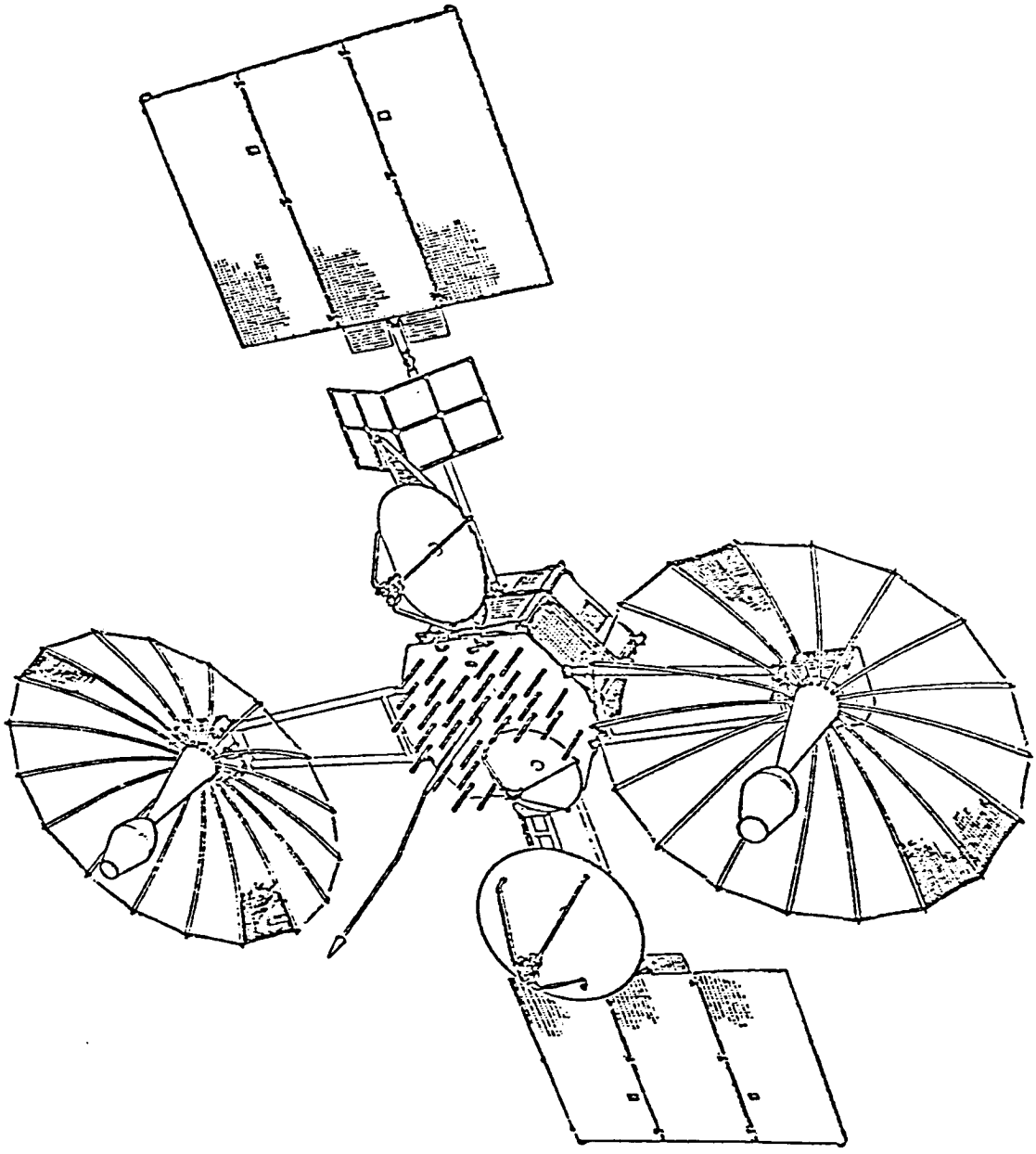

FIGURE 1.1 THE TDRS SATELLITE

TABLE 1.1

DETAILS OF 69-COMPONENT MODEL

Component #	Description	Area (m^2)	Reflectivity	Components of Normal X	Y	Z
1	Solar Panel 1	14.7553	0.0	Normal makes minimum angle with sun		
2	Solar Panel 2	14.7553	0.0	"	"	"
3	SGL Antenna	3.13761	0.5	Points to White Sands		
4	C-Band Antenna	2.67112	0.5	Points to Los Angeles		
5	Solar Sail	0.90593	1.0	0	0	1
6	Antenna Feed 1 (top)	0.00462	1.0	0	0	1
7	Antenna Feed 2 (top)	0.00462	1.0	0	0	1
8	Antenna Feed 1 (bottom)	0.29570	1.0	0	0	-1
9	Antenna Feed 2 (bottom)	0.29570	1.0	0	0	-1
10	Antenna Feed 1 (side)	1.11771	1.0			
11	Antenna Feed 2 (side)	1.11771	1.0			
12	Main Body (top)	4.03665	0.5	0	0	1
13	Main Body (bottom)	4.03665	0.5	0	0	-1
14	Main Body (side 1)	1.1599	0.5	0	1	0
15	Main Body (side 2)	1.1599	0.5	.866	.5	0
16	Main Body (side 3)	1.1599	0.5	.866	-.5	0
17	Main Body (side 4)	1.1599	0.5	0	-1	0
18	Main Body (side 5)	1.1599	0.5	-.866	-.5	0
19	Main Body (side 6)	1.1599	0.5	-.866	.5	0
20-69	Sections of stationary antennae	Computed by POLYN	1.0	Computed by POLYN		

SECTION 2 - ANALYSIS

This section is concerned with the analysis of a differential correction procedure to obtain the values of the four solve-for parameters incorporated into the two-plate model.

For convenience, let us introduce the following notation:

$\vec{f}(t)$ = position vector of 69-component TDRS at time t

$\vec{g}(t, \vec{\alpha})$ = position vector of two-plate model at time t

$\vec{\alpha} = (\alpha_1, \alpha_2, \alpha_3, \alpha_4)$ = 4 parameters for two-plate model

Q = loss function defined as $\sum_{i=1}^{25} \left| \vec{f}(t_i) - \vec{g}(t_i, \vec{\alpha}) \right|^2$

The problem is then to obtain the values of $\vec{\alpha}$ such that Q is a minimum. It is obvious that the minimum of Q is given by the necessary condition $\partial Q / \partial \alpha_j = 0$ where j = 1, 2, 3, 4.

The loss function Q may also be written as

$$Q = \sum_{i=1}^{25} \left[\vec{f}(t_i) - \vec{g}(t_i, \vec{\alpha}) \right] \cdot \left[\vec{f}(t_i) - \vec{g}(t_i, \vec{\alpha}) \right] \tag{2-1}$$

The necessary condition for minimum is

$$\frac{\partial Q}{\partial \alpha_j} = -2 \sum_{i=1}^{25} \left\{ \left[\vec{f}(t_i) - \vec{g}(t_i, \vec{\alpha}) \right] \cdot \frac{\partial \vec{g}(t_i, \vec{\alpha})}{\partial \alpha_j} \right\} = 0 \qquad j = 1,2,3,4 \tag{2-2}$$

The function $\vec{g}(t_i,\vec{\alpha})$ may be expanded in a Taylor series about an a priori value $\vec{\alpha}_o$.

$$\vec{g}(t_i,\vec{\alpha}) = \vec{g}(t_i,\vec{\alpha}_o) + \sum_{k=1}^{4} \left.\frac{\partial \vec{g}(t_i,\vec{\alpha})}{\partial \alpha_k}\right|_{\vec{\alpha}=\vec{\alpha}_o} \Delta\alpha_k + \cdots \tag{2.3}$$

where $\Delta\alpha_k$ is defined as

$$\Delta\alpha_k = \alpha_k - \alpha_{o,k} \qquad k=1,2,3,4 \tag{2.4}$$

Let $$\Delta\vec{f}(t_i,\vec{\alpha}_o) \equiv \vec{f}(t_i) - \vec{g}(t_i,\vec{\alpha}_o) \tag{2.5}$$

Substitution of equations (2.3) and (2.5) into (2.2) yields to first order

$$\sum_{i=1}^{25} \left\{ \left[\Delta\vec{f}(t_i) - \left(\sum_{k=1}^{4} \left.\frac{\partial \vec{g}(t_i,\vec{\alpha})}{\partial \alpha_k}\right|_{\vec{\alpha}=\vec{\alpha}_o} \Delta\alpha_k \right) \right] \cdot \left.\frac{\partial \vec{g}(t_i,\vec{\alpha})}{\partial \alpha_j}\right|_{\vec{\alpha}=\vec{\alpha}_o} \right\} = 0$$

$$j=1,2,3,4 \tag{2.6}$$

Interchanging the order of summation yields

$$\sum_{k=1}^{4} \left\{ \sum_{i=1}^{25} \left[\left.\frac{\partial \vec{g}(t_i,\vec{\alpha})}{\partial \alpha_j}\right|_{\vec{\alpha}=\vec{\alpha}_o} \cdot \left.\frac{\partial \vec{g}(t_i,\vec{\alpha})}{\partial \alpha_k}\right|_{\vec{\alpha}=\vec{\alpha}_o} \right] \right\} \Delta\alpha_k$$

$$= \sum_{i=1}^{25} \left[\left.\frac{\partial \vec{g}(t_i,\vec{\alpha})}{\partial \alpha_j}\right|_{\vec{\alpha}=\vec{\alpha}_o} \cdot \Delta\vec{f}(t_i,\vec{\alpha}_o) \right] \tag{2.7}$$

$$j=1,2,3,4$$

Let $$a_{jk} \equiv \sum_{i=1}^{25} \left[\left.\frac{\partial \vec{g}(t_i,\vec{\alpha})}{\partial \alpha_j}\right|_{\vec{\alpha}=\vec{\alpha}_o} \cdot \left.\frac{\partial \vec{g}(t_i,\vec{\alpha})}{\partial \alpha_k}\right|_{\vec{\alpha}=\vec{\alpha}_o} \right] \qquad j,k=1,2,3,4 \tag{2.8}$$

$$b_j \equiv \sum_{i=1}^{25} \left[\left.\frac{\partial \vec{g}(t_i,\vec{\alpha})}{\partial \alpha_j}\right|_{\vec{\alpha}=\vec{\alpha}_o} \cdot \Delta\vec{f}(t_i,\vec{\alpha}_o) \right] \tag{2.9}$$

Equation (2.7) then becomes

$$\sum_{k=1}^{4} a_{jk} \Delta\alpha_k = b_j \qquad j=1,2,3,4 \qquad (2.10)$$

It remains to solve for $\Delta\alpha_k$ where k=1,2,3,4. This constitutes the first iteration in the differential correction procedure to solve for the value of $\vec{\alpha}$ such that Q is a minimum.

SECTION 3 - RESULTS

This section summarizes the numerical results in this feasibility study, and presents tabulated and graphical results for rapid comparisons.

Numerous computer runs were made for the TDRS with epoch elements:

$$X_o = 31{,}662{,}513.0 \text{ m}$$
$$Y_o = -27{,}523{,}890.0 \text{ m}$$
$$Z_o = 0.0 \text{ m}$$

$$\dot{X}_o = 2{,}012.15997 \text{ m/sec}$$
$$\dot{Y}_o = 2{,}314.7253 \text{ m/sec}$$
$$\dot{Z}_o = 376.58528 \text{ m/sec}$$

One set of runs had epoch time set at Day 183.0, Year 1980 (i.e., July 1, 1980 which is close to the summer solstice), and another set had epoch time set at Day 275.0, Year 1980 (i.e., October 1, 1980 which is close to the autumnal equinox). Each of these sets of runs was made for the cases of N=1,2,3 and 4 parameters. The parameters were aligned in the following sequence which is probably the order of decreasing importance:

α_1 = area of sun-pointing plate (M^2)
α_2 = area of earth-pointing plate (M^2)
α_3 = reflectivity of earth-point plate
α_4 = reflectivity of sun-pointing plate

The initial values of these parameters used in the first iteration of the differential correction procedure were taken to be the following:

N	=	1	2	3	4
$\alpha_{0,1}$	=	36.6	29.5	29.5	29.5
$\alpha_{0,2}$	=	0.0	18.81	18.81	18.81
$\alpha_{0,3}$	=	0.0	0.0	0.74	0.74
$\alpha_{0,4}$	=	0.0	0.0	0.0	0.0

The tolerance ε for testing convergence of the iterations

(i.e., $|\Delta\vec{\alpha}|<\epsilon$) was taken to be 0.01. The values for the stepsize $\vec{\delta}$ for computing the partial derivatives was taken to be 0.1. In the runs described above, convergence was achieved after two or three iterations. Figures 3.1 and 3.2 summarize the results of these computer runs. The symbols appearing on the horizontal axis in these figures have the following connotations:

O = The sun is overhead with respect to the satellite

U = The sun is underfoot with respect to the satellite

A = The satellite is moving away from the sun

T = The satellite is moving toward the sun

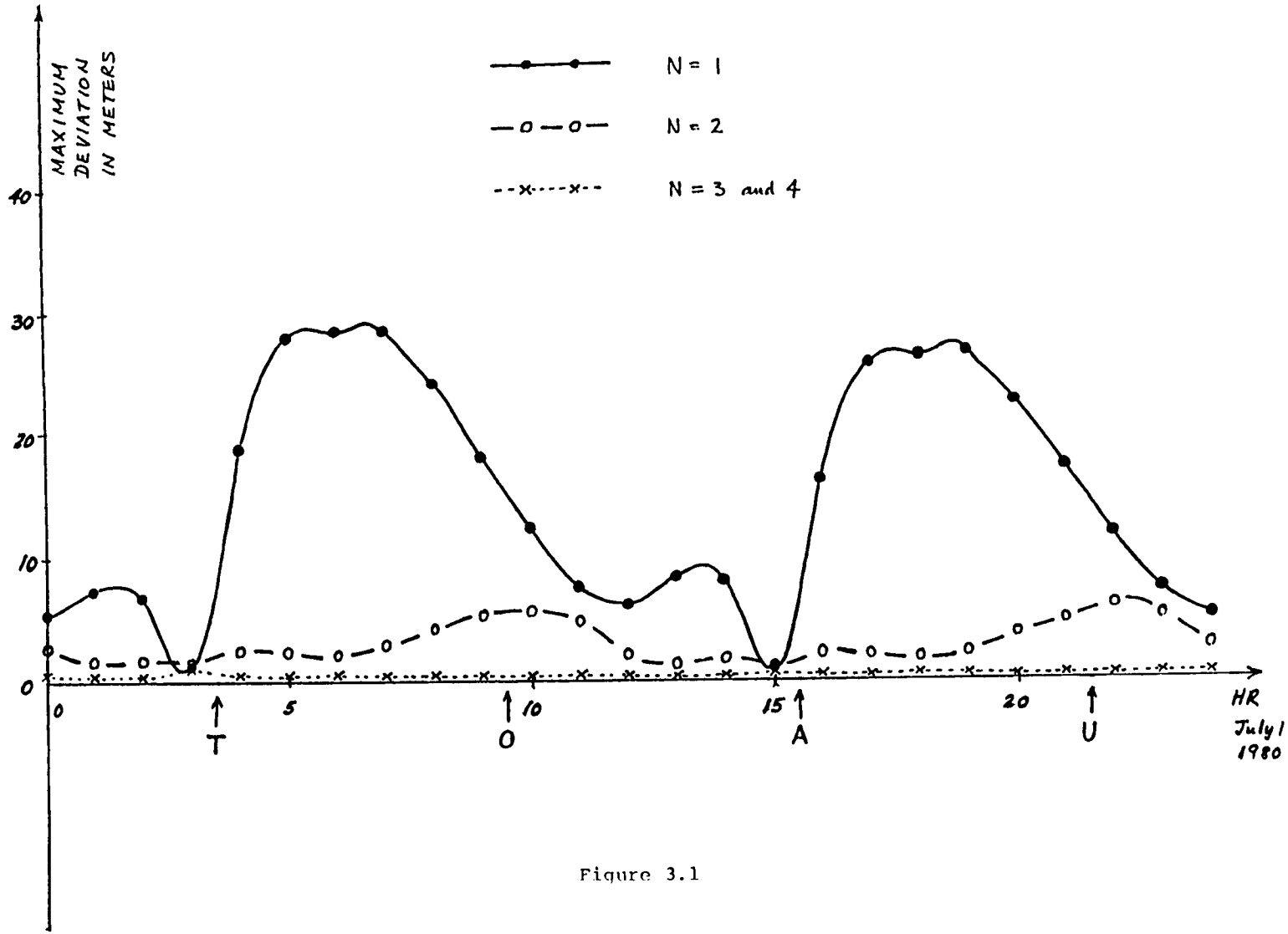
MAXIMUM DEVIATION IN METERS
N = 1
N = 2
N = 3 and 4
40
30
20
10
0
0
5
10
15
20
HR
July 1
1980
T
O
A
U

Figure 3.1

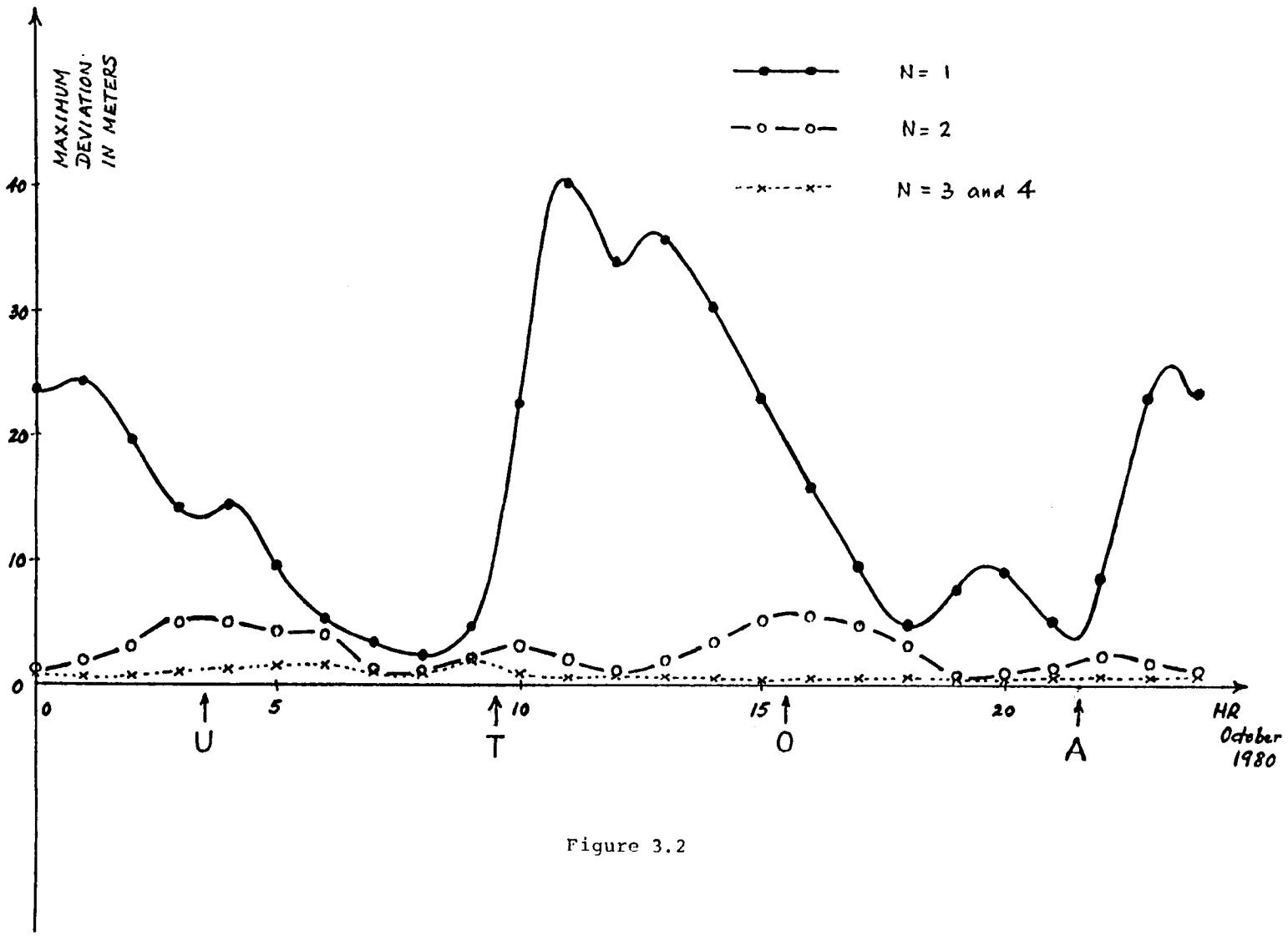
MAXIMUM DEVIATION IN METERS
40
30
20
10
0
N = 1
N = 2
N = 3 and 4
0
5
10
15
20
HR
October 1980
U
T
O
A

Figure 3.2

SECTION 4 - CONCLUSION

This section is concerned with a brief discussion of the results obtained in Section 3, and also an attempt to relate them to results obtained in other investigations.

From Figures 3.1 and 3.2, it is seen that the following observations may be made:

1. The maximum deviation of the two-plate model from the 69-component TDRS is essentially cyclical with a 12-hour period.
2. The magnitude of these deviations decreases as the number N of parameters increases, as would be expected.
3. There is a pronounced phase change of this period curve in going from the case of N=1 to N=2.
4. The curves for the cases of N=3 and N=4 are essentially identical. Moreover, the amplitude of oscillation is so small that they are almost constant.

A computer run was also made comparing the 69-component TDRS with and without solar radiation pressure effects. The results are plotted in Figure 4.1.

It is noted that in this case the curve is essentially sinusoidal, unlike those in Figure 3.1 and 3.2. Moreover, the maximum deviation occurs when the sun is overhead or underfoot in Figure 4.1, unlike the cases of N=1 and N=2 in Figures 3.1 and 3.2.

Finally, it is interesting to recall the results obtained by Fang[2] who observed that:

1. In orbit propagation, the least perturbation occurs when the sun vector is parallel to the satellite velocity vector in the beginning, and the worst perturbation occurs when the sun is overhead or underfoot in the beginning.
2. TDRS orbits determined from a one-day tracking arc tend to be less sensitive to solar pressure errors if the tracking arc begins when the sun is directly overhead or underfoot. This is contrary to the (previous) result for solar pressure perturbations in the absence of tracking.

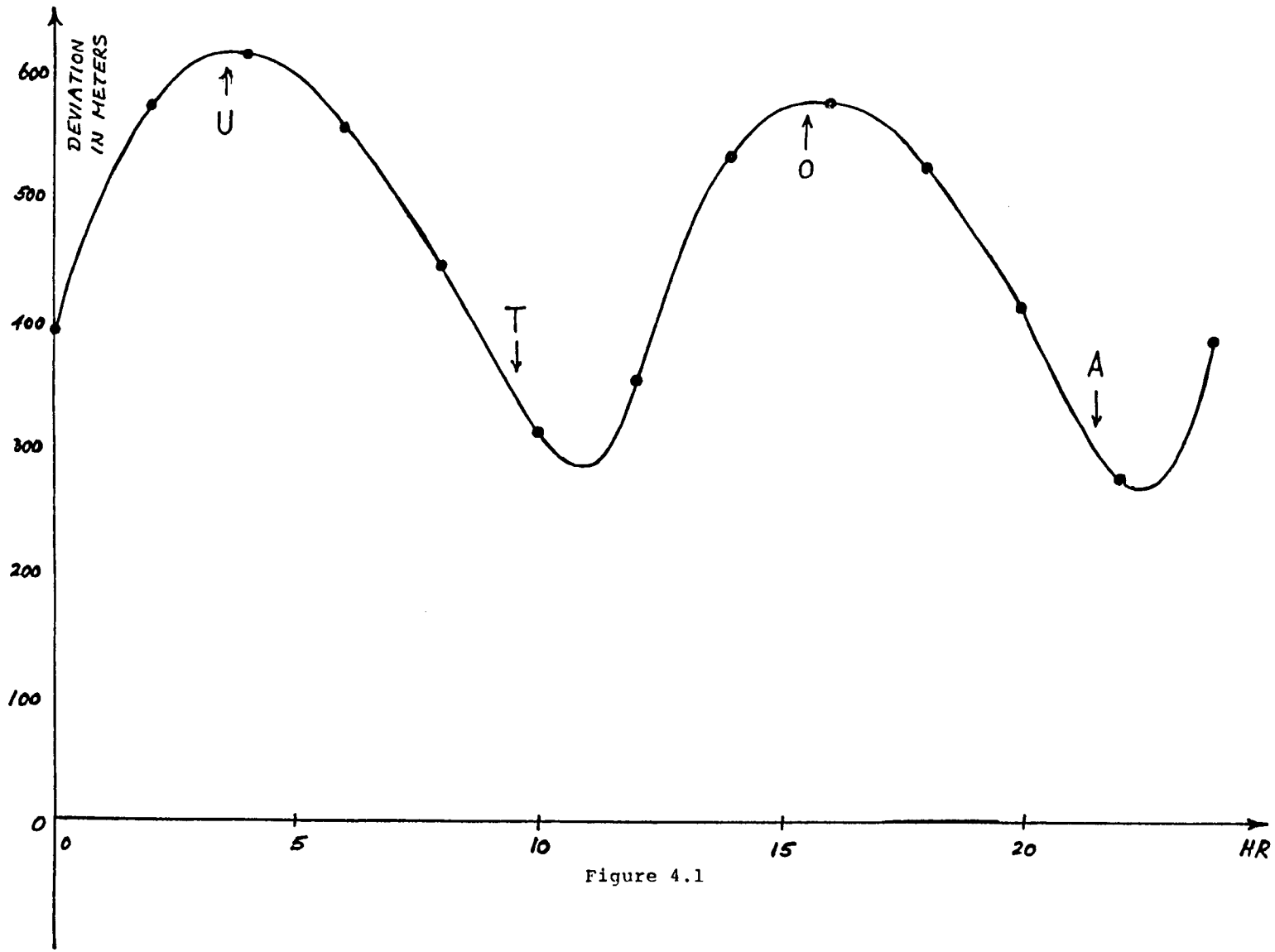
DEVIATION IN METERS
600
500
400
300
200
100
0
0
5
10
15
20
HR
U
T
O
A

Figure 4.1

From the numerical results of this feasibility study, it is seen that the 69-component TDRS can be accurately replaced by the two-plate model. It suffices to take only three parameters to achieve an accuracy to within about one meter. Moreover, it is sufficient to use only one approximating orbit throughout the 24 hour period, instead of 24 approximating orbits regularly spaced throughout the day.

REFERENCES

(1) Eliasberg, P.E., "Introduction to the Theory of Flight of Artificial Earth Satellites," Moscow (1965). Translation, Jerusalem (1967).

(2) Fang, B.T., "Short-Term Solar Pressure Effect and GM Uncertainty on TDRS Orbital Accuracy--A Study of the Interaction of Modeling Error with Tracking and Orbit Determination," EG&G/Washington Analytical Services Center, Inc., Report No. 002-78 (1978).

(3) Georgevic, R.M., "The Solar Pressure Force and Torque Model," J. Astron. Sc., Vol. XX, No. 5, pp. 257-274. (1973).

Improved Chebyshev Series Ephemeris Generation Capability of GTDS

S. Y. Liu*, J. Rogers*†

Computer Sciences Corporation

and

J. J. Jacintho

Goddard Space Flight Center

ABSTRACT

This paper describes an improved implementation of the Chebyshev ephemeris generation capability in the operational version of the Goddard Trajectory Determination System (GTDS). Preliminary results of an evaluation of this orbit propagation method for three satellites of widely different orbit eccentricities are also discussed in terms of accuracy and computing efficiency with respect to the Cowell integration method. An empirical formula is also deduced for determining an optimal fitting span which would give reasonable accuracy in the ephemeris with a reasonable consumption of computing resources.

*Work was supported by the Mission Software Section, Code 571.2, Goddard Space Flight Center, NASA, under Contract No. NAS 5-24300.

†Now at University of Arizona

TABLE OF CONTENTS

Section 1 - Introduction. 2-4

Section 2 - The Use of Chebyshev Polynomials to Generate Ephemerides. 2-6

2.1 Advantages of Using Chebyshev Polynomials as Interpolating Polynomials. 2-6
2.2 Computation Scheme in GTDS 2-7

Section 3 - Applications of the Improved Implementation of the Chebyshev Ephemeris Generation Method. 2-10

3.1 Near Circular Orbit. 2-10
3.2 Elliptical Orbit 2-23
3.3 Highly Eccentric Orbit 2-23
3.4 An Empirical Formula to Determine the Optimal Fitting Span. 2-25

Section 4 - Conclusions 2-31

Appendix A - Mathematical Theory of the Chebyshev Orbit Generation Method. 2-33

Appendix B - Comparison Between the Improved Implementation and the Previous Implementation of the Chebyshev Methods 2-43

References. 2-46

LIST OF ILLUSTRATIONS

Figure

3-1 GEOS-3 Ephemeris Accuracy for the Chebyshev Polynomial Fit Compared With the Cowell Method 2-12

3-2 Calibration Curve of CPU Time Consumed by Computer Runs Used for This Study. 2-14

3-3 CPU Time Versus Degree of Chebyshev Polynomials for Various Fitting Spans for GEOS-3 2-16

3-4 CPU Time Versus Fitting Span for Various Degrees of Chebyshev Polynomials for GEOS-3. . 2-17

3-5 Changes in Relative Accuracy and Efficiency for a Fitting Span of P/4 for the GEOS-3 Orbit. 2-18

3-6 Changes in Relative Accuracy and Efficiency for a Fitting Span of P/2 for the GEOS-3 Orbit. 2-19

3-7 Changes in Relative Accuracy and Efficiency for a Fitting Span of P for the GEOS-3 Orbit. 2-20

3-8 Changes in Relative Accuracy and Efficiency for a Fitting Span of 2P for the GEOS-3 Orbit. 2-21

3-9 IMP-7 Ephemeris Accuracy for the Chebyshev Polynomial Fit Compared With the Cowell Method 2-24

3-10 ISEE-1 Ephemeris Accuracy for the Chebyshev Polynomial Fit Compared With the Cowell Method 2-26

A-1 Chebyshev Polynomials of Degrees 0 to 3. . . . 2-37

LIST OF TABLES

Table

3-1 Ephemeris Accuracies for Fitting Spans Determined Using the Empirical Formula. . . 2-28

A-1 The Chebyshev Polynomials 2-35

A-2 An Algebraic Function Expressed in Terms of a Linear Combination of the Chebyshev Polynomial. 2-36

B-1 Comparison Between New and Previous Chebyshev Implementations With Respect to the Cowell Method. 2-44

SECTION 1 - INTRODUCTION

This document presents an improved implementation of the Chebyshev ephemeris generation capability in the Goddard Trajectory Determination System (GTDS). The reimplementation was necessary to resolve a System Failure Report on the operational version of GTDS and to improve the clarity of the computer program code to make it more readable and maintainable. The improved implementation employs the same Chebyshev polynomial/Picard iteration scheme as previously implemented (described in References 1 and 2) but exhibits a marked improvement in accuracy and efficiency (see Appendix B). The improved implementation fits the Chebyshev polynomial to satellite ephemeris data displaced as a function of time in accordance with the roots of the Chebyshev polynomial. This displacement is dependent on the degree of the polynomial.

The advantages of using Chebyshev polynomials as interpolating polynomials and the computational scheme in GTDS are briefly described in Section 2. Section 3 discusses general application of the improved implementation of the Chebyshev method to orbits over a wide range of eccentricity. The results are analyzed in deducing an empirical formula for determining an optimal fitting span that would consume a reasonable amount of computer resources and still provide a reasonably accurate ephemeris. A brief summary of conclusions is presented in Section 4.

Appendix A briefly discusses the properties of Chebyshev polynomials, the formulation of an interpolating polynomial consisting of a linear combination of Chebyshev polynomials of different degrees to represent acceleration, and the integration of the interpolating

polynomial to generate satellite ephemerides. Appendix B contains the results of a comparison of the new and previous implementations of the Chebyshev ephemeris generation method in GTDS.

SECTION 2 - THE USE OF CHEBYSHEV POLYNOMIALS TO GENERATE EPHEMERIDES

2.1 ADVANTAGES OF USING CHEBYSHEV POLYNOMIALS AS INTERPOLATING POLYNOMIALS

In principle, any function characterized by a discrete set of values can be approximated by a polynomial or a linear combination of polynomials. Such polynomials may be expressed as Chebyshev polynomials, Legendre polynomials, Laguerre polynomials, or any other polynomial form which is expedient for mathematical/computational analysis. For instance, in the case of a satellite trajectory, the positions at a series of selected times determine a polynomial consisting of a Chebyshev series within the time interval. The significant advantages of using Chebyshev polynomials to fit a satellite trajectory are that the error in the approximation is distributed evenly over the interval and that the maximum error is reduced to the minimum or near-minimum value (References 3 and 4).

Once this interpolating polynomial is established, the position of any other time within the interval can be easily interpolated. If a long ephemeris is to be stored for any reason, it is plausible to use a small amount of computer storage to store only coefficients for the interpolating polynomial instead of using a large amount of space to store the entire ephemeris. One familiar example is the Solar/Lunar/Planetary Ephemeris File (SLP File), which is stored as coefficients of Chebyshev polynomials for GTDS and other trajectory determination systems to interpolate noncentral body positions for evaluating perturbations on a satellite. Another possible application would be to store the coefficients of Chebyshev polynomials to represent the ephemeris of a Tracking and

Data Relay Satellite (TDRS) in the onboard computer of a user satellite for autonomous orbit determination.

2.2 COMPUTATION SCHEME IN GTDS

In order to apply the mathematical theory described in Appendix A, one must know the acceleration, $\ddot{x}(\xi)$, as a function of time to fit a Chebyshev interpolating polynomial. However, this is not the case for near-Earth spacecraft because of the nonlinearity of the perturbing forces, namely $\ddot{x}$ depends on x which is in turn determined from $\ddot{x}$. Therefore, the Picard iteration method is used in GTDS to incorporate the Chebyshev series ephemeris generation method. The computational procedure is described in the following paragraphs. For discussions related to the mathematical aspects of the method, see Reference 1.

Suppose an ephemeris is requested from t_a to t_z with a fitting span (or equivalent step size) of H which is equal to $(t_b - t_a)$. The entire ephemeris will consist of a series of spans which are represented by different Chebyshev interpolating polynomials. The default fitting span in GTDS is 5400 seconds. The allowable range of the degree of the Chebyshev interpolating polynomial is from 4 to 48 with a default of 36.

Within a fitting span, the roots (ξ_k of the Chebyshev polynomial of the highest degree plus 1, (n + 1)) in the interpolating polynomial are first computed according to Equation (A-7). These roots are then transformed back into time, i.e., $\xi_k \rightarrow t_k$, k = 1, 2, ..., n + 1.

GTDS uses boundary conditions at the beginning of the fitting span, i.e., the position and velocity at t_a, to obtain positions and velocities at t_1, t_2, ..., t_k, ..., t_{n+1} with a two-body central force field to start the iteration scheme. With the positions and velocities

at t_k available, the perturbations, $\ddot{x}(\xi_k)$ can now be estimated at these instants and the Chebyshev coefficients, C_i, are subsequently computed using Equation (A-11). At this point, the Chebyshev interpolating polynomial for the acceleration, Equation (A-8), is established.

The next step is to successively integrate the Chebyshev interpolating polynomial twice according to Equations (A-14) and (A-17) to obtain interpolating polynomials, Q_{n+1} and R_{n+2}, for velocity and position, respectively, in the fitting span (t_a, t_b). The position and velocity with perturbations included at the end of the fitting span, t_b, or any other time can be easily interpolated. The first loop of the iterative scheme is essentially completed at this point.

In the next loop, GTDS uses positions and velocities interpolated from the interpolating polynomials, Q_{n+1} and R_{n+2}, at the roots to estimate acceleration. After fitting the polynomial to the accelerations, it is again integrated twice to obtain polynomials for velocity and position. The position interpolated at the end of the fitting span in this loop is compared with that obtained in the previous loop.

This iterative scheme is repeated until the differences of the position components of the two successive loops at t_b are less than a tolerance (default value = 10^{-6} kilometers). At this moment, the fitting procedure for the span (t_a, t_b) is completed.

After ephemerides are generated and the Chebyshev coefficients for velocity and position are optionally saved, the

fitting span is advanced one step forward to $(t_b, t_b + H)$. This scheme is continued until all the spans are fitted.

SECTION 3 - APPLICATIONS OF THE IMPROVED IMPLEMENTATION OF THE CHEBYSHEV EPHEMERIS GENERATION METHOD

The improved implementation of the Chebyshev ephemeris generation method is applied to satellites of different orbital eccentricities to study the behavior of the Chebyshev polynomial representation in order to find an optimal set of parameters, such as fitting span and degree of the Chebyshev polynomial, for different satellites. A series of computer runs on GTDS with the new Chebyshev implementation was obtained. The ephemerides from the Chebyshev ephemeris generation method are compared with those from the Cowell integration method in terms of accuracy and efficiency. The results are discussed separately for a near-circular orbit, an elliptical orbit, and a highly eccentric orbit in the following sections. An attempt to find an empirical formula for determining the optimal fitting span for these orbits is also discussed.

3.1 NEAR CIRCULAR ORBIT (ECCENTRICITY = 10^{-3})

The GEOS-3 satellite was chosen for this case study. The eccentricity of the GEOS-3 orbit is 0.00098 and the semi-major axis is 7225 kilometers. The fitting spans used in this case range from P/4 to 2P, where P is the period of the satellite. For each fitting span, several runs with different degrees of Chebyshev polynomials were made. The ephemeris of every run was compared by using the GTDS Ephemeris Comparison Program with the reference ephemeris generated by the Cowell integration method with a 24-second step size using perturbations identical to those used in the Chebyshev method. The maximum differences in position vector, $\left|\Delta\vec{R}\right|_{max}$, between the two

ephemerides are plotted in Figure 3-1 as a function of the degree of Chebyshev polynomials and the fitting span.

The maximum difference decreases very rapidly as the degree of Chebyshev polynomials increases. However, after reaching a critical degree of the Chebyshev polynomials, the maximum difference bottoms out and does not decrease any further.

The saturation of the maximum difference occurs at a lower degree of the Chebyshev polynomials for a shorter fitting span. This saturation level generally increases with the fitting span.

Since the step size of ·24 seconds used in the Cowell integration method in generating the reference ephemeris is relatively very small, the maximum difference in position vectors between the Chebyshev and Cowell ephemerides can be loosely regarded as the accuracy of the fit of the Chebyshev polynomials. Therefore, Figure 3-1 demonstrates one significant phenomenon: once the saturation level is reached, for a particular fitting span, adding higher degrees of the Chebyshev polynomials not only does not improve its accuracy, but decreases its efficiency. This is further evaluated by examining the computer resources, mainly CPU time, consumed by each of the computer runs.

All the runs for GEOS-3 satellite were executed on the GSFC IBM S/360-75 C1 computer. However, some of the runs were executed in the "low-speed" core of the CPU, which is

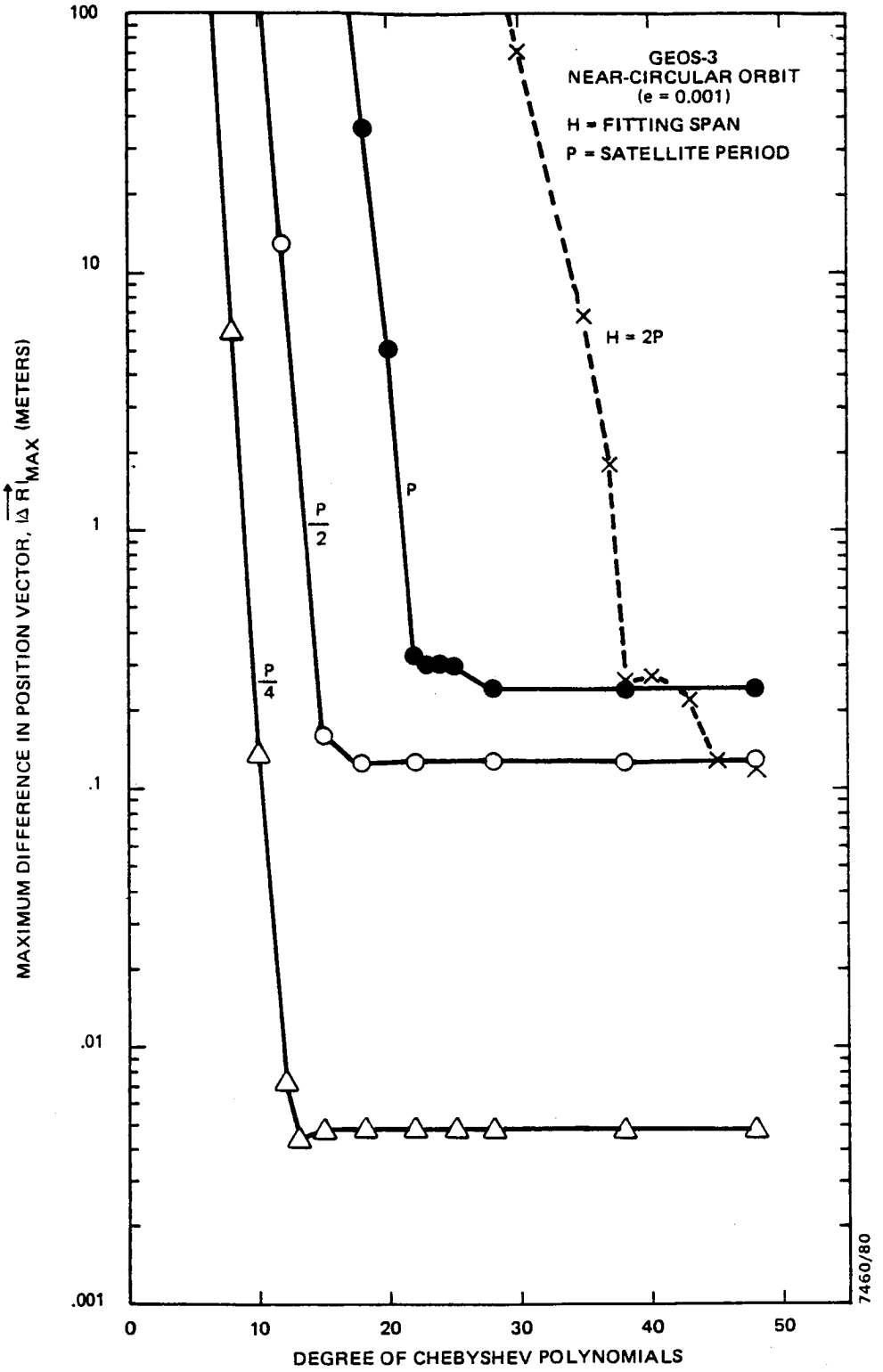

Figure 3-1. GEOS-3 Ephemeris Accuracy for the Chebyshev Polynomial Fit Compared With the Cowell Method

roughly three times slower than "high-speed" core. Also, there are a number of runs executed partly in low-speed core and partly in high-speed core. The CPU time consumed depends on the proportion of high-speed core and low-speed core used. This nonuniform CPU scale makes the comparison not so straightforward. Instead of reexecuting these runs in high-speed core, the CPU time of these runs are calibrated through force model calls, as described below.

In GTDS, the "Number of Times Forces Called For Full Model" in the statistics report is provided at the end of a run. For a numerical integration method, such as the Cowell method or the Chebyshev method, the full perturbing force, including harmonic geopotential field, noncentral body gravitational field, and nonconservative forces, is evaluated at each integration grid point according to the options specified. The number of times the full perturbing force is evaluated is proportional to the CPU time used in a run. In Figure 3-2 this number is plotted against CPU time for only those runs executed in high-speed core. Although the points plotted are somewhat scattered, there is a linear relationship between this number and the CPU time.

For comparison, the number of times the full force is evaluated (7236 times) and the CPU time (0.85 minute) are also plotted in Figure 3-2 for the reference run of Cowell method with a 24-second step size. It is interesting to note that the Chebyshev method with any reasonable accuracy is much slower than the Cowell method. Consequently, for ordinary purposes other than those that require Chebyshev coefficients, it is at least not recommended to use the Chebyshev method to generate ephemerides for a spacecraft of circular orbit at a lower altitude.

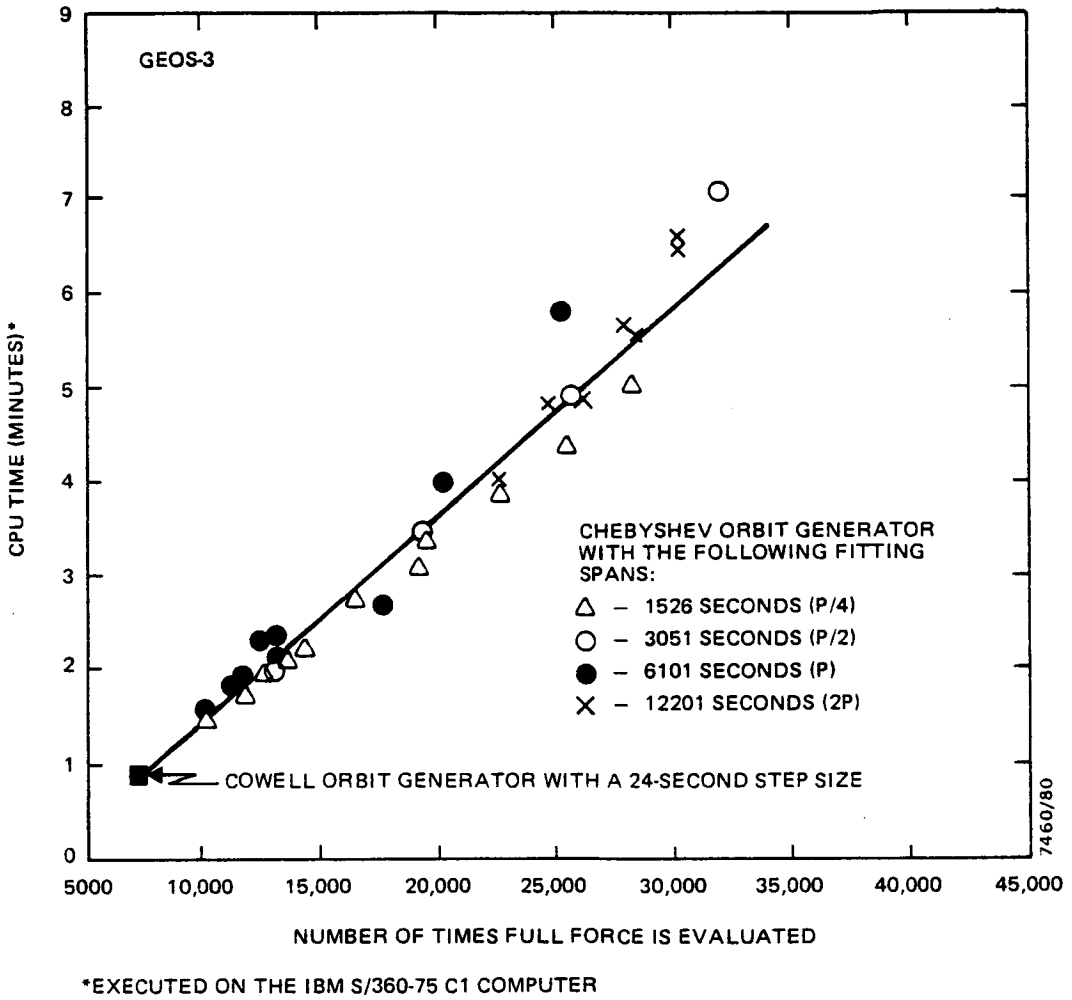

Figure 3-2. Calibration Curve of CPU Time Consumed by Computer Runs Used for This Study

After the CPU time of the runs which were executed partly in high-speed core are calibrated by using this linear relationship,[1] the CPU time of all the runs of Chebyshev method is plotted against the degree of the Chebyshev polynomials in Figure 3-3 for different fitting spans. The CPU time consumed is approximately linearly proportional to the degree of the Chebyshev polynomials. The CPU time is also plotted in Figure 3-4 against the fitting spans for degrees 18, 28, 38, and 48.

The curves in both Figures 3-3 and 3-4 give the impression that the fitting span of one satellite period would be the most desirable one to use for the Chebyshev method as far as CPU time is concerned. However, the accuracy of the fit may not be desirable for the situation. For this reason, the accuracy information is also included in Figures 3-3 and 3-4 by different shadings of the plot symbols to avoid the possibility of drawing misleading conclusions.

Since the accuracy of the Chebyshev method bottoms out at a critical degree of the polynomial (Figure 3-1) and the CPU time used increases linearly with the degrees of the polynomials, a trade-off can be performed to study the benefit or penalty of using a higher degree than is necessary.

The results of the trade-off study are presented in Figures 3-5, 3-6, 3-7, and 3-8 for fitting spans P/4, P/2, P, and 2P, respectively, by combining the results in Figures 3-1 and 3-3. The CPU time or the accuracy is normalized with respect to that of a data point

[1] This calibration curve is not necessarily valid for other experimental conditions or other satellites.

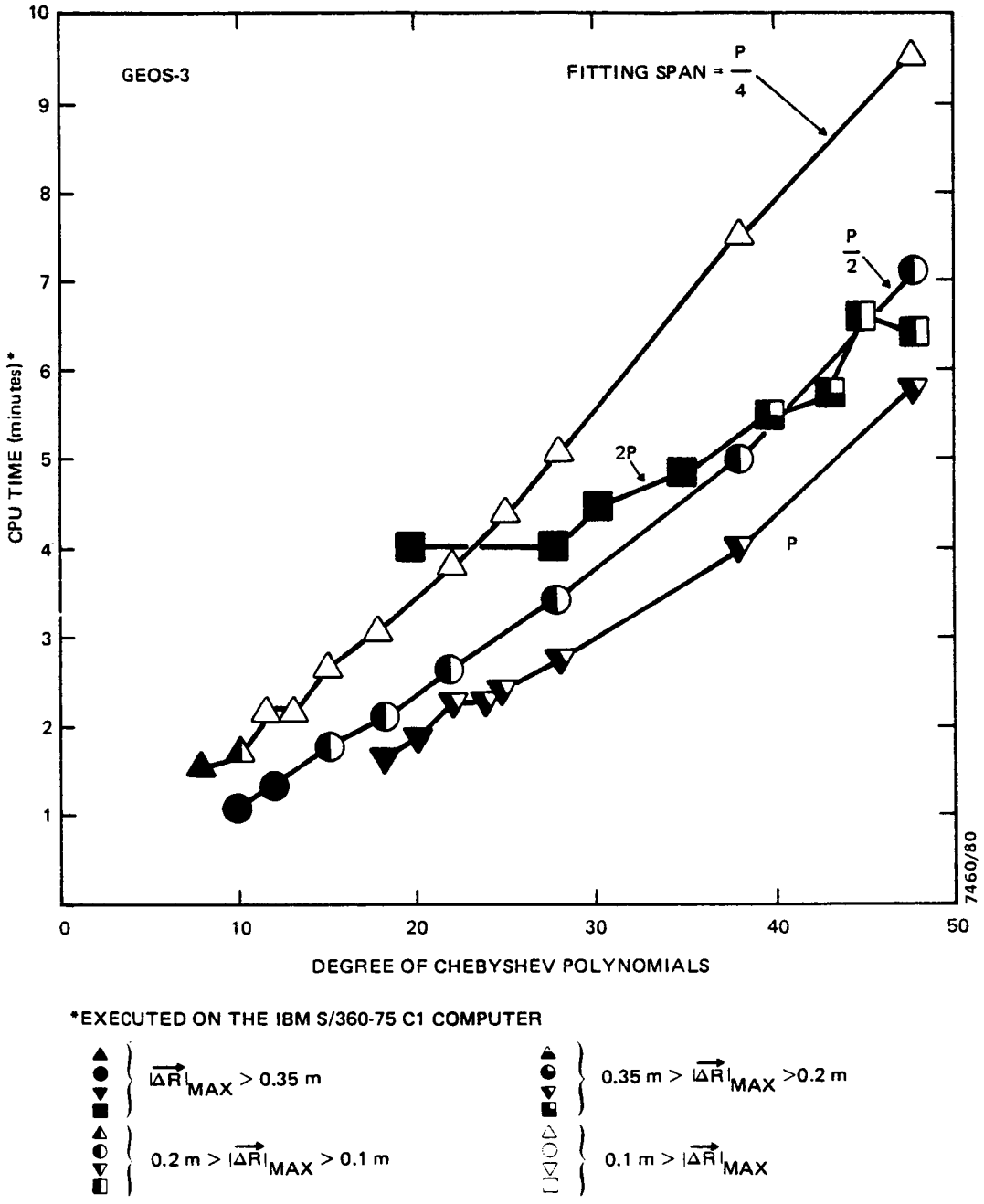

Figure 3-3. CPU Time Versus Degree of Chebyshev Polynomials for Various Fitting Spans for GEOS-3

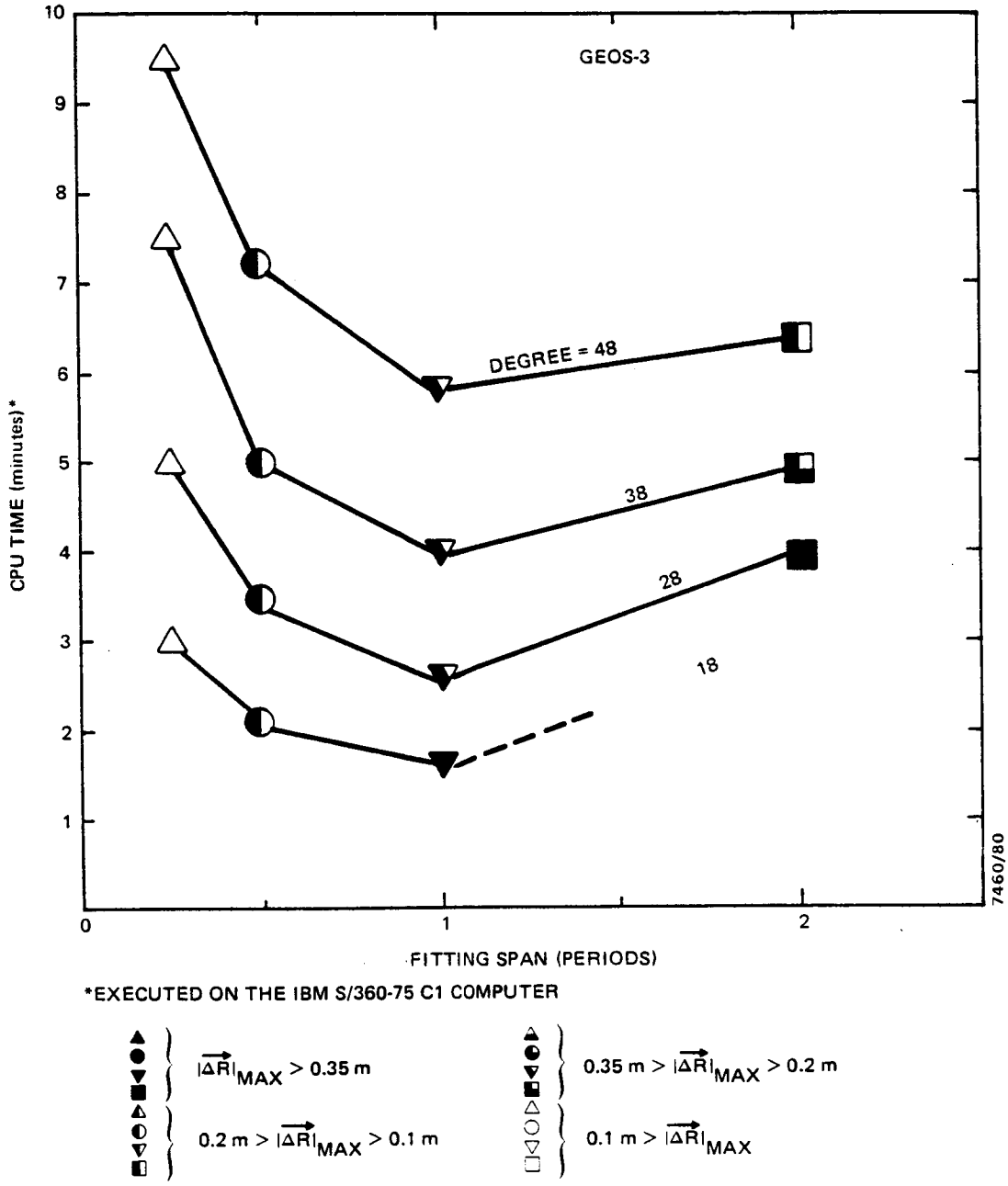

Figure 3-4. CPU Time Versus Fitting Span for Various Degrees of Chebyshev Ploynomials for GEOS-3

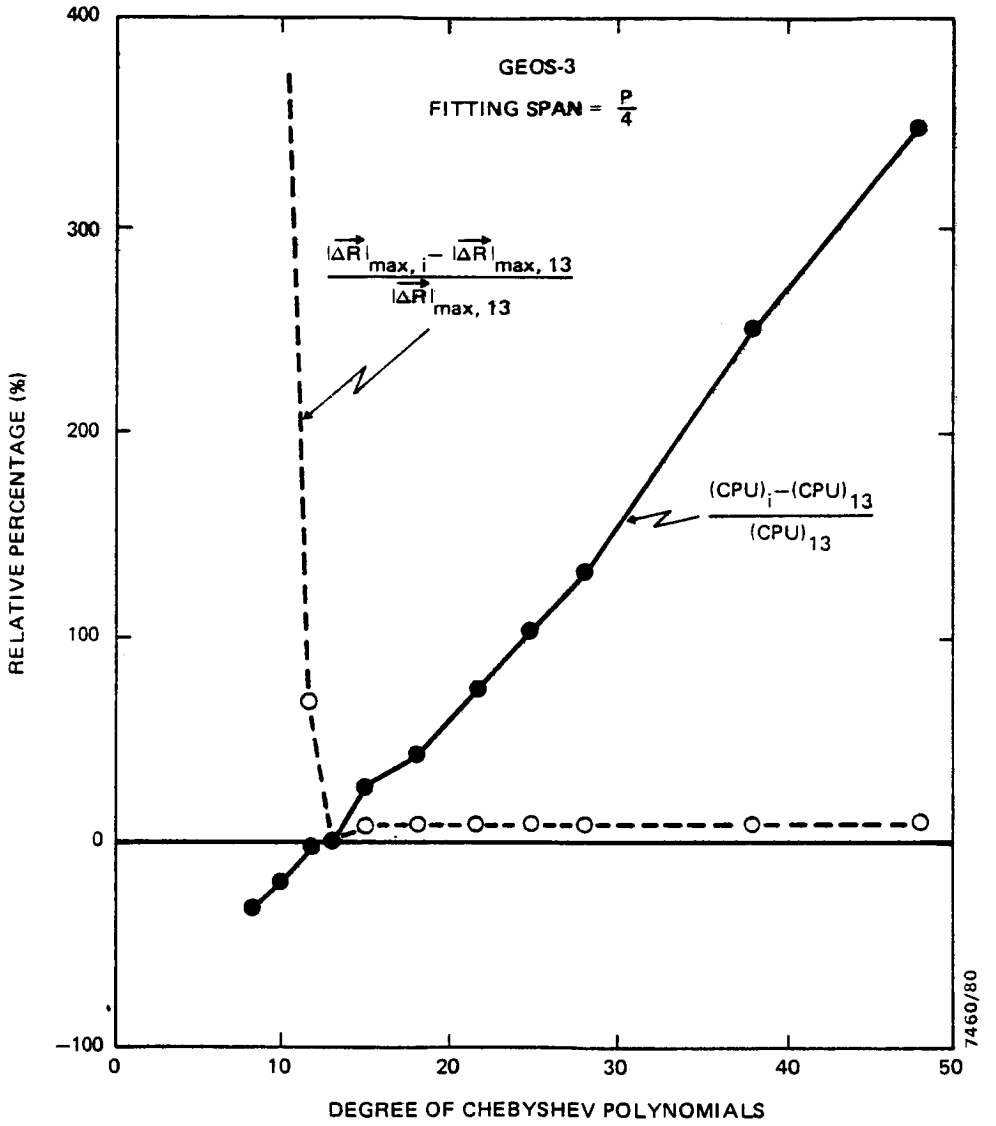

Figure 3-5. Changes in Relative Accuracy and Efficiency for a Fitting Span of P/4 for the GEOS-3 Orbit

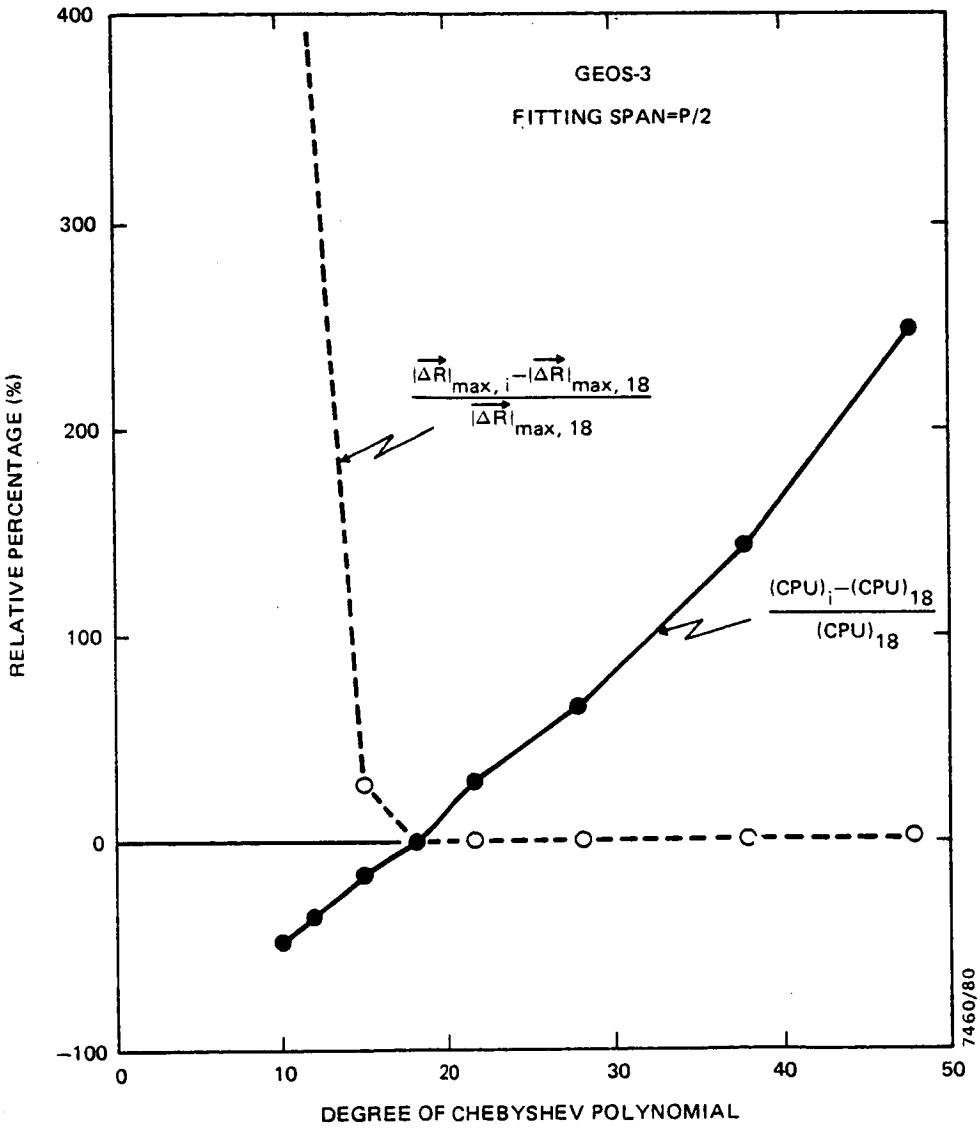

Figure 3-6. Changes in Relative Accuracy and Efficiency for a Fitting Span of P/2 for the GEOS-3 Orbit

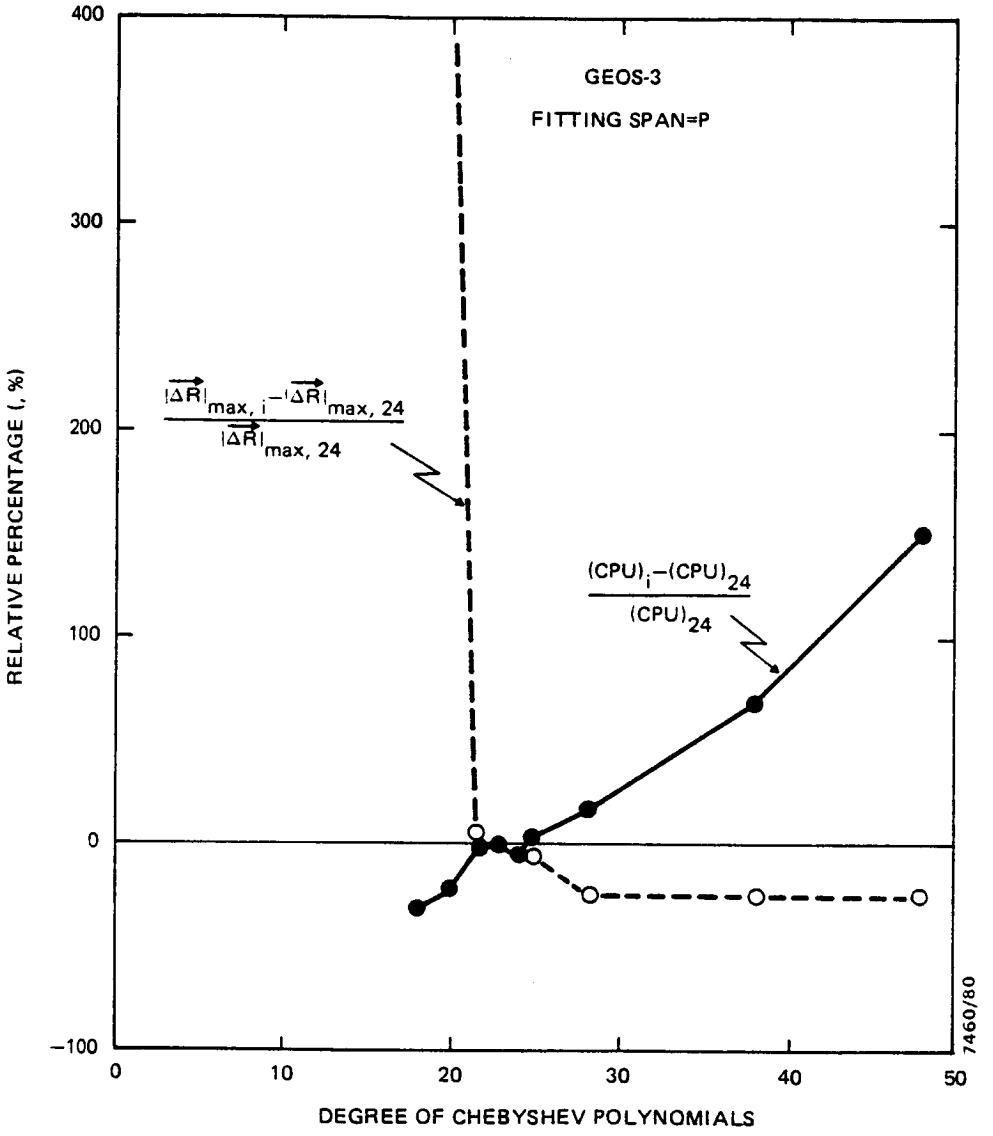

Figure 3-7. Changes in Relative Accuracy and Efficiency for a Fitting Span of P for the GEOS-3 Orbit

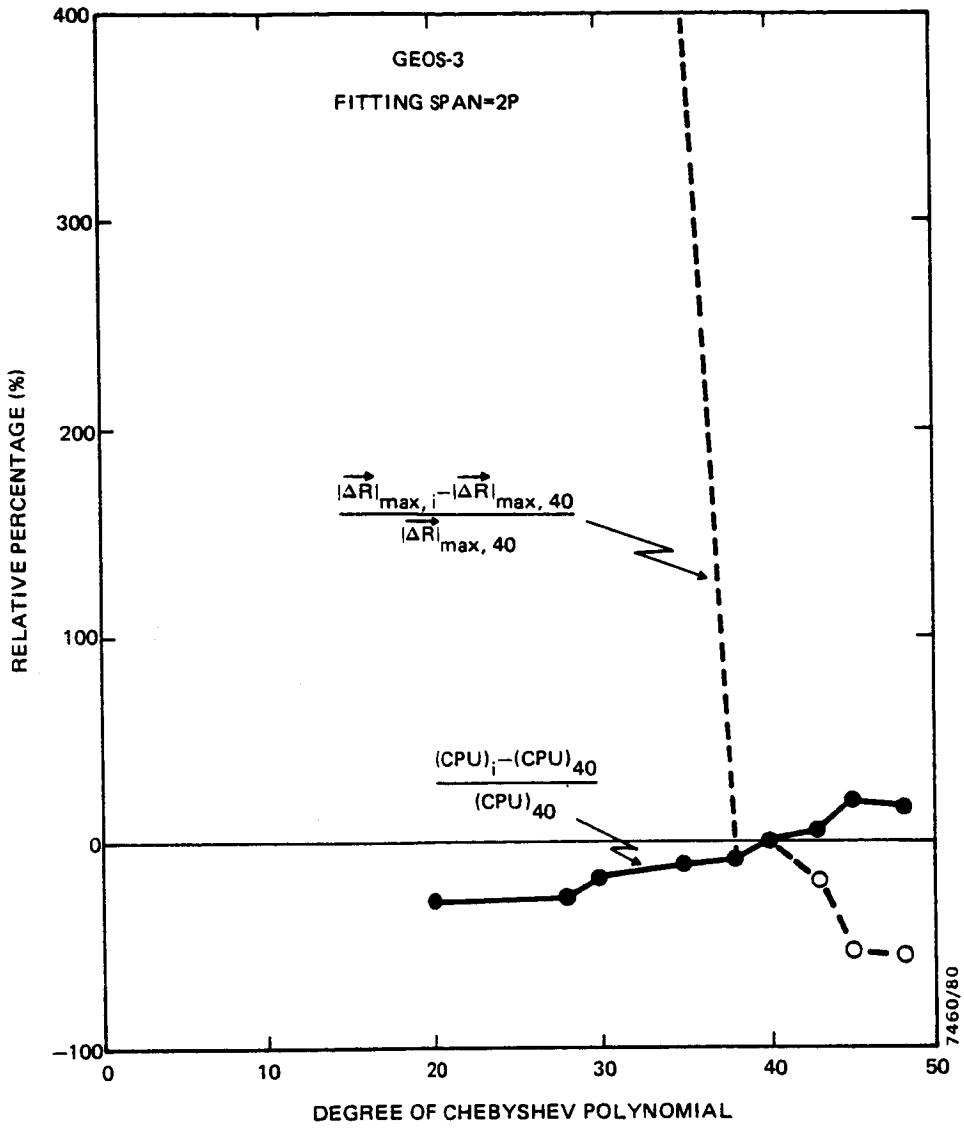

Figure 3-8. Changes in Relative Accuracy and Efficiency for a Fitting Span of 2P for the GEOS-3 Orbit

corresponding to the critical degree of the polynomial on the saturated portion of the accuracy curve. For example, the CPU time used in a computer run for fitting a Chebyshev polynomial of the ith degree over a span of P/4 is normalized with respect to the CPU time consumed for fitting 13th-degree Chebyshev polynomials over the same span, i.e.,

$$[(CPU)_i - (CPU)_{13}]/[(CPU)_{13}]$$

Likewise, the accuracy of the fit is also normalized with respect to the 13th-degree Chebyshev polynomials, i.e.,

$$(|\Delta\vec{R}|_{max,i} - |\Delta\vec{R}|_{max,13})/(|\Delta\vec{R}|_{max,13})$$

For the fitting span of P/4, CPU usage doubles without any benefit at all when the degree is increased from 13th to 25th. Actually, the accuracy has deteriorated by about 10 percent. If the degree is reduced from 13th to 12th, the CPU consumption saved is only 0.6 percent, but the penalty is a significant 70 percent decrease in accuracy. Therefore, it is very desirable to predefine the requirement for support to be accuracy-bound or CPU-bound for selecting the fitting span and the degree of the Chebyshev polynomials. An arbitrary combination of these parameters may either produce an ephemeris with accuracy so poor that it is not usable or consume more computer resources than necessary.

Another area of trade-off consideration is whether support is accuracy-bound or storage-bound. The total number of Chebyshev coefficients is directly proportional to the degree of the Chebyshev polynomials and inversely

proportional to the fitting span over a predefined arc length. If these coefficients are to be saved in a limited amount of space for general applications, such as ephemeris representation on an onboard computer for satellite navigation or autonomous spacecraft, an appropriate combination of degree and fitting span must be selected for an efficient usage of the storage within a required accuracy constraint.

3.2 ELLIPTICAL ORBIT (ECCENTRICITY = 0.1)

The IMP-7 spacecraft, with an orbit eccentricity of 0.11 and a semimajor axis of 223,670 kilometers, was selected to represent the elliptical orbit. Three sets of computer runs were obtained for fitting spans of P/4.5, P/2, and P. The results are shown in Figure 3-9.

The behavior in the variation of accuracy with the degree of the Chebyshev polynomials is essentially the same as that shown in Figure 3-1 for a near-circular orbit. The accuracy improves very rapidly as the degree increases and then saturates after a critical degree is reached.

3.3 HIGHLY ECCENTRIC ORBIT (ECCENTRICITY = 0.9)

The ISEE-1 spacecraft orbit, with an eccentricity of 0.91 and a semimajor axis of 75,500 kilometers, was selected as representative of a highly eccentric orbit. With a fitting span of P/4, equivalent to 51,600 seconds, the best accuracy of the ephemeris represented by Chebyshev polynomials of the 48th degree over one satellite revolution (equivalent to a 2.4-day arc) is 228 kilometers with respect to the reference ephemeris generated by the Cowell method. An ephemeris with accuracy this poor may not be very useful.

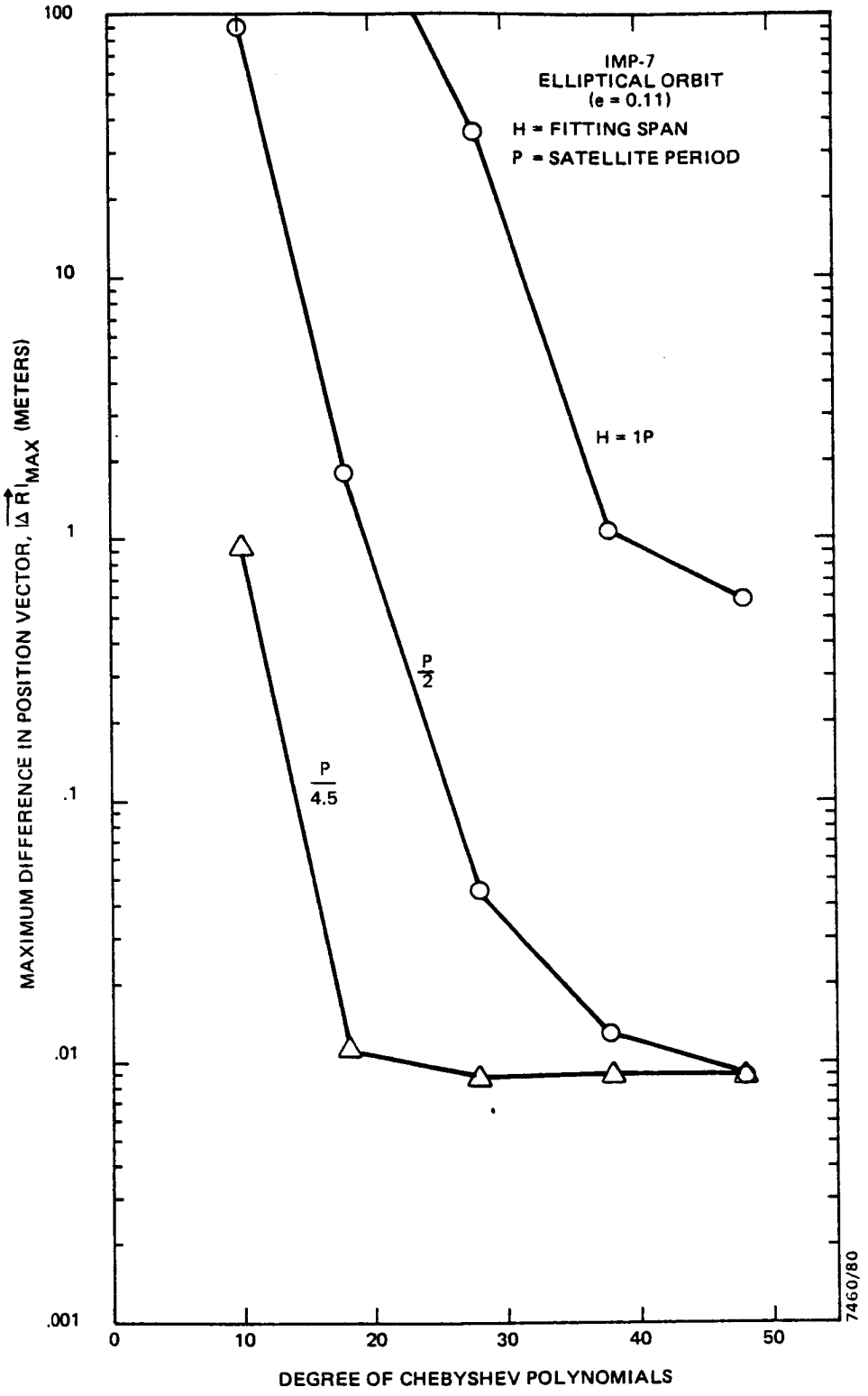

Figure 3-9. IMP-7 Ephemeris Accuracy for the Chebyshev Polynomial Fit Compared With the Cowell Method

Further tests were conducted with drastically reduced fitting spans of P/40 and P/80. The results are presented in Figure 3-10. The accuracy obtained was comparable to that shown in Sections 3.1 and 3.2. As in the cases of circular orbit and elliptical orbit, the accuracy curves show the similar behavior in the variation of accuracy with the degree of the Chebyshev polynomials.

3.4 AN EMPIRICAL FORMULA TO DETERMINE THE OPTIMAL FITTING SPAN

Ideally, in applying the Chebyshev method, one would like to obtain the highest accuracy with a minimum amount of CPU time for the lowest possible degree and the longest possible fitting span. However, so straightforward an application is not possible because those factors compete with each other in a rather complicated fashion as demonstrated in Sections 3.1, 3.2, and 3.3. An attempt was made to find an empirical formula for determining an optimal fitting span in terms of satellite period.

From Figures 3-1, 3-9, and 3-10, it is obvious that a longer fitting span requires a higher degree for the Chebyshev polynomials in order to achieve acceptable fitting accuracy, i.e., the fitting span should be proportional to the degree of the Chebyshev polynomials. Furthermore, the fitting span must be substantially smaller for a highly eccentric orbit than for a circular orbit. From these arguments, a very crude empirical formula results:

$$H = C \cdot DP \, (1 - e)^2 \qquad (3\text{-}1)$$

where H = the fitting span of Chebyshev polynomials in terms of satellite period

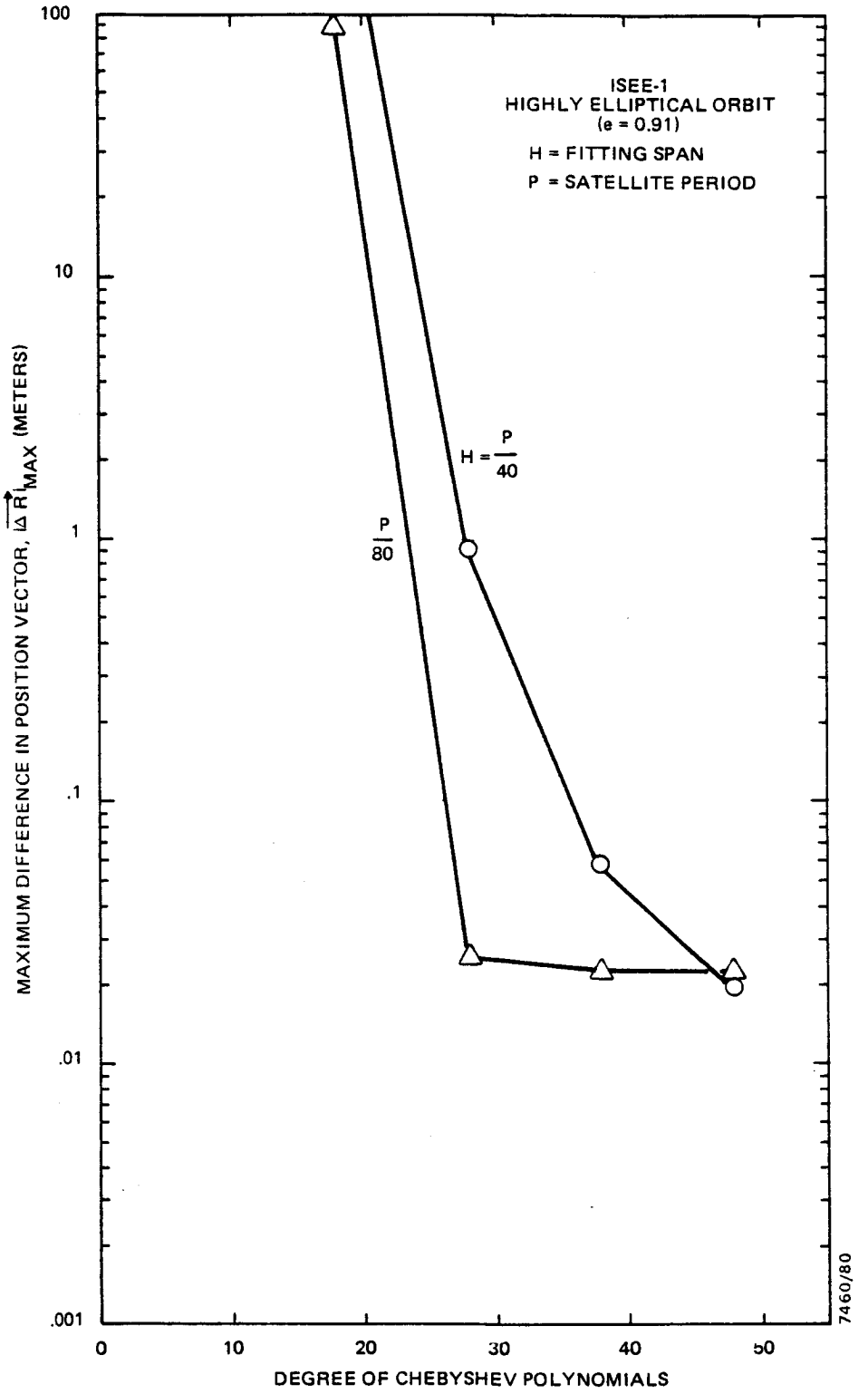

Figure 3-10. ISEE-1 Ephemeris Accuracy for the Chebyshev Polynomial Fit Compared With the Cowell Method

D = the degree of the Chebyshev polynomials

P = the satellite period

e = the eccentricity of the orbit

C = an empirical constant

The value of the constant, C, depends on the degree of the Chebyshev polynomials,

$$C = \frac{1}{40} \qquad D \leq 20$$

$$C = \frac{1}{20} \qquad D > 20$$

To demonstrate the validity of this empirical formula, the following examples are given and results are shown in Table 3-1.

To represent the GEOS-3 ephemeris ($e \simeq 0$) with Chebyshev polynomials of the 10th degree, the fitting span computed using Equation (3-1) is 2P, which gives an accuracy of 0.27 meter over 28 periods (2 days). If Chebyshev polynomials of the 20th degree are desired for GEOS-3, the fitting span given by the empirical formula is P/2, which gives an accuracy of 0.13 meter.

For IMP-7 ($e \simeq 0.1$), the fitting span computed from the empirical formula for a 40th-degree Chebyshev polynomial is roughly 3P/2 with an accuracy of 20 meters. For a 20th-degree Chebyshev polynomial, the fitting span would be P/2.5, giving an accuracy better than 0.2 meter.

In the case of ISEE-1 ($e \simeq 0.9$), fitting a 48th-degree Chebyshev polynomial requires a fitting span of P/40 to achieve 0.02 meter accuracy. For a 30th-degree Chebyshev polynomial, a fitting span of P/70 gives an accuracy of 0.03 meter.

Table 3-1. Ephemeris Accuracies for Fitting Spans Determined Using the Empirical Formula

CATEGORY	NEAR CIRCULAR ORBIT				ELLIPTICAL ORBIT				HIGHLY ECCENTRIC ORBIT	
SATELLITE	GEOS-3		TDRS		IMP-7		SATELLITE-X		ISEE-1	
ECCENTRICITY, e	10^{-3}		10^{-3}		0.1		0.5		0.9	
DEGREE OF CHEBYSHEV POLYNOMIALS, D	20	40	20	40	20	40	20	40	30	48
FITTING SPAN DETERMINED BY USING EMPIRICAL FORMULA, H	$\frac{P}{2}$	2P	$\frac{P}{2}$	2P	$\frac{P}{2.5}$	$\frac{3P}{2}$	$\frac{P}{8}$	$\frac{P}{2}$	$\frac{P}{70}$	$\frac{P}{40}$
ACCURACY OF EPHEMERIS* (METERS)	0.13	0.27	0.14	1.6	0.18	20.0	0.55	0.62	0.03	0.02
EPHEMERIS ARC LENGTH, DAYS (REVOLUTIONS)	2 (28)	2 (28)	31 (31)	31 (31)	13.6 (1)	13.6 (1)	2 (11.5)	2 (11.5)	2.4 (1)	2.4 (1)

7460/80

*ACCURACY IS MEASURED WITH RESPECT TO COWELL METHOD.

The empirical formula is applied to the Tracking and Data Relay Satellite (TDRS) and the results are also included in Table 3-1. The TDRS is to be a geosynchronous satellite with an eccentricity of nearly zero and a semimajor axis of 42,000 kilometers. The fitting span computed from the empirical formula for a 20th-degree Chebyshev polynomial is P/2 which gives an accuracy of 0.14 meter for the ephemeris over a 31-day arc of 31 revolutions. If a 40th-degree Chebyshev polynomial is chosen, the computed fitting span is 2P which gives an accuracy of 0.16 meter over the same arc length.

To further verify the validity of the empirical formula, a nonexistent Satellite-X with an eccentricity of 0.5 and a semimajor axis of 13,200 kilometers was tested. The perigee height is 6,600 kilometers, about 200 kilometers above the surface of the Earth, and the apogee height is 19,800 kilometers. The relative importance of all perturbing forces, such as a higher-order harmonic geopotential field, atmospheric drag, and solar radiation pressure, exerted on Satellite-X varies at different positions on the orbit causing the magnitude of the trajectory variation to differ along the orbit. Near the perigee, a shorter fitting span and a higher degree of Chebyshev polynomials may be needed to meet required accuracy criteria because of the effects of a higher-order harmonic geopotential field and the atmospheric drag. Near the apogee, a medium fitting span and medium degrees of the Chebyshev polynomials may be required because of the large curvature of the trajectory in combination with the trajectory variation due mainly to the solar radiation pressure. While in the vicinities of 90 degrees and 270 degrees of anomaly of the orbit, the trajectory is rather linear and a lower degree and a longer fitting span may be sufficient. It is not possible, however, to apply

several different fitting spans and degrees over each revolution in a single computer run setup with the current GTDS, which only allows a uniform fitting span and a single choice of degree for the Chebychev polynomials.

Two test runs were made with fitting spans of P/8 and P/2 computed by using the empirical formula, Equation (3-1), for Chebyshev polynomials of the 20th and 40th degrees, respectively. The accuracy for a P/8 fitting span with a 20th-degree Chebyshev polynomial is 0.55 meter, and 0.62 meter for a P/2 fitting span with a 40th-degree polynomial over a two-day arc of 11.5 revolutions.

With the exception of the case of the 40th-degree polynomial with a 3P/2 fitting for IMP-7, all the cases seem to favorably support the validity of the empirical formula. However, the formula still should be used with extreme caution, perhaps only as a rough guideline to establish a preliminary set of parameters for the Chebyshev ephemeris generation method.

SECTION 4 - CONCLUSIONS

The Chebyshev ephemeris generation method is reimplemented in the operational version of GTDS. The conclusions from the testing results for this new implementation are summarized below.

- The new implementation is more efficient and produces more accurate ephemerides.
- The accuracy of the ephemeris generated by the Chebyshev method increases with the degree of the Chebyshev polynomials very rapidly but bottoms out after a critical degree is reached.
- The accuracy is generally better for smaller fitting spans.
- The efficiency of the Chebyshev method is mainly related to the degree of the Chebyshev polynomials and the fitting span.
- The Chebyshev method is slower than the Cowell method. Unless Chebyshev coefficients are required, the Chebyshev method is not recommended for use in general applications. A study is currently underway to further improve the efficiency of the Chebyshev method by using the Brouwer-Lyddane theory instead of the two-body theory for the starter.
- A preliminary empirical formula was deduced to determine an optimal fitting span with a desirable degree of Chebyshev polynomials in terms of high accuracy of the satellite ephemeris and low consumption of computer resources.

- It is also recommended that the conclusions of any study involving the use of Chebyshev ephemerides obtained from the previous version of GTDS should be re-evalutated, especially in regard to accuracy.

APPENDIX A - MATHEMATICAL THEORY OF THE CHEBYSHEV ORBIT GENERATION METHOD

A.1 PROPERTIES OF CHEBYSHEV POLYNOMIALS

The properties of the Chebyshev polynomials are most easily examined in the normalized interval [1, -1]. Any arbitrary finite interval $[t_a, t_b]$ can be transformed to the normalized interval [1, -1] by the change of variable:[1]

$$\xi = 1 - 2\left(\frac{t - t_a}{t_b - t_a}\right) \qquad \text{(A-1)}$$

where ξ = the normalized time variable

t_a = the start time of a polynomial fitting span, (i.e., the start time of an integration step in GTDS terminology)

t_b = the end time of a polynomial fitting span, (i.e., the end time of an integration step and, therefore, $t_b - t_a$ corresponds to the "step size")

The Chebyshev polynomials are defined as a set of polynomials

$$T_i(\xi) = \cos i\theta \qquad i = 0, 1, \ldots \qquad \text{(A-2)}$$

---

[1]The transformation could have been defined as

$$\xi = 2\left(\frac{t - t_a}{t_b - t_a}\right) - 1$$

so that t_a would correspond to -1, and t_b would correspond to +1. Since Reference 1 and the GTDS software have consistently used the definition as shown in Equation (A-1), this transformation is retained throughout this document and the new software.

generated from the sequence of cosine functions using the transformation

$$\theta = \cos^{-1}\xi \qquad -1 \leq \xi \leq 1 \tag{A-3}$$

Clearly for the zeroth degree

$$T_0(\xi) = \cos\ (0) = 1 \tag{A-4}$$

and for the first degree

$$T_1(\xi) = \xi \tag{A-5}$$

By repeated trigonometric manipulations, higher-degree Chebyshev polynomials can be computed yielding the recursion relation

$$T_i(\xi) = 2\xi T_{i-1}(\xi) - T_{i-2}(\xi) \qquad i = 2,\ 3,\ \ldots \tag{A-6}$$

Table A-1 contains the first ten Chebyshev polynomials. With simple algebraic manipulation, the algebraic functions, ξ^n, can be expressed in terms of a linear combination of the Chebyshev polynomials. This is shown in Table A-2. All the Chebyshev polynomials have a maximum magnitude of 1 in the interval [1, -1]. The Chebyshev polynomials of degrees 0 to 3 are plotted in Figure A-1. The function of a parabola, ξ^2, is also plotted in the figure as a linear combination of T_0 and T_2. Except for T_0, all other Chebyshev polynomials cross the ξ-axis. The number of times that axis is crossed is equal to the degree of the Chebyshev polynomial and only those

Table A-1. The Chebyshev Polynomials

$$T_0 = 1$$

$$T_1 = \xi$$

$$T_2 = 2\xi^2 - 1$$

$$T_3 = 4\xi^3 - 3\xi$$

$$T_4 = 8\xi^4 - 8\xi^2 + 1$$

$$T_5 = 16\xi^5 - 20\xi^3 + 5\xi$$

$$T_6 = 32\xi^6 - 48\xi^4 + 18\xi^2 - 1$$

$$T_7 = 64\xi^7 - 112\xi^5 + 56\xi^3 - 7\xi$$

$$T_8 = 128\xi^8 - 256\xi^6 + 160\xi^4 - 32\xi^2 + 1$$

$$T_9 = 256\xi^9 - 576\xi^7 + 432\xi^5 - 120\xi^3 + 9\xi$$

Table A-2. An Algebraic Function Expressed in Terms of a Linear Combination of the Chebyshev Ploynomial

$$1 = T_0$$
$$\xi = T_1$$
$$\xi^2 = (T_0 + T_2)/2$$
$$\xi^3 = (3T_1 + T_3)/4$$
$$\xi^4 = (3T_0 + 4T_2 + T_4)/8$$
$$\xi^5 = (10T_1 + 5T_3 + T_5)/16$$
$$\xi^6 = (10T_0 + 15T_2 + 6T_4 + T_6)/32$$
$$\xi^7 = (35T_1 + 21T_3 + 7T_5 + T_7)/64$$
$$\xi^8 = (35T_0 + 56T_2 + 28T_4 + 8T_6 + T_8)/128$$
$$\xi^9 = (126T_1 + 84T_3 + 36T_5 + 9T_7 + T_9)/256$$

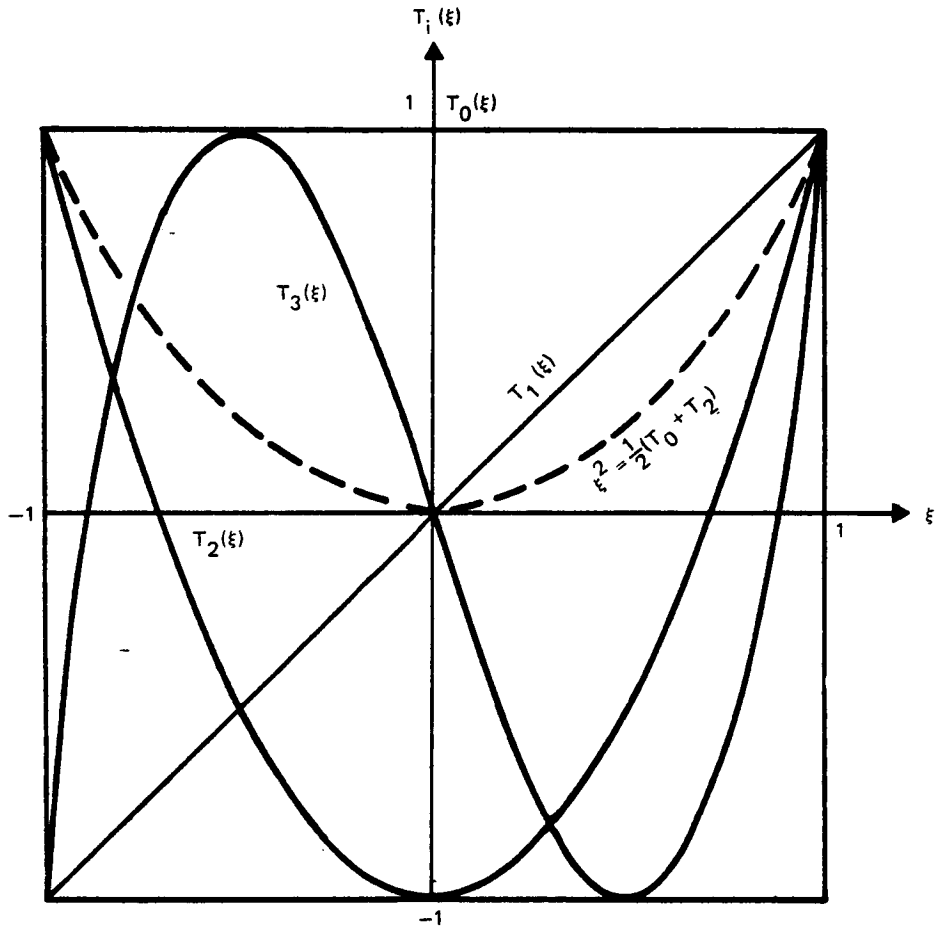

Figure A-1. Chebyshev Polynomials of Degrees 0 to 3

of odd degrees will cross the origin. The n locations at which the Chebyshev polynomial $T_n(\xi)$ crosses the ξ-axis are the n roots in the interval [1, -1] and are given by

$$\xi_k = \left[\cos \frac{(2k - 1)\pi}{2n}\right] \qquad k = 1, \ldots, n \qquad \text{(A-7)}$$

The significant properties of using the Chebyshev polynomials to fit an arbitrary function are that the error in the approximation is distributed evenly over the interval and the maximum error is reduced to the minimum or near-minimum value (References 3 and 4).

A.2 INTERPOLATING POLYNOMIALS CONSISTING OF A LINEAR COMBINATION OF CHEBYSHEV POLYNOMIALS OF DIFFERENT DEGREES TO REPRESENT ACCELERATION

Each component of the acceleration vector exerted on the spacecraft can be approximated by an interpolating polynomial consisting of a linear combination of Chebyshev polynomials:

$$\ddot{x}(\xi) = P_n(\xi) = \sum_{i=0}^{n} C_i T_i(\xi) \qquad \text{(A-8)}$$

where $\ddot{x}$ = the Cartesian component of the acceleration vector

P_n = the interpolating polynomial of degree n

C_i = Chebyshev coefficients for an acceleration component

ξ = the transformed time variable

The accuracy of this approximation is better when the higher degrees of Chebyshev polynomials are included. However, the benefit of including higher degrees drops off quickly. This point is further illustrated in Section 4.

It is well known that the Chebyshev polynomials are one of the families which possess the property of orthogonality (References 3 and 4). They are orthogonal in the interval [1, -1] with respect to the weighting function, $w(\xi) = 1/\sqrt{1 - \xi^2}$, i.e.,

$$\int_{-1}^{1} \frac{1}{\sqrt{1 - \xi^2}} T_i(\xi)\, T_j(\xi)\, d\xi = 0, \qquad i \neq j$$

$$\int_{-1}^{1} \frac{1}{\sqrt{1 - \xi^2}} \left[T_i(\xi)\right]^2 d\xi = A_i \neq 0 \tag{A-9}$$

where A_i is a normalization factor which depends on i. Making use of the property of orthogonality, as demonstrated in Equation (A-9), the Chebyshev coefficients can be evaluated

$$C_i = \frac{1}{A_i} \int_{-1}^{1} \frac{1}{\sqrt{1 - \xi^2}} T_i(\xi)\, \ddot{x}(\xi)\, d\xi$$

$$i = 0, 1, \ldots, n \tag{A-10}$$

The above integral is difficult to evaluate because of the complexity of $\ddot{x}(\xi)$. However, it has been shown (References 3, 4, and 5) that Equation (A-10) may be approximated by

$$C_0 = \frac{1}{n + 1} \sum_{k=1}^{n+1} \ddot{x}(\xi_k)$$

$$C_i = \frac{2}{n + 1} \sum_{k=1}^{n+1} T_i(\xi_k)\ddot{x}(\xi_k) \qquad i = 1, 2, \ldots, n \tag{A-11}$$

where ξ_k are the roots of the Chebyshev polynomial of degree n + 1, $T_{n+1}(\xi)$. Therefore, with the accelerations evaluated at all the n + 1 roots, the variation of the acceleration in the interval [1, -1], corresponding to the time interval $[t_a, t_b]$, can be represented by the interpolating polynomial, $P_n(\xi)$, of degree n.

A.3 INTEGRATION OF CHEBYSHEV INTERPOLATING POLYNOMIAL TO GENERATE EPHEMERIS

With the acceleration components represented by Chebyshev interpolating polynomials as shown in Equation (A-8), integrating the equation once gives the velocity components, $\dot{x}$:

$$\dot{x}(\xi) = \int P_n(\xi)\, d\xi = \sum_{i=0}^{n} C_i \int T_i(\xi)\, d\xi \qquad \text{(A-12)}$$

Through the use of Equations (A-4), (A-5), and (A-6), the integration of the Chebyshev polynomials of different degrees can be obtained:

$$\int T_0(\xi)\, d\xi = T_1(\xi) + K_0$$

$$\int T_1(\xi)\, d\xi = \frac{1}{4}\left[T_0(\xi) + T_2(\xi)\right] + K_1 \qquad \text{(A-13)}$$

$$\int T_i(\xi)\, d\xi = \left[\frac{1}{2}\,\frac{1}{i+1}\,T_{i+1}(\xi) - \frac{1}{i-1}\,T_{i-1}(\xi)\right] + K_i,$$

$$i = 2, 3, \ldots, n$$

where K_0, K_1, and K_i are integration constants.

Substituting Equation (A-13) into Equation (A-12) and collecting terms of Chebyshev polynomials of the same degrees yields another interpolating polynomial of the following form for the velocity components:

$$\dot{x}(\xi) = \int P_n(\xi)\, d\xi = Q_{n+1}(\xi) = \sum_{i=0}^{n+1} b_i\, T_i(\xi) \qquad \text{(A-14)}$$

where Q_{n+1} = the interpolating polynomial of degree n + 1

b_i = Chebyshev coefficients for a velocity component

with

$$\begin{aligned} b_0 &= K_0 + K_1 + \ldots + \frac{C_1}{4} T_0 \\ b_1 &= C_0 - \frac{1}{2} C_2 \\ b_i &= \frac{1}{2i}\left[C_{i-1} - C_{i+1}\right] \qquad i = 2, 3, \ldots, n+1 \\ C_{n+1} &= C_{n+2} = 0 \end{aligned} \qquad \text{(A-15)}$$

The integration constants in the expression for b_0 may be evaluated from the initial velocity, i.e., $\dot{x}(t_a) = \dot{x}(\xi = 1)$:

$$\dot{x}(\xi = 1) - \sum_{i=1}^{n+1} b_i\, T_i(\xi = 1) = b_0\, T_0(\xi = 1) = b_0 \qquad \text{(A-16)}$$

The interpolating polynomials for position components, $x(\xi)$, can be obtained by the same procedure:

$$x(\xi) = \int Q_{n+1}(\xi)\, d\xi = R_{n+2}(\xi) = \sum_{i=0}^{n+2} a_i\, T_i(\xi) \qquad \text{(A-17)}$$

$$a_0 = x(\xi = 1) - \sum_{i=1}^{n+2} a_i\, T_i(\xi = 1)$$

$$a_1 = b_0 - \frac{1}{2} b_2$$

$$a_i = \frac{1}{2i}\left[b_{i-1} - b_{i+1}\right], \qquad i = 2, 3, \ldots, n + 2$$

$$b_{n+2} = b_{n+3} = 0$$

where R_{n+2} = the interpolating polynomial of degree n + 2 for the position component

With velocity and position represented by Equations (A-14) and (A-17) in the interval $[t_a, t_b]$, the ephemerides of spacecraft at any other time within the interval can now be accurately and easily interpolated.

APPENDIX B - COMPARISON BETWEEN THE IMPROVED IMPLEMENTATION AND THE PREVIOUS IMPLEMENTATION OF THE CHEBYSHEV METHODS

A series of GTDS computer runs was executed to compare the new and the previous software implementations in terms of their accuracy and efficiency. The accuracy was measured with respect to the ephemeris generated with the high-precision Cowell numerical integration method by using the GTDS Ephemeris Comparison Program. The efficiency is simply a comparison of the CPU and I/O times consumed by the two different Chebyshev implementations.

Three sets of test runs were made on GTDS with the GEOS-3 satellite (arbitrarily chosen) over a two-day span using the Cowell method and the Chebyshev polynomial method of the new and previous implementations. The comparison results are presented in Table B-1. In these tests, the ephemeris generated by the Cowell integration method with a 24-second step size was used as a reference. The perturbation (or force model) included in the Cowell method was identical to that used in the Chebyshev methods.

Table B-1 shows that the maximum difference in position vector of the ephemeris generated by the previous Chebyshev implementation with a 48th degree polynomial over a two-day arc is 97 meters with respect to the ephemeris generated by the Cowell method, while the new Chebyshev implementation with the same degree of polynomial has a maximum position difference of only 0.25 meter. This represents an improvement of better than two orders of magnitude in the relative accuracy.

The efficiency which is expressed as CPU time and I/O time consumed on the IBM S/360-75 computer is also examined.

Table B-1. Comparison Between New and Previous Chebyshev Implementations With Respect to the Cowell Method

PERTURBATION INCLUDED IN INTEGRATION PARAMETERS FOR CHEBYSHEV AND COWELL ORBIT INTEGRATORS	METHOD	DEGREE OF CHEBYSHEV POLYNOMIAL	$\lvert\Delta\vec{R}\rvert_{max}$* (meters)	$\sigma_{\Delta\vec{R}}$ (meters)	EFFICIENCY** (CPU Minutes/ I/O Minutes)	NUMBER OF TIMES FULL FORCE IS EVALUATED
4 x 4 GEOPOTENTIAL, SUN, MOON	NEW IMPLEMENTATION	48	0.25	0.11	5.806/0.142	25,143
		20	5.17	2.36	1.835/0.142	11,339
		18	36.6	16.76	1.604/0.138	10,353
	PREVIOUS IMPLEMENTATION	48	97.32	51.73	8.012/0.154	39,562
8 x 8 GEOPOTENTIAL, 14TH ORDER RESONANCE GEOPOTENTIAL, SUN, MOON, DRAG, SOLAR RADIATION PRESSURE	NEW IMPLEMENTATION	38	4.87	2.22	7.118/0.176	20,213
	PREVIOUS IMPLEMENTATION	38	20.09	11.02	7.272/0.177	31,408

*$\lvert\Delta\vec{R}\rvert_{max}$ = MAXIMUM $\left|\vec{R}(t)_{CHEBYSHEV} - \vec{R}(t)_{COWELL}\right|$ OVER A 2-DAY ARC

**EXECUTED ON AN IBM S/360-75 COMPUTER

NOTE: GEOS-3 ORBIT CHARACTERISTICS AT EPOCH, JULY 18, 1977, WERE AS FOLLOWS:

a = 7224.6628 KILOMETERS
e = 0.0009758
i = 114.98 DEGREES
Ω = 341.14 DEGREES
ω = 210.90 DEGREES
M = 126.14 DEGREES

THE PERIOD WAS 6100 SECONDS. STEP SIZES WERE 6101 SECONDS FOR THE CHEBYSHEV ORBIT INTEGRATOR AND 24 SECONDS FOR THE COWELL ORBIT INTEGRATOR.

The previous implementation used 8.012 minutes of CPU time and 0.154 minute of I/O time, while the new implementation used only 5.806 minutes of CPU time, a saving of 38 percent, and a comparable 0.142 minute of I/O time.

The saving of computer resources can be viewed from another angle by lowering the degree of Chebyshev polynomials from 48 to 20 and 18. The results are also shown in Table B-1. Fitting Chebyshev polynomials with much lower degrees, the new implementation consumes four to five times less CPU resources yet maintains better accuracy than the previous implementation.

Results in Table B-1 indicate similar conclusions with more elaborate perturbation models, i.e., 8x8 geopotential field, 14th order resonance geopotential field, atmospheric drag, and solar radiation pressure as well as solar and lunar gravitational fields.

The results presented in Table B-1 are obtained with a fitting span of one satellite period for both the new and previous implementation. When the fitting span is increased to two satellite periods, the new implementation gives excellent results ($\left|\Delta\vec{R}\right|_{max}$ = 0.12 meter). However, after 80 loops in the iterative scheme, the previous implementation has simply failed to satisfy the 10^{-6} kilometer tolerance in fitting the first span and the computer run was subsequently terminated without generating an ephemeris.

REFERENCES

1. Goddard Space Flight Center, X-582-73-176, Description of the Numerical Integration of the Equations of Motion of a Space Vehicle Using Chebyshev Series, T. Feagin, June 1973

2. Goddard Space Flight Center, X-582-76-77, Mathematical Theory of the Goddard Trajectory Determination System (GTDS), J. O. Capellari, C. E. Velez, and A. J. Fuchs, April 1976.

3. Fox, L., and I. B. Parker, Chebyshev Polynomials in Numerical Analysis. London: Oxford University Press, 1972.

4. Carnahan, B., H. A. Luther, and J. O. Wilkes, Applied Numerical Methods. New York: John Wiley and Sons, Inc., 1969

5. Snyder, M. A., Chebyshev Methods in Numerical Approximation. Englewood Cliffs, New Jersey: Prentice-Hall, 1966

AN ECONOMICAL SEMI-ANALYTICAL ORBIT THEORY FOR RETARDED SATELLITE MOTION ABOUT AN OBLATE PLANET

Robert A. Gordon
Goddard Space Flight Center

ABSTRACT

Brouwer and Brouwer-Lyddanes' use of the Von Zeipel-Delaunay method is employed to develop an efficient analytical orbit theory suitable for micro-computers. A succinctly simple pseudo-phenomenologically conceptualized algorithm is introduced which accurately and economically synthesizes modeling of Drag effects. The method epitomizes and manifests effortless efficient computer mechanization. Simulated (Space Telescope) trajectory data is employed to illustrate the theory's ability to accurately accommodate oblateness and Drag effects for micro-computer ground based or on-board predicted orbital representation. Real (SMM – Solar Maximum Mission) tracking data is used to demonstrate that the theory's orbit determination and orbit prediction capabilities are favorably adaptable to and are comparable with results obtained utilizing complex "Definitive Cowell Method" solutions on satellites experiencing significant Drag effects.

AN ECONOMICAL SEMI-ANALYTICAL ORBIT THEORY FOR RETARDED SATELLITE MOTION ABOUT AN OBLATE PLANET

BY: ROBERT A. GORDON
(NASA/GSFC)

INTRODUCTION:

Brouwer[1] derived a first-order perturbation solution expressing the secular, short and long periodic variations in the motion of an artificial satellite about an oblate planet. Brouwer obtained separation of all the periodic terms by adapting Von Zeipel's[2] technique to modify Delaunay's method for calculating the coefficients of the periodic terms through a succession of canonical transformations. Delaunay's variables were introduced in order to simplify the canonical expressions for the equations of motion. Brouwer developed the periodic terms to $O(J_2)$ and obtained the secular variations to $O(J_2^2)$. The resultant formulas are piecewise continuous with singularities existing for certain values of the eccentricity and inclination which occur as poles in the algebraic expressions. Thus, the equations are valid, except in the regions for which $e'' = 0$, $i'' = 0$ deg. , and $1 - 5\cos^2 i'' = 0°$ i.e., $i'' = 63.43°$, the critical inclination. Lyddane[3] introduced Poincaré's variables and reformulated Brouwer's expressions as to remove the poles, and thus the singularities arising from small eccentricities or inclinations in the Brouwer theory.

This paper is the fruition of an effort to provide an optimal on-board ephemeris representation employing an efficient analytical orbit theory suitable for microcomputers. Brouwer/Brouwer-Lyddane's method is modified to develop an economical

analytical orbit theory for satellite motion about an oblate planet which accommodates J_2, J_3, and parts of the J_4 zonal effects with the true argument of latitude as the fast variable. The theory is applicable to circular and non-circular satellites but singular for $i=0$. This is satisfactory for the vast majority of our satellite support. The choice of the true argument of latitude as the fast variable in difference to Brouwer-Lyddane's choice of the true longitude is a major contribution to the economical variation presented here; it simplifies the computation of the osculating inclination. J_3 and portions of the J_4 zonal effects are considered in the theory in relation to their primary effects on the radial and cross-track errors respectfully, and truncated in accordance with economical computational consideration. Lyddane remarks that l'' and g'' must be used for computing f' and r' in his version; however, as demonstrated by Gordon[4] et al., this results in a relative large radial error with respect to Brouwer for moderate values of the eccentricity. This can be avoided by evaluating f' and r' with l', g' for moderate values of the eccentricity and with l'', g'' for relative low values of the eccentricity. The theory presented here also computes f' and r' with the long-period contribution (J_3) to the eccentricity. For some orbital parameters, this can result in a significant improvement in accounting for intrack error due to the oblateness perturbation and compares favorably with respect to the Brouwer and Brouwer-Lyddane's orbit theories for the satellite cases presented in Reference 4. The theory presented here is further modified to incorporate a "cheap" algorithm which accounts for drag effects semi-analytically. A succinctly simple pseudo-phenomenologically conceptualized algorithm is introduced which accurately and economically synthesizes modeling of drag effects. The method epitomizes and manifests effortless efficient computer mechanization. Simulated (Space Telescope) trajectory data is employed to illustrate the theory's ability to accurately accommodate oblateness and drag effects for microcomputer ground-based or on-board

predicted orbital representation. Real (SMM-Solar Maximum Mission) tracking data is used to demonstrate that the theory's orbit determination and orbit prediction capabilities are favorably adaptable to and comparable with results obtained utilizing complex "Definitive Cowell Method" solutions on satellites experiencing significant drag effects.

FORMULAS FOR COMPUTATION:

A computational flow diagram of a subroutine with a description of input and output parameters for that part of the modified Brouwer theory which accounts for the oblateness effects is presented in the Appendix. Henceforth, this analytic part of the current orbit theory will be represented by the symbolic function Bg(t), where t designates the time of theory evaluation.

The theory is adapted to accommodate retarded motion due to drag by a pseudo-physical secular relationship to describe decay in the semi-major axis. This representation is inferred phenomenologically from the signature of the semi-major axis Locus defined by osculating to mean[5] conversions of state vectors of a drag perturbed satellite ephemeris.

OSCULATING-TO-MEAN CONVERSION:

Walter's algorithm[5] for osculating to mean conversion is unstable for low e in Keplerian space; the apparent instability of the iterative osculating-to-mean element conversion is removed by translating the iteration from mean Keplerian space to mean Cartesian space.

Define:

$\bar{\underline{\Omega}} \equiv (a'', e'', i'', g'', h'', l'')$ -- Mean Keplerian Elements

$\underline{\Omega} \equiv (a, e, i, g, h, l)$ -- Osculating Keplerian Elements

$X \equiv (x'', y'', z'', \dot{x}'', \dot{y}'', \dot{z}'')$ -- Mean Cartesian State Elements

$Y \equiv (x, y, z, \dot{x}, \dot{y}, \dot{z})$ -- Osculating Cartesian State Elements

Given an osculating Cartesian state Y we determine

$$\bar{\underline{\Omega}}_i^{(0)} \longleftarrow f_{2B}(Y_i)$$

Where f_{2B} represents the Keplerian state two-body functional relationship to the Cartesian state. Then employing the iterative algorithm,

$$\underline{\Omega}^{(j)} \leftarrow B_g(\Delta t = 0, \bar{\underline{\Omega}}^{(j)})$$

$$Y^{(j)} \leftarrow f_{2B}(\underline{\Omega}^{(j)})$$

$$X_i^{(j+1)} = X_i^{(j)} + (Y_i - Y_i^{(j)}), \quad i = 1, 2, \ldots, 6$$

$$\bar{\underline{\Omega}}^{(j+1)} \longleftarrow f_{2B}^{-1}(X^{(j+1)})$$

For j = 0, 1, 2, . . ., 10 or until the following criterion is satisfied:

$$\left| Y_i - Y_i^{(j)} \right| \leq \epsilon$$

Where ϵ is some preassigned small positive number. Let this algorithm be represented by the symbolic functional relationship,

$$\bar{\underline{\Omega}} \leftarrow \Pi(Y)$$

SEMI-MAJOR AXIS DECAY RATE:

Applying the osculating to mean conversions at one period (P) intervals, we determine the semi-major axis decay over M periods, i.e., with

$$a_i'' \leftarrow \Pi_i(\underline{\Omega})$$

Given for i = 1, 2, . . ., M; we compete the mean semi-major axis decay rate as

$$\dot{a}_i'' = \sum_{i=1}^{M} \left(\frac{a_i'' - a_{i-1}''}{M} \right)$$

ORBIT PROPAGATION WITH "$\dot{B}g$":

To update the orbital elements to time ($\Delta t = t - t_o$) with the $\dot{B}g$ theory, we assume the orbital elements remain constant over one period and rectify the theory's constants at one period intervals (with the $\dot{a}$ decay rate) up to the Nth period where

$$N = \mathrm{int}\left(\frac{\Delta t}{P}\right) .$$

Employing the above iterative method we have

$$a''_j = a_{j-1} + \dot{a} P_{j-1}$$

$$e''_j = e''_{j-1} + \frac{(1 - e''_{j-1})}{a_{j-1}} \dot{a} P_{j-1}$$

$$(l''_o)_j = (l''_o)_{j-1} - \frac{3}{4}\left(\frac{n_{j-1}}{a''_{j-1}}\right) \dot{a} P^2_{j-1} \quad , \quad n = \sqrt{\frac{\mu}{a''^3}}$$

Evaluating the secular part of Bg we obtain

$$\bar{\underline{\Omega}}_j \leftarrow B''_g(P_{j-1})$$

Where $j = 1, 2, \ldots, N \Rightarrow$

$$\bar{\underline{\Omega}}_N \equiv (a''_N, e''_N, i''_N, g''_N, h''_N, l''_N)$$

Then at time Δt the osculating elements are given by evaluating the full Bg theory with

$$\underline{\Omega}(\Delta t) \leftarrow B_g\left(\bar{\underline{\Omega}}(T_N), \Delta t - T_N\right)$$

With $T_N = N \times P$. Let us represent the semi-analytic theory with the rectification algorithm for retarded motion symbolically by "$\dot{B}g$."

TRAJECTORY DATA:

Trajectory data, i.e., osculating state vectors are used in a simulation to demonstrate the $\dot{B}g$ orbit theory capability in representing retarded satellite motion about an oblate planet. It has been proposed that a secular analytic orbit theory be employed for the on-board ephemeris representation of the Space Telescope. The

Space Telescope can experience significant drag effects over a three-day span. State vectors generated from a sample set of Space Telescope elements demonstrates the $\dot{B}g$ theory's superior ability to represent the Space Telescope ephemeris. This will be demonstrated by three steps in the simulation.

Step No. 1:

A comparison is made between two Cowell ephemeris generations at two-hour intervals, the "Truth Ephemeris" with drag included with a drag model constant C_D = 2.0 versus the Cowell ephemeris with C_D = 0, i.e., no drag consideration over a three-day span. The Space Telescope epoch elements is defined as:

a =	6778.140 km	A =	117.6 m^2
e =	0.001	m =	10134 kg
i =	28.2 degrees		
h =	19.78 degrees	h_p =	393.222 km
g =	0 degree	h_a =	406.778 km
l =	0 degree		

Note: Table No. 1 -- the maximum total error growth realized was (262.88 km).

Step No. 2:

An analytical method without drag model effects is fitted to the "Truth Ephemeris" over a three-day span with the "Truth Ephemeris" state vectors as observation data at two-hour intervals for a Differential Correction of the epoch mean elements of the analytical orbit theory. The analytical theory used is the Brouwer-Lyddane which includes periodic terms.

Note: Table No. 2 -- the post trajectory data DC compare at the two-hour frequency yields a maximum total error of (43.71 km).

Step No. 3:

Step No. 2 was repeated employing the $\dot{B}g$ orbit theory.

Note: Table No. 3 -- the post trajectory data DC compare at the two-hour frequency yields a maximum total error of (1.30 km).

TRACKING DATA:

Real tracking data demonstrates the $\dot{B}g$ orbit theory's favorable orbit determination and prediction capabilities. An orbit determination for a number of different epochs employs real (SMM-Solar Maximum Mission) tracking data over a two-day span to differentially correct the epoch state and drag model parameter for a "Definitive Cowell Method" and the epoch mean elements for the $\dot{B}g$ orbit theory. The predicted ephemeris of the "Definitive Cowell Method" and the $\dot{B}g$ orbit theory is then compared with a series of state solutions determined over a two-day DC arc at two-day intervals. A table of the comparable response of the Cowell and $\dot{B}g$ method is presented in Table 4.

CONCLUSIONS:

1. The osculating to mean algorithm described herein provides an accurate first-order estimate to the semi-major axis decay rate.

2. Tables 1 and 2 graphically demonstrates that the $\dot{B}g$ orbit theory can accurately accommodate significant drag effects on orbital motion and that the $\dot{a}$ parameter can absorb virtually all of the significant drag effects.

3. Table 4 implies that the $\dot{B}g$ theory is competitive with a "Definitive Cowell Method" in a least squares batch filter orbit determination for

satellites experiencing significant drag effects. Thus this can expand the class of satellites which can be operationally supported with a semi-analytic orbit theory.

4. The $\dot{B}g$ theory is suited for a ground-based or on-board microcomputer applications, providing an orbital ephemeris generation which does not require a density table or analytic density model.

RECOMMENDATIONS:

1. Some adaptation of the $\dot{B}g$ theory should be employed for the on-board ephemeris representation of the Space Telescope.

2. Develop the state transition matrix for a truncated secular version of $\dot{B}g$ for Karman Filter state estimation applications on microcomputers.

3. $\dot{B}g$ be adapted by those various sites who require orbit ephemeris generation but does not have an orbit determination capacity. The mean orbital constants and the $\dot{a}$ parameter can be determined and distributed by Goddard for satellites of interest as are now the Brouwer Mean Orbital elements. This would lead to a uniform method at each of the various sites who require such elements with a significant improvement in ephemeris representation for satellites experiencing significant drag effects.

DATE OF DATA		POSITION DIFFERENCES (METERS)			POSITION DIFFERENCES DEGREES			SEC.S	POSITION DIFFERENCES (METERS)		(KM.)	POSITION DIFFERENCES (METERS)		(DEG.)
YYMMDD	HHMMSS	DA	PPM DE	(10**3) DI	DELH	DELG	DELM	DELTIME	TOTAL ERROR	RADIAL	IN TRACK	ALONG TRACK	CROSS TRACK	TRUE ANOMALLY
800101	0.	0.00	0.0	0.00	-0.00	-0.00	0.00	-0.0000	0.00	0.00	-0.00	-0.00	0.00	360.00
800101	20000.	83.59	24.41	-1.53	-2.27	-0.05	0.06	0.0102	240.24	-80.42	0.08	78.15	-212.47	350.43
800101	40000.	-127.00	-8.17	-0.96	-3.62	-0.94	0.94	0.0927	721.76	-69.67	0.71	711.72	-97.69	1.24
800101	60000.	17.94	-10.19	-0.11	-3.63	0.57	-0.56	0.1455	1132.85	70.73	1.12	1116.69	177.08	13.49
800101	80000.	-178.12	33.25	-0.24	-1.98	0.73	-0.71	0.3103	2410.19	-369.06	2.38	2381.77	5.03	339.56
800101	100000.	-151.31	3.92	-0.25	-1.10	357.70	-357.67	0.6499	4994.55	-172.92	4.99	4991.17	-61.86	1.60
800101	120000.	-143.57	-62.50	-0.59	0.54	-0.57	0.62	0.7995	6143.41	276.48	6.14	6136.94	54.85	19.13
800101	140000.	-267.31	30.37	-1.96	0.80	3.47	-3.40	1.0115	7776.03	-375.61	7.76	7764.87	-179.85	344.47
800101	160000.	-208.34	54.51	-1.34	-3.09	-1.15	1.25	1.5163	11659.37	-565.02	11.64	11643.32	-234.01	1.41
800101	180000.	-300.10	-18.26	0.49	-3.84	-2.48	2.60	1.9604	15050.25	-134.43	15.05	15049.23	-112.15	7.71
800101	200000.	-328.03	-16.43	1.80	-2.37	1.17	358.99	2.4166	18554.05	-190.65	18.55	18552.48	147.85	359.38
800101	220000.	-463.20	10.98	1.76	-0.07	1.43	-1.23	3.0486	23409.93	-489.38	23.40	23404.04	191.29	355.61
800102	0.	-346.01	9.18	-0.61	-0.56	-1.21	1.45	3.7498	28793.71	-355.66	28.79	28791.50	22.34	357.94
800102	20000.	-387.82	-30.11	-0.96	-5.09	0.87	-0.58	4.3352	33282.49	-116.42	33.28	33280.88	306.77	9.53
800102	40000.	-535.87	23.41	-1.00	-6.99	2.68	-2.35	4.9812	38241.07	-543.28	38.24	38237.20	-24.84	346.46
800102	60000.	-450.74	25.05	-0.78	-4.87	-1.39	1.77	5.8524	44943.41	-477.19	44.94	44940.08	-267.50	359.53
800102	80000.	-558.16	-59.85	-0.11	-2.89	-0.35	0.78	6.5768	50486.37	41.35	50.49	50486.29	78.00	12.65
800102	100000.	-505.33	55.42	-1.28	-1.15	4.61	-4.12	7.3302	56277.95	-564.37	56.28	56275.10	-52.92	348.25
800102	120000.	-582.19	70.86	-1.36	-1.87	-2.18	2.72	8.4557	64931.37	-728.67	64.93	64927.05	-171.64	4.62
800102	140000.	-621.43	-64.72	-1.83	-3.82	356.46	-355.86	9.3871	72060.31	207.04	72.06	72059.81	169.50	3.15
800102	160000.	-672.69	-34.59	-1.31	-3.82	4.05	356.62	10.1744	78116.10	22.44	78.12	78115.85	196.97	357.14
800102	180000.	-646.32	61.29	1.11	-5.38	1.95	-1.21	11.3165	86879.22	-509.12	86.88	86877.73	-12.47	2.72
800102	200000.	-739.65	13.62	1.48	-3.37	-1.51	2.33	12.6381	97034.61	-166.98	97.03	97034.12	-259.67	354.53
800102	220000.	-692.36	-25.74	1.37	-2.44	0.91	-0.01	13.8261	106155.76	313.94	106.16	106155.28	46.86	6.65
800103	0.	-734.94	31.32	-1.29	-5.87	3.78	-2.79	15.0265	115351.96	48.73	115.35	115351.91	-95.41	355.39
800103	20000.	-935.52	19.92	-1.56	-5.78	-0.64	1.71	16.4412	126243.38	95.53	126.24	126242.99	-296.90	357.94
800103	40000.	-715.54	-34.64	0.02	-8.97	-1.16	2.32	17.7319	136131.57	914.00	136.13	136128.31	230.72	8.14
800103	60000.	-1029.21	-3.00	-0.89	-7.32	5.57	-4.32	18.9784	145708.60	606.19	145.71	145707.18	216.61	352.29
800103	80000.	-868.53	73.62	0.40	-5.34	-0.52	1.86	20.6096	158243.87	505.38	158.24	158242.86	-252.15	5.82
800103	100000.	-945.72	-78.58	-0.56	-6.83	-3.02	4.46	22.1222	169827.86	1682.91	169.82	169819.52	12.59	357.00
800103	120000.	-1120.45	-48.86	-1.89	-1.87	6.08	355.45	23.4078	179744.87	1619.19	179.74	179737.56	63.59	355.90
800103	140000.	-870.93	108.63	-1.23	-8.39	4.08	-2.44	25.1243	192892.69	1114.23	192.89	192889.14	-357.96	8.79
800103	160000.	-1203.34	-29.79	-1.36	-9.34	-3.35	5.10	26.9431	206860.50	2062.75	206.85	206850.07	-242.30	352.43
800103	180000.	-1000.10	-55.88	2.04	-7.64	2.47	-0.61	28.5222	219028.26	2918.11	219.01	219008.62	296.97	2.94
800103	200000.	-1209.92	11.27	1.93	-9.26	7.35	-5.36	30.2842	232502.55	2673.50	232.49	232487.01	281.67	2.13
800103	220000.	-1187.26	48.39	-0.02	-3.44	0.19	1.92	32.3532	248429.29	3026.44	248.41	248410.78	-190.99	356.58
800104	0.	-1008.66	-31.85	0.08	-11.63	-0.11	2.34	34.2400	262918.02	4321.32	262.88	262882.30	329.56	2.74

Table No. 1 -- Cowell Drag Versus Cowell No Drag

DATE OF DATA		POSITION DIFFERENCES (METERS)				POSITION DIFFERENCES DEGREES		SEC.S	POSITION DIFFERENCES (METERS)		(KM.)	POSITION DIFFERENCES (METERS)		(DEG.)
YYMMDD	HHMMSS	DA	PPM DE	(10**3) DI	DELH	DELG	DELM	DELTIME	TOTAL ERROR	RADIAL	IN TRACK	ALONG TRACK	CROSS TRACK	TRUE ANOMALLY
800101	0.	594.11	44.91	0.34	1.32	-0.79	1.15	5.6939	43709.82	428.87	43.71	43707.65	-75.40	360.00
800101	20000.	691.75	-13.88	-1.07	-1.54	-1.96	2.27	4.7809	36712.55	842.27	36.70	36702.59	-147.85	350.43
800101	40000.	447.19	-36.69	-0.76	-2.31	1.36	-1.11	3.7730	28981.16	752.25	28.97	28971.34	-52.64	1.24
800101	60000.	624.41	35.66	0.33	-2.13	2.26	-2.06	2.9374	22550.98	373.43	22.55	22547.76	76.82	13.49
800101	80000.	410.42	9.69	0.07	-0.53	-2.85	3.00	2.2598	17349.19	277.66	17.35	17346.96	16.03	339.56
800101	100000.	441.00	-42.49	0.09	0.75	-1.42	1.51	1.5277	11755.50	742.22	11.73	11731.97	42.31	1.60
800101	120000.	449.28	-45.24	-0.25	2.52	3.19	-3.14	0.6968	5387.36	647.62	5.35	5348.24	-21.96	19.13
800101	140000.	331.87	46.47	-1.58	2.92	0.27	-0.27	0.1031	829.90	35.60	0.79	791.73	-246.24	344.47
800101	160000.	376.14	4.31	-1.07	-0.82	-1.87	-358.16	-0.3938	3045.76	349.40	-3.02	-3023.72	-108.08	1.41
800101	180000.	300.53	-20.72	0.90	-1.12	1.18	-1.24	-1.0090	7758.30	427.55	-7.75	-7745.61	-118.39	7.71
800101	200000.	268.32	30.87	2.16	0.01	-0.12	0.03	-1.3814	10605.06	67.12	-10.60	-10604.83	16.26	359.38
800101	220000.	113.58	-25.71	1.97	3.08	-1.55	1.44	-1.6586	12739.52	287.15	-12.73	-12733.15	282.25	355.61
800102	0.	275.[illegible]	-14.00	-0.05	2.42	0.65	-0.78	-2.0490	15738.25	391.59	-15.73	-15733.01	108.21	357.94
800102	20000.	174.56	11.24	-0.86	-2.09	1.67	-1.82	-2.3653	18159.49	85.55	-18.16	-18158.63	154.23	9.53
800102	40000.	74.89	13.16	-0.52	-3.00	-2.03	1.86	-2.5524	19592.75	-19.64	-19.59	-19592.72	-22.86	346.46
800102	60000.	150.54	-21.82	-0.37	-1.95	-1.27	1.09	-2.7453	21083.82	327.99	-21.08	-21081.00	-105.67	359.53
800102	80000.	-1.57	-45.45	-0.05	1.45	2.56	-2.76	-3.0155	23149.74	278.33	-23.15	-23148.05	-28.80	12.65
800102	100000.	142.42	85.35	-0.52	2.75	0.94	-1.14	-3.0665	23545.54	-360.06	-23.54	-23542.26	-157.24	348.25
800102	120000.	-38.63	16.98	-1.40	1.81	-3.91	3.71	-2.9293	22492.86	-91.48	-22.49	-22492.67	10.46	4.62
800102	140000.	-4.51	-64.70	-1.30	1.48	-0.12	-0.08	-3.0666	23546.17	473.65	-23.54	-23540.81	166.61	3.15
800102	160000.	-61.32	16.54	-0.83	-0.35	2.35	-2.54	-3.1158	23922.35	-121.59	-23.92	-23922.04	6.10	357.14
800102	180000.	-110.15	28.16	1.02	0.06	-2.18	1.99	-2.8687	22025.45	-259.32	-22.02	-22023.66	109.29	2.72
800102	200000.	-68.41	-5.10	2.43	1.49	-0.14	-0.03	-2.6386	20259.68	-3.32	-20.26	-20259.19	-141.42	354.53
800102	220000.	-167.17	10.30	1.19	1.89	0.99	-1.14	-2.3659	18167.15	-230.43	-18.17	-18164.99	-159.35	6.65
800103	0.	-114.23	36.11	-0.74	0.74	-1.60	1.47	-1.9904	15283.48	-350.93	-15.28	-15279.18	-92.45	355.39
800103	20000.	-312.41	-26.13	-0.99	-1.73	-1.40	1.29	-1.6309	12523.54	-132.41	-12.52	-12522.60	-76.87	357.94
800103	40000.	-202.76	-26.22	-0.25	-2.43	0.99	-1.07	-1.3481	10349.61	-34.61	-10.35	-10349.14	92.37	8.14
800103	60000.	-333.42	41.72	0.24	-1.44	1.72	-1.77	-0.9065	6985.24	-587.53	-6.96	-6960.07	76.68	352.29
800103	80000.	-359.05	18.86	0.10	-0.41	-3.44	3.42	-0.2492	1966.27	-453.53	-1.91	-1913.18	-16.52	5.82
800103	100000.	-324.62	-78.69	0.00	1.11	0.09	-0.08	0.1867	1448.63	208.29	1.43	1433.56	6.91	357.00
800103	120000.	-482.02	7.34	-1.20	2.77	4.04	-3.99	0.6277	4849.92	-508.58	4.82	4819.67	-183.93	355.90
800103	140000.	-383.08	81.50	-1.69	-0.83	-1.19	1.29	1.4640	11277.53	-902.64	11.24	11239.63	-196.35	8.79
800103	160000.	-483.05	-45.31	-0.05	-2.38	-2.53	2.67	2.1916	16826.88	-202.48	16.83	16825.45	-84.94	352.43
800103	180000.	-502.62	-25.42	1.64	-2.15	1.96	-1.77	2.8421	21825.75	-311.47	21.82	21823.49	38.26	2.94
800103	200000.	-592.34	30.79	2.46	-0.01	1.88	-1.63	3.7878	29089.01	-744.17	29.08	29078.04	290.13	2.13
800103	220000.	-530.78	4.23	0.81	1.82	-1.59	1.89	4.8126	36954.96	-477.29	36.95	36951.80	77.16	356.58
800104	0.	-545.68	-32.20	-0.58	-3.09	1.36	-0.98	5.6795	43605.44	-192.70	43.60	43604.75	152.50	2.74

Table No. 2 -- Cowell Drag Versus Brouwer-Lyddane

DATE OF DATA		POSITION DIFFERENCES (METERS)			POSITION DIFFERENCES DEGREES			SEC.S	POSITION DIFFERENCES (METERS)		(KM.)	POSITION DIFFERENCES (METERS)		(DEG.)
YYMMDD	HHMMSS	DA	PPM DE	(10**3) DI	DELH	DELG	DELM	DELTIME	TOTAL ERROR	RADIAL	IN TRACK	ALONG TRACK	CROSS TRACK	TRUE ANOMALLY
800101	0.	-42.47	62.17	0.35	2.03	-358.28	358.27	-0.1073	954.03	-466.68	-0.82	-824.03	-115.61	360.00
800101	20000.	66.62	16.37	-1.19	-0.25	-4.77	4.77	0.0799	642.93	-135.65	0.61	613.21	-137.60	350.43
800101	40000.	-118.56	-69.17	-0.61	-1.59	-0.22	0.21	-0.0216	389.17	350.83	-0.17	-165.82	-29.60	1.24
800101	60000.	51.51	9.18	0.22	-1.57	4.16	-4.16	-0.1189	923.44	-126.79	-0.91	-912.82	58.43	13.49
800101	80000.	-89.44	42.92	0.11	0.13	-3.89	3.88	0.0184	499.63	-479.18	0.14	141.08	10.87	339.56
800101	100000.	-38.35	-48.08	0.10	0.97	357.28	-357.28	0.0902	752.99	289.41	0.69	692.99	54.86	1.60
800101	120000.	-7.36	-72.28	-0.27	2.78	3.27	-3.28	-0.1217	999.30	354.11	-0.93	-934.12	-25.10	19.13
800101	140000.	-68.59	62.26	-1.57	3.01	1.05	-1.06	-0.1309	1128.02	-447.29	-1.00	-1005.04	-249.53	344.47
800101	160000.	2.55	14.83	-1.05	-0.84	-2.44	-357.56	0.0026	146.23	-96.83	0.02	19.79	-107.77	1.41
800101	180000.	-51.13	-31.02	0.88	-1.31	0.63	-0.63	-0.0936	743.38	149.16	-0.72	-718.39	-119.49	7.71
800101	200000.	-55.72	26.83	2.16	-0.10	0.49	-0.49	-0.0145	262.78	-237.10	-0.11	-111.13	22.10	359.38
800101	220000.	-151.16	-20.50	2.03	2.68	-1.07	1.07	0.0831	696.32	-21.06	0.64	637.59	279.11	355.61
800102	0.	20.43	-7.68	-0.12	2.08	0.61	-0.61	0.0746	586.02	74.89	0.57	572.64	99.47	357.94
800102	20000.	-32.88	10.26	-0.77	-2.44	1.24	-1.23	0.0857	690.05	-126.49	0.66	657.81	165.72	9.53
800102	40000.	-97.39	-1.20	-0.56	-3.68	-0.94	0.95	0.0776	605.80	-107.66	0.60	595.88	-18.37	346.46
800102	60000.	7.59	-8.99	-0.39	-2.24	-0.35	0.36	0.0692	549.87	67.90	0.53	531.76	-122.39	359.53
800102	80000.	-104.01	-24.18	0.05	0.73	1.62	-1.61	0.0147	117.54	23.03	0.11	113.18	-21.78	12.65
800102	100000.	64.74	52.19	-0.64	2.20	0.67	-0.67	0.0025	303.85	-267.28	0.02	19.35	-143.22	348.25
800102	120000.	-61.07	12.10	-1.29	1.37	-1.94	1.94	0.0909	709.17	-125.79	0.70	697.89	-6.14	4.62
800102	140000.	-19.66	-25.66	-1.34	0.66	-0.25	0.25	0.0136	247.69	154.95	0.10	104.43	162.59	3.15
800102	160000.	-49.10	-2.82	-0.85	-0.69	0.59	-0.59	-0.0382	295.43	-26.36	-0.29	-293.16	25.36	357.14
800102	180000.	-29.96	-10.66	1.11	-0.62	0.30	-0.30	-0.0928	720.75	40.78	-0.71	-712.25	102.51	2.72
800102	200000.	13.21	41.95	2.33	0.98	1.54	-1.54	-0.0334	393.08	-255.27	-0.26	-256.60	-153.30	354.53
800102	220000.	-35.76	33.74	1.28	1.52	-1.74	1.74	0.1652	1299.38	-240.64	1.27	1268.57	-145.61	6.65
800103	0.	55.94	-30.70	-0.75	0.15	-0.84	0.85	0.1061	858.98	257.09	0.81	814.74	-89.15	355.39
800103	20000.	-115.94	-2.63	-1.01	-1.95	1.84	-1.83	0.0085	144.01	-92.77	0.07	65.00	-88.92	357.94
800103	40000.	28.90	40.77	-0.20	-2.79	-1.40	1.41	0.0945	766.54	-228.20	0.73	725.44	96.13	8.14
800103	60000.	-60.04	-29.71	0.22	-1.65	-0.82	0.83	0.0566	460.23	126.22	0.43	434.76	82.85	352.29
800103	80000.	-53.59	-17.44	0.12	-0.49	0.57	-0.57	-0.0213	173.73	55.90	-0.16	-163.35	-19.36	5.82
800103	100000.	5.78	11.21	0.01	1.12	0.14	-0.14	-0.0072	89.17	-69.49	-0.06	-55.58	5.74	357.00
800103	120000.	-124.11	-18.77	-1.18	2.81	-0.28	0.27	-0.0027	187.01	0.01	-0.02	-20.75	-185.86	355.90
800103	140000.	18.98	-13.34	-1.73	-0.52	1.44	-1.44	-0.1340	1049.67	84.16	-1.03	-1028.69	-191.13	8.79
800103	160000.	-37.35	44.10	0.05	-1.97	1.08	-1.09	-0.1558	1240.43	-320.32	-1.20	-1195.81	-78.09	352.43
800103	180000.	-53.15	21.69	1.56	-1.81	356.96	-356.96	0.0241	266.36	-189.68	0.19	185.40	24.35	2.94
800103	200000.	-76.11	-83.95	2.50	0.99	0.05	-0.05	-0.0561	715.62	491.93	-0.43	-430.82	290.71	2.13
800103	220000.	19.77	32.17	0.91	2.34	-355.94	355.94	-0.1480	1155.90	-184.94	-1.14	-1136.43	102.10	356.58
800104	0.	-7.22	76.00	-0.78	-1.87	-2.69	2.70	0.0979	921.52	-515.32	0.75	751.99	134.73	2.74

Table No. 3 -- Cowell Drag Versus $\dot{B}g$

Table # 4

SMM IN TRACK ERROR (km.)

		COWELL	$\dot{B}g$		COWELL	$\dot{B}g$		COWELL	$\dot{B}g$	
	EPOCH	80/03/14	80/03/14		80/03/20	80/03/20		80/08/0/	80/08/0/	
0	L.C.	-0.02	-.0.32		0.13	0.06		0.09	0.71	
2	ARC	-0.05	0.22		-0.18	-0.04		0.12	0.85	
	PREDICTS									
2	"	-0.44	0.66		-2.96	-1.87		2.41	2.31	
4	"	-2.82	-0.81		-6.78	-4.08		6.43	4.67	
6	"	-10.39	-7.46		-19.62	-14.66		13.02	8.73	
8	"	-27.15	-23.28		-42.60	-34.60		22.88	15.28	
10	"	-51.66	-46.88		-77.20	-65.26		38.18	26.60	
12	"	-91.94	-86.26		-123.75	-106.96		62.09	45.88	
14	"	-149.09	-142.39		-176.93	-154.47		95.58	74.00	
16	"	-224.58	-216.62		-237.02	-208.23		141.93	114.11	

REFERENCES

1. Brouwer, D., "Solution of the Problem of Artifical Satellite Theory Without Drag," The Astronomical Journal, Volume 64, October, 1959, pages 378-397.

2. Von Zeipel, H., Arkiv Mathematics, Astronomy, Physics, Volume 11, No. 1, 1916.

3. Lyddane, R. H., "Small Eccentricities or Inclinations in the Brouwer Theory of Artifical Satellite Motion," The Astronomical Journal, Volume 68, June, 1963, pages 555-558.

4. Gordon, R. A., Mistretta, G. D., and Watson, J. S., "A Comparison of Classical Analytic Theories for the Motion of Artifical Satellites," Journal of Guidance and Control, Volumes 2 and 3, May and June, 1979, page 184.

5. Walter, H. G., "Conversion of Osculating Orbital Elements into Mean Elements," The Astronomical Journal, Volume 72, October 1967, pages 994-997.

Appendix

$$\underline{\Omega}(t) = \underline{B}_g(\bar{\underline{\Omega}}(t_o), t)$$

Geodynamic Constants:

$Gm = 398600.8 \ km^3/sec^2$

$a_e = 6378.14 \ km$

$u = 1$

$R_e = 1$

$k_e = \sqrt{\frac{Gm}{a_e^3}}$

Zonal Harmonics:

$J_2 = -0.0010826517$

$J_3 = 0.0000025450306$

$J_4 = 0.0000016714987$

$k_2 = -\frac{1}{2} J_2 R_e^2$

$k_3 = J_3 R_e^3$

$k_4 = J_4 R_e^4$

Define fractions:

$1/2, 1/3, 1/4, 3/2, 3/8, 3/32, 5/4, 5/16, 15/16$

Input: BRWGOR$(\bar{\underline{\Omega}}, \underline{\Omega}$, IDPERT, IDPASS, IDMEAN, $\underline{B}, t)$

$\bar{\underline{\Omega}}(t_o) \equiv (a_o'', e_o'', i_o'', h_o'', g_o'', l_o'')$ epoch mean elements.

a = Semi-major axis

e = eccentricity

i = inclination

g = argument of perigee

h = Longitude of ascending Node

l = Mean anomaly

$$\text{IDPERT} = \begin{cases} 1 \rightarrow B_g''(\bar{\underline{\Omega}}(t_o), t) & \text{evaluate secular elements} \\ \neq 1 \rightarrow B_g(\underline{\Omega}(t), t) & \text{evaluate osculating elements} \end{cases}$$

$$\text{IDPASS} = \begin{cases} 1 \rightarrow B_g(\bar{\underline{\Omega}}(t_o), t) & \text{initialize theory at } t=0 \text{ epoch} \\ 2 \rightarrow B_g(\underline{\Omega}(t), t) & \text{evaluate theory at time } (t) \end{cases}$$

$$IDMEAN = \begin{cases} 0 \rightarrow B_g(t=0, \underline{\Omega}) & \text{osculating elements input for osculating to mean conversion} \\ \neq 0 \rightarrow B_g(t, \bar{\underline{\Omega}}) & \text{Mean elements input for updating osculating elements} \end{cases}$$

<u>Output</u>:

$$\bar{\underline{\Omega}}_i \equiv (a_o'', e_o'', i_o'', h'', g'', l'')$$
$$\underline{\Omega}_i \equiv (a, e, i, h, g, l)$$
$$\mathcal{B}_i \equiv (E', P, g', n, f')$$

E' -- long Period Eccentric Anomaly
P -- mean Period
g' -- long Period argument of perigee
n -- "mean" mean motion
f' -- long Period true anomaly

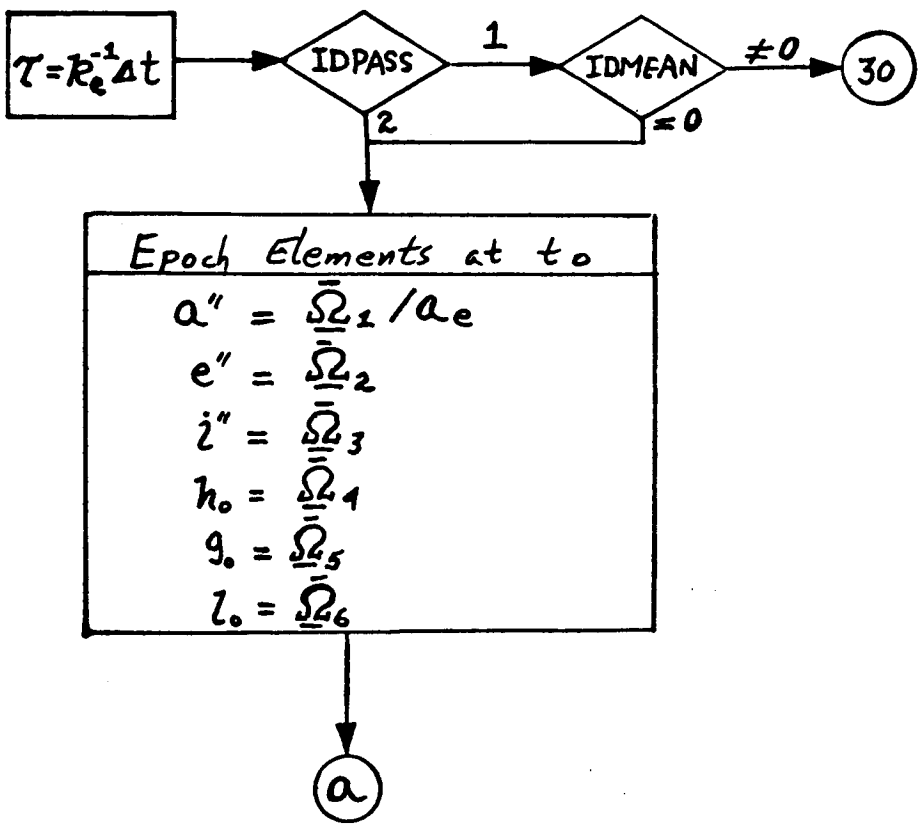

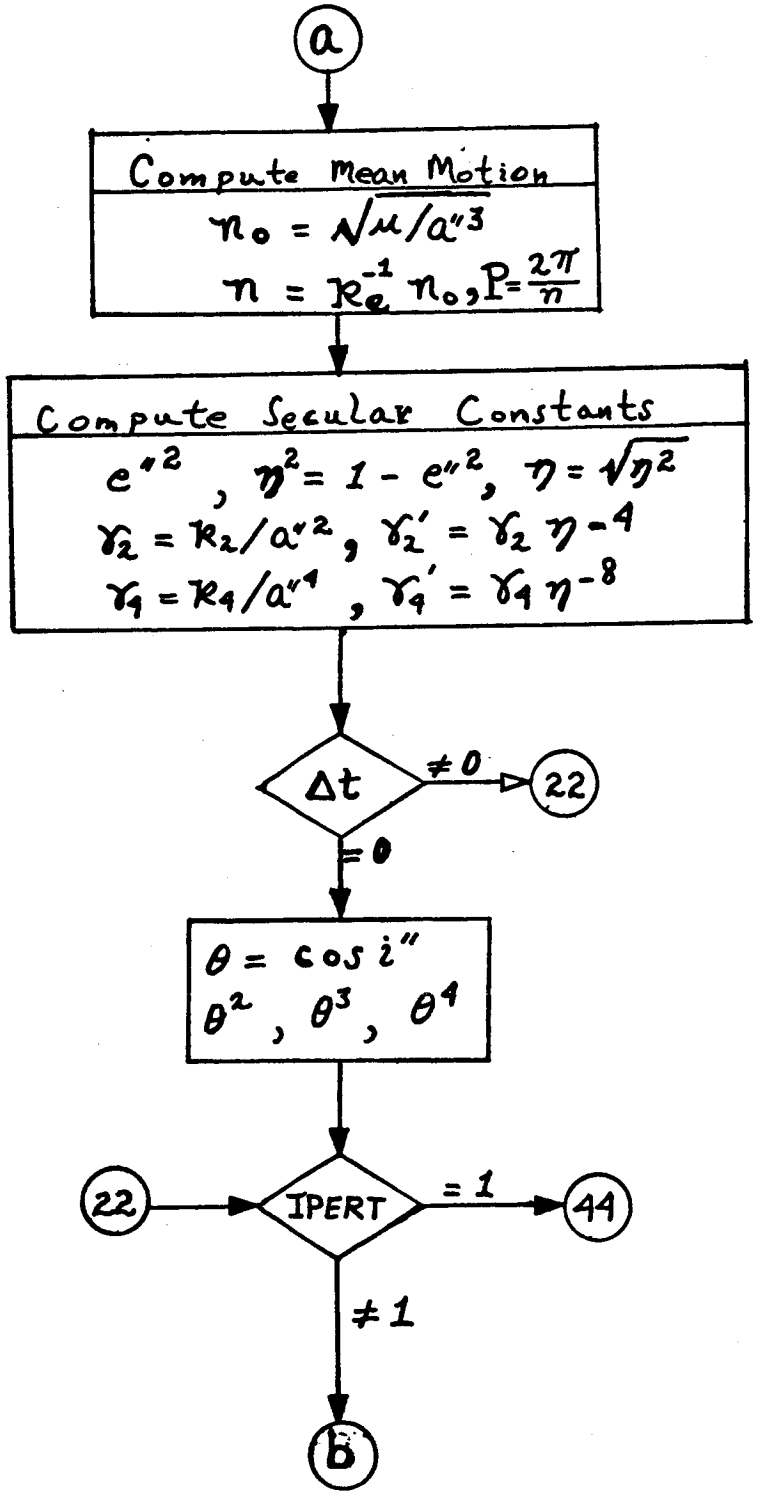
a
Compute Mean Motion
$n_0 = \sqrt{\mu / a''^3}$
$n = k_e^{-1} n_0, P = \frac{2\pi}{n}$
Compute Secular Constants
$e''^2, \eta^2 = 1 - e''^2, \eta = \sqrt{\eta^2}$
$\gamma_2 = k_2 / a''^2, \gamma_2' = \gamma_2 \eta^{-4}$
$\gamma_4 = k_4 / a''^4, \gamma_4' = \gamma_4 \eta^{-8}$
Δt
$\neq 0$
22
$= 0$
$\theta = \cos i''$
$\theta^2, \theta^3, \theta^4$
22
IPERT
$= 1$
44
$\neq 1$
b

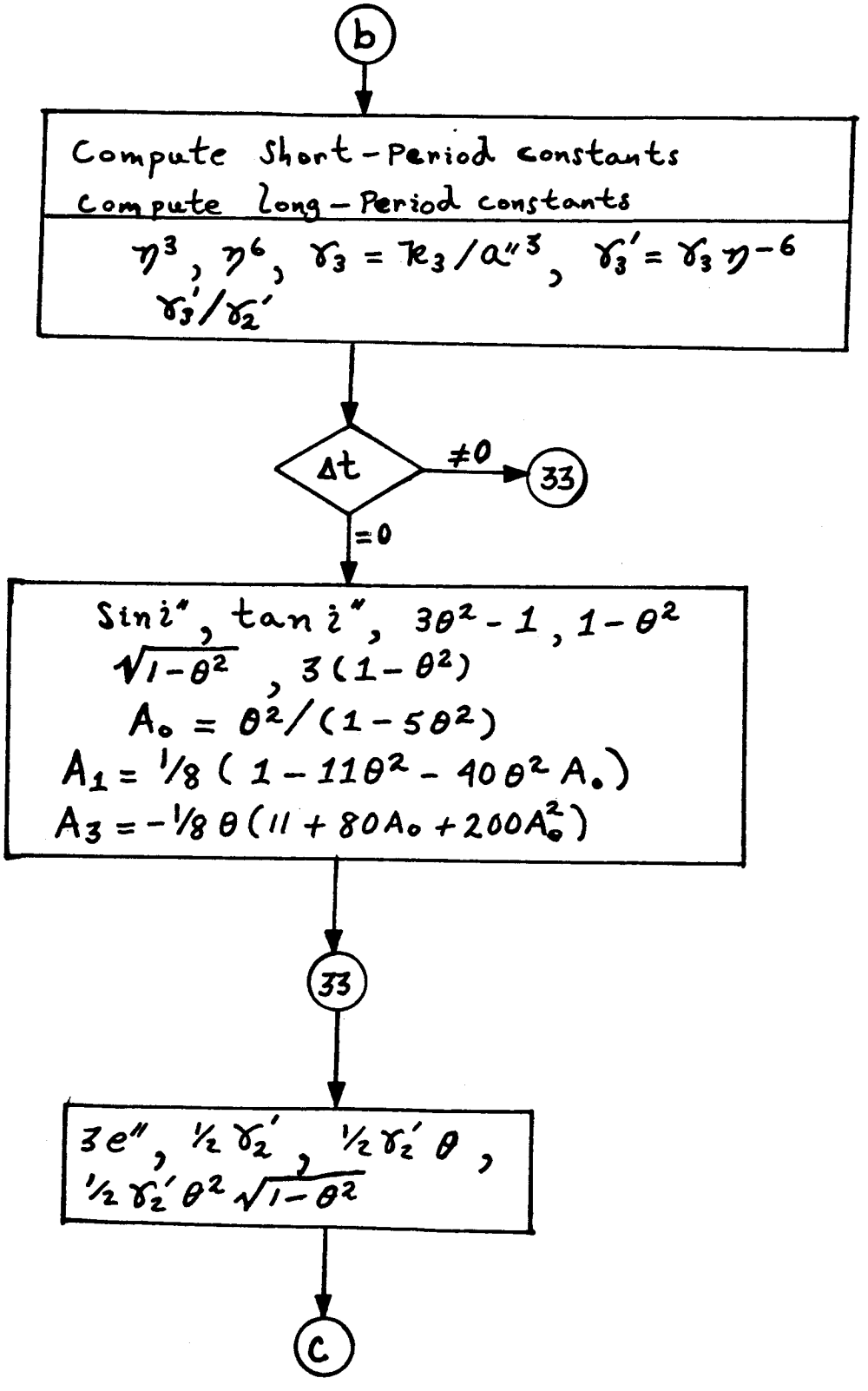
b
Compute Short-Period constants
Compute Long-Period constants
η^3, η^6, $\gamma_3 = k_3/a''^3$, $\gamma_3' = \gamma_3 \eta^{-6}$
γ_3'/γ_2'
Δt
$\neq 0$
33
$= 0$
$\sin i''$, $\tan i''$, $3\theta^2 - 1$, $1 - \theta^2$
$\sqrt{1-\theta^2}$, $3(1-\theta^2)$
$A_0 = \theta^2/(1-5\theta^2)$
$A_1 = 1/8\,(1 - 11\theta^2 - 40\theta^2 A_0)$
$A_3 = -1/8\,\theta(11 + 80A_0 + 200A_0^2)$
33
$3e''$, $1/2\,\gamma_2'$, $1/2\,\gamma_2'\theta$,
$1/2\,\gamma_2'\theta^2\sqrt{1-\theta^2}$
c

C

$$A_2 = \eta^3 \gamma_2' A_1 - \tfrac{1}{16}\gamma_2' \left\{ \begin{array}{l} 2 + e''^2 - 400 e''^2 \theta^2 A_0^2 \\ -40(5e''^2 + 2)\theta^2 A_0 \\ -11\theta^2(3e''^2 + 2) \end{array} \right\}$$

$$A_4 = \tfrac{1}{4}(\gamma_3'/\gamma_2') \sin i'' \quad , \quad A_5 = e''\theta A_4/(1+\theta)$$

44 → IDMEAN $=0$ → 50

IDMEAN $\neq 0$ → IDPASS

30 → IDPASS $=2$ → 40

IDPASS $\neq 2$ →

Compute $\dot{i}''$, $\dot{g}''$, $\dot{h}''$

$$\dot{i}'' = \left\{ \begin{array}{l} \gamma_2' \left[\frac{3}{2}(3\theta^2 - 1) + \gamma_2' \left(\frac{3}{32}\right)[\theta^2(30 - 96\eta - 90\eta^2) \\ \quad + (16\eta + 25\eta^2 - 15) + \theta^4(144\eta + 25\eta^2 + 105)] \right] \\ \quad + e''^2 \gamma_4' \left(\frac{15}{16}\right)(3 + 35\theta^4 - 30\theta^2) \end{array} \right\} \eta n_0$$

$$\dot{g}'' = n_0 \left\{ \begin{array}{l} \frac{3}{2}\gamma_2'(5\theta^2 - 1) + \frac{3}{32}\gamma_2'^2 [25\eta^2 + 24\eta - 35 \\ \quad + (90 - 192\eta - 126\eta^2)\theta^2 + (385 + 360\eta + 45\eta^2)\theta^4] \\ + \frac{5}{16}\gamma_4'[21 - 9\eta^2 + (126\eta^2 - 270)\theta^2 + (385 - 189\eta^2)\theta^4] \end{array} \right\}$$

$$\dot{h}'' = n_0 \left\{ \begin{array}{l} -3\gamma_2'\theta \\ \frac{3}{8}\gamma_2'^2 [(9\eta^2 + 12\eta - 5) + (-5\eta^2 - 36\eta - 35)\theta^3] \\ \frac{5}{4}\gamma_4'(5 - 3\eta^2)\theta(3 - 7\theta^2) \end{array} \right\}$$

d

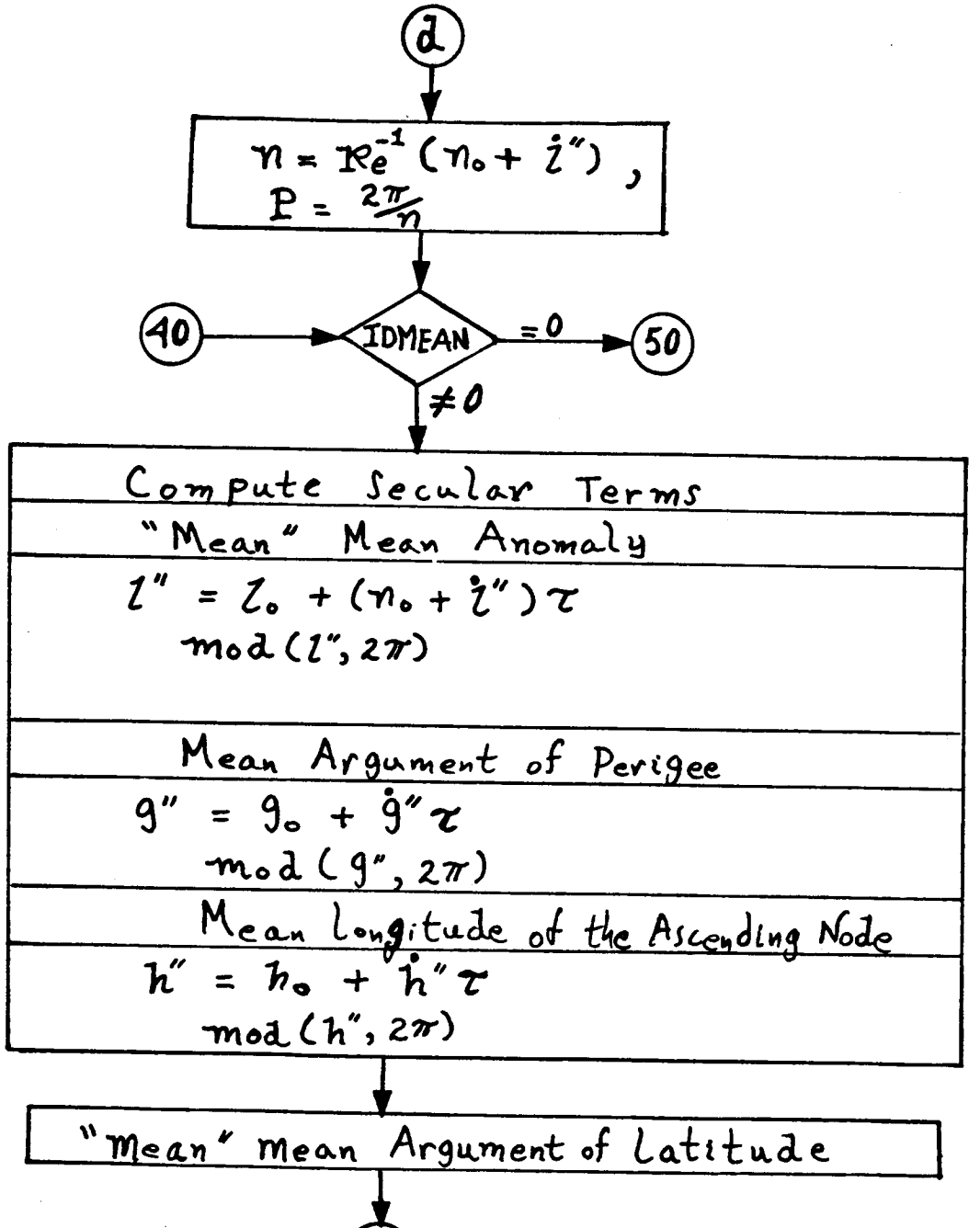
d
$n = R_e^{-1}(n_0 + \dot{l}'')$,
$P = 2\pi/n$
40
IDMEAN
=0
50
≠0
Compute Secular Terms
"Mean" Mean Anomaly
$l'' = l_0 + (n_0 + \dot{l}'')\tau$
$\mathrm{mod}(l'', 2\pi)$
Mean Argument of Perigee
$g'' = g_0 + \dot{g}''\tau$
$\mathrm{mod}(g'', 2\pi)$
Mean Longitude of the Ascending Node
$h'' = h_0 + \dot{h}''\tau$
$\mathrm{mod}(h'', 2\pi)$
"Mean" Mean Argument of Latitude
50
$a = a''$, $e = e''$, $l = l''$
$e' = e''$, $g' = g''$, $l' = l''$
e

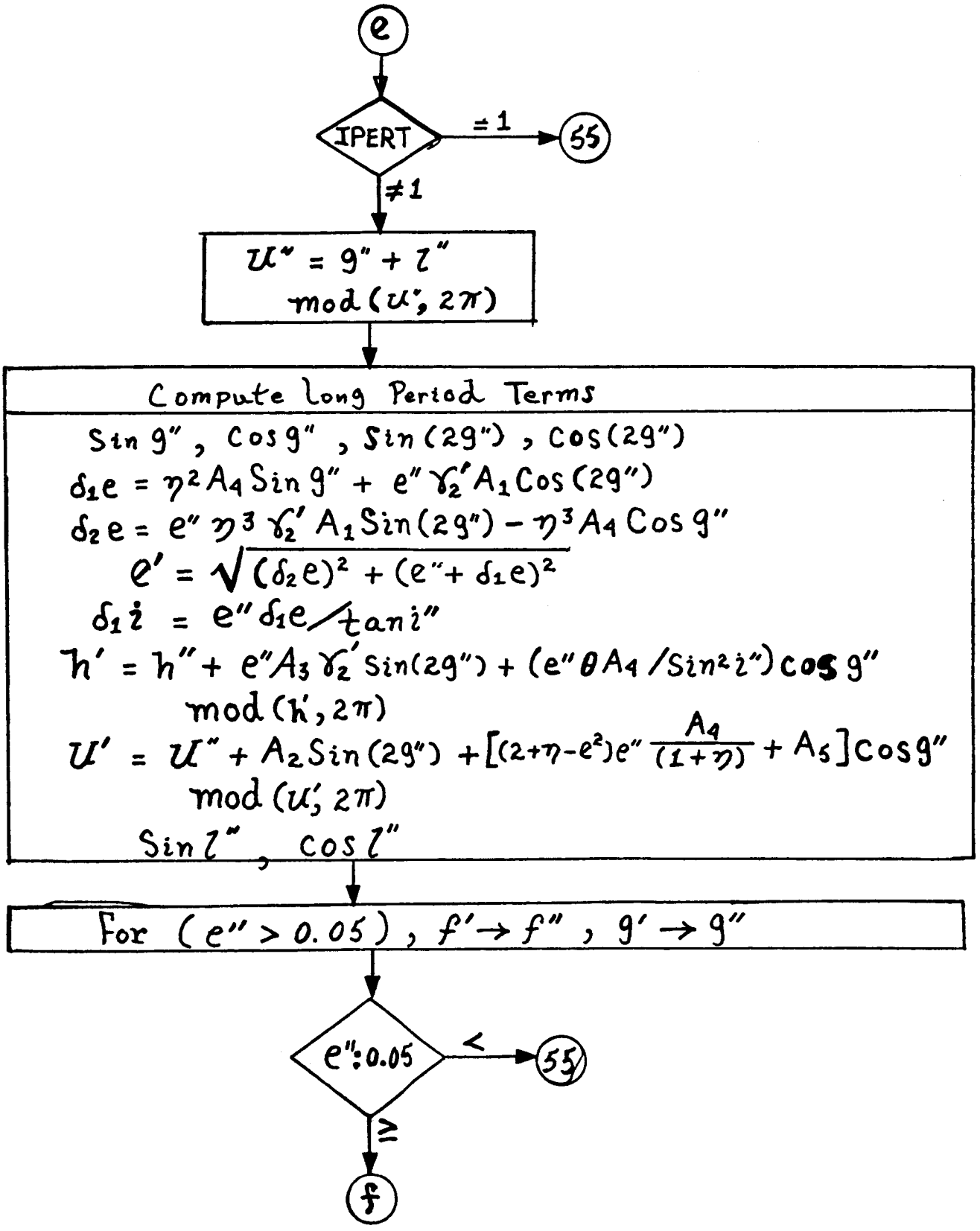
e
IPERT
= 1
55
≠ 1
$u'' = g'' + l''$
$\mod(u'', 2\pi)$
Compute Long Period Terms
$\sin g''$, $\cos g''$, $\sin(2g'')$, $\cos(2g'')$
$\delta_1 e = \eta^2 A_4 \sin g'' + e'' \gamma_2' A_1 \cos(2g'')$
$\delta_2 e = e'' \eta^3 \gamma_2' A_1 \sin(2g'') - \eta^3 A_4 \cos g''$
$e' = \sqrt{(\delta_2 e)^2 + (e'' + \delta_1 e)^2}$
$\delta_1 i = e'' \delta_1 e / \tan i''$
$h' = h'' + e'' A_3 \gamma_2' \sin(2g'') + (e'' \theta A_4 / \sin^2 i'') \cos g''$
$\mod(h', 2\pi)$
$u' = u'' + A_2 \sin(2g'') + [(2+\eta-e^2)e'' \frac{A_4}{(1+\eta)} + A_5] \cos g''$
$\mod(u', 2\pi)$
$\sin l''$, $\cos l''$
For $(e'' > 0.05)$, $f' \to f''$, $g' \to g''$
$e'' : 0.05$
<
55
≥
f

f

$$l' = \tan^{-1}\left(\frac{\delta_2 e \cos l'' + (e'' + \delta_1 e)\sin l''}{(e'' + \delta_1 e)\cos l'' - (\delta_2 e \sin l'')}\right)$$

$$\mathrm{mod}(l', 2\pi)$$

$$g' = u' - l'$$

$$\mathrm{mod}(g', 2\pi)$$

$$\sin g'' \leftarrow \sin g', \quad \cos g'' \leftarrow \cos g'$$

$$\sin(2g'') \leftarrow \sin(2g'), \quad \cos(2g'') \leftarrow \cos(2g')$$

55

$E' \Leftarrow K(l', e')$

(Solve Kepler's Eq.)

Compute True Anomaly f'

$$f' = \tan^{-1}\left(\frac{\sqrt{1 - e'^2}\,\sin E'}{\cos E' - e'}\right)$$

$$\mathrm{mod}(f', 2\pi)$$

IPERT

$= 1$ → 60

$\neq 1$ → 9

9

$$\alpha = \frac{1}{1 - e' \cos E'}$$

$$\alpha^2 \ , \ \alpha^3$$

$$\sin f' = \alpha \sqrt{1 - e'^2} \sin E'$$

$$\cos f' = \alpha (\cos E' - e')$$

$$\cos^2 f' , \ \cos(2f') , \ \sin(2f') , \ \cos(3f') , \ \sin(3f')$$

$$\sin(2g' + f') , \ \sin(2g' + 2f') , \ \sin(2g' + 3f')$$

$$\cos(2g' + f') , \ \sin(2g' + 2f') , \ \sin(2g' + 3f')$$

Semi - major Axis

$$a = a'' \left\{ 1 + \tfrac{1}{2} \left[(3\theta^2 - 1)(\alpha^3 - \eta^{-3}) + 3(1 - \theta^2)\alpha^3 \cos(2g' + 2f') \right] \right\}$$

h

h

Compute eccentricity

$$\delta_1 e = \delta_1 e + \frac{1}{2}\eta^2 \left\{ \begin{array}{l} 3\left(\frac{1}{\eta^6}\right)\gamma_2(1-\theta^2)\cos(2g'+2f')\left[3e''\cos^2 f' + 3\cos f' + e''^2\cos^3 f' + e''\right] \\ -\gamma_2'(1-\theta^2)\left[3\cos(2g'+2f') + \cos(3f'+2g')\right] \\ (3\theta^2-1)\gamma_2\left(\frac{1}{\eta^6}\right)\left[e''\eta + \left(\frac{e''}{1+\eta}\right) + 3e''\cos^2 f' + 3\cos f' + e''^2\cos^3 f'\right] \end{array} \right\}$$

$$\delta_2 e = \delta_2 e - \frac{1}{4}\eta^3\gamma_2' \left\{ \begin{array}{l} 2(3\theta^2-1)(\alpha^2\eta^2 + \alpha + 1)\sin f' \\ +3(1-\theta^2)\left[\begin{array}{l}(-\alpha^2\eta^2 - \alpha + 1)\sin(2g'+f') \\ +(\alpha^2\eta^2 + \alpha + \frac{1}{3})\sin(3g'+f')\end{array}\right] \end{array} \right\}$$

$$e = \sqrt{(\delta_2 e)^2 + (e'' + \delta_1 e)^2}$$

compute i inclination

$$i = i'' + \delta_1 i + \frac{1}{2}\gamma_2'\theta\sqrt{1-\theta^2}\left[3\cos(2g'+2f') + 3e''\cos(2g'+f') + e''\cos(2g'+3f')\right]$$
$$\mathrm{mod}(i, 2\pi)$$

compute h longitude of the ascending node

$$h = h' - \frac{1}{2}\gamma_2'\theta\left[6(f' - l' + e''\sin f') - 3\sin(2g'+2f') - 3e''\sin(2g'+f') - e''\sin(2g'+3f')\right]$$
$$\mathrm{mod}(h, 2\pi)$$

i

i

Compute ($\mathcal{U}$) - Mean Argument of latitude

$$\mathcal{U} = \mathcal{U}' + \left(\frac{1}{\eta+1}\right)\frac{1}{4}e''\gamma_2'\eta^2\left\{\begin{array}{l} 3(1-\theta^2)\left[\begin{array}{l}(1/3+\alpha^2\eta^2+\alpha)\sin(3f'+2g') \\ (1-\eta^2\alpha^2-\alpha)\sin(2g'+f')\end{array}\right] \\ +2(3\theta^2-1)(\eta^2\alpha^2+\alpha+1)\sin f' \end{array}\right\}$$

$$+\frac{3}{2}\gamma_2'(5\theta^2-1)(e''\sin f'+f'-l')$$

$$+\frac{1}{4}\gamma_2'(3-5\theta^2)\left\{\begin{array}{l} e''\sin(2g'+3f') \\ 3[\sin(2g'+2f')+e''\sin(2g'+f')] \end{array}\right\}$$

$$\mathrm{mod}(\mathcal{U}, 2\pi)$$

Compute l mean Anomaly

$$l = \tan^{-1}\left(\frac{\delta_2 e\cos l'' + (e''+\delta_1 e)\sin l''}{(e''+\delta_1 e)\cos l'' - (\delta_2 e\sin l'')}\right)$$

$$\mathrm{mod}(l, 2\pi)$$

j

j

Compute g Argument of Perigee

$$g = u - l$$
$$\bmod (g, 2\pi)$$

Store Secular, Osculating arrays

$$a'' = a'' a_e$$
$$a = a a_e$$
$$\bar{\Omega}, \Omega, \mathcal{B}$$

END

ANOTHER SEMI-ANALYTIC ORBIT THEORY

K. T. Alfriend*
Naval Research Laboratory

ABSTRACT

The Naval Research Laboratory for the past several years has been working on the development of an accurate analytic orbit theory. The major stumbling block has been the large number of terms in the coordinate (canonical) transformations. Recent research has been directed toward the development of techniques for reducing the number of terms. A recent development by Deprit shows considerable promise in this regard. A spin-off of Deprit's break through is the framework of a semi-analytic theory which (i) allows recovery of short period terms, a drawback of many semi-analytic theories, (ii) is accurate to $0(J_2^3)$, (iii) allows the use of any set of non-singular variables. Currently the theory is restricted to the zonal perturbations but it is felt it can be extended to include other perturbations.

*Head, Advanced Systems Branch, Space Systems Division, Naval Research Laboratory, Washington, D.C. 20375

SEMIANALYTICAL ORBIT DETERMINATION

P. Cefola*
Charles Stark Draper Laboratory

ABSTRACT

This paper describes an orbit determination capability based upon a semianalytical satellite theory. The goal is to achieve Special Perturbations accuracy with a significant increase in computational efficiency, while maintaining the flexibility to simply include new physical models and to easily truncate the theory based on actual accuracy requirements.

The semianalytical theory includes theoretical developments for the averaged equations of motion, the coefficients in the Fourier series expansions for the short-periodic variations in the orbit elements, and the partial derivatives of perturbed motion. The resulting algorithms employ the recursive analytical approach for gravitational and third-body paint mass perturbations and numerical quadrature constructions for the atmospheric drag and solar radiation pressure perturbations. The development also includes a generalized interpolator architecture whose goal is the rapid evaluation of the position, velocity, and partial derivatives at the output times. The interpolator architecture includes Hermite interpolation processes for the averaged elements and the partial derivatives of the averaged elements, and a Lagrangian interpolator for the coefficients in the short-periodic expansions. A short-arc interpolator for position, velocity, and the partial derivatives of position and velocity is also included; this option is advantageous when the output times are closely spaced. These capabilities have been implemented into a modified version of the Research and Development Goddard Trajectory Determination System that operates on the Amdahl 470/V8 computer at CSDL. Differential Correction (DC) tests of the semianalytical orbit determination package will be discussed.

*Section Leader, Space Systems Analysis, Air Force Programs Department.

SEMIANALYTICAL SATELLITE THEORY AND SEQUENTIAL ESTIMATION

Stephen P. Taylor
Massachusetts Institute of Technology
and
Charles Stark Draper Laboratory

Paul J. Cefola
Massachusetts Institute of Technology
and
Charles Stark Draper Laboratory

ABSTRACT

Kalman filtering techniques are combined with a semianalytical orbit generator to develop a sequential orbit determination algorithm. The algorithm is investigated for computational efficiency, accuracy, and radius of convergence by comparison with truth ephemerides and a Cowell Special perturbations filter (GTDS FILTER). Test cases relevant to satellite navigation are examined.

Notation and Symbols

sub-bar (e.g., $\underline{x}$) = vector

super-bar (e.g., $\bar{x}$) = average or mean; also statistical mean

ϵ (e.g., $\epsilon\underline{\eta}$) = formal indication of the order of the quantity

(ϵ = first, ϵ^2 = second, ...)

$\underline{\varepsilon}_6 = [0\ 0\ 0\ 0\ 0\ 1]^T$

n = mean motion = $\sqrt{\frac{\mu}{a^3}}$

Equinoctial Elements

a = semimajor axis

$h = e \sin(\omega + I\Omega) \quad k = e \cos(\omega + I\Omega)$

$p = \tan^I(1/2) \sin \Omega \quad q = \tan^I(i/2) \cos \Omega$

$\lambda = M + \omega + I\Omega$ = mean longitude

I = retrograde factor

super-hat (e.g., $\hat{x}$) = predicted estimate

super-tilde (e.g., $\tilde{x}$) = updated estimate

1. INTRODUCTION

The current trends in Earth satellite orbit determination are toward sequential filtering and onboard computation [1]. The Global Positioning System (GPS) currently employs an orbit determination algorithm that updates a batch estimated nominal trajectory in real-time with an extended Kalman filter [2]. This system is designed to achieve an operational accuracy within 1.5 m. Telesat, a satellite communications system, has been using a sequential system to support all station keeping operations for several years now, with both improved accuracy and reduced costs [3]. Many other applications exist and will develop for which the timeliness, accuracy, and efficiency of a real-time orbit determination system are highly desirable.

Orbit determination processes require two capabilities: the ability to accurately propagate an orbit, given initial conditions; and some estimation algorithm indicating how observations of the satellite should be used in updating the ephemeris. Advances in the technology of either capability imply corresponding advances in orbit determination processes. Recently, much work has been done by P. Cefola, et al. [4], [5], [6], [7] of CSDL in extending Semianalytical Satellite Theory to allow highly accurate and efficient orbit propagation. A. Green [4] developed and used some of these results in a batch DC estimation algorithm, finding accuracies and convergence properties quite comparable to high precision Cowell results. This paper explores the implications of these advances in Semianalytical Satellite Theory for sequential orbit determination, considering both accuracy and efficiency through comparison with batch and sequential filters available from GTDS and Green [4].

The organization of the paper is dictated by the structure of the orbit determination problem. Summaries of semianalytical satellite theory and sequential filtering are presented first. Then their combination into an orbit determination algorithm is developed to give the algorithm as it was finally implemented. Results are not included here; they will be presented at the conference.

2. SEMIANALYTICAL SATELLITE THEORY

The accurate and efficient propagation of an ephemeris requires both a precise model of the forces acting on the satellite and an accurate and efficient means of integrating the equations of motion. The equations of motion are given by Newton's Second Law as

$$\frac{d^2\underline{r}}{dt^2} + \frac{\mu}{r^3}\,\underline{r} = \underline{a}_d \qquad [1]$$

The terms from left to right are the satellite's acceleration, the point-mass gravitational attraction, and all other (disturbing) accelerations, due to drag, third bodies, solar radiation, etc. The disturbing accelerations are typically several orders of magnitude smaller than the point-mass force.

Now any integrator is most accurate and efficient for systems with only small nonlinearities and low frequencies in the force model. Historically, this fact has motivated tradeoffs between analytical methods, which use simplified force models and analytical approximations to obtain the integrated ephemeris efficiently, and numerical methods, which retain the full force model and use high precision numerical integrators to obtain the integrated ephemeris quite accurately.

To increase the efficiency of an ephemeris generator, it is necessary to decrease both the magnitude of the nonlinearities as well as the high frequency content of the force model. The magnitude of the nonlinearities can be reduced by choice of the orbital elements. For example, Keplerian and equinoctial elements incorporate the effects of the point mass acceleration, leaving only the disturbing acceleration to be accounted for. The transformation from cartesian position and velocity to such an element set is the basis of Gauss' VOP equations. [In the early days of modern satellite orbit determination, many element sets incorporating different components of the disturbing acceleration were experimented with; while they could very efficiently propagate an ephemeris subject to only their selected perturbations, to achieve real-world accuracy they had to sacrifice all efficiency gains with the inclusion of additional perturbations.] The high frequency content is removed by averaging these frequencies out; more formally, by transforming from the current osculating elements described by the VOP equations, to mean elements described by "averaged VOP equations." For analytical theories, this whole process was done by hand, necessitating simplified force models and approximate methods. Semianalytical satellite theory, developed after computers became inexpensive and versatile, uses numerical methods to handle those force models that cannot be averaged analytically. Since the tradeoff between numerical averaging of the force model and the use of a high precision integrator on it is in favor of averaging by a factor of 10 to 100, semianalytical satellite theory is much more efficient than purely numerical theories. There is one problem: the transformation back from the mean elements to the osculating elements. The high frequency components or short periodics were averaged out and must be recovered before the mean elements can be used for anything other than long term, approximate prediction. The practical recovery of the short periodics constitutes one of the important contributions of the recent work at CSDL.

Semianalytical Satellite Theory at CSDL

Semianalytical satellite theory at CSDL is implemented in equinoctial elements to avoid singularity problems. The basic equations are shown formally in Table I. Key things to note are the dependence of the mean element rates on only the slowly varying elements $\bar{\underline{a}}$, and the expansion of the short periodics $\underline{n}$ ($\bar{\underline{a}}$, $\bar{\lambda}$) as a Fourier series whose coefficients similarly depend on only the slowly varying elements $\bar{\underline{a}}$. Thus the elements $\bar{\underline{a}}$ * and short periodic coefficients $\epsilon\underline{C}\sigma(\bar{\underline{a}})$ and $\epsilon\underline{D}\sigma(\bar{\underline{a}})$ can be and are interpolated, allowing efficient evaluation of the osculating elements for many output times other than those on the integration grid. This is significant since for all averaged theories the computational cost is proportional to the number of integration steps. Averaging allows large steps, but frequent output points could require small steps.

3. SEQUENTIAL FILTERING THEORY

The equations of motion for the osculating and mean orbital elements are shown in Table I. They are nonlinear, as are the equations for range and range rate observations given in Table II. The orbit determination problem is to estimate the satellite's orbit given some initial (a priori) information and a series of observations over time. It can be formulated as an optimal estimation problem:

$$\begin{array}{llll} \text{estimate} & \hat{\underline{x}}(t)\text{, given} & & \\ \text{plant} & \dot{\underline{x}} = \underline{f}(\underline{x}) + \underline{w} & , \quad \underline{x}(t_o) = \underline{x}_o & \\ \text{observations} & y_k = & h(\underline{x}(t_k), t_k) + v & \end{array} \qquad [2]$$

using the y_k, such that the variance of the error $\underline{x} - \underline{x}$ is minimum. $\underline{x}_o$, $\underline{w}$, and v are random and uncorrelated, $\underline{w}$ and v are white noise processes.

The resulting equations require propagating the probability density function of $\underline{x}$ (t) and are very difficult and expensive to solve. As a result, most sequential orbit determination schemes use some suboptimal filter, usually adapted from the Kalman filter, which solves the linear optimal estimation problem. The two most common adaptations are the Linearized Kalman Filter and the Extended Kalman

Table I. The Equations of Semianalytical Satellite Theory*

Osculating Elements	$\underline{a}^* = [a,h,k,p,q,\lambda]^T$
	$\underline{a} = [a,h,k,p,q]^T$
Mean elements	$\bar{\underline{a}}^* = [\bar{a},\bar{h},\bar{k},\bar{p},\bar{q},\bar{\lambda}]^T$
	$\bar{\underline{a}} = [\bar{a},\bar{h},\bar{k},\bar{p},\bar{q}]^T$
Osculating to mean transformation (the near identity transformation)	$\underline{a}^* = \bar{\underline{a}}^* + \varepsilon\underline{\eta}_1(\bar{\underline{a}},\bar{\lambda})$
Osculating VOP equations	$\frac{d\underline{a}^*}{dt} = \bar{n}\underline{\varepsilon}_6 + \varepsilon\,\underline{F}(\underline{a},\lambda)$
Mean VOP equations	$\frac{d\bar{\underline{a}}^*}{dt} = \bar{n}\underline{\varepsilon}_6 + \varepsilon\,\underline{A}_1(\bar{\underline{a}})$
Mean Element Rate	$\underline{A}_1(\bar{\underline{a}}) = \frac{1}{2\pi}\int_0^{2\pi} \varepsilon\,\underline{F}(\bar{\underline{a}},\bar{\lambda})\,d\bar{\lambda}$
Short Periodics	$\varepsilon\underline{\eta}_1(\bar{\underline{a}},\bar{\lambda}) = \frac{1}{\bar{n}}\int[\varepsilon\underline{F}(\bar{\underline{a}},\bar{\lambda}) - \varepsilon\underline{A}_1(\bar{\underline{a}})]d\bar{\lambda}$
	$- \frac{3}{2\bar{a}}\int \varepsilon\eta_{11}(\bar{\underline{a}},\bar{\lambda})\,\underline{\varepsilon}_6\,d\bar{\lambda}$
Periodicity of short periodics	$\underline{\eta}_1(\bar{\underline{a}},\bar{\lambda} + 2\pi) = \underline{\eta}_1(\bar{\underline{a}},\bar{\lambda})$
	$\int_0^{2\pi} \underline{\eta}_1(\bar{\underline{a}},\bar{\lambda})\,d\bar{\lambda} = 0$
Series Expansion of Short Periodics	
Assume	$\varepsilon\underline{F}(\bar{\underline{a}},\bar{\lambda}) = \sum_{\sigma=0}^{\infty} \varepsilon\underline{X}_\sigma(\bar{\underline{a}})\cos\sigma\bar{\lambda} + \varepsilon\,\underline{Z}_\sigma(\bar{\underline{a}})\sin\sigma\bar{\lambda}$

* Extracted from Green [4], which contains a good derivation

where

$$\varepsilon \underline{X}_{\sigma}(\bar{\underline{a}}) = \frac{1}{2\pi}\int_0^{2\pi} \varepsilon \underline{F}(\bar{\underline{a}},\bar{\lambda})\, d\bar{\lambda} = \varepsilon \underline{A}_1(\bar{\underline{a}})$$

$$\varepsilon \underline{X}_{\sigma}(\bar{\underline{a}}) = \frac{1}{\pi}\int_0^{2\pi} \varepsilon \underline{F}(\bar{\underline{a}},\bar{\lambda}) \cos \sigma\bar{\lambda}\, d\bar{\lambda}$$

$$\varepsilon \underline{Z}_{\sigma}(\bar{\underline{a}}) = \frac{1}{\pi}\int_0^{2\pi} \varepsilon \underline{F}(\bar{\underline{a}},\bar{\lambda}) \sin \sigma\bar{\lambda}\, d\bar{\lambda}$$

then

$$\varepsilon \underline{\eta}_1(\bar{\underline{a}},\bar{\lambda}) = \sum_{\sigma=1}^{\infty} \varepsilon \underline{C}_{\sigma}(\bar{\underline{a}}) \sin \sigma\bar{\lambda} - \varepsilon \underline{D}_{\sigma}(\bar{\underline{a}}) \cos \sigma\bar{\lambda}$$

where

$$\varepsilon \underline{C}_{\sigma}(\bar{\underline{a}}) = \frac{1}{\sigma\bar{n}}\, \varepsilon \underline{X}_{\sigma}(\bar{\underline{a}}) + \frac{3}{2\sigma\bar{a}}\, \varepsilon D_{1\sigma}(\bar{\underline{a}})\, \underline{\varepsilon}_6$$

$$\varepsilon \underline{D}_{\sigma}(\bar{\underline{a}}) = \frac{1}{\sigma\bar{n}}\, \varepsilon\, \underline{Z}_{\sigma}(\bar{\underline{a}}) - \frac{3}{2\sigma\bar{a}}\, \varepsilon C_{1\sigma}(\bar{\underline{a}})\, \underline{\varepsilon}_6$$

Partials

Solve Vector

$$\underline{x}^T = [\bar{\underline{a}}^{*T}\ \underline{c}^T]$$

$\underline{c}$ = parameter vector in force model

define partials

$$\Phi(t,t_o) = \frac{\partial \bar{\underline{a}}^*(t)}{\partial \bar{\underline{a}}^*(t_o)} = B_2$$

$$\Psi(t,t_o) = \frac{\partial \bar{\underline{a}}^*(t)}{\partial \underline{c}} = B_3$$

State partials equation

$$\frac{d}{dt}\Phi(t,t_o) = \left[\underline{\varepsilon}_6 \frac{\partial \bar{n}}{\partial \bar{\underline{a}}^*} + \frac{\partial \varepsilon \underline{A}_1}{\partial \bar{\underline{a}}^*}\right] \Phi(t,t_o)$$

Parameter Partials Equation

$$\frac{d}{dt}\Psi(t,t_o) = \left[\underline{\varepsilon}_6 \frac{\partial \bar{n}}{\partial \bar{\underline{a}}^*} + \frac{\partial \varepsilon \underline{A}_1}{\partial \bar{\underline{a}}^*}\right] \Psi(t,t_o) + \frac{\partial \varepsilon \underline{A}_1}{\partial \underline{c}}$$

Initial Conditions

$$\Phi(t,t_o) = \underline{I},\ \Psi(t,t_o) = \underline{O}$$

Table II. Range and Range-Rate Satellite Observations

Orbital elements

Mean equinoctial elements $\bar{\underline{a}}^* = [\bar{a},\bar{h},\bar{k},\bar{p},\bar{q},\bar{\lambda}]^T$

Osculating elements $\underline{a}^* = [a,h,k,p,q,\lambda]^T$

Cartesian inertial element transformation

$$\begin{bmatrix} \underline{P} \\ \underline{v} \end{bmatrix} = T(\underline{a}^*)$$

Cartesian local tangent element transformation

$\underline{r}_s$ = radius to origin of fram on earth's surface

$$\underline{P}_{LT} = D_{\underline{P}} - \underline{r}_s$$

$$\underline{v}_{LT} = D\underline{v} + \dot{D}_{\underline{P}}$$

range observation $\rho = \sqrt{\underline{P}_{LT} \cdot \underline{P}_{LT}}$

range rate observation $\dot{\rho} = \frac{1}{\rho} \underline{P}_{LT} \cdot \underline{v}_{LT}$

Filter. These and other nonlinear filters are discussed in Gelb [8].

The Linearized Filter is the most basic adaptation. The a priori mean state $\bar{\underline{x}}(t_o)$ is propagated forward in time to generate the nominal trajectory

$$\dot{\underline{x}}_N(t) = \underline{f}(\underline{x}_N) \quad ; \quad \underline{x}_N(t_o) = \bar{\underline{x}}_o(t_o) \qquad [3]$$

The plant and observation equations [2] are then linearized about this trajectory to obtain the linear problem

estimate $\quad \Delta\hat{\underline{x}}(t)$, given

plant $\quad \Delta\dot{\underline{x}}(t) = F(t)\,\Delta\underline{x}(t) + \underline{w} \quad ; \quad \Delta\underline{x}(t_o) = \Delta\underline{x}_o$

observation $\quad \Delta y_k = H(t_k)\,\Delta\underline{x}(t_k) + v$

$$\Delta y_k = h(\underline{x}(t_k),t_k) - h(\underline{x}_N(t_k),t_k)$$

where

$$F(t) = \left.\frac{\partial \underline{f}}{\partial \underline{x}}\right|_{\underline{x}_N(t)} \qquad [4]$$

$$H(t_k) = \left.\frac{\partial h}{\partial \underline{x}}\right|_{\underline{x}_N(t_k),t_k}$$

The statistics of $\Delta\underline{x}_o$, $\underline{w}$, and v carry over from above.

A Kalman filter can solve the explicit problem [4] optimally, but here the implicit dependence on $x_N(t)$ makes the solution suboptimal. An Extended Kalman Filter is essentially a linearized filter that starts over, computing a new nominal trajectory, after every observation. Though an Extended Filter performs better than a Linearized Filter, since the nominal trajectory itself is corrected, the use of large step sizes and interpolators for efficiency in the semianalytical ephemeris propagator precludes its use here. Rather, a modification of the Linearized Filter will be used, as discussed below. The equations for a Linearized Kalman Filter are given in Table III.

Table III. Linearized Kalman Filter Equations

Estimation Problem

$\underline{x}(t)$ = state to be estimated

$y(t)$ = scalar observation of $\underline{x}(t)$

$\underline{w}(t)$ = white state process noise

$v(t)$ = white observation noise

plant $\dot{\underline{x}}(t) = \underline{f}(\underline{x},t) + \underline{w} \quad ; \quad \underline{x}(t_o) = \underline{x}_o$

observations $y(t) = h(\underline{x},t) + v$ at times t_i

statistics $E(\underline{w}) = \underline{0} \quad , \quad E(\underline{w}(t)\ \underline{w}^T(\tau)) = Q\delta(t-\tau)$,

$E(v) = 0 \quad , \quad E(v(t)\ v(\tau)) = r\delta(t-\tau)$,

$E(\underline{x}_o) = \bar{\underline{x}}_o \quad , \quad E(\underline{x}_o\ \underline{x}_o^T) = \underline{P}_o$

$\underline{x}_o$, $\underline{w}$, v are uncorrelated.

Linearized Kalman Filter Solution

nominal trajectory $\dot{\underline{x}}_N(t) = \underline{f}(\underline{x}_N,t) \ ; \ \underline{x}_N(t_o) = \bar{\underline{x}}_o$

prediction of estimate and covariance

transition matrix

$$\dot{\Phi}(t,t_{i-1}) = \left[\frac{\partial \underline{f}}{\partial \underline{x}_N}(\underline{x}_N,t)\right] \Phi(t,t_{i-1}) \ ;$$

$$\Phi(t_{i-1},t_{i-1}) = I$$

state prediction

$$\Delta\hat{\dot{\underline{x}}}(t_i) = \Phi(t_i,t_{i-1})\ \Delta\hat{\underline{x}}(t_{i-1}) \ ;$$

$$\Delta\hat{\underline{x}}(t_{i-1}) = \Delta\tilde{\underline{x}}(t_{i-1})$$

covariance prediction

$$\hat{P}(t_i) = \Phi(t_i,t_{i-1})\ \hat{P}(t_{i-1})\Phi^T(t_i,t_{i-1}) + \Lambda(t_i,t_{i-1})$$

$$\hat{P}(t_{i-1}) = \tilde{P}(t_{i-1})$$

$$\Lambda(t_i,t_{i-1}) = \int_{t_{i-1}}^{t_i} \Phi(t_i,\tau)Q(\tau)\Phi^T(t_i,\tau)d\tau$$

Update of estimate and covariance

observation partial $\quad H_i = \frac{\partial h}{\partial \underline{x}_N}(\underline{x}_N,t_i)$

Kalman gain $\quad \underline{K}_i = \frac{\hat{P}(t_i)H_i^T}{H_i\hat{P}(t_i)H_i^T + r}$

observation $\quad \Delta y(t_i) = y(t_i) - h(\underline{x}_N, t_i)$

state update $\quad \Delta\tilde{\underline{x}}(t_i) = \Delta\hat{\underline{x}}(t_i) + \underline{K}_i\ [\Delta y(t_i) = H_i\Delta\hat{\underline{x}}(t_i)]$

covariance update $\quad \tilde{P}(t_i) = (I - \underline{K}_i\ H_i)\ \hat{P}(t_i)$

initialization

$$\Delta\tilde{\underline{x}}(t_o) = 0$$

$$\tilde{P}(t_o) = \underline{P}_o$$

4. SEMIANALYTICAL KALMAN FILTER DESIGN

The Kalman Filter equations as given in Table III usually allow the means of propagating the nominal trajectory and the transition matrices to be arbitrary, since the filter only requires the values at observation times. However, when optimizing the computations for efficiency, the structures of the integrator and the filter may become intertwined to produce a more efficient result. This is the case for a Semianalytical Kalman Filter, where the use of interpolators for the state, the transition matrices, and the short periodic coefficients has definite implications for the overall filter design.

The Linearized Kalman Filter uses observations over time to improve the estimate of a satellite's orbit. Typically the observation times are not known in advance, so the underlying ephemeris generator must be able to efficiently generate the values of the state and the transition matrices at essentially arbitrary times and arbitrarily frequently. This requirement does not decrease the efficiency of high precision numerical integrators (such as Adams-Cowell, etc.), since they are constrained to small step sizes anyway and automatically generate the required values at many points in time. Analytical and Semianalytical integrators, on the other hand, use very large step sizes, generating the required state and transition matrices at only a few points in time. Such integrators use interpolators to obtain the values at intermediate points in time. The contribution at CSDL has been to develop an interpolation method that retains the efficiency of analytical integrators and also gives values with the accuracies of numerical integrators.

In the optimization of the Semianalytical Kalman Filter for efficiency, the semianalytical integrator and the Kalman Filter each place requirements on the other.

The use of interpolators by the integrator over the integration grid dictates the use of a Linearized Kalman filter inside the integration grid, although the solve vector can be updated after processing all the observations in that grid.

The filter, on the other hand, requires the transition matrices $\Phi(t_i,t_{i-1})$, $\Psi(t_i,t_{i-1})$ between adjacent observation times t_{i-1} and t_i. The integrator can most readily supply the transition matrices from the beginning of the integration grid, $\Phi(t_i,t_o)$, $\Psi(t_i,t_o)$. By using the equations

$$\Phi(t_i,t_{i-1}) = \Phi(t_i,t_o)\ \Phi(t_o,t_{i-1})$$

$$\Phi(t_o,t_{i-1}) = \Phi^{-1}(t_{i-1},t_o) \qquad [5]$$

$$\Psi(t_i,t_{i-1}) = \Psi(t_i,t_o) - \Phi(t_i,t_{i-1})\ \Psi(t_{i-1},t_o)$$

we can restate the filter's requirement as supplying $\Phi(t_i, t_o)$, $\Psi(t_i, t_o)$, and $\Phi^{-1}(t_i, t_o)$. While $\Phi^{-1}(t_i, t_o)$ could be calculated directly from $\Phi(t_i, t_o)$, the expense of computing matrix inverses motivates another solution. $\Phi(t_i, t_o)$ is calculated from a Hermite interpolator using integration grid values and rates. Since the rate of $\Phi^{-1}(t, t_o)$ can be calculated as

$$\dot{\Phi}^{-1}(t,t_o) = -\Phi^{-1}(t,t_o)\,\dot{\Phi}(t,t_o)\,\Phi^{-1}(t,t_o) \qquad [6]$$

a similar Hermite interpolator can be constructed for $\Phi^{-1}(t_i, t_o)$. This interpolator is included in the semianalytical integrator.

The last requirement of the filter on the integrator is the calculation of Λ, the contribution of the state process noise. Due to the difficulty in defining Q, the process noise strength, Λ, will be calculated as linear in time

$$\Lambda = \Lambda(t_i - t_{i-1}) \qquad [7]$$

This follows the procedure already incorporated in GTDS [9] and appears to work quite well.

The implementation of the rest of the filter equations is straightforward and follows software already in the GTDS FILTER subroutines.

A procedural statement of the final algorithm for implementing this Semianalytical Kalman Filter design is given in Table IV.

5. CONCLUSIONS

An algorithm for implementing a Semianalytical Kalman Filter has been presented. Its implementation is currently being completed. Results will be presented at the conference.

Table IV. The Semianalytical Kalman Filter Algorithm

Due to use of a Runge kutta integrator, we may consider only one integration grid step; all others are processed identically.

Operations on the Integration Grid

1. $t = t_o$ update $\tilde{\underline{x}} = \hat{\underline{x}} + \hat{\Delta\underline{x}}$ $\underline{x} = \begin{bmatrix} \bar{\underline{a}}^* \\ \underline{c} \end{bmatrix}$

update $\tilde{P} = \hat{P}$

inititalize $\tilde{\Delta\underline{x}} = 0$

$\Phi(t_o, t_o) = I$

$\Psi(t_o, t_o) = 0$ save in Ψs

$\Phi^{-1}(t_o, t_o) = I$ save in Φs

2. $t = t_o + \Delta t$ do averaged integration

obtain $\hat{\underline{x}}(t)$, $\Phi(t, t_o)$, $\Psi(t, t_o)$

set up mean interpolators $\hat{\underline{x}}$, Φ, Ψ, Φ^{-1}

3. $t = t_o + \Delta t$ set up interpolators for short periodic coefficients $\varepsilon \underline{C}_\sigma(\bar{\underline{a}})$, $\varepsilon \underline{D}_\sigma(\bar{\underline{a}})$

Operations on the Observation Grid

1. obtain the new observation, $y(t_i)$, at time $t = t_i$.

2. interpolate for $\hat{\underline{x}}(t_i)$, $\Phi(t_i,t_o)$ $\Psi(t_i,t_o)$

   we already have $\Phi^{-1}(t_o,t_{i-1})$ in Φs

3. interpolate for short periodic coefficients

$$\varepsilon\underline{C}_\sigma(\bar{\underline{a}}(t_i)) \ , \ \varepsilon\underline{D}_\sigma(\bar{\underline{a}}(t_i))$$

4. construct the osculating elements

$$\underline{a}^*(t_i) = \bar{\underline{a}}^*(t_i) + \sum_{\sigma=1}^{N} \varepsilon\underline{C}_\sigma(\bar{\underline{a}}) \sin \sigma\bar{\lambda} - \varepsilon\underline{D}_\sigma(\bar{\underline{a}}) \cos \sigma\bar{\lambda}$$

5. transform to cartesian elements and construct the nominal observation

$$h(\hat{\underline{x}}(t_i),t_i)$$

   the observation residual

$$\Delta y(t_i) = y(t_i) - h(\hat{\underline{x}}(t_i),t_i)$$

   and the observation partials

$$H_i = \frac{\partial h}{\partial \hat{\underline{x}}} (x_N,t_i) = \frac{\partial h}{\partial \underline{a}^*} [I + B_1 \mid B_4]$$

$$B_1 = \frac{\partial \varepsilon\underline{\eta}_1(\bar{\underline{a}},\bar{\lambda})}{\partial \bar{\underline{a}}^*}$$

$$B_4 = \frac{\partial \varepsilon\underline{\eta}_1(\bar{\underline{a}},\bar{\lambda})}{\partial \underline{c}}$$

6. Compute the transition matrices

$$\Phi(t_i,t_{i-1}) = \Phi(t_i,t_o)\ \Phi^{-1}(t_{i-1},t_o) = \Phi(t_i,t_o)\ \Phi s$$

   using $\Phi_s = \Phi^{-1}(t_{i-1},t_o)$, and $\Psi_s = \Psi(t_{i-1},t_o)$

$$\Psi(t_i,t_{i-1}) = \Psi(t_i,t_o) - \Phi(t_i,t_{i-1})\ \Psi_s$$

7. Obtain predicted solve vector and covariance

$$\hat{\Delta x}(t_i) = \Phi(t_i,t_{i-1})\ \tilde{\Delta x}(t_{i-1})$$

$$\hat{P}(t_i) = \begin{bmatrix} \Phi(t_i,t_{i-1}) & \Psi(t_i,t_{i-1}) \\ 0 & I \end{bmatrix} \tilde{P}(t_{i-1}) \begin{bmatrix} \Phi(t_i,t_{i-1}) & \Psi(t_i,t_{i-1}) \\ 0 & I \end{bmatrix}$$

$$+ \Lambda(t_i,t_{i-1})$$

$$\Lambda(t_i,t_{i-1}) = \dot{\Lambda} \cdot (t_i - t_{i-1})$$

8. Complete the update phase of the filter.

Calculate the gain $K_i = \dfrac{\tilde{P}(t_i)\ H_i^T}{(H_i\ \hat{P}(t_i) H_i^T + R)}$

update the state $\tilde{\Delta \underline{x}}(t_i) = \hat{\Delta \underline{x}}(t_i) + K_i(\Delta y(t_i) - H_i\ \hat{\Delta \underline{x}}(t_i))$

update the covariance $\tilde{P}(t_i) = (I - KH)\hat{P}(t_i)$

9. Save transition matrices for next observation

$\Phi_s = \Phi^{-1}(t_i,t_o)$ interpolated

$\Psi_s = \Psi(t_i,t_o)$ interpolated in 2

Go to step 1.

6. ACKNOWLEDGEMENTS

The authors wish to thank L. Early and W. McClain (CSDL) for their comments and suggestions, and A. Green for his extensive previous work on which this paper is based. The authors also wish to thank K. Smith for returning from California to prepare this manuscript. S. Taylor thanks the Fannie and John Hertz Foundation for their support of his education, of which this is part. This work was partially funded by the USAF Space Division under contract number F04701-79-C-0062.

7. REFERENCES

(1) Fuchs, A. J., and Kolenkiewicz, R., "An Overview of Earth Satellite Orbit Determination," AAS/AIAA Astrodynamics Specialist Conference, Provincetown, MA, June 25-27, 1979.

(2) Van Dierendonck, A. J., Melton, W. C., Birnbaum, M., and Harkins, M. D., "The Approach to Satellite Ephemeris Determination for the NAVSTAR Global Positioning System," Navigation, Vol. 23, No. 1, Spring 1976.

(3) Kes, F. C., Lagowski, R. G., Grise, A. J., "Performance of the Telesat Real-Time State Estimator," AIAA Paper No. 80-0573

(4) Green, A. J., Orbit Determination and Prediction Processes for Low Altitude Satellites, Ph.D. Thesis, Massachusetts Institute of Technology, December 1979.

(5) Collins, S. K., and Cefola, P. J., "Double Averaged Third Body Model for Prediction of Super-synchronous Orbits over Long Time Spans," AAS/AIAA Astrodynamics Specialist Conference, Provincetown, MA, June 25-27, 1979.

(6) Green, A. J., and Cefola, P. J., "Fourier Series Formulation of the Short Periodic Variations in Terms of Equinoctial Variables," AAS/AIAA Astrodynamics Specialist Conference, Provincetown, MA, June 25-27, 1979.

(7) McClain, W. D., and Slutsky, M., "A Theory for the Short Period Motion of an Artificial Satellite," AIAA/AAS Astrodynamics Conference, Danvers, MA, August 11-13, 1980.

(8) Gelb, A., ed., Applied Optimal Estimation, The MIT Press, Massachusetts Institute of Technology, Cambridge, MA, 1974.

(9) Cappellari, J. O., Velez, C. E., and Fuchs, A. J., eds., Mathematical Theory of the Goddard Trajectory Determination System, Goddard Space Flight Center, X-582-76-77, April 1976.

SESSION II

G. D. Mistretta, Chairman

Estimation of Kalman Filter Model Parameters from an Ensemble of Tests

by

B. P. Gibbs, D. R. Haley, W. Levine, D. W. Porter,
and C. J. Vahlberg
Business and Technological Systems, Inc.

ABSTRACT

This paper presents a methodology for estimating initial mean and covariance parameters in a Kalman filter model from an ensemble of non-identical tests. In addition, the problem of estimating time constants and process noise levels is addressed. The work is motivated by practical problems such as developing and validating inertial instrument error models from laboratory test data or developing error models of individual phases of a test.

1.0 INTRODUCTION

This paper presents a methodology for estimating initial mean and covariance parameters in a Kalman filter model from an ensemble of non-identical tests. In addition, the problem of estimating time constants and process noise levels is addressed. The work is motivated by practical problems such as developing and validating inertial instrument error models from laboratory test data or developing error models of individual phases of a test.

Previous results in the literature [2,3] employ a Kalman smoother to obtain a sufficient statistic for the estimation of initial mean and covariance. Then the Expectation-Maximization (EM) algorithm [1] is applied to iteratively obtain maximum likelihood estimates of the entire initial mean vector and covariance matrix. The previous results are extended in this paper to account for parameter constraints such as constraining variables that are physically unrelated to each other to be uncorrelated. Further, the results are extended to consider time constant and process noise level parameters. Previous techniques capable of estimating initial mean and covariance parameters and dynamic parameters require re-reunning a Kalman filter for each value of the parameter vector considered. The new approach presented here is more efficient in that the filter need be re-run only for dynamic parameters.

System testing (for example, of inertial instruments in the laboratory and error mechanisms from flight data) is often done in multiple phases that are physically different but linked dynamically in a given test. In order to obtain models for different phases, the previous results could be applied where the phase dynamics are stacked one on top of the other. New results are presented that provide a simpler and computationally improved approach that deals with each phase individually. The new results are also useful when only one multiple phase test is conducted, it is only desired to estimate the state in each phase, and the state is unobservable in a given phase but observable over all phases.

In practical testing situations, suboptimal filters are often used. Results are presented that account for filter suboptimality.

Theoretical convergence results for the present application of the iterative EM algorithm are presented. Both the case of observable and unobservable per test dynamics are addressed. Also included are some references regarding rate of convergence and the effect of constraints on elements of the estimated covariance matrix.

2.0 THE DL/EM APPROACH

The Data Likelihood (DL) algorithm was derived in [2, 3] during analyses directed toward the estimation of mean and covariance parameters of the initial distribution of certain discrete-time multi-dimensional Gaussian random processes. The essential idea is to use Kalman smoother (Bayesian) estimates of realizations of the initial conditions to estimate the mean and variance of these initial condition distributions and to test certain statistical hypotheses thereabout. The iterative DL scheme arose in the process of attempting to divorce the a priori model to be validated from the estimated model, and was observed to be of the form of the Generalized Expectation-Maximization method described by Dempster, et al [1].

The context of the problem is as follows. For each test, j, the realization of the r.v. x is assumed to be described by

$$x_{k,j} = \Phi_{k,j} x_{k-1,j} + w_{k,j} \quad , \; k=1,2,\cdots,n_j \; , \; j=1,\cdots,N \; . \tag{1}$$

and to be observed by

$$z_{k,j} = M_{k,j} x_{k,j} + v_{k,j} \; . \tag{2}$$

Here w and v are assumed zero mean, white, uncorrelated, Gaussian, and independent of $x_{o,j}$ for all j. It is assumed that $x_{o,j}$ are realizations from a Gaussian distribution with mean μ and covariance Σ, μ and Σ unknown. In [2, 3] it is shown that the log likelihood function for the process can be written as

$$\log \; L(\mu,\Sigma) = \log \; L_{ML}(\mu,\Sigma) + R \; ,$$

where

$$\log L_{ML}(\mu,\Sigma) = -\frac{1}{2}\sum_{j=1}^{N} \log \left|\Sigma+P(j)\right| \tag{3}$$

$$-\frac{1}{2}\sum_{j=1}^{N} (\hat{x}_{o,j}-\mu)^t \, [\Sigma+P(j)]^{-1} \, (\hat{x}_{o,j}-\mu)$$

and R is independent of μ , Σ . Here $\hat{x}_{o,j}$ are maximum likelihood (non-Bayesian batch least squares) estimates of $x_{o,j}$, and $P(j)$ are the associated estimation error covariances. Differentiating Log L_{ML} with respect to μ and Σ and setting the derivative to zero yields the equations

$$\sum_{j=1}^{N} [\Sigma+P(j)]^{-1} \, [\hat{x}_{o,j}-\mu] = 0 \tag{4}$$

$$\sum_{j=1}^{N} [\Sigma+P(j)]^{-1} \, (\hat{x}_{o,j}-\mu) \, (\hat{x}_{o,j}-\mu)^t \, [\Sigma+P(j)]^{-1}$$

$$- \sum_{j=1}^{N} [\Sigma+P(j)]^{-1} = 0 \, . \tag{5}$$

It is further noted that the Kalman smoother (Bayesian) estimates $\hat{x}_{o,j} \equiv \hat{\hat{x}}_{o,j}(\mu,\Sigma)$ and associated estimation error covariance $\hat{P}_j \equiv \hat{P}_j(\Sigma)$ are related to $\hat{x}_{o,j}$ and $P(j)$ by

$$\hat{x}_{o,j} = [\Sigma+P(j)] \, \Sigma^{-1} \, [\hat{\hat{x}}_{o,j}-\mu] \, , \tag{6}$$

$$\hat{P}_j = (P(j)^{-1}+\Sigma^{-1})^{-1} \, . \tag{7}$$

Then the iterative DL loop can be defined:

$$\hat{\mu}_s = \frac{1}{N} \sum_{j=1}^{N} \hat{\hat{x}}_{o,j} (\hat{\mu}_{s-1}, \hat{\Sigma}_{s-1}) , \tag{8}$$

$$\hat{\Sigma}_s = \frac{1}{N} \sum_{j=1}^{N} \{\hat{P}_j(\hat{\Sigma}_{s-1}) + [\hat{\hat{x}}_{o,j}(\hat{\mu}_{s-1}, \hat{\Sigma}_{s-1}) - \hat{\mu}_s] \times [\hat{\hat{x}}_{o,j}(\hat{\mu}_{s-1}, \hat{\Sigma}_{s-1}) - \hat{\mu}_s]^t\} , \tag{9}$$

$$\hat{P}_j(\hat{\Sigma}_s) = [\hat{\Sigma}_s^{-1} + P_j^{-1}]^{-1} , \tag{10}$$

$$\hat{\hat{x}}_{o,j}(\hat{\mu}_s, \hat{\Sigma}_s) = \hat{\mu}_s + \hat{P}_j(\hat{\Sigma}_s) P_j^{-1} [\hat{x}_{o,j} - \hat{\mu}_s] , \tag{11}$$

with iteration on s .

2.1 Theoretical Convergence

Theoretical convergence of the DL algorithm is addressed in detail in references [4] and [5]. The first note begins by proving that the DL algorithm is a Generalized Expectation Maximization algorithm. It then follows that the DL algorithm produces a monotone increasing sequence of likelihoods. It also follows, under the additional assumption that there exists a pair $\underline{\Sigma}^*$, $\underline{\mu}^*$ that maximizes the likelihood, that $\underline{\Sigma}^*$, $\underline{\mu}^*$ is a fixed point of the DL algorithm. Finally, it is shown that the sequence $\{\underline{\mu}_s, \underline{\Sigma}_s\}_{s=0}^{\infty}$ converges to some $\underline{\mu}^o$, $\underline{\Sigma}^o$ assuming that $\underline{\Sigma}_s \leq c\underline{I}$ for all s and some c .

There are two defects in this result. First, it is not guaranteed that $\underline{\mu}^o$, $\underline{\Sigma}^o$ maximize the log likelihood. There is probably nothing to be done about this. Dempster et al [1] remark, as is probably true, that

$\underline{\mu}^o$, $\underline{\Sigma}^o$ will, in almost all applications, occur at a local, if not global, maximum of the likelihood. Second, it would be desirable to relax the assumption that $\Sigma_s \leq c\,\underline{I}$. In [5] it is shown that $\Sigma_s \leq c\underline{I}$ is automatically true provided all the tests are identically set-up. It seems reasonable, but has not yet been proven, that a similar result holds in general.

2.2 Constrained DL Estimates

In many potential applications of the DL method, the random variable of interest (whose mean and covariance we desire to estimate) is of rather large dimension. It is also often true that several of the parameters to be estimated are simultaneously poorly estimable and of relatively little interest. The judicious constraint of some parameters thus presents itself as a reasonable possibility. For example, if there is reason to believe that some components of the random variable are physically uncorrelated, and any correlation is believed to be largely irrelevant, little is likely to be lost if the estimated covariance is constrained to exhibit zero correlation.

It is desired to obtain those values μ and Σ of the mean and covariance of the r.v. under consideration which maximize the log likelihood

$$L = \log L(\mu,\Sigma)_{ML} = -\frac{1}{2}\sum_{1}^{N} \log\left|\Sigma+P(j)\right| - \frac{1}{2}\sum^{N} (\hat{x}_{o,j}-\mu)^t\,[\Sigma+P(j)]^{-1}\,(\hat{x}_{o,j}-\mu)\ , \tag{12}$$

subject to appropriate constraints. Three forms of constraints have been explicitly considered. Within the DL iterative context, it seems that a rather wide variety of constraints may be handled quite easily.

The general approach taken here is to use Lagrange multipliers to reduce the constrained maximization problem to a modified but unconstrained problem.

The first forms of constraint on $\mu = [\mu_i]$ and $\Sigma = [\sigma_{jk}]$ under consideration here are

$$\phi_i = \delta_i(\mu_i - \mu_i^*) = 0 \ , \tag{13}$$

$$\psi_{jk} = \delta_{jk}(\sigma_{jk} - \sigma_{jk}^*) = 0 \ . \tag{14}$$

Here $[\delta_i]$ and $[\delta_{jk}]$ are "selectors",

$$\delta_i = \begin{cases} 0 \text{ if } \mu_i & \text{unconstrained} \\ 1 \text{ if } \mu_i & \text{constrained} \end{cases} \tag{15}$$

$$\delta_{jk} = \begin{cases} 0 \text{ if } \sigma_{jk} & \text{unconstrained} \\ 1 \text{ if } \sigma_{jk} & \text{constrained} \end{cases} \tag{16}$$

Clearly, reasonableness dictates that $[\delta_{jk}]$ and $[\sigma_{jk}^*] = \Sigma^*$ be symmetric, and that $\Sigma \geq 0$. The problem now becomes that of obtaining an unconstrained maximum to

$$\begin{aligned} L^* = L^*(\mu,\Sigma) = L &+ \sum_i \lambda_i \ \delta_i(\mu_i - \mu_i^*) \\ &+ \sum_{j,k} \lambda_{jk} \ \delta_{jk}(\sigma_{jk} - \sigma_{jk}^*) \ . \end{aligned} \tag{17}$$

(Again, it is clear that $[\lambda_{jk}]$ must be symmetric.) To extremize L^* , we set

$$\frac{\partial L^*}{\partial \mu} = \frac{\partial L}{\partial \mu} + \mathrm{diag}(\delta\ )[\lambda\ ]$$

$$= \frac{\partial L}{\partial \mu} + \Delta\lambda = 0\ , \tag{18}$$

and

$$\frac{\partial L^*}{\partial \Sigma} = \frac{\partial L}{\partial \Sigma} + [\lambda_{jk}\delta_{jk}]$$

$$= \frac{\partial L}{\partial \Sigma} + \Lambda = 0\ . \tag{19}$$

The explicit computations and solutions become rather tedious and are not reproduced here. The complete details and several examples are found in [6]. It should be noted that the use of Lagrange multipliers has an important advantage that is not mentioned in [6]. It is shown in [7] that $\lambda_{jk} = \frac{\partial L}{\partial \sigma_{jk}}\Big|_{\sigma_{jk}=\sigma^*_{jk}}$ and $\lambda_i = \frac{\partial L}{\partial M_i}\Big|_{\mu_i=\mu^*_i}$. In words, solving Lagrange multipliers gives the sensitivity of the log likelihood to the constraint.

Consider the case where the mean μ is partitioned as $\mu = \begin{bmatrix}\mu_u \\ \mu_c\end{bmatrix}$ into its constrained and unconstrained parts. It is rather straightforward to show (see [6]) that the solution for $\hat{\mu}$ at each DL step is given by

$$\hat{\mu} = \begin{bmatrix}\hat{\mu}_u \\ \hat{\mu}_c\end{bmatrix} = \begin{bmatrix}\frac{1}{N}\left[\sum_1^N \hat{x}_i^u + \Sigma_{12}\Sigma_{22}^{-1}\left\{N\mu_c^* - \sum_1^N \hat{x}_i^c\right\}\right] \\ \mu_c^*\end{bmatrix}\ , \tag{20}$$

from which the effect of the constraints on $\hat{\mu}$ at each iteration is clearly visible. (Here the state estimates $\hat{x}_i$ are also assumed partioned as μ ,

$$\hat{\hat{x}}_i = \begin{bmatrix} \hat{\hat{x}}_i^u \\ \\ \hat{\hat{x}}_i^c \end{bmatrix} .)$$

Such a formal solution is not generally available for the covariance equations. However, several specific cases yield results of some interest. One such case arises when Σ is partioned as

$$\Sigma = \begin{bmatrix} \Sigma_{11} & \Sigma_{12} \\ \Sigma_{21} & \Sigma_{22} \end{bmatrix} ,$$

and we wish to constrain $\Sigma_{12} = \Sigma_{12}^*$, $\Sigma_{21} = \Sigma_{12}^t = \Sigma_{12}^{*t}$, and $\Sigma_{22} = \Sigma_{22}^*$. Denoting

$$\Sigma^* - M = \tilde{M} = \begin{bmatrix} \tilde{M}_{11} & \tilde{M}_{12} \\ \tilde{M}_{21} & \tilde{M}_{22} \end{bmatrix} , \tag{21}$$

where

$$M = \frac{1}{N} \{\sum_1^N (\hat{\hat{x}}_i - \mu)(\hat{\hat{x}}_i - \mu)^t + \hat{P}_i\} , \tag{22}$$

It is shown in [6] that

$$\Sigma_{11} = M_{11} + \Sigma_{12} \Sigma_{22}^{-1} \tilde{M}_{12}^t + \tilde{M}_{12} \Sigma_{22}^{-1} \Sigma_{21} - \Sigma_{12} \Sigma_{22}^{-1} \tilde{M}_{22} \Sigma_{22}^{-1} \Sigma_{21} , \tag{23}$$

$$\Sigma_{12} = \Sigma_{12}^* , \tag{24}$$

$$\Sigma_{22} = \Sigma_{22}^* . \tag{25}$$

One slightly disconcerting question which does arise though regards the positivity of Σ_{11} in (23). It is presently not clear what conditions on $\Sigma_{12}^*, \Sigma_{22}^*$ yield $\Sigma_{11}^* > 0$. The conditions on Σ_{12}^* are more open to question since Σ_{22}^* is more naturally restricted. Perhaps a relevant question is "how does one place a reasonable <u>a priori</u> constraint on a cross-covariance matrix?" One reasonable choice for the problem at hand might well be $\Sigma_{12}^* = 0$. In this case $\Sigma_{11} = M_{11}$, and the difficulty regarding definiteness disappears.

A slightly different sort of result arises from the more specific desire to constrain Σ to be of the form

$$\Sigma = \begin{bmatrix} \Sigma_{11} & \Sigma_{12} \\ \Sigma_{21} & \Sigma_{22} \end{bmatrix} ,$$

with $\Sigma_{12} = \Sigma_{21}^t = 0$, and $\Sigma_{22} = \text{diag}\,(\sigma_{22i})$.

Then it is shown in [6] that the solution is

$$\Sigma_{11} = M_{11} , \tag{26}$$

$$\Sigma_{12} = \Sigma_{12}^* = 0 , \tag{27}$$

$$\Sigma = \begin{cases} M_{22ii} & i=j, \\ \sigma_{22ij}^* = 0 , & i=j . \end{cases} \tag{28}$$

It is clear that the constrained lack of correlation forces Σ_{11} and Σ_{22} to exactly follow the data observed for each. It is important to note that the above result can be applied to cases where elements of Σ_{12} or off-diagonal elements of Σ_{22} are constrained to known non-zero values. Suppose the $x_{o,j}$ can be expressed as

$$x_{o,j} = \mu + x_{1j} + x_{2j} \tag{29}$$

where x_{2j} is uncorrelated with x_{1j}, the covariance of x_{2j} is known and carries the known non-zero values mentioned above, and the covariance of x_{1j} is to be estimated subject to the constraints $\Sigma_{12} = \Sigma_{21}^T = 0$, $\Sigma_{22} = \text{diag}\,(\sigma_{22i})$. Then the results of equations (26), (27), (28) can be applied where $x_{o,j}$ is re-defined to be

$$x_{o,j} = \mu + x_{1j} \tag{30}$$

A second form of constraint on μ and Σ is

$$\mu = \alpha\mu^*, \quad \text{and}$$

$$\Sigma = \beta\Sigma^* .$$

Here μ^*, Σ^* are assumed to be given, and α, β are undetermined constants. For purposes of analysis, these constraints may be more conveniently stated as

$$\phi_i = \mu_1^*\mu_i - \mu_i^*\mu_1 = 0 , \qquad p \geq i \geq 2, \tag{31}$$

$$\psi_{jk} = \sigma_{11}^*\sigma_{jk} - \sigma_{jk}^*\sigma_{11} = 0 \qquad 1 \leq j,k \leq p , \quad (j,k) \neq (1,1) \tag{32}$$

The Lagrange multipliers λ_i, λ_{jk}, then enter in the unconstrained maximization of

$$L^* = L + \sum \lambda_i \phi_i + \sum \lambda_{jk}\psi_{jk} . \tag{33}$$

The explicit extremizing solution for α is given by

$$\alpha = \frac{1}{N} \frac{\mu^{*t} \sum^{-1} \{\sum^{N} \hat{x}_{o,i}\}}{\mu^{*t} \sum^{-1} \mu^{*}} \quad . \tag{34}$$

A similar but quite complicated analytic solution for β is obtained. As was the case for identity constraints, this value of β and derivational details are contained in [6].

A third form of constraint of potential interest, applying only to the covariance estimation problem, is that of a specified correlation matrix, $R = [\rho_{ij}]$, so that the covariance takes the form

$$\sum = \text{diag}\ (\sqrt{\sigma_{ii}})\ R\ \text{diag}\ (\sqrt{\sigma_{jj}}) \tag{35}$$

with σ_{ii} being the individual variance components. Then the constraint functions are

$$\phi_{ij} = \sigma_{ij} - \sqrt{\sigma_{ii}}\ \rho_{ij}\ \sqrt{\sigma_{jj}} = 0 \ . \qquad (i \neq j) \tag{36}$$

Clearly the usual properties of a correlation matrix are required.

The modified likelihood function is then

$$\begin{aligned} L^{*} &= L + \sum_{i \neq j} \lambda_{ij}\ \phi_{ij} \ . \\ &= L + S \ . \end{aligned} \tag{37}$$

We wish to find $\sum$ such that $\frac{\partial L^{*}}{\partial \sum} = 0$. Again, the details of the solution are found in [6].

2.3 Observability

The effect of unobservable tests on the DL algorithm is discussed in detail in reference [8]. The results can be summarized as follows:

(1) The state space can be divided into an observable subspace and an unobservable subspace.

(2) On the observable subspace the DL algorithm performs as if the observable subspace is the whole space. Data and estimates of $\underline{\Sigma}$ and $\underline{\mu}$ on the unobservable space have no effect on the DL algorithm as applied to the observable subspace.

(3) The data and estimates on the observable subspace do effect the algorithms results on the unobservable subspace and the correlations between unobservable and observable subspaces.

(4) If the DL algorithm is initialized with zero correlation between observable and unobservable subspaces then the correlation will remain zero and the DL algorithm will not change the mean and covariance on the unobservable subspace.

2.4 Estimation of Markov Parameters

In addition to estimating parameters of initial distributions, it is often of interest to use data from multiple tests to estimate dynamic parameters of the system, particularly parameters of Markov processes. Several possibilities exist for such estimation, and three are discussed very briefly here. It should be noted that such estimation likely is most useful for consistency checking because of the innately poor identifiability of such parameters during system tests of short time duration. Further, all methods for their estimation are likely to be computationally costly.

In [9], Goodrich and Caines have presented a methodology for maximum likelihood idenfication of system parameters based on data from repeated independent tests. The likelihood function is based, as in the original derivation of [3], on Kalman filter innovations, and the assumption of independence of realization yields a rather tractable form. Methods for modification of the procedure to allow for correlated tests should be studied further. The computational burden can be high for this approach since multiple Kalman filter passes are needed at each iteration.

Sun [10] has presented an application of the E-M procedure to the simultaneous estimation of system initial state, process and measurement noise levels, and system dynamics based on data from a single test. The paper indicates that an extension to repeated tests may be possible. Again, further study and extension seem necessary.

A third possibility combines several aspects of the DL methods as previously described, the ideas of Goodrich and Caines, and other work in maximum likelihood estimation.

Consider a dynamical system as described in equation (1), where Φ and Q may depend on some parameter vector α (e.g., time constants and process noise levels). Whether to solve for α,μ,Σ simultaneously or separately seems unclear as yet. For a given value of α, one might obtain via DL the maximum likelihood estimates $\hat{\mu}(\alpha),\hat{\Sigma}(\alpha)$. Then, fixing μ,Σ, numerical/gradient methods could be used to obtain the value α to maximize the likelihood. Also open to question is the variability of α -- one might assume α to be universally constant, constant over groups of tests or unique from test to test.

An illustration of a possible implementation loop on such a procedure is found in Figure 1. We desire, again, to estimate $\mu=E(x_{0,i})$, $\Sigma=E((x_{0,i}-\mu)(x_{0,i}-\mu)^t)$, and the Markov parameter vector α. Dropping the individual test indicator i for the moment, we have

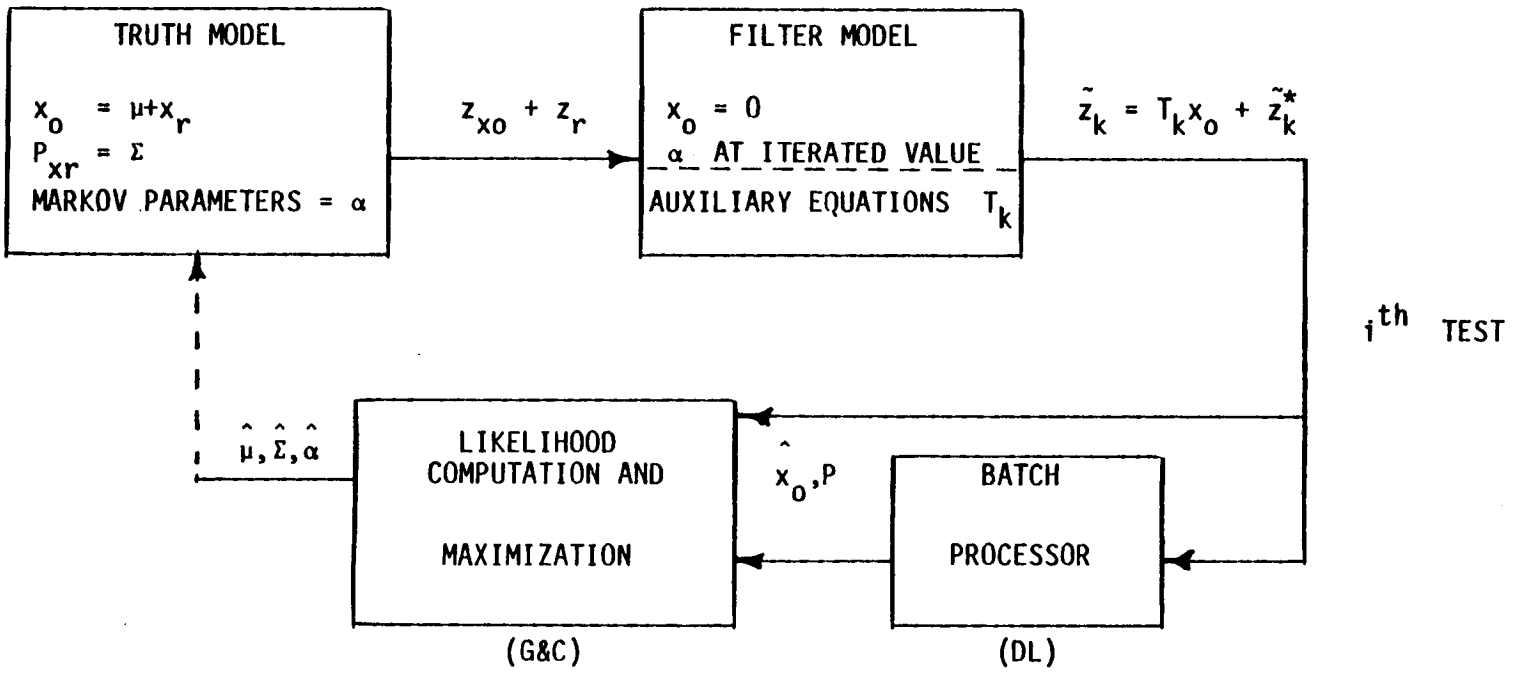

Figure 1 Proposed Markov Parameter Estimation Loop

$$x_o = \mu + x_r ,$$

x_r the random part of x_o , and

$$P_{xr} = \Sigma .$$

The observation z may be decomposed into

$$z = z_{xo} + z_r ,$$

a part due to x_o and a random part. In Reference [11] it is shown that the innovations $\tilde{z}_k$ may be decomposed as

$$\tilde{z}_k = T_k x_o + \tilde{z}_k^* . \tag{38}$$

where $\tilde{z}_k^*$ is computed based on assumed filter and truth models of $x_o=0$. It is then possible to write the log likelihood function, given μ,Σ,α, and indexing repeated tests by i,

$$-2 \log p(z|\mu,\Sigma,\alpha) + \text{constant} =$$

$$\sum_i \{\log|\Sigma+P(i)|+(\hat{x}_{o,i}-\mu)^t (\Sigma+P(I))^{-1} (x_{o,i}-\mu) \tag{39}$$

$$- \log|P(i)|-\hat{x}_{o,i}^t P^{-1}(i)\hat{x}_{o,i}\}$$

$$+ \sum_{i,k} \{\log|P_{\tilde{z}_{i,k}}|+\tilde{z}_{i,k}^t P_{\tilde{z}_{i,k}}^{-1} \tilde{z}_{i,k}\} .$$

If α is known, this procedure reduces to the DL algorithm. If α is unknown then gradient procedures may be used in the maximization. This requires differentiating the estimate for α , but not for μ,Σ . Another idea is to solve for α for each test, and only for μ,Σ for repeated tests. The proposed iterative loop is illustrated as the dotted closure in Figure 1.

In summary, the detailed analysis of the effect of Markov parameters is a difficult problem which has really only been recently addressed. It is felt that substantial additional effort may be required to fully develop adequate analysis methodology, but that failure to attempt to address the problem in detail may lead to inadequate analysis capabilities in some areas.

3.0 MULTIPLE PHASE THEORY

Many systems are operated and evaluated in a sequence of phases. The analysis of performance in one phase is carried out relatively independent of results from other phases, and then results are combined at the end. Although this procedure is not a constraint for many systems, there is interest in studying it. This section presents the theory necessary to combine the results from several phases on one test, then to analyze the results using a cumulative methodology such as DL. An approximation is presented which allows for reasonably accurate quick cumulative evaluations. An extension of the theory is discussed at the end.

Some framework, nomenclature, and assumptions need to be stated before the theory is presented. It is assumed that the effects of least squares estimates of errors from previous phases have been removed from the data prior to its analysis in a Bayesian per phase filter, or equivalently removed after data analysis is complete. The per phase analysis is actually done with a Bayes filter, but the theory is developed starting with a least squares (infinite prior) filter. The least squares estimate of errors in the ith phase can be represented by (see Reference [12])

$$\hat{x}_{i_{LS}} = \mu_i + x_{r_i} + \tilde{x}_i - \tilde{x}_{T_{i-1}} , \tag{40}$$

where

μ_i = Systematic error in this phase,

x_{r_i} = Random error introduced in this phase,

$\tilde{x}_i$ = Residual estimation error from this phase due to Q_i , R_i ,

$\tilde{x}_{T_{i-1}}$ = Residual estimation error from previous phase due to Q_{i-1}, R_{i-1} .

The covariance of this estimate is

$$E((\hat{x}_{LS}-\mu)(\hat{x}_{LS}-\mu)^T) = \Sigma_i + P_i + P_{T_{i-1}} \tag{41}$$

where

$$\Sigma_i = E(x_{r_i} x_{r_i}^T)$$

$$P_i = E(\tilde{x}_i \tilde{x}_i^T)$$

$$P_{T_{i-1}} = E(\tilde{x}_{T_{i-1}} \tilde{x}_{T_{i-1}}^T) \ .$$

The error at the transition time can be represented by (see References [11], [13])

$$\tilde{x}_T = C\,\tilde{x}_i + \tilde{x}'_{T_i} \tag{42}$$

where the following statistics are obtained suppressing the i subscript

$$\begin{aligned} E(\tilde{x}_i \tilde{x}_i)^T &= P \\ E(\tilde{x}_T \tilde{x}_T^T) &= CPC^T + P'_T = P_T \\ E(\tilde{x}_i \tilde{x}_T^T) &= PC^T = P_C \\ E(\tilde{x}_T \tilde{x}_o^T) &= 0 \end{aligned} \tag{43}$$

These statistics can be calculated following data analysis using a conventional Bayesian filter. If the initial states are augmented to the state vector to provide a fixed-point estimate of errors, all necessary covariances and correlations are obtained. For the state vector definition

$$x^* = \begin{bmatrix} x_i \\ x_T \end{bmatrix} \tag{44}$$

the covariance of estimation errors obtained from a fixed-point Bayesian smoother will be

$$P_N^* = \begin{bmatrix} P_N & P_{CN}^T \\ P_{CN} & P_{TN} \end{bmatrix} \tag{45}$$

Using the above, the correlation matrix C and the covariance of transition-time errors which are independent of initial estimation errors can be calculated

$$\begin{aligned} C &= P_{CN}^T P_N^{-1} \\ P_T' &= P_{TN} - CP_{CN} \end{aligned} \tag{46}$$

The max-likelihood information matrix is obtained as

$$P^{*-1} = \begin{bmatrix} P_N & P_{CN}^T \\ P_{CN} & P_{TN} \end{bmatrix}^{-1} - \begin{bmatrix} \Sigma^{-1} & 0 \\ 0 & 0 \end{bmatrix} \tag{47}$$

Assuming that it is invertible, the max-likelihood covariance is obtained and is given by

$$P^* = \begin{bmatrix} P & P_C^T \\ P_C & P_T \end{bmatrix} = \begin{bmatrix} P & CP \\ PC^T & CPC^T + P_T' \end{bmatrix} \tag{48}$$

The discussion thus far has focused upon manipulation of data and covariances from one phase of a multiple phase system. The result is the

max-likelihood covariance and by similar procedures, the estimate for the combined state vector at the initial and transition times. Since the error in the max-likelihood estimate, as represented by Equation (40) is unbiased, the error in the estimate of the ith phase, although correlated with the previous phase, is uncorrelated with all phases previous to that. Hence, the multiphase max-likelihood covariance of the max-likelihood estimate for the stacked vector of $\mu_i + x_{ri}$ vectors is of the banded form (see Reference [12]).

$$P = \begin{bmatrix} P_1 & -P_{c_1}^T & 0 & 0 & 0 \\ -P_{c_1} & P_2+P_{T_1} & -P_{c_2}^T & 0 & 0 \\ 0 & -P_{c_2} & P_3+P_{T_2} & -P_{c_3}^T & 0 \\ 0 & 0 & -P_{c_3} & P_4+P_{T_3} & -P_{c_4}^T \\ 0 & 0 & 0 & -P_{c_4} & P_5+P_{T_4} \end{bmatrix} \tag{49}$$

This banded form has some interesting properties that lead to a useful result, especially when the following often practical assumptions are made:

(1) The derivations presented have already assumed that all states in each phase are observable -- so that the max-likelihood information matrix is invertible

(2) Interphase correlations can be ignored for preliminary cumulative analysis giving an algorithm suboptimal in the sense that information is thrown away but not in the sense that an approximation is made.

Although the first assumption may not always be true, it may be possible to redefine the state vector so that the unobservable states do

not enter the system until the phase in which they are observable. This can be accomplished automatically in a mathematical sense utilizing the Singular Value Decomposition (SVD) algorithm. Thus, although the first assumption may not be able to be satisfied explicitly, there are ways to accomplish its effect without degrading the fidelity of the model.

4.0 USE OF SUBOPTIMAL STATE ESTIMATES IN MULTIPHASE ANALYSIS

It is often the case that data from the several phases under consideration are obtained from Kalman-Schmidt filter/fixed point smoother algorithms. Thus the algorithm for processing a test phase should be capable of handling suboptimal gains. Even if the filter were optimal, the equations for the suboptimal case would be applicable, and, in some situations, might be preferable to equations assuming optimality.

It is also desirable that the processing for each phase be done independently. In some cases, the processing for different phases may be done by different organizations. Thus, the per phase data reduction must use no information from other phases. The combination of phase estimates is done as the final step in the data reduction.

Reference [14] defines the equations required for the phase data reduction. These equations are fairly general and would apply to most suboptimal filters. Also presented there are the additional recursive equations which must be computed in a consider filter so that the phases may be combined. These equations only apply to a Kalman-Schmidt filter (which automatically computes the correct covariance matrix) but could be modified for other suboptimal filters. The following section presents the algorithm for combining the suboptimal (or optimal) estimates from different phases.

4.1 Multiphase Reduction Using Suboptimal Estimates

The output of each phase will be a suboptimal, smoothed estimate of the state at initial time and transition time. Also obtained are the various covariance and sensitivity matrices. The true state at the epoch of each phase is assumed to have a mean and random component; i.e., for phase i

$$x_0^i = \mu^i + x_r^i \, . \tag{50}$$

The DL method attempts to estimate μ^i and cov (x_r^i) by combining results of different phases and tests. To do this, the state estimates for each phase are manipulated so that they are in the familiar form

$$z = Hx_0 + v \ . \tag{51}$$

Consider the combination of phase 1 and 2 shown in Figure 2. The value of x_T^1 is

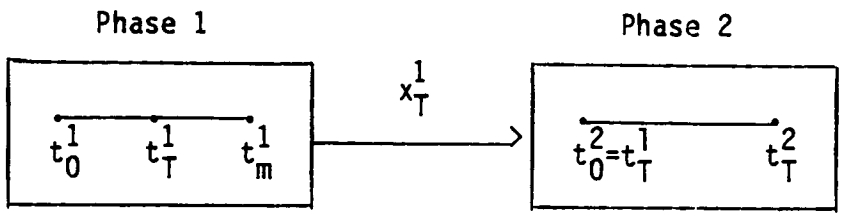

Figure 2 Phase Combination

directly included in the phase 2 initial condition, i.e.,

$$x_0^2 = \mu^2 + x_r^2 + Tx_T^1 \tag{52}$$

where T is a transformation matrix (not to be confused with transition time t_T).

Now consider the estimates obtained from phase 1:

$$\begin{aligned} \hat{x}_0^1 &= \mu^1 + x^1 + \tilde{x}_0^1 \\ &= D_{10}^1(\mu^1+x_r^1) + D_{20}^1 w^T + v_0^1 \end{aligned} \tag{53}$$

$$\hat{x}_T^1 = D_{1T}^1 \phi_T x_0^1 + D_{2T}^1 w_T + v_T^1 \tag{54}$$

and from phase 2

$$\begin{aligned}\hat{x}_0^2 &= \mu^2 + x_r^2 + Tx_T^1 + \tilde{x}_0^2 \\ &= D_{10}^2(\mu^2 + x_r^2 + Tx_T^1) + v_0^2 \ .\end{aligned} \tag{55}$$

These equations can be combined in matrix notation as:

$$\begin{bmatrix} \hat{x}_0^1 \\ \hat{x}_T^1 \\ \hat{x}_2^2 \end{bmatrix} = \begin{bmatrix} D_{10}^1 & D_{20}^1 & 0 \\ D_{1T}^1\phi_T & D_{2T}^1 & 0 \\ D_{10}^2 T\phi_T & D_{10}^2 T & D_{10}^2 \end{bmatrix} \begin{bmatrix} y^1 \\ w_T \\ y^2 \end{bmatrix} + \begin{bmatrix} v_0^1 \\ v_T^1 \\ v_0^2 \end{bmatrix} \tag{56}$$

where $y^1 = \mu^1 + x_T^1$ and $y^2 = \mu^2 + x_T^2$. Notice that v_0^1 and v_T^1 are correlated but are uncorrelated with v_0^2 . Also notice that there is no <u>a priori</u> information on y^1 and y^2 but that the <u>a priori</u> variance of w_T is Q_T . Thus, equation (56) can be treated as three measurements in a Bayesian least squares estimator for $\hat{y}^1$, $\hat{w}_T$ and $\hat{y}^2$

where

$$E\left\{ \begin{bmatrix} V_0^1 \\ V_T^1 \\ V_0^2 \end{bmatrix} \begin{bmatrix} V_0^{1T} & V_T^{1T} & V_0^{2T} \end{bmatrix} \right\}$$

is calculated in [14].

If all states are observable, then $\hat{y}^1$ and $\hat{y}^2$ should be maximum likelihood estimates.

In order to better understand the result of this processing, we assume that the first two measurements in equation (56) were processed first (to estimate $\hat{y}^1$ and $\hat{w}_T$) the third measurement was processed separately to estimate

$$y_s^2 = y^2 + Tx_T \ . \tag{57}$$

This can be done because the measurement errors are uncorrelated. Then we want to combine the estimates. Since y^2 had infinite <u>a priori</u> variance, all information in the third measurement will be used to estimate y^2 if y^1 and w_T were observable from the first two measurements, i.e., the estimates of y^1 and w_T will not change. Thus,

$$\hat{y}_2 = \hat{y}_s^2 - T(\phi_T\hat{y}^1+\hat{w}_T) = y^2 + \tilde{y}_s^2 - T(\phi_T\tilde{y}^1+\tilde{w}_T) \tag{58}$$

and the covariance of the error in the estimate of y_2 is

$$P_{\tilde{y}_s^2} + T[\phi_T \vdots I] \, P_{\begin{matrix}\tilde{y}^1\\ \tilde{w}T\end{matrix}} \begin{bmatrix}\phi_T^T \\ \hdashline I\end{bmatrix} T^T \ . \tag{59}$$

The above analysis is similar to that given previously in the sense that data processing and requirements analysis can be done phase by phase.

5.0 BIBLIOGRAPHY

[1] Dempster, A. P., N. M. Land and D. B. Rubin, "Maximum Likelihood from Incomplete Data via the EM Algorithm", J. Roy. Stat. Soc., Series B, Vol. 39, No. 1, 1977.

[2] Levy, L. J., R. H. Shumway, D. E. Olsen and F. C. Deal, Jr., "Model Validation From an Ensemble of Kalman Filter Tests", Proc. 21st Midwestern Symposium on Circuits and Systems, 1978.

[3] Shumway, R. H., D. E. Olsen and L. J. Levy, "Estimation and Tests of Hypothesis for the Initial Mean and Covariance in the Kalman Filter", American Statistical Association, San Diego, August, 1978.

[4] Levine, W. L., "Convergence of the DL Algorithm", BTS, May, 1980.

[5] Levine, W. L., "Boundedness of $\hat{\hat{\Sigma}}_k$ in the DL Algorithm", BTS, July, 1980.

[6] Haley, D. R., "Modifications and Extensions to the DL Algorithm to Allow for Constrained Max Likelihood Estimation", BTS, May, 1980.

[7] Varaiya, P. O., Notes on Optimization, Von Nostrand Reinhold, New York, 1972.

[8] Levine, W. L., "Behavior of the DL Algorithm for Unobservable Tests", BTS, July, 1980.

[9] Goodrich, R. L., and P. E. Caines, "Linear System Identification from Nonstationary Cross-Sectional Data", IEEE Trans. AC. Vol. AC-24, No. 3, June, 1979.

[10] Sun, F. K., "An Alternative Approach for Maximum Likelihood Identification", 18th Conf. Dec. Cont., Ft. Lauderdale, Florida, December 1979.

[11] Porter, D. W., "Relationships Required to Implement Generalized Likelihood Approach", BTS, October, 1978.

[12] Porter, D. W., To Appear.

[13] Porter, D. W., and T. S. Englar, Jr., "Multi-Object Tracking via a Recursive Generalized Likelihood Approach", 18th Conf. Dec. Cont., Ft. Lauderdale, Florida, December, 1979.

[14] Gibbs, B. P., "Suboptimal Per-Phase Data Reduction", BTS, May, 1980.

Analysis of Estimation Algorithms for Autonomous Navigation with TDRSS DATA[1]

By

J. Dunham, A. Long, P. Gural
K. Preiss, and H. Sielski

Computer Sciences Corporation

ABSTRACT

An investigation was performed to determine an appropriate estimation technique for onboard orbit determination using Tracking and Data Relay Satellite System (TDRSS) data. The two user satellite orbits which were studied are similar to Landsat-D (near-circular, 700-kilometers altitude, near-polar inclination). The following estimation algorithms were identified as candidates for use in autonomous navigation: (1) the extended Kalman filter (EKF) with process noise, (2) the EKF with consider parameters (CEKF), (3) the sequential Kalman filter with consider parameters (CKF), and (4) the batch least-squares differential correction technique (DC). The candidate estimators were evaluated with respect to their performance with both baseline and worst case TDRSS measurement errors and tracking configurations.

Two different modes of operation were studied. The one-way uses Doppler data which are collected on the user satellite. The two-way mode uses range and Doppler data which are collected on the ground and transmitted in the command stream to the user satellite for processing.

The actual data used in this study were simulated satellite-to-satellite range and delta range from TDRS East and West to the user, scheduled in 10-minute passes of six pairs of range/delta-range observations per minute. Various tracking frequencies were used, ranging from tracking once per orbit

[1]Work performed under NASA Contract NAS 5-24300

to tracking every third orbit. Data sets of 12 or 24 hours length were generated which simulated the expected range of errors in the TDRS ephemerides, the onboard force model, and the user clock (one-way only). Transient problems were also simulated such as TDRS ephemeris updates, and passes of data with large biases or high noise.

Identical data sets were used in evaluating the estimation algorithms. The user satellite state was estimated for both modes. For the one-way mode, the onboard oscillator frequency bias was also estimated. The user ephemeris resulting from each estimation process was compared to the truth model to determine the accuracy and reliability of that estimation process was compared to the truth model to determine the accuracy and reliability of that estimation process in both baseline and worst cases. The process noise levels in the EKF were varied to determine the optimum range. The performances of the CEKF and CKF were analyzed to determine an appropriate set of consider parameters and their a priori variances. In addition, a method of automating the DC processing was evaluated.

I. INTRODUCTION

National Aeronautic and Space Administration operational support of satellite missions of the future will require the annotation of data collected onboard with ancillary data, which includes the spacecraft orbit, attitude, and time. If the spacecraft position and velocity can be determined entirely onboard, it will improve the system responsiveness by providing fully annotated payload data without the requirement for post facto processing or other ground support. Onboard data annotation will also decrease the ground support requirements for spacecraft and attitude control and instrument operations.

Toward this end, Goddard Space Flight Center (GSFC) is currently investigating the feasibility of autonomous spacecraft navigation with Tracking and Data Relay Satellite System (TDRSS) data. The use of TDRSS data for onboard estimation has the advantage that the NASA will already be using TDRSS for ground-based satellite tracking and the relay of command and telemetry data. Therefore, TDRSS interfaces will already exist, and NASA spacecraft will be equipped with TDRSS transponders. However, the major constraint in the use of TDRSS is that only a limited number of users may use the forware link over a given time span, which limits the frequence of tracking contacts.

An onboard orbit determination algorithm must be selected for use with TDRSS data that will provide both reliability and accuracy. Three estimation algorithms are being studied to determine their suitability for onboard use with TDRSS data: the extended Kalman Filter (EKF), the batch least-squares estimator, and the consider filter. The performance of these estimators was compared with respect to: 1) accuracy using a nominal tracking schedule, 2) effect of reducing the tracking schedule, 3) effect of large TDRS ephemeris errors,

and 4) accuracy in the presence of anomalous or deleted passes of data. This paper presents an overview of the results of the studies made, which are described in detail in References 1,2, and 3. The work described herein was carried out under Contract NAS 5-24300 using the capabilities of the Research and Development Goddard Trajectory Determination System (R&D GTDS) available at the time of the study (References 4, 5, and 6).

II. PROTOTYPE SYSTEM

A prototype onboard orbit determination system for use with TDRSS data is being developed by the Advanced Systems Program of the Office of Space Tracking and Data Systems (OSTDS) to demonstrate its feasibility. This work includes analysis to select a suitable estimation technique, and design and implementation of a candidate system on a LSI-11/23 microprocessor. The prototype system will be a combination of hardware and software designed to simulate the onboard operation and ground support of the orbit determination system.

Two tracking modes are being studies for use onboard, one-way Doppler and two-way range and/or Doppler. The one-way Doppler measurements are extracted onboard the user satellite from tracking signals originating on the ground, relayed through a TDRS, and received by the user spacecraft. The accuracy of the one-way measurements will be degraded by any errors in the user frequency standatd that is used in extracting the Doppler measurements. The geometry of this measurement is illustrated in Figure 2-1. The two-way data are extracted on the ground from the round-trip propagation of the tracking signals; the resulting data are collected and relayed back to the user spacecraft through the communications link. The two-way measurement geometry is illustrated in Figure 2-2. Comparison of Figure 2-1 and 2-2 shows that the

one-way data is from the forward link of the round-trip measurement which produces the two-way data.

A diagram of the proposed orbit determination concept and its interaction with other satellite systems is shown in Figure 2-3 (adapted from Ref. 7). Those areas outlined by the dashed lines indicate the additional requirements for the onboard orbit determination. Both one-way and two-way data types will require additional onboard computer capability for the orbit determination. One-way navigation will require modification of the standard TDRSS transponder to permit Doppler extraction and signal acquisition.

For both navigation modes, the Payload Operations Control Center (POCC) transmits the TDRSS ephemerides via the TDRSS to the user spacecraft. For two-way tracking data, the measurements, along with accurate time tags and frequency reference provided by the standard clock at White Sands Tracking Facility (WSTF), are placed in the command stream and transmitted to the user via TDRSS. In the one-way navigation mode, the navigation computer uses the TDRSS ephemeris and the a priori satellite state estimate to predict the Doppler measurement for signal acquisition. The two-way data navigation mode can be one for estimation recovery after a user spacecraft maneuver, or any event requiring estimation initialization, and then the navigation mode switched to one-way data. Once measurements are available, they are passed to the orbit determination module for estimating the user satellite ephemeris and, for one-way data, the oscillator frequency bias. Other modeling parameters related to the effects of atmospheric drag or to the frequency standard may also be estimated. The satellite ephemeris produced by the estimation process is passed to the general purpose onboard computer for use instead of the ground-uplinked ephemeris.

III. ESTIMATORS

Four estimation techniques were selected for study; an extended Kalman filter (EKF), a sliding batch differential corrector (SBDC), a consider Kalman filter (CKF), and a consider extended Kalman filter (CEKF). The EKF was available in R&D GDTS, and the SBDC, CKF, and CEKF were made available through temporary modifications to the R&D GTDS software. These orbit determination techniques were studied to determine their reliability and accuracy in the presence of measurement errors and data problems associated with TDRSS data. Figure 3-1 lists the major characteristics of each estimator.

Extended Kalman Filter (EKF)

The R&D GTDS Filter Program (Reference 5) contains an EKF estimator with a simple process noise covariance matrix model. It was recognized that the sequential processing capability of the EKF would be advantageous for onboard orbit estimation, although the data coverage would be sparse (at most, a 10-minute pass of data per orbit), not an optimal configuration for a filter. The operational flow of an EKF is given in Figure 3-2.

In the EKF, the state, clock, and drag covariance process noise rates were modeled using the linear model

$$Q(t_k) = \dot{Q} \cdot (t_k - t_{k-1})$$

where $Q(t_k)$ = process noise

$\dot{Q}$ = diagonal matrix of constants that are the assumed noise variance rates of change for the solve-for parameter set

t_k = measurement time

t_k-1 = measurement time of previous observation

The state covariance is augmented by $Q(t_k)$ at each measurement time, t_k. In the current study, nonzero process noise rates of change were used for the velocity, clock drift, and drag terms.

Sliding Batch Differential Correction (SBDC)

The batch least-squares estimation (DC) program of R&D GTDS, described in References 4 and 6 was modified, as described in Reference 2, to sequentially process a series of data spans through a large data set. The program starts with a span of data approximately 12 hours, with which it estimates the satellite position and velocity state, and other parameters, as requested. After converging to a solution, a new data span is created by adding new data and deleting old data. A new solution is then attempted on this data. In a typical run selecting 12 hour spans from a file covering 24 hours, five solutions and five separate DC Program runs qre made.

The SBDC flow is described in Figure 3-3.

Consider Kalman Filter (CKF) and Consider Extended Kalman Filter (CEKF)

The FILTER Program of R&D GTDS, as described in Reference 5, was modified to include a consider feature, used in place of the process noise covariance matrix. The motivation for this investigation was to compare the CKF and CEKF results to those of the EKF and the SBDC to see if the consider feature, which models the estimation error in a more physically meaningful way, would perform better than the EKF or SBDC or lead to a better understanding of the estimation results from the EKF and SBDC.

The KF and EKF can be easily modified to the CKF and CEKF be setting the relevant gain terms to zero. If the state

update equation is partitioned into the solve-for (X) and consider (Z) portions, then the state update, x, is

$$\begin{bmatrix} \hat{x} \\ \hat{z} \end{bmatrix} = \begin{bmatrix} \bar{x} \\ \bar{z} \end{bmatrix} + \begin{bmatrix} K \\ 0 \end{bmatrix} \left\{ y - \begin{bmatrix} H_x & H_z \end{bmatrix} \begin{bmatrix} \bar{x} \\ \bar{z} \end{bmatrix} \right\}$$

where Hx and Hz are the partial derivatives of the observation equation with respect to the solve and the consider parameters, respectively.

The covariance is also partitioned to be

$$P = \begin{bmatrix} P_x & P_{xz} \\ P_{zx} & P_z \end{bmatrix}$$

If the a priori cross terms P_{xz} and P_{zx} are assumed to be zero, the Kalman gain is

$$K = \bar{P}x \; H_x^T \left[H_x \bar{P}_x H_x^T + H_z P_z H_z^T + R \right]^{-1}$$

$$P_x = \left[I - K \; H_x \right] \bar{P}_x$$

$$P_{xz} = -K \; H_z P_z$$

The propagated estimate to the error in Z, $\bar{z}$, will be zero, since no estimate is made of the Z error. Then the state update will be

$$\hat{x} = \bar{x} + K(y - H_x \; \bar{x})$$

For the CKF, the processing done until the last data point is processed, and then the state is updated

$$\hat{X}_\ell = X_\ell + \hat{x}_\ell$$

If the CKF has not converged, the updated state $\hat{X}_\ell$ is propagated back to the first observation and the process begins again.

For the CEKF, the state update becomes:

$$\hat{X}_K = X_K + K_k y_k$$

which are then the initial conditions for integration to the next data point.

IV Evaluation Procedure

Several programs available in R&D GTDS were used in the evaluation of the orbit determination accuracy. Figure 4-1 illustrates the evaluation procedure by which the ephemeris of a "truth" model for the user satellite was compared with the ephemeris produced by the estimator. Deviations between the two ephemerides provide a measurement of the accuracy obtained by the estimator for a particular test case. The simulated data used by the estimator is supplied by the DATASIM Program, which has the capability to corrupt the range and delta-range measurements with measurement errors and random measurement noise.

The time spans for the comparisons for each estimator are chosen to cover times which correspond to those in which an operational onboard estimator would be annotating data. In the case of the CKF, and the SBDC, this is a span covering at least one orbit, and possibly two, beyond the last data points. For the EKF and the CEKF, this comparison time span is one covering an orbit or more well beyond (that is, several orbits) the initial data. This time span should be one in which the effects of initialization of the filter are not noticeable, and the filter has settled to a steady state or equilibrium condition. Since it is of some interest to learn how long this settling process takes, two comparison spans are used, one at the mid-point and one at the end of the data.

The analysis procedure used in comparing the ephemerides involved examining (1) the solve-for parameter report, (2) the root mean square (rms) and the maximum deviations of the position and velocity errors, and (3) the radial, along-track, and cross-track ephemeris comparison plots of the position and velocity errors for the full estimation time

span. These statistics were recorded for all cases, along with pass frequency, numbers of TDRSs observed, and measurement and modeling errors applied.

Test Cases

The Landsat-D and Gamma Ray Observatory, (GRO) spacecraft were selected as the sample test cases for onboard orbit estimation. Landsat-D has a near-polar inclination and a medium altitude. GRO, on the other hand, has a lower altitude and a less inclined orbit. Table 4-1 lists the Landsat-D and GRO orbital elements and spacecraft parameters. The TDRSS satellites were placed in nearly circular stationary orbits 130° apart with periods of 1436.2 minutes.

Measurement Models for TDRSS Data

For the purpose of this study, three separate data-type cases were considered for evaluation: one-way Doppler data, two-way Doppler data, and two-way range and Doppler data. The Doppler measurement was simulated as a delta-range measurement so that existing R&D GTDS capabilities could be used.

The range and delta-range measurements were simulated using the pseudo-TDRSS data capabilities in the Data Simulation (DATASIM) program of R&D GTDS. A discussion of these measurements can be found in Reference 1. A set of range and/or delta-range measurements constitute a pass of data. In all cases, it was assumed that the user satellite was in contact with a single TDRS for 10 minutes for each pass of data. The time between range and delta-range measurements and the delta-range computation interval were set at 10 seconds, which yields 30 delta-range measurements for every complete pass of data. For both measurement types combined, there are 30 range and 30 delta-range measurements.

TDRSS Tracking Schedules

The TDRSS observation simulation determines the TDRSS visibility from the user spacecraft by testing to see if the TDRSS falls within the user antenna and that it is not occulted by the Earth. The effects of atmospheric refraction are not included in the observation modeling. With an antenna modeled as a cone pointing along the radial direction with a half-angle of 100^0, the time span of line-of-sight contact between Landsat-D or GRO and any single TDRS ranges from 40 to 60 minutes. During the early phases of the feasibility study, several models were run to investigate the dependence of the prediction accuracy on the time from the first or last possible contact with a TDRS. It was determined that tracking measurements made consistently at the beginning or end of a visibility interval (edge-justified data) yield better estimation accuracy than those centered in the visibility arc (center-justified data). Since neither data set represents a realistic case, a more random model was selected for use in the remainder of the study. Another variable in the tracking schedule was the length of time between subsequent passes of data. To study this, estimation was done with time gaps of one, two, or three user-satellite revolutions between data passes. For the one revolution gap, a Landsat-D data set covering a 24-hour time span will have 17 passes of data. For the same time span, a set with a two revolution gap will contain 9 passes of data, and, with a three revolution gap, 6 passes of data. For any given pass of data, the user satellite was restricted to tracking by only one TDRS. However, most models were run with alternating TDRS contacts on subsequent passes of data.

Figure 4-2 shows the TDRS visibility for the GRO satellite, and the location of the data sets used for the one revolution gap GRO studies.

Measurement Error Models And Anomalous Data

Each observation in a data set, consists of the observed quantity, range or delta-range, its time tag, and the TDRS identification and coordinates at the time of the observation. The scheduling of the observations and the delta-range integration time are supplied by the user. The R&D GTDS DATASIM Program applies biases and random errors to the measurements. Errors on the TDRS ephemeris are applied to the TDRS coordinates included in each observational record. The frequency bias is added to the delta-range observation and the user clock error is applied to the observation time tag.

The nominal values for each of these error sources are listed in Tables 4-2, 4-3 and 4-4, respectively.

To study the performances of the estimators in the presence of transitory data problems, data sets were created in which one or more ten-minute passes of data were given anomalously large errors. The operation of this data simulation technique is explained in detail in Reference 2.

The errors may include any or all of the following:

- Larger TDRS ephemeris errors in the along-track(L), cross-track(C), radial(H) and/or $\dot{L}$ components
- Larger range and/or delta-range measurement noise
- Larger bias on the range data
- Bias on the delta-range data

These errors are applied to one or more specific passes in a 24-hour data set. In this way, the effects of transitory problems which are periodic or create larger random errors or a bias on the data can be studied.

Dynamic Modeling Errors

Dynamic modeling errors are simulated by a mismatch of the

spacecraft acceleration and frequency standard that are used in the data simulation from those used in the estimation.

Physically, these errors arise from the lack of precise models for the accelerations acting on the spacecraft and the behavior of onboard clocks. The dynamic modeling errors affect the accuracy of the propagation of the orbital and clock state vectors. The dynamic models used in the truth model, and in the estimators, the EKF, the SBDC, the CKF and the CEKF, are given in Table 4-5.

Table 4-6 gives the maximum deviation in 24 hours due to the dynamic modeling differences between the truth and the estimation models for the SBDC. Figures 4-3 and 4-4 show the along-track growth of these errors over 12 hours for Landsat-D and GRO. Similar results for the EKF force model show a larger error growth.

Baseline Parameters

Table 4-7 lists the parameters that were estimated and those from which the consider parameters were chosen. Table 4-8 lists the a priori offsets or values, a priori covariances associated with the estimated parameters, and the measurement standard deviations that were used in the baseline runs.

The clock drift term (frequency bias), $\dot{b}$, is estimated in addition to the orbital state vector when using one-way data. For the GRO satellite, the atmospheric drag parameter (ρ_1) can be either estimated or considered. The values in Table 4-7 for ρ_1 and its a priori covariance are for cases in which ρ_1 is estimated.

For the CKF and CEKF estimators, the central body term (GM), and any of the geopotential coefficients can be considered. For one-way data, the clock drift rate ($\ddot{b}$) can also be considered. The atmospheric drag parameter (ρ_1) can be considered when estimating the GRO orbital state.

V. Evaluation Results

The four estimation algorithms were studied to determine their best performance with data with the baseline error levels. In the case of the EKF, this included tuning the process noise parameters to give optimal results. For the CEKF and the CKF, the selection of the considered parameters and tuning their variances was studied. All baseline runs and their variations used a tracking schedule of 10 minutes every N revolutions of the user satellite and alternating observations of the two TDRSs. Figure 4-2 shows the periods of visibility of TDRS-E and TDRS-W from GRO for 24 hours from the time of epoch (October 1, 1980). The shaded areas represent the data spacing for cases with one contact per revolution. A similar visibility pattern is used for the Landsat-D satellite.

Some representative results taken from the Landsat-D satellite studies are shown in Table 5-1, and some results when the user satellite is GRO are shown in Table 5-2. The run numbers in these tables refer to the run numbers used in references 1, 2, and 3.

The runs are grouped to allow comparison of the performance of an extended estimation (EKF, CEKF) against a batch processor (SBDC, CKF). Statistics for an extended estimator are given for two periods, 9-12 hours and 21-24 hours after the beginning of the data spans. The later period is to assess the estimator accuracy unaffected by transients associated with initializing the estimator. For some of the runs, the differences between the 9-12 hour span and 21-24 hour span evaluations show that the extended estimator has not reached an equilibrium solution at 12 hours, but requires a longer time. In the case of the batch (SBDC, CKF) estimators, the statistics are associated with a

typical ephemeris prediction that uses an initial state derived from processing data spanning the previous 12 hours.

Effect of the Baseline Data Errors

The error in the along-track direction for the Landsat-D B5 EKF run is shown in Figure 5-1. The behavior of these errors is characteristic of the EKF, in which a large initial deviation (reaching, in this case, a maximum of 2549m), is reduced to an acceptable level as the data processing proceeds and the filter achieves an equilibrium solution. For comparison, the along-track error for the L02 SBDC run is shown in Figure 5-2. In this case, Figure 5-2a is a plot of the definitive solution error over the data span, and 5-2b the predictive error after the end of the data. These errors behave in a manner characteristic of a DC estimator, in which the definitive solution errors have a mean of zero. The predictive errors behave as would be expected from the differences in the truth and estimator force models, as shown in Figure 4-1.

The additional errors in the modeling from increased drag on the GRO satellite decrease the accuracy attainable by the estimators, as can be seen by comparing the Table 5-2 baseline results to those in Table 5-1. The statistics for the P12 EKF run as compared to the B5 run show the EKF requiring more than 12 hours to reach an equilibrium solution, and producing a little larger rms and maximum deviation after the equilibrium solution is reached.

The CEKF run 200E, whose along-track errors are plotted in Figure 5-3 is using the J_2 harmonic coefficient as a consider parameter.

Effect of Reduced Data Sets

Using less data, delta-range data only (run H3) or a pass of data every other revolution (runs L5, L12, 114E) does not affect the solution accuracy significantly. When the data is decreased even further, to data only every third revolution, there is some growth in the error, with the run D2 statistics as compared to B5 as an example.

The effect of using less data is more pronounced with the GRO satellite. The CEKF run 113E shows rms and maximum deviations approximately double those in run 200E. This CEKF run is using the Earth geoptential constant (GM) as a consider parameter. Run P24, with along track errors plotted in Figure 5-4, shows that when the EKF estimator has a data pass once every three revolutions, or 6 contacts (360 observations) over 24 hours, approximately 15 hours is required to reach an equilibrium solution for a drag perturbed satellite.

The Effect of TDRS Ephemeris Errors

Runs E4 and L15 are examples of the effect of larger TDRS ephemeris errors in the Landsat-D data. It was found that the estimators perform about as well using only delta-range data as when both range and delta-range data are used as long as the weighting on the range data reflects the larger error in that data type from the TDRSS ephemeris errors. When the TDRS ephemeris errors were not reflected in the range measurement noise (that is, the estimator assumed a more accurate measurement than was available), the estimation accuracy was degraded. Proper use of the range data assumes a good knowledge of the level of error in the TDRS ephemeris, a factor which increases the risk of using that data type.

The SBDC run L15 also included the effect of a TDRS ephemeris update 14 hours after the beginning of the Landsat-D data set.

The first two data spans of the SBDC are data processed with increasing TDRS ephemeris errors, and, as the SBDC processes successive 12 hour spans, the level of the total TDRS ephemeris error becomes less. This can be seen in Figure 5-5 of the along-track errors in the first and fifth data spans. The rms of the predicted solution is 202m for the second span and 139 for the fifth; the maximum deviations are 304m and 190m, respectively. (The statistics given in Table 5-1 are from the first data span).

The effects of additional $\dot{L}$ error in the TDRS ephemeris for the GRO satellite are shown in the runs Q17 of the EKF and G6 of the SBDC in Table 5-2. The SBDC shows and increasing effect as the successive spans of data are processed. The statistics given are from the third data span. At the fifth, they are 323m rms and 507m maximum deviation. The errors in the G1 run, by comparison, stay more uniform over the data arc; the statistics given are for the fifth span of that run.

The SBDC run G15 includes a TDRS ephemeris update at 14 hours. The plot of the along-track error in Figure 5-6 is over the first 12 hours, showing the solution accuracy as the maximum TDRS ephemeris error is approached.

Effect of Onboard Clock Errors

Use of one-way data degrades the solution accuracy as compared to the two-way data results. Landsat-D runs M4, L08 and the GRO run R8, show this. One-way data has increased error due to the user clock errors, especially the frequency bias and drift, and the larger delta-range measurement noise. Also, the estimators must now solve for one or two additional terms with no increase in the amount of data. The EKF requires a larger processing span to achieve an equilibrium solution than when using two-way data, as can be seen in Figure 5-7 of EKF run M4. The SBDC L08 run exhibits the type of errors common to a DC estimator trying to estimate a

quadratic clock error (linear frequency bias error) with a linear equation (constant). The plot of the definitive solution along-track errors, in Figure 5-8, show this effect, with the errors containing a linear term.

Estimating with one-way GRO data is considerably more difficult than with one-way Landsat-D data. Figure 5-9 shows the along-track errors for EKF run R8, estimating the frequency bias for the accurate clock. The effect of the drag errors, and the necessity for solving for the drag parameter, can be seen by comparing Figure 5-9 with the comparable run for Landsat-D, in Figure 5-7.

Replacing the accurate oscillator in the one-way data model with the NASA standard transponder, whose frequency drift is 200 times larger, produces much worse results. The errors in the SBDC grow to hundreds of kilometers when attempting to model this oscillator as one with a constant frequency bias. The EKF run N14 with Landsat-D data, shows that when both the frequency bias and drift are estimated, the solutions are as accurate as with the two-way data. However, this should not be construed as demonstrating that the frequency drift must be estimated for accurate solutions. It is only a demonstration of the need for correctness in the estimator modeling of one-way data as the data is simulated with the same oscillator as is used in the estimator.

The NASA transponder oscillator produces even worse results when used with GRO data. Runs comparable to the EKF run with this data gave solutions accurate only to 1-10 kilometers. All of the estimators need to estimate the frequency drift to perform well with GRO data with the transponder oscillator error.

Effect of Anomalous Data

Data sets were generated in which one or two passes had anomalous data errors; large increases in any or all of the errors sources beyond what is expected by the estimators. If the estimator can recognize that the data pass is in error and edit it, it has virtually no effect on the solution accuracy. If the estimator does not recognize the data pass as having larger errors, then it can, and does, corrupt the solution accuracies. Runs O4 and L17 are two in which the Landsat-D data with anomalous errors were not all edited. Plots of the solution accuracies are shown in Figures 5-10 and 5-11, respectively. For run L17, the bad data occurs at $4^h\ 45^m$ after the beginning of the data span. The definitive solution from Figure 5-11a is for the first span in which the data, nearly centered in this span, shows a more significant effect than Figure 5-11b, where the bad data are the first points encountered.

The along-track errors in the two runs with anomalous data in Table 5-2, the T3 EKF run and the G19 SBDC run, are plotted in Figures 5-12 and 5-13, respectively. In both cases the errors are such that the anomalous data are not all edited. The bad data pass for G19 has a significant effect on the second span of the SBDC, as seen in Figure 5-13a, but the estimator is recovering by the fourth span, as shown in Figure 5-13b. The statistics given are those for the second span; for the fourth they are 377m rms and 566m maximum deviation.

VI. Conclusions

These studies have been done by modifying an existing satellite-to-satellite tracking system in an attempt to study relevant data error sources. While it is an analyst's axiom that no simulation can adequately model the real world effects, it does allow some conclusions as to the appropriate procedure for onboard navigation.

- All estimators give solutions using the baseline data sets to an accuracy of 500m or better, often to better than 100m.
- Use of the two-way range data with the delta-range data produces the same results as using the delta-rang data alone only as long as the TDRS ephemeris errors are well known and accounted for in the data weighting. If their effect is underestimated, the range data will degrade the solution accuracy.
- The model used for the frequency standard should be examined further to determine appropriate models for estimation of realistic errors. The solution accuracy depends strongly on the accuracy of this estimation when one-way data is used.
- The SBDC estimator needs no tuning for optimal performance with the two-way data.
- The EKF, CEKF, and CKF estimators must be tuned to the specific circumstances for which they are intended for optimal performance. With this data type, these estimators perform best when tuned to respond somewhat slowly to new data.
- The estimator which requires the least processing from the onboard computer is the EKF. The one which requires the most is the CKF.

- The EKF and CEKF need between 6-15 hours to reach an equilibrium solution, depneding on the data type and frequency. The SBDC and CKF need 2 to 4 iterations to converge to an acceptable solution.

REFERENCES

1. CSC/TM-80/6176, Onboard Orbit Determination with Tracking and Data Relay Satellite System (TDRSS) Data, Volume 1, Extended Kalman Filter (EKF) Evaluation, A. C. Long, P. S. Gural, October 1980

2. CSC/TM-80/6234, Onboard Orbit Determination with TDRSS Data, Volume 2, Sliding Barch Differential Corrector (SBDC) Evaluation, K. A. Preiss, J. B. Dunham, in preparation

3. CSC/TM-80/6235, Onboard Orbit Determination with TDRSS Data, Volume 3, The Consider Filter Evaluation, J. B. Dunham and H. M. Sielski, in preparation

4. CSC, Goddard Trajectory Determination System Research and Development (GTDS R&D) User's Guide (draft), August 1978

5. CSC/SD-79/6032, The Research and Development Goddard Trajectory Determination System (R&D GTDS) Filter Program Software Specifications and User's Guide, J. B. Dunham, December 1968

6. Mathematical Theory of the Goddard Trajectory Determination System, J. O. Cappellari, C. E. Velez, and A. J. Fuchs (eds), GSFC, X-582-76-77, April 1979

7. NASA, End-to-End Data System (NEEDS) Ancillary Data and Support Computing (ADSC) Concept Document, NEEDS/ADSC Team, June 1980

Table 4-1. Landsat-D and GRO Orbital Elements, Area, and Mass

PARAMETER	LANDSAT-D	GRO
EPOCH	OCTOBER 1, 1980	OCTOBER 1, 1980
COORDINATE SYSTEM	TRUE OF DATE	TRUE OF DATE
SEMIMAJOR AXIS (km)	7086.901	6778.140
ECCENTRICITY	0.001	0.0017
INCLINATION (deg)	98.181	28.0
LONGITUDE OF ASCENDING NODE (deg)	354.878	0.0
ARGUMENT OF PERIGEE (deg)	180.0	0.0
MEAN ANOMALY (deg)	0.0	0.0
PERIOD (min)	98.956	92.56
AREA (m^2)	20.0	20.0
MASS (kg)	1700.0	1700.0

7657/80

Table 4-2. Data Simulation Measurement Errors

PARAMETER	BASELINE STANDARD DEVIATION	
	ONE-WAY DATA	TWO-WAY DATA
Random Range Error(m)	-	1
Random Delta-Range Error(cm)	10	1
Range Measurement Bias(m)	-	7
Delta-Range Measurement Bias(cm)	+	-

+The delta-range measurement bias due to the user clock is

= 60,000 + 0.0069t cm for the accurate clock,

= 300,000 + 0.69t cm for the NASA standard transponder,

t measured in seconds from the clock epoch.

Table 4-3. Data Simulation TDRS Ephemeris Error Model

PARAMETER	VALUE
PERIOD OF SINUSOID[1] (hr)	24
RADIAL AMPLITUDE (m)	35
CROSS-TRACK AMPLITUDE (m)	35
ALONG-TRACK AMPLITUDE (m)	80
ALONG-TRACK GROWTH RATE (m/day)	250

7526/80

[1]SINUSOIDAL PERIOD FOR RADIAL, CROSS-TRACK, AND ALONG-TRACK TDRS EPHEMERIS ERRORS.

Table 4-4. Data Simulation Quadratic User-Clock Error Model

COEFFICIENT	ONE-WAY DATA		TWO-WAY DATA
	NASA STANDARD TRANSPONDER	ACCURATE ONBOARD CLOCK	PERFECT CLOCK
USER-CLOCK BIAS (sec)	0	0	0
USER-CLOCK DRIFT (sec/sec)	1×10^{-6}	2×10^{-7}	0
USER-CLOCK DRIFT RATE (sec/sec/day)	2×10^{-7}	2×10^{-9}	0

7526/80

Table 4-5. Dynamic Models

PARAMETER	DATA SIMULATION VALUE	EKF/CEKF VALUE	SBDC/CKF VALUE
GEOPOTENTIAL	15x15, GEM-9	8x8,GEM-1	8x8,GEM-7
RESONANCE (GRO ONLY)	YES	NO	NO
SOLAR FLUX	150×10^{-22} watt/m^2/Hz	200×10^{-22} watt/m^2/Hz	200×10^{-22} watt/m^2/Hz
AERODYNAMIC DRAG COEFFICIENT	2.0	2.2	2.2
SUN AND MOON	YES	YES	NO
SOLAR RADIATION PRESSURE	NO	NO	NO
INTEGRATOR	COWELL 12th-ORDER	RUNGE-KUTTA 3(4+)	RUNGE-KUTTA 3(4+) (CKF) COWELL 12th-ORDER (SBDC)

Table 4-6. Error Growth in Ephemeris over 12 Hours

SATELLITE	MAX. POS. DIFFERENCE (M)			
	ΔH	ΔC	ΔL	ΔR
LANDSAT-D	45.	94.	1232.	1235.
GRO	367.	103.	26573.	26575.

Table 4-7. Estimator Solve-for and Consider Parameters

PARAMETERS	ONE-WAY DATA	TWO-WAY DATA
$x, y, z, \dot{x}, \dot{y}, \dot{z}$	solve	solve
$\dot{b}$	solve	-
$\ddot{b}$		
EKF and SBDC	ignore/solve	-
CKF and CEKF	ignore/solve/ consider	-
ρ_1 (GRO only)		
EKF and SBDC	solve	solve
CKF and CEKF	solve/ consider	solve/ consider
GM CKF and CEKF	consider	consider
geopotential harmonic coefficients CKF and CEKF	consider	consider

Table 4-8. A Priori Values and Measurement Standard Deviations

PARAMETER	BASELINE INPUT VALUE	
	ONE-WAY DATA	TWO-WAY DATA
A PRIORI STATE OFFSETS		
X,Y,Z	100 m	100 m
$\dot{X},\dot{Y},\dot{Z}$	30 cm/sec	30 cm/sec
A PRIORI USER CLOCK PARAMETERS		
b(BIAS)	0 sec	-
$\dot{b}$(DRIFT)		
NASA STANDARD TRANSPONDER	1.1×10^{-6} sec/sec	-
ACCURATE ONBOARD CLOCK	2.2×10^{-7} sec/sec	-
$\ddot{b}$ (DRIFT RATE)	0 sec/sec/day	-
A PRIORI ρ_1	0.0	0.0
A PRIORI COVARIANCES(EKF, CKF, & CEKF)		
X,Y,Z	0.1 km^2	0.1 km^2
$\dot{X},\dot{Y},\dot{Z}$,	1.0 m^2/sec^2	1.0 m^2/sec^2
$\dot{b}$	1×10^{-6} sec/sec	-
ρ_1 (GRO ONLY)	1.0	1.0
A PRIORI COVARIANCES (SBDC)		
X,Y,Z	∞	∞
$\dot{X},\dot{Y},\dot{Z}$,	∞	∞
$\dot{b}$	∞	-
ρ_1 (GRO ONLY)	∞	∞
STANDARD DEVIATION OF MEASUREMENT ERROR		
RANGE	-	40 m
DELTA-RANGE	10 cm	1 cm

Run	Estimator	Data Type	Tracking Schedule	rms/max position deviations (m)			Data Error Model
				$9^h - 12^h$	typical 3hr prediction	$21^h - 24^h$	
B5 LO2	EKF SBDC	2-Way $\rho, \Delta\rho$	1 Rev	78/130 -	81/124	41/65 -	baseline
H3	EKF	2-Way $\Delta\rho$	1 Rev	66/95	-	49/82	baseline
C5 L12 114E	EKF SBDC CEKF	2-Way $\rho, \Delta\rho$	2 Rev	67/99 - 61/92	- 120/174 -	39/55 - 88/134	baseline
D2	EKF	2-Way $\rho, \Delta\rho$	3 Rev	83/162	-	73/119	baseline
E4	EKF	2-Way $\rho, \Delta\rho$	1 Rev	41/85	-		8H, 8C
L15	SBDC	2-Way $\Delta\rho$	1 Rev	-	187/262	-	8H, 8C, TDRS Ephemeris Update
M4 LO8	EKF SBDC	1-Way $\Delta\rho$	1 Rev	282/418 -	- 345/531	87/169 -	accurate clock
N14	EKF	1-Way $\Delta\rho$	1 Rev	110/190	-	47/92	NASA transponder, $\ddot{b}$ estimated
O4	EKF	2-Way $\rho, \Delta\rho$	1 Rev	66/95	-	140/228	anomalous data 13hrs ρ error = 7 km $\Delta\rho$ error = 300 cm
L17	SBDC	2-Way $\rho, \Delta\rho$	1 Rev	-	58/101	-	anomalous data 5hrs ρ error = 5 km $\Delta\rho$ error = 500cm

Table 5-1. Results for Landsat-D

Run	Estimator	Data Type	Tracking Schedule	rms/max position deviations (m)			Data Error Model
				$9^h - 12^h$	typical 3hr prediction	$21^h - 24^h$	
P12 200E	EKF CEKF	2-Way $\rho, \Delta\rho$	1 Rev	141/234 174/274	- -	60/88 64/139	baseline
G1	SBDC	2-Way $\Delta\rho$	1 Rev	-	252/420	-	baseline
113E	CEKF	2-Way $\rho, \Delta\rho$	2 Rev	368/637	-	120/230	baseline
P24	EKF	2-Way $\rho, \Delta\rho$	3 Rev	1090/2048	-	102/157	baseline
Q17 G6	EKF SBDC	2-Way $\Delta\rho$	1 Rev	173/315 -	- 245/380	109/194 -	4L
G15	SBDC	2-Way $\Delta\rho$	1 Rev	-	174/249	-	8H, 8C, TDRS Ephemeris Update
R8	EKF	1-Way $\Delta\rho$	1 Rev	306/453	-	129/235	Accurate clock
T3 G19	EKF SBDC	2-Way $\Delta\rho$	1 Rev	162/248 -	- 693/896	226/379 -	anomalous data 13hrs $\Delta\rho$ error = 300 cm

Table 5-2. Results for GRO

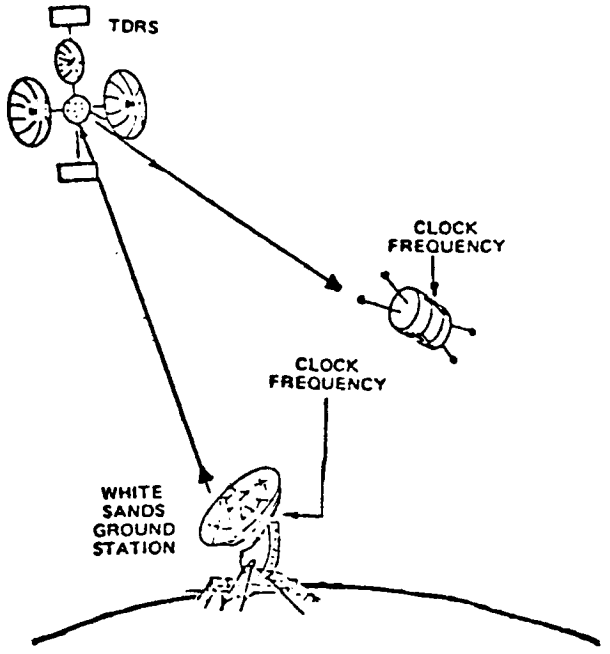

Figure 2-1. One-Way Tracking Signal Geometry

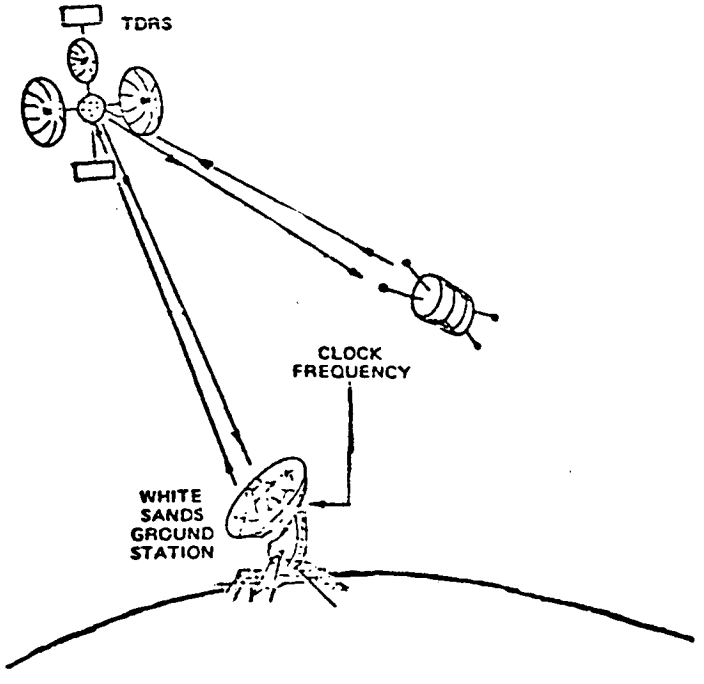

Figure 2-2. Two-way Tracking Signal Geometry

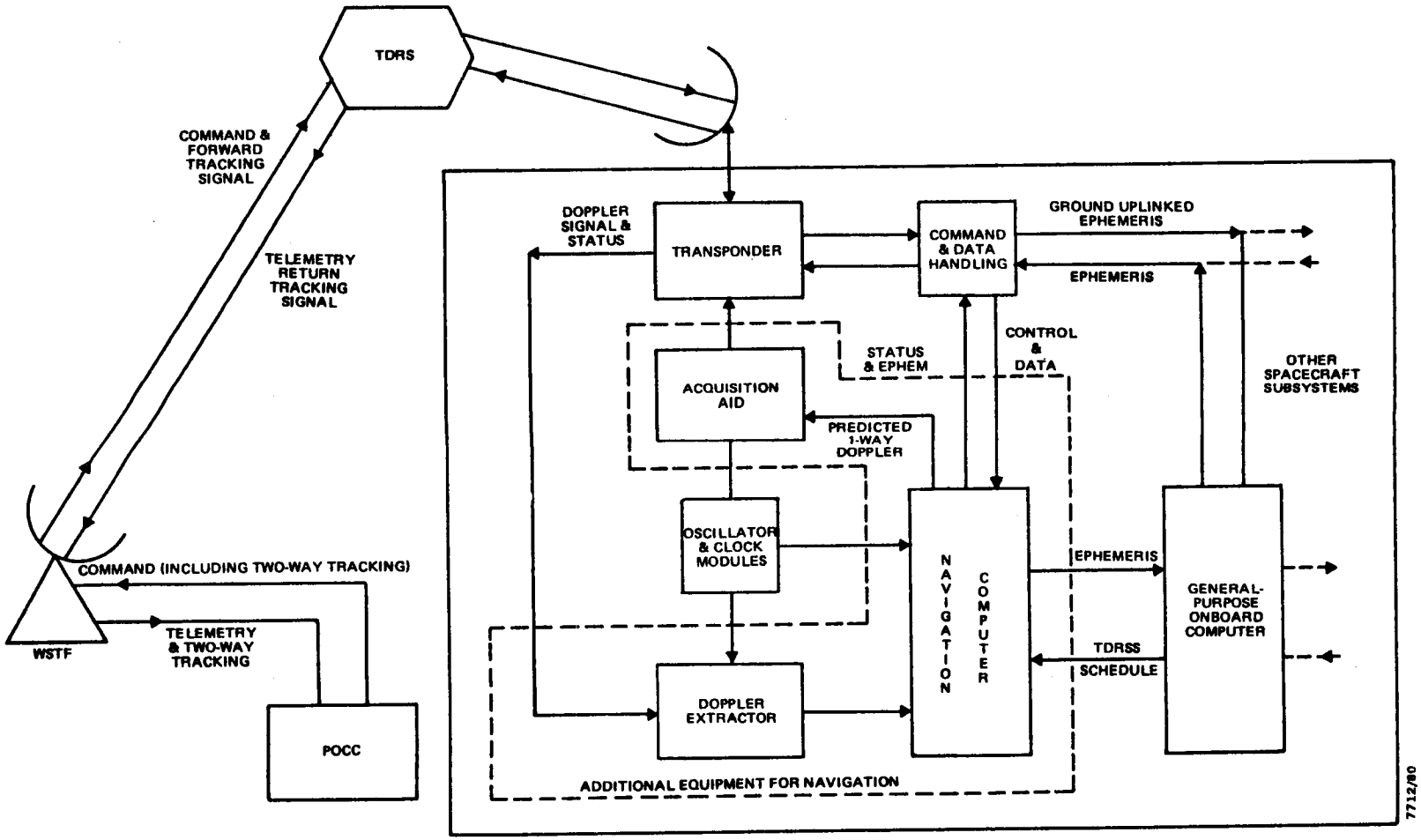

Figure 2-3. One-Way and Two-Way Tracking With TDRSS

EKF

- state update at each observation
- simple process noise covariance model
  $Q = \dot{Q}\,(t_i - t_{i-1})$
- tunable parameters
  - a priori covariance
  - $\dot{Q}$ matrix

SBDC

- State update at epoch
- Data in 12-hour spans, new solution generated when each pass of data is collected
- Initial state solution from previous data span propagated to new epoch
- No a priori covariance

CKF, CEKF

- State update at epoch (CKF) or each observation (CEKF)
- Consider covariance used instead of process noise
- Tunable parameters
  - a priori covariance
  - consider parameter selection and variance

Figure 3-1. Estimator Characteristics

given the initial state, $X_{k-1} = \hat{X}_{k-1}$, the covariance, P_{k-1}, and an observation Y_k

1. Propagate to t_k to obtain X_k

   state: $\dot{X}_k = F(X, t_k)$ with X_{k-1} as the initial conditions

   state transition matrix:

   $$\dot{\Phi}(t, t_{k-1}) = A(t)\ \Phi(t, t_{k-1}) \text{ with } \Phi(t_{k-1}, t_{k-1}) = I$$

   the initial conditions,

   and where $A(t) = \left|\frac{\partial F}{\partial X}\right|$ evaluated at $X = X_{k-1}$

2. Propagate the covariance to t_k

   $$\bar{P}_k = \Phi(t_k, t_{k-1})\ P_{k-1}\ \Phi^T(t_k, t_{k-1}) + \dot{Q} \times (t_k - t_{k-1})$$

   where $\dot{Q}$ is the state process noise covariance rate.

3. Compute observation (G_k), residual (y_k), and observation partial derivatives (H_k)

   $$G_k = G(X_k, t_k)$$

   $$y_k = Y_k - G_k$$

   $$H_k = \left|\frac{\partial G}{\partial X}\right| \text{ evaluated at } X = X_k$$

4. Compute gain (K_k), update covariance (P_k), and state $(\hat{X}_k)$

   $$K_k = \bar{P}_k H_k^T \left[H_k \bar{P}_k H_k^T + R_k\right]^{-1}$$ where R_k is the observation weight

   $$P_k = \left[I - K_k H_k\right] \bar{P}_k$$

   $$\hat{X}_k = X_k + K_k y_k$$

5. If there is more data, return to step 1.

Figure 3-2. EKF Operational Flow

Input: state $X(t_o)$

1. Select observation span, Y_k to Y_ℓ, and new epoch, t_k. Propagate state to the new epoch, t_k.

2. Integrate state and state transition matrix to each observation state: $\dot{X} = F(X,t)$ with $X(t_i)$ as the initial conditions

   state transition: $\dot{\Phi}(t,t_i)=A(t)\Phi(t,t_i)$ with $\Phi(t_i,t_i)=I$ as the initial conditions

3. Compute observation, residual, and observation partials

   $G_i = G(X_i,t_k)$,

   $y_i = Y_i - G_i$

   $H_i = \tilde{H}_i \; \Phi(t_i,t_k)$, where $\tilde{H}_i$ is the observation partials at t_i

4. When all observations are processed, compute update at epoch, t_k,

   $\hat{x}_k = (H^T R H)^{-1} H^T R y$, where R is the observation weighting matrix

   $\hat{X}_k = X_k + \hat{x}_k$

5. Determine if the SBDC has converged over this span. If not, repeat steps 2 to 4.
   If it has, go to step 1 and select the next data span.

Figure 3-3. SBDC Flow

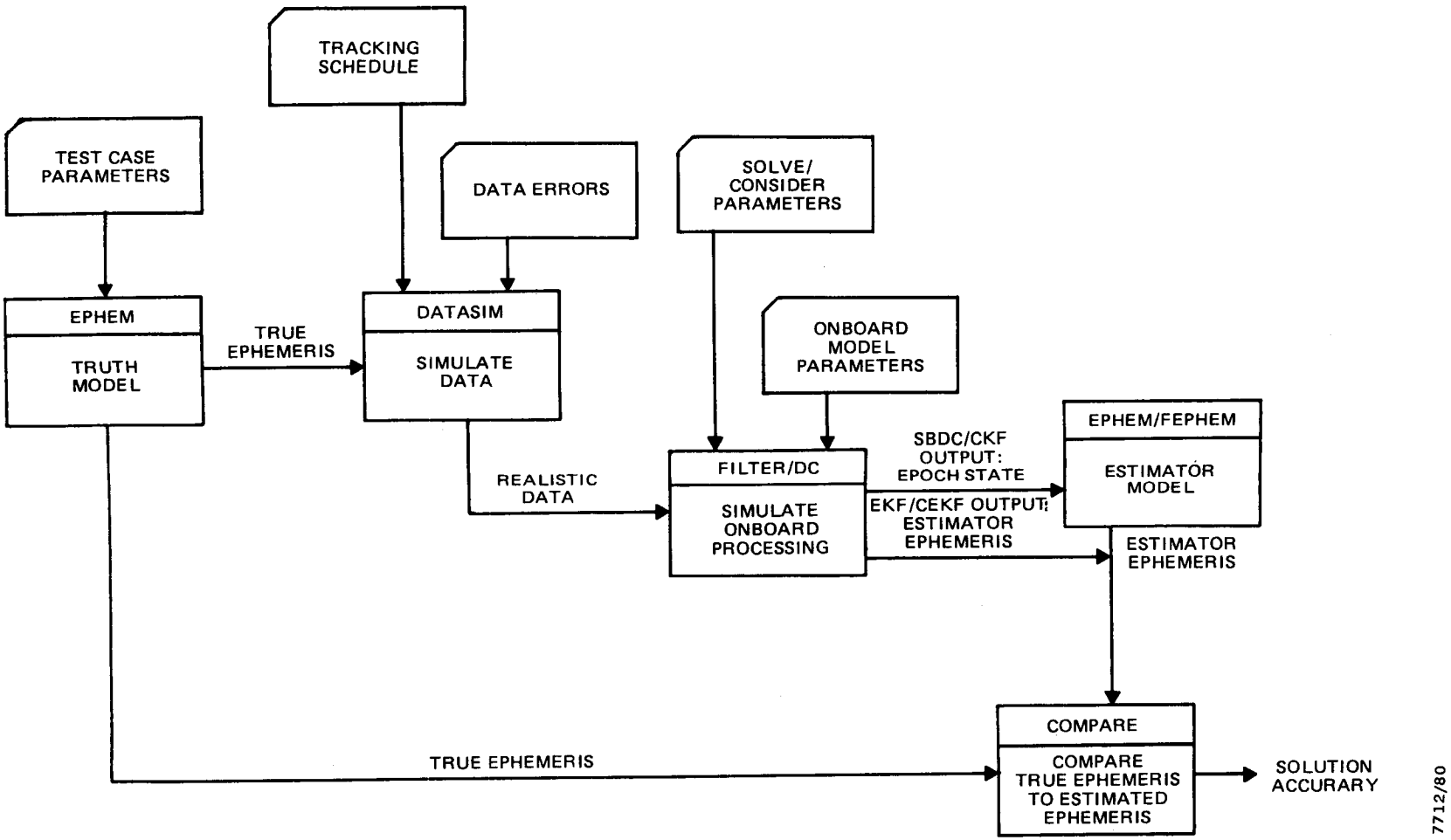

Figure 4-1. Evaluation Procedure for TDRSS Study

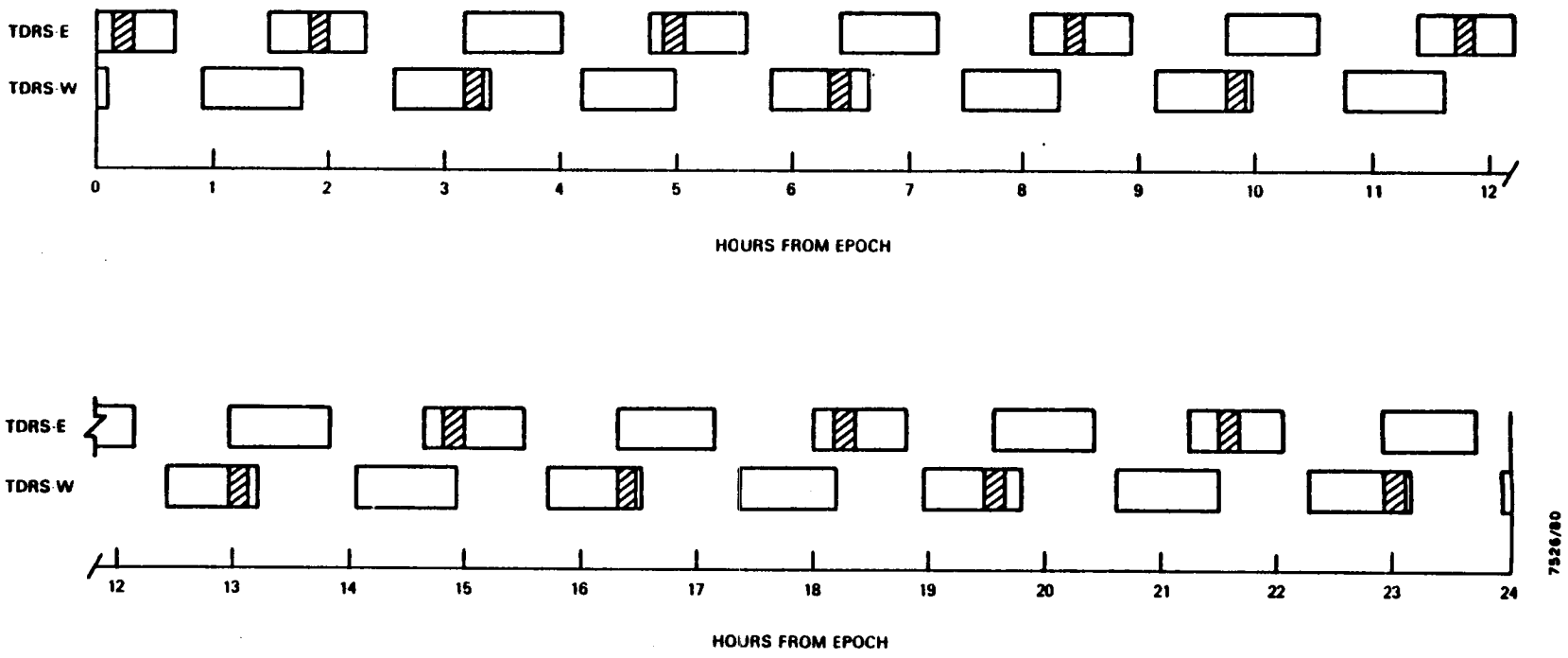

NOTES: 1. EPOCH = OCTOBER 1, 1980.

2. SHADED AREAS CORRESPOND TO ONE PASS PER REVOLUTION DATA SET.

Figure 4-2. Contacts for the Every Revolution Case for GRO

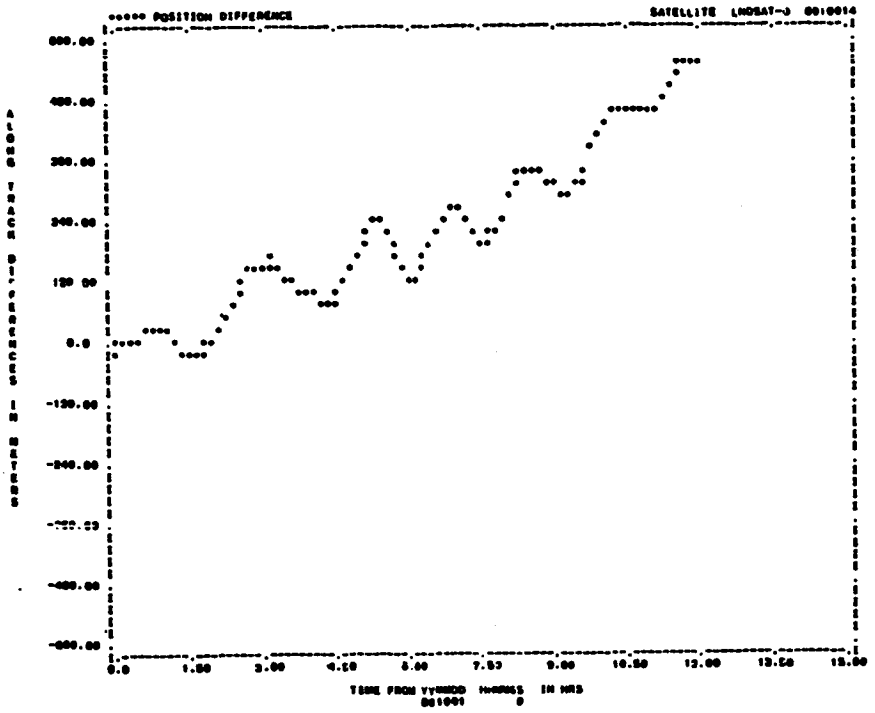

Figure 4-3. Along-Track Error Growth Over 12 Hours for Landsat-D

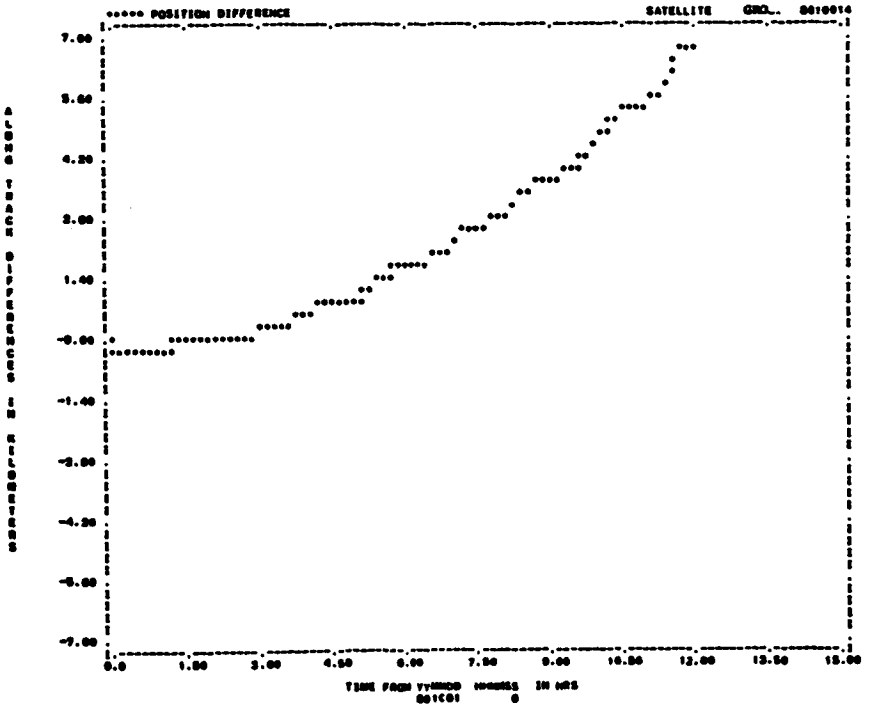

Figure 4-4. Along-Track Error Growth Over 12 Hours for GRO

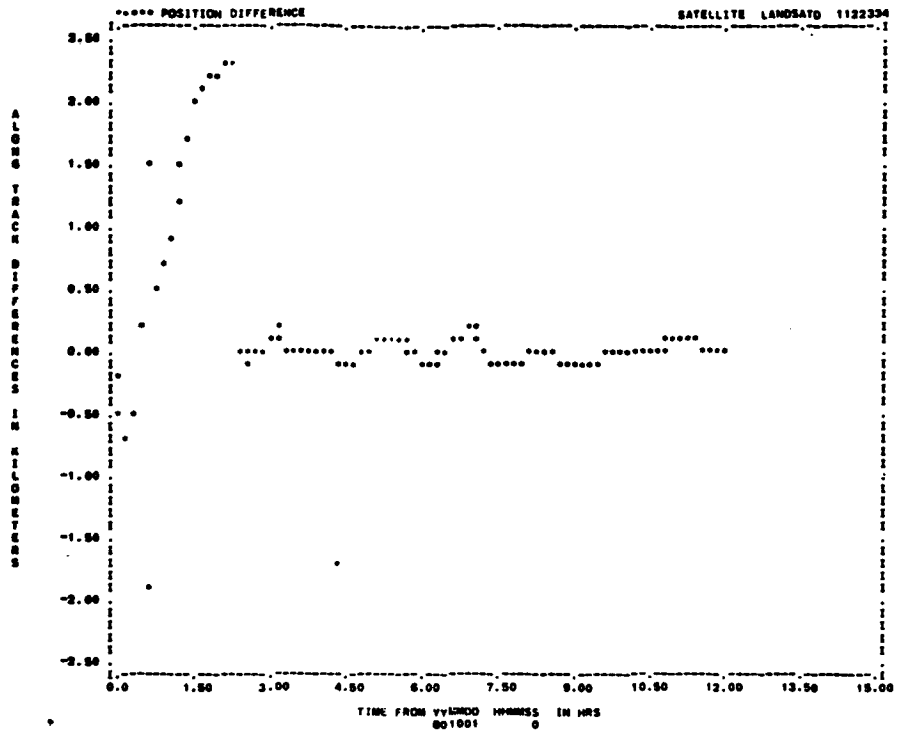

a. 0 to 12 hours

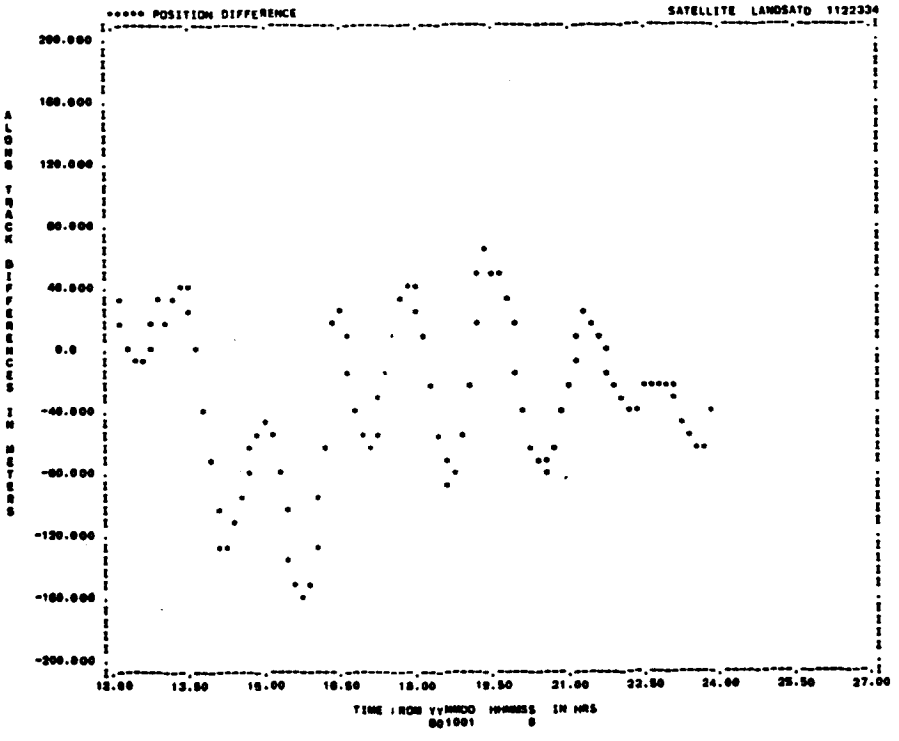

b. 12 to 24 hours

Figure 5-1. Along-Track Error for EKF Run B5

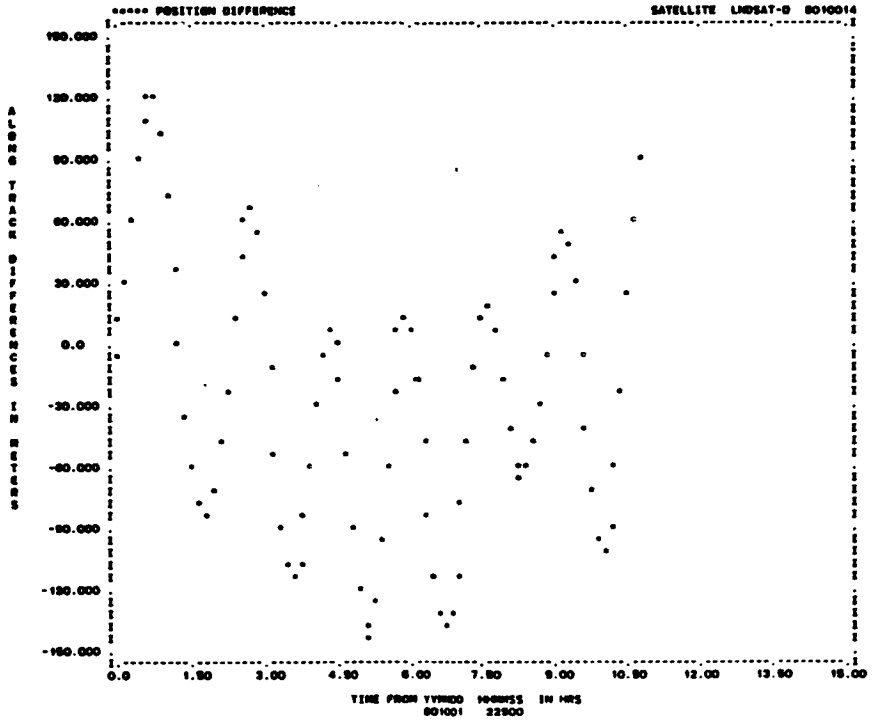

a. Definitive Arc

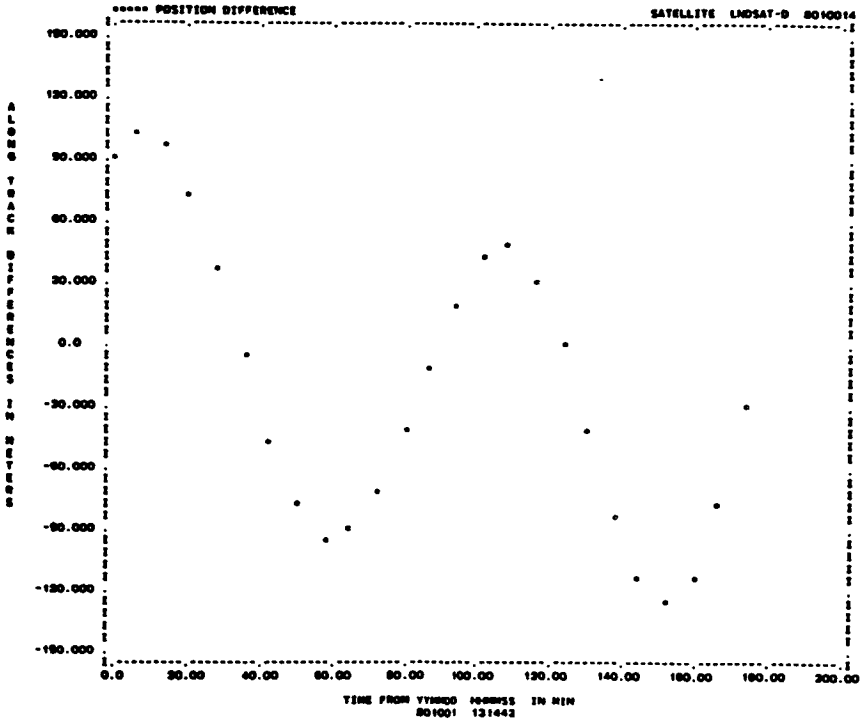

b. Predictive Arc

Figure 5-2. Along-Track Error for SBDC Run LO2

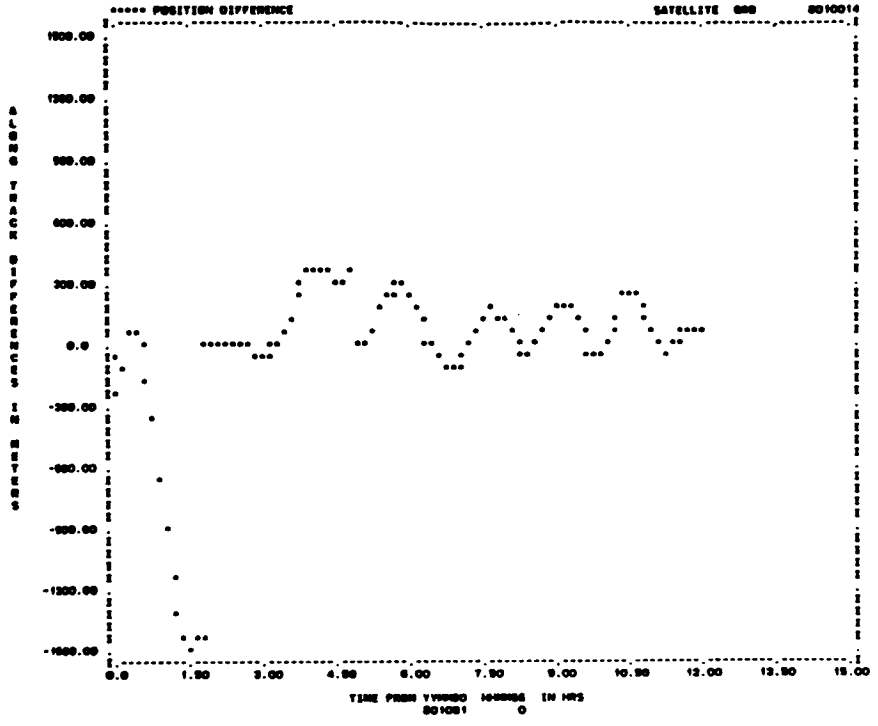

a. 0 to 12 Hours

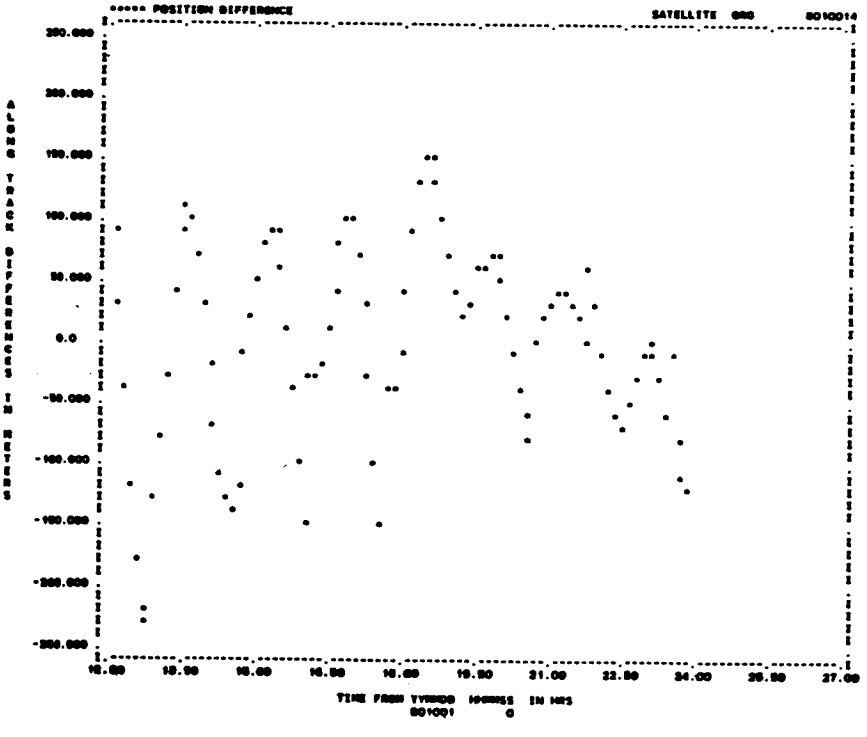

b. 12 to 24 Hours

Figure 5-3. Along-Track Error for CEKF Run 200E

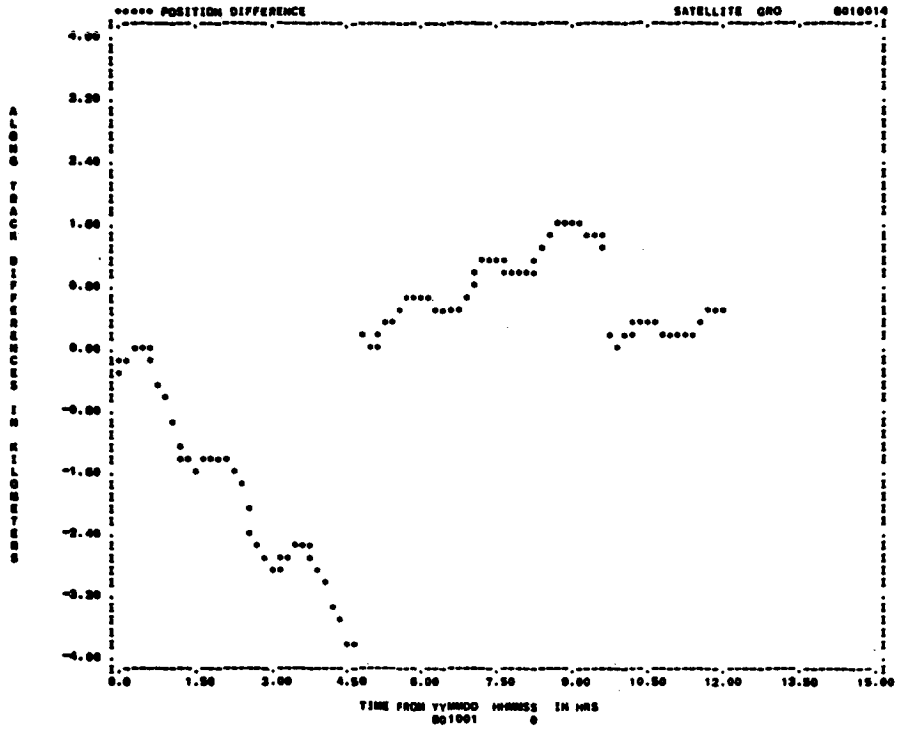

a. 0 to 12 Hours

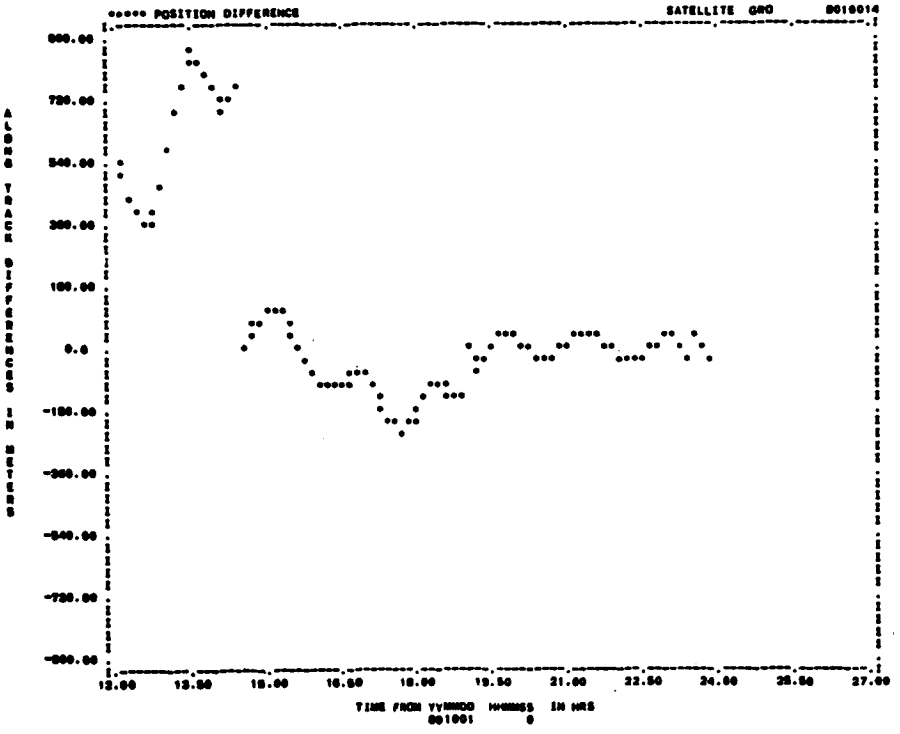

b. 12 to 24 Hours

Figure 5-4. Along-Track Error for EKF Run P24

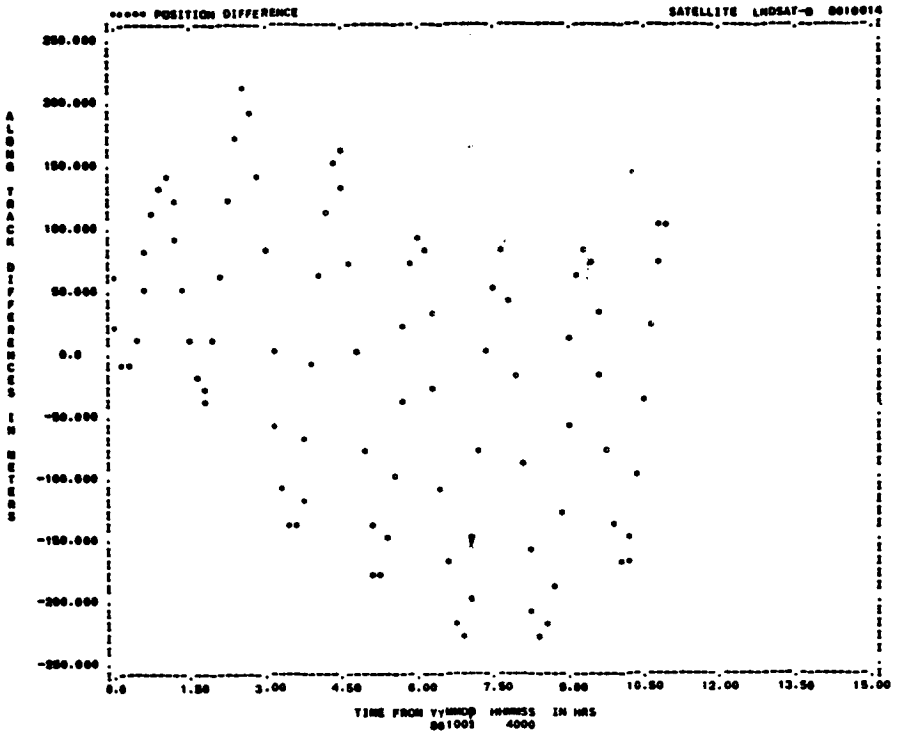

a. First Span

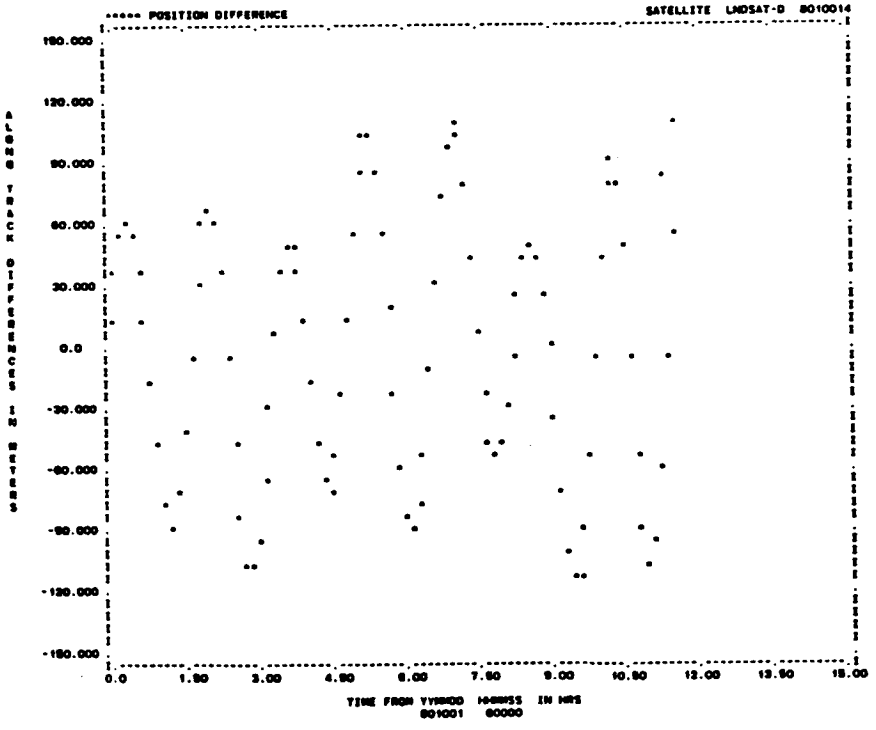

b. Fifth Span

Figure 5-5. Along-Track Error for SBDC Run L15

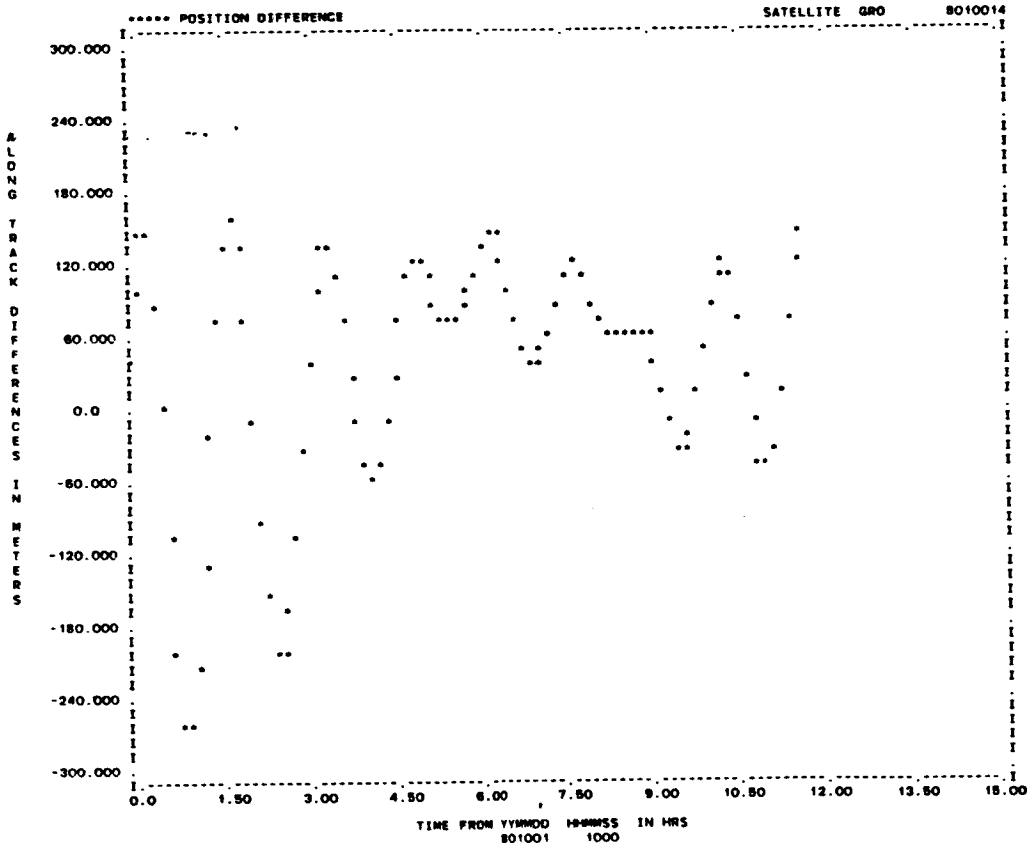

Figure 5-6. Along-Track Error for SBDC Run G15

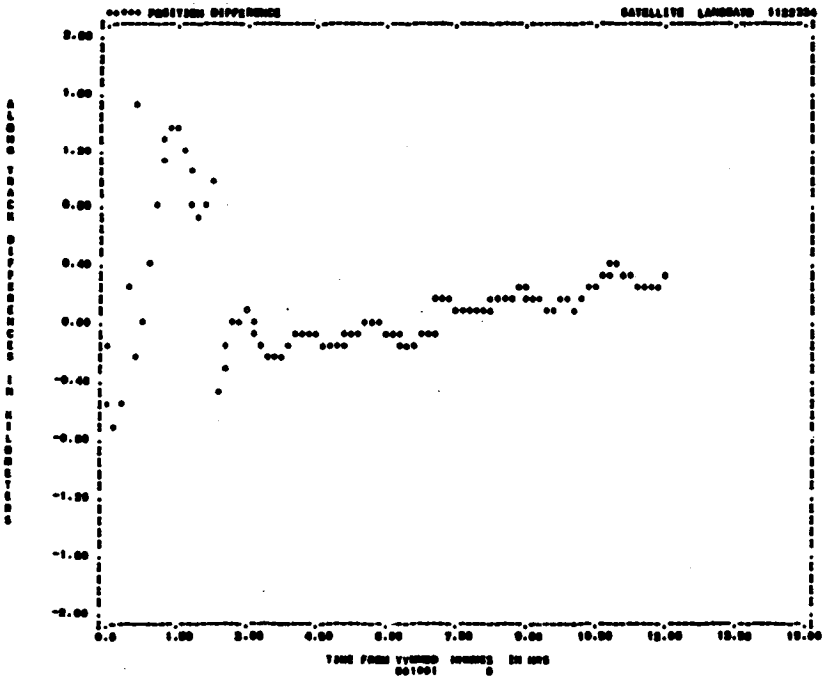

a. 0 to 12 Hours

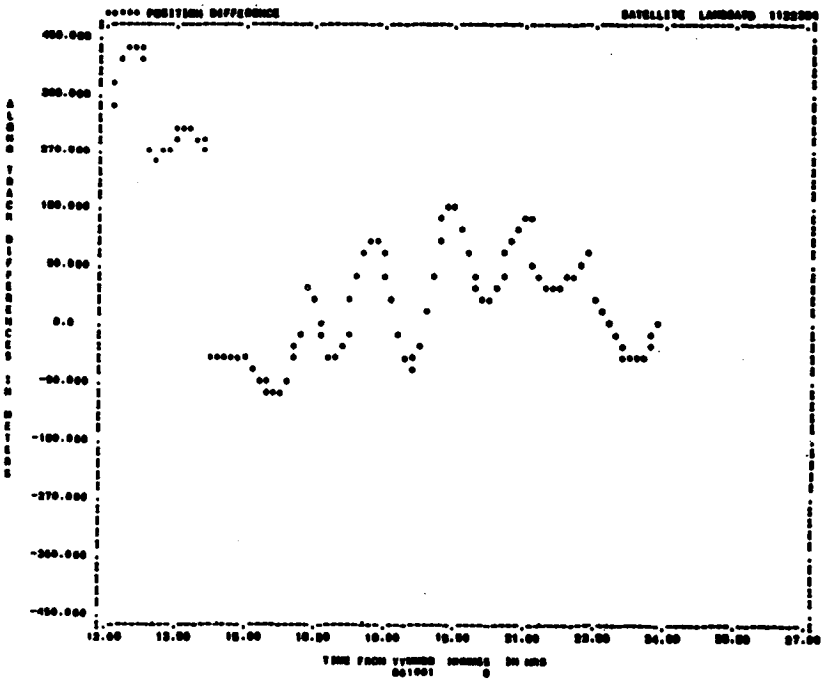

b. 12 to 24 Hours

Figure 5-7. Along-Track Errors for EKF Run M4

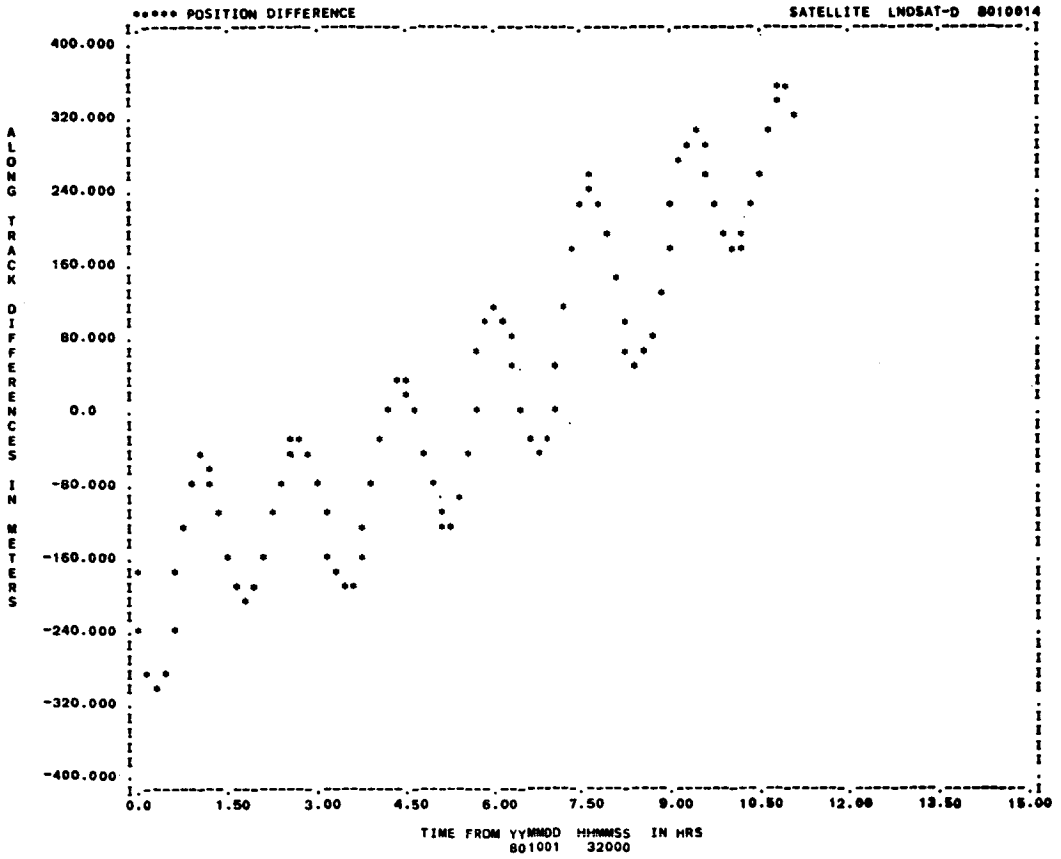

Figure 5-8. Along-Track Error for SBDC Run LO8

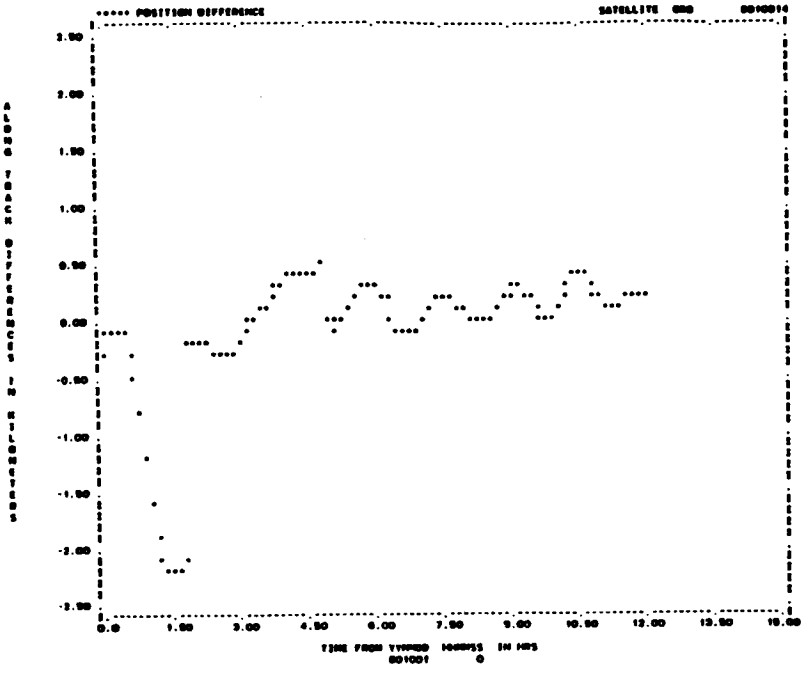

a. 0 to 12 Hours

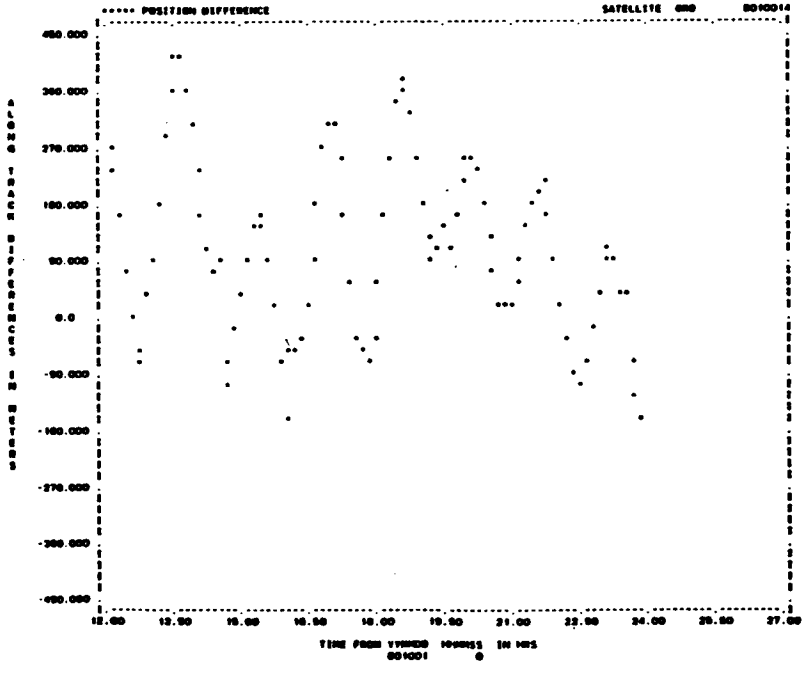

b. 12 to 24 Hours

Figure 5-9. Along-Track Error for EKF Run R8

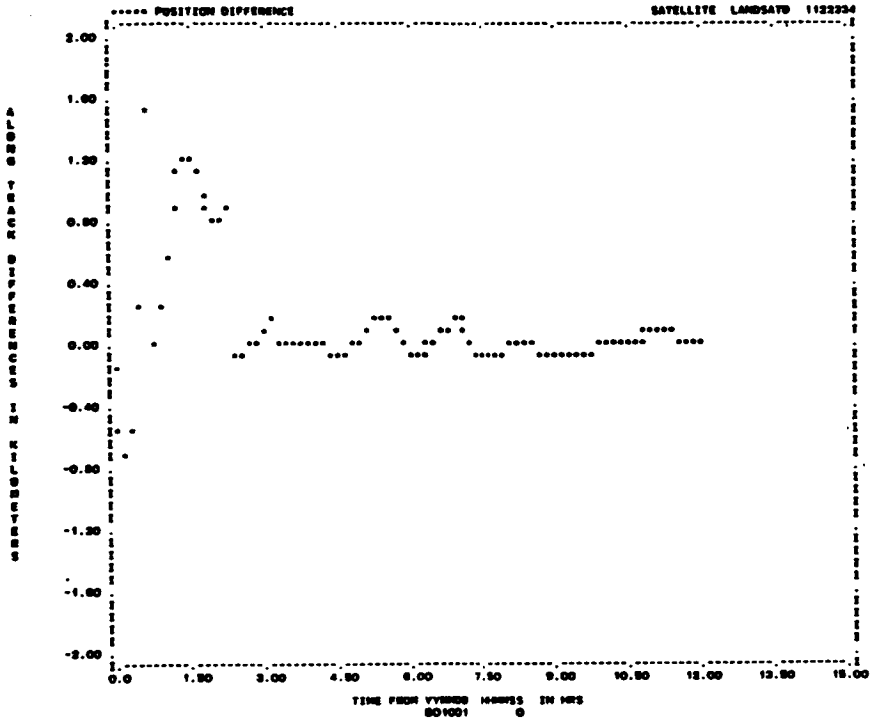

a. 0 to 12 Hours

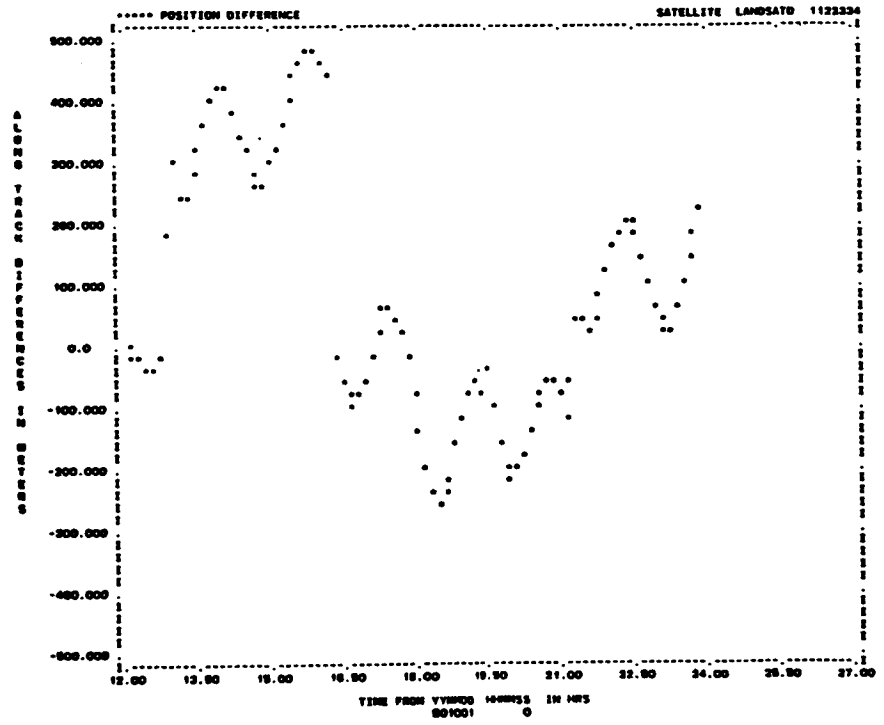

b. 12 to 24 Hours

Figure 5-10. Along-Track Error for EKF Run 04

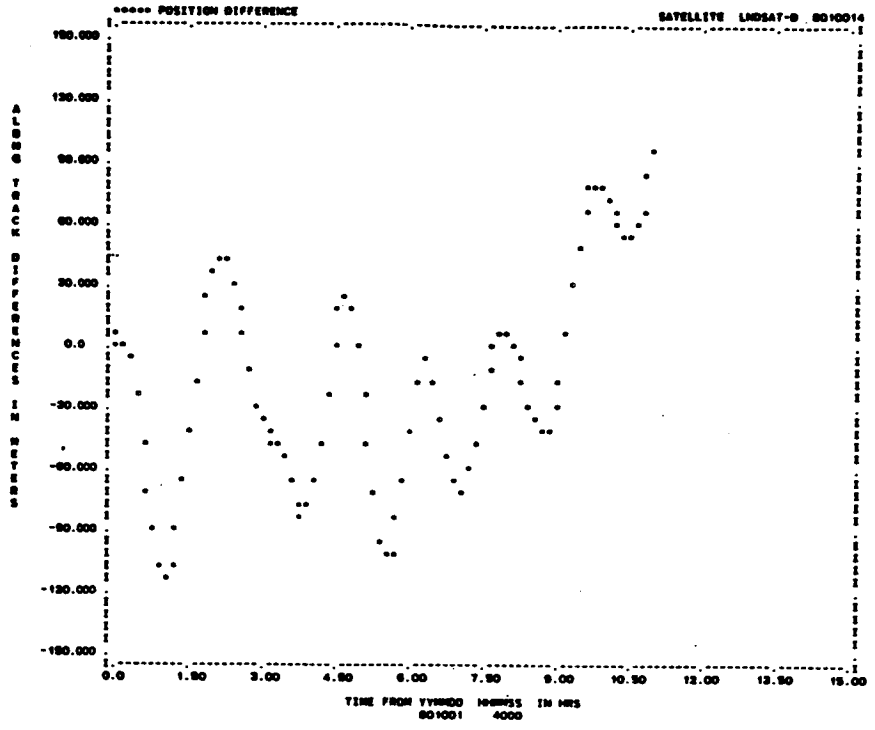

a. First Span

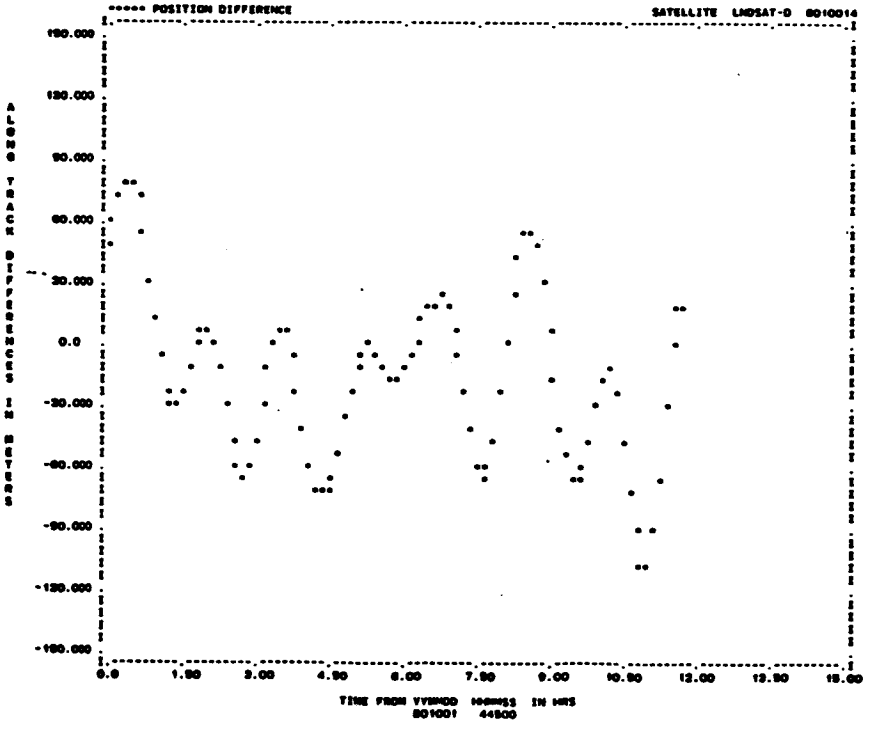

b. Fourth Span

Figure 5-11. Along-Track Errors for SBDC Run L-17

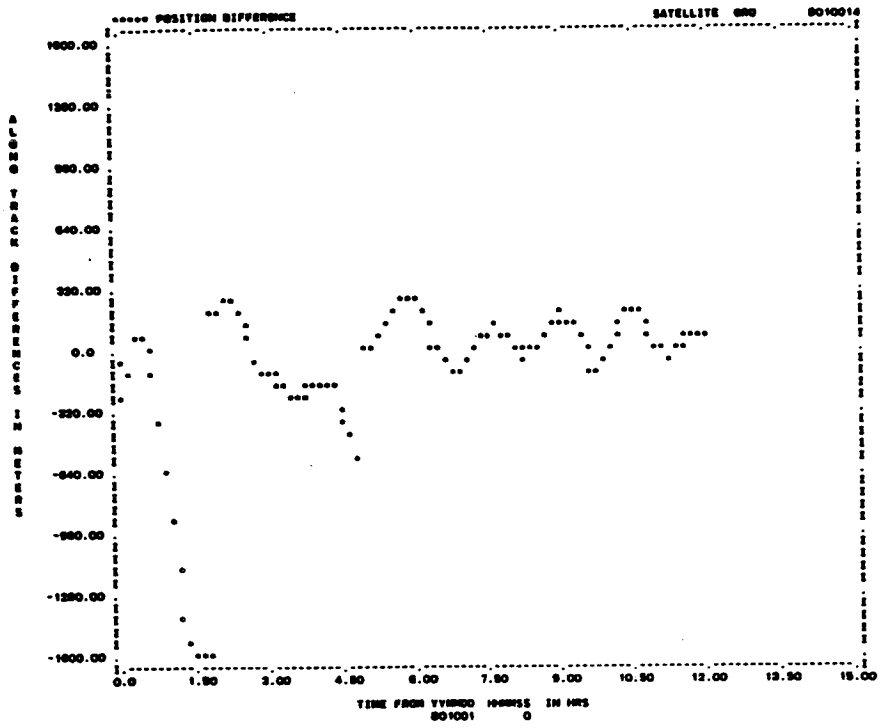

a. 0 to 12 Hours

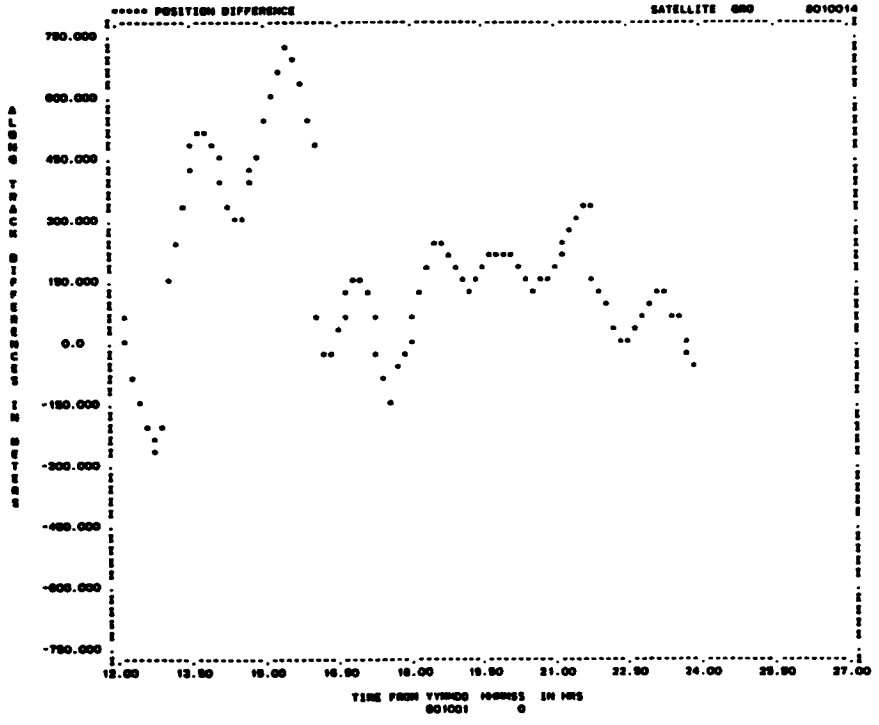

b. 12 to 24 Hours

Figure 5-12. Along-Track Errors for EKF Run T3

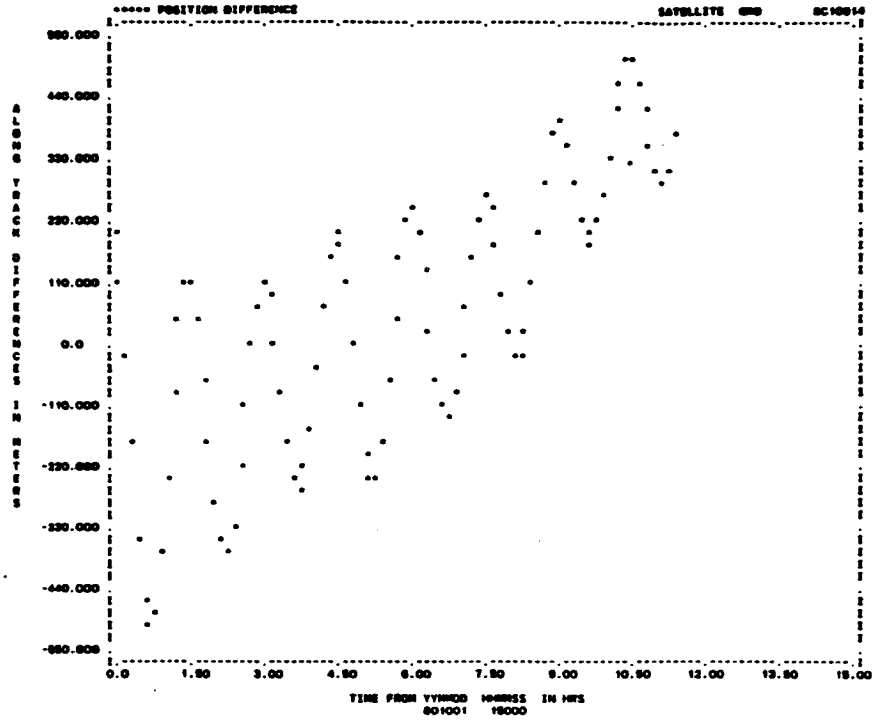

a. Second Span

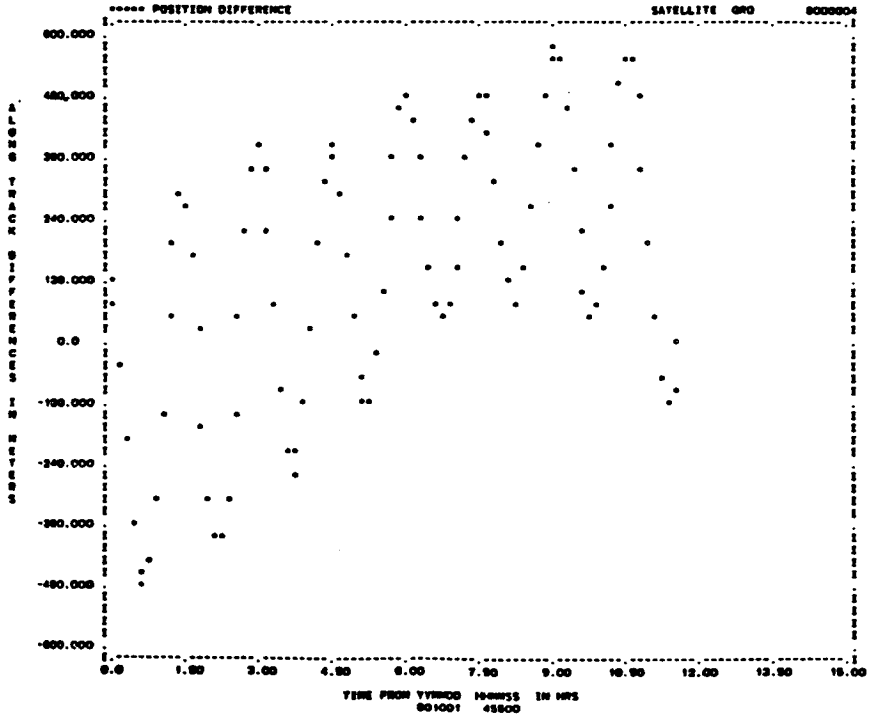

b. Fourth Span

Figure 5-13. Along-Track Errors for SBDC Run G19

GSFC PRECISION ORBIT ANALYSES IN SUPPORT OF THE SEASAT ALTIMETER EXPERIMENT

James G. Marsh
Geodynamics Branch
National Aeronautics and Space Administration
Goddard Space Flight Center
Greenbelt, Maryland

Ronald G. Williamson
EG&G Washington Analytical Services Center, Inc.
6801 Kenilworth Avenue
Riverdale, Maryland

August 1980

Paper to be Submitted to the
Journal of Astronautical Sciences

ABSTRACT

Analyses have been conducted at the Goddard Space Flight Center (GSFC) to improve the accuracy of Seasat ephemeris computations so that the altimeter data can be used for determinations of global ocean topography. After improvements to models for the earth's gravity field, atmospheric drag, solar radiation pressure, and the tracking station coordinates, an r.m.s. radial ephemeris accuracy of 1.5 meters has been achieved. Most of this error is still attributed to the model of the earth's gravity field. Preliminary gravity model solutions incorporating GEOS-3 altimeter data have provided a significant improvement in the accuracy of Seasat ephemeris computations.

The long continuous tracks of Seasat altimeter data intersect one another several thousand times in a few days. Differencing the sea surface heights computed from the altimeter range measurements at these crossover points has provided important insight into the nature of the ephemeris error. The ephemeris error is long wavelength in nature so that over tracks of a few thousand kilometers, the radial error can be represented by a linear trend.

Comparisons of the Seasat ephemerides computed at the GSFC with those independently computed at the Naval Surface Weapons Center (NSWC) have provided important information on the source and magnitude of the ephemeris errors. In addition to providing insight into gravity model errors the comparisons also have revealed the existence of an apparent 4 meter difference between GSFC and NSWC Z components of tracking station coordinates.

Additional analyses of Seasat and GEOS-3 altimeter data, in combination with laser and Unified S-Band tracking data, are ultimately expected to produce an r.m.s. radial orbital accuracy of about 50 cm.

Introduction

The altimeter experiment on Seasat produced a global set of data with a precision better than 10 cm. The use of these data for sea surface topography determinations has placed very stringent requirements on the ephemeris determination. The objectives of the precision orbit determination work at GSFC have been: to evaluate the accuracy with which the Seasat orbit can be computed, to identify the sources of error which limit the satellite ephemeris accuracy, and to improve the ephemeris accuracy by developing improved models for the orbit error sources.

Initial orbit computations with existing geodetic data, gravity, atmospheric drag, and solar radiation pressure models resulted in radial ephemeris errors of several meters. These errors occur because the altitude of 800 km. and the very complex nature of the spacecraft structure make the task of accurately modeling the forces on Seasat difficult. Analyses of the orbit perturbations due to the earth's gravity field indicated that significant radial perturbations (10-30 cm.) were caused by spherical harmonic coefficients even out to degree and order 36. The specularly reflecting spherical model for the spacecraft which is typically used in the drag and solar radiation pressure computations of orbit determination programs is no longer adequate. The choice of atmospheric models is quite important, particularly in longer arcs as is discussed in Schutz and Tapley [1].

A series of improvements were made to the gravity model and tracking station coordinates, with the most recent model based upon an analysis of the Seasat laser and Unified S-Band (USB) data and the GEOS-3 altimeter data. Improvements in models and techniques to account for drag and solar radiation pressure also have been implemented. Using these model improvements and the set of Seasat laser and USB data, orbital solutions have been computed at GSFC for the extent of the Seasat mission.

The following sections present a summary of these developments. The primary measures of orbit accuracy we have relied upon are the r.m.s. of fit, the intercomparison of ephemerides, and the use of altimeter sea surface height discrepancies at the intersections of the ground tracks. The GSFC ephemerides have been compared with those computed independently at NSWC using Doppler data [2]. These comparisons have provided a direct means of assessing the nature and magnitude of the gravity model error and also have revealed significant coordinate system differences.

Laser and Unified S-Band Orbits

The Seasat orbits computed by the Geodynamics Branch at GSFC were based upon a combination of laser and USB tracking data. These two data types were complementary in the sense that the laser data provided high accuracy (i.e., 10 cm. for the GSFC lasers and 50 cm. for the Smithsonian Astrophysical Observatory (SAO) lasers) and absolute scale for the orbit computations while the USB average range rate data provided global coverage both geographically and in time. The USB data were found to be particularly valuable in the development of the gravity model for Seasat. The amount of tracking data provided by these systems averaged 5 passes per day for the laser network and 18 passes per day for the USB network. This rather sparse data set necessitated the use of orbital arc lengths of several days.

The GSFC Geodyn computer program [3,4] was used for the orbit computations. This program uses numerical techniques to integrate the equations of motion and Bayesian least squares adjustment techniques for the improvement of the orbital parameters. The earth's gravity field, the luni-solar direct gravitational perturbations, and the solid earth tidal perturbations including the geometric tracking station displacements due to the tidal effects have been modeled. The JPL planetary ephemeris DE-96 was adopted for these computations along with the BIH polar motion and UT1 data. The non-conservative forces of solar radiation pressure and drag have also been modeled. The Jacchia 1971 model atmosphere [5] implemented in Geodyn was selected for this effort.

The spacecraft model currently employed in the Geodyn program for Seasat uses the conventional specularly reflecting sphere. In the computations described here a radiation pressure coefficient and a number of drag coefficients were adjusted for each orbital arc in order to best fit these complex perturbations in an average sense with this spherical model. A more accurate variable-area model of the complex structure of the Seasat spacecraft is being developed for implementation in the drag and solar radiation pressure computations.

The major source of error in the initial SEASAT-1 orbit computations was the modeling of the earth's gravitational field. Orbit computations using the GSFC GEM gravity models available at the time of launch indicated that the most accurate orbits were obtained with the GEM-10B model [6] which is complete to degree and order 36 in the spherical harmonic coefficients. The observation residuals and other orbit accuracy assessments indicated that improved geopotential coefficients were required. An initial gravity model designated PGS-S1 [7] was computed by incorporating Seasat laser data into the GEM-9 gravity model normal equations [8] which are based solely upon satellite observational data. Although this PGS-S1 model provided an improvement in orbit accuracy over the GEM-10B model, radial orbit errors of several meters still existed due to the sparsity and poor distribution of the laser data for the adjustment of a Seasat gravity model. Subsequent analyses of the USB average range-rate data permitted the inclusion of these data into another solution which was designated PGS-S2 [7]. This latter model is complete to degree and order 30, with selected coefficients to degree 36. An example of the degree of improvement of the PGS-S2 model versus previously available models is presented in Table 1 from Lerch and Marsh [7]. This table presents orbit overlap differences for a set of five two day arcs when the GEM 9, GEM 10B and PGS-S2 gravity models were used. The reduction from 2.6 meters for the GEM 9 model to 0.7 meters for the PGS-S2 model in the radial r.m.s. difference illustrates almost a factor of four improvement in the orbit consistency.

A detailed evaluation of the PGS-S2 model indicated that orbital height errors of several meters due to gravity field mis-modeling were still present, particularly in the mid-Pacific ocean area [9]. The lack of high accuracy tracking data over the ocean areas is believed to be the limiting factor in the development of the gravity model for Seasat. Previous GSFC experience in the development of the GEM 10B gravity model indicated that the addition of altimeter data provided an important contribution, particularly over the remote ocean areas where surface gravity data and tracking data were sparse. Based upon this experience, the same set of GEOS-3 altimeter data which was used in the computation of the GEM 10B model was combined with the data used in computing the PGS-S2 gravity model. The resulting model, designated PGS-S3 [10], is complete to degree and order 36. This model has been used for

most of the orbit computations described in this paper and has been used for the orbits contained on the final set of the Seasat altimeter data released by the Jet Propulsion Laboratory (JPL). Coordinates for the laser and USB stations were derived simultaneously with the gravity models. The PGS-S3 gravity coefficient and station coordinate values are contained in the November 1979 Seasat Altimeter/Orbit Determination Team Workshop Report [10].

Table 2 presents a comparison of the orbital r.m.s. fits obtained when the PGS-S2 and PGS-S3 models were used for 6 day orbit computations. The significant point in this table is the indication of an improved global orbit by the reduction in the USB r.m.s. of fit from 1.40 cm/s to 1.25 cm/s. The USB data provides a better measure of orbit accuracy because of the more global distribution. The minor changes in the laser fits are not considered meaningful measures of orbit accuracy, even though a reduction was noted for the first arc, since most of the laser data were recorded in regions of the world where the gravity model errors are minimal. The tracking data residuals <u>only</u> provide a measure of orbit accuracy where tracking data exist.

Table 3 presents a summary of the r.m.s. radial, crosstrack and alongtrack position differences between three day arcs computed using the PGS-S2 and PGS-S3 gravity models. These values represent the r.m.s. of the differences computed every 5 minutes around the orbits. The r.m.s. radial position difference is 74 cm; however, maximum excursions as large as 3 meters are noted. These maximum differences primarily occur in the remote ocean regions where tracking data are not available. Along track differences in excess of 10 meters are also noted in this comparison.

Improving the accuracy of the earth's gravity model for Seasat is quite difficult. Even with PGS-S3, gravity model error is still the largest error source for Seasat. Sensitivity analyses [7] have shown that a large number of coefficients above degree 30 produce radial perturbations greater than 10 cm. Further gravity model adjustments using the Seasat altimeter data in conjunction with the PGS-S3 data set are in progress and should provide a significant reduction in orbit errors.

Atmospheric drag perturbations on the Seasat orbit also present a difficult modeling problem. Solar activity during the Seasat mission was quite high and large variations have been noted in the day to day flux values used in modeling drag. The adjustment of atmospheric drag parameters (C_D, $\dot{C}_D$) was found to be adequate for arc lengths up to three days in length. For longer arcs, tests indicated that it was necessary to employ a technique of adjusting multiple drag coefficients in each orbital arc. This technique permitted the extension of the orbital arc lengths so that dynamics could be used to compensate for the sparsity of tracking data and the preponderance of data in the northern hemisphere. Using this technique orbital arcs as long as 17 days were fitted with only a minor degradation in accuracy noted. Table 4 illustrates this fact for arc lengths of three, six, twelve and seventeen days. The PGS-S2 gravity model was used in this study. The r.m.s. fits for the S-Band data remained essentially the same in the 6 and 12 day arcs as in the 3 day arc. The laser r.m.s. fit increased by about 30 cm. This is attributed to the fact that most of the laser data is from North America and Arequipa, Peru and the three day orbit was distorted to fit these regions at the expense of poorer accuracy in other unobserved areas. The increased dynamical strength of the longer arcs is believed to have provided a better distribution of the orbit errors and thus provided a more accurate global solution with less dependence upon the actual times and locations of the tracking data. Even the 17 day arc showed only a slight degradation in the r.m.s. fit.

Table 5 presents a comparison of a series of 3 day ephemerides with a 12 day ephemeris covering the same time span. The r.m.s. radial differences of the orbits range from 0.4 meters to 1 meter. This comparison does not represent an absolute measure of orbit accuracy since both orbits were computed with the same gravity model, however, there appears to be no radial accuracy loss in the longer arc. The availability of such long dynamically consistent orbits is believed to be quite advantageous for the interpretation of the altimeter data. Additional tests of the accuracy of the 3 day arcs versus the 12 day arc were carried out through the altimeter derived sea surface height discrepancies at ground track intersections during the 12 day period. These tests indicated that the 12 day arc was everywhere equal to the 3 day arcs in accuracy. In the

more remote ocean areas such as the mid-Pacific the 12 day arc was more accurate, again reflecting the increased dynamical strength of the longer arc. After further analyses, six day arcs with the adjustment of daily C_D values were selected as optimum for Seasat with the present level of force model error.

For the Seasat ephemerides distributed with the altimeter data, an orbit fit span of six days was employed where feasible. Table 6 presents a summary of the laser range and USB range rate r.m.s.. fits for these orbits which cover most of the mission. The overall laser range r.m.s. value is 1.1 meters and the overall USB range rate r.m.s. value is 1.4 cm/s. The variation in the laser r.m.s. values from arc to arc is primarily due to the difference in the precision of the laser data available in each arc. The SAO data has a larger uncertainty (50 cm.) than the GSFC data (10 cm.) and the relative proportions of SAO and GSFC data vary from arc to arc.

Ephemeris Evaluation

The observational data r.m.s. fits and the internal orbit consistency evaluations discussed earlier are necessary but not sufficient tests of the global Seasat orbit accuracy. Other comparisons are available which provide a more direct measure of the ephemeris accuracy, specifically, by using the altimeter data and by comparison of ephemerides produced by other independent investigators.

Use of the altimeter data at orbit ground track intersections provides a means of evaluating the radial ephemeris error over the open ocean areas. At the crossing points, the constant part of the ocean surface height above the reference ellipsoid, the geopotential contribution, is the same on both tracks. Thus the sea surface height differences will reflect unmodeled changes in time dependent ocean topography, orbit modeling errors, and time tag biases or height bias changes in the altimeter data. Investigations of these crossover differences (defined as the sea surface height corresponding to the ascending pass minus the

sea surface height on the descending pass at the intersection of the ground tracks) are particularly meaningful in the case of Seasat since several thousand globally distributed crossover points are established in just a few days. Except for tidal errors, which may be of order 50 cm. in local areas, one would generally expect oceanographic topography variations to be small over time periods of a few days, so that the primary contribution to the crossover differences will be radial orbit errors. Crossover differences thus provide a powerful test of radial orbit accuracy. However, it is should be noted that even this test is not absolute, as orbit modeling errors are known to produce correlated ephemeris errors at the crossover point.

Earlier investigations had revealed the existence of a substantial time tag error associated with the altimeter observations [9]. A time tag error will propagate directly into a height error according to the rate of change of the sea surface height. Because the height rate has a different sign on an ascending pass than on a descending pass, the sea surface height discrepancies at ground track intersections provide a sensitive measure of the time tag error. The detailed formulation for deriving a time tag correction from the crossover sea height differences was presented in [9]. Using this approach, several solutions were computed for the timing bias using the PGS-S2 and PGS-S3 gravity model and a variety of 3 day, 6 day and 12 day orbits covering the period July 28 to August 8, 1978. The results of this investigation are presented in Table 7.

The initial solution was based upon four three day orbits covering the 12 day time period. The orbits were computed using the USB and laser tracking data and the PGS-S2 gravity model and station coordinates. This solution, based upon almost 8500 crossover points, resulted in a value of -76.4 ms. for the timing bias. Crossover differences larger than 8 meters were eliminated from the solution. A single ephemeris covering the 12 day time period which was previously described was also used to compute the time bias. This resulted in a change of only 1 ms. from the previous solution. The timing bias was next estimated using two 6 day arcs based upon the PGS-S3 gravity model and the daily drag parameters. This solution was identical to the 12 day ephemeris

solution. Finally, a time bias was calculated based upon the NSWC ephemeris for this time period. This solution provided a significantly different value of -64.2 ms. The accuracy of the solutions based upon the GSFC orbits are believed to be better than 5 ms. The cause for the large GSFC/NSWC discrepancy is not known. A possible cause may be the differences in reference coordinate systems or gravity models used at NSWC and GSFC which are discussed later. A subsequent analysis of the altimeter instrument internal time delays provided a time tag correction of -79.38 ms. as part of the Seasat post-launch calibration effort. This hardware analysis is therefore corroborated at the 5 ms. level by these orbital analyses at GSFC and by similar independent orbital analyses at the University of Texas [1,9].

Regional solutions for the time bias based upon the two GSFC gravity models differed by several ms.; however, the regional differences appear to have been averaged out in the global solution. These regional variations primarily reflect the variations in Seasat ephemeris accuracy with respect to geographic area. In order to illustrate in detail these variations, we have divided the area of altimeter coverage into 24 blocks. The two six day orbits using the PGS-S3 gravity model and with C_R and daily C_D coefficients adjusted formed the basis for this investigation. Ocean tides were modeled using the Estes (1977) model [11] as provided on the preliminary set of altimeter data distributed by JPL. The time tags on the altimeter data were modified to account for the -79.38 ms. bias.

Figure 1 presents a summary of the crossover difference statistics in each of the geographic areas. The mean and the r.m.s. about the mean for the crossover differences in each of the 24 blocks is shown in the figure. The overall r.m.s. crossover difference was 1.64 meters. Crossover differences in the N. Atlantic and N.E. Pacific are approximately 1 meter whereas those in the Central Pacific and in the South Atlantic are approximately 2 meters. This is attributed to the fact that the tracking data are sparse and gravity model errors are larger in the latter areas. Also in some areas, e.g., the central Pacific block, a large mean difference exists (226 cm.), although the r.m.s. about the mean is much smaller (151 cm.). Thus, even though the computed sea surface heights on the ascending passes are systematically different from those corresponding to the descending passes in that area, each set of passes (ascending or descending) is quite consistent. As shown in the simulation by Anderle and Hoskins [12], correlation of gravity model errors produces this type of signature and we feel this is the cause. Certain other patterns are noted in the crossover differences. For example, crossover differences are small in the calibration block off the east coast of the U.S. and the blocks south of Australia and New Zealand. A similar pattern is noted between the block immediately east of Japan where large crossover differences are observed and the block between South Africa and Brazil. This phenomenon is obviously related to the periodic nature of the orbit errors which is discussed later.

A similar crossover analysis was performed for the altimeter data recorded in regions of the northern hemisphere during the 1978 September/ October 3 day repeat ground track orbit. These crossover differences exhibited the same regional accuracy trends noted in the previous analysis.

The collinear ground track data recorded during the last month of the Seasat mission provide an additional means of evaluating the nature of the ephemeris errors. Figure 2 presents a typical plot of the differences between the sea surface height as computed from the Seasat altimeter data and the GSFC 5' gravimetric geoid [13] for a ground track in the N.W. Atlantic. These profiles, which are approximately 2000 km. in extent, show very good repeatibility with little evidence of relative tilts. The major differences between the profiles are characterized by a different constant bias associated with each pass and short wavelength dynamic topography variations. The different biases, which appear to vary over a range of 1.25 meters with respect to their common mean, are attributed to ephemeris error. The short wavelength dynamic topography variations in the N.W. Atlantic as observed in these Seasat altimeter data have been discussed by Cheney and Marsh [14].

Still another means of assessing the Seasat ephemeris error is through the comparison of independently computed orbits. The NSWC ephemerides have been independently computed using entirely different data (Doppler vs. laser and USB), force models, computer programs and data analysis procedures. In contrast to the orbital arc lengths of several days used at GSFC, arc lengths of two revolutions were used at the NSWC. This was possible because of the large amount of globally distributed Doppler tracking data available (10-25 passes per arc). Because of this, the respective ephemeris differences provide a meaningful measure of the magnitude of Seasat radial orbit errors. The NSWC ephemeris used here is the one provided with the final Seasat altimeter data - the NSWC smoothed ephemeris. This ephemeris was constructed from overlapping two revolution Doppler orbits using a numerical interpolation procedure to generate a continuous smoothed ephemeris. The details of this smoothing procedure are explained by Malyevac and Colquitt elsewhere in this issue [2]. Because the NSWC ephemeris was based on independently computed two revolution orbits, it is not likely to contain long period force model errors.

Table 8 presents a comparison of ephemerides for two six day GSFC arcs with the NSWC smoothed ephemeris. The GSFC orbits were computed first with the PGS-S2 gravity model and then with the more recent PGS-S3 model. A solar radiation pressure coefficient and daily drag parameters were adjusted in these six day orbits. The r.m.s. radial position difference about the mean was 2.2 meters for the PGS-S2 orbits and was reduced to 2.1 meters with the PGS-S3 orbits. Comparisons were also made between the remaining six day PGS-S3 ephemerides included with the final set of Seasat data and the NSWC ephemeris. The results were nearly identical to those presented in Table 8. A GSFC 12 day arc computed with the PGS-S2 gravity models was also compared with the NSWC smoothed ephemeris. The differences for the 12 day arc were virtually the same as for these two six day arcs. This is consistent with the results presented earlier in Table 5. These comparisons indicate that, with the force models presently being used for Seasat, orbit arc lengths as long as 12 days do not exhibit degradation due to force model error.

Inspection of the NSWC/GSFC ephemeris differences indicated that the satellite ephemeris position Z values were systematically different with an offset of about 3 meters. In addition, a comparison of the GSFC tracking station coordinates with the NSWC Doppler station coordinates at nearby stations through the use of survey data conducted by Hothem [15] indicated that a systematic difference of about 5 meters existed in the Z station coordinate values. That is, $Z_{GSFC} = Z_{NSWC} + 5$ meters. Comparisons of a global set of Doppler derived tracking station coordinates by Grappo and Huber [16] with the GEM 10 geoid [8] have also indicated the presence of a similar 5 meters systematic difference in the Z coordinates of the Doppler stations.

To investigate the relationship between the station coordinate Z differences and the ephemeris Z differences, an experiment was conducted using the GSFC 12 day orbit. The GSFC Z components of the station coordinates were modified by subtracting 5 meters and an orbit was computed with these modified values. The r.m.s.'s of fit for the laser and USB data in the modified orbit were only slightly larger than the values obtained for the nominal orbit. This ephemeris was in turn compared with the nominal ephemeris. The ephemeris Z values were systematically different by about 4 meters. Thus the Z station coordinate shift propagates significantly into the orbital differences. Since the mean ephemeris Z difference in the GSFC orbit experiment is about a meter larger than that indicated in the GSFC/NSWC comparison it appears that the 5 meter station coordinate Z shift used in the GSFC orbit experiment may be slightly too large for this specific set of Seasat tracking station coordinates.

The r.m.s height difference between this Z shifted case and the nominal ephemeris was 1.92 meters while the r.m.s. height difference between the GSFC and NSWC orbits was 2.14 meters. This experiment suggests that at least half of the GSFC/NSWC radial orbit differences can be accounted for by the station coordinate reference system differences. These analyses cannot establish whether the Z error is in the GSFC system or in the NSWC system or partially in both.

This 5 meter difference in the Z coordinate values could be due to an error in the GEM-10 geoid, an error in the Doppler or GSFC station coordinates, or a combination of errors. An error in the odd zonal coefficients of the GEM-10 model would also produce such an effect. King-Hele et al. [17] have computed an independent set of odd zonal coefficients based upon orbital arcs several hundred days in length. The geoid computed from these odd zonal coefficients agrees generally better than a meter with the GSFC GEM-10B model and a recent SAO model. Schaab and Groten [18] have compared the origins of the GSFC, SAO, Centre National D'Etudes Spatiales (CNES) and Ohio State University (OSU) coordinate systems through geoid data obtained from their respective spherical harmonic coefficient models for the earth's gravity field. This comparison showed that the origins typically agreed to better than a meter except for the OSU system where the Z origin differed by 2 meters. This large difference was attributed to the fact that the OSU model was based purely on surface gravity data. Thus it seems likely that most of the Z coordinate discrepancy is due to the NSWC gravity model or tracking station coordinates.

In addition to the reference coordinate system difficulty, there are two other factors which may produce differences in the GSFC/NSWC Seasat ephemeris computations: force model differences and the distribution, amount, and quality of the tracking data. In an attempt to provide more insight into the effect of the Z coordinate system differences and to isolate these two latter factors, an additional test was devised. The NSWC ephemeris data was treated as observational data for the Geodyn program and a solution was computed adjusting the orbital state, resonance coefficients, GM, and coefficients for drag and solar radiation pressure. The NSWC ephemeris was converted to the Cartesian true of date inertial system ("PCE" data format in Geodyn) for this purpose. Since the NSWC ephemeris data was continuous around the orbit (sampled every 5 minutes), and since the smoothed 2-rev NSWC orbits should be relatively free of long periodic force model errors, the objective of the test was to see if the remaining GSFC/NSWC orbit differences were primarily due to errors in the force models or the uneven distribution of the laser and USB tracking data. In this test it is believed that the Z coordinate system differences were accommodated in the adjustment process; that is, the fitted Geodyn PCE orbit conformed to the NSWC geodetic system.

The resulting Geodyn PCE orbit was compared with the GSFC PGS-S3 orbit. The radial r.m.s. difference was 1.58 meters, which compares reasonably well with the 1.92 meters obtained in the previous analyses where the station Z components were perturbed by the 5 meters. To further assess this comparison, the spectra of the respective radial orbit differences associated with each of these two analyses were intercompared. The spectral analyses were performed with a Fast Fourier Transform package, sampling the radial orbit differences once a minute for the 12 day span. Use of a 12 day span results in a spectral frequency interval of .0833 cycles/day. The amplitude spectrum of the radial orbit differences of the PCE orbit vs. the GSFC PGS-S3 orbit shown in Figure 3a has a simple spectral behaviour, with just two detectable peaks. The dominant amplitude is 201 cm. at the once per revolution orbit frequency of 14.3 cycles/day. The other detectable peak amounts to 34 cm. at a frequency of 14.0 cycles/day. This latter peak is due to the adjustment of the resonant coefficients in the PCE orbit determination run, and hence slightly different amplitudes for the long period gravitational terms of order 14 were used.

The amplitude spectrum shown in Figure 3b for the radial orbit differences due to the 5 meter station coordinate Z shift has a single peak of 250 cm. amplitude at 14.3 cycles/day. It is remarkably similar to the Geodyn PCE/GSFC PGS-S3 spectrum, except that it is 25% larger at the once/rev peak. The phase spectra corresponding to these amplitude spectra are virtually identical outside the area of resonance effects. The similarity of these spectra leads us to postulate that all of the effect related to the once/rev peak is due to the apparent station Z shift. Assuming this and recalling the phase agreement noted above, the theoretical spectrum due to the station Z shift may be linearly scaled by a factor of 80% (which reduces it to 4 meters) and removed from the spectrum of the radial differences between the PCE orbit and the GSFC PGS-S3 orbit. This computation is consistent with assuming that the station Z shift effect propagates linearly into the orbit. The resulting adjusted spectrum has only a single peak above a centimeter in amplitude and that is an 11.3 cm. amplitude at the 14.0 cycles/day frequency mentioned previously. Again, this last feature is an artifact of having adjusted resonant coefficients.

The results of this comparison strongly indicate that the differences between the GSFC PGS-S3 orbit and the Geodyn PCE orbit are explained by the two factors of coordinate system differences and resonant coefficient adjustment. The 4 meter effect we have determined is in good agreement with the 5 meter station coordinate differences indicated by Hothem [15] and by Grappo and Huber [16]. It must be kept in mind that the origin of this apparent coordinate system error has not been resolved. Nevertheless, the recovered orbit ephemeris difference has the identical signature to an overall Z coordinate error. A further conclusion is that errors contributed by the GSFC laser and USB tracking data appear to be quite small, as only the GSFC PGS-S3 orbit used these data.

The Geodyn PCE ephemeris derived above was in turn compared with the NSWC orbit. The r.m.s. radial orbit difference was 1.47 meters with maximum differences as large as 6 meters noted. Recalling that the above analyses indicated that coordinate system differences produced an r.m.s. radial difference of 1.58 meters, the r.m.s. of 1.47 m. is consistent with the overall r.m.s. NSWC/GSFC orbit differences of 2.14 m., i.e., $(1.58^2 + 1.47^2) \approx 2.14^2$. This 1.47 meters is a good measure of the agreement between these independent investigations after taking into account the differences in coordinate system definition.

An analysis of the amplitude spectrum, Figure 4, of the radial differences between the Geodyn PCE orbit and the NSWC orbit indicates the presence of many frequencies. A comparison of the unique orbit referenced frequencies due to the geopotential with this amplitude spectrum demonstrates that most of the terms are at these frequencies and hence are probably gravitational in origin. As is shown by Kaula [19], the frequencies due to the geopotential are given by

$$f = (\ell - 2p + q)(\dot{\omega} + \dot{M}) - q\dot{\omega} + m(\dot{\Omega} - \dot{\theta}_g)$$

where ℓ and m are the degree ℓ and order m of a particular gravitational term; p and q are the indices of sub-harmonics which arise due to the expression of the potential in Kepler elements; $\dot{\omega}$ is the perigee rate, which for Seasat is small; $\dot{M}$ is the mean anomaly rate; $\dot{\Omega}$ is the node rate; and $\dot{\theta}_g$ is the rotation rate of

the earth. Because the orbit of Seasat is nearly circular, and the amplitudes of the perturbations drop off as $e^{/q/}$, only perturbations where $/q/ \leq 1$ can be expected to produce much of an effect on the Seasat orbit. The fact that the perigee rate on Seasat is small means that in our spectral analysis, the $q\dot{\omega}$ fine structure cannot be resolved. Thus the basic orbit frequencies found in the Seasat NSWC/GSFC orbit differences are characterized by the basic period of the orbit, $\dot{\omega}+\dot{M}$; by the node rate and rotation rate of the earth, $\dot{\Omega} - \dot{\theta}_g$; and by the two integers ℓ-2p+q and m. The fundamental $\dot{M}+\dot{\omega}$ orbit frequency for Seasat is the 14.3 cycles/day; the "daily" frequency is very close to 1 cycle per day (.997).

For the most part the frequencies indicated in the spectral analysis correspond to the orbit referenced frequency terms with (ℓ-2p+q) =1 and order m ranging up to about 16. There are also m daily terms (ℓ-2p+q=0) indicated. Figure 4 has been annotated to indicate the class of geopotential terms which are possibly associated with the significant amplitudes. All of the terms above 8 cm. amplitude have been identified as corresponding to these gravitationally implied frequencies. The largest amplitude is associated with geopotential terms of order two which have a frequency of 12.32 cycles/day and an amplitude of 74 cm. An amplitude of 38 cm. corresponds to the fourth order terms at the frequency of 10.32 cycles/day. Note that for example 43rd order terms are not necessarily present in either the NSWC or GSFC gravity models, but the frequency of their effects is very close to some of the determined frequencies in the spectral analyses. While some of the features may have other origins such as tides, the clearly identifiable harmonic constituents are attributed to gravity model differences.

The effect of the major harmonics on the Geodyn PCE/NSWC radial r.m.s. orbit difference is easily estimated if we restrict ourselves to the 71 terms with amplitudes in excess of 10 cm. These specific harmonics provide a contribution to the r.m.s. of 133 cm. If we remove the effect of these terms from the r.m.s. difference between NSWC and the GSFC PCE ephemerides, the effect is to reduce the r.m.s. from 147 cm. to 63 cm. Thus much of the 147 cm. r.m.s. is demonstrably due to the effect of these terms which are attributed to gravity model differences. Moreover, much of the 63 cm. r.m.s. remaining is due to specific terms at the gravitational frequencies with amplitudes less than 10 cm. The effects of other error sources are not obvious in this harmonic evaluation.

This ephemeris accuracy evaluation has thus far shown that the GSFC orbits are internally consistent at the 1-2 meter r.m.s. level, and that comparisons with a totally independent source of ephemerides, NSWC, indicate agreement to 1.5 meters r.m.s. after the coordinate system difference is taken into account. While we have yet to evaluate the effects of drag and solar radiation pressure errors using a comprehensive spacecraft model, these effects are clearly much smaller than the probable geopotential error which dominates the 1.5 meter r.m.s.

An inspection of the amplitude spectrum presented in Figure 4 shows that most of the major effects occur near the frequency of once/orbit revolution. The amplitudes for the effects with a wavelength shorter than a third of a revolution are less than 5 cm. which is consistent with the Seasat prelaunch simulation presented by Cutting et al. [20]. Thus the orbit error is long wavelength in nature and over distances of a few thousand kilometers it can be represented by a linear trend.

Because the orbit error is long wavelength, Goad et al. [21] were able to derive a technique which, based on global geoid data and the Seasat altimeter data, has provided an independent estimate of the GSFC orbit error in the July 28-August 8, 1978 time period. This error estimate agrees with the 1.5 meter radial orbit accuracy we have presented. The 50 cm. r.m.s. altimeter crossover difference obtained by Goad et al. after using this technique to improve the ephemeris radially is also in good agreement with the 63 cm. r.m.s. residual noted above in the GSFC/NSWC ephemeris comparison after the removal of the major long wavelength harmonics.

This analysis has established the fact that the dominant source of the orbit differences between NSWC and GSFC orbits is due to coordinate system differences. Gravity model error is clearly the dominant effect in the remaining differences. We cannot attribute this error to either the NSWC or GSFC gravity models. However, it is clear from this investigation that the current gravity models are inadequate for the task of 10 cm. orbit determination.

Conclusions

Several conclusions have resulted from the orbit analyses in support of the Seasat altimeter experiment. Major improvements have been made in the GSFC geodynamic models for Seasat. The results of the orbit analyses including comparisons of GSFC laser and USB orbits with independently computed NSWC Doppler orbits and the evaluation of global altimeter data crossover differences have indicated that the Seasat ephemeris error is currently about 1.5 meters r.m.s. with occasional excursions to about six meters. Based upon an anlysis of altimeter crossover differences, the GSFC Seasat altitude ephemeris error is regional in nature. The ephemerides are most accurate in the N. Atlantic, N.E. Pacific and the S.E. Indian Ocean and least accurate in the Central Pacific and the S. Atlantic.

Currently the dominant error source in Seasat ephemeris computation is the uncertainty in modeling the earth's gravity field. Significant errors are also due to atmospheric drag and solar radiation pressure modeling. Comparisons of GSFC and NSWC Seasat ephemerides have indicated the presence of an unexplained difference of about 4 m. in the location of the center of mass along the Z axis. This difference is consistent with that obtained with earlier geoid and station coordinate comparisons performed by other investigators.

The ephemeris error is not random but is serially correlated in time due to the inadequacies of the force and geodetic models used to compute the accelerations of the satellite. The behavior of the orbit error is such that over ground tracks up to a few thousand kilometers in length, the error has the character of a linear trend. Hence, investigations of geoid undulations and sea surface variations with wavelengths shorter than a few thousand kilometers should not be affected by the ephemeris error. Furthermore, collinear satellite ground tracks result in ephemeris errors which are highly correlated geographically. Since the geoid is the same along collinear tracks, these data can be used to study time variations of the sea surface topography.

Future combinations of Seasat and Geos-3 altimeter data, together with laser and Unified S-Band tracking data, are ultimately expected to produce a gravity field which allows computations of a global Seasat ephemeris with an r.m.s. radial accuracy of about 50 cm.

ACKNOWLEDGEMENTS

This work has been performed as part of the activities of the Seasat Altimeter/Precision Orbit Determination Experiment Team. The interaction provided by this Team has been invaluable in performing the analyses presented here. The gravity model development work performed under the leadership of Frank Lerch was crucial to improving the Seasat ephemeris accuracy. The authors acknowledge the help of Neader Boulware in performing the computer runs necessary for this work.

REFERENCES

[1] SCHUTZ, B.E. and TAPLEY, B.D., "Orbit Accuracy Studies for Seasat-1," Journal of the Astronautical Sciences, This Issue, 1980.

[2] MALYEVAC, C.W., COLQUITT, E.S., "NSWC Doppler Computed Seasat-1 Orbits," Journal of the Astronautical Sciences, This Issue, 1980.

[3] PUTNEY, B.H., "General Theory for Dynamical Satellite Geodesy," National Geodetic Satellite Program, NASA SP-365, pp. 319-334, 1977.

[4] MARTIN, T.V., OH, I.H., EDDY, W.F., and KOGUT, J.A., Geodyn System Description, Volume 1, prepared by EG&G Washington Analytical Services Center, Inc., Wolf Research and Development Group, for the National Aeronautics and Space Administration, Goddard Space Flight Center, Greenbelt, MD, August 1976.

[5] JACCHIA, L.B., "Revised Static Models of the Thermosphere and Exosphere with Empirical Temperature Profiles," Smithsonian Astrophysical Observatory, Special Report 332, 1971.

[6] LERCH, F.J., WAGNER, C.A., KLOSKO, S..M., BELOTT, R.P., LAUBSCHER, R.E., and TAYLOR, W.A., "Gravity Model Improvement Using GEOS-3 Altimetry (GEM 10A and 10B)," paper submitted to the Journal of Marine Geodesy, 1978.

[7] LERCH, F.J., and MARSH, J.G., "Gravity Model Improvement Using Seasat," Presented at the Spring AGU Meeting, May 1979; Abstract published in EOS, Transactions of the AGU, Vol. 60, No. 18, p. 232, 1979.

[8] LERCH, F.J., KLOSKO, S.M., LAUBSCHER, R.E., and WAGNER, C.A., "Gravity Model Improvement Using GEOS-3 (GEM 9 and 10), J. Geophys Res., Vol. 84, No. B8, 3897, 1979.

[9] TAPLEY, B.D., SCHUTZ, B.E., MARSH, J.G., TOWNSEND, W.F., and BORN, G.H., (editors), "Accuracy Assessment of the SEASAT Orbit and Altimeter Height Measurement," University of Texas, Austin, Inst. for Advanced Study in Orbital Mechanics IASOM TR 79-5, October 1979.

[10] TAPLEY, B.D., MARSH, J.G., and BORN, G.H., (editors), "Seasat Orbit Accuracy Assessment and Bias Calibration Workshop," GSFC TM, September 1980.

[11] ESTES, R.H., "A Computer Software System for the Generation of Global Ocean Tides Including Self Gravitation and Crustal Loading Effects," X-920-77-82, Goddard Space Flight Center, Greenbelt, Maryland, 1977.

[12] ANDERLE, R.J., and HOSKINS, R.L., "Correlated Errors in Satellite Altimetry Geoids," Geophysical Research Letters, Vol. 4, No. 10, pp. 421-424, October 1977.

[13] MARSH, J.G., and CHANG, E.S., "5' Detailed Geoid in the Northwestern Atlantic Ocean," Marine Geodesy, Vol. 1, No. 3, pp. 253-261, 1978.

[14] CHENEY, R.E., and MARSH, J.G., "Seasat Altimeter Observations of Dynamic Topography in the Gulf Stream Region," Journal of Geophysical Research, in press, June 1980.

[15] HOTHEM, L.D., "Determination of Accuracy, Orientation and Scale of Satellite Derived Point Positioning Coordinates," Proceedings of the Second International Geodetic Symposium on Satellite Doppler Positioning, Applied Research Lab, University of Texas Report, Austin, Texas, 1979.

[16] GRAPPO, G.A., and HUBER, D.N., "Determination of the Earth's Mean Equatorial Radius and Center of Gravity from Doppler-Derived and Gravimetric Geoid Heights," General Assembly of the IUGG, Canberra, Australia, 2-15, December 1979.

[17] KING-HELE, D.G., BROOKES, C.J., and COOK, G.E., "Odd Zonal Harmonics in the Geopotential, From Analysis of 28 Satellite Orbits," Royal Aircraft Establishment Technical Report 80023, Farnborough, Hants, England, February 1980.

[18] SCHAAB, H., and GROTEN, E., "Comparison of Geocentric Origins of Global Systems from Uniformly Distributed Data," Bulletin Geodesique, Vol. 53, pp. 11-17, 1979.

[19] KAULA, WILLIAM M., Theory of Satellite Geodesy, Blaisdell, Waltham, Mass., 1966.

[20] CUTTING, E., BORN, G.H., and FRAUTNICK, J.C., "Orbit Analysis for SEASAT-A," Journal of Astronautical Sciences, Vol. XXVI, No. 4, pp. 315-348, October-December, 1978.

[21] GOAD, C.C., DOUGLAS, B.C., and AGREEN, R.W., "On the Use of Satellite Altimeter Data for Ephemeris Improvement," Journal of the Astronautical Sciences, This Issue, 1980.

TABLE 1

SEASAT ORBIT OVERLAP COMPARISONS
GRAVITY MODEL EFFECTS ON ORBIT CONSISTENCY

AVERAGE RMS DIFFERENCE*	GRAVITY MODEL		
	GEM-9	GEM-10B	PGS-S2
RADIAL DIFFERENCE	2.6 METERS	2.1 METERS	0.7 METERS
ALONG TRACK DIFFERENCE	9.8	8.1	3.4

*BASED UPON 5 CASES OF 2 DAY ARCS OVERLAPPING BY ONE DAY

TABLE 2

SEASAT GRAVITY MODEL TESTS
SIX DAY ARCS, C_R, DAILY C_D ADJUSTED

GRAVITY MODEL	EPOCH-JULY 28, 1978 RMS OF FIT		EPOCH-AUGUST 3, 1978 RMS OF FIT	
	LASER	USB	LASER	USB
PGS-S2	1.14 M.	1.40 CM/S	1.30 M.	1.41 CM/S
PGS-S3	0.98	1.24	1.33	1.25

TABLE 3

SEASAT ORBIT COMPARISON

THREE DAY ARC, C_R , DAILY C_D ADJUSTED, AUGUST 10-13, 1978

PGS-S2 ORBIT
VS.
PGS-S3 ORBIT

	RMS POSITION DIFFERENCE		
	RADIAL	CROSSTRACK	ALONGTRACK
MAXIMUM	2.9 M.	3.0 M.	11.4 M.
RMS	0.7	0.8	2.4

TABLE 4

SEASAT ORBITS BASED UPON A COMBINATION OF LASER AND USB DATA

PGS-S2 GRAVITY MODEL

	1978 EPOCH	RMS OF FIT	
		LASER	USB
3-DAY ARC	JUL 29	0.9 M	1.4 CM/S
C_D, C_R, $\dot{C}_D$ ADJUSTED	AUG 1	0.8	1.3
	AUG 4	1.2	1.5
	AUG 7	0.9	1.4
	AUG 10	1.0	1.3
	AUG 13	0.7	1.2
6-DAY ARCS	JUL 28	1.4	1.7
C_R, DAILY C_D ADJUSTED	AUG 3	1.3	1.4
	AUG 9	1.0	1.4
12-DAY ARC	JUL 19	1.4	1.4
C_R, DAILY C_D ADJUSTED			
17-DAY ARC	JUL 29	1.6	1.6
C_R, DAILY C_D ADJUSTED			

TABLE 5

SEASAT ORBIT COMPARISON

GSFC LASER AND USB ORBITS

12 DAY ORBIT, C_R, DAILY DRAG ADJUSTED

VS.

3 DAY ORBIT, C_R, C_D, $\dot{C}_D$ ADJUSTED

PGS-S2 GRAVITY MODEL USED

EPOCH TIME		POSITION DIFFERENCE RADIAL	CROSSTRACK	ALONGTRACK
JULY 29, 1978	MAXIMUM DIFF.	1.0 M.	2.0 M.	10.5 M.
	RMS	0.4	1.4	2.4
AUGUST 1, 1978	MAXIMUM DIFF.	1.6	1.8	7.2
	RMS	0.6	1.2	2.1
AUGUST 7, 1978	MAXIMUM DIFF.	1.5	2.2	4.8
	RMS	1.0	1.5	2.3

TABLE 6

SEASAT LASER AND UNIFIED S-BAND RMS RESIDUALS IN SIX DAY GSFC ORBITS

PGS-S3 GRAVITY MODEL

C_R AND DAILY DRAG COEFFICIENTS ADJUSTED

1978 DATE		LASER RANGE NO. OBS.	LASER RANGE RMS (M)	USB RANGE RATE NO. OBS.	USB RANGE RATE (CM/S)
JULY	09-15	1218	1.1	1041	1.4
	15-21	1280	1.4	1087	1.4
	21-27	1374	0.8	1454	1.3
	27-02	803	1.1	1190	1.3
AUGUST	02-08	963	0.9	1795	1.3
	08-14	1494	1.0	1309	1.3
	15-18	418	1.2	696	1.3
	18-23	478	0.8	1286	1.3
	23-26	345	0.8	765	1.1
	26-01	1120	0.4	1246	1.0
SEPTEMBER	01-05	621	0.5	1059	1.1
	05-10	645	1.1	1131	1.7
	10-17	1376	1.2	1637	1.2
	17-23	1740	0.9	1233	1.3
	23-29	1791	1.2	1411	1.6
	29-05	2057	1.4	1318	1.7
OCTOBER	05-11	1441	1.5	1097	1.7
OVERALL		19164	1.1	20755	1.4

TABLE 7

ALTIMETER TIME BIAS SOLUTIONS BASED UPON SEA SURFACE HEIGHT DISCREPANCIES AT GROUND TRACK INTERSECTIONS

JULY 28 TO AUGUST 9, 1978

ORBIT	NO. OF INTERSECTIONS	ESTIMATED TIMING BIAS
GSFC – FOUR-3 DAY ARCS C_R, C_D, $\dot{C}_D$ ADJUSTED PGS-S2 GRAVITY MODEL	8476	– 76.4 M.S.
GSFC – ONE-12 DAY ARC C_R, DAILY C_D PGS-S2 GRAVITY MODEL	7448	– 75.5
GSFC – TWO-6 DAY ARCS C_R, DAILY C_D PGS-S3 GRAVITY MODEL	7464	– 75.5
NSWC – SMOOTHED EPHEMERIS	7447	– 64.2

TABLE 8

SEASAT ORBIT COMPARISON — RADIAL COMPONENT

NSWC — 2 REV SMOOTHED ORBITS, DOPPLER DATA

VERSUS

GSFC — 6 DAY ORBITS, LASER AND USB DATA, C_R, DAILY C_D ADJUSTED

	PGS-S2	PGS-S3
JULY 28 TO AUGUST 3, 1978		
MAXIMUM DIFF.	7.1 METERS	6.6 METERS
RMS	2.2	2.1
AUGUST 3 TO AUGUST 9, 1978		
MAXIMUM DIFF.	6.9	6.5
RMS	2.2	2.1

FIGURE 1

SEA SURFACE HEIGHT DISCREPANCIES AT GROUND TRACK INTERSECTIONS

(~ 7500 INTERSECTIONS)

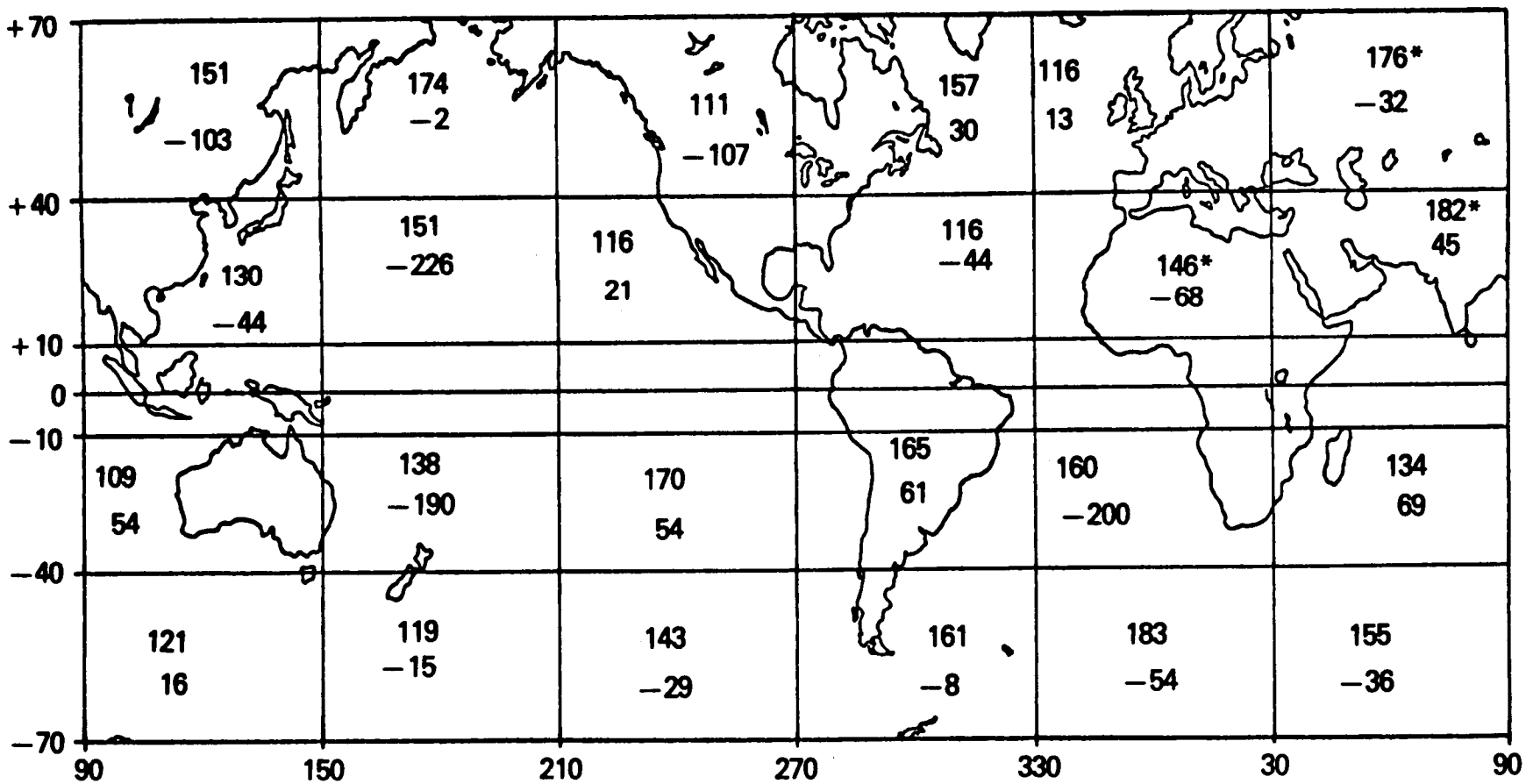

[RMS ABOUT MEAN
MEAN]

UNITS ARE cm.

* TIDES NOT MODELED - INLAND SEAS

FIGURE 2

DIFFERENCES BETWEEN THE SEASAT SEPTEMBER/OCTOBER 1978 COLLINEAR ALTIMETER DATA AND THE GSFC 5′ GRAVIMETRIC GEOID

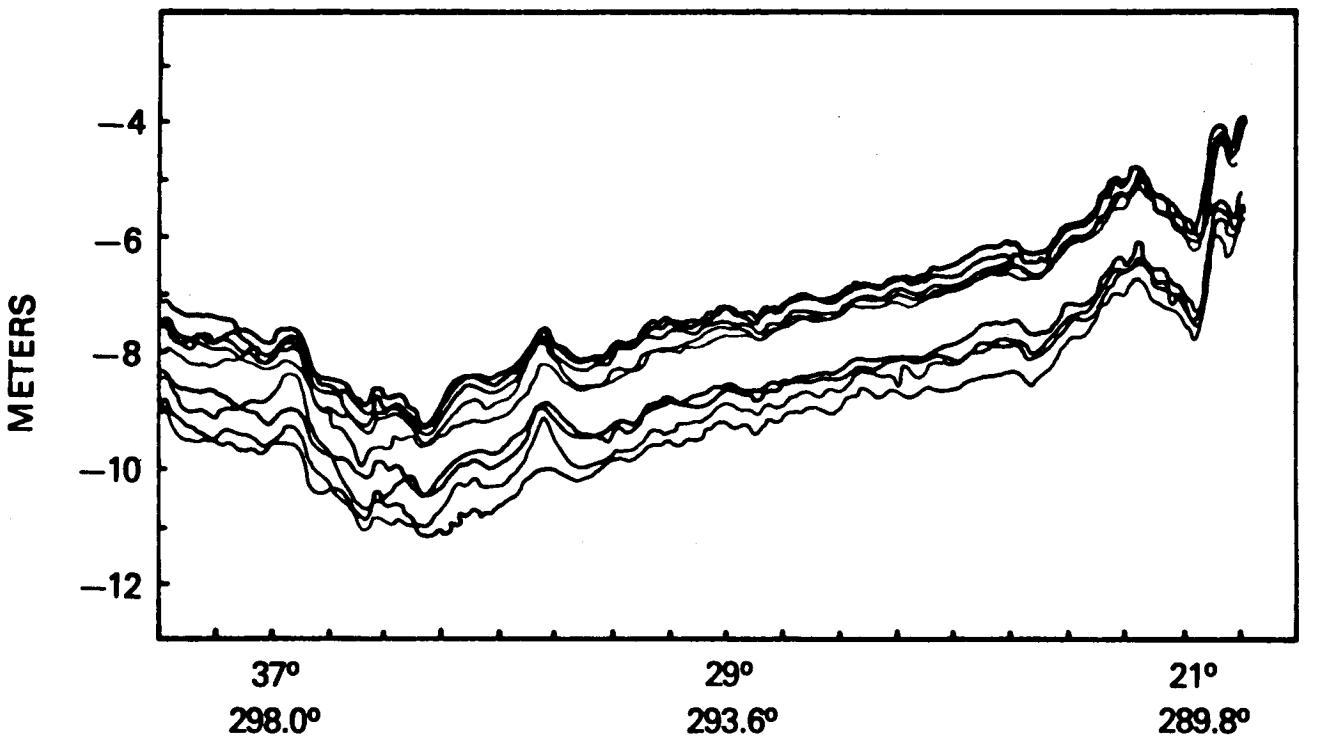

DESCENDING REV NO.

1117	1246	1375
1160	1289	1418
1203	1332	1461

FIGURE 3a POWER SPECTRAL ANALYSIS OF RADIAL EPHEMERIS DIFFERENCES
GEODYN PCE ORBIT
VS.
GEODYN PGS-S3 NOMINAL ORBIT

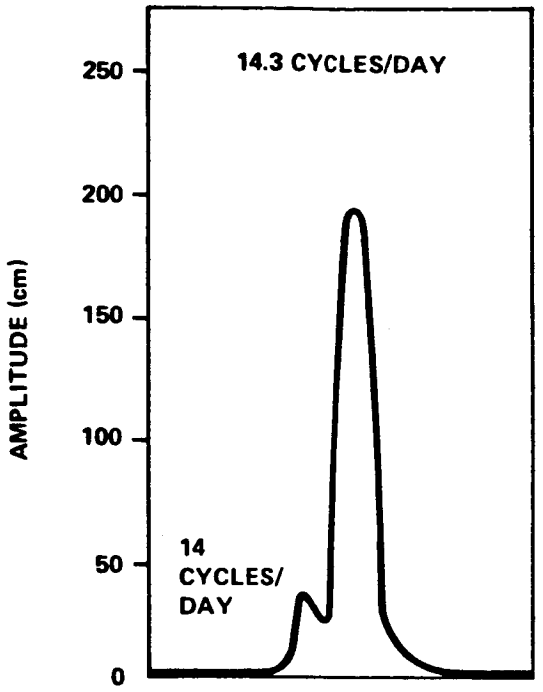

FIGURE 3b GEODYN PGS-S3 NOMINAL ORBIT
VS.
GEODYN PGS-S3 ORBIT WITH MODIFIED STATION COMPONENTS

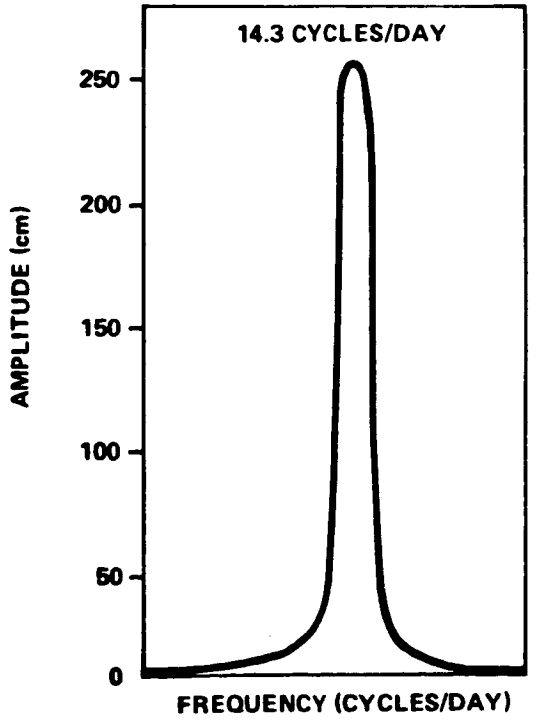

FIGURE 4

POWER SPECTRAL ANALYSIS OF ORBITAL DIFFERENCES GEODYN PCE ORBIT VS. NSWC CONTINUOUS EPHEMERIS

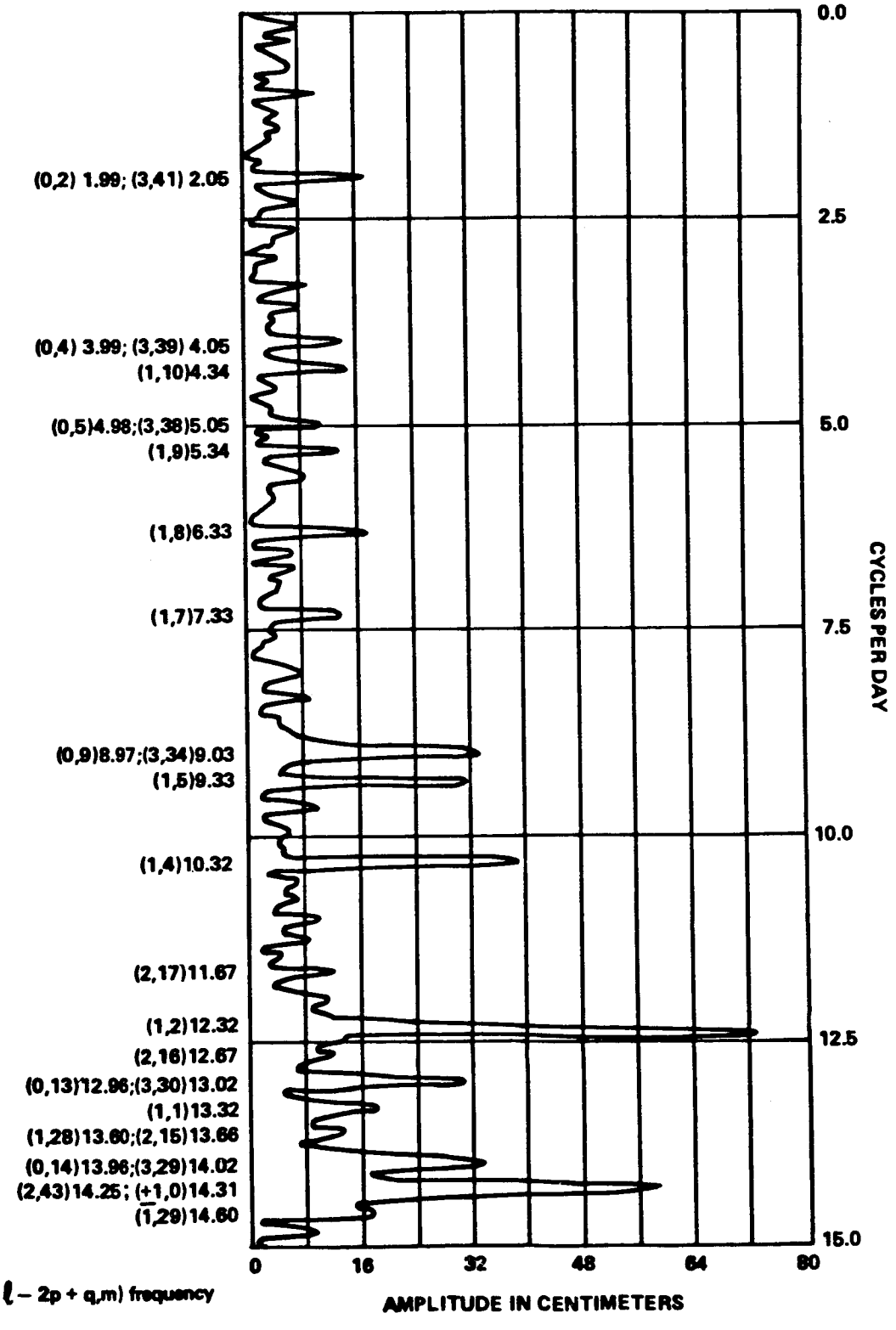

FIGURE 4 (Continued)

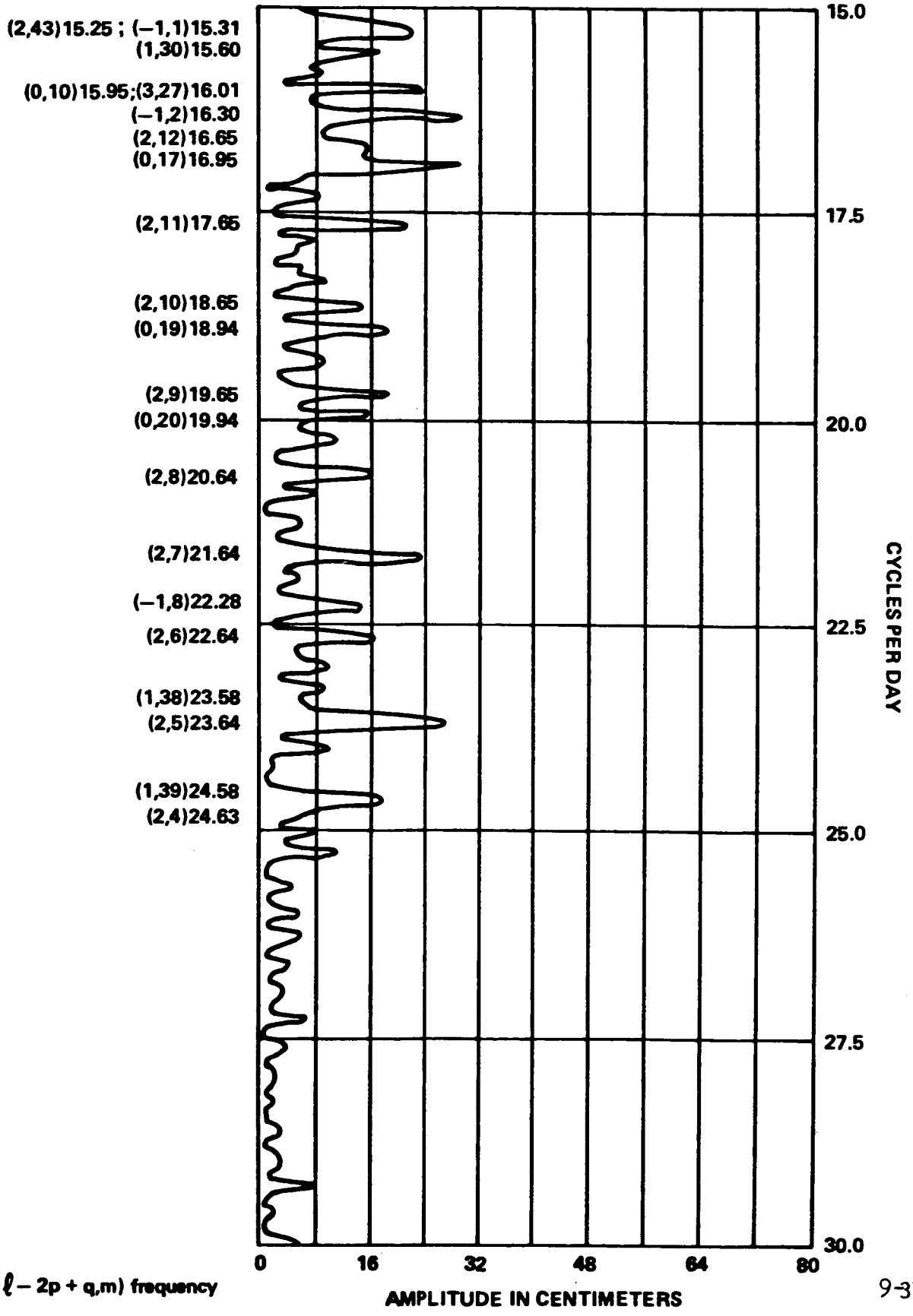

FIGURE 4 (Continued)

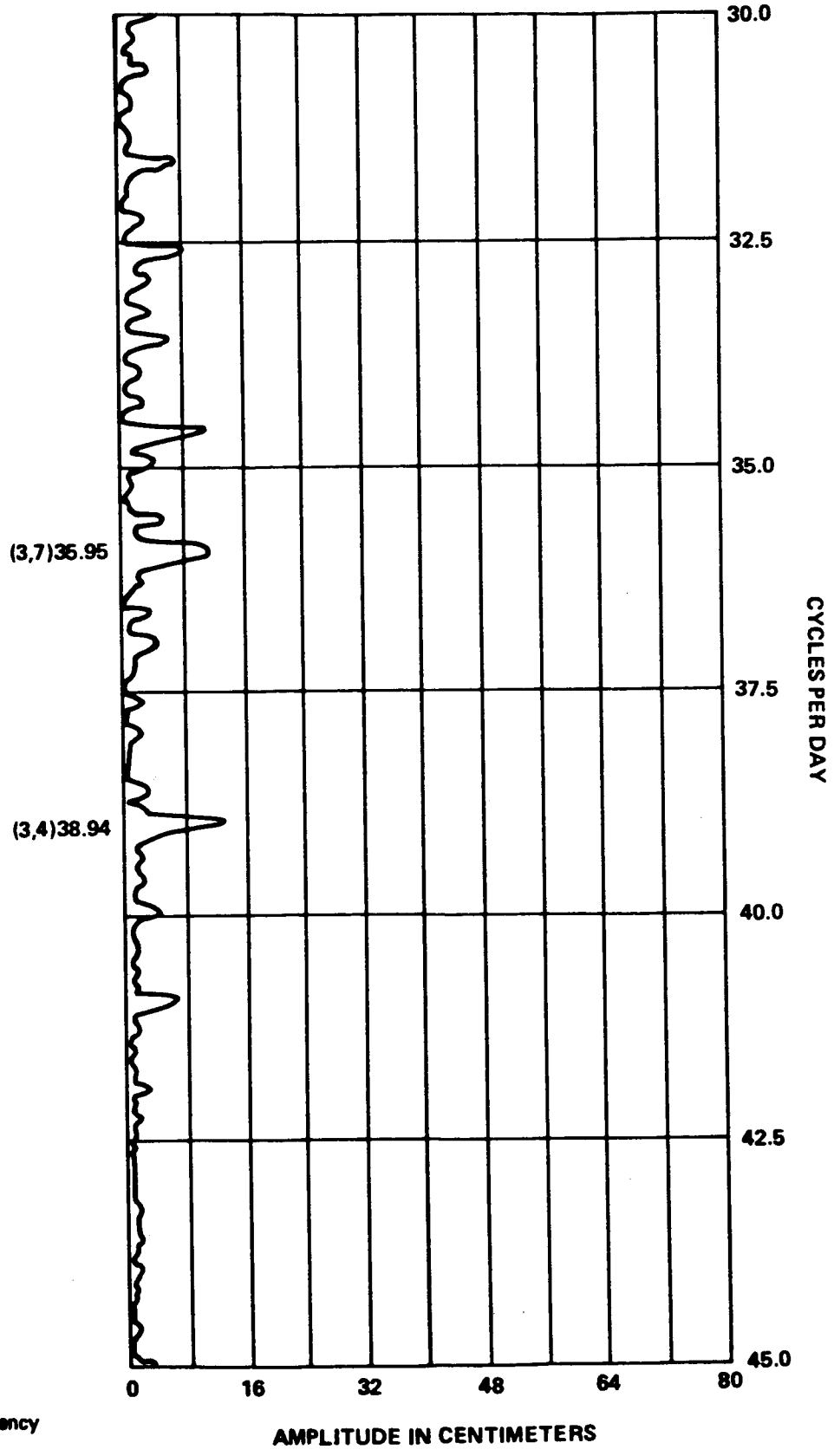

(ℓ – 2p + q,m) frequency

AUTONOMOUS NAVIGATION ACCURACY USING SIMULATED HORIZON SENSOR AND SUN SENSOR OBSERVATIONS

by

G. E. PEASE

and

H. T. HENDRICKSON

The Aerospace Corporation

Post Office Box 92957

Los Angeles, California 90009

This work was supported under the U.S. Air Force Space Division Contract # F4701-79-C-0080.

AUTONOMOUS NAVIGATION ACCURACY USING SIMULATED HORIZON SENSOR AND SUN SENSOR OBSERVATIONS

G. E. PEASE
and
H. T. HENDRICKSON

Summary

Infrared Earth horizon sensors in combination with a sun sensor have proven useful for autonomous station keeping of geosynchronous satellites but the complexity of a fully self-contained autonomous navigation system for low altitude satellites has discouraged implementation of such a scheme. A relatively simple system which would use horizon crossing indicators, a sun sensor, a quartz oscillator, and a microprogrammed computer is being studied.

The sensor combination is required only to effectively measure the angle between the centers of the Earth and the Sun. Simulations for a particular orbit indicate that 2 km r. m. s. orbit determination uncertainties may be expected from a system with $0.^{\circ}06$ measurement uncertainty. A key finding is that knowledge of the satellite orbit plane orientation can be maintained to this level because of the annual motion of the Sun and the predictable effects of Earth oblateness. The basic system described above can be updated periodically by transits of the Moon through the IR horizon crossing indicator fields of view. The extent to which these conclusions may be applied to a larger class of satellite orbits is under study.

Introduction

Previous autonomous navigation schemes (references 1 and 2) have had two characteristics which have caused them to be noncompetitive with normal ground navigation techniques; they tend to be low accuracy systems, yet they require inordinate onboard processing capability. Higher accuracy autonomous systems such as the Space Sextant are even more complex and require a large sacrifice of payload capability to perform the optical measurements and complex data reductions. To date, the most successful applications of the autonomous navigation concept have been for limited functions, most notably automatic longitude station keeping of geosynchronous satellites LES 6, LES 8, and LES 9 (references 3 and 4).

The present application of interest is for a self-contained low accuracy (12 k.m., 3σ) system with minimal payload allocation requirements. The success of this approach hinges less on accuracy than on degree of autonomy and simplicity. The trap we wish to avoid is the common one of proposing a massive and complex system that is able to overcome all possible problems other than those of cost, practicality, and self-sufficiency.

As envisioned, the completely self-contained on board navigation system will use one or more IR Earth horizon crossing indicators, a Sun sensor, a quartz oscillator, and a microprogrammed computer to deliver the desired overall orbit position accuracy of 12 k.m., 3σ, or better throughout a six month lifetime mission. Such a system has the potential to provide this level of self-contained autonomous navigation accuracy over very long mission lifetimes measured in years instead of months. It is important to keep in mind that the proposed system is truly autonomous in the sense that it is independent of other systems such as ground or orbiting radio beacons which are susceptible to jamming or destruction.

To date, a 470 km circular orbit with 34° inclination has been studied using a special version of the FLEXSAT program. A brief description of this program is given in Appendix B.

Sensor Measurement System

Figure 1 illustrates a conventional attitude sensor configuration that is well suited to perform autonomous navigation functions. The spinning satellite uses one or more narrow angle IR horizon crossing indicators and a wide angle Sun sensor. For autonomous navigation with horizon crossing indicators it is desirable to orient the spacecraft spin axis normal to the orbit plane as shown. This may be controlled by monitoring attitude throughout the orbital period and minimizing variations in the horizon scanner pulse widths by means of attitude maneuvers when required. The attitude measurements allow determination of the direction to the center of the Earth with respect to the Sun at each scan. As indicated, the horizon sensors can also detect the Moon. This opportunity will occur at least twice in a sidereal month. The moon observations provide an inertial reference update that normally would require the extra complexity of a separate star sensor system. For the system shown in figure 1, a wide angle sun sensor is used to measure the times of Sun crossings through the instrument field of view and the elevation of the sun with respect to the optical axis of the sun sensor. The horizon and Sun transit times, along with the Sun elevation, yield the angle between the centers of Earth and Sun as seen from the satellite.

An ambiguity exists in this measurement system, in that a rotation of the satellite orbit plane about the Earth-Sun line would be undetectable in the observations if the gravitational potential field of the Earth were that of a sphere rather than that of an oblate spheroid, and if the direction of the Sun in inertial space were fixed. The proposed system takes advantage of the known nature of Earth oblateness effects (see Appendix A) and of the orbital motion of Earth in the plane of the ecliptic. The dynamical effects of oblateness include regression of the nodes along the equator; the orbital motion of Earth defines the ecliptic plane. Periodic Moon observations remove any remaining ambiguity. Initial orbit knowledge at time of orbit injection should be sufficiently accurate (528 meters, 0.61 m/sec) to provide confidence that the ambiguity will not be a problem in practice.

Error Model

For the initial studies, the sensor measurements have been simulated in the form of angular distance between the centers of Earth and Sun at one minute intervals during the portion of the orbit in which the Sun is visible to the satellite. An uncertainty of 1700 m (reference 5) was assumed for the uncertainty in the height of the 14-16 micron absorption layer of Earth's atmosphere. This translates to a horizon sensor angular measurement error of

$$\sigma_{\theta_h} = 0.^{\circ}042$$

for a 470 km altitude orbit.

The Sun sensor can measure angular position of the Sun to

$$\sigma_{\theta_s} = 0.^{\circ}03$$

and the angular uncertainty between the optical axes of the horizon and Sun sensors is

$$\sigma_{\theta_a} = 0.^{\circ}02.$$

We consider time-tag uncertainties resulting from instrumental delay and clock error to be similar in magnitude to σ_{θ_a}. The uncertainty, σ_θ in the angle between the center of Earth and center of Sun is approximately the r.s.s. of these errors or

$$\sigma_\theta = (\sigma_{\theta_h}{}^2 + \sigma_{\theta_s}{}^2 + 2\,\sigma_{\theta_a}{}^2)^{1/2} \approx 0.^{\circ}06 ,$$

which is the angular uncertainty used in the simulations.

FLEXSAT was used to generate state vector covariance matrices based on the angular measurement uncertainties. The ballistic drag value, $C_D A/W$, was also estimated. In addition, the Kalman filter performance was tested by perturbing the initial values of the estimated parameters

by the amount of the a priori uncertainties. These uncertainties are listed in Table 1. The reference trajectory value of $C_D A/W$ was 0.037 m^2/kg.

Additional filter errors were introduced by modelling an eighth degree, eighth order geopotential field in the numerical integration of the reference trajectory used to generate the simulated observations, whereas a second degree, zero order fit model was used. Corresponding covariance uncertainties were roughly approximated by adding process noise to the covariances in the form of acceleration uncertainties,

$$\sigma_{\ddot{x},\ddot{y},\ddot{z}} = 80.2\mu g,$$

to represent high frequency geopotential accelerations and unmodeled aerodynamic drag variations. The low frequency J_2 term, in contrast, produces accelerations of up to about 1000μg. The simple analytic disturbing function of Appendix A serves to model the J_2 accelerations very precisely. The velocity vector of a satellite in an inclined orbit is therefore surprisingly determinable in equatorial coordinates without a stellar reference.

Effect of Orbit/Sun Geometry

Figure 2 illustrates the various possible extremes of geometry for a 34° inclination orbit, depending upon the time of day of launch and the time of year. Consider the Sun 1, Sun 2 and N axes to be in the plane of the drawing. The Sun 3 axis, equatorial plane, and satellite orbit plane are normal to the plane of the drawing. As shown, the Sun can be within $\pm 23.^\circ 5$ of the equator, depending upon the time of year. Sun 1 and Sun 2 positions are extremes of solar declination. In the drawing they are placed normal to the satellite line of nodes so that at Sun 2 the maximum angle of the orbit plane to the sun line of $57^\circ.5$ is attained. That this is unfavorable geometry is evident. At the limit, 90° is singular, for if the satellite attempted

to navigate by observing a celestial object at N, normal to the orbit plane, it is seen that in a circular orbit the Earth-object angle would not change as a function of time, to first order.

The Sun 3 geometry is also unfavorable, as the sunline is coplanar with the satellite orbit. Since this particular configuration again places the satellite line of nodes on the ecliptic line of nodes, the orbital inclination of the satellite is not directly observable.

Position Uncertainties

Table 2 contains the peak remaining radial, intrack, and crosstrack position standard deviations for each of the three extreme Sun orientations after nine simulated orbital revolutions of the satellite, using FLEXSAT covariances. An advantage of a recursive real time filter is that the customary prediction errors are limited to data gaps, which in this case are somewhat less than half of each orbit revolution.

The largest crosstrack errors are associated with Sun 1 orientation, with Sun 3 a close contender. Figures 3 and 4 plot the time history of these covariance-derived uncertainties as a function of time from injection. It is seen that the orbit solutions are stable but not overly convergent. Simulations with a spherical Earth model produce crosstrack uncertainties that increase with time, as expected, in the presence of the $80\mu g$ acceleration noise that simulates unmodeled high frequency geopotential and drag terms. This results from the ambiguity in the orientation of the orbit plane that would exist except for the measurable presence of the J_2 disturbing function.

The largest position uncertainty was found to be the intrack standard deviation in the Sun 2 configuration, which also produces the largest radial uncertainty (see Table 2). The time history from injection of these errors is plotted in figures 5 and 6. As expected, these exhibit more convergent behavior than do the crosstrack uncertainties, which more closely reflect orbit plane orientation errors. However, it should be noted that the highest intrack errors are initially large and do not converge to the extent of recovering *a priori* knowledge. The Earth horizon measurement errors, of course, map directly into intrack orbit errors.

Effect of Injection Knowledge

The previously described cases used the somewhat conservative orbit injection knowledge uncertainties and errors in Table 1 of

$$\tilde{\sigma}_{x,y,z} = \tilde{\Delta}_{x,y,z} = 3048 \text{ m}$$

$$\tilde{\sigma}_{\dot{x},\dot{y},\dot{z}} = \tilde{\Delta}_{\dot{x},\dot{y},\dot{z}} = 3.048 \text{ m/sec.}$$

The crosstrack errors for a typical nominal case (Sun at first point of Aries, $\Omega_{Sat} = 90^{\circ}$) are plotted from injection through nine orbit revolutions in Figure 7.

To verify the dependence of orbit plane orientation knowledge on injection knowledge and to test the capability of retaining this knowledge, a similar case with more realistic injection knowledge and errors was run using

$$\tilde{\sigma}_{x,y,z,} = \tilde{\Delta}_{x,y,z} = 528 \text{ m}$$

$$\tilde{\sigma}_{\dot{x},\dot{y},\dot{z},} = \tilde{\Delta}_{\dot{x},\dot{y},\dot{z}} = 0.61 \text{ m/sec.}$$

Radial uncertainty was reduced from about 600 m (nominal case) to 400 m on the ninth orbit revolution, while intrack uncertainty was reduced from 2700m (nominal case) to 1900m on the ninth revolution. The important crosstrack uncertainty is plotted in Figure 8. It is seen that the injection knowledge of 528 m is retained through the ninth orbit revolution and even improved slightly between the first and ninth revolutions. This is certainly encouraging in light of the importance of minimizing orbit plane orientation errors. As expected, however, the solution displays slightly divergent characteristics. In time the errors might be expected to grow to the size of those in Figure 7.

Filter Errors

The largest filter estimate difference from the "truth" state vector or from the "truth" ballistic drag value is less than 3σ, where the value of σ is obtained from the covariance matrix associated with the particular

estimate. Assuming a Gaussian error distribution, one would normally expect to see an occasional 3σ estimate. The great majority of estimates are less than 1σ from the "truth" model. The actual estimates are accordingly better than Table 2 and Figures 3 - 8 indicate. In these cases the conservative process noise of 80.2μg served to maintain the filter covariance matrix at a reasonably high level. The fact that there was convergence and that the actual errors showed reasonable conformity with the sigmas from the covariance analysis indicates that the filter covariances are realistic. Since in theory they represent an infinite sample of Monte Carlo trials they are the numbers tabulated and plotted in this paper.

Moon Observations

Figure 1 illustrates how the horizon crossing indicator will, in general, view two portions of the Moon's orbit (the second view area is on the opposite sides of the satellite and Moon orbits). When the Moon enters these view areas, once every sidereal month for each portion, the 14-16 micron bandwidth horizon sensor will detect the Moon for several satellite orbit revolutions on each occasion. The exact length of viewing time depends upon the horizon sensor field of view and the inclination of the satellite orbit plane to the orbit plane of the Moon.

The Moon observations can be used to periodically update the orbit knowledge with independent observations. These observations fix the satellite state in inertial space in a direct manner. If two horizon crossing indicators are used in order to scan both north and south of the orbit plane, then two additional Moon viewing periods are available in each sidereal month. This system would seem to be superior to a system using only one horizon crossing indicator in any event, when the attitude determination problem is examined.

The principal value of Moon observations is to provide periodic recovery capability in the event that orbit knowledge is lost or degraded owing to larger than expected injection errors, degraded sun sensor performance, transient data stream/clock/microprocessor failures or unexpectedly large perturbations to the satellite orbit. A very compact,

pre-calculated lunar ephemeris would suffice because of the infrequency of Moon observations. With two horizon sensors, the Moon would nominally be observable for four or five orbit revolutions per week. To account for the large IR radiation differences between the illuminated hemisphere of the Moon and the dark side, a lunar phase-dependent model of the asymmetric sensor response would be a necessary part of the pre-calculated ephemeris. Figure 9 shows the essential elements of the navigation system, including the Moon data capability. The dashed lines indicate that the Sun elevation measurements are optional for attitude control, but may prove useful.

Clock Errors

All horizon, Sun, and Moon observations must be time-tagged by the onboard oscillator. A typical quartz oscillator is stable to one part in 10^9, or 30 msec/year. To make use of 500 m injection accuracy we desire clock errors no larger than

$$\Delta t \leq \frac{500 \times 5640}{6848252 \times 2\pi} \approx 66 \text{ msec}$$

during the intervals between Moon observations, which is clearly not a problem. In the above example the orbital period is 5640 seconds and the orbit semimajor axis is 6848252 m.

Onboard Computer Requirements

The products of the autonomous system diagrammed in Figure 9 are the satellite ephemeris at bottom center and the attitude control function at upper right of the chart. The recursive orbit filter and attitude computations, ephemeris evaluation, and information management throughout the system could be performed by a microprogrammed I/O and central processor system. The requirements are currently being studied, but it is estimated that a 32k word memory and 16 bit fixed word length should be adequate.

Conclusions

An autonomous navigation system such as the one diagrammed in Figure 9 would appear to be capable of delivering accuracies normally associated with horizon sensors in conjunction with a stellar attitude system (reference 7). It is felt that the extra complication of a star sensor may be unwarranted considering the relatively good performance of a horizon sensor and sun sensor system. To fully assess the value of such a system, however, it is important to study the particular orbital characteristics of the intended mission. For example, simulations indicate that some high inclination missions may be a poor choice or would at least require further study. Accuracy will also be dependent to some extent on orbit altitude.

References:

1. "Autonomous Navigation Systems Technology Assessment," J. W. Lowrie, Martin Marietta Aerospace, AIAA Report No. 79-0056, January 1979.

2. "High Altitude Reference System Development Study," N. Westheimer, P. Andrews, J. Samson, Rockwell International Technical Report AFAL-TR-79-1111, Volume II, August 1979.

3. "Automatic Stationkeeping," A. Braga-Illa, J. Spacecraft, Vol. 6, No. 4, April 1979.

4. "Navigation Schemes for LES-8/9 Autonomous Stationkeeping System," S. Srivastava, MIT, Lincoln Laboratory Technical Note 1973-18, 20 April 1973.

5. "Located Horizon Variation Study," L. Bradfield, G. Nelson, Honeywell Inc. Report, NASA CR-6678, N69-36001, January, 1969.

6. "Digital Hardware for Use in Spacecraft Control Applications," G. Gilley, AAS 80-031, February, 1980.

7. "Analysis of an Horizon Scanner Autonomous Orbital Navigation System," J. S. Meditch, J. L. LeMay, J. P. Janus, Aerospace Corp., Report No. TDR-469(5540-10)-6, July 1965.

Appendix A

The disturbing function of an equatorial bulge is

$$D = \frac{-\mu}{2r^3} J_2 (3 \sin^2\delta - 1)$$

where μ is GM_{Earth},

r is the instantaneous radius vector,

J_2 is the second degree Legendre polynomial coefficient for Earth,

δ is the instantaneous declination of the satellite.

The secular perturbations are then

$$D_s = \frac{1}{2\pi}\int_0^{2\pi} D \, d M$$

where M is the mean anomaly.

In terms of orbital elements a, e, i, ω, Ω, M_o, the principal secular effect is a regression of the nodes along the equator,

$$d\Omega_s = - \frac{3n J_2}{2a^2(i-e^2)^2} \cos i \, dt,$$

where n is the mean motion.

Depending upon whether orbital inclination is less than or greater than $i = \arcsin (2/\sqrt{5}) = 63.^{\circ}43$, the line of apsides will secularly advance or regress according to

$$d\omega_s = \frac{3n J_2}{2a^2(1-e^2)^2} \left(\frac{5}{2} \sin^2 i - 2\right) dt.$$

Secular changes in the orbital period are also a function of a, e, and i as the mean anomaly changes by

$$d M_s = n \, d t \left[1 - \frac{3 J_2}{2a^2(1-e^2)^{3/2}} \left(\frac{3}{2} \sin^2 i - 1\right)\right].$$

APPENDIX B

SIMULATION SOFTWARE

- program: FLEXSAT
- author: H. Hendrickson
- compiles on: CDC 7600, CDC 176 FORTRAN compiler
- trajectory: Runge-Kutta fourth order integrator
- filter: Kalman
- partial derivatives: finite difference

$$\Delta\theta = f(p_1, \ldots, p_j + \Delta p_j, \ldots p_k)(t_i) - f(p_1, \ldots, p_k)(t_i)$$

at the ith observation, θ_i and jth estimated parameter, p_j at time t_i for the data equation

$$\theta = f(p_1, \ldots, p_k) + \epsilon$$

having k parameters, ϵ observation noise.

- Additive parameter noise model:
  White acceleration noise,

$$\sigma_{q_{\frac{\cdot}{r}}} = \sigma_{q_{\frac{\cdot}{r}}} / (t_{i+1} - t_i)^{1/2}.$$

APPENDIX C

ONBOARD CALCULATIONS FOR HORIZON/SUN SENSOR AUTONOMOUS ATTITUDE AND NAVIGATION SYSTEM

- Polynomial evaluation, one second intervals for observation angles,

3 Annual Terms	$\theta_t(a, e, M_o)_{Earth}$
8 Monthly Terms (use different $\Delta\Omega$, $\Delta\omega$ each month)	$\theta_t(a, e, i, \Omega, \omega, M_o, \Delta\Omega, \Delta\omega)_{Moon}$
3 Secular terms (Satellite orbit)	$\theta_t(\Delta\Omega, \Delta\omega, \Delta M)_{J_{2,0} J_{2,2}}$

- Sequential filter recursive estimation at each observation time

  2 attitude angles (α, δ spin axis)

  5 satellite orbit parameters
  $(a, e, i, \Omega, \omega, C_D A/W)_{Satellite}$ and ballistic drag

  (assume M_0 known at injection)

- Satellite ephemeris calculation

  geocentric position
  as a function of time $(x, y, z)_t$
  at one minute intervals

Table 1.

Simulation *a priori* Uncertainties/Initial Perturbations

parameter, p	$\tilde{\sigma}_p = \Delta p$ (initial)
x, y, z	3048 meters
$\dot{x}, \dot{y}, \dot{z}$	3.048 m/sec
$C_D A/W$	8.19×10^{-3} m^2/kg

Table 2.

EFFECTS OF EXTREME SUN VIEW GEOMETRY

9th REV	SUN 1 ($10^{\circ}.5$)	SUN 2 ($57^{\circ}.5$)	SUN 3 (COPLANAR)
σ RADIAL (M)	490	730	430
σ INTRACK (M)	1860	3440	1830
σ CROSSTRACK (M)	2960	1620	2740
σ r.m.s. (M)	2040	2230	1920

Figure 1

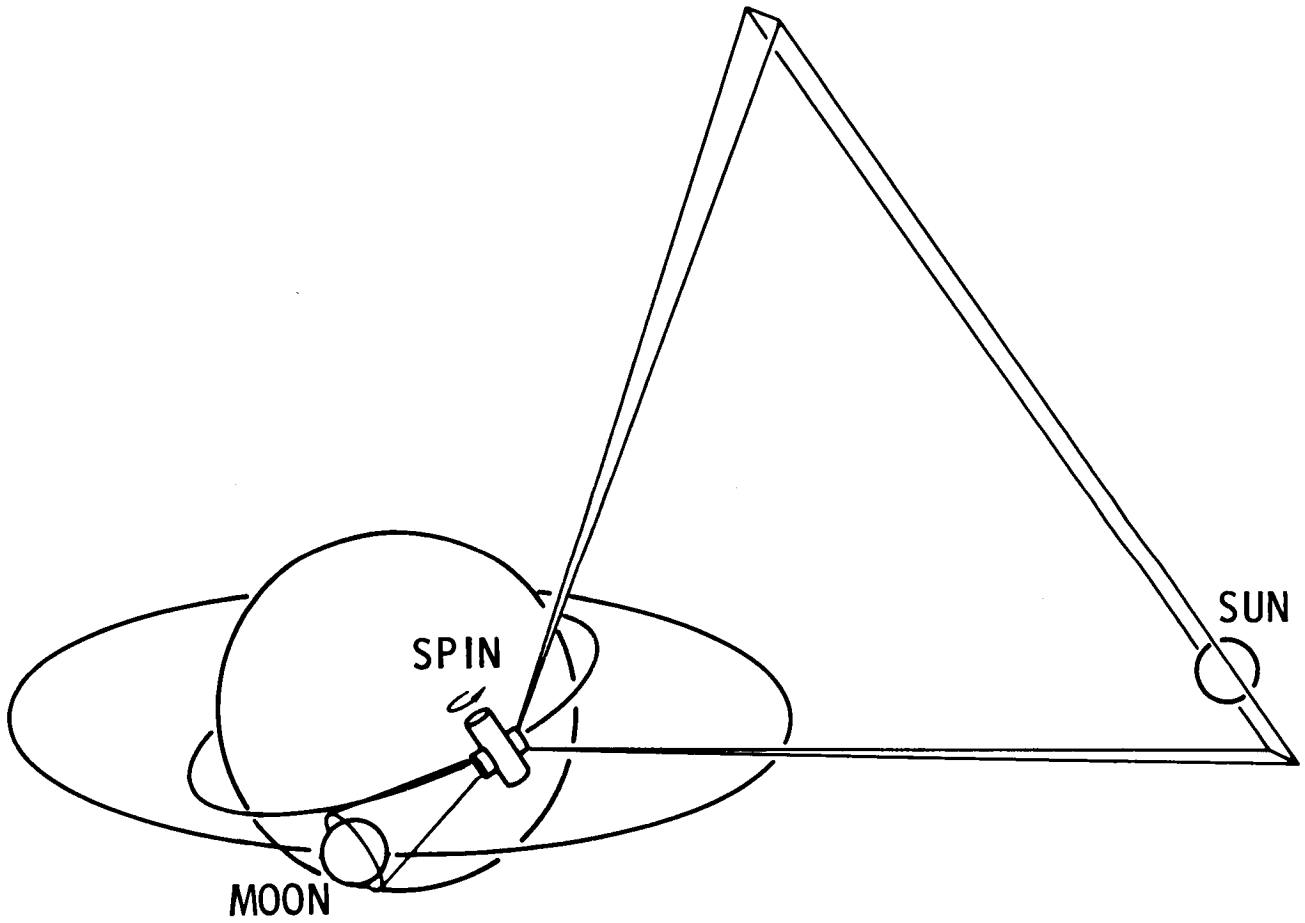

SCHEMATIC OF PROPOSED HORIZON CROSSING INDICATOR AND WIDE ANGLE SUN SENSOR CONFIGURATION ON A SPINNING SATELLITE WITH SPIN AXIS NORMAL TO THE SATELLITE ORBIT PLANE

Figure 2

Extremes of Possible Sun View Geometry

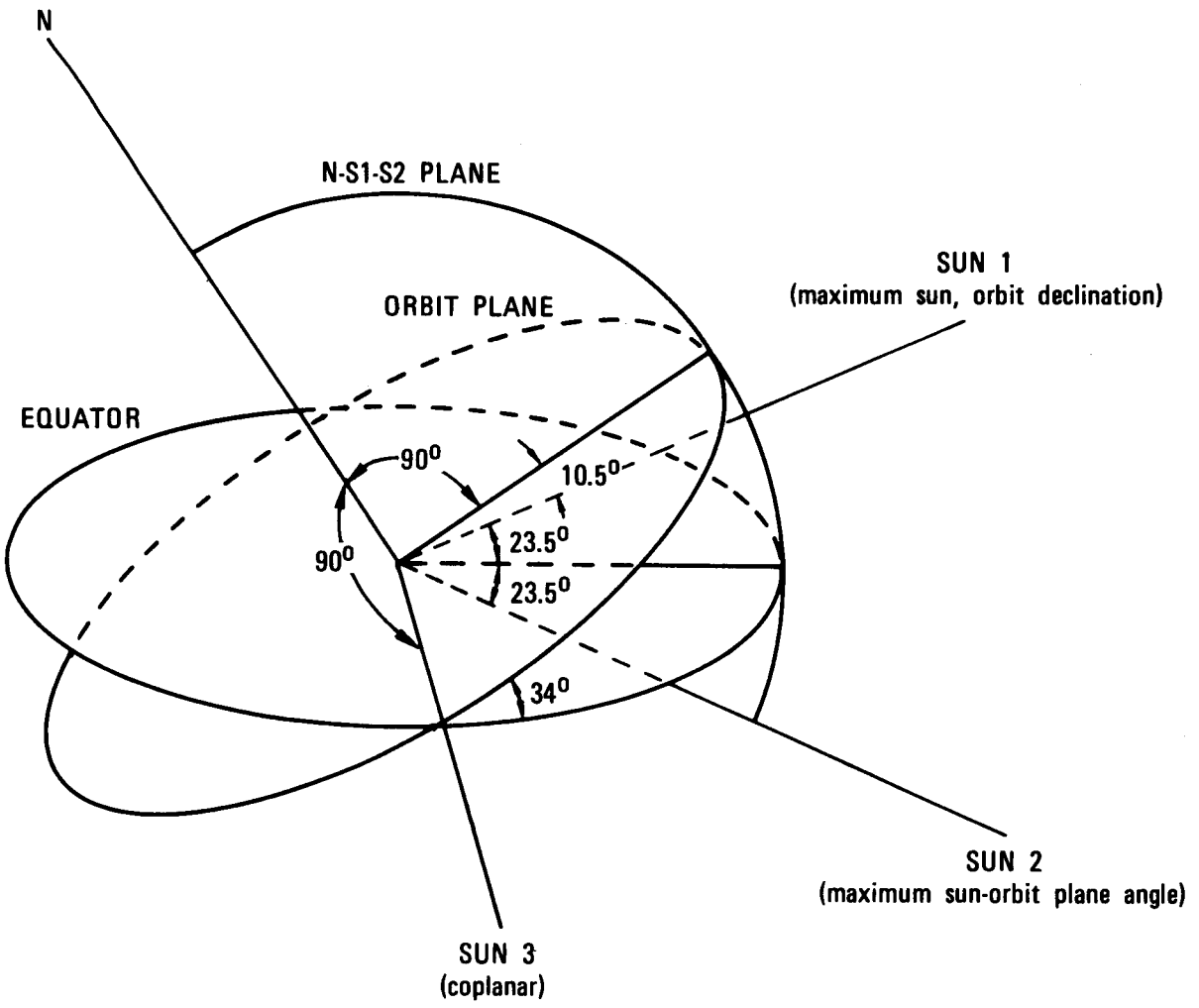

Figure 3

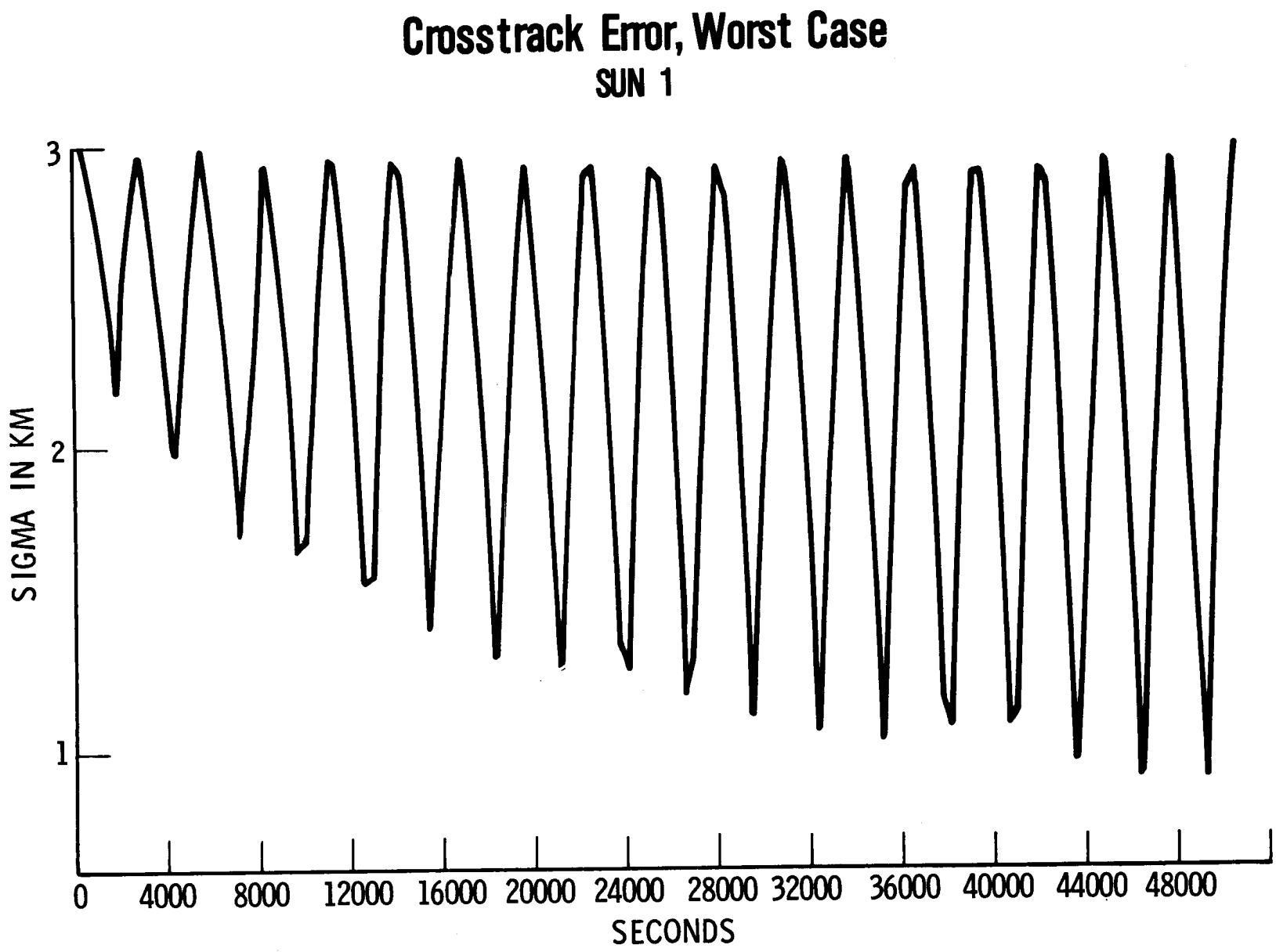
Crosstrack Error, Worst Case
SUN 1
SIGMA IN KM
3
2
1
0
4000
8000
12000
16000
20000
24000
28000
32000
36000
40000
44000
48000
SECONDS

Figure 4

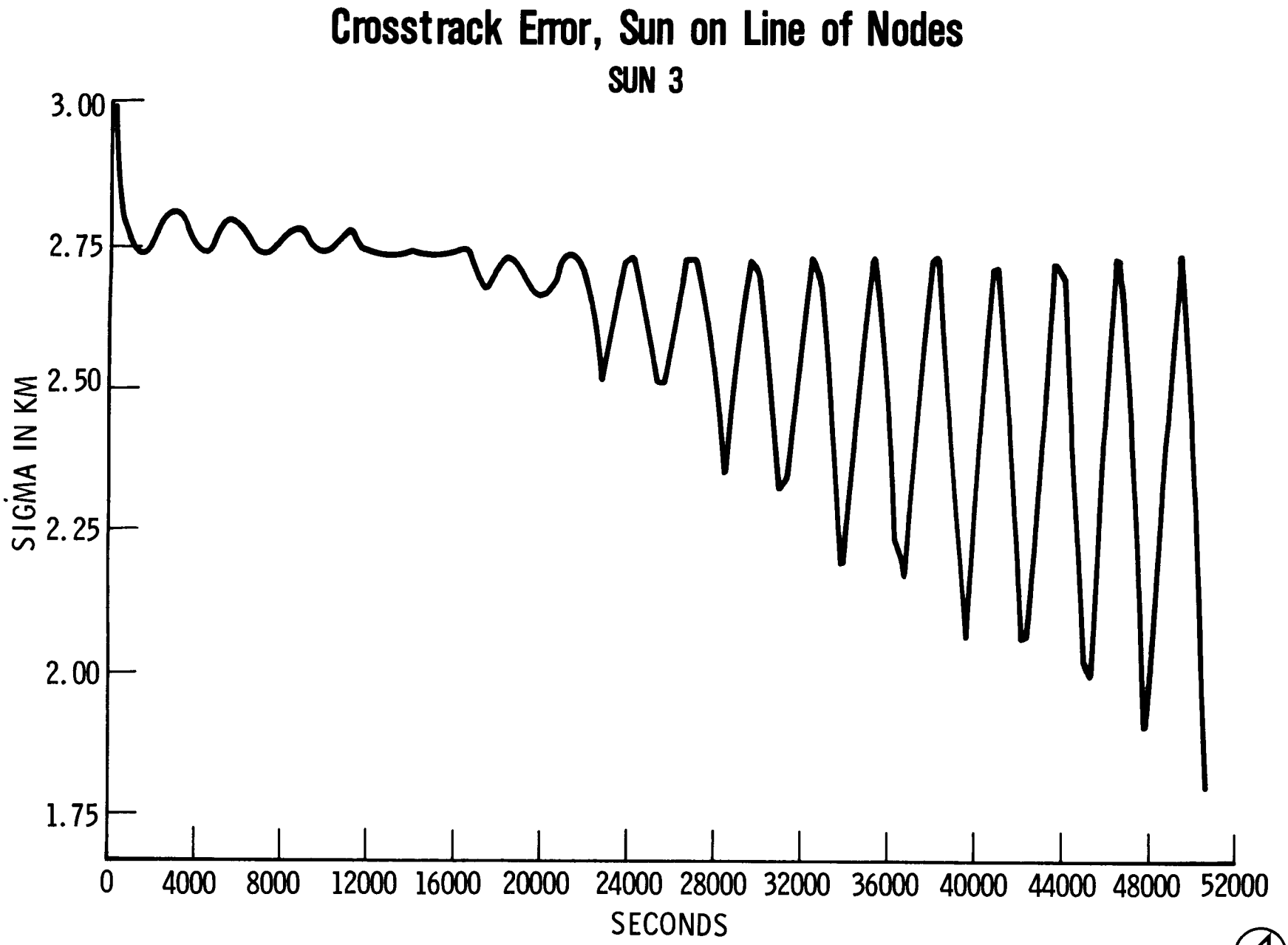
Crosstrack Error, Sun on Line of Nodes
SUN 3
3.00
2.75
2.50
2.25
2.00
1.75
SIGMA IN KM
0
4000
8000
12000
16000
20000
24000
28000
32000
36000
40000
44000
48000
52000
SECONDS

Figure 5

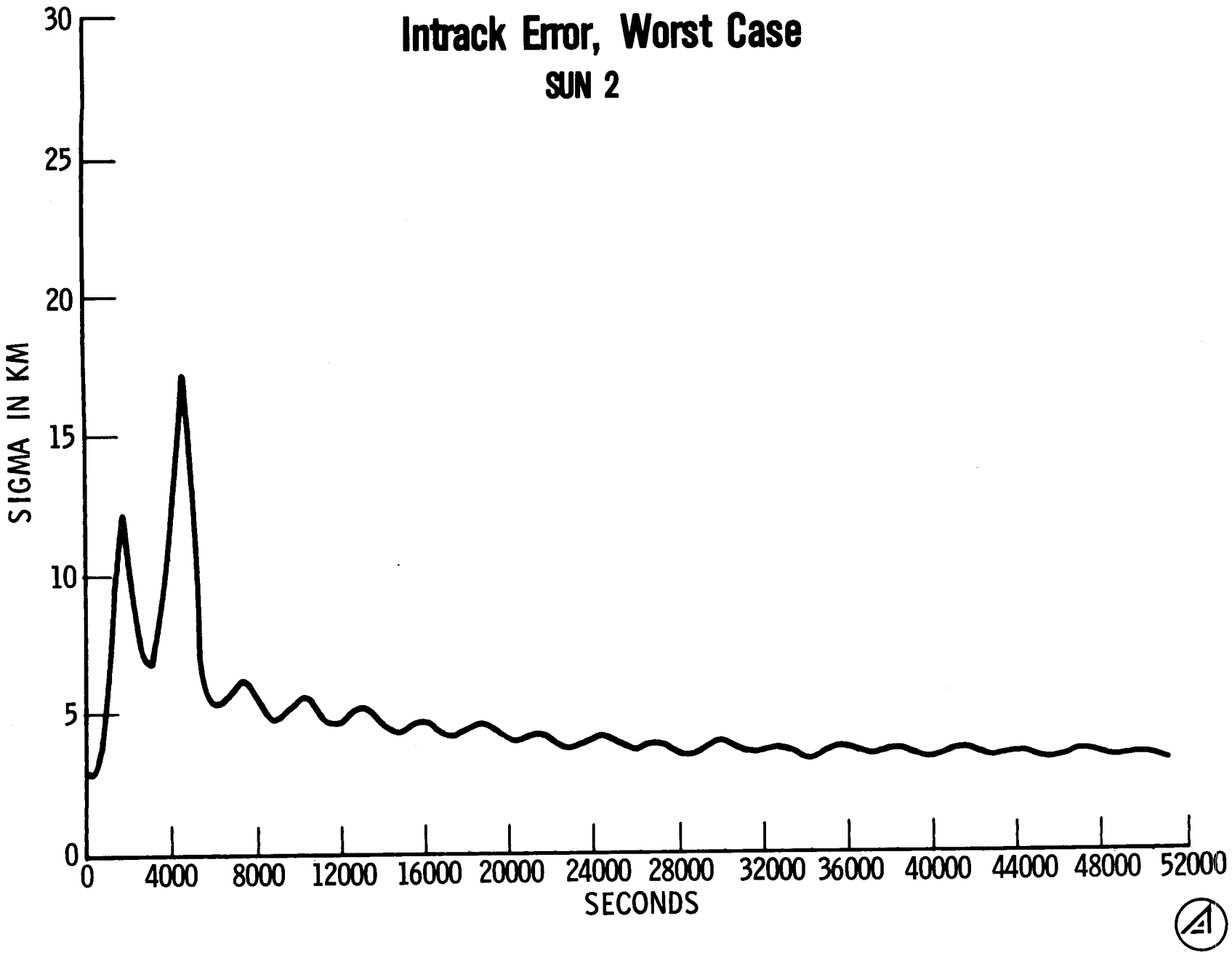
Intrack Error, Worst Case
SUN 2
SIGMA IN KM
30
25
20
15
10
5
0
0
4000
8000
12000
16000
20000
24000
28000
32000
36000
40000
44000
48000
52000
SECONDS

Figure 6

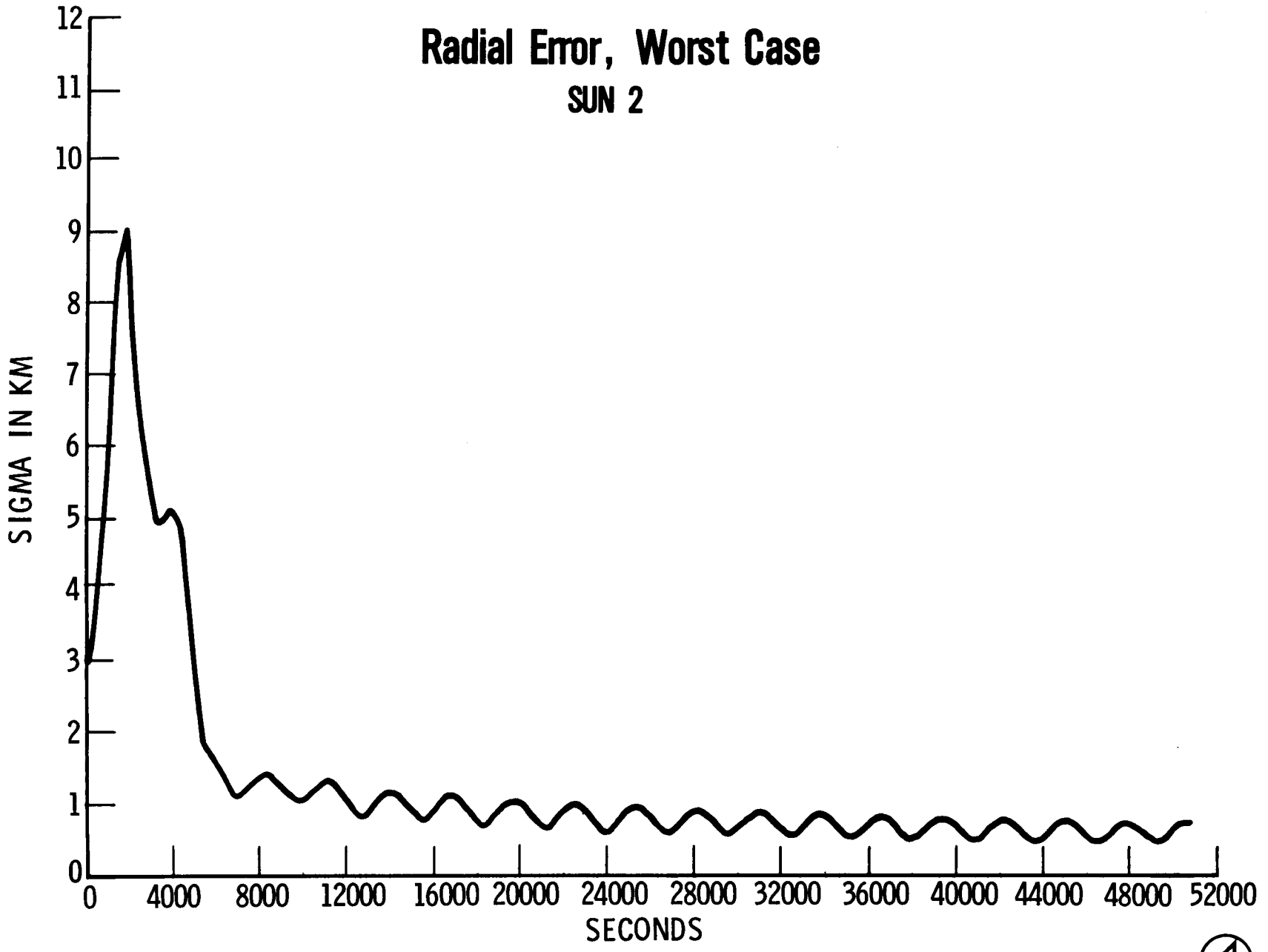
Radial Error, Worst Case
SUN 2
SIGMA IN KM
0
1
2
3
4
5
6
7
8
9
10
11
12
0
4000
8000
12000
16000
20000
24000
28000
32000
36000
40000
44000
48000
52000
SECONDS

Figure 7

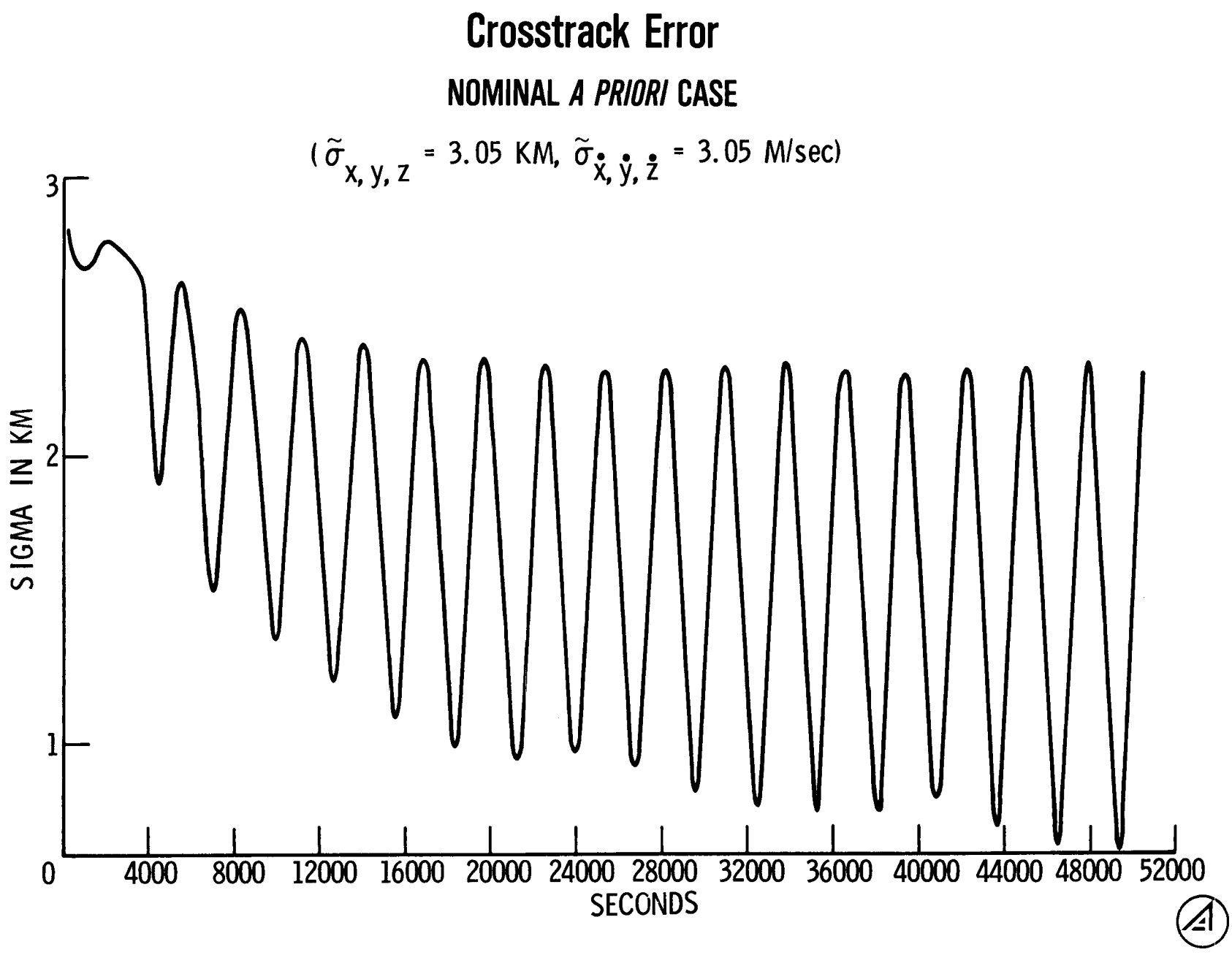
Crosstrack Error
NOMINAL A PRIORI CASE
($\tilde{\sigma}_{x,y,z}$ = 3.05 KM, $\tilde{\sigma}_{\dot{x},\dot{y},\dot{z}}$ = 3.05 M/sec)
SIGMA IN KM
3
2
1
0
4000
8000
12000
16000
20000
24000
28000
32000
36000
40000
44000
48000
52000
SECONDS

Figure 8

Crosstrack Error

IMPROVED *A PRIORI* CASE

($\tilde{\sigma}_{x,y,z}$ = 528 METERS, $\tilde{\sigma}_{\dot{x},\dot{y},\dot{z}}$ = 0.61 M/sec

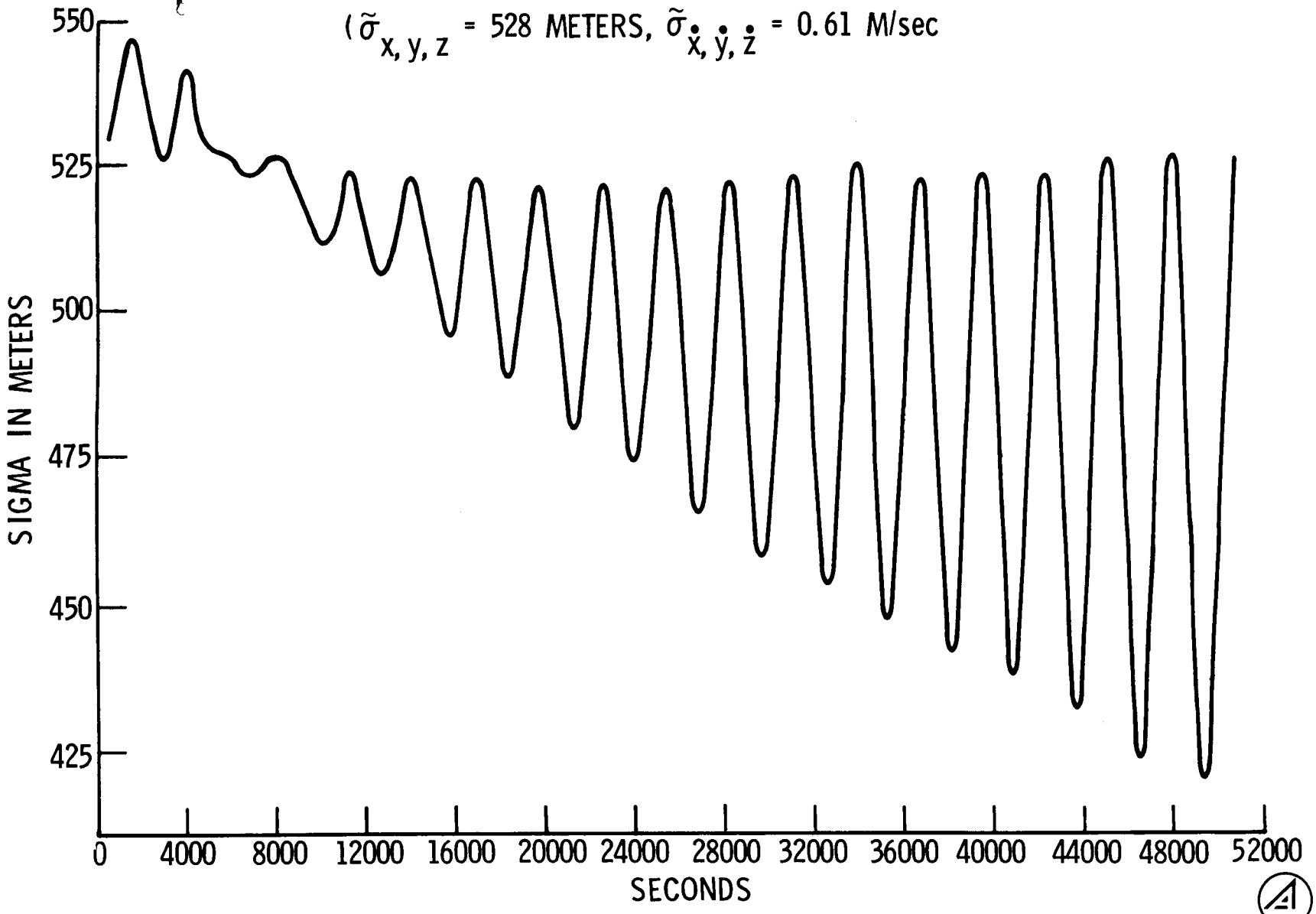

Figure 9

Horizon Indicator/Sun Sensor

AUTONOMOUS NAVIGATION SYSTEM FOR SPINNING SATELLITE

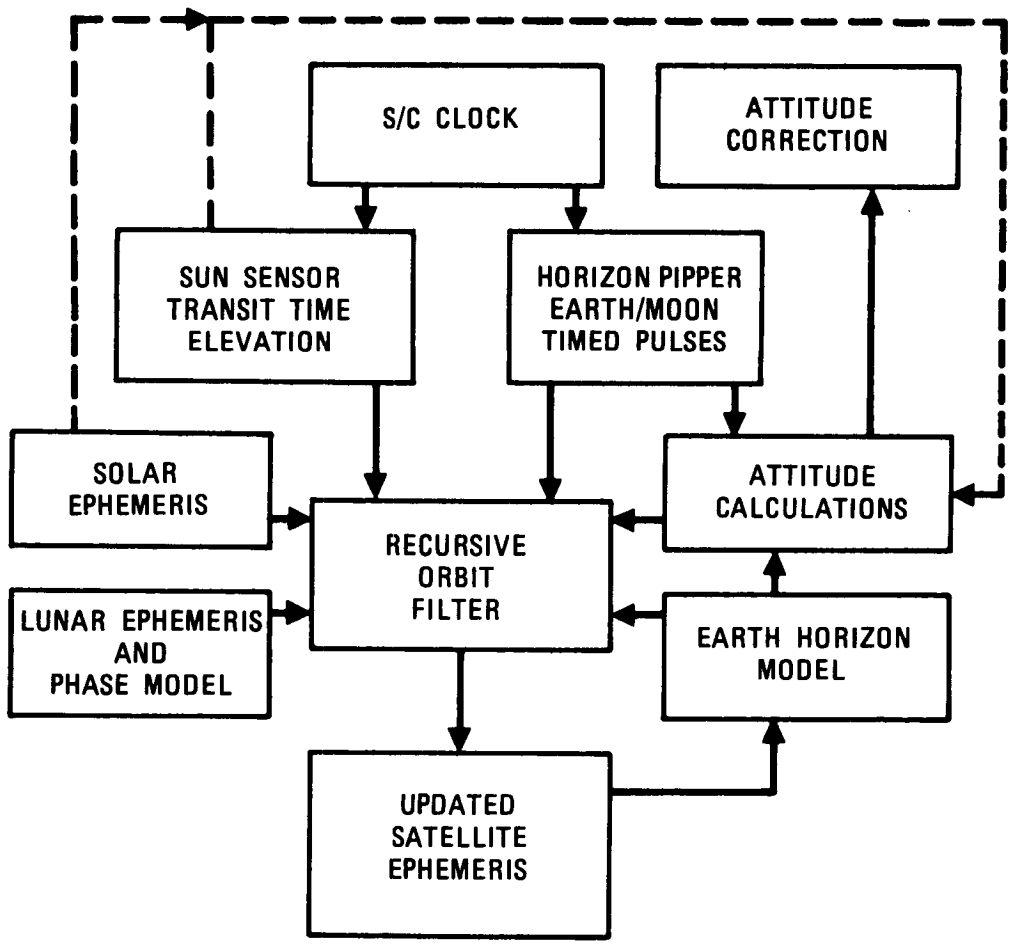

AN EVALUATION OF GALILEO - VIKING DIFFERENCED RANGE IN GALILEO - MARS FLYBY NAVIGATION

F. B. Winn, E. W. Walsh, M. P. Ananda, F. T. Nicholson

Jet Propulsion Laboratory
California Institute of Technology

ABSTRACT

The navigational requirements of Galileo as it swings by Mars [flyby distance is 275 km from the Martian surface; 25 km (1σ)] are going to be met with interferometric angular measurements (VLBI) and range and range-rate measurements. Like VLBI, dual spacecraft differenced range is less sensitive to Mars ephemeris errors and tracking station location errors than conventional range and Doppler. Similarly, differenced range provides angular information about the separation between the Mars Viking Lander I and the Galileo spacecraft. In covariance studies, dual spacecraft range coupled with conventional range and Doppler is shown to estimate the Galileo-Mars flyby distance to better than 10 km (1σ) which is comparable to the VLBI performance. For the Galileo-Mars flyby, dual spacecraft differenced range promises to be an excellent backup to VLBI if the Mars Viking Lander remains operational.

This paper presents the results of one phase of research carried out at the Jet Propulsion Laboratory, California Institute of Technology, under Contract NAS7-100, sponsored by the National Aeronautics and Space Administration.

I. INTRODUCTION

Galileo, a NASA spacecraft to be launched in 1984 by the Space Shuttle/IUS launch vehicle, will travel from earth to a Mars flyby on an ultra fast trajectory: a flight time of less than 100 days. On such a high acceleration trajectory (Fig. 1), conventional Galileo radiometric tracking data, 2-way range and Doppler, can establish the heliocentric position of the probe to a standard deviation of 11 km.

The Mars ephemeris has an additional 40 km 'in-track' position uncertainty such that the Mars-Galileo relative position uncertainty exceeds 40 km (1σ). It is essential to know the Mars-Galileo relative position to better than 25 km (1σ). The closer Galileo can be flown past Mars, the smaller the Galileo rocket maneuver that will be required to send Galileo on to the Jupiter system (Fig. 2). The ΔV requirement of Galileo's rockets increases 40 m/s per 100 km increase in the flyby distance (Fig. 3). The Mars flyby is being used to provide a controlled acceleration to the Galileo spacecraft.

Deep space probes, such as Galileo, are tracked and navigated from earth. That is, a radio carrier is beamed to a distant space probe. The probe transponds the radio tone back to earth. The frequency difference between the earth transmitted and received signal is the Doppler shift - a measure of the spacecraft radial velocity. Modulation placed on the radio carrier is used to measure the light time separation between earth transmission to and reception from the spacecraft. These conventional radio metric data types, Doppler and range, measure in the radial direction only.

Because of topocentric parallax, at any instant of time the radial velocity of a probe is different at each terrestrial tracking station. This uniqueness of Galileo and Viking* range and range-rate, that is dependent on topocentric position, permits the determination of the relative Galileo-Viking angular separation.

In covariance studies, Galileo conventional range and Doppler could estimate the Galileo-Mars flyby distance to 40 km (σ) while a combination of doubly differenced range which exploits the relative topocentric parallax in conventional range and Doppler yields a standard deviation of less than 10 km and does so 25 days before Mars encounter (Fig. 4).

Galileo Project plans call for the Galileo spacecraft to flyby Mars 275 km (σ_d = 25 km) above the planet's surface (Ref. 1). To achieve this accurate flyby two new technological advances must be accomplished: one, the Mars ephemeris must be improved to better than 25 km (σ) and this effort is in progress; two, a wide-band Very Long Base Interferometry technology must be developed that will permit the Galileo spacecraft and Mars trajectories to be defined in a quasar inertial reference frame. This latter effort is underway also and offers not only a means to reduce the Galileo-Mars relative trajectory errors but VLBI cancels the preponderance of the Deep Space Station (DSS) location effects on orbit determination.

---

* The Viking Mars Lander I softly touched down on the Martian surface on July 4, 1976, and it still functions. It is expected to be operational in the Galileo era.

As circumstances are now, the current Mars Ephemeris and DSS locations uncertainties limit the Galileo-Mars relative navigation such that a $\sigma_d \leq 25$ km is not achievable with Galileo radiometric range and doppler alone. Galileo-Viking doubly differenced range provides a promising approach to Galileo's navigation objectives independent of an improved Mars ephemeris or a new VLBI technology. It does require the survival of the Viking Lander, however, in 1984.

II. DOUBLY DIFFERENCED RANGE DEFINITION

Figure 5 shows two Deep Space Station (DSS) tracking first one spacecraft and then the other. Thus, four range measurements are obtained and although the order of the range measurements taken in Figure 5 are DSS-1 to Viking, DSS-1 to Galileo, DSS-2 to Viking and DSS-2 to Galileo, the order is arbitrary.

With a restricted view to a single spacecraft, it is easy to show that the relative topocentric range (Fig. 6) involving 2 DSS is

$$\Delta\rho = \Delta Z \sin \delta + \Delta L \cos \delta$$

where

$$\Delta\rho = \rho_2 - \rho_1$$

ΔZ = north-south projection of the DSS baseline on that plane possessing the baseline and the spacecraft

ΔL = east-west projection of the baseline

or

$$\Delta L = \Delta\lambda \cos (\alpha - LST)$$

with

$\Delta\lambda$ being a linear separation between the DSS in the earth equatorial plane

LST = local sidereal time at the λ of the baseline

$$\lambda = \left(\lambda_{DSS_1} + \lambda_{DSS_2}\right)/2$$

Now if the relative range, $\Delta\rho$, from 2 spacecraft are combined in a second difference

$$\Delta^2\rho = \Delta\rho_G - \Delta\rho_V \qquad \begin{bmatrix} \text{G signifies Galileo} \\ \text{V signifies Viking} \end{bmatrix}$$

$$\begin{aligned} \Delta^2\rho = \Delta Z & \left[\cos\delta_G \quad \Delta\delta\right] \\ - \Delta\lambda & \left[\sin\ \alpha_G - LST\right) \cos\delta_G\ \Delta\alpha \\ & + \cos\left(\alpha_G - LST\right) \sin\delta_G\ \Delta\delta \end{aligned} \qquad (1)$$

$\Delta^2\rho$ is a function of the relative plane-of-sky coordinates of the two spacecraft and the baseline projection onto the plane-of-sky. It's sensitivity to the Mars ephemeris is less than that of $\Delta\rho$ or ρ.

$$\frac{\partial\Delta^2\rho}{\partial\mathcal{S}(\text{state})} = \frac{\partial\Delta\rho_G}{\partial\mathcal{S}(\text{state})} - \frac{\partial\Delta\rho_V}{\partial\mathcal{S}(\text{state})}$$

but

$$\frac{\partial\Delta^2\rho}{\partial(\text{Galileo State})} = \frac{\partial\Delta\rho}{\partial(\text{Galileo State})}$$

Specifically, $\Delta^2\rho$ is 20% (2 months before Mars encounter) to 50% (at encounter) less sensitive to the Mars ephemeris error than $\Delta\rho_G$ as is shown by the RSS of $\Delta\rho$ and $\Delta^2\rho$ partials with respect to the heliocentric position of Mars (Fig. 7).

In Figure 7 there are three graphs, one for each baseline used in the study.

DSS43 is located in Woomera, Australia. DSS63 is located in Madrid, Spain, and DSS14 is at Goldstone, California. The DSS approximate spherical coordinates are tabulated in Table I.

Since the DSS are separated in longitude, from 94° to 154°, Mars is in view over each baseline at different times. The Viking Lander can only be ranged in the cool morning Martian hours and only ranged once per Martian day. Thus, as indicated in Figure 7, the Viking Lander can be ranged about 50% of the days that Galileo is in flight. Table II presents the 43 different occasions. Each baseline can range the Lander for 8 to 12 days repetitively.

Each baseline's performance is not only time dependent, but is also governed by the alignment of the baseline with respect to the Galileo-Mars angular separation at encounter (Eq 1). In essence, the Viking and the Galileo $\Delta\rho$ measurements provide information as to the direction of each spacecraft with respect to the baseline but only in the direction of the baseline. Orthogonal to the baseline there is no information. And, of course, when $\Delta\rho$ measurements are differenced to obtain $\Delta^2\rho$, $\Delta^2\rho$ defines the earth centered angular separation between the two spacecraft only in the baseline direction. Figure 8 shows the baseline orientations relative to the Mars-Galileo direction at encounter. The DSS43 - DSS63 baseline which is approximately 4° offset, yields the strongest information concerning the flyby distance while the DSS63 - DSS14 ($\sim$12° offset) and the DSS14 - DSS43 ($\sim$60° offset) baselines provide progressively less information.

Table III itemizes the theoretical error assessments of $\Delta^2\rho$ resulting from instrumentation and transmission media.* From Table III it is apparent

*Philip Callahan, Jet Propulsion Laboratory, private communication

that it is thermal noise [galactic background (6°K), receiver front end electronics (6°-11° K), antenna cable (3° K), transmission media (10° K), etc.] when subjected to high gain that dominates the $\Delta^2\rho$ error budget. A full 90% of the $\Delta^2\rho$ RSS noise is from this source. The result is that $\Delta^2\rho$ should have an RMS error of $\sim$2 m and 2m is the a priori standard diviation used in covariance study. Most of the systematic errors due to solar plasma, troposphere, ionosphere, DSS clock errors, spacecraft and station delays cancel. In addition, since tracking stations are used redundantly to track both Galileo and Viking, DSS longitude errors tend to cancel in the formation of $\Delta^2\rho$ (Fig. 9). DSS uncertainties in the other two coordinates are of little consequence since their effect upon $\Delta^2\rho$ is from one to two orders of magnitude smaller yet.

III. THE GALILEO-MARS FLYBY DISTANCE COVARIANCE STUDY

The covariance analysis performed in this paper allows a maximum likelihood estimated with gaussian errors on the observations. The assumed observations include two-way coherent Doppler data from the Galileo spacecraft using the three Deep Space Network stations continuously, one Doppler measurement every one hour, one range measurement from the Goldstone station every day and the available doubly differenced range measurements as shown in the Table II. Since the dynamic state parameters are non-linear functions of the measurements, the observation equations are linearized and the results obtained are based on a linear estimator. When a standard maximum likelihood estimator is constructed, the computed statistics based on data noise errors, do not reflect the effect of model errors in the solution. Thus the statistics must be adjusted to

account for these effects.

The measurement equation can be written in the form

$$\bar{Z} = A\bar{x} + C\bar{p} + \bar{e}$$

where $\bar{Z}$ is the vector of measurements, $\bar{x}$ the vector of estimated parameters, $\bar{p}$ the vector of model parameters whose effects on the estimated parameters are to be investigated and $\bar{e}$ the measurement errors. A weighted least squares estimator of $\hat{\bar{x}}$ can be obtained by (Bryson and Ho, 1969)

$$\hat{\bar{x}} = \left(A^{R}P^{-1}A\right)^{-1} \quad A^{T}P^{-1}\bar{z}$$

with the assumption that $\bar{p}$ is a random vector of zero mean with covariance P_c, $E(\bar{e}) = o$, $Cov\ (\bar{e}) = P$ and $E\left(\bar{p}\bar{e}^{T}\right) = 0$ and the covariance of $\hat{\bar{x}}$ is given by

$$P_x^{\ c} = Cov\left(\hat{\bar{x}}\right) = P_x + P_x\ A^{T}P^{-1}CP_cC^{T}P^{-1}AP_x$$

where $P_x = \left(A^{T}P^{-1}A\right)^{-1}$ is the voir covariance matrix. The matrix $P_x^{\ c}$ is known as the 'consider' covariance matrix and the matrix A and C are the partial derivatives of the measurements with respect to the estimated and the consider parameters. Both the Galileo orbital state and Mars ephemeris parameters are treated as estimated parameters, and the station locations, Viking lander locations and Mars mass are treated as 'considered' parameters. The apriori uncertainties of the parameters are given in Table IV.

In the model used to assess $\Delta^2\rho$, the trajectory parameters of the Galileo probe was estimated in a manner that considered the uncertainties associated with the Mars Ephemeris, the DSS location set, the mass of Mars, the Viking Lander position (Table IV).

With this parameter set and the Galileo data set (Table V), the Galileo

heliocentric position can be estimated to 35 km (σ), Figure 10, and this uncertainty stems principally from DSS location uncertainties. The Galileo trajectory does not sense the gravitational effect of Mars until the last day before encounter. Galileo travels over a million kilometers on that last day.

Figure 10, the 'Standard Deviation of Galileo Heliocentric Position', shows σ_ρ in kilometers as a function of time in days from Mars encounter or when each simulated Galileo data arc stops. All estimates of σ_ρ involve data that starts 88 days before Mars encounter. Each estimate, following the $E\text{-}85^d$ estimate, has an additional five days of data added to the solution. All of the standard deviation plots presented have this same format.

Galileo, Mars-centered, position estimates have a standard deviation equal to the RSS of Galileo's heliocentric position sigma and the Mars ephemeris position standard deviation (Fig. 11a).

Figure 11 not only exhibits the standard deviation of the Galileo flyby but shows the components of σ_d related to the Mars Ephemeris $(\sigma_d \mid \text{Mars Ephemeris})$, the DSS locations $(\sigma_d \mid \text{DSS Locations})$ and data noise $(\sigma_d \mid \text{data noise})$.

Since Galileo is over a million kilometers away from Mars at $E\text{-}1^d$, Galileo does not see Mars gravitationally until $E\text{-}2^h$ and any effort to utilize Galileo tracking data to improve the Mars ephemeris fails. Hence, the ephemeris provides a near constant 40 plus kilometer component to σ_d(RSS).

As indicated in Figure 11, $\sigma_d \mid \text{DSS Locations}$ increases as the earth-probe distance increases. That is, DSS angular location uncertainty in an Euclidian solar system results in larger and larger spacecraft linear position uncertainty with increased topocentric range. However, if DSS coordinates were estimated,

instead of considered, this procedural artifact would disappear as in Fig. 2.

And lastly, in Figure 11, the data noise is shown to fall off with the square-root of the number of observations.

When these $\Delta^2\rho$ observations of Table II are added to the conventional Galileo data of Table V, the effects of the Mars ephemeris and the DSS location uncertainties are reduced. This should be expected since the RSS of the partials of the Mars position coordinates (Fig. 7) and the DSS coordinates (Fig. 9) with respect to $\Delta^2\rho$ are 2 to 10 times smaller than those with respect to $\Delta\rho$. That is, each $\Delta^2\rho$ observation is less sensitive to these error sources, but $\Delta^2\rho$ and $\Delta\rho$ possess the same sensitivity to the Galileo-Mars relative state. Figure 12 exhibits the ephemeris, DSS, and data noise contributions to σ_d. The data ensemble of $\Delta^2\rho$, conventional range and Doppler yields a $\sigma_d < 10$ km (σ) 25 days before Mars encounter. This is an improvement over conventional data reductions of four-fold. As can be seen in Figure 12, the correlated ephemeris and DSS locations uncertainties in each ρ observation cancel in the formation of $\Delta^2\rho$. As modeled, Mars ephemeris and DSS location uncertainties still dominate the standard deviation of the Galileo-Mars encounter distance estimate, however, their combined RSS contribution is less than 10 km (σ).

Summary

This covariance study shows that Galileo-Mars navigation is improved four-fold when dual station range from both Galileo and Viking are added to conventional Galileo tracking data and reduced. In essence, the Mars ephemeris and the tracking station uncertainties are differenced out of the new doubly differenced range data type, to a large extent, while little Galileo-Mars relative state information is lost. The information content of doubly differenced range is analogous to that of wideband very long baseline interferometry and promises to be an efficient backup the Galileo Project planned VLBI. Doubly differenced range coupled with conventional tracking data can be used to estimate Galileo-Mars flyby distance to better than 10 km (σ).

Reference

Project Galileo Navigation Requirements, PD 625-565, JPL 19 April 1979, JPL Internal Document.

TABLE I: Tracking Station Spherical Coordinates

DSS	Longitude	Latitude
43	149°0	35°3
63	355.8	-35.3
14	243.1	40.3

TABLE II: VIKING LANDER DIRECT LINK RANGING OPPORTUNITIES

for

GALILEO NAVIGATION, 1984

POINT	DSS BASELINE	DATE
1	63-14	22 March 84
2	"	23 March 84
3	"	24 March 84
4	"	25 March 84
5	63-14	26 March 84
6	14-43	29 March 84
7	"	30 March 84
8	"	31 March 84
9	"	1 April 84
10	"	2 April 84
11	"	3 April 84
12	"	5 April 84
13	14-43	6 April 84
14	43-63	14 April 84
15	"	15 April 84
16	"	16 April 84
17	"	17 April 84
18	43-63	18 April 84
19	63-14	25 April 84
20	"	26 April 84
21	"	27 April 84
22	"	29 April 84
23	"	30 April 84
24	63-14	1 May 84

POINT	DSS BASELINE	DATE
25	14-43	4 May 84
26	"	6 May 84
27	"	7 May 84
28	"	8 May 84
29	"	9 May 84
30	"	10 May 84
31	14-43	11 May 84
32	43-63	17 May 84
33	"	18 May 84
34	"	20 May 84
35	"	21 May 84
36	"	22 May 84
37	14-43	23 May 84
38	63-14	27 May 84
39	"	29 May 84
40	"	30 May 84
41	"	31 May 84
42	"	1 June 84
43	63-14	2 June 84

DSS 14 (Goldstone, California)
DSS 43 (Woomera, Australia)
DSS 63 (Madrid, Spain)

TABLE III: Doubly Differenced NSR Error Budget

INSTRUMENTATION:	
STATION CLOCK STABILITY (15 MIN)	4 CM
STATION DELAY CALIBRATION	--
SNR (THERMAL NOISE)	200 CM
WAVEFORM DISTORTION	88 CM
SPACECRAFT DELAY	28 CM
MEDIA:	
TROPOSPHERE (25° ELEVATION)	20 CM
IONOSPHERE (25° ELEVATION)	6 CM
SOLAR WIND	15 CM
RSS	222 CM

ASSUMPTIONS:

VIKING LANDER - GALILEO SEPARATION ~ 5°

DATA AT OPPOSITION ~ 0.7 AU

TWO STATIONS OBSERVE LANDER IN TURN APPROX. 15 MIN EACH

SAME TWO STATIONS OBSERVE GALILEO IN TURN APPROX. 15 MIN EACH

TABLE IV: Galileo-Viking Parameter Set

PARAMETERS	MODEL STATUS	A PRIORI
Galileo State	Estimated	$\sigma_x = \sigma_y = \sigma_z = 10^7$ km; $\sigma_{\dot{x}} = \sigma_{\dot{y}} = \sigma_{\dot{z}} = 100$ km/s
Mars State	Considered	$\sigma_{radial} = 10$ km; $\sigma_{in\ track} = 40$ km; $\sigma_{out\text{-}of\text{-}plane} = 70$ km
DSS Locations*	Considered	$\sigma_\lambda = 3.0$ m; $\sigma_{r_s} = 1.5$ m; $\sigma_{r_z} = 15.0$ m
Viking Lander Locations	Considered	$\sigma_x = 10.0$ m; $\sigma_y = 40.0$ m; $\sigma_z = 300.0$ m; $\sigma_x = \sigma_y = \sigma_z = 10^{-3}$ m/day
Mars GM	Considered	$\sigma = 0.1$ km^3/Sec^2

* r_s = DSS distance from terrestrial spin-axis

r_z = DSS distance from earth equator plane

TABLE V: Schedule for Conventional Data

DATA TYPE	(σ)	RATE	DSS ACQUIRING
Galileo Doppler	1 mm/s	1 pt/hr	14, 43, 63
Galileo Range	1 km	1 pt/pass	14
Start: 6 March 1984 ($E_{♂}$ - 88 days)		Stop: 2 June 1984 ($E_{♂}$ - 20 min)	

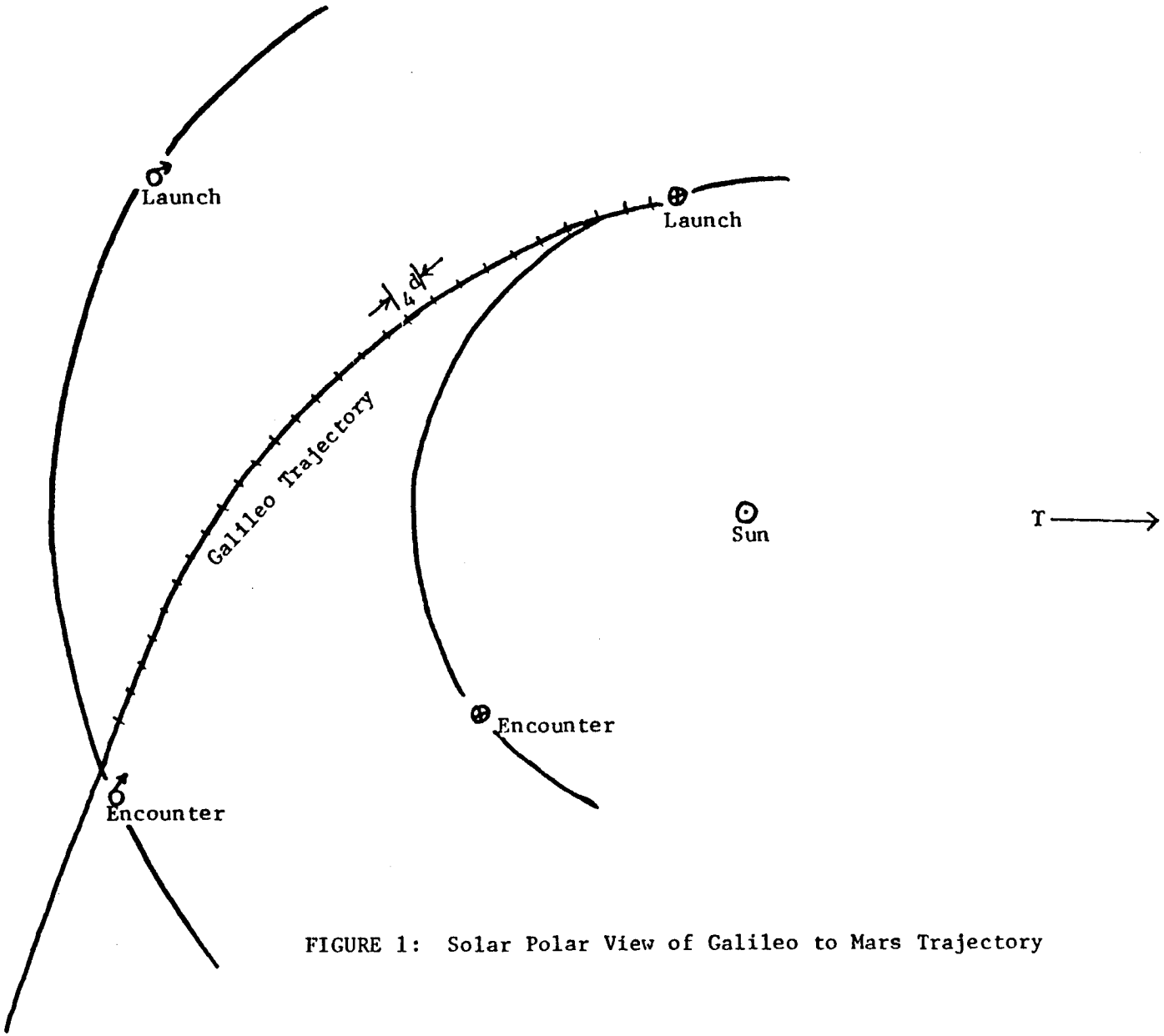

FIGURE 1: Solar Polar View of Galileo to Mars Trajectory

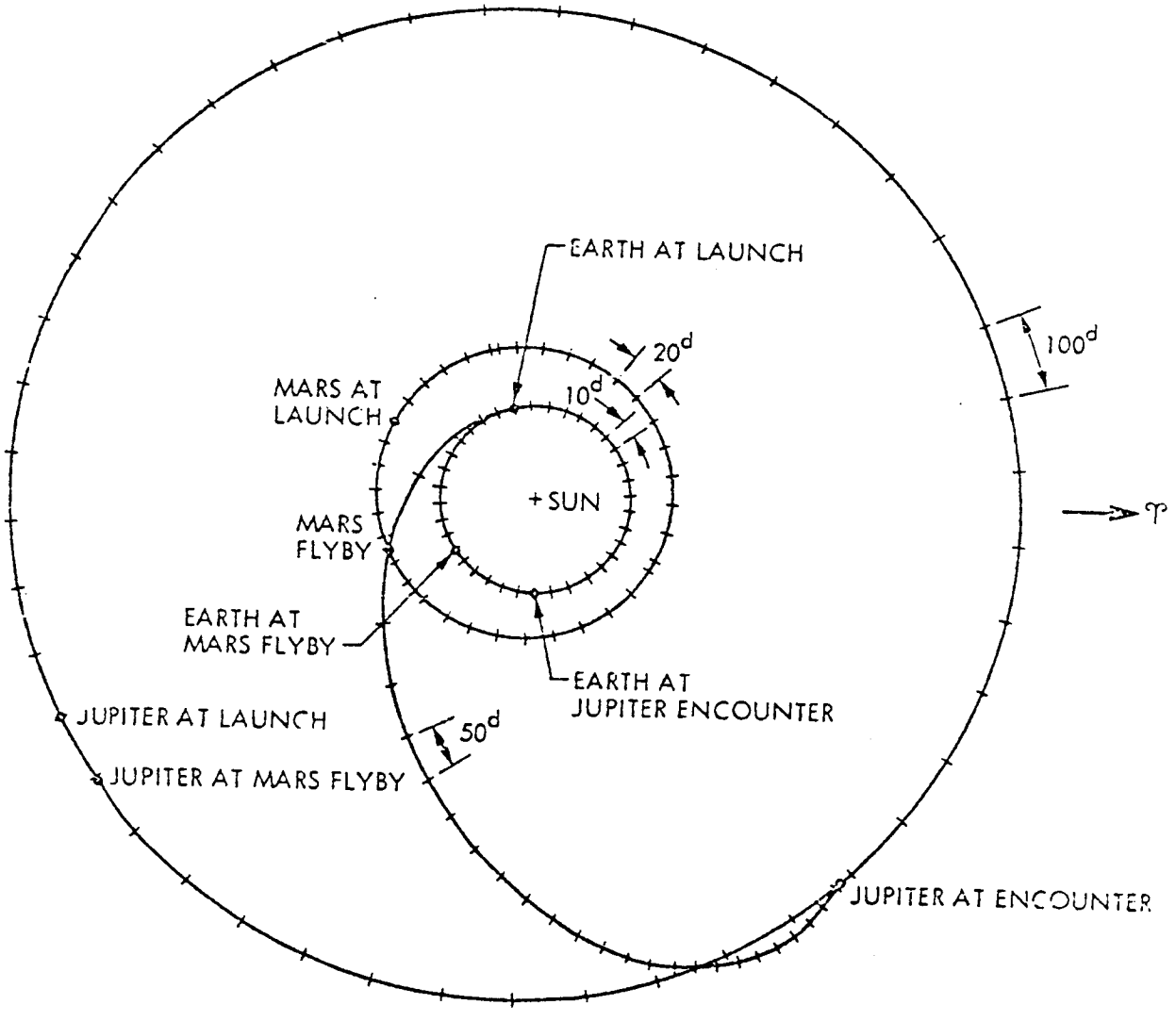

Figure 2 Heliocentric Ecliptic Pole View of Interplanetary Trajectory

FIGURE 3: ΔV and Flyby Distance Relationship

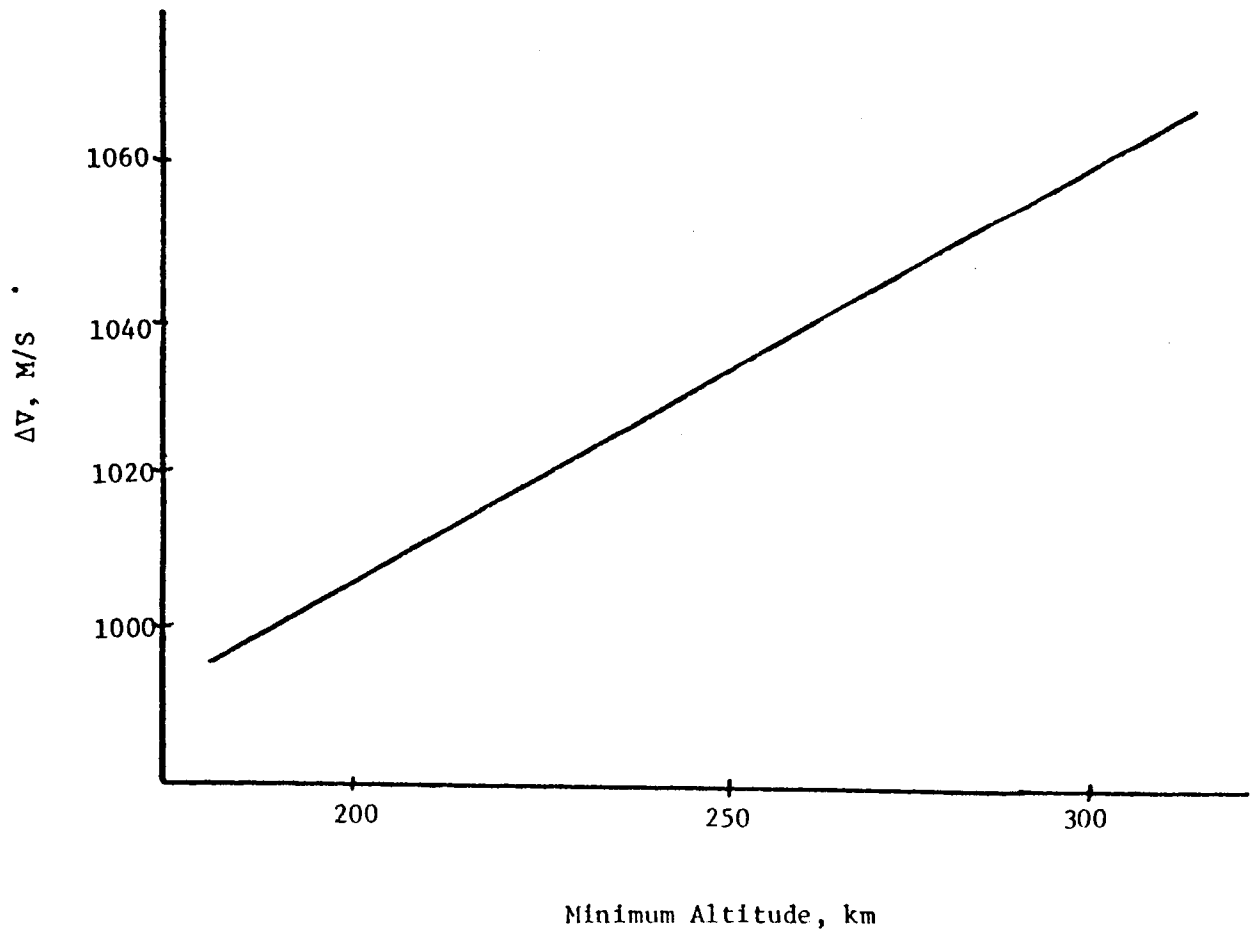

FIGURE 4: Uncertainty of Galileo-Mars Flyby Distance as a Function of Time-to-GO

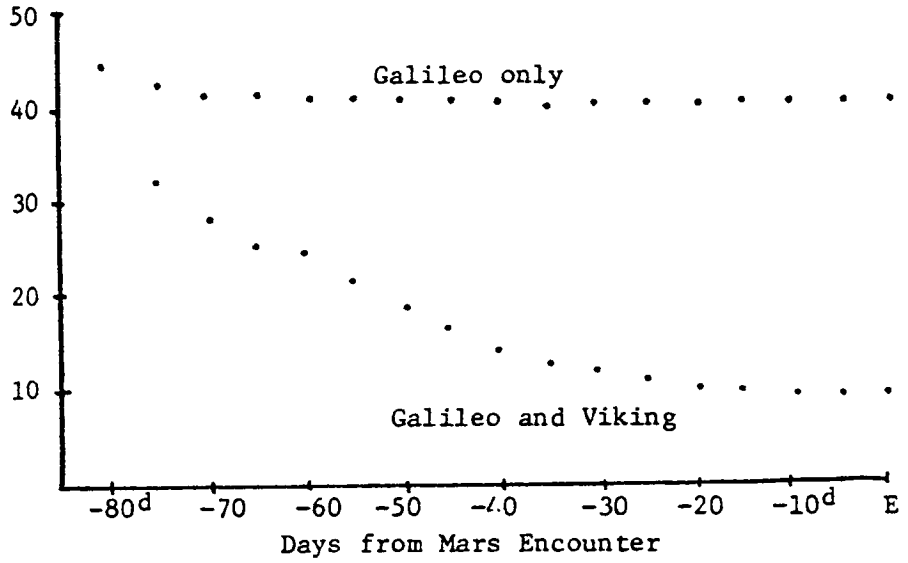

First data occurs at E-88^d and continues uniformly until Mars encounter. Estimates of flyby distance are obtained every 5^d after E-85^d until Encounter.

FIGURE 5: Range Components of Doubly Differenced Range

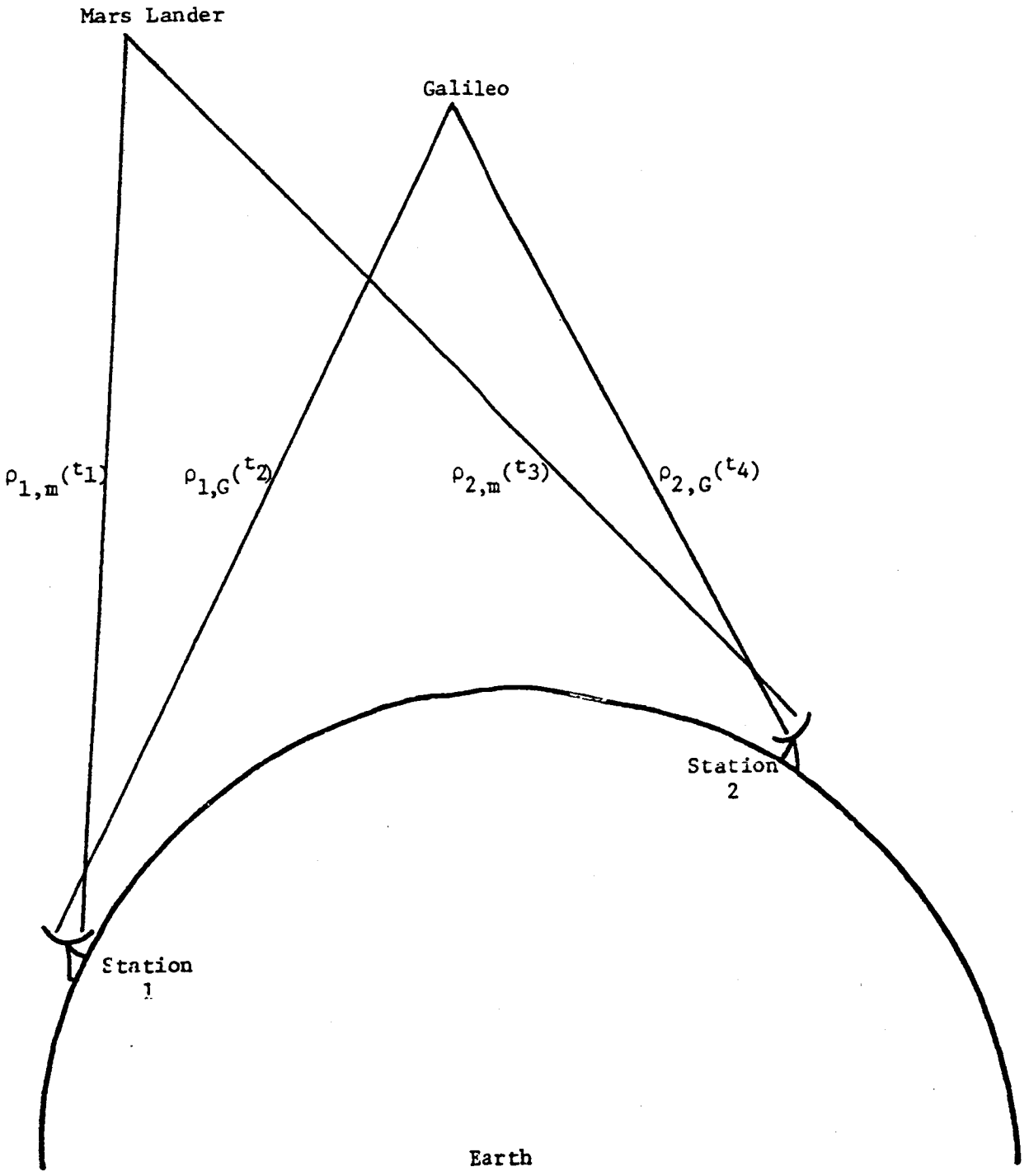

FIGURE 6: The Plane Geometry of Relative Range

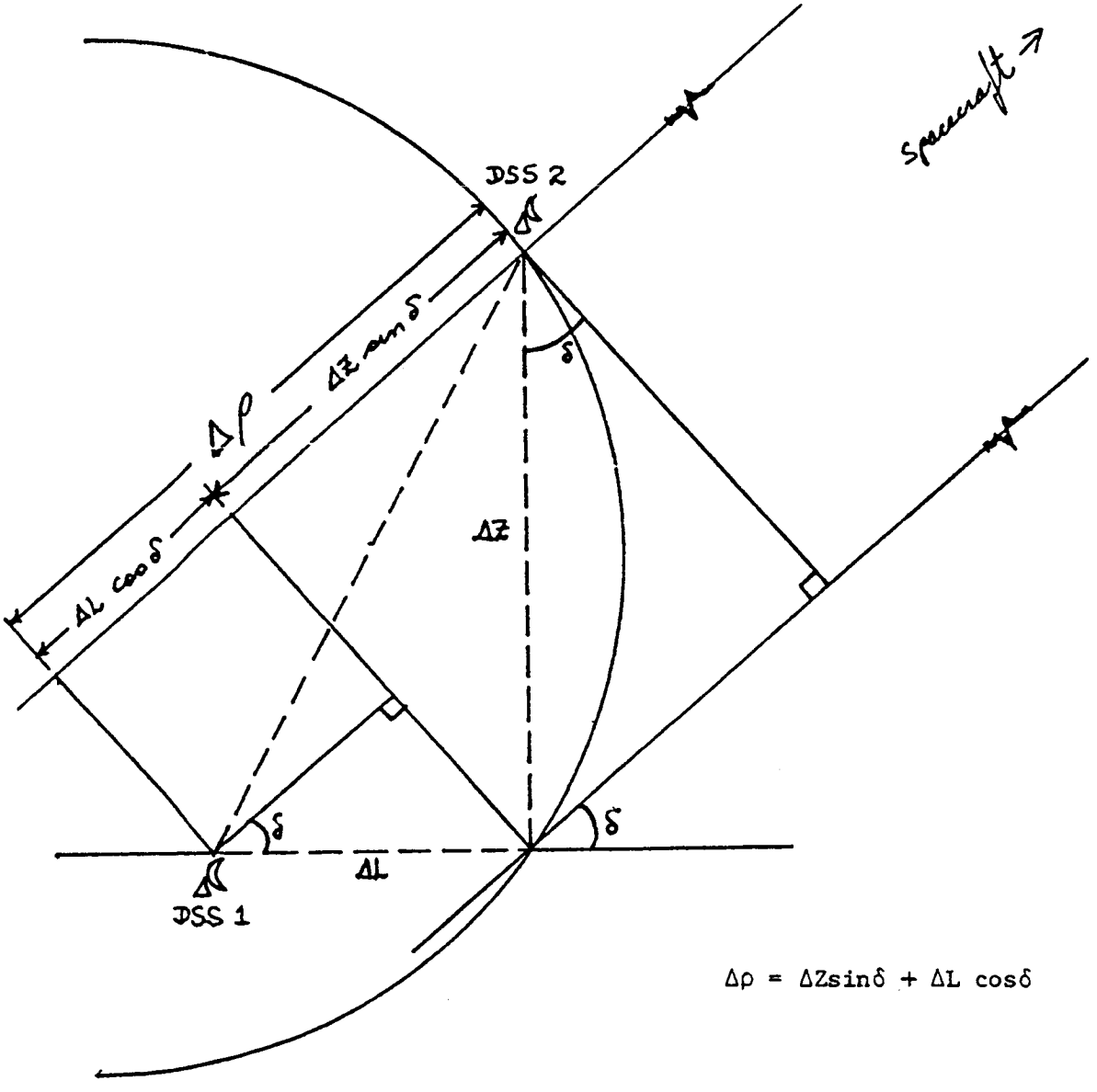

$$\Delta\rho = \Delta Z \sin\delta + \Delta L \cos\delta$$

DSS ≡ Deep Space Station of NASA's Deep Space Net

FIGURE 7: Sensitivity of $\Delta\rho$ and $\Delta^2\rho$ to Mars Position

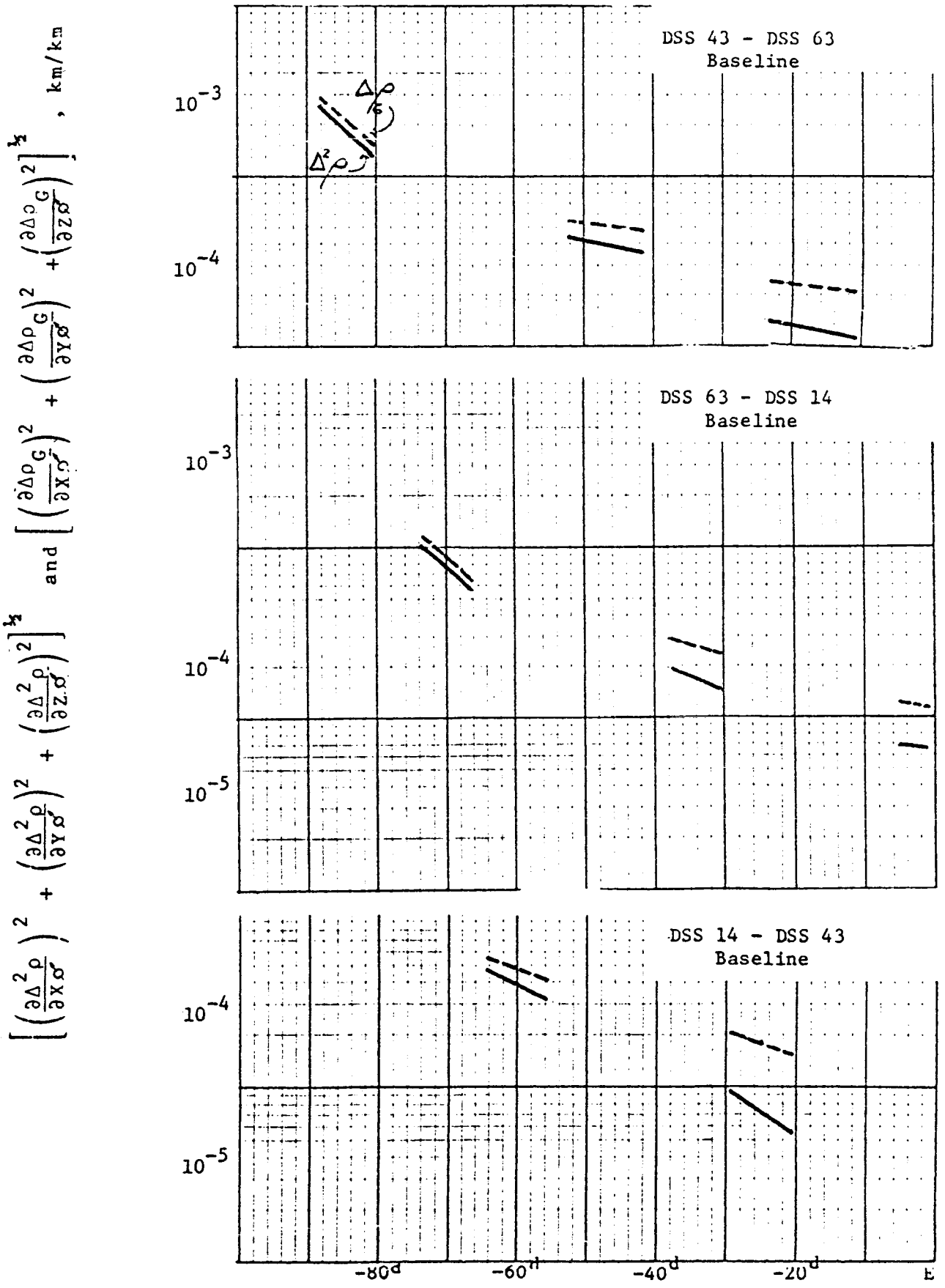

FIGURE 8: Relative Orientation of Baselines and Mars-Galileo Direction

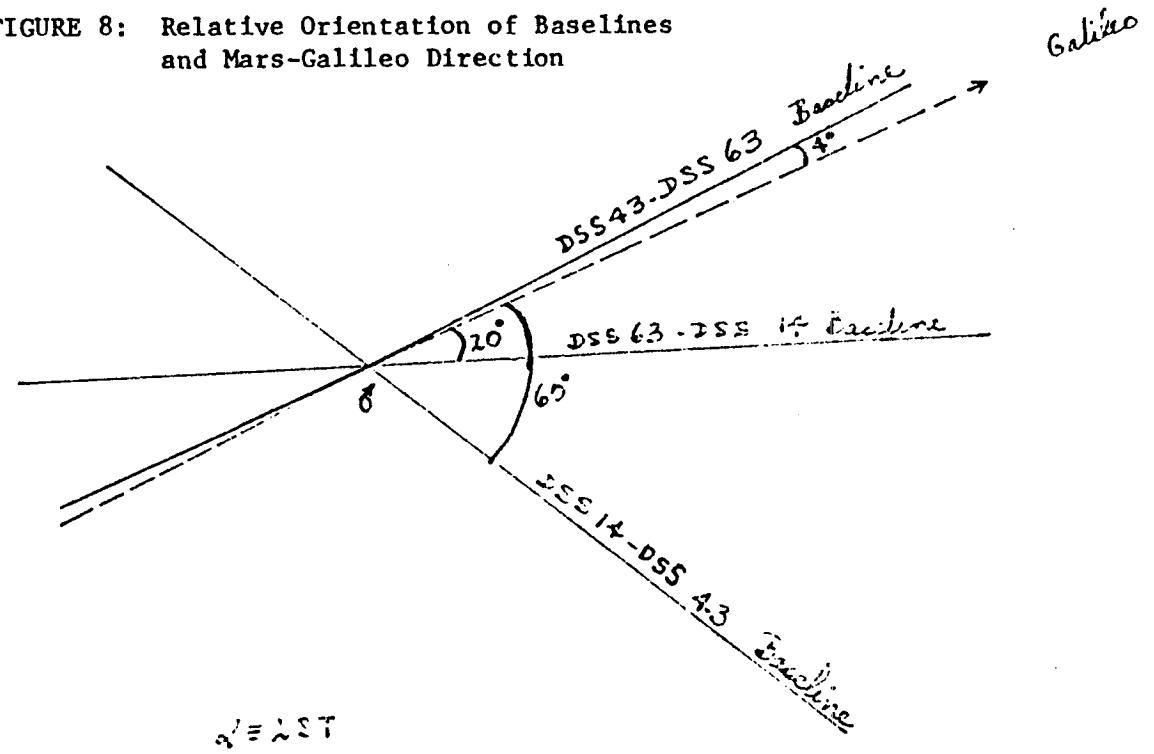

FIGURE 9: Sensitivity of $\Delta\rho$ and $\Delta^2\rho$ to DSS Locations

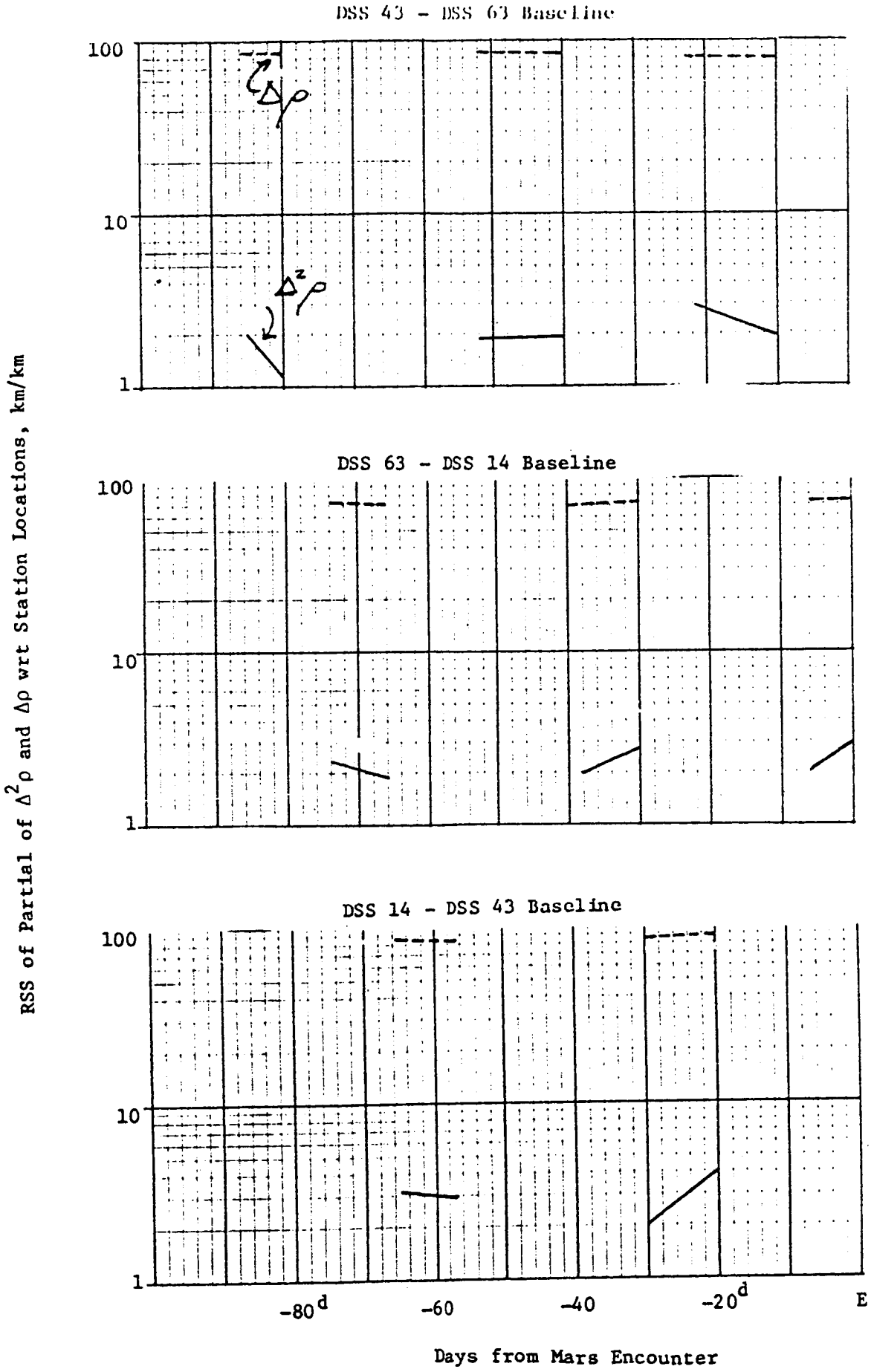

FIGURE 10: Standard Deviation of Galileo Heliocentric Position Estimates, σ_p

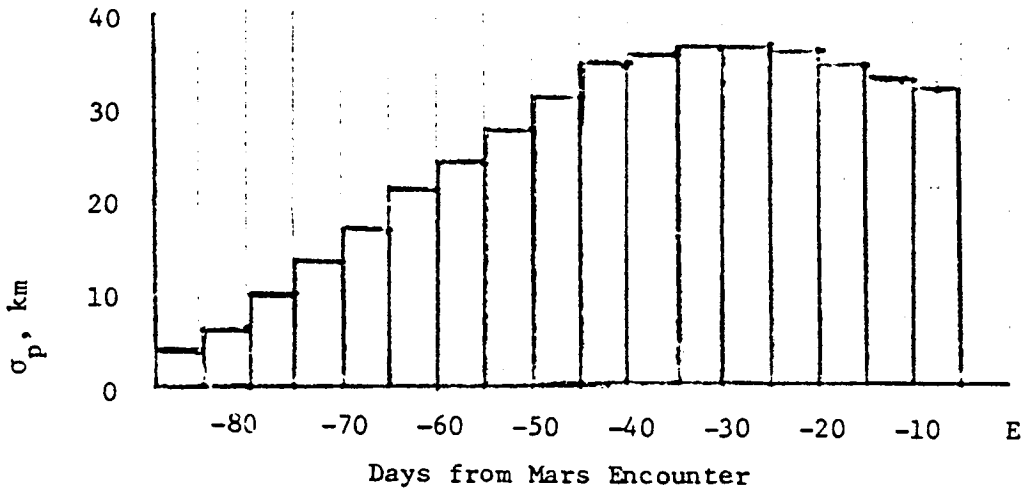

FIGURE 11: Standard Deviation of Galileo Flyby Distance From Mars
(Convention Galileo Tracking Data Only)

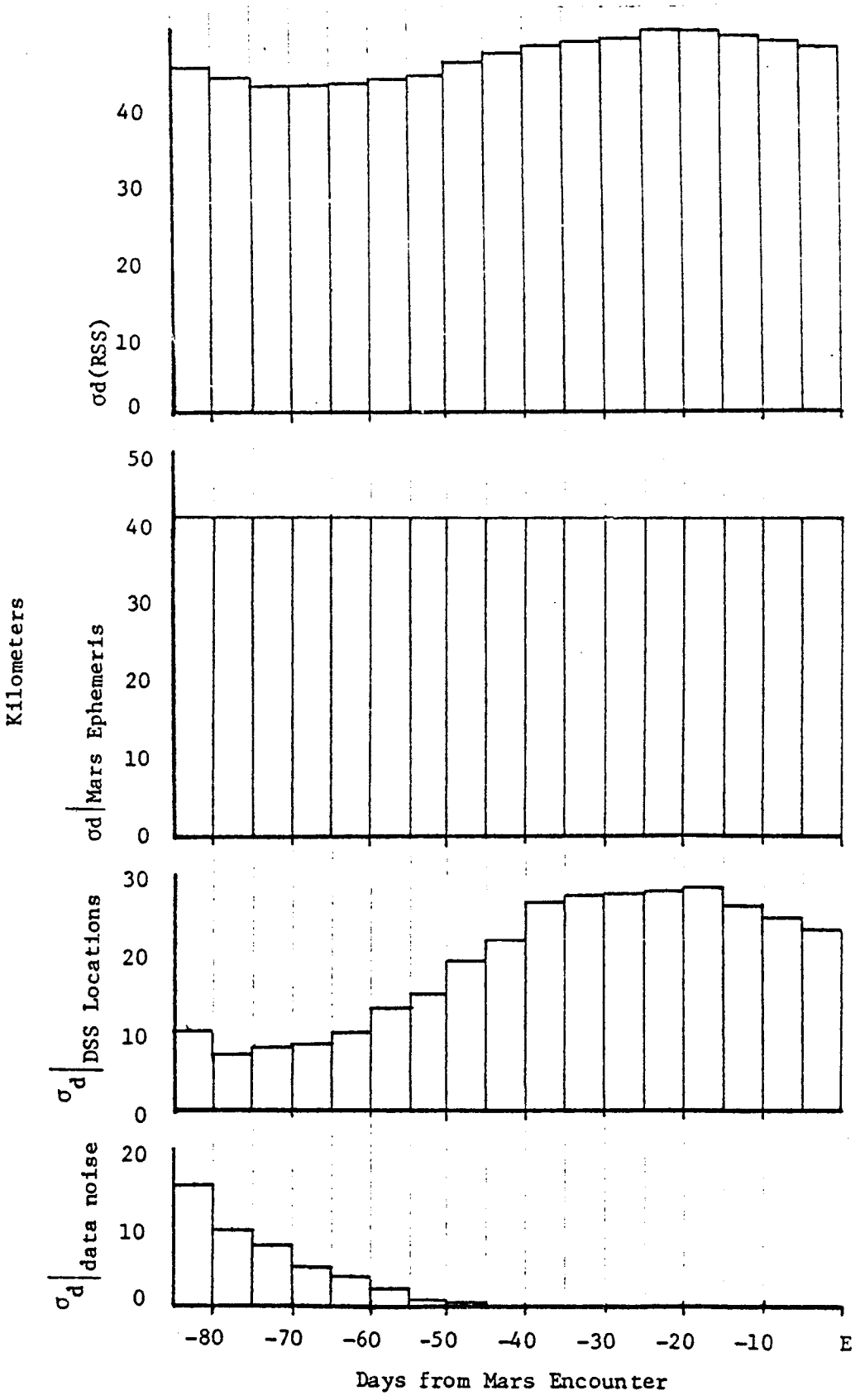

FIGURE 12: Standard Deviation of Galileo Flyby Distance from Mars (with Galileo-Viking $\Delta^2\rho$)

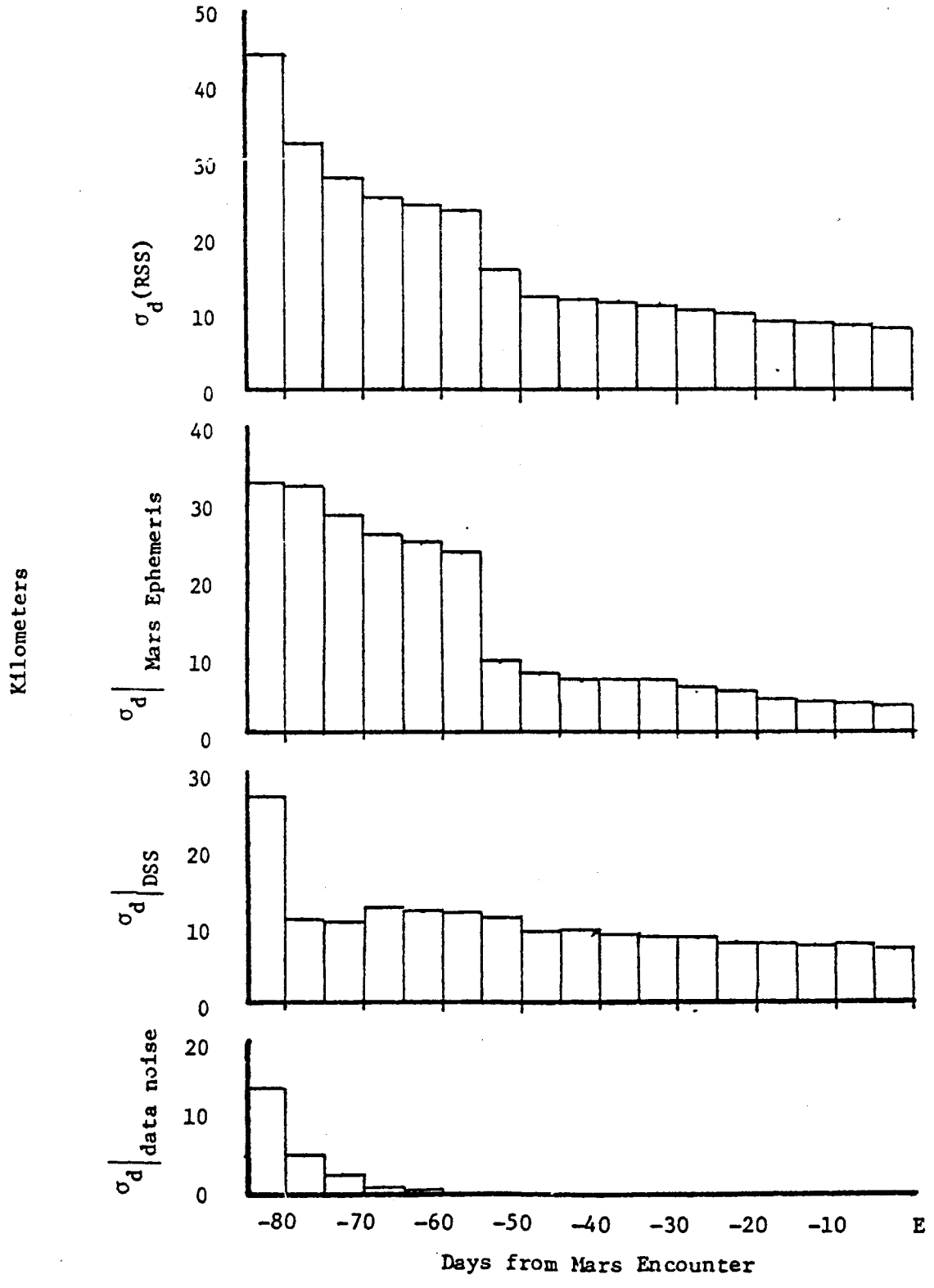

SESSION III

H. S. Heuberger, Chairman

An Analysis of GDOP in Global Positioning System Navigation

Bertrand T. Fang
Computer Sciences Corporation, Silver Spring, MD

ABSTRACT

The accuracy of user navigation fix based on the NAVSTAR Global Positioning System is described by a 4x4 position-time error covariance matrix. The "trace" of this matrix serves as a convenient navigation performance index and the square-root of the trace is called Geometric Dilution of Precision (GDOP). In this paper, certain theoretical results concerning the general properties of the navigation performance are derived. An efficient algorithm for the computation of GDOP is given. Applications of the results are illustrated by numerical examples.

An Analysis of GDOP in Global Positioning System Navigation

Bertrand T. Fang*
Computer Sciences Corporation, Silver Spring, MD

INTRODUCTION

The NAVSTAR Global Positioning System (GPS), when fully operational in the early 1990's, will provide world-wide navigation through synchronized transmissions from a constellation of eighteen 12-hour period satellites in three 55°-inclination orbital planes. An accurate user navigation fix (position and time) will be obtainable by receiving transmissions from four satellites and decoding the signal transit times.

One may relate the measurements, referred to as the pseudo-ranges, to the navigation state as follows

$$C T_j = \sqrt{(X_1 - x_1)^2 + (X_2 - x_2)^2 + (X_3 - x_3)^2} + X_4 + n_j \quad (1)$$

where
- C = velocity of light
- T_j = Signal transit time from GPS satellite "j" to user, not corrected for user clock offset, Δt
- X_1, X_2, X_3, X_4 = user naviagation state, the first three represent a set of convenient Cartesian user coordinates, $X_4 = C\Delta t$ is a range bias equivalent of user clock offset
- x_1, x_2, x_3 = corresponding Cartesian coordinates of GPS satellite "j"
- n_j = random measurement noise

---

*Senior Principal Engineer, Orbit Operations, System Sciences Division.

From a set of four measurements, a user navigation fix may be determined. The accuracy of the fix is characterized by the following 4x4 position-time navigation error covariance matrix

$$P = (H^T W H)^{-1} \tag{2}$$

where H = measurement parital derivative matrix = $\begin{bmatrix} a^T & \vdots & \vdots \\ \hline b^T & \vdots & \vdots \\ \hline c^T & \vdots & \vdots \\ \hline d^T & \vdots & \vdots \end{bmatrix}$ (3)

a, b, c and d = line-of-sight unit vectors from a set of four GPS satellites to the user, W = 4x4 covariance matrix of random measurement noise, superscript "T" = transpose of matrix.

The measurement error covariance matrix W is generally taken to be diagonal, which is strictly true for uncorrelated measurements only. In practice, assignments of quantitative values to the elements of W also takes into consideration such factors as the elevation and health status of individual GPS satellites. Thus W may be more appropriately be referred to as the weighting matrix. For uniform weighting, P is proportional to $(H^T H)^{-1}$, which depends only on the relative geometry of the user and the four GPS satellites, as is evident from Equation (3). The square-root of the "trace" of $(H^T H)^{-1}$ is referred to as Geometric Dilution of Precision (GDOP), a self-explanatory name. Whatever the weighting strategy, the "trace" of the navigation error covariance matrix serves as a covenient and natural performance index

characterizing the accuracy of the naviagation fix. For a diagonal weighting matrix W,

TRACE "P" = sum of diagonal terms of $(H^T H)^{-1}$ weighted by the inverses of the corresponding elements of W

Thus the evaluation of the GPS naviagation performance is essentially equivalent to the computation of the diagonal terms of $(H^T H)^{-1}$, which may be called the GDOP matrix for convenience.

The navigation performance index, Trace "P", also serves as a criterion for the selection of a set of four best GPS satellites among those visible, which may be as many as ten for users which are satellites themselves. If, for optimum performance, each of the different combinations of four has to be evaluated, the computational burden can be considerable. In the following, certain theoretical results concerning the general properties of the GDOP matrix are derived. An efficient algorithm for the computation of GDOP matrix and the navigation performance index is given. Applications of the results are illustrated by numerical examples.

ANALYTICAL RESULTS

To solve for a navigation fix from four measurements, the partial derivative matrix H must be non-singular. Since

$$\text{determinant } H = \begin{vmatrix} a^T - d^T & 0 \\ b^T - d^T & 0 \\ c^T - d^T & 0 \\ d^T & 1 \end{vmatrix} = \begin{vmatrix} a & -d \\ b & -d \\ c & -d \end{vmatrix}$$

a navigation fix can be determined from four GPS satellites with line-of-sight directions a, b, c, d, if and only if the three vectors (a-d), (B-d), and (c-d) are linearly independent, i.e., non-coplanar. This shall be assumed to be the case in the following development.

Since Trace $(H^TH)^{-1}$ = Trace $(HH^T)^{-1}$, by making use of Equation (3) and the fact that a, b, c, d, are unit vectors, one obtains,

$$\text{Trace } (H^TH)^{-1} = \text{Trace } (HH^T)^{-1}$$

$$= \text{Trace} \begin{bmatrix} 2 & a^Tb+1 & a^Tc+1 & a^Td+1 \\ & 2 & b^Tc+1 & b^Td+1 \\ & & 2 & c^Td+1 \\ \text{(symmetric)} & & & 2 \end{bmatrix}^{-1} \qquad (4)$$

The advantages of dealing with HH^T instead of H^TH will become obvious below.

The following may be observed from Equation (4):

1. The matrix HH^T in Equation (4) is non-negative, symmetric, and with identical diagonal terms which are greater than the off-diagonal terms. (Expressions such as a^Tb are scalar product of unit vectors and are less than unity). These properties give rise to good behaviour in numerical operations.

2. Since the Trace of a matrix is equal to the sum of its eigenvalues and the eigenvalues of the matrix inverse are inverses of the eigenvalues of the matrix itself, one has the following results:

a. Trace $(HH^T)^{-1} = \frac{1}{\lambda_1} + \frac{1}{\lambda_2} + \frac{1}{\lambda_3} + \frac{1}{\lambda_4}$, where the λ's are eigenvalues of (HH^T) with

$$\lambda_1+\lambda_2+\lambda_3+\lambda_4 = 8.$$

b. From "a" above and the fact that the λ's are non-negative, one may conclude that

$$\text{Trace } (HH^T)^{-1} \geq 2 \qquad (5).$$

c. Let us order the eigenvalues of HH^T as

$$0 < \lambda_1 \leq \lambda_2 \leq \lambda_3 \leq \lambda_4 < 8.$$

One has the obvious inequality

$$\text{Trace } (HH^T)^{-1} = \frac{1}{\lambda_1} + \left(\frac{1}{\lambda_2} + \frac{1}{\lambda_3} + \frac{1}{\lambda_4}\right)$$

$$> \frac{1}{\lambda_1} + \underset{\lambda_2+\lambda_3+\lambda_4<8}{\text{lower bound}} \left(\frac{1}{\lambda_2} + \frac{1}{\lambda_3} + \frac{1}{\lambda_4}\right),$$

or,

$$\text{Trace } (HH^T)^{-1} > \frac{1}{\lambda_1} + \frac{9}{8} \qquad (6)$$

Thus knowledge of the smallest eigenvalue of HH^T provides another lower bound for the navigation performence index. Sometimes this lower bound also serves as a good estimate.

d. The 2x2 principal submatrix of HH^T, e.g. $\begin{bmatrix} 2 & a^Tb+1 \\ a^Tb+1 & 2 \end{bmatrix}$ has eigenvalues $3+a^Tb$ and $1-a^Tb$. From the Theorem of Root Separation for Symmetric Matrices[1] one obtains the following bounds on the eigenvalues of HH^T

$$\lambda_1 \leq 1-a^Tb \leq \lambda_3 \tag{7}$$

$$\lambda_2 \leq 3 + a^Tb \leq \lambda_4 \tag{8}$$

These inequalities have no preferences for the labeling of the unit vectors. That is, a, b may be replaced by c, d, etc., to obtain sharper bounds. In particular, one must have $\lambda_1 < 2$ and $\lambda_4 > 2$. Therefore, the eigenvalues of HH^T cannot be all identical and the equality sign in (5) may be deleted. Physically, this follow from the fact that the four unit vectors in three-dimensional space cannot play identical roles in the four-dimensional position-time space. Combining inequalities (6) and (7), one obtains another inequality.

$$\text{Trace } (HH^T)^{-1} > \frac{9}{8} + \frac{1}{1-\cos\theta} \tag{9}$$

where θ = smallest angle subtended by two line-of-sight vectors.

This inequality, although not sharper than Inequality (8), is easier to calculate, and expresses the intuitive rule of thumb that an accurate navigation should not rely on a GPS constellation that is clustered together. We shall see later that with good geometry, navigation performance index of magnitude less than 3 may be obtained. On the other hand, as indicated by Inequality (9), a navigation performance index in excess of 8.5 would result if any two line-of-sight vectors to GPS satellites are separated by 30° or less.

An upper bound for the navigation performance index may be obtained as

$$\text{Trace}\,(HH^T)^{-1} < \frac{3}{\lambda_1} + \frac{1}{2} \tag{10}$$

by noting $\lambda_1 \leq \lambda_2 \leq \lambda_3$ and $\lambda_4 > 2$.

It may also be pointed out that because the determinant of a matrix product is equal to the product of the individual determinants, and that the determinant of a matrix is equal to the product of its eigenvalues, one has the relation

$$\lambda_1 \lambda_2 \lambda_3 \lambda_4 = (\text{determinant } H)^2 = \begin{vmatrix} a-d \\ b-d \\ c-d \end{vmatrix}^2 .$$

The maximization of $\begin{vmatrix} a-d \\ b-d \\ c-d \end{vmatrix}$ has been suggested as a convenient GPS selection criterion[3]. It is seen from the above equation that this criterion is equivalent to a maximization of the denominator of our performance index,

$$\text{Trace}\,(HH^T)^{-1} = \frac{1}{\lambda_1} + \frac{1}{\lambda_2} + \frac{1}{\lambda_3} + \frac{1}{\lambda_4}$$

$$= \frac{\lambda_1\lambda_2\lambda_3 + \lambda_1\lambda_2\lambda_4 + \lambda_2\lambda_3\lambda_4 + \lambda_1\lambda_3\lambda_4}{\lambda_1\lambda_2\lambda_3\lambda_4}.$$

ALGORITHM

An efficient algorithm for the computation of the GDOP matrix may be obtained by noting the following decomposition of the measurement partial derivative matrix:

$$H = \left[\begin{array}{c|c} a^T & 1 \\ \hline b^T & 1 \\ \hline c^T & 1 \\ \hline d^T & 1 \end{array}\right] = \left[\begin{array}{c|c} a^T & 1 \\ b^T & 1 \\ c^T & 1 \\ \hline 0 & 1 \end{array}\right] + \begin{bmatrix} 0 \\ 0 \\ 0 \\ 1 \end{bmatrix} \left[\begin{array}{c|c} d^T & 0 \end{array}\right]$$

$$\triangleq A + BD^T$$

From this decomposition, the Sherman-Morrison Formula[2] gives us

$$H^{-1} = A^{-1} - (A^{-1}B)(D^TA^{-1}) / (1 + D^TA^{-1}B) \qquad (11).$$

Let $$(f \mid g \mid h) \triangleq \left([a \mid b \mid c]^{-1}\right)^T \qquad (12).$$

Then one has, by straight-forward simple algebra,

$$A^{-1} = \left[\begin{array}{c|c|c|c} f & g & h & -q \\ \hline 0 & 0 & 0 & 1 \end{array}\right]$$

and

$$H^{-1} = \frac{1}{\alpha}\left[\begin{array}{c|c|c|c} \alpha f + (d^T f) q & \alpha g + (d^T g) q & \alpha h + (d^T h) q & -q \\ \hline -d^T f & -d^T g & -d^T h & 1 \end{array}\right] \tag{13}$$

where $q \triangleq f + g + h$

$\alpha \triangleq 1 - d^T q.$

When H^{-1} is obtained, one may obtain the GDOP matrix as $(HH^T)^{-1} = (H^{-1})^T (H^{-1})$. In particular,

Trace $(HH^T)^{-1}$ = sum of the squares of the elements of H^{-1}

$$= f^T f + g^T g + h^T h + \frac{2}{\alpha}\left\{ (d^T f) q^T f + (d^T g) q^T g + (d^T h) q^T h \right\}$$

$$+ \frac{q^T q + 1}{\alpha^2}\left\{ 1 + (d^T f)^2 + (d^T g)^2 + (d^T h)^2 \right\} \tag{14}$$

Equations (11), (13) and (14) constitute the algorithm. It reduces the inversion of the 4x4 matrix HH^T to the inversion of a 3x3 matrix (a | b | c) plus the scalar products of several 3x1 vectors. Notice that Eq. (13) may also be obtained from inverting H by partitioning[2]. But the Sherman-Morrison Formula provides additional flexibility as will be discussed below.

An important advantage of this algorithm is that very little recomputation is required when the fourth GPS satellite is switched. In selecting the best set of four GPS satellites from the many possible combinations, a simple combinatorial test logic may be advantageous. For this purpose, one may need the flexibility of changing any one of the rows of H. Although Eq. (14) remains valid provided one interprets the vectors f, g, and h accordingly, this does mean these vectors have to be recomputed. In that case it is preferable to use Eq. (11) directly instead of Eq. (14). To illustrate let us assume that for a particular GPS configuration, $H^{-1}=G$ is already obtained. If the nth (n = 1, 2, 3, 4) GPS Satellite with line of sight vector r is to be replaced by another satellite with line-of-sight vector p, the new measurement partial derivative matrix may be written as

$$H' = H + \begin{bmatrix} \delta_{1n} \\ \delta_{2n} \\ \delta_{3n} \\ \delta_{4n} \end{bmatrix} \left[(p-r)^T \;\vdots\; 0 \right]$$

where δ_{in} is the Kronecker delta ($\delta_{in}=0$ for $i \neq n$ $\delta_{in}=1$ for $i = n$).

From the above decomposition the Sherman-Morrison Formula gives us

$$H'^{-1} = G - \frac{\begin{bmatrix} G_{1n} \\ G_{2n} \\ G_{3n} \\ G_{4n} \end{bmatrix} \left([p-r]^T \begin{bmatrix} G_{11} & G_{12} & G_{13} & G_{14} \\ G_{21} & G_{22} & G_{23} & G_{24} \\ G_{31} & G_{32} & G_{33} & G_{34} \end{bmatrix} \right)}{1 + [p-r]^T \begin{bmatrix} G_{1n} \\ G_{2n} \\ G_{3n} \end{bmatrix}} \tag{15}$$

The computational economy provided by this equation is obvious.

APPLICATIONS

Intuitively, orthogonal line-of-sight user-to-GPS satellite configurations are favorable. In three-dimensional space, it is, of course, impossible to have a set of four mutually orthogonal unit vectors. An alternative has three of the line-of-sight vectors a, b, c orthogonal. For this case the vectors f, g and h become the same orthogonal unit vectors as a, b, c and Eq. (14) simplifies to

$$\begin{aligned} \mathrm{Trace}\,(HH^T)^{-1} &= 3 + 2(d_1+d_2+d_3)/\alpha + 4(1+d_1^2+d_2^2+d_3^2)/\alpha^2 \\ &= 1 + \{8+2(1-d_1-d_2-d_3)\}/(1-d_1-d_2-d_3)^2 \end{aligned}$$

where d_1, d_2, d_3 with $d_1^2+d_2^2+d_3^2 = 1$ are components of the line-of-sight unit vector d along the orthogonal a, b, c directions. It is of interest to note that for this case the Navigation Peformance Index depends only on $(d_1+d_2+d_3)$, the simplest symmetric function of the components of the vector d. The best performance index of 2.80 is achieved for $d^T = (-1,-1,-1)/\sqrt{3}$. This is the situation that the line of sight to GPS satellite "d" shows no preference to, but is directed away from the other GPS satellites, an artificial but not improbable configuration for an user satellite. For $d^T = (1,1,1)/\sqrt{3}$, i.e., d having the same general direction as the other three lines-of-sight, the performance index degrades to 13.20. This degradation reminds us of the statement made earlier about avoiding closely-grouped GPS satellites. For d = -a, i.e. for an user located between two GPS satellites, the performance index has the value 4.00.

There is reason to think that a GPS constellation with a-d, b-d, c-d orthogonal may give good navigation performance.

This may be realized with the set of line-of-sight vectors $a^T = (-1, 1, 1)\sqrt{3}$, $b^T = (1, -1, 1)/\sqrt{3}$, $c^T = (1, 1, -1)/\sqrt{3}$ and $d^T = (1, 1, 1)/\sqrt{3}$. However, for this configuration, the angle between the vector d and any other vector is $\cos^{-1}(2/3)$, which is comparatively small, and may be undesirable from the consideration of the preceeding section. Indeed, it follows immediately from Inequality (10) that the navigation performance index must be in excess of $9/8 + 1/(1 - 2/3) = 4\frac{1}{8}$, a lower bound which may be compared with the exact index of 5.5 obtainable from straightforward simple computation. On the other hand, by reversing the direction of the vector d given above, one has the completely symmetrical configuration that the line-of-sight vectors are all separated by the same angle $\cos^{-1}(-1/3)$. For this configuration one may compute the eigenvalues of HH^T as $\lambda_1 = \lambda_2 = \lambda_3 = 4/3$ and $\lambda_4 = 4$, giving rise to a navigation performance index

$$\text{Trace } (HH^T)^{-1} = \frac{3}{4} + \frac{3}{4} + \frac{3}{4} + \frac{1}{4} = 2.5.$$

Notice that for this configuration,

1. The upper bound for λ_1 given in Inequality (7) is achieved.

2. Any perturbation of the configuration will result in a decrease in the minimum angle between two line-of-sight vectors, and therefore a decrease in λ_1.

Thus this configuration maximizes the smallest eigenvalue of HH^T, or equivalently, minimizes the largest eigenvalue of $(HH^T)^{-1}$. Whether this also happens to be the best configuration remains to be investigated.

ACKNOWLEDGEMENT

This work was sponsored by NASA Goddard Space Flight Center under Contract No. NAS 5-24300. The author is in debt to Dr. Dale Headrick of Computer Sciences Corporation for pointing out the completely symmetrical configuration described above.

REFERENCES

1. Pearson, C. E., ed., "Handbook of Applied Mathematics," 1st Ed., Van Nostrand, New York, 1974, p. 926.
2. Householder, A. S., "Principles of Numerical Analysis," McGraw-Hill, New York, 1953, pp. 78-79.
3. Bogen, A. H., "Geometric Performance of the Global Positioning System," Aerospace Corporation, El Sengundo, CA, SAMSO-TR-74-169, June 1974.

A QUADRILATERALIZED SPHERICAL CUBE EARTH DATA BASE

F. K. Chan
Systems and Applied Sciences Corporation
6811 Kenilworth Avenue Suite 500
Riverdale, Maryland 20840

ABSTRACT

A Quadrilateralized Spherical Cube has been constructed to form the basis for the rapid storage and retrieval of high resolution data obtained of the earth's surface. The structure of this data base is derived from a spherical cube, which is obtained by radially projecting a cube onto its circumscribing sphere. An appropriate set of curvilinear coordinates is chosen such that the resolution calls on the spherical cube are of equal area and are also of essentially the same shape.

The main properties of the earth data base are that the indexing scheme is binary and telescopic in nature, the resolution cells are strung together in a two-dimensional manner, the cell addresses are easily computed, and the conversion from geographic to data base coordinates is comparatively simple.

Based on numerical results obtained, it is concluded that this data base structure is perhaps the most viable one for handling remotely-sensed data obtained by satellites. It can be used either as a data base for individual satellites or as a composite one for multiple satellites.

This work was supported by Navy Contract No. N66314-74-C-1340. The author wishes to acknowledge the programming assistance provided by Michael O'Neill, presently of Dilks Company.

SECTION 1 - INTRODUCTION

In the numerous satellites presently orbiting the Earth, enormous amounts of data are continuously taken of the Earth's surface and atmosphere. These data are of a varied nature: topography, crop distribution, sea surface temperature, cloud coverage, etc. The measurements are used by research and applications personnel of diverse scientific disciplines. These users usually employ and Earth-oriented coordinate system, such as the traditional geographic frame of reference. Thus, it is not surprising that almost all existing Earth data bases have been constructed with latitudes and longitudes as gridlines, either in a patched-up partial fashion or in the entire outlay.

However, what is convenient to the user is not necessarily also efficient from the standpoint of data management and data processing by the computer. Efficiency is especially important because of the large amounts of data rapidly acquired in global coverage, the necessity to update data continually for operational use, and the desire to access directly relatively small amounts of data corresponding to selected geographic regions at appropriate times.

The high computer overhead encountered in processing can therefore be minimized by designing an Earth data base structure with constant (but selectable) geometric resolution cells, which are also locally invariant in shape along a translation in any direction. This would eliminate the necessity to account for nonequal-area resolution cells, and also the need to compute the location of every resolution cell in the data base. Moreover, the design should also utilize a fairly simple transformation between the user-preferred geographic coordinates and the internal data base coordinates. This would greatly facilitate arithmetic and transfer operations desired by the user in mathematical computations or in graphic display.

The Quadrilateralized Spherical Cube[1] or the Chan Projection was especially constructed to form the basis for an earth data base of remotely-sensed satellite data. In this model, the sphere is visualized as a spherical cube, as illustrated in Figure 1-1. This spherical cube is obtained by radially projecting the edges of an inscribed cube, as shown in Figure 1-2.

From Figure 1-2, it is obvious that equal-area elements on the plane square do not radially project as equal-area elements on the spherical square. For example, those elements near the center of the plane square have larger projections than those elements near the edges of the plane square. Hence, if a rectangular grid of equal-area elements is first constructed on the plane square, it is then necessary to distort this grid into a curvilinear network so that the elements near the center are smaller than those near the edges. The distortion is such that when the curvilinear elements are projected radially, equal-area elements are again obtained on the spherical square. The desired sequence of transformations is illustrated in Figure 1-3 through 1-5. The mathematical details of deriving these transformations are discussed in Section 2.

For the present, it suffices to say that it is possible to obtain a world map such as Figure 1-6. This map illustrates the continental outlines as they would appear on the cube with the original undistorted rectangular coordinates. This is accomplished by reversing the sequence of transformations previously illustrated by Figures 1-3 through 1-5. Thus, in Figure 1-6, equal-area regions correspond to equal-area regions on the spherical Earth. An examination of this planar equal-area world map shows that the distortion of the continental outlines is not as great as might be expected.

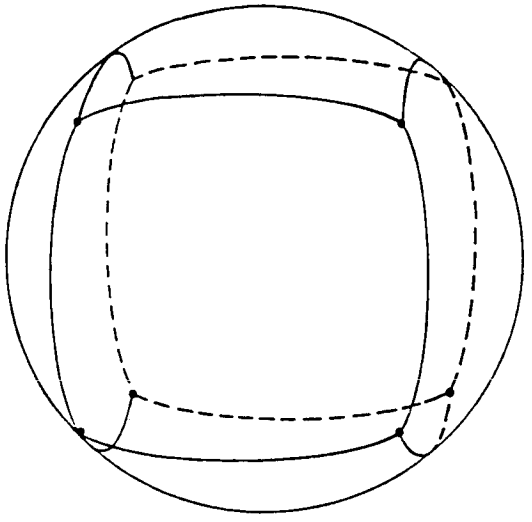

Figure 1-1. Spherical Cube

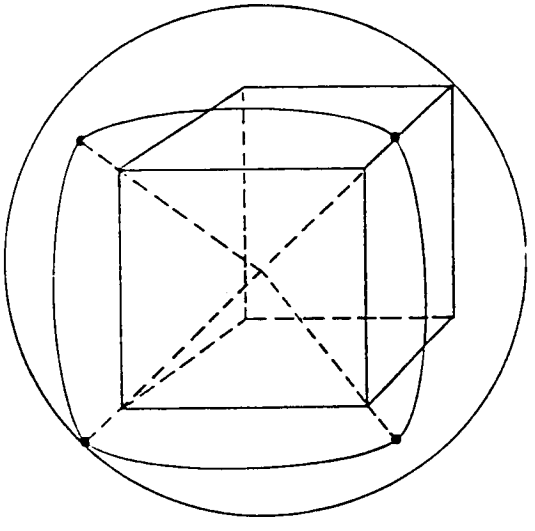

Figure 1-2. Construction of the Spherical Cube

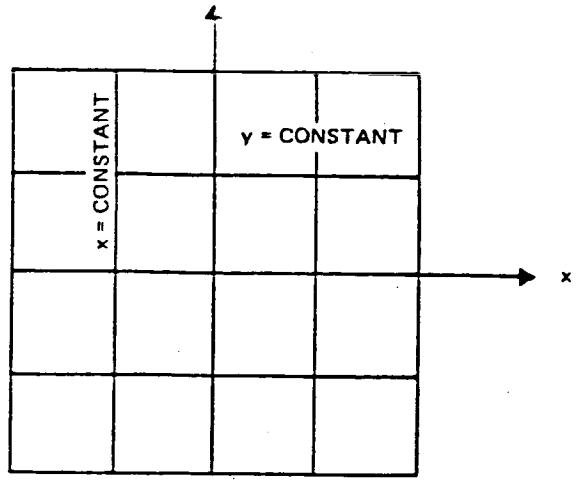

Figure 1-3. Plane Square With Cartesian Coordinates

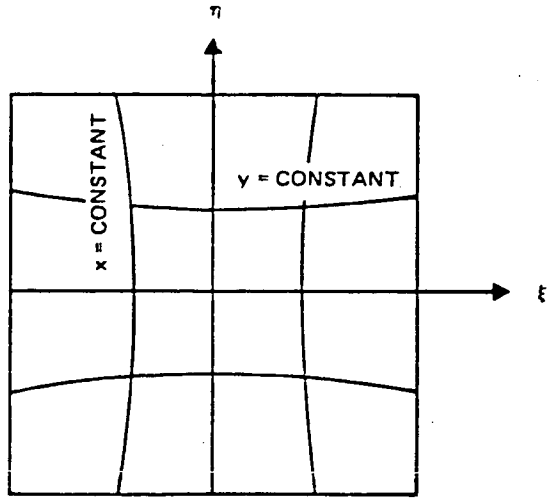

Figure 1-4. Plane Square With Curvilinear Coordinates

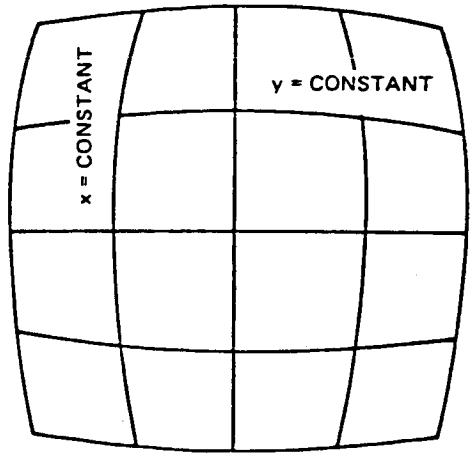

Figure 1-5. Spherical Square With Curvilinear Coordinates

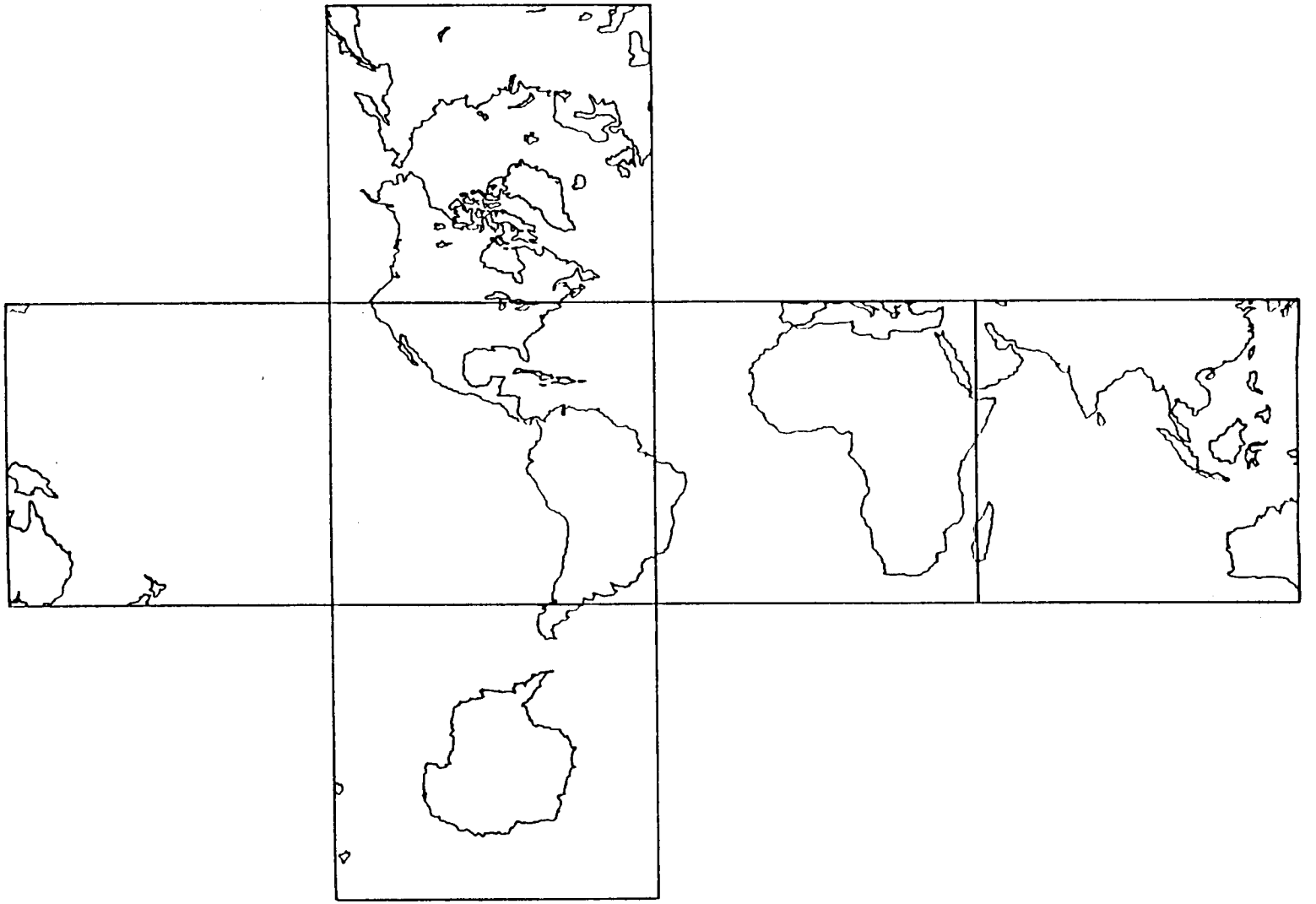

Figure 1-6. World Map on Equal-Area Cube

SECTION 2 - MATHEMATICAL FORMULATION OF DATA BASE STRUCTURE

DERIVATION OF DIRECT MAPPING FUNCTION

First, consider a plane surface subtended by a spherical surface with radius R. Let $\vec{r}_o$ be the vector from the center of the sphere to the given plane. As shown in Figure 2-1, let dA_p be an area element on this plane, and let $\vec{r}$ be the vector from the center of the sphere to the area element dA_p.

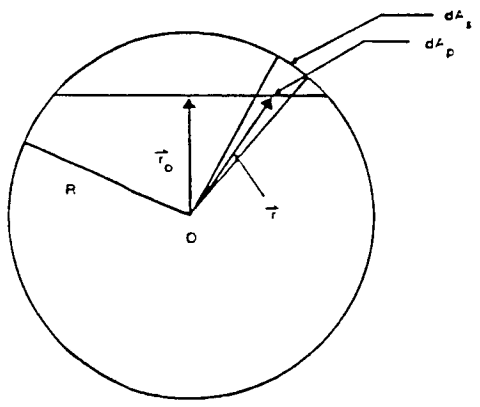

Figure 2-1. Relation Between Plane and Spherical Area Elements

Let dA_s be the spherical area element obtained by projecting dA_p radially onto the sphere. Then, it can be readily shown that the following relation between dA_p and dA_s holds:

$$dA_s = \frac{R^2 \cos^3 (\vec{r}, \vec{r}_o)}{r_o^2} dA_p \tag{2-1}$$

where $(\vec{r}, \vec{r}_o)$ denotes the angle between $\vec{r}$ and $\vec{r}_o$.

Let (ξ, η, r_o) denote the components of the vector $\vec{r}$. Then, it follows that

$$\cos(\vec{r}, \vec{r}_o) = \frac{r_o}{r} = \frac{r_o}{\left(r_o^2 + \xi^2 + \eta^2\right)^{1/2}} \tag{2-2}$$

Moreover, for convenience, let the unit of length be chosen such that the radius, R, of the sphere is equal to unity. Then, Equations (2-1) and (2-2) yield

$$dA_s = \frac{r_o}{\left(r_o^2 + \xi^2 + \eta^2\right)^{3/2}} dA_p \tag{2-3}$$

Next, consider a cube together with a circumscribing spherical surface. On each of the six plane faces of the cube, a rectangular coordinate system (x, y) may be defined, the domain of definition being $-r_o \leq x, y \leq r_o$. It may be easily verified that

$$r_o = \frac{1}{\sqrt{3}} \tag{2-4}$$

Let a new coordinate system (ξ, η) be defined by

$$\begin{aligned} \xi &= \xi(x, y) \\ \eta &= \eta(x, y) \end{aligned} \tag{2-5}$$

where $\xi(x, y)$ and $\eta(x, y)$ are independent arbitrary functions.

The new area element $d\xi\, d\eta$ is related to the original area element $dxdy$ by

$$d\xi\, d\eta = J\left(\frac{\xi,\ \eta}{x,\ y}\right) dxdy \tag{2-6}$$

where $J\left(\frac{\xi,\ \eta}{x,\ y}\right)$ is the Jacobian of transformation

$$J\left(\frac{\xi,\ \eta}{x,\ y}\right) = \begin{vmatrix} \frac{\partial \xi}{\partial x} & \frac{\partial \xi}{\partial y} \\ \frac{\partial \eta}{\partial x} & \frac{\partial \eta}{\partial y} \end{vmatrix} \tag{2-7}$$

If this new area element is projected radially onto the surface of the sphere, Equations (2-3) and (2-6) yield

$$dA_s = \frac{r_o}{\left(r_o^2 + \xi^2 + \eta^2\right)^{3/2}}\ J\left(\frac{\xi,\ \eta}{x,\ y}\right) dxdy \tag{2-8}$$

which relates the spherical area element dA_s to the original area element $dxdy$. For original equal-area plane elements $dxdy$ to transform into equal-area spherical elements dA_s, it follows that

$$\frac{r_o}{\left(r_o^2 + \xi^2 + \eta^2\right)^{3/2}}\ J\left(\frac{\xi,\ \eta}{x,\ y}\right) = \lambda^2 \tag{2-9}$$

or

$$\frac{r_o}{\left(r_o^2 + \xi^2 + \eta^2\right)^{3/2}} \left(\frac{\partial \xi}{\partial x}\frac{\partial \eta}{\partial y} - \frac{\partial \xi}{\partial y}\frac{\partial \eta}{\partial x}\right) = \lambda^2 \tag{2-10}$$

where λ^2 is a constant.

It is easy to verify that the value of λ^2 is equal to the ratio of the area of the spherical square to the area of the plane square, i.e.,

$$\lambda^2 = \frac{2\pi/3}{4\, r_o^2} = \frac{\pi}{2} \tag{2-11}$$

An alternative form of Equation (2-10) is

$$\frac{\partial \xi}{\partial x}\frac{\partial \eta}{\partial y} - \frac{\partial \xi}{\partial y}\frac{\partial \eta}{\partial x} = \gamma^2 \left(1 + \frac{\xi^2}{r_o^2} + \frac{\eta^2}{r_o^2}\right)^{3/2} \tag{2-12}$$

where

$$\gamma^2 = r_o^2 \lambda^2 = \frac{\pi}{6} \tag{2-13}$$

From Equations (2-7) and (2-12), it is seen that γ^2 may be interpreted as the area-scale of transformation at the point $(\xi = 0\ ,\ \eta = 0)$.

Equation (2-12) in itself is quite general. It is now desirable to specify the following general properties for the transformation from (x, y) to (ξ, η).

1. To preserve symmetry in the transformation Equation (2-5), it is required that

$$\begin{aligned} \xi &= f(x, y) \\ \eta &= f(y, x) \end{aligned} \tag{2-14}$$

Equation (2-14) states that ξ and η have exactly the same form of dependence on x and y, except that the roles of x and y are interchanged. Moreover, symmetry preservation also requires that the function $f(x, y)$ be odd in x and even in y, i.e.,

$$\begin{aligned} f(-x, y) &= -f(x, y) \\ f(x, -y) &= f(x, y) \end{aligned} \tag{2-15}$$

As a consequence of Equations (2-14) and (2-15), it is seen that the origin maps back into itself, i.e.,

$$f(0, y) = 0 \tag{2-16}$$

2. To map points on the sides of the square back into points on the same sides, it is necessary that

$$f(r_o, y) = r_o \tag{2-17}$$

As a consequence of all the above requirements, it may be shown that $\frac{\partial \xi}{\partial y}$ and $\frac{\partial \eta}{\partial x}$ are zero at the points $(0, 0)$ and (r_o, r_o). Therefore, from Equation (2-12), it follows that

$$\left.\frac{\partial \xi}{\partial x}\right|_{\substack{x=0\\y=0}} = \left.\frac{\partial \eta}{\partial y}\right|_{\substack{x=0\\y=0}} = \gamma = \sqrt{\frac{\pi}{6}} = 0.72360\ 12545\ 582 \tag{2-18}$$

$$\left.\frac{\partial \xi}{\partial x}\right|_{\substack{x=r_o\\y=r_o}} = \left.\frac{\partial \eta}{\partial y}\right|_{\substack{x=r_o\\y=r_o}} = \mu = \sqrt{\frac{\sqrt{3}\pi}{2}} = 1.6494\ 54166\ 187 \tag{2-19}$$

If $f(x, y)$ can be expanded in a power series in x and y, then Equation (2-16) requires that

$$f(x, y) = x \sum_{i=0}^{\infty} \sum_{j=0}^{\infty} a_{ij}\, x^{2i}\, y^{2j} \tag{2-20}$$

The condition in Equation (2-18) yields

$$a_{00} = \gamma \tag{2-21}$$

The condition in Equation (2-17) may be incorporated into $f(x, y)$ by writing it in the form

$$f(x, y) = \gamma x + \frac{(1-\gamma)}{r_o^2} x^3 + \left(r_o^2 - x^2\right) x \sum_{(i+j)\geq 1}^{\infty} b_{ij}\, x^{2i}\, y^{2j} \tag{2-22}$$

It may be shown that Equation (2-12), together with the conditions given by Equations (2-16) through (2-18), are not sufficient to determine uniquely the transformation in Equation (2-14). This nonuniqueness is manifested by the fact that there are more unknowns (b_{ij}) than equations when Equation (2-22) is substituted into Equation (2-12) and terms of the same degree are equated.

Finally, to incorporate the condition in Equation (2-19), it is most efficient to express $f(x, y)$ in the following form. The details for arriving at this form are given in Reference 1.

$$
\begin{aligned}
f(x, y) = {} & \gamma x + \frac{(1-\gamma)}{r_o^2} x^3 \\
& + xy^2 \left(r_o^2 - x^2\right) \left[\delta + \left(r_o^2 - y^2\right) \sum_{\substack{i \geq o \\ j \geq o}} c_{ij} x^{2i} y^{2j}\right] \\
& + x^3 \left(r_o^2 - x^2\right) \left[\omega + \left(r_o^2 - x^2\right) \sum_{i \geq o} d_i x^{2i}\right]
\end{aligned}
\tag{2-23}
$$

where

$$
\begin{aligned}
\delta &= \frac{1}{4r_o^4} \left[-(\mu + 2\gamma) + \sqrt{(\mu^2 - 4\mu\gamma + 4\gamma^2 + 16\sqrt{2}\,\gamma^2)}\right] \\
&= 0.79048\ 64491\ 208
\end{aligned}
\tag{2-24}
$$

$$
\begin{aligned}
\omega &= \frac{1}{2r_o^4} \left(3 - 2\gamma - \mu - 2r_o^4 \delta\right) \\
&= -\ 1.2254\ 41487\ 984
\end{aligned}
\tag{2-25}
$$

An approximate mapping function may be obtained by truncating the series expansion in Equation (2-23) at some degree, and then obtaining the coefficients c_{ij} and d_i which minimize the following residual function:

$$\phi(c_{ij}, d_i) \equiv \int_{-r_o}^{r_o} \int_{-r_o}^{r_o} \left[r_o^{-2} \left(1 + \frac{\xi^2}{r_o^2} + \frac{\eta^2}{r_o^2} \right)^{-3/2} \times \left(\frac{\partial \xi}{\partial x} \frac{\partial \eta}{\partial y} - \frac{\partial \xi}{\partial y} \frac{\partial \eta}{\partial x} \right) - \lambda^2 \right]^2 dxdy \tag{2-26}$$

This residual function is obtained by considering Equation (2-10) or (2-12). Then, $\phi(c_{ij}, d_i)$ is evidently equal to zero for the exact transformation function $f(x, y)$. For computational purposes, Equation (2-26) is replaced by

$$\phi(c_{ij}, d_i) = \sum_{x_k} \sum_{y_l} \left[r_o^{-2} \left(1 + \frac{\xi^2}{r_o^2} + \frac{\eta^2}{r_o^2} \right)^{-3/2} \times \left(\frac{\partial \xi}{\partial x} \frac{\partial \eta}{\partial y} - \frac{\partial \xi}{\partial y} \frac{\partial \eta}{\partial x} \right) - \lambda^2 \right]^2 \tag{2-27}$$

where the points (x_k, y_l) are chosen to form a regular grid over the plane square. A computer software program for performing this minimization problem is given in Reference 1. For a second-degree approximation of the series in Equation (2-23), the following values of c_{ij} and d_i are obtained:

$$c_{00} = -2.7217\ 05366\ 1814$$

$$c_{10} = -5.5842\ 16830\ 5430$$

$$c_{01} = 2.1711\ 17480\ 9423$$

$$c_{20} = -3.4578\ 62747\ 3390$$

$$c_{11} = -6.4160\ 15152\ 6783$$

$$c_{02} = 1.9736\ 26575\ 8872$$

$$d_0 = 1.4833\ 12929\ 4187$$

$$d_1 = 1.1199\ 72606\ 9742$$

$$d_2 = 6.0515\ 38216\ 1464$$

The corresponding mapping function $f(x, y)$ is accurate to about five significant figures.

DERIVATION OF INVERSE MAPPING FUNCTION

Corresponding to the symmetrical direct mapping function expressed in Equation (2-14), it may be verified that the inverse mapping function is also symmetrical, i.e.,

$$\begin{aligned} x &= f^*(\xi, \eta) \\ y &= f^*(\eta, \xi) \end{aligned} \tag{2-28}$$

As discussed in Reference 1, $f^*(\xi, \eta)$ must be expressed in the form

$$\begin{aligned} f^*(\xi, \eta) = {} & \gamma^* \xi + \frac{(1-\gamma^*)}{r_o^2} \xi^3 \\ & + \xi\eta^2 \left(r_o^2 - \xi^2\right) \left[\delta^* + \delta_1^* \left(r_o^2 - \xi^2\right) + \left(r_o^2 - \eta^2\right) \sum_{\substack{i \geq 0 \\ j \geq 0}} c_{ij}^* \xi^{2i} \eta^{2j}\right] \\ & + \xi^3 \left(r_o^2 - \xi^2\right) \left[\omega^* + \left(r_o^2 - \xi^2\right) \sum_{i \geq 0} d_i^* \xi^{2i}\right] \end{aligned} \tag{2-29}$$

where

$$\gamma^* = \frac{1}{\gamma}$$

$$\mu^* = \frac{1}{\mu}$$

$$\gamma_1{}^* = \frac{1}{\gamma + r_o^4\,\delta}$$

$$\mu_1{}^* = \frac{1}{\mu + 2r_o^4\,\delta} \qquad (2\text{-}30)$$

$$\delta^* = \frac{(\mu_1{}^* - \mu^*)}{2r_o^4}$$

$$\omega^* = \frac{1}{2r_o^4}\left(3 - 2\gamma^* - \mu^* - 2r_o^4\,\delta^*\right)$$

$$\delta_1{}^* = \frac{1}{r_o^2}\left[\frac{(\gamma_1{}^* - \gamma^*)}{r_o^4} - \delta^*\right]$$

An approximate inverse mapping function may be obtained by truncating the series expansion in Equation (2-29) at some degree, and then obtaining the coefficients $c_{ij}{}^*$ and $d_i{}^*$ which minimize the following residual function:

$$\phi^*(c_{ij}{}^*,\ d_i{}^*) \equiv \int_{-r_o}^{r_o}\int_{-r_o}^{r_o}\left\{\left[x - f^*\left(f(x,y),\ f(y,x)\right)\right]^2 + \left[y - f^*\left(f(y,x),\ f(x,y)\right)\right]^2\right\}^{1/2} dx\,dy \qquad (2\text{-}31)$$

In obtaining this residual function, the direct mapping function $f(x, y)$ is considered, as given by Equation (2-23). Then, $\phi^* (c_{ij}^*, d_i^*)$ is evidently equal to zero for the exact inverse mapping function $f^* (\xi, \eta)$. Again, for computational purposes, Equation (2-31) is replace by

$$\phi^*(c_{ij}^*, d_i^*) = \sum_{x_k} \sum_{y_\ell} \left\{ \left[x - f^* \left(f(x,y), f(y,x) \right) \right]^2 + \left[y - f^* \left(f(y,x), f(x,y) \right) \right]^2 \right\}^{1/2} \tag{2-32}$$

A computer software program for performing this minimization problem is also given in Reference 1. For a second-degree approximation of the series in Equation (2-29), the following values of c_{ij}^* and d_i^* were obtained:

$$c_{00}^* = 3.973\ 89249$$

$$c_{10}^* = 6.591\ 19476$$

$$c_{01}^* = -25.368\ 92536$$

$$c_{20}^* = -73.064\ 97000$$

$$c_{11}^* = 77.381\ 61133$$

$$c_{02}^* = 21.685\ 89623$$

$$d_0^* = 1.811\ 28250$$

$$d_1^* = 37.635\ 47857$$

$$d_2^* = 63.000\ 23655$$

The corresponding mapping function $f^* (\xi, \eta)$ is accurate to about five significant figures.

SECTION 3 - ORGANIZATION OF DATA BASE

The underlying principle in organizing the data base is specifically related to the binary division and the stringing pattern discussed below. In this scheme, the process starts at the level of the faces in the spherical cube, numbering these faces 1 through 6 as in Figure 3-1.

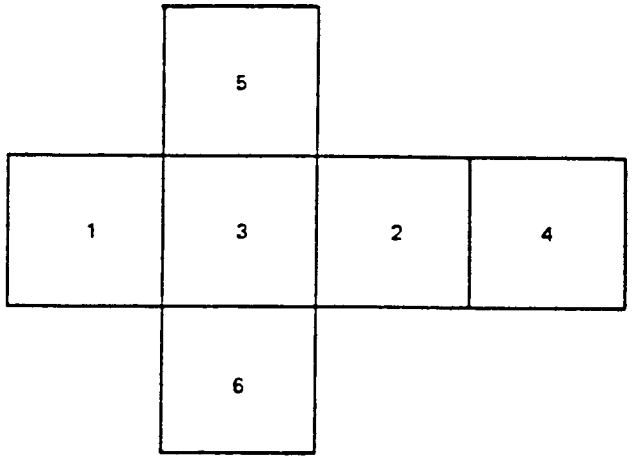

Figure 3-1. Face Numbering Scheme

Each face is divided, to the requisite resolution level, by a two dimensional binary grid, as shown in Figure 3-2. On each level of division, the areas are divided into quadrants, which are labeled by a 2-bit binary number. Each level of division, k, is indicated by the addition of two binary bits to the least significant end of a 2k bit binary number. Figure 3-3 illustrates the indexing scheme corresponding to the third level of division. Suppose there are n levels of division altogether. Then, the binary index defines the serial location of a point in the 2n array.

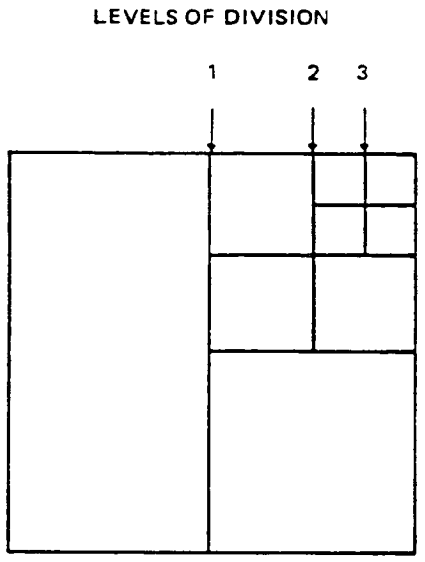

Figure 3-2. Binary Division Scheme

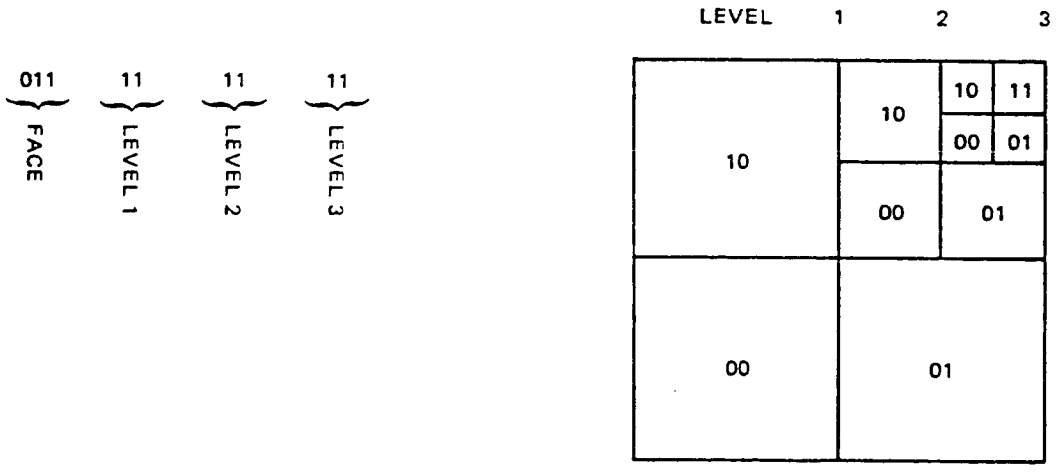

Figure 3-3. Illustrative Labeling by Binary Bits

In comparison to the normal row and column addressing scheme, the present one has the following advantages:

1. Reduction in I/O time through maintenance of near-neighbor relationships
2. Compactness of arrays containing addresses
3. Maintenance of a consistent addressing scheme regardless of resolution level

The serial addressing scheme reduces I/O time for disk type storage devices because more near neighbors of a point are within the range which requires no arm motion for accessing. The expression of addresses as a single bit string allows storage of addresses as single machine words, whereas a two-dimensional addressing scheme would require two or three words, including one for the face number. Finally, the expandibility and generality of the serial string permit the use at any resolution level without regard to physical storage considerations, such as record size. Any reasonable matrix type storage scheme would require a dual (or multiple) level of addresses for record and item within record location in the serial scheme. This is accomplished simply by considering the high order m bits as the record number, and the low order n-m bits as the address within record.

Implicit in the manner of binary labeling at each level, it is obvious that one obtains an ordering pattern whose basic nature is that of an upside-down Z. Figures 3-4 and 3-5 illustrate the binary indexing and the stringing sequence for the first two levels of division.

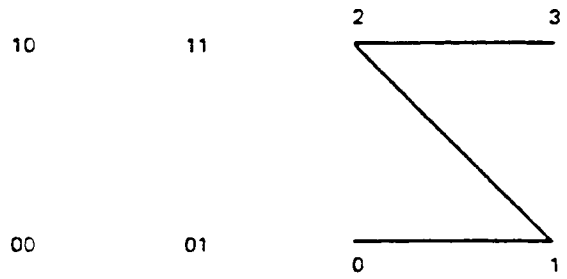

Figure 3-4. First Level of Division

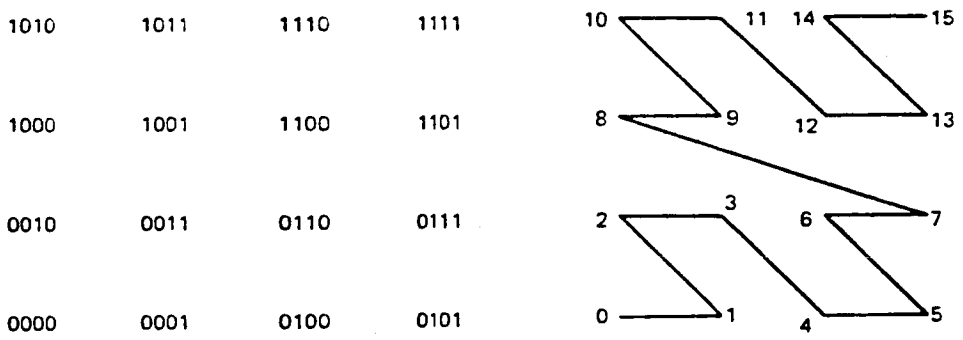

Figure 3-5. Second Level of Division

Next, suppose that a point (or cell) is represented by its rectangular coordinates (x,y). A little consideration of Figure 3-4 which illustrates the basic nature of each level of division reveals that, in general, the x and y coordinates respectively can only be associated with the odd and even bits in the binary index (or serial address) s of the cell, no matter how many levels of division there are. Furthermore, a more important property is that the x and y coordinates respectively can be directly obtained by merely masking out the even and odd bits in the serial address. Conversely, this important property means that if the x and y coordinates are given, then the serial address s may be obtained by

1. Representing x and y in binary form of n bits.
2. Expanding the n-bit format to 2n-bit format by appropriately inserting O in the even bits for x and in the odd bits for y, as illustrated in Table 3-1.
3. Adding the modified forms for x and y to obtain s.

Table 3-1. Binary Representation of Coordinates

DECIMAL VALUE	BINARY	X-COORDINATE (ODD)	Y-COORDINATE (EVEN)
1	1	01	10
2	10	100	1000
3	11	101	1010
4	100	10000	100000
5	101	10001	100010
6	110	10100	101000
7	111	10101	101010

As an example, consider the cell (2,3). Thus, from Table 3-1, we obtain

$$x = 10 \Longrightarrow 100$$

$$y = 11 \Longrightarrow 1010$$

$$s = 100 + 1010 = 1110$$

which checks with Figure 3-5.

The calculation of the serial string index may also be accomplished by the construction of a very simple hardware device. This device would consist of three registers: an x register, a y register, and a s register. Two register-to-register instructions would provide packing from x , y to s and unpacking s to x , y . These instructions would initiate parallel transfer from the two n-bit coordinate registers to the 2n-bit serial register and vice versa. The interconnection is shown in Figure 3-6.

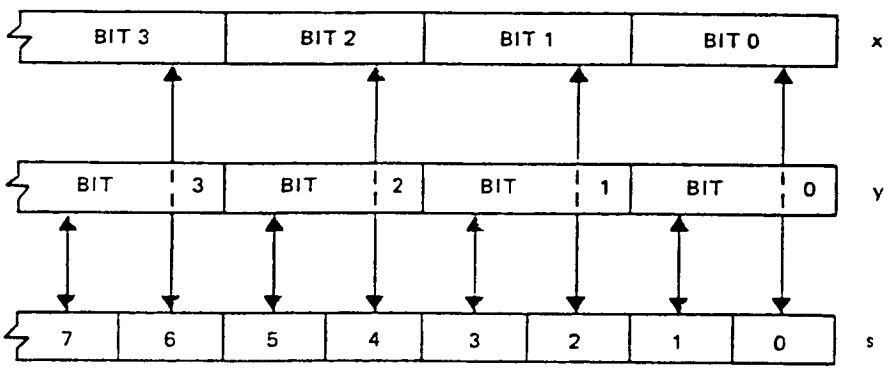

Figure 3-6. Transfer Between Registers

SECTION 4 - CONCLUSION

The main properties of the Quadrilateralized Spherical Cube Earth Data Base are:

1. The indexing scheme is binary in nature, and telescopic in the sense that each additional level of resolution is addressed by appending additional binary bits. Thus, minimal work is needed for indexing cells of higher resolution.

2. The resolution cells are strung together in a two-dimensional manner, so as to accomplish area coverage with a serial bit string. Consequently, a higher degree of proximity is achieved for near-neighbors in this stringing pattern than in the usual one-dimensional array of stringing by rows and columns.

3. The cell addresses are readily computed because of the indexing scheme which is the same regardless of the resolution level, and because of the stringing pattern which permits the decomposition of the cell address into two independent binary indices.

4. The conversion from geographic coordinates to data base coordinates is comparatively simple because of the simplicity of the data base structure.

5. Incoming data can be stored rapidly by interpolation, using benchmarks only occasionally. This method of fast-filling is made possible by the equal-area nature and translational shape invariance of the data base resolution cells.

6. Input/output operations with this data base are also simplified because of the rectangularized nature of the data base records and the rhombic nature of the interpolation blocks.

7. The user can rapidly and directly access data corresponding to specified geographic regions of arbitrary shape and size. This data-accessing is accomplished by retrieving the relatively few bit-strings which lie within the associated data base records. The rapidity and directness of data access are the result of equal-area resolution, translational invariance, indexing scheme, stringing pattern, and relatively simple coordinate transformation.

8. The primary contemplated uses of the retrieved data are mathematical computations and visual display. For the former, the equal-area resolution property eliminates the need to distinguish between density measurements and integrated measurements. For the latter, the quadrilateralized nature of the resolution cells on the spherical cube and the comparative simplicity of coordinate transformation both simplify and minimize the internal operations.

REFERENCES

1. Chan, F. K., and O'Neill, E. M., "Feasibility Study of Quadrilateralized Spherical Cube Earth Date Base," Computer Sciences Corporation, Silver Spring, Maryland. EPRF Technical Report 2-75 (CSC), (1975).

Adaptive Guidance and Control for Future Remote Sensing Systems

James W. Lowrie† and John E. Myers ††

Martin Marietta Aerospace

Abstract

Remote sensing missions past the era of LANDSAT D require the dissemination of high quality image data to users in near real time. Martin Marietta has developed a unique approach to onboard processing which is directed at this goal. The first step of this approach was the development of an onboard cloud detection system which has flown on an aircraft flight test and will fly on the first Shuttle experimental pallet. The second step of the approach was the development of a Landmark tracker, which has also been flown on an aircraft flight test. This paper outlines the results of these two developments and summarizes the requirements of an operational guidance and control system capable of providing continuous estimation of the sensor boresight position.

Introduction

All forecasts of advanced technology and the future space mission models have pointed to massive increases in image data return from spaceborne sensor platforms designed to provide global monitoring of agriculture, minerals, forest, and water resources. Concurrently, the user community is requesting high quality image products in a shorter amount of time. Examination of existing and near-term mission models reveals that the end to end remote sensing system is inefficient. Over 50% and closer to 80% of all data acquired by the Landsat series remains unused due to either undesirable effects such as cloud coverage or disinteresting scene content. Also, the turnaround time between data acquisition and dissemination to the user can exceed two months due to tremendous processing requirements necessary to correct imagery for distortions. This situation is intolerable to both NASA and the user community. In summary, two major limitations of existing remote sensing missions are deterministic acquisition of high quality imagery and the timely correction of imagery for distortions. This paper outlines an approach to remote sensing which will meet future mission goals by overcoming these limitiations. The approach is centered around two subsystems. The first subsystem provides real time classification of features within a scene so that onboard decisions affecting data acquisition can be made. The second subsystem incorporates a landmark tracker into a state of the art navigation system in order to continuously predict the sensor boresight position in earth fixed coordinates.

---

†James W. Lowrie is a senior engineer at Martin Marietta Aerospace, Denver Division, working in the Advanced Automation Technology area.

††John E. Myers is a Professor of Electronics Engineering Technology at Metropolitan State College, Denver, Colorado, and consultant to Martin Marietta Aerospace, Denver Division.

Deterministic Data Acquisition

In order to solve the problem of acquiring only desirable scenes, it is necessary to define the features which are desirable or undesirable and then to develop a system which will automatically classify scenes according to their content. For remote sensing missions, it is certainly necessary to distinguish clouds from other features, but it is also desirable to separate others such as vegetation, bare earth, and water. For example, a mission dedicated to water pollution monitoring has no desire to acquire bare earth or vegetation scenes. Therefore, for this application it is necessary to discriminate between water and other classes. Table I presents a list of mission models and the types of data selection criteria they might use.

Table I. Data Selection Criteria for Advanced Mission Models

Mission Model	Data Selection Criteria
Biomass Estimation	Cloud Vegetation
Flood Detection	Cloud Water
Forest Fire Detection	Cloud Vegetation Fire
Water Pollution Monitoring	Cloud Water Water/Land Interface
Ice Mapping	Cloud Snow Ice
General Remote Sensing (Landsat)	Cloud

The Feature Identification and Location Experiment (FILE) was first conceived in 1976 as the first segment of a truly autonomous remote sensing system (Ref. 1). The experiment, which has flown on an aircraft flight test in early 1980 and is scheduled to fly on shuttle OFT-2, is designed around the concept that generic classes of features may be separated by spectral signature using simple algorithms. It is important to note that this experiment eliminates the need for detailed ground truth information by avoiding the temptation to separate generic clusters into finer detail. The FILE algorithm utilizes the ratio of the sensor voltages in two bands centered at .65μm and .85μm. Although the observed radiance from a feature is a function of its reflectance, incident illumination, and radiance absorption of the medium through which it is viewed, the ratio of the radiance at these two wavelengths is reasonably independent of all factors except reflectance. This principle is the basis of the FILE system and is the key to avoiding the need for ground truth. Figure I shows how various feature types can be classified with the algorithm. Water and vegetation can be separated on the basis of the ratio alone. However, since the radiance ratio

for bare land is essentially the same as for clouds and snow, these features must be separated on the bases of absolute radiance.

Although the FILE experiment has been designed to classify clouds, vegetation, bare earth, and water, the technique may be extrapolated to other target types as long as the statistics of the signatures are seperable. For example, forest fire detection could be implemented using a thermal and visual band.

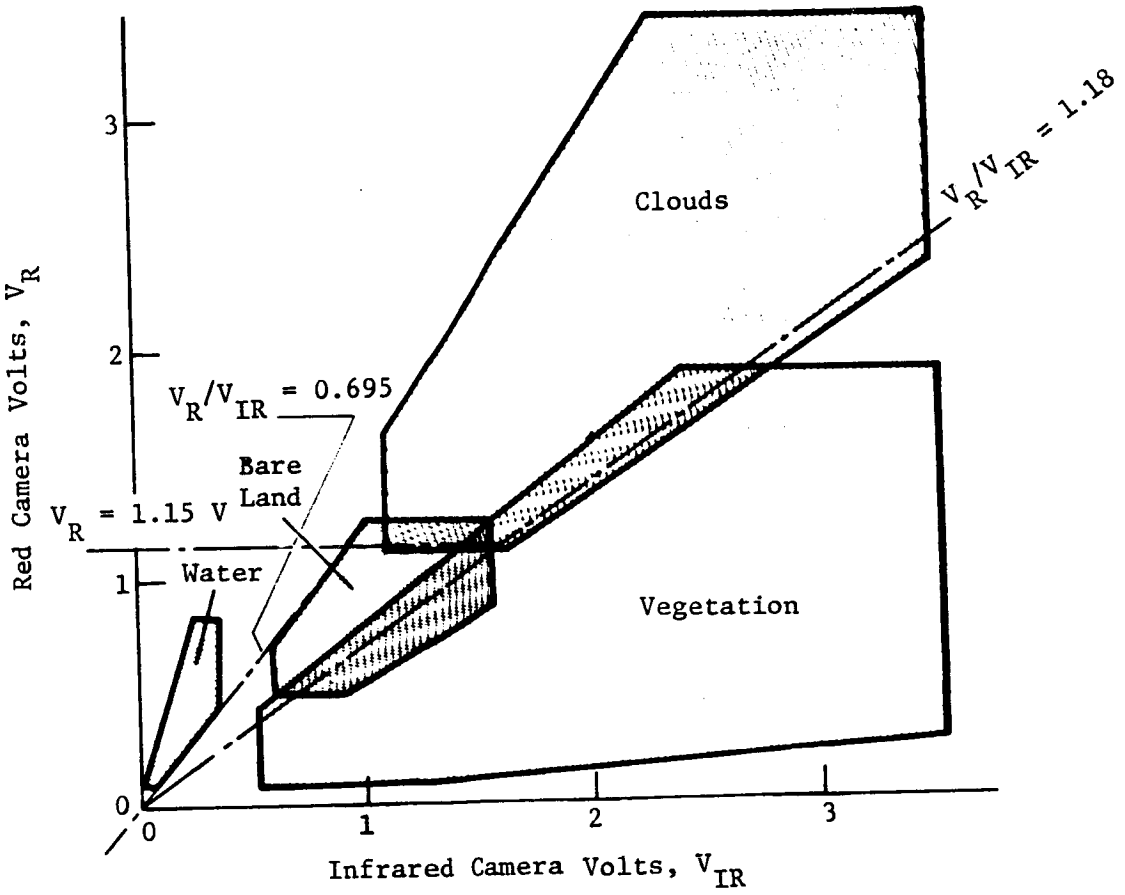

Figure I. 99% Confidence Polygons, Sun 41 to 60 Degrees from Zenth

Image Correction

The advancement of spaceborne processors has made real time correction of imagery a feasible goal for near-term mission models provided the distortions can be measured onboard to sufficient accuracy. The primary sources of image distortion can be separated into sensor peculiarities, viewing perspective, and spacecraft characteristics (Ref. 2). With the development of linear arrays, the primary sensor-caused distortions will be the individual placement of detector elements and the orientation of the array relative to the sensor prior to flight. Viewing perspective, which is a combination of curvature of the field of view and look angle geometry, is a slowly varying function

of local earth radius and can also be considered deterministic over short intervals. The primary error source remaining, therfore, is spacecraft-caused distortions. The spacecraft error sources can be catagorized as follows:

Attitude determination

Ephemeris prediction

Misalignment between sensor and body coordinates

Mathematical inaccuracies in inertial to earth fixed coordinate transformation

These general sources have been broken down in more detail in Table II.

Table II. Spacecraft Induced Error Sources in Temporal Registration

Attitude determination
- Star tracker accuracy
- Star tracker configuration
- Knowledge of star tracker misalignment
- Error in star catalogue
- Gyro noise
- Knowledge of gyro bias, nonorthogonality, misalignment
- Numerical accuracy

Ephemeris prediction
- GPS accuracy
- Numerical accuracy

Misalignment between sensor and body coordinates
- Knowledge of linear array or scan mirror orientation
- Accuracy of thermal deflection model
- Vibration modes between two coordinates
- Calibration technique and frequency
- Numerical accuracy

Transformation error between inertial and earth fixed coordinates
- Knowledge of UT1
- Knowledge of earth precession, nutation, polar wander, and tidal deformation
- Numerical accuracy

For the sake of discussion, assume that all the error is due simply to the attitude determination system. In order to achieve a temporal registration accuracy of 15 meters, it will be necessary to predict the attitude to within 4 sec as illustrated in Figure II. Accuracy of current state-of-the-art systems using the NASA standard star tracker and gyro is 15 sec (2σ) as discussed in the "Onboard Attitude Determination System" study (Ref. 3).

Figure II. Error Budget for Registration Accuracy of 15m

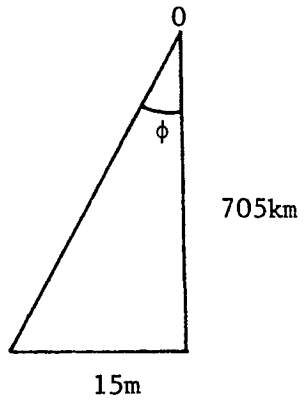

$$\phi = \tan^{-1} \frac{15\text{m}}{705\text{km}}$$

$$\approx 4 \text{ sec}$$

Even with the advancement of CCD star trackers, the attitude determination capability will be around 6 sec (2σ). Note that two sigma numbers have been used here corresponding to 95% of the data. If a one sigma number corresponding to 67% of the data is used, the accuracy goal can be met. However, by adding just one more error term such as a misalignment between sensor and body coordinates of 2 sec (2-axis accuracy achievable with an optical alignment cube), the total error exceeds the design goal. From the previous discussion, which ignored many error sources, it is clear that another approach is required.

Solution of the temporal registration problem requires that the sensors boresight position in earth fixed coordinates be periodically measured. This can be accomplished using a correlator which registers known Ground Control Points (GCP) within the sensor data. Onboard registration of GCPs allows many of the error terms listed in Table II to be accurately estimated in real time.

Shortly after the experimental definition of FILE, Martin Marietta began the development of a landmark tracker or GCP detector centered around our experience with terminal guidance systems. The primary function of the landmark tracker is to provide periodic measurements of the science sensors boresight position to be used as an input to a navigation system. Previous studies (Ref. 4-7) have shown that the landmark tracker will not adequately solve for both position and attitude without supplemental measurements from another source. For this reason the remote sensing navigation system has been configured with a GPS receiver to provide position measurements. Another limitation of the landmark tracker operating in the visual spectrum is that measurements are sometimes obscured by clouds and no measurements can be taken over water. For this reason, two star trackers have been added to the configuration to bound the maximum attitude error and to reduce the convergence time of the state when GCP sightings are acquired. A block diagram of the navigation system is shown in Figure III.

The registration processor is centered around a Sequential Similarity Detection Algorithm (SSDA) first identified by Barnea and Silverman (Ref. 8). Other algorithms were considered, but after significant analysis (Ref. 9), results indicate that for the advanced Landsat mission model, the SSDA is superior to other techniques due to its low probability of false lock, time required for registration, and ease of implementation in a hardwired system.

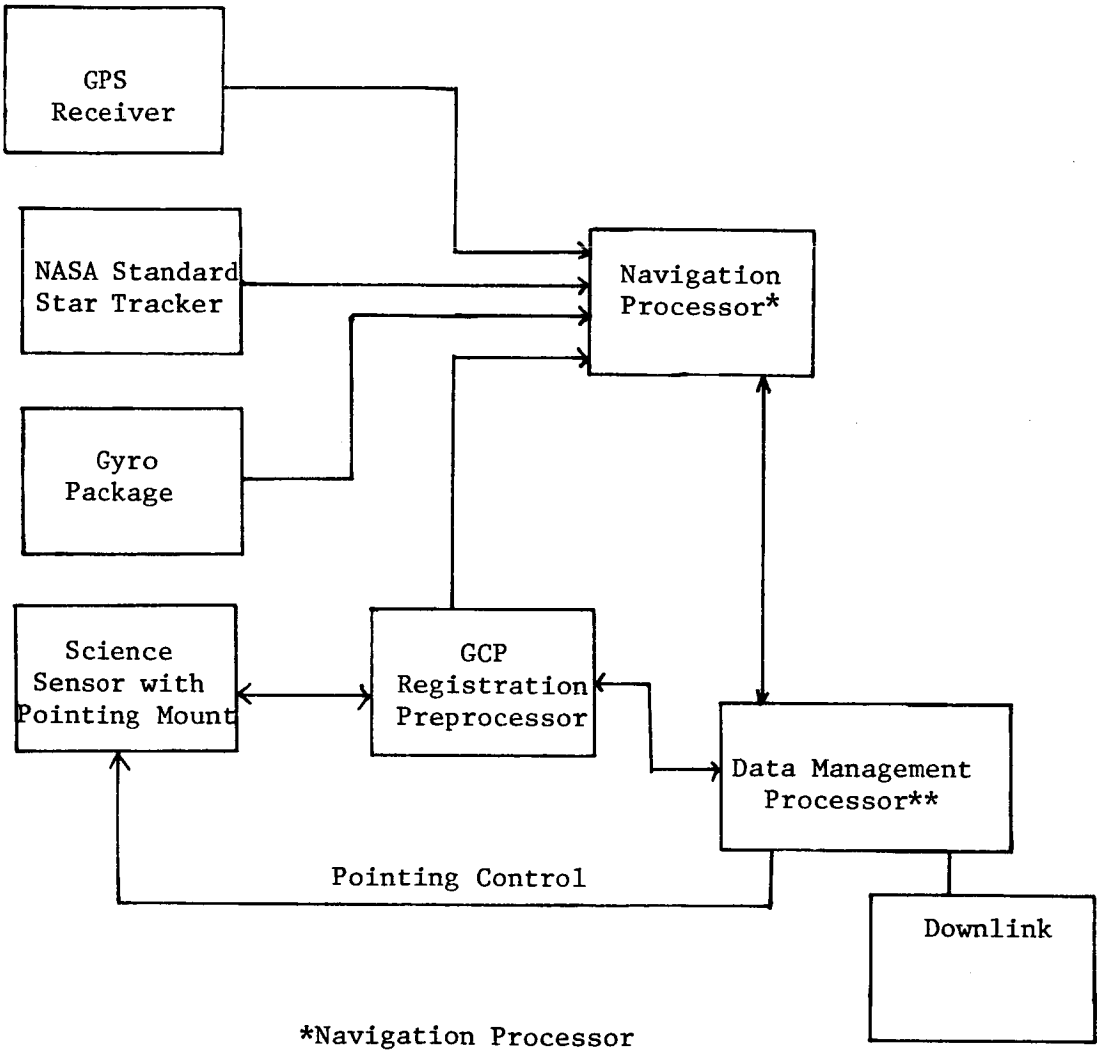

*Navigation Processor

- Vehicle State Solution
- Sensor Boresight
  Position Determination

**Data Management Processor

- Data Annotation
- Image Correction
- Sensor Pointing
- Information Extraction
- Telemetry Management

Figure III. GPS Detection System Configuration

GCP Registration

To perform GCP registration it is not necessary to process imagery from the entire Field of View (FOV) but only an area whose size ensures the GCP will be located within its boundary.

Let this search area be defined as an LxL area of digital picture elements. The image may be defined by a function, S, that describes the gray scale, or recorded radiance, in relation to position coordinates, i.e.,

$S(i,j) = W_{i,j}$

where $W_{i,j}$ is the gray scale of the i,j^{th} picture element of the search area

$1 \leq (i, j) \leq L$.

Let the ground control point be defined similarly as an MxM area with an image function

$G(\ell,m) = R_{l,m}$

where $R_{l,m}$ is the gray scale of the l,m^{th} picture element of the GCP

$1 \leq (\ell, m) \leq M$.

A subimage (Figure IV) of the SA may be defined as an MxM area whose upper left coordinates (n,o) lie in the range

$1 \leq (n, o) \leq L - M + 1$.

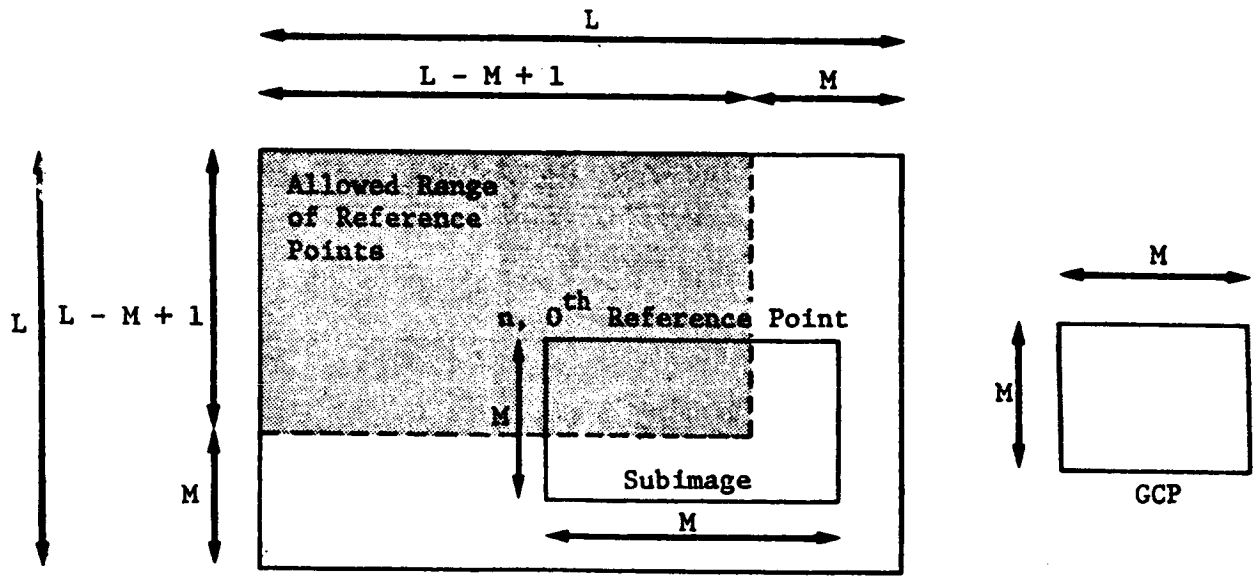

Figure IV. Subimage Definition

A subimage whose upper left coordinates are n,o will be referred to as the n,o^{th} reference point.

The sensor data are registered by measuring the similarity between each MxM subimage within the search area and the representation of the GCP stored onboard. The reference point that produces the highest degree of similarity with the GCP is then the best registration of the SA and can be labeled with the same earth fixed coordinates as the GCP.

The SSDA algorithm may be implemented to detect similarity between a reference point and the GCP through the following equation:

$$\text{Similarity} = \sum_{i-1}^{M} \sum_{j-1}^{M} \left| \left(S(i+n,\ j+0) - \overline{S}_{n,o}\right) - \left(G(i,j) - \overline{G}\right) \right|$$

where

S_{no} ≡ n,oth reference point,

$\overline{S}_{no}$ ≡ mean value of the subimage located at the n,oth reference point

$\overline{G}$ ≡ mean value of the GCP.

The entire registration process can then be described by the algorithm shown in Figure V.

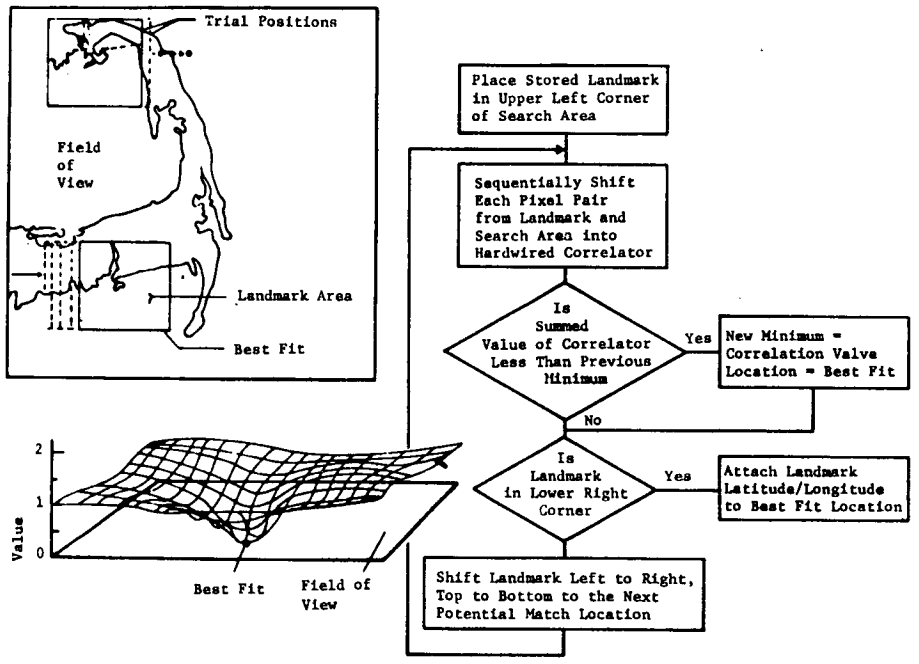

Figure V. Registration of an Area Landmark

Approaches to automatic registration have typically been limited by the effect of cloud coverage on accuracy and the inability to detect correlator false lock. A technique for reducing the effects of cloud coverage was developed under an independent research project (Ref. 9). The technique incorporates the FILE classification capability into the correlator so that every pixel representing a cloud is eliminated from the correlator computation. Results indicate that the tolerance for clouds within the search area has increased from 10% to 40%. An algorithm was also developed to detect correlation false lock. Basically, the algorithm compares the rate of convergence of the correlation surface with the rate of convergence found when the GCP is correlated with itself. If false lock is detected, no registration vector is passed to its navigation filter.

System Model

Under contract to NASA-GSFC, Martin Marietta is currently investigating the operational requirements of an onboard GCP detection system designed to meet the goals of accurate image correction. The analysis is centered around a simulation program which models the environment of the spacecraft, generates measurements, and estimates the state of the vehicle using an extended Carlson square root filter. The program was set up to provide analysis of true errors rather than simply evaluating the covariance matrix. Although the covariance analysis provides a great deal of information, interpretation of results can be inaccurate and misleading. For example, there are many cases where the covariance matrix converges over a period of time while the actual state estimate diverges from the true state. A conceptual diagram of the modeling is shown in Figure VI.

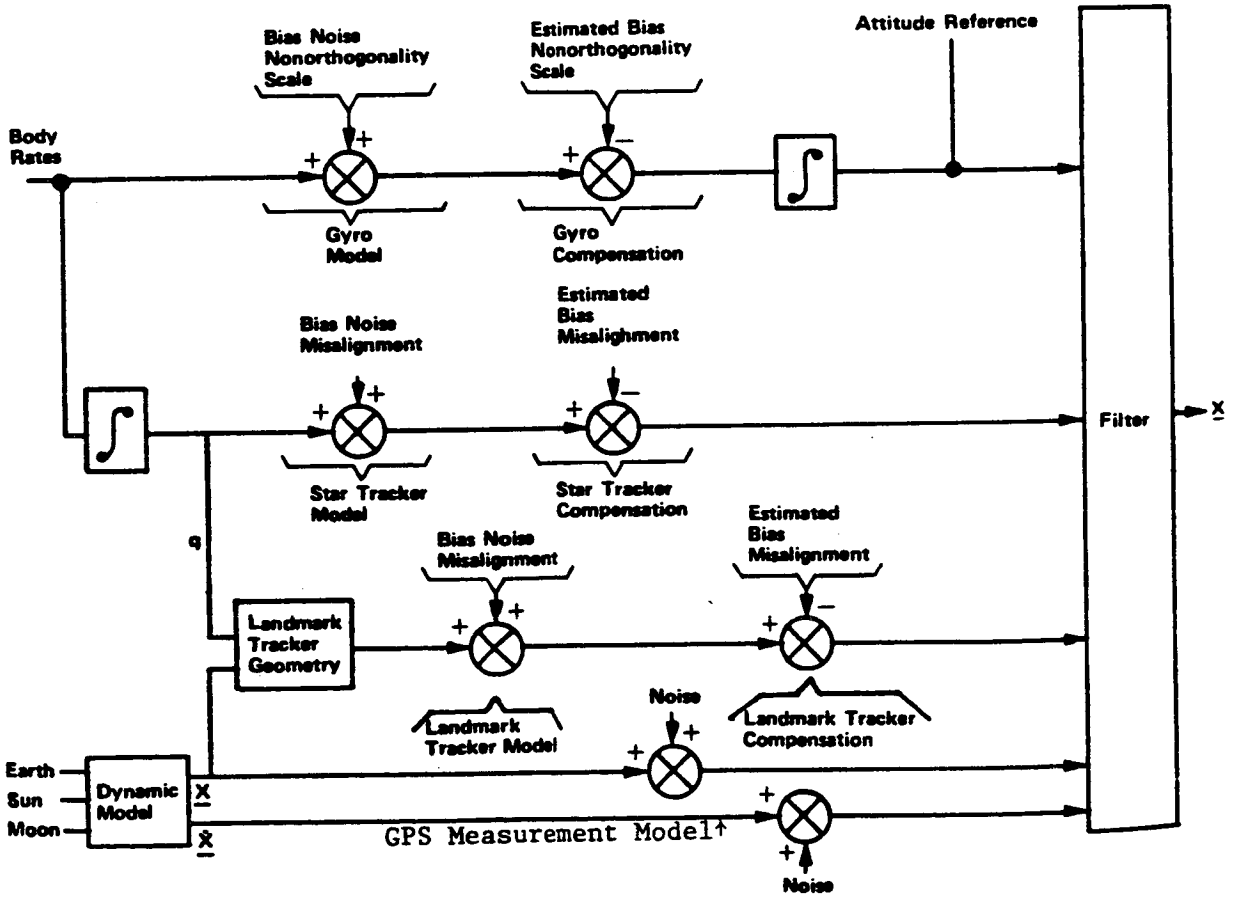

Figure VI. Overview of Measurement Models

The design philosophy behind the measurement models is that the actual vehicle state is used with a geometry model to yield an ideal measurement vector. This ideal vector is then corrupted with bias, noise, and misalignment to provide the actual sensor output. The sensor output is then compensated for some estimate of the error terms and is used by the filter to estimate the vehicle state. The benefit behind this design approach is that it enables a

detailed analysis of sensitivity to misalignments and compensation ability. It is also expected that the severe requirements associated with onboard image correction will require the onboard estimate of misalignment terms such as those between the science sensor and body coordinates. With this approach, it will not be difficult to modify the filter to solve for these terms. It is possible to understand the mathematics of most of the measurement models simply by interpreting Figure VI. However, the landmark tracker model is somewhat more complex and is described more fully here.

The landmark location on the surface of the earth in Local Landmark Coordinates (Figure VII) will be a function of the altitude (A_L) above the earth's mean radius.

$$\underline{L}_L = \begin{bmatrix} A_L \\ 0 \\ 0 \end{bmatrix}$$

However, in earth fixed coordinates, the landmark will have the earth's mean radius ($\overline{r}_E$) added to the altitude. Using the angular transformation from local landmark to earth fixed coordinates produces

$$\underline{L}_E = {}_E T_L \, \underline{L}_L = {}_E T_L \begin{bmatrix} \overline{r}_E + A_L \\ 0 \\ 0 \end{bmatrix} = (\overline{r}_E + A_L) \begin{bmatrix} CLC\lambda & -SL & -CLS\lambda \\ SLC\lambda & CL & -SLS\lambda \\ S\lambda & 0 & C\lambda \end{bmatrix} \begin{bmatrix} 1 \\ 0 \\ 0 \end{bmatrix}$$

$$= (\overline{r}_E + A_L) \begin{bmatrix} CLC\lambda \\ SLC\lambda \\ S\lambda \end{bmatrix}$$

As shown in Figure VII, the position vector of the spacecraft ($P_{S/C}$), when subtracted from the landmark position in some coordinate frame, will provide the measurement vector ($\underline{M}$).

$$\underline{M}_I = ({}_I T_E \, \underline{L}_E) - \underline{P}_{S/C_I}$$

Accounting for hardware misalignments, the same measurement vector in landmark tracker coordinates is:

$$\underline{M}_\ell = {}_\ell T_I \left(({}_I T_E \, \underline{L}_E) - P_{S/C_I} \right)$$
$$= {}_\ell T_E \, \underline{L}_E - {}_\ell T_I \, \underline{P}_{S/C_I}$$

From examination of Figure VIII, the unit measurement vector in landmark tracker coordinates is:

$$\underline{U}\ell = \frac{\underline{M}\ell}{|\underline{M}\ell|} = \begin{bmatrix} U\ell x \\ U\ell y \\ U\ell z \end{bmatrix} = \begin{bmatrix} \mathrm{Cos}\Delta V \mathrm{Sin}\Delta H \\ \mathrm{Sin}\Delta V \\ \mathrm{Cos}\Delta V \mathrm{Cos}\Delta H \end{bmatrix}$$

However, the tracker instrument has no sensitivity to projections along its boresight axis. Therefore, the tracker response to the unit vector $\underline{U}\ell$ will be:

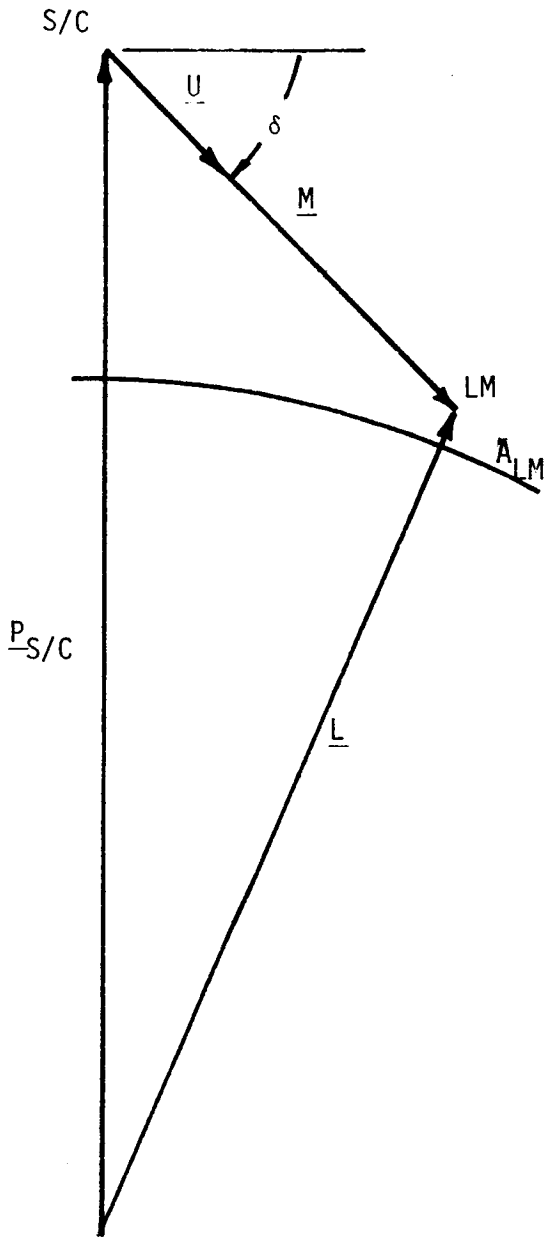

Figure VII

Landmark Tracker Geometry - Sighting Plan

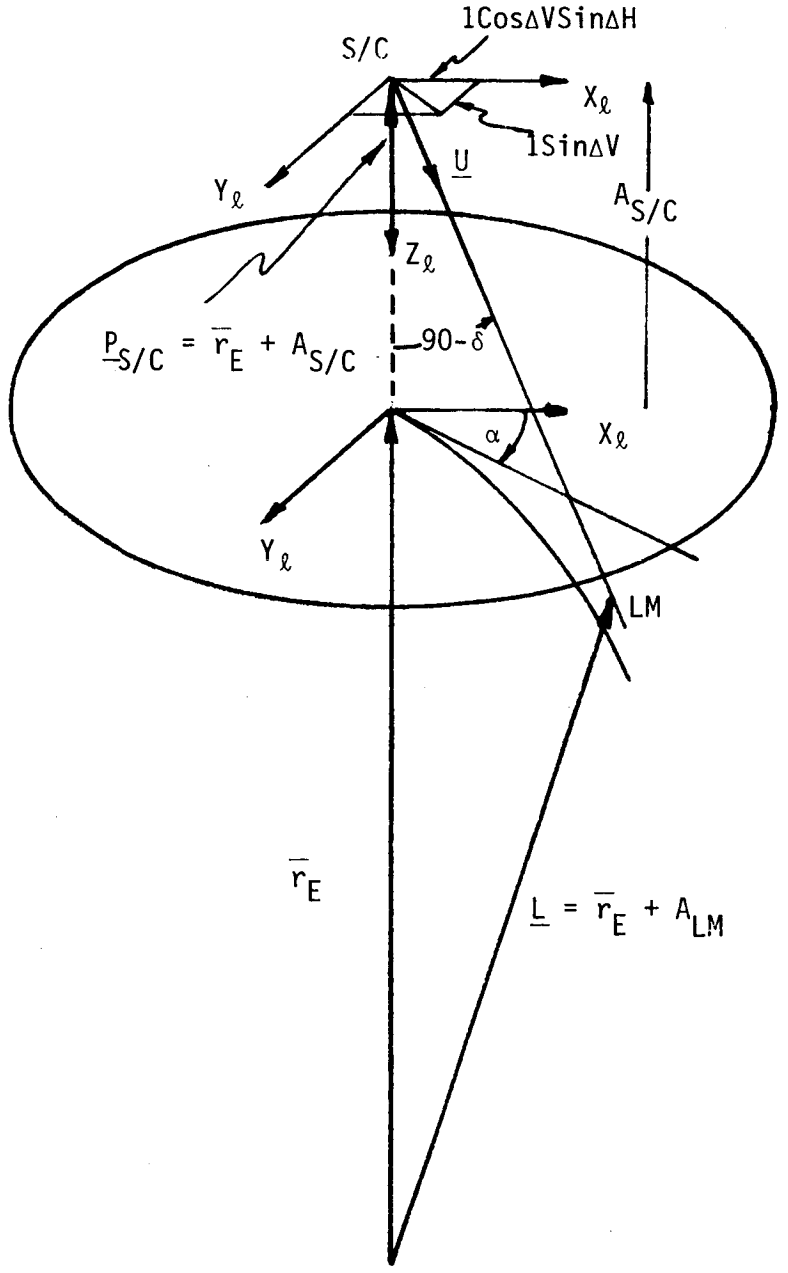

Figure VIII

Landmark Tracker Geometry - General

$$\underline{U\ell}' = \begin{bmatrix} U\ell x \\ U\ell y \end{bmatrix} = \begin{bmatrix} \mathrm{Cos}\Delta V \mathrm{Sin}\Delta H \\ \mathrm{Sin}\Delta V \end{bmatrix}$$

producing a H and V as shown in Figure VIII as sensor outputs. Since the sensor output will be corrupted by bias and noise, the sensed measurement will be:

$$\underline{Z\ell} = \begin{bmatrix} \Delta H_s \\ \Delta V_s \end{bmatrix} = \begin{bmatrix} \Delta H + b_H + v_H \\ \Delta V + b_V + v_V \end{bmatrix}$$

Where:

b_H, b_V = Component landmark tracker bias

V_H, V_V = Component landmark tracker zero mean random noise, $N(0,\sigma^2)$

The component biases and standard deviations (σ) are user selectables.

The landmark tracker measurement may be compensated for knowledge of instrument bias. The bias knowledge may be a priori or through estimation. The compensated sensor output will be:

$$\underline{\hat{Z}\ell} = \begin{bmatrix} \Delta H_c \\ \Delta V_c \end{bmatrix} = \begin{bmatrix} \Delta H_s - \hat{b}_H \\ \Delta V_s - \hat{b}_V \end{bmatrix}$$

Where:

LM = the landmark being used = f (L, λ, A_L)

A_L = the altitude of the landmark above the mean radius of the earth

L = longitude of the landmark

λ = latitude of the landmark

$\underline{L}$ = vector position of the landmark relative to the center of the earth

$\underline{P}_{S/C}$ = vector position of the spacecraft relative to the center of the earth

$A_{S/C}$ = altitude of the spacecraft above the mean radius of the earth

$\underline{M}$ = measurement vector from the spacecraft to the landmark

$\underline{U}$ = unit vector along $\underline{M}$

ΔH = the landmark tracker horizontal place angular deflection from the boresight axis

ΔV = the landmark tracker vertical plane angular deflection from the boresight axis

The dynamics model calculates the derivative of the spacecraft navigational state, which will be integrated to produce the navigational state vector. This is done in part by calculating the total acceleration of the spacecraft due to solar pressure and gravitation effects of the sun, moon, and earth, including fourth zonal harmonic terms. The total acceleration of the spacecraft can be

found by solving the following simultaneous equations:

$$\ddot{X}_1 = -X_1 \cdot \frac{\mu}{R^3} + g_1(t,X) + a_1(t,X)$$

$$\ddot{X}_2 = -X_2 \cdot \frac{\mu}{R^3} + g_2(t,X) + a_2(t,X)$$

$$\ddot{X}_3 = -X_3 \cdot \frac{\mu}{R^3} + g_3(t,X) + a_3(t,X)$$

where

$X = (X_1, X_2, X_3)^T$

μ = earth gravitational constant (3.98549120E + 14m^3/sec^2)

$R = (X_1^2 + X_1^2 + X_1^2)^{\frac{1}{2}}$

X_1, X_2, X_3 = coordinates of spacecraft

g_1, g_2, g_3 = accelerations caused by zonal harmonics of earth gravity

a_1, a_2, a_3 = solar radiation pressure perturbations, sun and moon gravity

The position state is advanced in time by numerical integration of the equations of motion consisting of external forces acting on the spacecraft. Analysis of various integration algorithms has shown that the Runge Kutta Gill 4th order numerical integration method is optimal for this application. It is self-starting, handles variable step sizes, and is sufficiently accurate. The Runge Kutta Gill method for numerically integrating differential equations is described here:

The change in the value of the function during the computing interval is calculated by

$$\Delta y = \frac{1}{6}\left(k_1 + 2(1-\mu)k_2 + 2(1+\mu)k_3 + k_4\right)$$

where

$k_1 = h \cdot f(t_n, y_n)$ $\qquad \mu = \sqrt{2/2}$

$k_2 = h \cdot f(t_n + \frac{1}{2}h, y_n + \frac{1}{2}k)$

$k_3 = h \cdot f\left(t_n + \frac{1}{2}h, y_n + (-\frac{1}{2}+\mu)k_1 + (1-\mu)k_2\right)$

$k_4 = h \cdot f\ t_n + h, y_n - \mu k_2 + (1+\mu)k_3\right)$

h = computing interval (seconds)

t_n = time of beginning of computing interval (seconds)

y_n = value of function at beginning of computing interval

The derivative function f is evaluated four times to calculate the change in the function being integrated during the computing interval.

Software Simulation

A Ground Control Point Simulation (GCPSIM) program has been configured to provide scientific simulations to predict the performance of the GCP detection system over a wide range of circumstances. Figure IX is a flow diagram of the

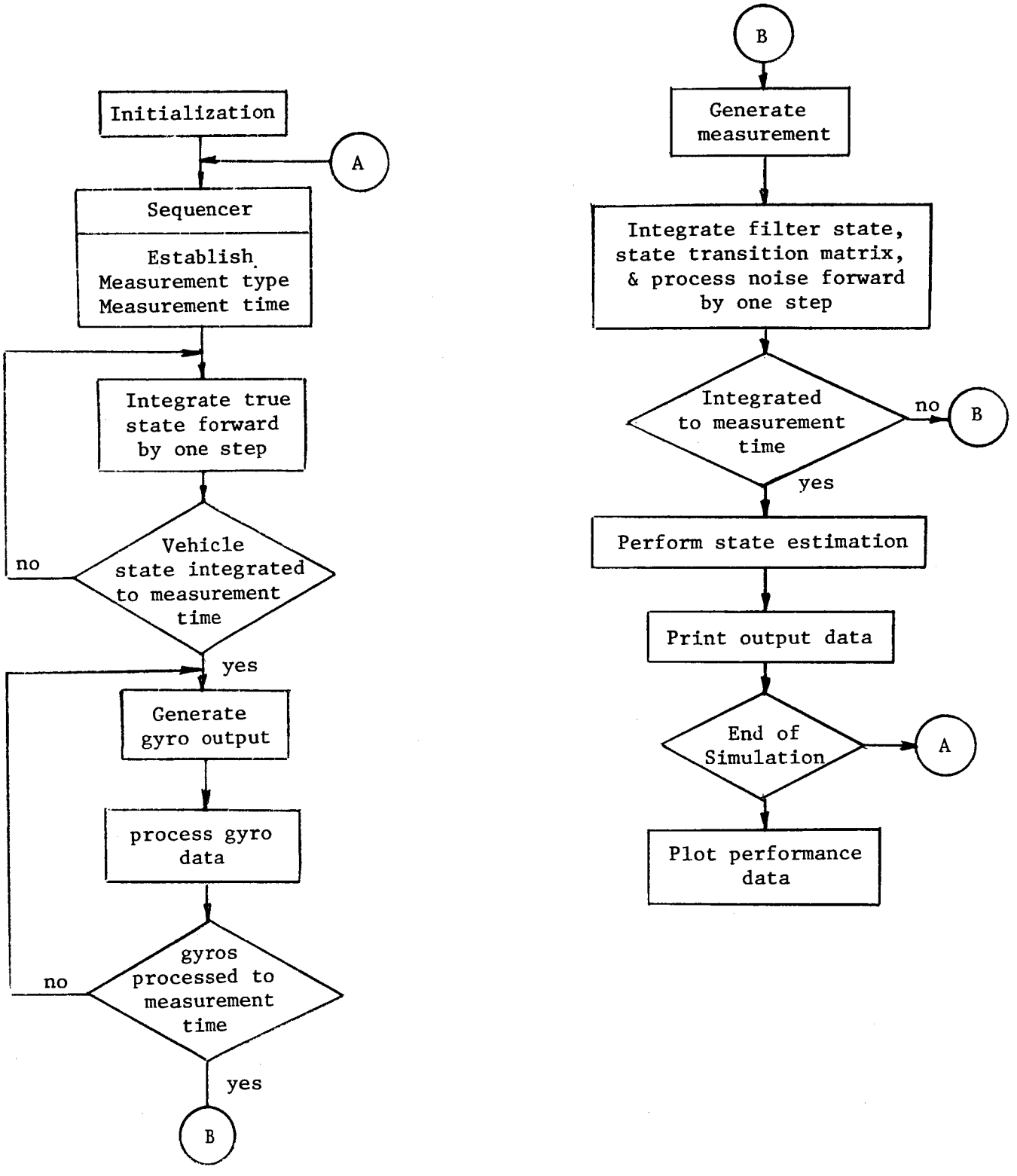

Figure IX. Flow Diagram of GCPSIM

simulation. GCPSIM has been designed to provide the ability to analyze the effect of various measurement sequences. This is especially important when studying the effect of GCP spacing, missed GCP sightings, and the expected accuracy after traversing a large body of water. The measurement sequencer designed for GCPSIM allows any mixture of GCP, GPS, or star tracker measurements and time delays (periods during which no measurements were made) of any length. The sequencer will determine the type of measurement and the time at which the measurement should be made. The true vehicle position state is then propagated forward to this time by integrating the nonlinear equations of motion with some additional process noise to account for modeling errors. The attitude state is propagated by looking up the body rates in an attitude profile table and integrating these rates.

The true vehicle state is used along with a measurement model to generate an ideal measurement vector. The ideal measurement is then corrupted with noise, bias, and misalignment terms and compensated for knowledge of these values. This allows a careful analysis of the effect of misalignment on the state solution. It is important to understand the effect of bias and misalignment between the landmark tracker and body axis because this is the largest unknown factor contributing to a pointing error. It is possible to calibrate the system for these misalignment errors, but it is difficult to model, for any length of time, the various processes which cause the misalignment. For example, thermal gradients across the vehicle and vibrational modes within the flexible structure are complex functions of such things as structural design, sun angle, physical properties of the material, and many other factors. These processes are the most difficult and least understood of all engineering problems. Therefore, significant emphasis will be placed on analyzing their effect on pointing accuracy.

The compensated measurements are used as inputs into an extended square root Kalman filter, which estimates the true vehicle state. The extended filter propagates the estimated navigation state, the state transition matrix, and the process noise array between measurements by integrating the various differential equations using a fourth order Runge Kutta Gill process. The estimated attitude state is propagated by a gyro model which corrupts the output with gyro drift, noise, nonorthogonality, scale factor, and misalignment. The gyro output is compensated, in a similar fasion to the measurement model, by subtracting off knowledge of these values.

The estimated state is used to form an estimated measurement which in turn is subtracted from the true measurement to obtain a residual. It is this measurement residual and a calculated Kalman gain which are used to update the state estimate. By comparing the state estimate with the true state, a direct error analysis can be performed. The entire process continues until the spacecraft is propagated forward to the run stop time.

GCPSIM has been designed to allow maximum flexibility in the analysis of an onboard landmark tracker. Types of analyses to be performed under the contract are indicated in Table III.

Table III. Detailed Breakdown of Analysis

- Sensitivity to:	sensor accuracies sensor misalignment GCP sighting frequencies GCP location in FOV knowledge of gyro bias, noise, non-orthogonality, misalignment knowledge of earth fixed coordinates measurement sequence
- Accuracy given:	1/10th pixel correlation 1 pixel correlation backup system (star tracker)
- Rate of Convergence:	after using backup using 1/10th pixel correlation accuracy using 1 pixel correlation accuracy
- Rate of Divergence:	when missing GCP sightings
- Ability to solve for:	sensor misalignment earth fixed coordinates

Summary

Development of a new generation of remote sensing systems has become a necessity for both NASA and the user community in order to fulfill the goals of future missions. In the past there has been a lack of coordination between the scientific user community and the engineers responsible for spacecraft design. This has resulted in a physical separation between the design and implementation of the science payload and the control system. This design philosophy must change if the future mission requirements are to be met.

The primary emphasis in the guidance and control system must shift from simply estimating the ephemeris and attitude of the spacecraft to estimating the position of the science sensors FOV on the earth's surface. This shift of emphasis will impact the design of the entire spacecraft. For example, if the science sensor is to be used as a primary attitude sensor, it is desirable to place the gyro package in close proximity to that sensor in order to reduce the misalignment between the two. This suggests that the current Multi-Mission Spacecraft (MMS) configuration, which provides a physical separation between the payload and the guidance and control system, will not satisfy the requirements of many future remote sensing missions.

Martin Marietta, under contract to NASA GSFC is developing an approach to remote sensing missions which eliminate the separation between the science instrument and the guidance and control system. Preliminary results obtained in the analysis of this system show great promise for automation of the end-to-end remote sensing process.

References

1) Schappell, R. T. and Tietz, J. C., "Landmark Identification and Tracking Experiments," Remote Sensing of Earth from Space: Role of "Smart" Sensors, edited by Roger A. Breckenridge, Vol. 67 of Progress in Astronautics and Aeronautics.

2) Final Report of "On-Board Image Registration Study" prepared by TRW for NASA GSFC under Contract NAS5-23725.

3) Carney, P. C., et al, "On-Board Attitude Determination System Final Report," Martin Marietta, 1978, NAS4-23428 Mod. 27.

4) White, R. L., et al, "Use of Known Landmarks for Satellite Navigation," 1975, AIAA Paper No. 75-1097.

5) White, R. L., et al, "Attitude and Orbit Estimation Using Stars and Landmarks," 1974, IEEE Transactions on Aerospace and Electronic Systems, Vol. AES-11, No. 2.

6) Toda, N. F. and Schlee, F. H., "Autonomous Orbital Navigation by Opitcal Tracking of Unknown Landmarks," 1967, Journal of Spacecrafts and Rockets, Vol. 4, No. 12.

7) Aldrich, D. H., "Interferometer Landmark Tracker Navigation System," 1974, NEACON Journal.

8) Barnea, D. I. and Silverman, H. F., "A Class of Algorithms for Fast Digital Image Registration," IEEE Transactions on Computers, Vol. C-21, No. 2, February, 1972.

9) Lowrie, J. W. and Schappell, R. T., "Guidance and Control for an Adaptive Information Retrieval System," 1980, American Astronautical Society Paper No. AAS 80-013.

THE RESURRECTION OF LANDSAT-2 ATTITUDE CONTROL SYSTEM (ACS)

Peter S. Hui
Goddard Space Flight Center

ABSTRACT

The yaw control reaction wheel in LANDSAT-2 failed in November, 1979. Attempts were made to maintain attitude control using magnetic and gravity-gradient torque commands from the ground. However, before definitive results could be obtained, the wheel decided to revive itself in May, 1980, and the ACS lived happily ever after.

DOUBLY-PERIODIC ORBITS IN THE SUN-EARTH-MOON SYSTEM

R. Farquhar and D. Muhonen
Goddard Space Flight Center
and
D. Dunham
Computer Sciences Corporation

ABSTRACT

A series of periodic orbits in the Earth-Moon circular restricted problem of three bodies has been found which is ideally suited for exploring the Earth's geomagnetic tail. The mean apsidal motion of the basic highly elliptical Earth orbit is maintained at about one degree per day by a sequence of lunar swingbys, keeping the apogees in the anti-Sun direction. Hence, the orbits are periodic in reference frames rotating at both lunar and solar rates. Apogee distances are alternately raised and lowered by the lunar swingby maneuvers. Several categories of these "Sun-synchronous" double lunar swingby orbits are identified. The strength and flexibility of this new trajectory concept is demonstrated with real-world simulations. A large variety of trajectory shapes can be used to explore the Earth's geomagnetic tail between 60 and 250 R_E. Some of these orbits will be shown in a movie. NASA plans to use this technique during its proposed four-spacecraft program called Origins of Plasmas in the Earth's Neighborhood (OPEN). More details can be found in AIAA Paper 80-0112, "A New Trajectory Concept for Exploring the Earth's Geomagnetic Tail."

The following plots are a representative sample of the many existing types of these doubly-periodic orbits. The gravity model employed consisted of the Earth and Moon point masses, and the Moon's orbit was assumed to be circular. A patched-conic method was used for orbit computations. All trajectories are in the moon's orbital plane, and a projection of the Sun-Earth line is shown as a fixed reference. A classification scheme is used whereby each periodic orbit is specified by four numbers, [A, B, C, D], where:

"A" is the approximate number of months between lunar swingbys in the inner segment.

"B" is the number of complete circuits (apogees) in the inner segment.

"C" is the approximate number of months between lunar swingbys in the outer segment.

"D" is the number of complete circuits (perigees) in the outer segment.

"D" equals zero with most orbits applicable to magnetospheric studies, so these are specified by only three numbers, [A, B, C]. For "D" larger than zero, the orbits become butterfly shaped, with the spacecraft spending most of its time far from the anti-Sun line outside the geomagnetic tail. For "C" greater than 3 and "D" equals zero, the outer loop extends well beyond the Sun-Earth L_2 libration point, where strong solar perturbations make the restricted Earth-Moon model unrealistic.

DOUBLE LUNAR SWINGBY ORBIT - (1.1.1) CLASS

PERIGEE 5.9 RE
APOGEE-1 86 RE
APOGEE-2 141 RE

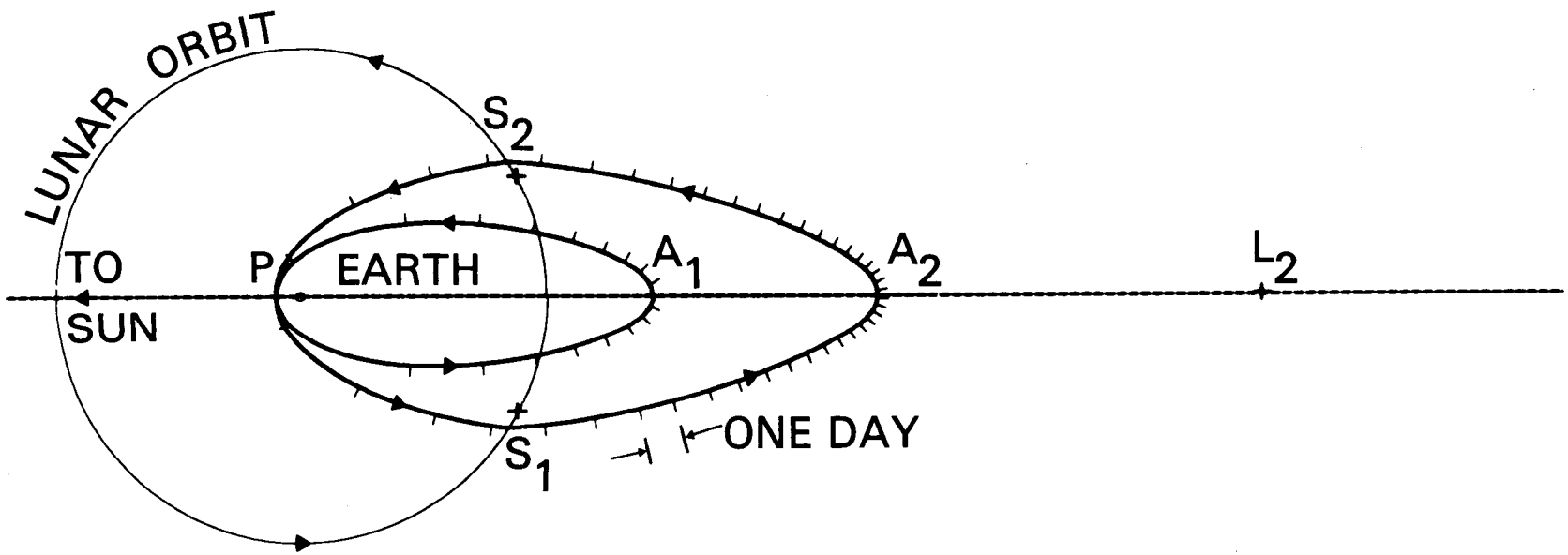

PERILUNE RADIUS AT LUNAR SWINGBYS 27.664 KM

DOUBLE LUNAR SWINGBY ORBIT - (1.1.2) CLASS

PERIGEE 5.4 RE
APOGEE-1 87 RE
APOGEE-2 205 RE

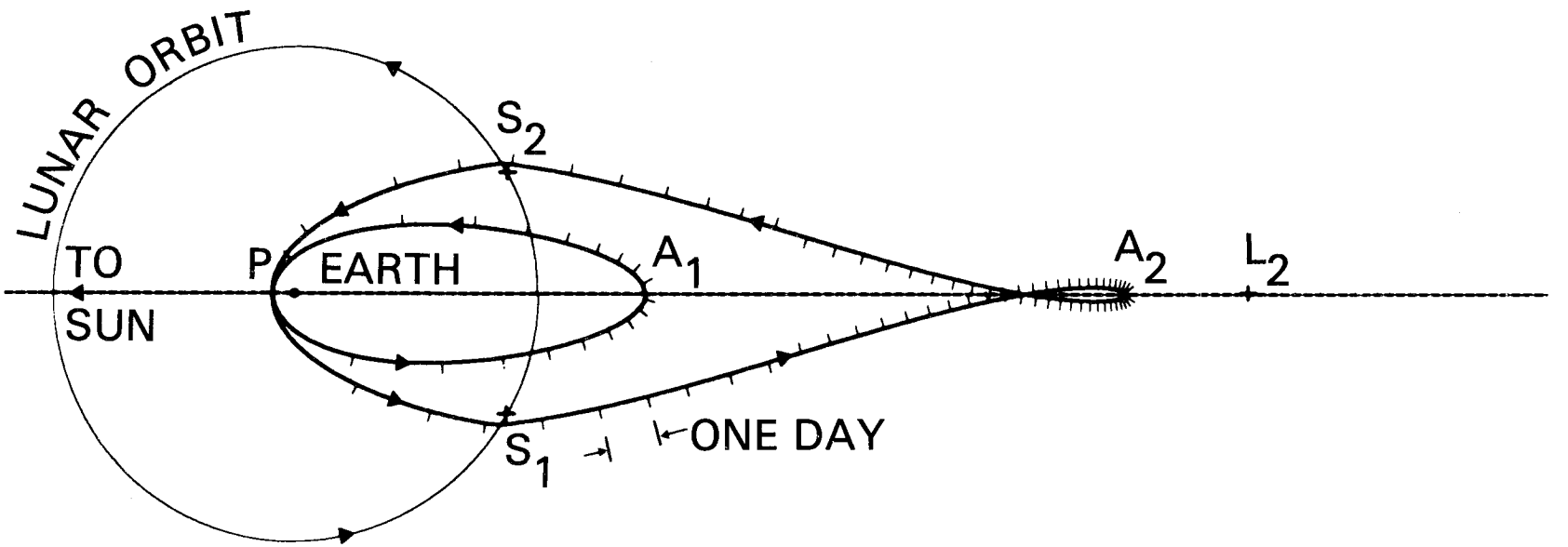

PERILUNE RADIUS AT LUNAR SWINGBYS 18.104 KM

DOUBLE LUNAR SWINGBY ORBIT - (1.1.3) CLASS

PERIGEE 7.1 RE
APOGEE-1 82 RE
APOGEE-2 257 RE

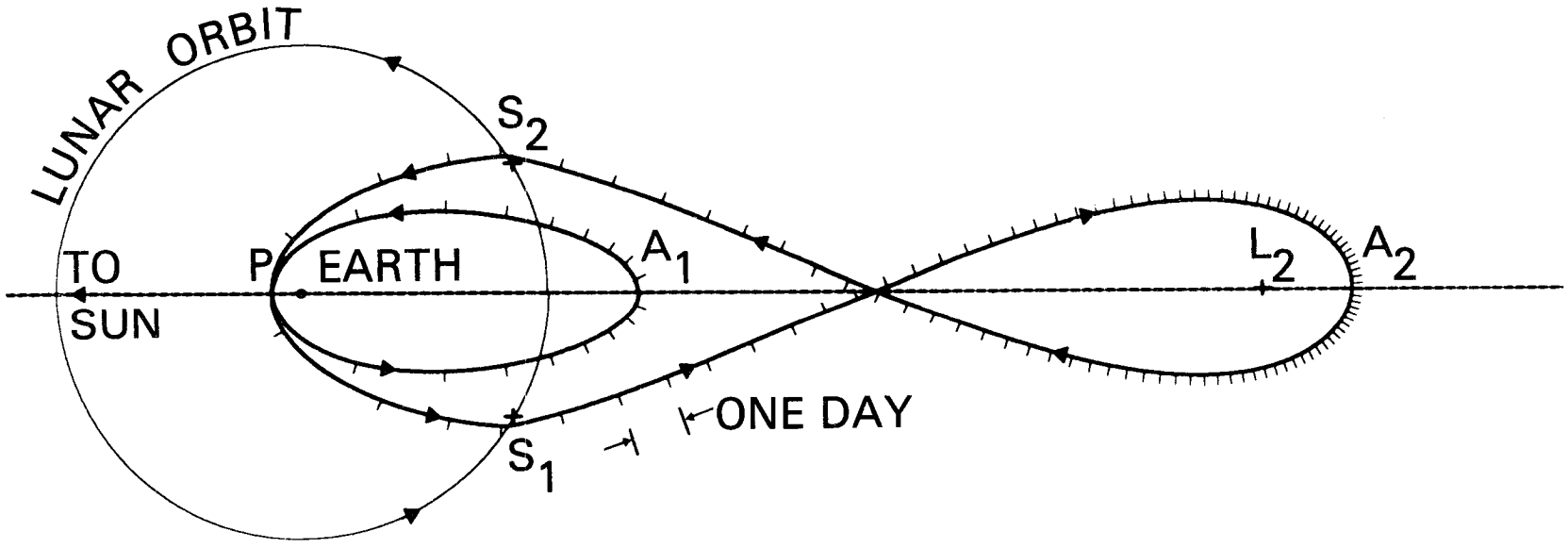

PERILUNE RADIUS AT LUNAR SWINGBYS 15.766 KM

DOUBLE LUNAR SWINGBY ORBIT - (2.3.1) CLASS

PERIGEE 6.0 RE
APOGEE-1 75 RE
APOGEE-2 141 RE

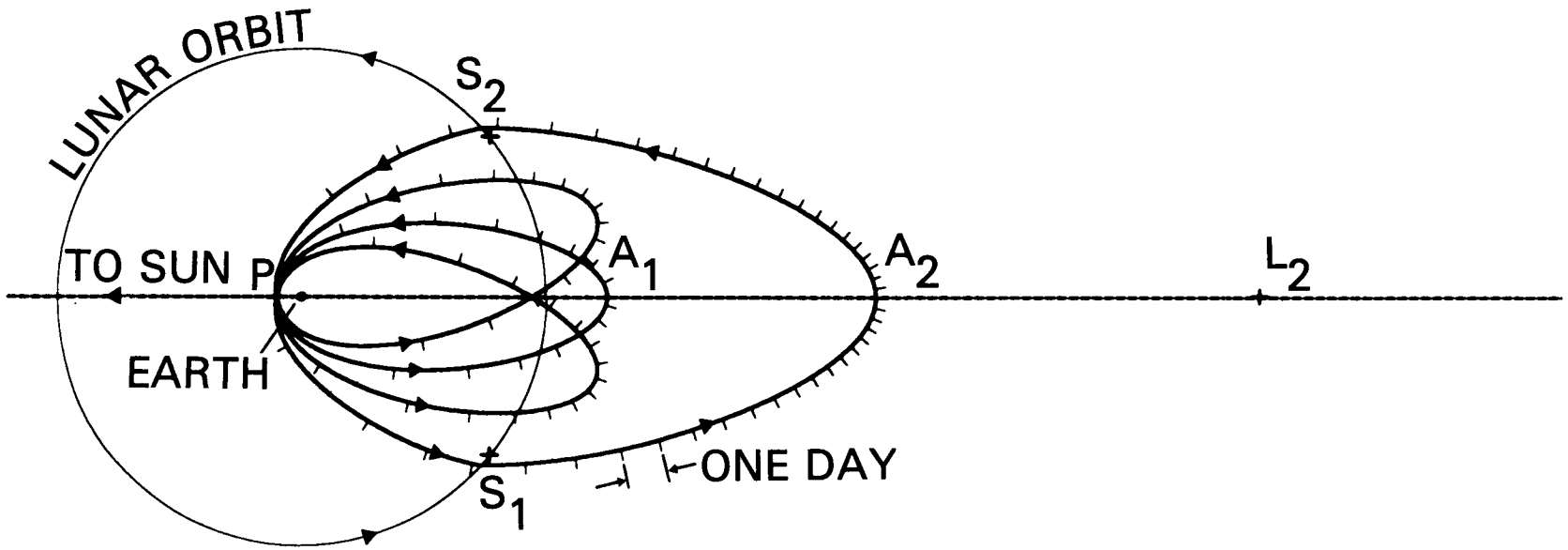

PERILUNE RADIUS AT LUNAR SWINGBYS 19.936 KM

DOUBLE LUNAR SWINGBY ORBIT - (2.4.2) CLASS

PERIGEE 1.0 RE
APOGEE-1 67 RE
APOGEE-2 205 RE

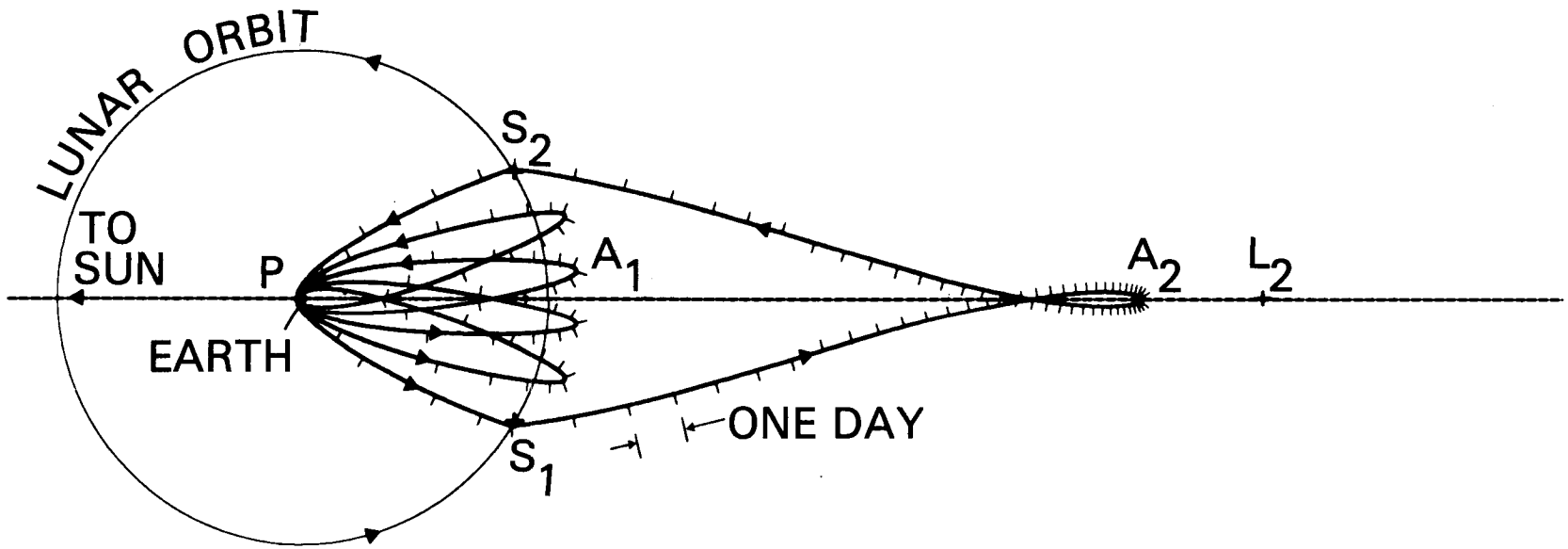

PERILUNE RADIUS AT LUNAR SWINGBYS 7.831 KM

DOUBLE LUNAR SWINGBY ORBIT - (3,4,3) CLASS

PERIGEE 16.2 RE
APOGEE-1 72 RE
APOGEE-2 249 RE

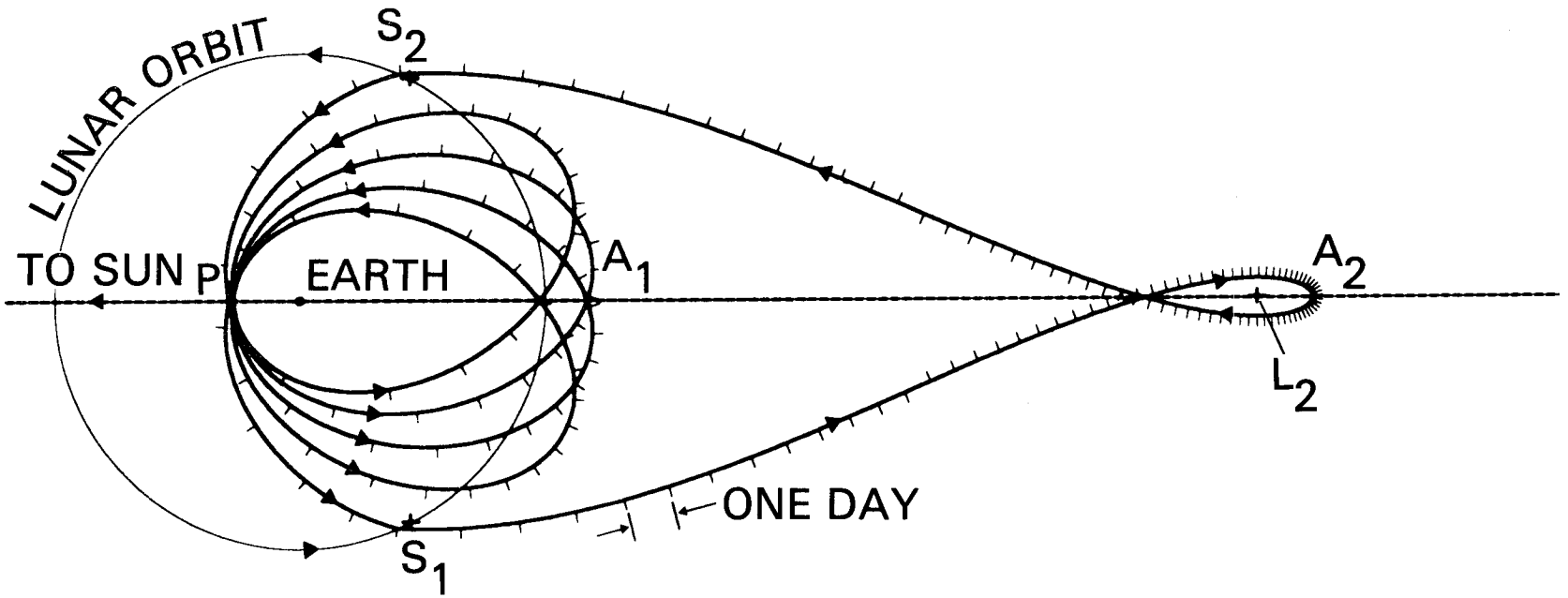

PERILUNE RADIUS AT LUNAR SWINGBYS 19.712 KM

DOUBLE LUNAR SWINGBY ORBIT - (3.5.1) CLASS

PERIGEE 8.5 RE
APOGEE-1 70 RE
APOGEE-2 139 RE

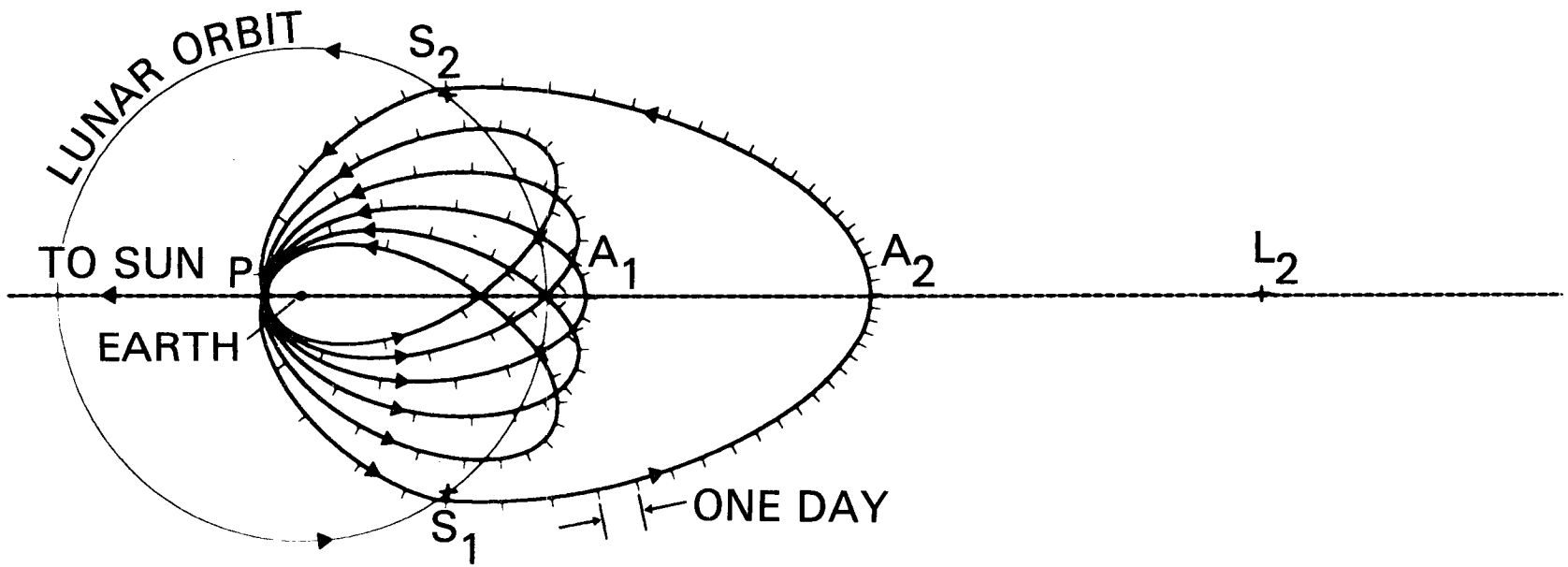

PERILUNE RADIUS AT LUNAR SWINGBYS 19.489 KM

DOUBLE LUNAR SWINGBY ORBIT - (3.6.2) CLASS

PERIGEE 3.9 RE
APOGEE-1 66 RE
APOGEE-2 202 RE

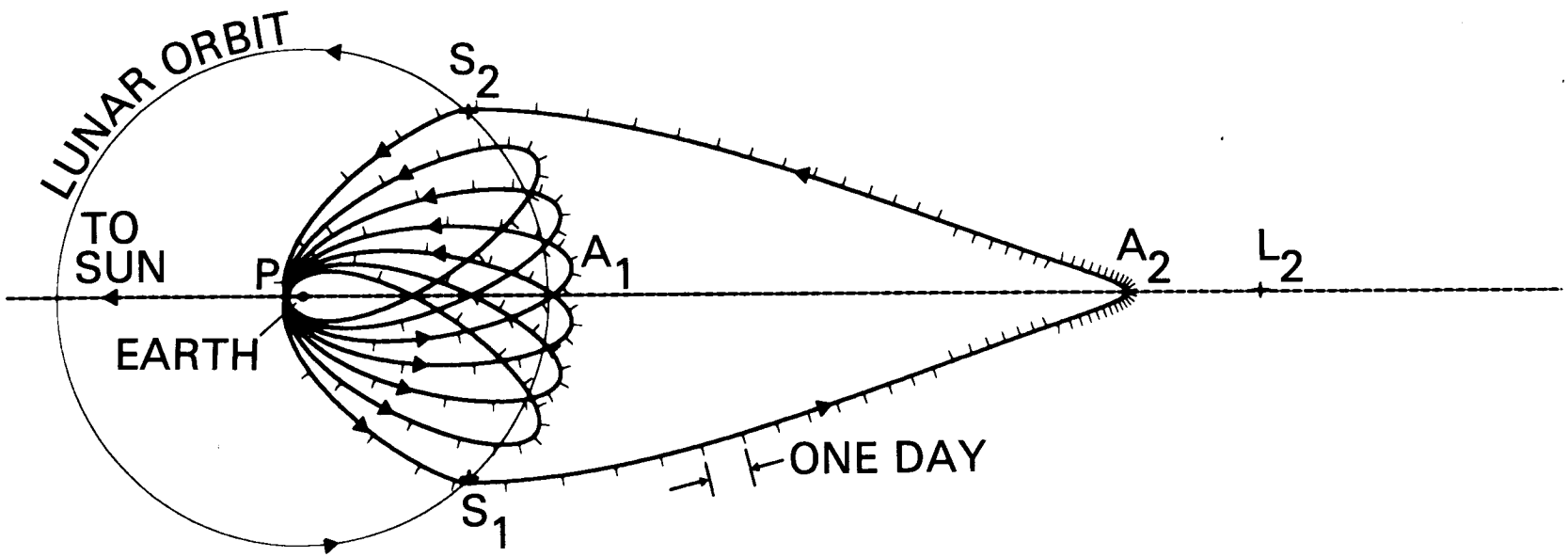

PERILUNE RADIUS AT LUNAR SWINGBYS 9.536 KM

DOUBLE LUNAR SWINGBY ORBIT - (3.7.3) CLASS

PERIGEE 2.0 RE
APOGEE-1 61 RE
APOGEE-2 256 RE

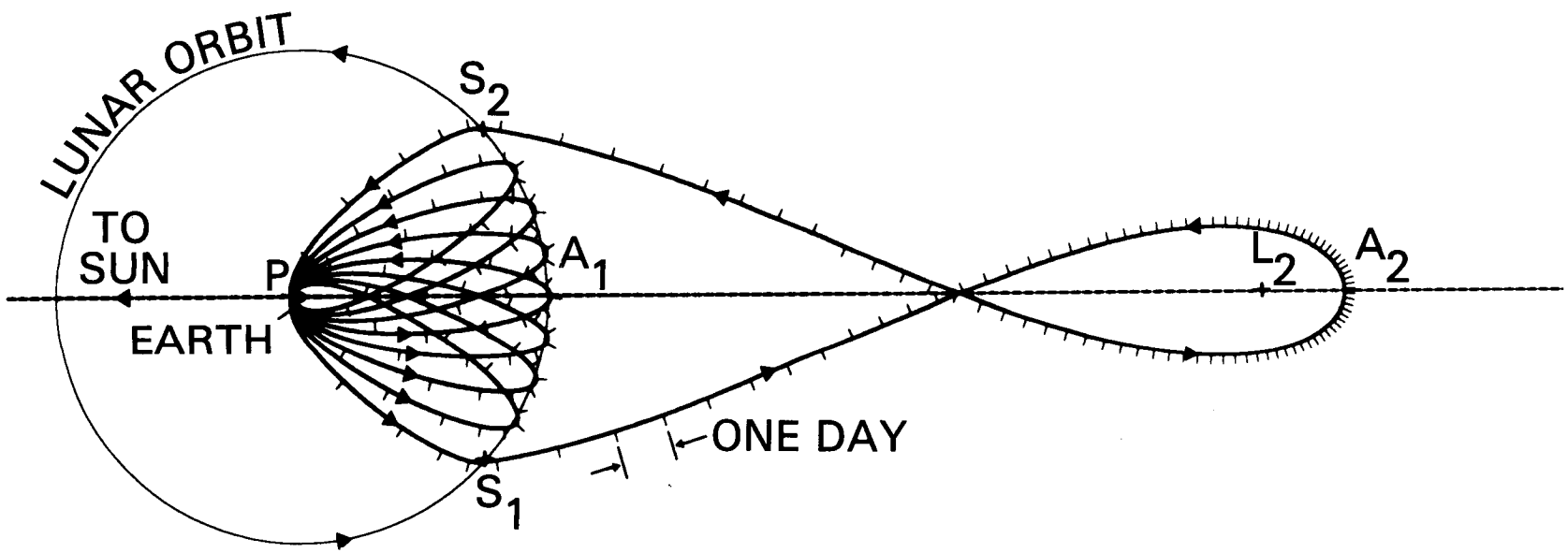

PERILUNE RADIUS AT LUNAR SWINGBYS 4.795 KM

DOUBLE LUNAR SWINGBY ORBIT - (4.8.1) CLASS

PERIGEE 7.1 RE
APOGEE-1 64 RE
APOGEE-2 139 RE

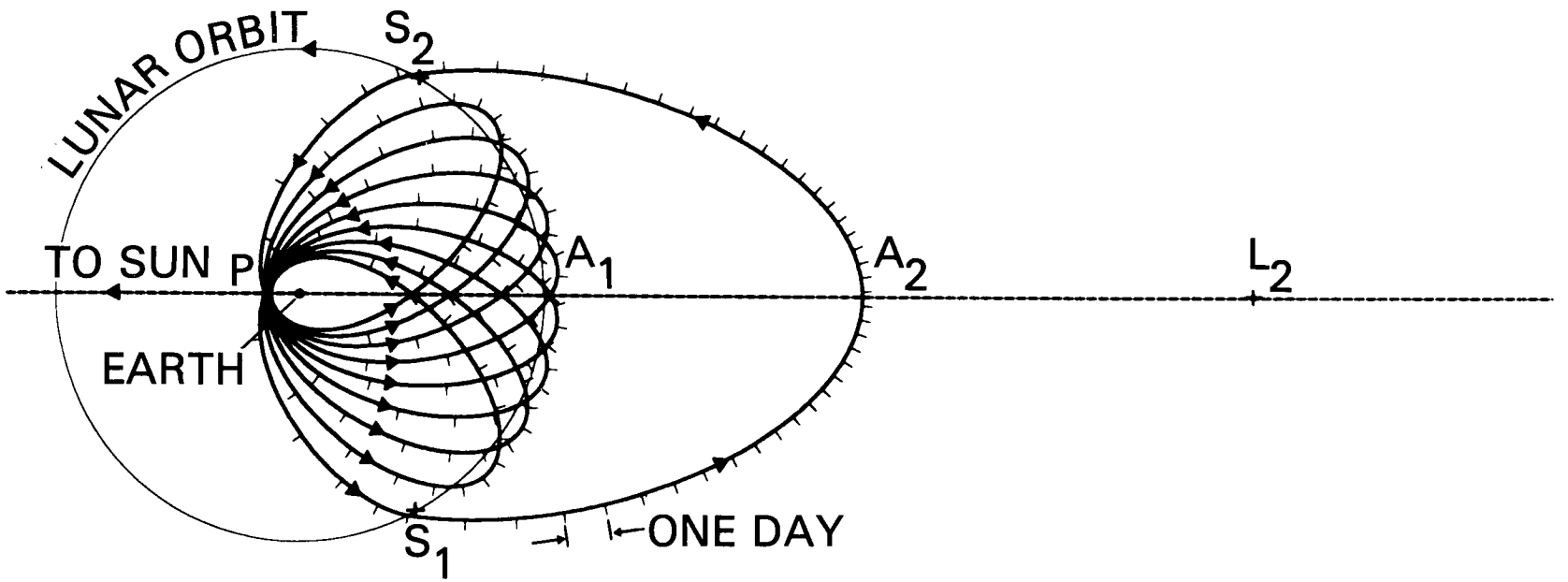

PERILUNE RADIUS AT LUNAR SWINGBYS 13.404 KM

DOUBLE LUNAR SWINGBY ORBIT - (4.9.2) CLASS

PERIGEE 4.1 RE
APOGEE-1 62 RE
APOGEE-2 200 RE

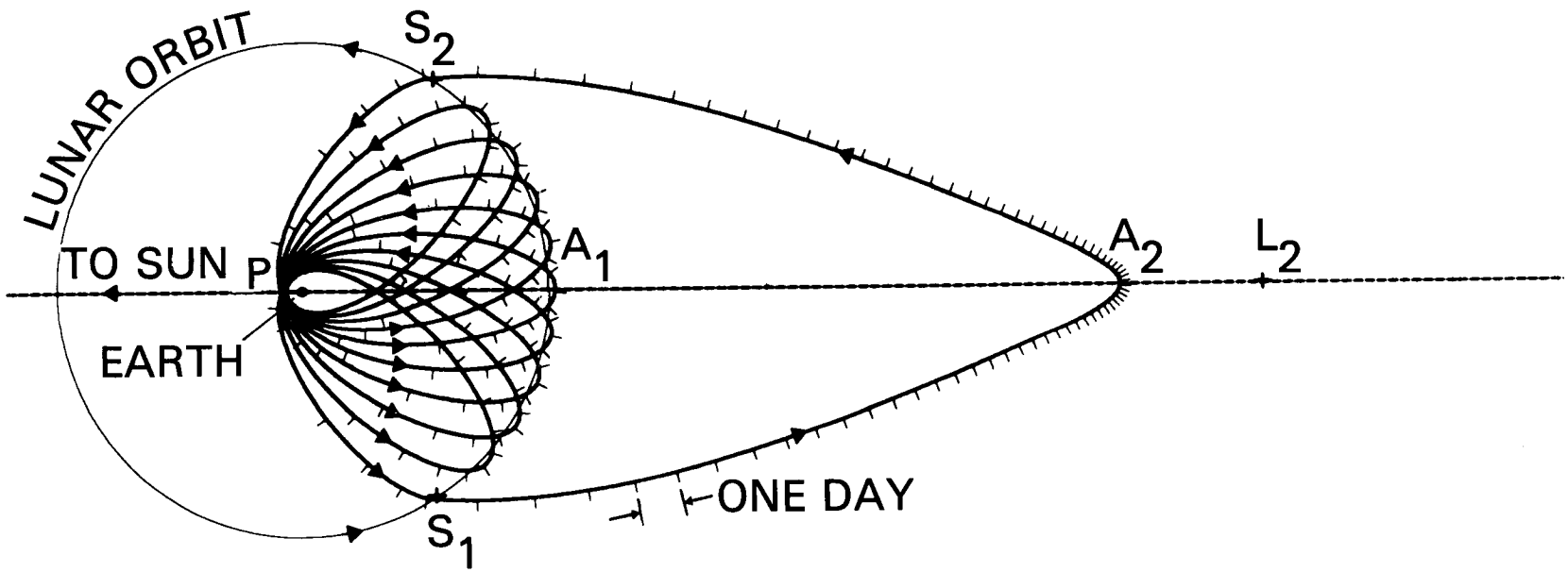

PERILUNE RADIUS AT LUNAR SWINGBYS 6.944 KM

DOUBLE LUNAR SWINGBY ORBIT - (5.10.3) CLASS

PERIGEE 9.9 RE
APOGEE-1 62 RE
APOGEE-2 248 RE

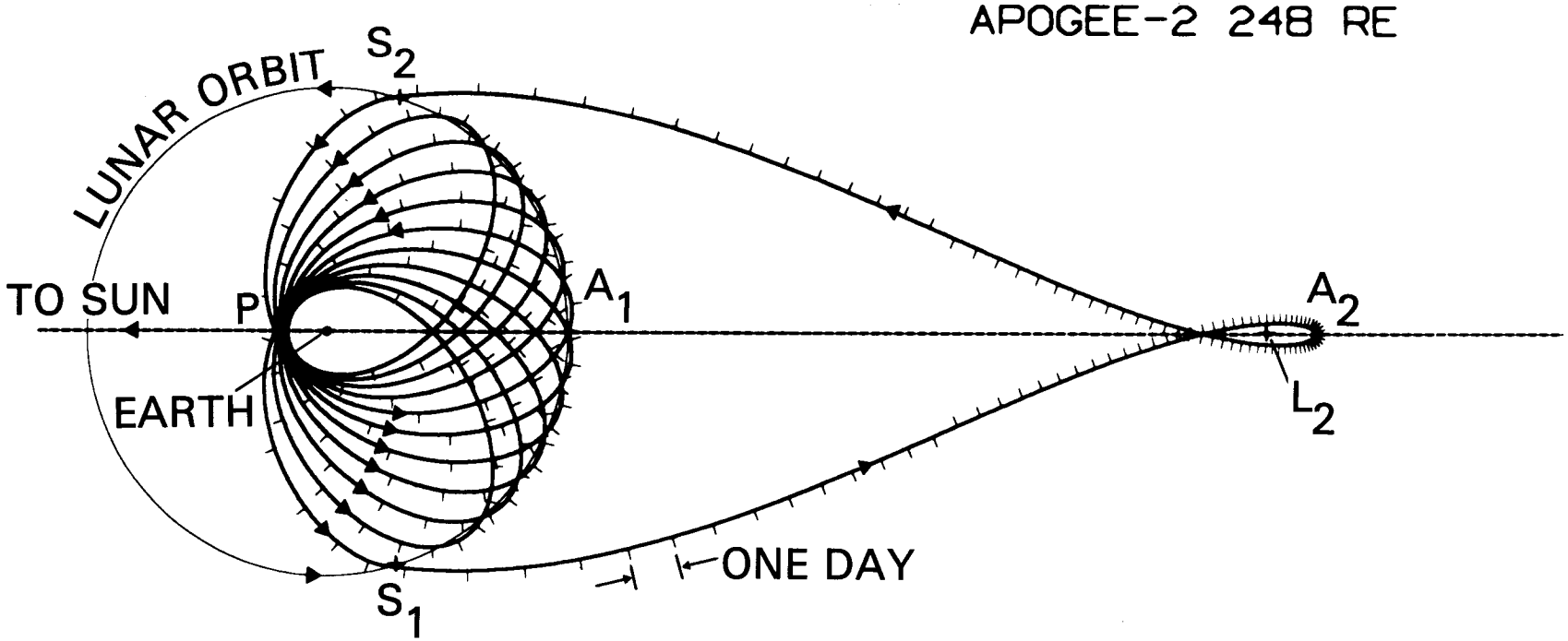

PERILUNE RADIUS AT LUNAR SWINGBYS 7.924 KM

DOUBLE LUNAR SWINGBY ORBIT - (5.11.1) CLASS

PERIGEE 6.7 RE
APOGEE-1 61 RE
APOGEE-2 138 RE

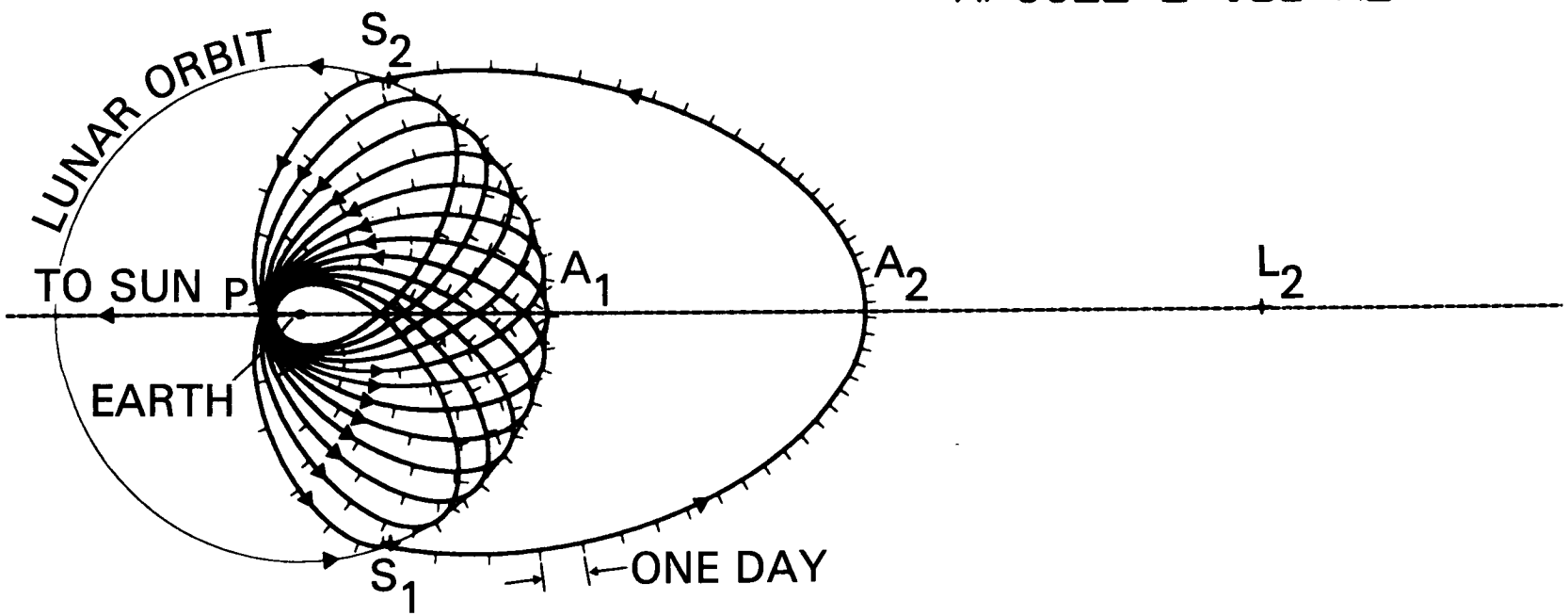

PERILUNE RADIUS AT LUNAR SWINGBYS 8.070 KM

DOUBLE LUNAR SWINGBY ORBIT - (1.1.3.1) CLASS

PERIGEE-1	11.4	RE
PERIGEE-2	33	RE
APOGEE-1	73	RE
APOGEE-2	148	RE

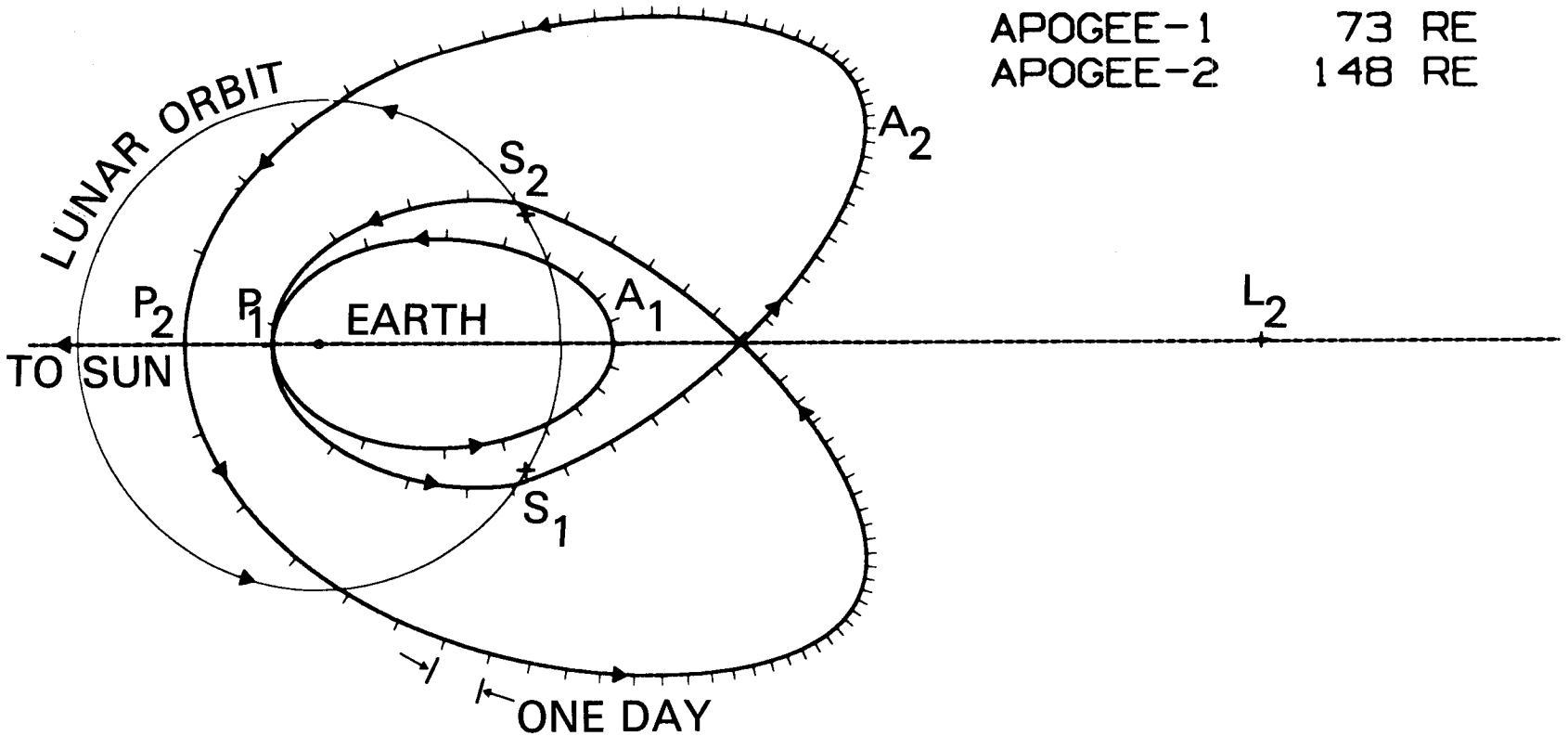

PERILUNE RADIUS AT LUNAR SWINGBYS 24.116 KM

DOUBLE LUNAR SWINGBY ORBIT - (1.1.4.2) CLASS

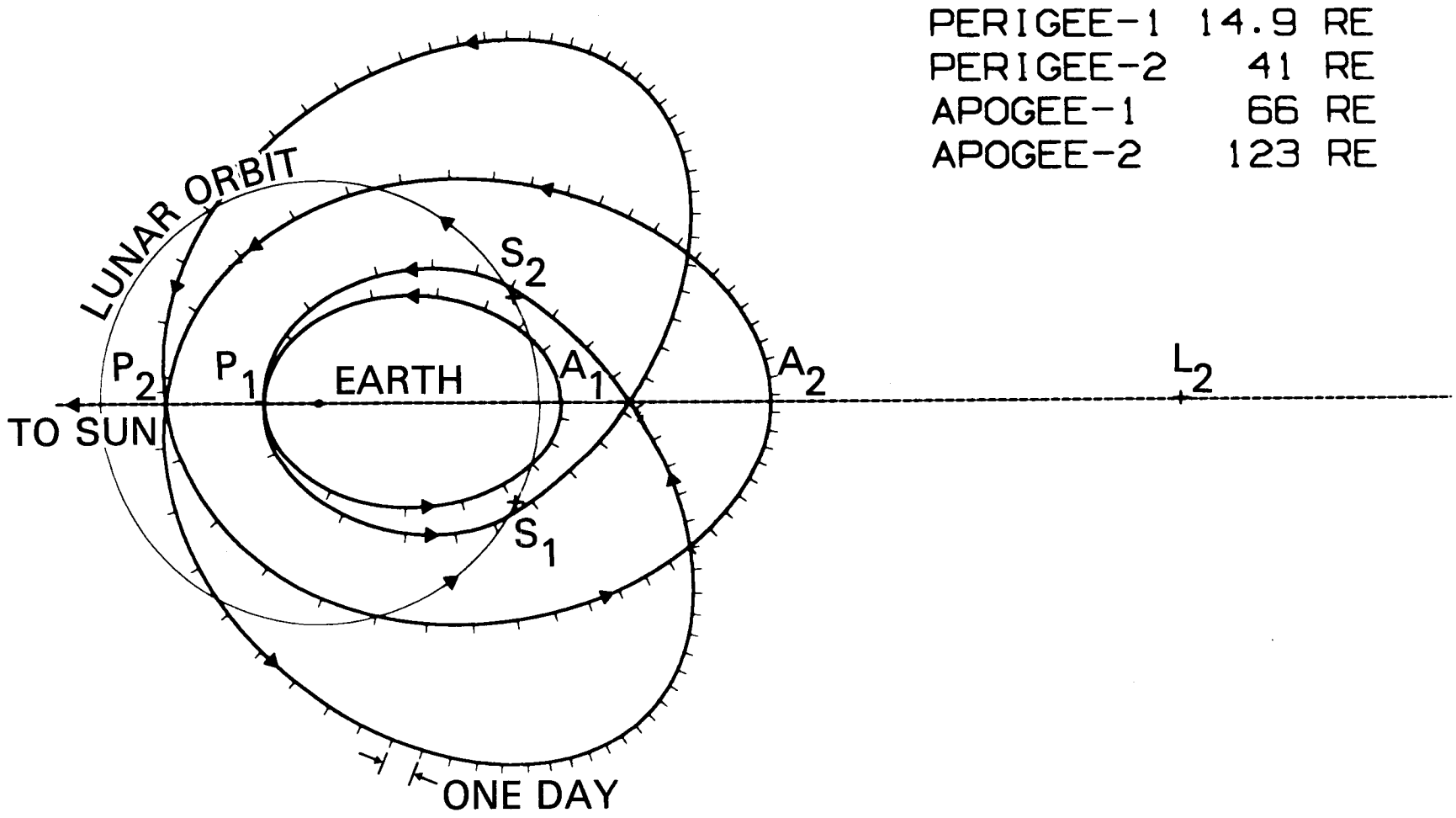

PERILUNE RADIUS AT LUNAR SWINGBYS 27.354 KM

DOUBLE LUNAR SWINGBY ORBIT - (2.4.2.1) CLASS

PERIGEE-1	4.4 RE
PERIGEE-2	27 RE
APOGEE-1	62 RE
APOGEE-2	118 RE

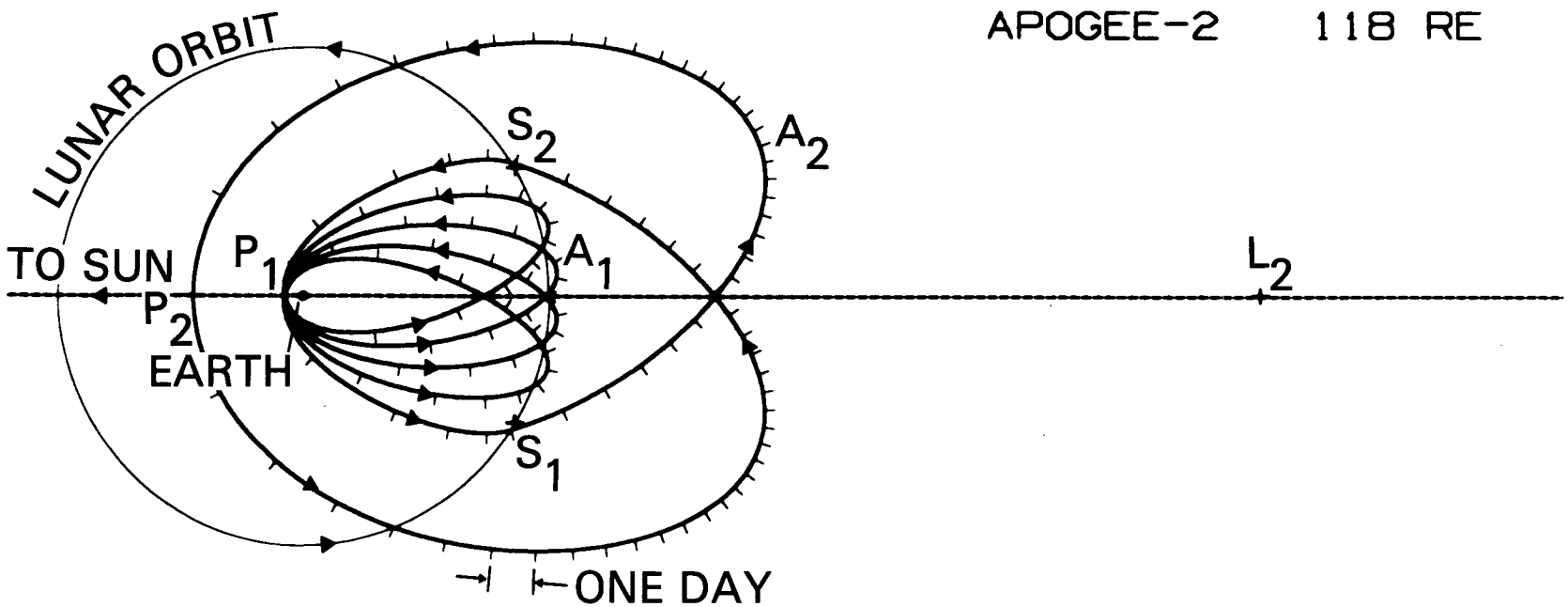

PERILUNE RADIUS AT LUNAR SWINGBYS 11.448 KM

DOUBLE LUNAR SWINGBY ORBIT - (3.6.2.1) CLASS

PERIGEE-1	7.8 RE
PERIGEE-2	35 RE
APOGEE-1	61 RE
APOGEE-2	113 RE

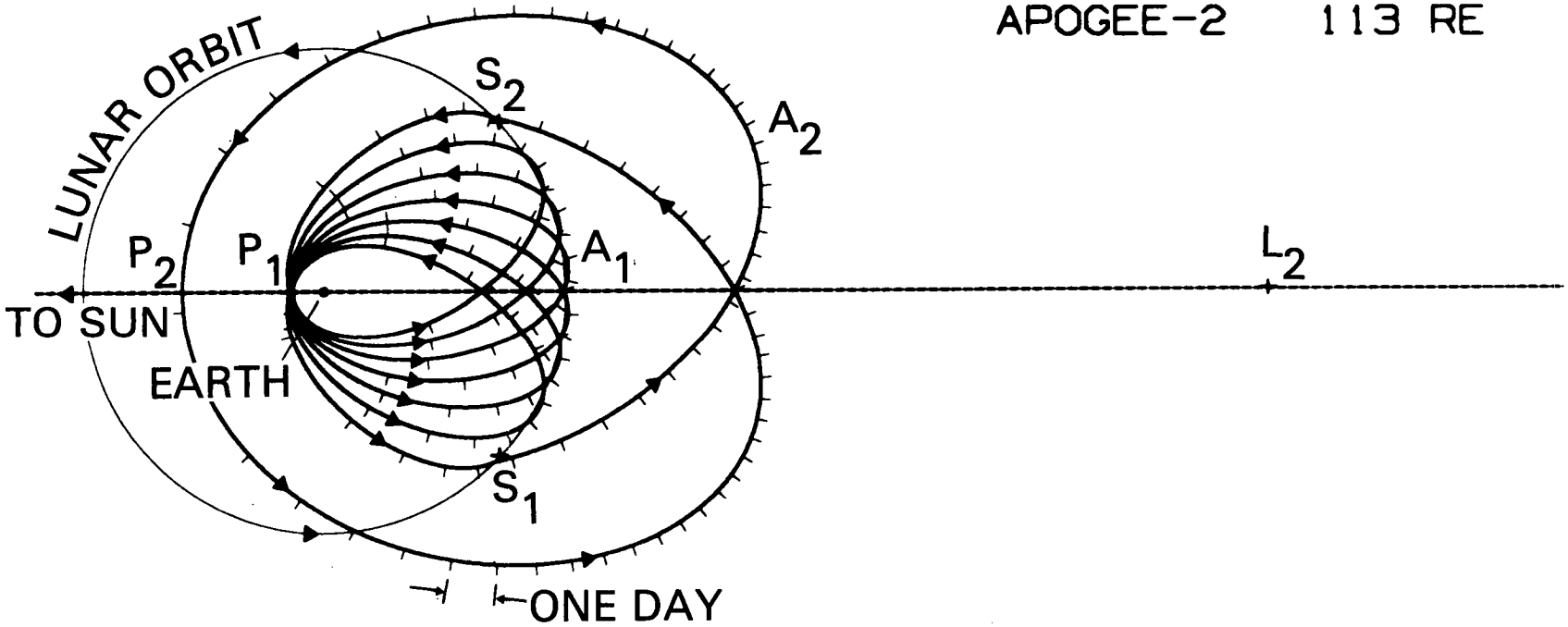

PERILUNE RADIUS AT LUNAR SWINGBYS 12.578 KM

SESSION IV

E. J. Lefferts, Chairman

ATTITUDE GROUND SUPPORT SYSTEM FOR THE SOLAR MAXIMUM MISSION SPACECRAFT

Dr. G. Nair

Computer Sciences Corporation, Silver Spring, Md.

ABSTRACT

The SMM Attitude Ground Support System (AGSS) supports the acquisition of spacecraft roll attitude reference, performs the in-flight calibration of the attitude sensor complement, supports onboard control autonomy via onboard computer data base updates, and monitors onboard computer (OBC) performance. Initial roll attitude acquisition is accomplished by obtaining a coarse 3-axis attitude estimate from magnetometer and Sun sensor data and subsequently refining it by processing data from the Fixed Head Star Trackers. In-flight calibration of the attitude sensor complement is achieved by processing data from a series of slew maneuvers designed to maximize the observability and accuracy of the appropriate alignments and biases. To ensure autonomy of spacecraft operation, the AGSS selects guide stars and computes sensor occultation information for uplink to the OBC. The onboard attitude control performance is monitored on the ground through periodic attitude determination and processing of OBC data in downlink telemetry. In general, the control performance has met mission requirements. However, software and hardware problems have resulted in sporadic attitude reference losses.

1. INTRODUCTION

The Solar Maximum Mission (SMM) spacecraft, first in the Multimission Modular Spacecraft (MMS) series, was launched on February 14, 1980. Seven payload instruments located in the SMM observatory study a large variety of solar-flare-related phenomena at the peak of the 11-year sunspot cycle. A summary of the experimental objectives of SMM is given by NASA GSFC (Reference 1). The SMM spacecraft components are shown in Figure 1. The attitude control objectives of SMM are to point the roll axis as defined by the experimenters as a result of coalignment to any point on the Sun's disk with an accuracy of ±5 arc-seconds and to maintain roll reference about the roll axis accurate to 0.1 degree. A comprehensive summary of the attitude determination and control functions as well as the attitude accuracy requirements for SMM are given by Guha (Reference 2). Notice, however, that the primary (roll) axis reference has been changed since then from the FPSS1 boresight to the experimenters' coalignment direction.

Ground attitude support for SMM is provided at the Goddard Space Flight Center (GSFC) by the Attitude Determination and Control Section (ADCS) and Computer Sciences Corporation. The major support functions are

- Acquisition of roll reference about the payload roll axis
- In-flight calibration of the attitude sensor complement consisting of two 3-axis magnetometers (TAMs), three 2-channel inertial reference units (IRUs), two Fine Pointing Sun Sensors (FPSSs), and two Fixed Head Star Trackers (FHSTs)
- Support of autonomous spacecraft operation under the control of an OBC for a period of up to 3 days

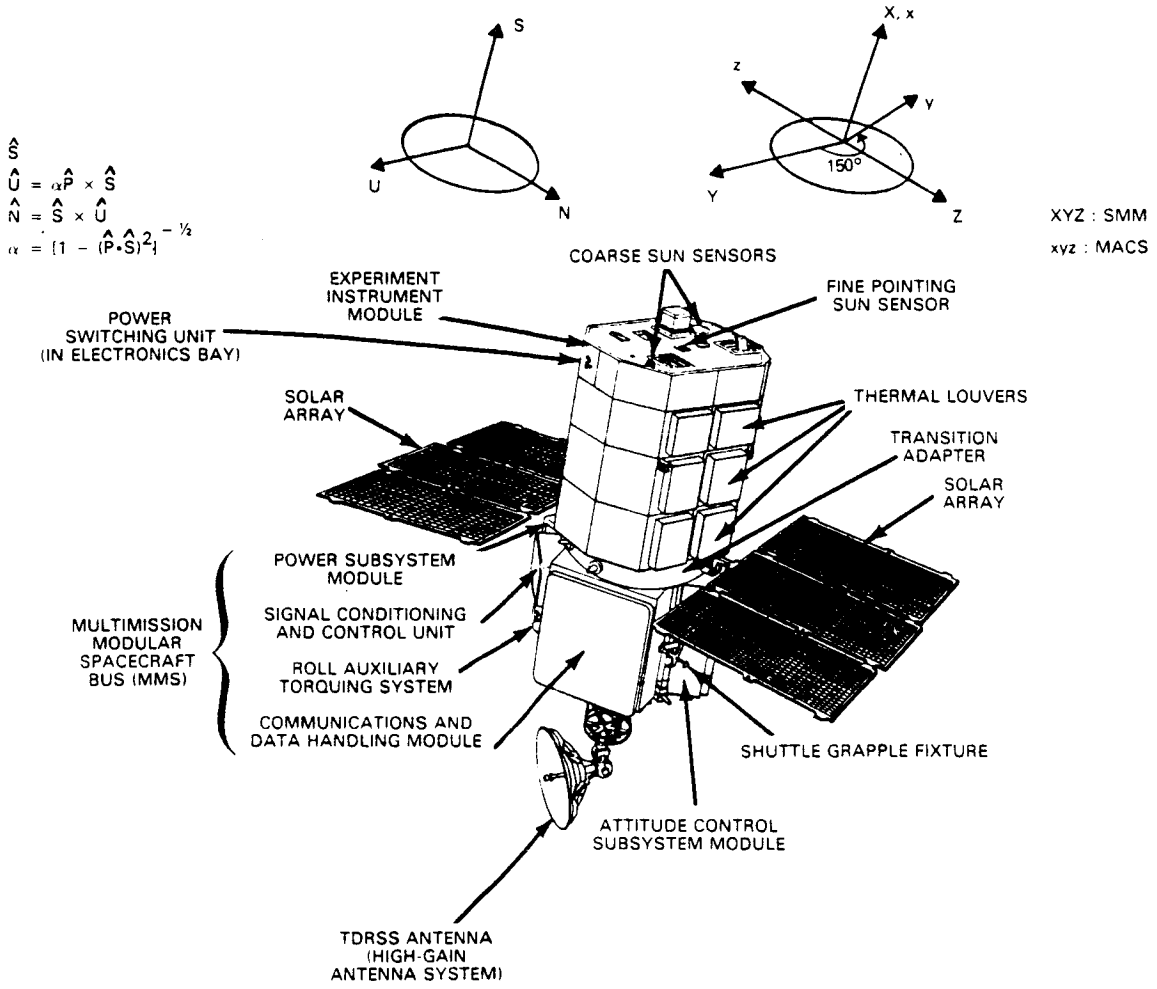

NOTE: ROLL, PITCH, YAW ARE 1-2-3 EULER ROATION ANGLES THAT TRANSFORM VECTORS FROM SUN FRAME TO SMM BODY FRAME.

Figure 1. SMM Spacecraft Components

- Verification of the OBC attitude determination and control performance

This paper presents a broad overview of the ground support software and discusses the performance of the spacecraft attitude system and sensors in the postlaunch period. The relationship between OBC processing and the corresponding ground support is described. Contingencies and anomalous situations encountered during the postlaunch period are also presented.

2. FUNCTIONAL OVERVIEW OF THE SMM AGSS

The sensor configurations, coordinate systems, attitude acquisition, and sensor calibration algorithms used in the ground processing are described in detail in Reference 3. Descriptions of the algorithms for onboard attitude control are given by Markley (Reference 4). A functional block diagram illustrating the relationship between onboard and ground attitude processing is given in Figure 2.

Table 1 summarizes the major functions of the various components of the SMM AGSS. The software is operational on the IBM S/360 computer system at GSFC. The spacecraft telemetry data are processed in an interactive environment to monitor the health and safety of the spacecraft and to quality-assure the performance of the onboard attitude determination and control system.

3. SMM AGSS PERFORMANCE IN THE POSTLAUNCH PERIOD

The performance of the ground attitude system is discussed in this section.

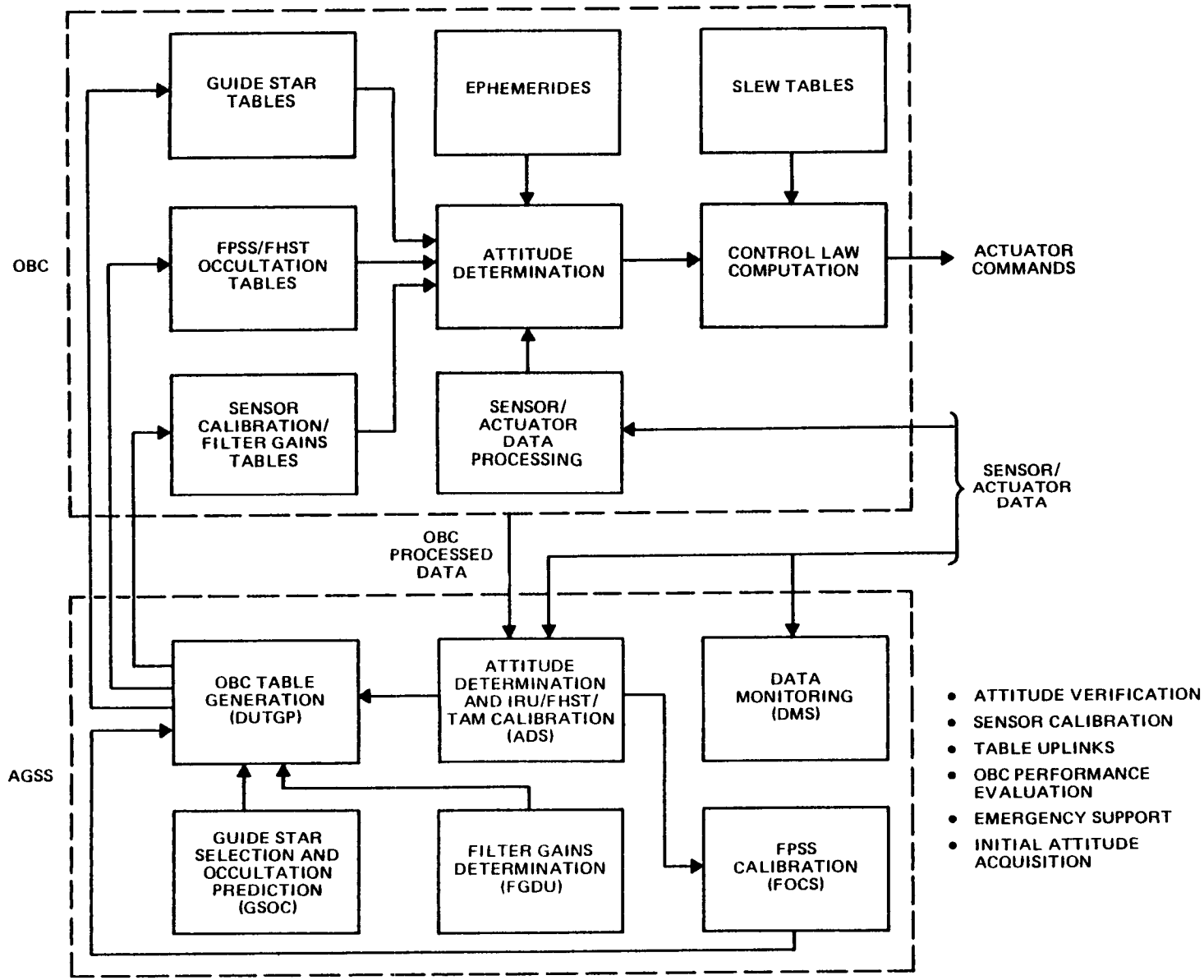

Figure 2. OBC and AGSS Attitude Processing Functional Block Diagram

Table 1. SMM Attitude Ground Support System

PROGRAM	FUNCTION
SMM/ADS	DETERMINES COARSE ATTITUDE TO AN ACCURACY OF 2 DEGREES FROM SUN AND MAGNETOMETER DATA. DETERMINES FINE ATTITUDE WITH SUN DATA TO AN ACCURACY OF BETTER THAN 5 ARC-SECONDS. DETERMINES FINE ATTITUDE WITH FHST DATA TO AN ACCURACY OF APPROXIMATELY 30 ARC-SECONDS. PERFORMS INITIAL ATTITUDE ACQUISITION AND SUPPORTS THE IN-FLIGHT CALIBRATIONS OF FHST, IRU, AND FPSS.
SMM/DMS	PERFORMS SENSOR AND OBC TELEMETRY DOWNLINK DATA MONITORING.
SMM/GSOC	SELECTS SUITABLE GUIDE STARS AND COMPUTES THEIR POSITIONS AND INTENSITIES IN THE FHST FIELD OF VIEW. PREDICTS OCCULTATIONS OF FHST AND FPSS BY THE EARTH, MOON, AND SOUTH ATLANTIC ANOMALY.
SMM/DUTGP	CONVERTS ENGINEERING DATA ON SENSOR CALIBRATION, GUIDE STARS, AND OCCULTATION PREDICTIONS INTO APPROPRIATE TABLE FORMAT FOR UPLINK TO THE ONBOARD COMPUTER.
SMM/FGDU	CALCULATES KALMAN FILTER GAIN MATRICES, CONTROL AND PROPAGATION MATRICES FOR ONBOARD ATTITUDE DETERMINATION AND CONTROL ESTIMATION.
SMM/FOCS	CALIBRATES THE FPSS IN THE OFF-NULL REGION. A NONLINEAR CALIBRATION CURVE IS FITTED TO THE FPSS DATA BY MINIMIZING THE RESIDUAL DIFFERENCES BETWEEN THE FPSS PITCH AND YAW ANGLES AND THE CORRESPONDING GYRO REFERENCE ANGLES. THE CALIBRATION ACCURACY IS BETTER THAN 2 ARC-SECONDS.

7697/80

3.1 INITIAL ATTITUDE ACQUISITION

Immediately after the launch, spacecraft control was under the safehold mode, in which data from the Coarse Sun Sensors (CSSs) were used to point the observatory roll axis to the Sun to within approximately 2 degrees. The spacecraft was placed under OBC control approximately 24 hours after launch. During this mode, the spacecraft was in an almost inertial orientation (the spacecraft roll axis tracks the Sun and, hence, moves approximately 1 degree per day) and data from the star trackers and IRU were available to determine 3-axis attitudes.

The primary procedure proposed for initial roll attitude acquisition consisted of two steps. In the first step, a coarse roll attitude is determined using the SMM/ADS subsystem. The coarse roll attitude, accurate to ±2 degrees, initializes the second step, fine roll attitude determination. The SMM/ADS computes fine roll solutions with an accuracy considerably better than the 0.1-degree mission requirement.

Several attempts to acquire fine roll attitude using the primary procedure were unsuccessful. Analysis showed that this was due to a misunderstanding in the definition of the star tracker coordinate system. This was verified by a careful analysis of the star motion in the camera fields of view during small slew maneuvers. After some investigation, the appropriate FHST documentation (Reference 5) was received and the correct tracker coordinate definition was established. The spacecraft roll attitude was established immediately thereafter.

3.2 SENSOR CALIBRATIONS

The in-flight calibrations of the attitude sensors are discussed in this subsection.

3.2.1 MAGNETOMETER CALIBRATION

The accuracy of coarse attitude determination is greatly improved by the in-flight determination of magnetometer biases. Magnetometer biases are determined by minimizing, in a least squares sense, the differences between the measured magnetic field magnitudes and those computed from a reference geomagnetic field model. The bias determination algorithm assumes that the magnetometer triad is orthogonal. It is of some interest to know the stability of these biases. The results of a long-term study of the SMM magnetometer biases are shown in Table 2. The bias B_x appears to be relatively stable and much larger in magnitude than the other biases; B_y and B_z are small but seem to reflect large fluctuations compared to their magnitude. This study indicates that to compute accurate attitudes, it is necessary to redetermine the biases at the time of attitude determination.

Table 2. Magnetometer Biases and Roll Attitudes

TIME (YYMMDD.HH)	MAGNETOMETER BIASES (MILLIGAUSS)			COARSE ROLL ATTITUDE (DEGREES)	TRUE ROLL (DEGREES)
	B_x	B_y	B_z		
800503.21	-66.4	-23.2	-18.5	-8.9	-7.8
800514.17	-72.9	-6.6	-5.1	0.5	0.0
800516.17	-70.6	-5.4	-2.7	1.8	0.0
800520.17	-85.2	3.3	3.8	-0.9	0.0
800522.17	-80.9	-1.5	22.3	13.1	12.7
800526.18	-68.6	3.3	0.6	0.4	0.0
800529.17	-72.9	14.6	-16.6	2.1	0.0
800604.12	-75.4	1.7	18.9	1.6	0.0

7697/80

It is believed that large, variable, uncompensated residual dipoles in the spacecraft contribute to the magnetometer biases. (SMM depends on the interaction between the geomagnetic field and torquer coils for momentum management.) However, the study also showed that the biases are relatively stable over a period of time of the order of a few orbits, and that reliable biases and coarse attitudes can be obtained if representative data points covering an entire orbit are processed. It is apparent from the results summarized in Table 2 that the accuracy of the coarse attitude determination is approximately 2 degrees when magnetometer biases are properly accounted for.

3.2.2 FHST/IRU/FPSS CALIBRATIONS

The SMM attitude sensors are calibrated so as to be consistent with each other. The FHST alignments and biases are determined using the output from the highly accurate FPSS. Attitudes determined from the calibrated FHSTs are then used to calibrate the IRUs. Finally, the off-null response of the FPSS is calibrated with reference to the IRUs.

It was noted during the early postlaunch period that the observed star separations in a given star tracker were different from the corresponding catalog star separations by as much as 35 to 90 arc-seconds. Moreover, attitudes determined from star data differed by as much as 100 arc-seconds from the FPSS reference attitudes. Consequently, an attempt was made to adjust the star tracker scale factor to reduce this discrepancy. Satisfactory results were obtained after this adjustment, which resulted in closer agreement with FPSS-measured attitudes (to within approximately 30 arc-seconds). A detailed account of the FHST alignment calibration as well as refinement of the prelaunch scale factors is given in References 6 and 7.

The IRU scale factor correction/alignment matrix and the 3-axis drift rates are determined by minimizing, in a least squares sense, the differences between IRU-propagated attitudes and the attitudes calculated using star and Sun data. There has been relatively little change in the IRU alignment in the postlaunch period. However, because of the failure of one of the three gyros, the primary gyro configuration was changed on September 1, 1980. A detailed account of the SMM IRU calibration is given in Reference 6.

The coefficients of the FPSS digital-to-analog nonlinear transfer function were determined by minimizing the residuals between the changes in pitch and yaw angles computed from FPSS measurements and the corresponding reference attitude changes obtained from IRU measurements of slew maneuvers executed to cover the FPSS field of view (References 6) and 8). The FPSS calibration accuracy was better than 1.2 arc-seconds in all instances. However, some degradations were observed in the FPSS, as discussed in the next subsection.

It is believed that the overall fine attitude determination accuracy with calibrated star tracker data is approximately 30 arc-seconds each in roll, pitch, and yaw, and with calibrated FPSS data is better than 5 arc-seconds in pitch and yaw.

3.2.3 RECALIBRATION OF FINE POINTING SUN SENSORS

Attitudes measured with FPSS1 and FPSS2 have been monitored regularly during the postlaunch period. As shown in Figure 3, the telemetry transfer function of the FPSS has been slowly changing with time, especially in the off-null region. To reduce the impact of these degradations and to ensure that the pitch and yaw pointing accuracy requirements are met, FPSS recalibration activities are being conducted on a regular basis.

Slew data to calibrate the FPSS were collected on March 4, June 21, July 10, August 1, and August 25, 1980. The first set of FPSS calibration parameters was uplinked on March 18, 1980. The second set of refined FPSS calibration parameters was uplinked with the new OBC flight software (version 13h) on July 31, 1980.

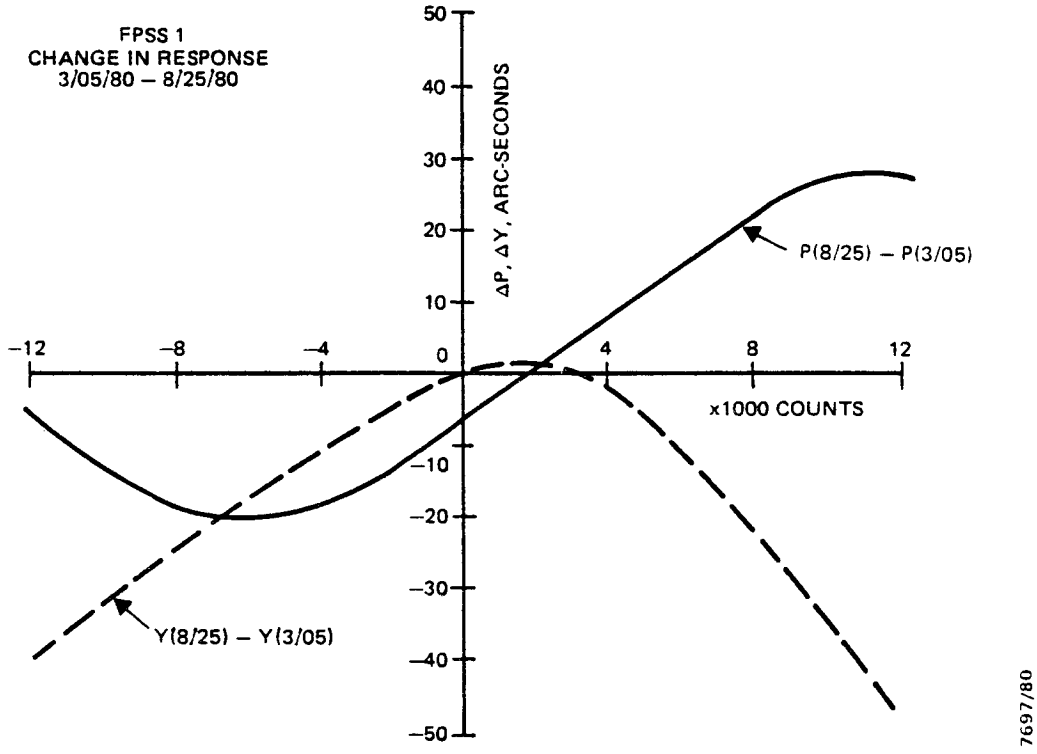

Figure 3. Change in Response of FPSS1 with Time as Measured by the Telemetry Function in the Field of View

3.3 GUIDE STAR SELECTION

The difference between the observed and predicted positions of the guide stars in the star tracker field of view is used

by the SMM control system to estimate the drift rates of the roll axis gyros. The major criteria used for the selection of guides stars are the following:

- Stars must remain within the FHST field of view during the entire period (nominally 3 days).
- Because of the finite size of the search area in the field of view, the star must be isolated within a fixed angular region (nominal tolerance of 1.15 degrees vertically and 1.10 degrees horizontally).

A more detailed account of the guide star selection criteria is given in Reference 6.

It was known from prelaunch studies that there would be periods of guide star scarcity during the SMM mission lifetime. Relaxing the criteria mentioned above to reduce the duration of the period to approximately 2 days and/or reducing the near-neighbor tolerance window slightly have worked successfully during most of these periods. In one instance (September 18, 1980, through September 23, 1980), it was necessary to change the nominal null roll attitude to -90 degrees in roll to guarantee the availability of guide stars.

It was also observed during the mission that the intensity responses of the trackers were somewhat different from those indicated by prelaunch calibrations. Thus, an in-flight intensity calibration of the trackers was performed (Reference 6), which resulted in more reliable guide star acquisitions by the OBC.

3.4 OCCULTATION PREDICTION

FPSS occultation predictions were biased to shorten the orbit day to avoid erroneous triggering of the attitude acquisition mode during day/night or night/day transitions. A similar procedure was adopted for FHST occultation predictions to prevent bad data from being processed by the OBC.

In general, no problems were encountered in the occultation prediction function. No measurable star data degradation was observed during the periods when the spacecraft passed through the regions of South Atlantic Anomaly.

4. SMM OBC PERFORMANCE MONITORING ON THE GROUND

4.1 PITCH/YAW POINTING CONTROL

Pitch and yaw pointing accuracy of the SMM observatory are frequently monitored. The results of a pitch/yaw slewing accuracy verification test, conducted with data taken on June 26, 1980, are presented in Table 3. It can be clearly seen that the relative slewing accuracy of the SMM control system using calibrated gyros and FPSS is within the accuracy requirements of 5 arc-seconds for the mission.

Table 3. SMM Control System Slewing Accuracy Verification

TIME (800626)		ΔPITCH (ARC-SECONDS)		PITCH ERROR (ARC-SECONDS)
START	STOP	FPSS1	GYRO	
0.083830	0.083859	−485.6	−486.3	0.7
0.084028	0.084109	822.7	821.8	0.9
0.084427	0.084516	−1641.2	−1640.5	0.7
0.084824	0.084918	1641.3	1644.8	3.5
0.085225	0.085312	−822.8	−820.4	2.4
TIME (800626)		**ΔYAW (ARC-SECONDS)**		**YAW ERROR (ARC-SECONDS)**
START	STOP	FPSS1	GYRO	
0.083928	0.084002	483.0	481.4	1.6
0.084226	0.084258	782.0	781.1	0.9
0.084628	0.084717	−1602.0	−1602.6	0.6
–	–	–	–	–
–	–	–	–	–

/491/80

4.2 ROLL POINTING CONTROL

The roll reference accuracy is well within the 0.1-degree mission requirement. Roll control has been maintained throughout, except on the occasions mentioned in Section 4.4. Roll slewing accuracy has also been monitored on the ground. For example, using calibrated gyros for a commanded roll of 90 degrees on August 1, 1980, the measured roll attitude difference was 89.98 degrees. Thus, the roll slew error is 0.02 degree--well within the 0.1-degree roll accuracy limit of the mission.

4.3 OBSERVATION OF A SPACECRAFT CONTROL ANOMALY NEAR ORBIT DUSK

A spacecraft control anomaly was observed at approximately 10 minutes before orbit dusk on June 30, 1980, when the gyros indicated a pitch change of approximately 10 arc-seconds while the pitch output from FPSS1 remained steady. Results from an extensive search of data dating back to the immediate postlaunch period summarized in Table 4 indicated that a probable cause of this problem could be the degradation of FPSS1 data due to the reflection of Earth albedo from a thermal vent, and the subsequent attempt by the onboard control system to compensate for this degradation by slewing the spacecraft.

Table 4. SMM Pitch/Yaw Control Anomalies Near Orbit Dusk

ORBIT DAWN (YYMMDD.HHMM)	TIME OF MAXIMUM GYRO SLEW FROM ORBIT DAWN (MINUTES)	ROLL ANGLE (DEGREES)	MAXIMUM FPSS2 DEVIATION (ARC-SECONDS)	MAXIMUM GYRO DEVIATION (ARC-SECONDS)
800223.1710	56	0	0.6 (PITCH)	7.2 (PITCH)
800327.1832	54	0	1 (PITCH)	
800429.1941	54	0		10.4
800522.2044	55	−12	0.2 (PITCH)	5.4 (PITCH)
800527.1902	52	0	0.3 (PITCH)	3.6 (PITCH)
800606.1703	59	180	0.5 (YAW)	7.2 (PITCH)
800614.1520	58	−90	0.2 (YAW), 1.3 (PITCH)	3.6
800630.1801	54	0	1.5 (PITCH)	10.4 (PITCH)
800708.1744	53	0	1 (PITCH)	
800709.1741	54	0	1 (PITCH)	7.9 (PITCH)

7491/80

An operational workaround for this problem was devised by increasing the FPSS occultation times duration in the OBC data base so that during the projected periods of potential anomalies, the control system enters the night mode--gyro reference--of control.

4.4 SPACECRAFT CONTINGENCIES

During the period from April 4, 1980, to September 1, 1980, the spacecraft lost attitude control 14 times. Guide star losses and OBC gyro drift update software problems caused half of these spacecraft contingencies. The remaining were directly attributable to other OBC problems. Table 5 gives a brief summary of these contingencies. Additional information is available in Reference 6.

Table 5. Spacecraft Control Problems During April 4, 1980 through September 1, 1980

NO.	DATE	NATURE OF PROBLEM	GROUND RESPONSE	COMMENTS
1	4/4/1980	ROLL REFERENCE LOST	ROLL ATTITUDE REACQUIRED	TIME JUMP IN S/C CLOCK
2	4/27/1980	ROLL REFERENCE LOST TEMPORARILY	MONITORING; ROLL REACQUISITION	TIME JUMP IN S/C CLOCK
3	5/2/1980	SAFEHOLD MODE	MONITORING AND ROLL REACQUISITION	PROBABLE TELEMETRY INTERFACE PROBLEM
4	5/10/1980	ROLL/PITCH/YAW REFERENCE LOST	THREE-AXIS ATTITUDE ACQUISITION	OBC SOFTWARE PROBLEM RELATED TO SUNSPOT TRACKING WHILE SLEWING
5	5/22/1980	ROLL/PITCH/YAW REFERENCE LOST	THREE-AXIS ATTITUDE ACQUISITION	OBC SOFTWARE PROBLEM
6	5/31/1980	GUIDE STAR LOST	GUIDE STAR TABLE REGENERATED	FHST2 STAR INTENSITY PROBLEM
7	6/13/1980	ROLL REFERENCE LOST	ROLL ATTITUDE REACQUIRED	ROLL GYRO DRIFT UPDATE PROBLEM
8	6/18/1980	GUIDE STAR LOST	GUIDE STAR TABLE REGENERATED	FHST2 INTENSITY PROBLEM
9	6/19/1980	ROLL REFERENCE LOST	ROLL REACQUIRED	ROLL GYRO DRIFT UPDATE PROBLEM
10	6/30/1980	SAFEHOLD MODE	ROLL ACQUISITION	OBC NEW FLIGHT SOFTWARE
11	8/1/1980	GUIDE STAR LOST	GUIDE STAR TABLE REGENERATED	FHST2 INTENSITY PROBLEM
12	8/4/1980	ROLL REFERENCE LOST	ROLL REACQUIRED	STAR PROCESSOR ON OBC WAS DISABLED
13	8/7/1980	ROLL REFERENCE LOST	ROLL REACQUIRED	PROBABLE OBC SOFTWARE PROBLEM
14	9/1/1980	SAFEHOLD MODE	THREE-AXIS ATTITUDE ACQUISITION	GYRO FAILURE; NEW GYRO CONFIGURATION RIPIYI

7697/80

5. CONCLUSIONS

The major conclusions based on the ground attitude support activities for SMM are as follows:

- Coarse attitude solutions accurate to within ±2 degrees were obtained from CSS and magnetometer data corrected for magnetometer biases that were determined for the particular data interval. These biases have shown appreciable time dependence.
- Fine attitude solutions accurate to approximately 30 arc-seconds were obtained with calibrated star tracker data. Pitch/yaw attitude solution accuracy was better than 5 arc-seconds using calibrated FPSSs.
- Star data sampling frequency (approximately 15 data points per minute) was comparatively low. The number of data points collected for each star varied from 4 to 15. The higher number of data points yielded better attitude estimates.
- In general, the guide star selection function worked very well. Periods of guide star scarcity were anticipated in advance and dealt with successfully.
- The sensor occultation function worked satisfactorily. Predicted periods were usually within 15 seconds of observed periods.
- Sensor calibration functions were performed reliably; self-consistent and accurate calibration parameters were generated. Overall pointing accuracy using calibrated sensors was better than 3.5 arc-seconds in pitch and yaw and better than 0.05 degree in roll.

REFERENCES

1. National Aeronautics and Space Administration, Goddard Space Flight Center, NASA-X-682-77-54, A Brief of Summary of the Solar Maximum Mission, February 1977

2. --, NASA-S-409-XXX, SMM Attitude Determination and Control Software Requirements Specification, A. Guha, March 1977

3. Computer Sciences Corporation, CSC/SD-78/6082, SMM Attitude System Functional Specifications and Requirements, R. Byrne et al., September 1978

4. F. L. Markley, "Attitude Control Algorithms for the SMM," (Paper presented at AIAA Guidance and Control Conference, Palo Alto, California, August 1978)

5. Ball Brothers Research Corporation, Aerospace Systems Division, Boulder, Colorado, TM 79-04, User's Guide for Standard Star Tracker

6. Computer Sciences Corporation, CSC/TM-80/6159, SMM Attitude Analysis Postlaunch Report, G. Nair et al., August 1980

7. R. Thompson and P. Gambardella, "In-flight Calibration and Performance Evaluation of the Fixed Head Star Trackers (FHSTs) for the Solar Maximum Mission" (Paper presented at GSFC Flight Mechanics/Estimation Theory Symposium, October 1980)

8. P. Gambardella and R. Thompson, "In-flight Calibration of the Fine Pointing Sun Sensor for the Solar Maximum Mission" (Paper presented at GSFC Flight Mechanics/Estimation Theory Symposium, October 1980)

IN-FLIGHT CALIBRATION AND PERFORMANCE EVALUATION OF THE FIXED HEAD STAR TRACKERS FOR THE SOLAR MAXIMUM MISSION

Dr. Richard H. Thompson
Computer Sciences Corporation, Silver Spring, Md.

Dr. Pascal J. Gambardella
Computer Sciences Corporation, Silver Spring, Md.

ABSTRACT

The Solar Maximum Mission (SMM) spacecraft, which was launched on February 14, 1980, provides an excellent opportunity for evaluating attitude determination accuracies achievable with star tracking instruments such as the Ball Brothers Research Corporation (BBRC) Fixed Head Star Trackers (FHSTs). SMM carries as a part of its payload a highly accurate Fine Pointing Sun Sensor (FPSS). The FPSS provides an independent check of the pitch and yaw parameters computed from observations of stars in the FHST field of view. This paper applies a method to determine the alignment of the FHSTs relative to the FPSS using spacecraft data. Also presented are two methods that were used to determine distortions in the 8-degree by 8-degree field of view of the FHSTs using spacecraft data. Finally, an evaluation is made of the attitude determination accuracy performance of the in-flight-calibrated FHSTs.

1. INTRODUCTION

Two NASA standard Fixed Head Star Trackers (FHSTs) were flown on the Solar Maximum Mission (SMM) spacecraft, which was launched on February 14, 1980. The FHSTs, manufactured by the BBRC Aerospace Systems Division, are electro-optical devices that use an image dissector to search for and track

stars in an 8-degree by 8-degree field of view. The SMM provides an excellent opportunity to evaluate the attitude determination accuracies attainable with the FHSTs. Included in the SMM payload is a highly accurate Fine Pointing Sun Sensor (FPSS), which provides an independent check of the pitch and yaw parameters computed from the stellar observations made by the SMM FHSTs. Two types of error are chiefly responsible for degrading the accuracy of attitude solutions based on FHST data. Uncertainty in the position of an observed star results from distortion of its image by electro-optical irregularities over the star sensor's field of view and by temperature, magnetic field, and star intensity effects. Errors of this type are predictable and can be compensated for by careful calibration of the star cameras on the ground. Uncorrected star camera misalignments are a second source of systematic errors in attitudes computed using star sensor data. Misalignment errors typically are eliminated by appyling to FHST data biases estimated by comparing attitudes determined from FHST and a reference attitude sensor data. This paper discusses a procedure that was developed for enhancing the accuracies of attitude solutions obtained with the SMM FHSTs. The procedure is based on (1) minimizing the errors in observed star positions by adjusting the scale factors in the equations calibrating the distortions in SMM star camera measurements and (2) minimizing the differences between the pitch and yaw attitudes derived from the SMM FHSTs and the reference FPSS by adjusting the FHST misalignment parameters. Application of the procedure to the case of the SMM FHSTs resulted in a two- to three-fold improvement in attitude accuracy when data from both star cameras were used to estimate attitude, and as much as a ten-fold improvement when data from single cameras

were used to determine attitude. Many details of the methods used in this paper are presented elsewhere (Reference 1) and only the main results of the calculations are given here.

2.0 EVALUATION OF FHST MEASUREMENT UNCERTAINTY

The angles θ and ϕ defining the measured star position relative to the FHST boresight are defined as shown in Figure 1. These angles are converted to a unit vector using the following equation:

$$\hat{S} = \cos\theta \cos\phi \ \hat{X} - \sin\theta \cos\phi \ \hat{Y} + \sin\phi \ Z \quad (1)$$

2.1 SMM FHST DATA REDUCTION

The raw FHST counts H and V are converted to angles θ and ϕ through a complicated set of calibration equations. The form at these calibrations is as follows (Reference 2):

$$\begin{aligned} f_1(H,V,X) = {} & C_1 + C_2V + C_3H + C_4X + C_5V^2 + C_6VH + C_7VX + C_8H^2 \\ & + C_9HX + C_{10}X^2 + C_{11}V^3 + C_{12}V^2H + C_{13}V^2X \\ & + C_{14}VH^2 + C_{15}VHX + C_{16}VX^2 + C_{17}H^3 + C_{18}H^2X \\ & + C_{19}HX^2 \end{aligned} \quad (2)$$

where
- H = horizontal axis output in counts
- V = vertical axis output in counts
- X = physical parameters as defined below
- $f_1(H,V,X)$ = H value corrected for X; f_1 in counts
- C = calibration coefficients corresponding to H value corrections

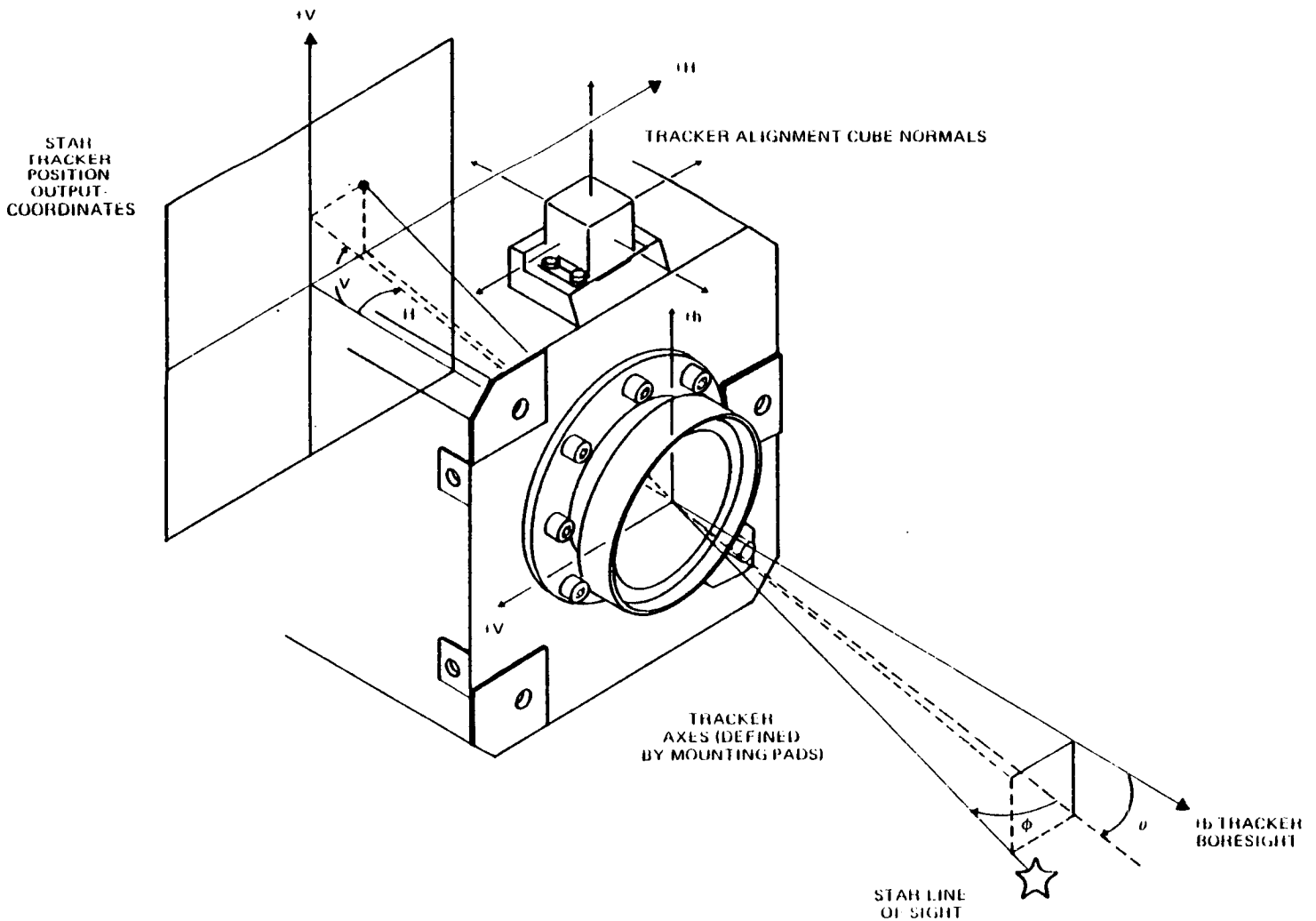

7491/8C

Figure 2-1. FHST Coordinate Definition (BBRC)

The expression $f_2(H,V,X)$ for the V value corrected for X is of the same form as $f_1(H,V,X)$ except for different calibration coefficients C.

Five separate applications of Equation (2) are necessary for each axis. The first application is a flat-field temperature calibration; X is the temperature in volts. The second application is for intensity, with X being the star intensity in volts. The third application has X equal to the magnetic field along the boresight axis in gauss; the fourth application has X equal to the magnetic field along the star tracker h axis in gauss; and the fifth application has X equal to the magnetic field along the star tracker v axis.

The angle θ and ϕ are then given by

$$\begin{aligned} \phi &= -S_H f_1 \\ \theta &= -S_V f_2 \end{aligned} \qquad (3)$$

where S_H and S_V are the scale factors for a particular FHST in degrees per count.

2.2 SMM FHST MEASUREMENT ERRORS WITH PRELAUNCH SCALE FACTORS

Star tracker flight data taken on March 2 and March 3, 1980, were used to evaluate this calibration. These data are composed of three different passes, referred to as ACN-I, ACN-II, and HAW. The data were rich in star information and represented the best data at the time the calibrations were completed. The stars present in each pass were identified, and the angle between each pair of stars was computed in the FHST reference frame. These angles were compared to the

corresponding angles computed from catalog stars. The difference between the catalog star separation angles and the measured separation angles was computed for every possible observed pair. The mean and standard deviation were computed for each of the three passes. These results are shown in Table 1.

Table 1. Mean and Standard Deviations of Differences Between Observed Star Pairs and the Corresponding Catalog Star Pairs

Pass	FHST1		FHST2	
	Mean (arc-sec)	σ^a (arc-sec)	Mean (arc-sec)	σ^a (arc-sec)
ACN-I	40.1	31.2	94.9	42.1
ACN-II	52.5	39.6	105.2	42.0
HAW	73.6	44.9	98.2	36.8

[a] σ = Standard deviation

The results shown in Table 1 are independent of the overall FHST alignment, since only angles between stars in one reference frame (the FHST frame) are being compared to the corresponding angles in a rotated reference frame (the geocentric inertial frame). Hence, these results reflect the inherent accuracy of the FHST data. The results in Table 1 indicate that the preflight calibration, when applied to actual flight data, leads to star position errors that are much larger than the 10- to 20-arc-second range desired for SMM.

Since temperature effects can greatly influence the FHST calibration, FHST temperature data around the SMM orbit were examined. There was virtually no change in temperature as the spacecraft made day-to-night transitions. In addition, the temperatures have been virtually the same from the time of launch through August 1980.

2.3 SMM FHST MEASUREMENT ERROR WITH REFINED SCALE FACTORS

Because of the large errors in star position given by the calibrated FHST data, as discussed in the previous subsection, it was decided to attempt an in-flight calibration of the FHST by treating the scale factors in Equation (3) as free parameters. These scale factors were originally specified by the manufacturer in the prelaunch specifications (Reference 2).

First it is assumed that $S^{(1)} = S_V^{(1)} = S_H^{(1)}$ and $S^{(2)} = S_V^{(2)} = S_H^{(2)}$; i.e., each FHST has only one scale factor associated with it. With this assumption, a straight line is expected when the angle between measured stars is plotted versus the angle between corresponding catalog stars. The deviation of the slope of this line from unity is related to the actual value of the scale factor.

Starting with a scale factor of 0.002079 degree per count, the following results were obtained:

$$S^{(1)} = 0.0020683 \text{ degree per count for FHST1}$$

$$S^{(2)} = 0.0020673 \text{ degree per count for FHST2}$$

These results, with the mean and standard deviation of the data, are given in Tables 2 and 3.

Separate horizontal axis and vertical axis scale factors were determined for each FHST by minimizing the angular differences in positions of three stars at one time and averaging the scale factors over as many triplets in the field of view as possible. For this method, stars that were near the edge of the field of view, that were very faint, or that for any reason showed large standard deviations in their positions were rejected.

Table 2. Angular Separation of Stars for FHST1 in Geocentric Inertial (GCI) and Pseudo-Geocentric Inertial (PGCI) Frames

FHST1 STAR PAIR	GCI SEPARATION (DEGREES)	PGCI SEPARATION[a] (DEGREES)	ANGULAR DIFFERENCE[b] (ARC-SECONDS)	PGCI[c] (DEGREES)	ANGULAR DIFFERENCE[d] (ARC-SECONDS)
1-2	2.6690691	2.6901166	-75.77	2.6916143	81.16
1-3	5.8430880	5.8559311	-46.24	5.85924730	-58.17
1-4	8.5593707	8.5717052	-44.40	8.57752340	-65.35
1-6	4.2783210	4.2864809	-29.38	4.28850445	-36.66
1-7	9.1755633	9.1740970	5.28	9.1792283	13.19
2-3	3.1760332	3.1677620	29.78	3.16958235	23.22
2-4	5.9347617	5.9266711	29.13	5.9308240	14.18
2-6	1.6897312	1.6770099	45.80	1.67765498	43.47
2-7	6.5068470	6.4844566	80.61	6.48801936	67.78
3-4	2.8523522	2.8528839	-1.91	2.8552865	-10.56
3-6	1.8074348	1.8078567	-1.52	1.80933849	-6.85
3-7	3.3448504	3.3309729	49.96	3.33272267	43.66
4-6	4.6575541	4.6588012	-4.49	4.6629900	-18.52
4-7	1.5609355	1.5600399	3.22	1.56080533	0.47
6-7	4.9774255	4.9656321	42.46	4.96875089	31.23

7491/80

[a] H&V SCALE FACTOR = 0.0020683 DEGREE PER COUNT

[b] MEAN = 5.50 ARC SECONDS; σ = 42.22 ARC-SECONDS

[c] HSF = 0.0020690 DEGREE PER COUNT; VSF = 0.0020704 DEGREE PER COUNT

[d] MEAN = 2.67 ARC-SECONDS; σ = 43.31 ARC SECONDS

Table 3. Angular Separation of Stars for FHST2 in GCI and PGCI Frames

FHST2 STAR PAIR	GCI SEPARATION (DEGREES)	PGCI SEPARATION[a] (DEGREES)	ANGULAR DIFFERENCE[b] (ARC-SECONDS)	PGCI[c] SEPARATION (DEGREES)	ANGULAR DIFFERENCE[d] (ARC-SECONDS)
9 10	1.99021294	1.9884488	6.35	1.98811031	7.57
9 12	5.18220145	5.18623851	-14.53	5.18555249	-12.06
9 13	3.10987769	3.10728594	9.33	3.10448100	19.43
9 17	3.49565583	3.49513002	1.89	3.49318537	8.89
10 12	3.83780618	3.83427703	12.70	3.83287884	17.74
10 13	3.30020267	3.30492505	-17.00	3.30333513	-11.28
10 17	1.99636914	2.00586208	-34.17	2.00413461	-27.96
12 13	7.11550992	7.11557903	-0.25	7.112602589	10.47
12 17	5.02159070	5.0259217	-15.62	5.02254775	3.45
13 17	2.73095274	2.72621958	17.04	2.72608318	17.53

7491/8C

[a]H&V SCALE FACTORS - 0.0020673 DEGREE PER COUNT

[b]MEAN - 3.43 ARC-SECONDS; σ - 16.25 ARC-SECONDS

[c]HSF = 0.0020654 DEGREE PER COUNT; VSF = 0.0020672 DEGREE PER COUNT

[d]MEAN - 2.69 ARC-SECONDS; σ 15.77 ARC-SECONDS

The following scale factors were obtained using the ACN data of March 2, 1980, at 9:23 GMT (see also Tables 2 and 3):

Tracker	Axis	Scale Factor (degree per count)
FHST1	Horizontal	0.0020690
FHST1	Vertical	0.0020704
FHST2	Horizontal	0.0020654
FHST2	Vertical	0.0020672

Table 4 shows the same pairs of stars used in scale factor determination with the prelaunch value.

3.0 EVALUATION OF SMM GHST ATTITUDE DETERMINATION ACCURACY PERFORMANCE

The misalignment angles are defined as corrections to the nominal 1-3-1 rotation from the Modular Attitude Control System (MACS) to FHST reference frame. This transformation is given by the following equation:

$$M \text{ (MACS to FHST)} = T_1(\beta_1 + \alpha_1)\ T_3(\beta_2 + \alpha_2)\ T_1(\beta_3 + \alpha_3) \quad (4)$$

where the β's are the nominal angles, the α's are the small misalignment angles, and T_i represents a rotation about the ith axis. The β's are given by the following:

FHST	β_3	β_2	β_1
1	-19.7724	53.34892	102.0137
2	-19.73046	126.5083	258.0593

3.1 FHST MISALIGNMENT BIAS DETERMINATION

To determine the misalignments, the attitude as computed from the FHST is adjusted to match the FPSS attitude for the pitch and yaw angles. Since there is no roll reference for the FHST, the absolute α_3 misalignment is not determined.

Table 4. Comparisons of Catalog and Observation Star Vector Separation With Prelaunch Scale Factors

FHST1 STAR PAIR	CATALOG ANGLE (DEGREES)	PGCI ANGLE (DEGREES)	ANGULAR DIFFERENCE* (ARC-SECONDS)
1–2	2.6690691	2.702847	−119.47
1–3	5.8430880	5.885778	−115.04
1–4	8.5593707	8.616201	−204.59
1–6	4.2783210	4.308378	−108.24
1–7	9.175563	9.221828	−166.55
2–3	3.176033	3.182881	−26.72
2–4	5.9347617	5.956749	−78.34
2–6	1.6897312	1.684136	20.85
2–7	6.506847	6.517856	−40.19
3–4	2.852352	2.866830	−55.27
3–6	1.8074348	1.816287	−38.73
3–7	3.3448504	3.348180	−17.14
4–6	4.6575541	4.682731	−90.90
4–7	1.5609355	1.568525	−31.18
6–7	4.9774255	4.991619	−53.00

FHST2 STAR PAIR	CATALOG ANGLE (DEGREES)	PGCI ANGLE (DEGREES)	ANGULAR DIFFERENCE** (ARC-SECONDS)
9–10	1.9902129	1.999312	−32.76
9–12	5.1822015	5.215897	−121.30
9–13	3.1098777	3.124387	−52.23
9–17	3.4956558	3.514408	−67.51
10–12	3.8378062	3.856123	−65.94
10–13	3.3002027	3.323802	−84.96
10–17	1.9963691	2.016582	−72.77
12–13	7.1155099	7.156287	−146.80
12–17	5.0215907	5.054222	−117.47
13–17	2.7309527	2.741496	−37.96

7491/80

*MEAN = −74.97 ARC-SECONDS; σ = 59.95 ARC-SECONDS

**MEAN = −79.97 ARC-SECONDS; σ = 37.67 ARC-SECONDS

However, $(\alpha_3)_{FHST2} - (\alpha_3)_{FHST1}$ is determined from the difference in the roll attitude computed independently with each star tracker at null atitude. The difference $(\alpha_3)_{FHST_2} - (\alpha_3)_{FHST1}$ was computed as 0.04378 degree.

3.2 PARTIAL DERIVATIVE METHOD FOR MINIMIZING ATTITUDE ERROR

The method used to obtain the α_1 and α_2 misalignments is referred to as the partial derivative method. The attitude is expanded in terms of the alignment angles about their nominal values. Using the FPSS as a reference produces a set of linear equations that result in solutions for α's. These solutions are given by the following set of equations:

$$\delta\alpha_1^{(1)} = \left(\delta Y^{(1)} \frac{\partial P^{(1)}}{\partial \alpha_2^{(1)}} - \delta P^{(1)} \frac{\partial Y^{(1)}}{\partial \alpha_2^{(1)}}\right) \Big/ J \qquad (5)$$

$$\delta\alpha_2^{(1)} = \left(-\delta Y^{(1)} \frac{\delta P^{(1)}}{\delta \alpha_1^{(1)}} + \delta P^{(1)} \frac{\delta P^{(1)}}{\delta \alpha_1^{(1)}}\right) \Big/ J \qquad (6)$$

where

$$J = \frac{\partial Y^{(1)}}{\partial \alpha_1^{(1)}} \frac{\partial P^{(1)}}{\partial \alpha_2^{(1)}} - \frac{\partial P^{(1)}}{\partial \alpha_1^{(1)}} \frac{\partial Y^{(1)}}{\partial \alpha_2^{(1)}} \qquad (7)$$

$$\delta\alpha_1^{(1)} = \alpha_1^{(1)} - \alpha_1^{(1)}(0) \qquad (8)$$

$$\delta\alpha_2^{(1)} = \alpha_2^{(1)} - \alpha_2^{(1)}(0) \qquad (9)$$

where $\alpha_1^{(1)}$ and $\alpha_2^{(1)}$ are the misalignments that are taken to force FHST1 to yield the same pitch and yaw as given by the FPSS and $\alpha_1^{(1)}(0)$ and $\alpha_2^{(1)}(0)$ are the starting values,

$$\delta P^{(1)} = P_{FPSS} - P^{(1)}(0) \tag{10}$$

$$\delta Y^{(1)} = Y_{FPSS} - Y^{(1)}(0) \tag{11}$$

where P_{FPSS} and Y_{FPSS} are the FPSS pitch and yaw and $P^{(1)}(0)$, $Y^{(1)}(0)$ is the attitude determined with the trial misalignments.

Since there is no absolute reference to determine α_3, the dependence of the attitudes on this parameter is ignored. This could lead to some difficulty, since the misalignment will also indirectly affect the determination of α_1 and α_2.

3.3 ATTITUDE ACCURACY RESULTS

Using the standard sets of data--ACN-I, ACN-II, and HAW--the best set of misalignment parameters is determined. These results are shown in Table 5, with the averaged values and the corresponding root-mean-square (rms) deviations. Certain conclusions are readily apparent from these computations. The misalignment around the boresight of the camera, α_1, is very poorly determined by the data. This result will not greatly affect the two-tracker attitudes. The misalignment α_2 is quite well determined, as shown by the results in Table 5.

Table 5. Misalignment Parameters

DATA	FHST1		FHST2	
	$\alpha_1^{(1)}$ (DEGREES)	$\alpha_2^{(1)}$ (DEGREES)	$\alpha_1^{(2)}$ (DEGREES)	$\alpha_2^{(2)}$ (DEGREES)
ACN-I	−0.059	0.1073	0.1696	−0.00555
ACN-II	−0.01867	0.1105	0.192	−0.0089
HAW	0.0108	0.1078	0.216	−0.0076
AVERAGED VALUES	−0.0223	0.1085	0.193	−0.0074
ROOT-MEAN-SQUARE DEVIATIONS	126 ARC-SECONDS	6 ARC-SECONDS	84 ARC-SECONDS	6 ARC-SECONDS

7491/80

NOTE: THE MISALIGNMENT PARAMETERS ARE SHOWN FOR FHST1 AND FHST2 FOR THREE SETS OF DATA. THE AVERAGED VALUES AND RMS DEVIATIONS IN ARC SEC ARE ALSO SHOWN.

The attitudes before and after the misalignments have been applied are shown in Table 6. It is apparent that a general overall improvement has been obtained in the computation of the pitch and yaw attitude components by the determined misalignments.

The overall attitude accuracy based on these results is on the order of ±30 arc-seconds.

ACKNOWLEDGMENTS

The authors thank R. Byrne, G. Nair, and J. Buckley of CSC and R. Werking of GSFC for countless discussions concerning the calibrations of the SMM FHST.

Table 6. Attitude Comparisons

DATA	FHST1				FHST2				BOTH			
	NEW		OLD		NEW		OLD		NEW		OLD	
	δP*	δY**	δP	δY	δP	δY	δP	δY	δP	δY	δP	δY
ACN I	30.1	46.1	25.2	32.8	17.6	18.5	-23.6	4.4	23.5	-24.1	-34.1	34.6
ACN II	4.2	10.1	104.4	-108.0	12.2	29.5	21.6	64.8	17.28	-28.8	-50.8	47.2
HAW	37.4	33.5	147.2	171.7	61.9	-83.0	61.2	105.8	13.3	-15.5	47.9	54.5

7491/80

*δP P_{FPSS} P_{FHST} (ARC SECONDS)

**δY Y_{FPSS} Y_{FHST} (ARC-SECONDS)

REFERENCES

1. Computer Sciences Corporation, CSC/TM-80/6159, Solar Maximum Mission (SMM) Attitude Analysis Postlaunch Report, G. Nair, R. H. Thompson, P. J. Gambardella, G. F. Neal, Y. R. Kwon, P. C. Kammeyer, and J. M. Buckley. J. M. Buckley, August 1980

2. Ball Brothers Research Corporation, Aerospace Systems Division, Boulder, Colorado, TM 79-04, User's Guide For Standard Star Tracker

IN-FLIGHT CALIBRATION OF THE FINE POINTING SUN SENSOR ON THE SOLAR MAXIMUM MISSION

Dr. Pascal J. Gambardella

Computer Sciences Corporation, Silver Spring, Md.

Dr. Richard H. Thompson

Computer Sciences Corporation, Silver Spring, Md.

ABSTRACT

The attitude control objectives of Solar Maximum Mission (SMM) are to point the boresight of the payload Fine Pointing Sun Sensor (FPSS) to any point within 30 arc-minutes of the Sun's center with an accuracy of 5 arc-seconds (3σ, pitch and yaw) and a jitter of less than 3 arc-seconds (3σ). To meet these stringent accuracy requirements, a procedure was developed for in-flight calibration of the FPSS. The spacecraft was maneuvered using FPSS offset commands to position the Sun at different points within the FPSS field of view. The coefficients of the FPSS digital-to-analog nonlinear transfer function were determined by minimizing the residuals between the pitch and yaw angles computed from the FPSS measurements and the corresponding reference angles obtained from Inertial Reference Unit (IRU) measurements.

In this paper, the actual in-flight calibration and the calibration algorithm are discussed. Spacecraft data are used to assess the range of validity of the FPSS transfer function. The Sun's diameter is computed with the FPSS calibration results and the Ultraviolet Spectrometer and Polarimeter (UVSP) experimenters' data. This calculation gives an independent verification of the calibration results.

1. INTRODUCTION

The attitude control objectives of the SMM are to point the boresight of the payload FPSS to any point within 30 arc-minutes of the Sun's center with an accuracy of 5 arc-seconds (3σ, pitch and yaw) and a jitter of less than 3 arc-seconds (3σ). To meet these stringent accuracy requirements, a procedure was developed for in-flight calibration of the FPSS. The spacecraft was maneuvered using FPSS offset commands to position the Sun at different points within the FPSS field of view. The coefficients of the FPSS digital-to-analog non-linear transfer function were determined by minimizing the residuals between the pitch and yaw angles computed from the FPSS measurements and the corresponding reference angles obtained from Inertial Reference Unit (IRU) measurements.

In this paper, spacecraft data are used to assess the range and validity of the FPSS transfer function. In addition, the Sun's diameter is computed with the FPSS calibration results and the Ultraviolet Spectrometer and Polarimeter (UVSP) experimenters' data.

2. EQUATIONS AND PROCEDURE

The Adcole transfer functions for each FPSS are (Reference 1)

$$\alpha = A_1 + A_2 N_\alpha + A_3 \sin (A_4 N_\alpha + A_5) + A_6 \sin (A_7 N_\alpha + A_8) \tag{1}$$

and

$$\beta = B_1 + B_2 N_\beta + B_3 \sin (B_4 N_\beta + B_5) + B_6 \sin (B_7 N_\beta + B_8) \tag{2}$$

where A_i and B_i $(1 \leq i \leq 8)$ are constants, N_α and N_β are the FPSS digital outputs, and the angles α and β are in radians.

During the calibration phase of the SMM mission, the spacecraft was maneuvered such that the Sun was positioned at different points within the reduced FPSS field of view. The angular displacement of each sample point from the FPSS null was measured independently by the FPSS and the calibrated SMM gyros. The coefficients A_i $(2 \leq i \leq 8)$ and B_i $(2 \leq i \leq 8)$ of the FPSS calibration equations were determined by minimizing the differences between the FPSS observed changes in pitch and yaw angles and the corresponding changes in the reference pitch and yaw angles measured by the gyros at each off-null sample point. The FPSS calibration algorithm employs a recursive least squares procedure which processes changes in pitch and yaw angles rather than absolute pitch and yaw angles to take advantage of the extreme accuracy with which gyros measure attitude changes. The coefficients A_1 and B_1 for each FPSS were determined from the equations

$$\begin{aligned} \alpha &= 0 \\ \beta &= 0 \end{aligned} \tag{3}$$

Calibration data were obtained using a discrete slew maneuver method and a continuous slew maneuver method. In the discrete slew maneuver method, the spacecraft was commanded to perform a series of slews (along the pitch and yaw axes) over the 1-degree by 1-degree FPSS reduced field of view. Gyro readings and FPSS readings were taken at each commanded slew position. To reduce the accumulation of errors, each slew maneuver was between null attitude and a specified off-null attitude. Changes in attitude resulting from a null attitude to an off-null attitude slew were input into the recursive least squares algorithm. The changes in attitude from an off-null attitude to a null attitude slew were also input.

For the continuous slew maneuver method, the spacecraft is commanded to perform bang-bang slews along the pitch and yaw axes of the FPSS 1-degree by 1-degree field of view. Gyro data and FPSS data were taken during the slew maneuver every 0.96 second.

The calibration results are presented in the following section.

The continuous slew data were not used because of the large residuals between the FPSS data and the gyro data. The large residuals resulted from the high slew rate of the spacecraft and the slight data sampling time shift between the FPSS and gyro data. Hence, the FPSS was calibrated with discrete slew data only.

The FPSS calibration uses the gyros as a reference and is dependent on the accuracy of the gyro calibration. The FPSS was calibrated with the gyro alignment/scale factor matrix, and gyro drifts computed in flight. The drift rates were adjusted slightly at each FPSS calibration to be consistent with that particular set of data.

3. CALIBRATION RESULTS

The results of the FPSS calibration algorithm are presented here and the accuracy of the algorithm is assessed. The FPSS was calibrated in flight on March 18, June 11, June 27, July 17, August 27, and September 4, 1980. These calibrations are summarized in Table 1, and the corresponding FPSS coefficients are given in Tables A-1 through A-7 in the appendix.

The mean pitch residuals $|\Delta P_{FPSS} - \Delta P_{GYRO}|$ and yaw residuals $|\Delta Y_{FPSS} - \Delta Y_{GYRO}|$ are a measure of the accuracy of the calibration algorithm. A comparison of the FPSS calibration

residuals from all of our calibrations as of this writing are given in Table 1. The maximum residuals are also tabulated.

After the March 18 calibration, the spacecraft was slewed +179 arc-seconds in pitch and -111 arc-seconds in yaw to facilitate the solar experiments on SMM. This will affect the A_1 and B_1 coefficients on calibrations III through V. Furthermore, on August 22 the spacecraft was slewed +44 arc-seconds in yaw. This will affect the A_1 and B_1 coefficients in calibration VI.

Both FPSSs have degraded since July 31, 1980. The overall degradation in FPSS1 is shown in Figures 1 and 2, where the FPSS1 pitch and yaw differences between various calibrations are shown.

As an independent verification of the calibration results, calibration VI was used to compute the solar diameter on August 6. This was accomplished by noting the FPSS raw counts when the UVSP experimental boresight made crossings of the Sun's limb, (Reference 2). These results are presented in Table 2. The results show that the Sun's diameter computed with the calibration results is consistent with the accepted value of the Sun's diameter for August 6.

Table 1. Summary of FPSS Calibration

CALIBRATION NO.	PITCH CALIB.	YAW CALIB.	FPSS	DATE OF CALIB.	DATE OF DATA	DATE OF GYRO CALIB.	RANGE OF CALIB. (deg)	MEAN RESIDUAL (arc-sec)	MAXIMUM RESIDUAL (arc-sec)	NO. OF DATA PTS.
PRELAUNCH	*		1					5.14 ± 5.58		
		*						9.38 ± 6.43		
	*		2					3.27 ± 2.24		
		*						6.22 ± 7.11		
I	*		1	3/18	3/5	3/18	0.43 TO −0.40	0.53 ± 0.03	1.3	25
		*					0.42 TO −0.39	0.40 ± 0.41	1.5	16
	*		2				0.43 TO −0.40	0.52 ± 0.43	1.7	25
		*					0.42 TO −0.39	0.56 ± 0.50	1.4	16
II	*		1	6/11	3/5	5/19	0.43 TO −0.40	–	0.9	25
		*					0.42 TO −0.39	–	1.2	16
	*		2				0.43 TO −0.40	–	1.2	25
		*					0.42 TO −0.39	–	1.2	16
III	*		1	6/27	6/21	5/19	0.25 TO −0.25	–	1.9	4
		*					0.41 TO −0.41	–	1.9	6
	*		2				0.25 TO −0.25	–	2.1	4
		*					0.41 TO −0.41	–	1.7	6
IV	*		1	7/17	7/3	5/19	0.32 TO −0.32	0.79 ± 0.72	1.7	10
		*					0.36 TO −0.38	0.68 ± 0.47	2.1	11
	*		2				0.32 TO −0.32	0.78 ± 0.93	1.7	10
		*					0.36 TO −0.38	0.68 ± 0.52	1.6	11
V	*		1	8/27	7/31	8/18	0.35 TO −0.32	0.28 ± 0.26	1.1	19
		*					0.35 TO −0.34	0.38 ± 0.46	1.0	21
	*		2				0.35 TO −0.32	0.26 ± 0.27	1.2	19
		*					0.35 TO −0.34	0.46 ± 0.50	1.0	21
VI	*		1	9/4	8/24	8/18	0.35 TO −0.36	0.29 ± 0.26	1.2	19
		*			8/25		0.35 TO −0.37	0.29 ± 0.23	1.0	21
	*		2		8/24		0.35 TO −0.36	0.31 ± 0.24	0.9	19
		*			8/25		0.35 TO −0.37	0.33 ± 0.22	0.9	21

7716/80

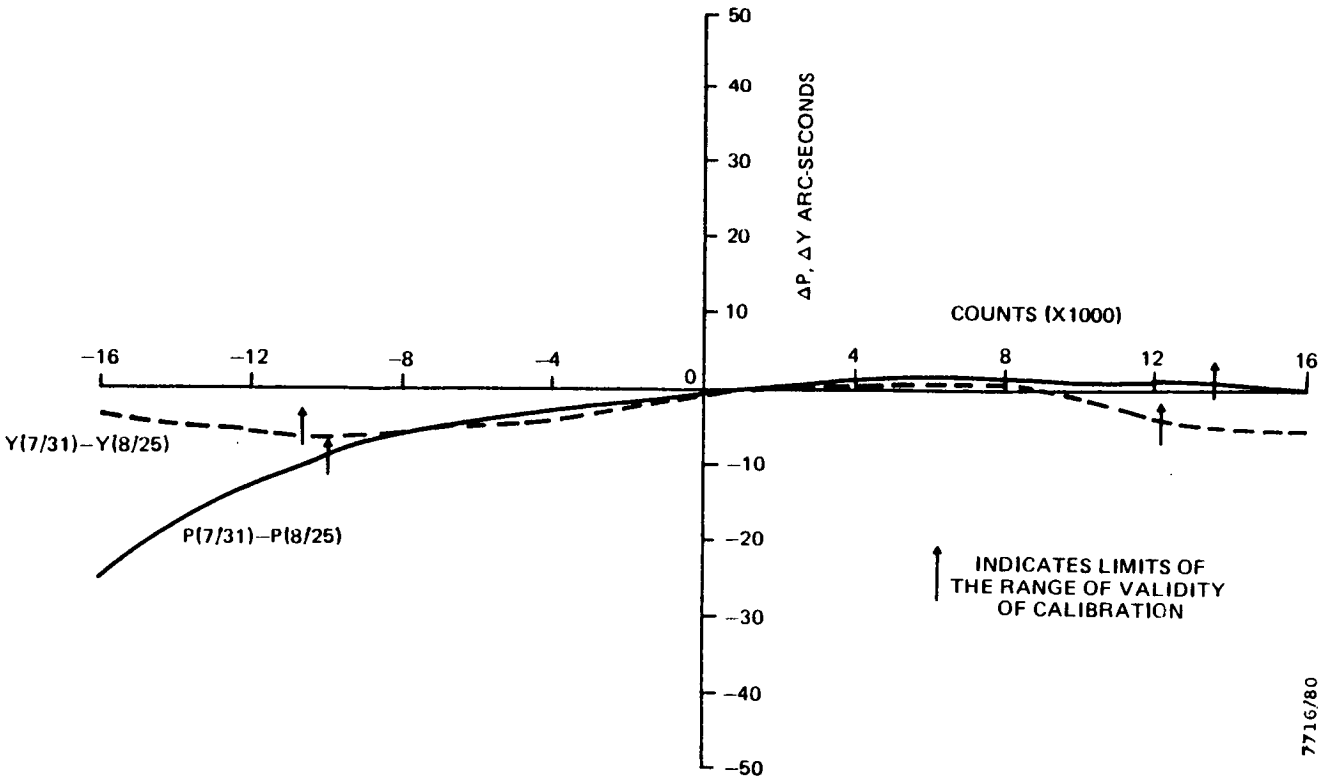

Figure 2. Plot of FPSS1 Pitch and Yaw Angle Difference Between July 31, 1980 (V) and August 25, 1980 (VI)

Table 2. UVSP Limb Crossing Results for August 6, 1980

Limb	FPSS Counts[a]	Time (HHMMSSMMM)	Pitch (arc-sec)	Yaw[b] (arc-sec)
South	+10394.5	0.104933450	946.5	
North	-6517.0	0.105327950	-945.8	
East	-7363.5	0.110137730		957.9
West	9812.0	0.110533200		-942.2

[a]Obtained from Reference 2 by dividing the numbers presented there by +0.109866 and -0.109866 (for pitch and yaw, respectively).

[b]The calibrated FPSS pitch and yaw angles were computed from the transfer function determined from the August 24, 1980, and the August 25, 1980 calibration slews.

NOTES: N-S diameter = 1892.3 arc-seconds
E-W diameter = 1900.1 arc-seconds
Accepted diameter for August 6, 1980 = 1895.36 arc-seconds (Reference 3)

APPENDIX A. SUMMARY OF FPSS COEFFICIENTS

Table A-1. I Prelaunch Calibration Coefficients

Coefficient	FPSS1	FPSS2
A_1	0.1090831×10^{-3}	$-0.8047742 \times 10^{-3}$
A_2	0.5326322×10^{-6}	0.5326322×10^{-6}
A_3	0.1335975×10^{-4}	0.2808313×10^{-4}
A_4	0.1917476×10^{-3}	0.1917476×10^{-3}
A_5	$0.29628831 \times 10^{+1}$	$-0.1695882 \times 10^{+1}$
A_6	0.1745964×10^{-4}	0.1150606×10^{-4}
A_7	0.3834951×10^{-3}	0.3834928×10^{-3}
A_8	0.8659915	$0.1223491 \times 10^{+1}$
B_1	-0.172264×10^{-3}	$-0.5874911 \times 10^{-3}$
B_2	0.5326322×10^{-6}	0.5326322×10^{-6}
B_3	0.1207313×10^{-4}	0.1443567×10^{-4}
B_4	0.1917476×10^{-3}	0.1917476×10^{-3}
B_5	$-0.1390673 \times 10^{+1}$	$-0.2480650 \times 10^{+1}$
B_6	0.1523304×10^{-4}	0.9449009×10^{-5}
B_7	0.3834951×10^{-3}	0.3834951×10^{-3}
B_8	$0.1206903 \times 10^{+1}$	0.9041772

Table A-2. I Postlaunch Calibration Coefficients Determined March 18, 1980

Coefficients	FPSS1	FPSS2
A_1	$-0.8467783 \times 10^{-4}$	0.8337881×10^{-3}
A_2	0.5320264×10^{-6}	0.5300202×10^{-6}
A_3	$-0.3860728 \times 10^{-5}$	$-0.3292304 \times 10^{-4}$
A_4	0.3072369×10^{-3}	0.1634355×10^{-3}
A_5	$0.3092502 \times 10^{+1}$	$-0.1704371 \times 10^{+1}$
A_6	$-0.2778208 \times 10^{-4}$	$-0.6869980 \times 10^{-5}$
A_7	0.2594346×10^{-3}	0.3717518×10^{-3}
A_8	$0.1737169 \times 10^{+1}$	$0.1595601 \times 10^{+1}$
B_1	$-0.1869254 \times 10^{-3}$	0.5601689×10^{-3}
B_2	0.5312469×10^{-6}	0.5317111×10^{-6}
B_3	0.1416509×10^{-4}	$-0.1834644 \times 10^{-4}$
B_4	0.4284356×10^{-3}	0.2224163×10^{-3}
B_5	$-0.1017843 \times 10^{+1}$	$-0.2684492 \times 10^{+1}$
B_6	0.2674199×10^{-4}	0.4998647×10^{-5}
B_7	0.2226275×10^{-3}	0.5214850×10^{-3}
B_8	$0.1267732 \times 10^{+1}$	$-0.3890319 \times 10^{-1}$

Table A-3. II Postlaunch Calibration Coefficients Determined June 11, 1980

Coefficient	FPSS1	FPSS2
A_1	$-0.8367909 \times 10^{-4}$	0.8259816×10^{-3}
A_2	0.5318888×10^{-6}	0.5300066×10^{-6}
A_3	$-0.4074826 \times 10^{-5}$	$-0.4318272 \times 10^{-4}$
A_4	0.2879776×10^{-3}	0.1498738×10^{-3}
A_5	$0.3085873 \times 10^{+1}$	$-0.1640329 \times 10^{+1}$
A_6	$-0.2873860 \times 10^{-4}$	$-0.9401628 \times 10^{-5}$
A_7	0.2495391×10^{-3}	0.3194979×10^{-3}
A_8	$0.1739822 \times 10^{+1}$	$0.1708081 \times 10^{+1}$
B_1	$-0.1922094 \times 10^{-3}$	0.5554837×10^{-3}
B_2	0.5310392×10^{-6}	0.5305829×10^{-6}
B_3	0.1485801×10^{-4}	$-0.2491201 \times 10^{-4}$
B_4	0.4229986×10^{-3}	0.1562029×10^{-3}
B_5	-0.7733552	$-0.2638508 \times 10^{+1}$
B_6	0.2962723×10^{-4}	0.6656607×10^{-5}
B_7	0.1890266×10^{-3}	0.4382294×10^{-3}
B_8	$0.1361674 \times 10^{+1}$	$-0.9191982 \times 10^{+1}$

Table A-4. III Postlaunch Calibration Coefficients Determined June 27, 1980

Coefficients	FPSS1	FPSS2
A_1	$-0.5005656 \times 10^{-3}$	0.3856357×10^{-3}
A_2	0.5321897×10^{-6}	0.5316871×10^{-6}
A_3	0.2804029×10^{-4}	0.8814421×10^{-5}
A_4	0.3004984×10^{-3}	0.5507673×10^{-3}
A_5	$0.4356816 \times 10^{+1}$	$-0.2294463 \times 10^{+1}$
A_6	$-0.1210886 \times 10^{-3}$	$-0.3935267 \times 10^{-4}$
A_7	0.1686625×10^{-3}	0.3279436×10^{-3}
A_8	$0.1556701 \times 10^{+1}$	$0.2645207 \times 10^{+1}$
B_1	$-0.1086737 \times 10^{-2}$	$-0.2948222 \times 10^{-3}$
B_2	0.5458022×10^{-6}	0.5415047×10^{-6}
B_3	0.2859741×10^{-4}	0.2531778×10^{-4}
B_4	0.4699715×10^{-3}	$-0.3735274 \times 10^{-3}$
B_5	$-0.1037046 \times 10^{+1}$	$-0.2593021 \times 10^{+1}$
B_6	0.2968237×10^{-4}	0.3284074×10^{-4}
B_7	0.1812999×10^{-3}	$-0.1052192 \times 10^{-3}$
B_8	$0.1252416 \times 10^{+1}$	$-0.1360665 \times 10^{+1}$

Table A-5. IV Postlaunch Calibration Coefficients Determined July 17, 1980

Coefficients	FPSS1	FPSS2
A_1	$-0.4818073 \times 10^{-3}$	0.3970052×10^{-3}
A_2	0.5318731×10^{-6}	0.5325560×10^{-6}
A_3	0.3316726×10^{-4}	$-0.3573487 \times 10^{-5}$
A_4	0.3004717×10^{-3}	0.5203074×10^{-3}
A_5	$0.3788808 \times 10^{+1}$	$-0.2229115 \times 10^{+1}$
A_6	$-0.1440138 \times 10^{-3}$	$-0.4843318 \times 10^{-4}$
A_7	0.1678243×10^{-3}	0.2682219×10^{-3}
A_8	$0.1678735 \times 10^{+1}$	$0.2263416 \times 10^{+1}$
B_1	$-0.1086574 \times 10^{-2}$	$-0.3003116 \times 10^{-3}$
B_2	0.5408410×10^{-6}	0.5396636×10^{-6}
B_3	0.4516499×10^{-4}	0.3816943×10^{-4}
B_4	0.3423773×10^{-3}	$-0.3097056 \times 10^{-3}$
B_5	-0.7504307	$-0.2698493 \times 10^{+1}$
B_6	0.3953853×10^{-4}	0.3490103×10^{-4}
B_7	0.1394383×10^{-3}	$-0.1010980 \times 10^{-3}$
B_8	$0.1192923 \times 10^{+1}$	$-0.1339042 \times 10^{+1}$

Table A-6. Postlaunch Calibration Coefficients Determined August 27, 1980

Coefficients	FPSS1	FPSS2
A_1	$-0.4508724 \times 10^{-3}$	0.4214450×10^{-3}
A_2	0.5289703×10^{-6}	0.5309641×10^{-6}
A_3	0.3533130×10^{-4}	$-0.3210337 \times 10^{-5}$
A_4	0.3166422×10^{-3}	0.5288627×10^{-3}
A_5	$0.3402219 \times 10^{+1}$	$-0.2474054 \times 10^{+1}$
A_6	$-0.1872402 \times 10^{-3}$	$-0.6040415 \times 10^{-4}$
A_7	0.1720052×10^{-3}	0.2535198×10^{-3}
A_8	$0.1743850 \times 10^{+1}$	$0.2169274 \times 10^{+1}$
B_1	$-0.1088536 \times 10^{-2}$	$-0.2967559 \times 10^{-3}$
B_2	0.5404148×10^{-6}	0.5396493×10^{-6}
B_3	0.5595529×10^{-4}	0.4825613×10^{-4}
B_4	0.3116594×10^{-3}	$-0.2824294 \times 10^{-3}$
B_5	-0.4978371	$-0.2923239 \times 10^{+1}$
B_6	0.3268151×10^{-4}	0.3803778×10^{-4}
B_7	0.1127492×10^{-3}	$-0.1327780 \times 10^{-3}$
B_8	$0.1187505 \times 10^{+1}$	$-0.1339587 \times 10^{+1}$

Table A-7. Postlaunch Calibration Coefficients Determined September 4, 1980

Coefficients	FPSS1	FPSS2
A_1	$-0.6776863 \times 10^{-3}$	0.1946652×10^{-3}
A_2	0.5284552×10^{-6}	0.5323566×10^{-6}
A_3	0.2988950×10^{-4}	$-0.4638057 \times 10^{-5}$
A_4	0.3252105×10^{-3}	0.4797970×10^{-3}
A_5	$0.3388264 \times 10^{+1}$	$-0.2600997 \times 10^{+1}$
A_6	$-0.1827369 \times 10^{-3}$	$-0.4252801 \times 10^{-4}$
A_7	0.1706592×10^{-3}	0.2589267×10^{-3}
A_8	$0.1830159 \times 10^{+1}$	$0.2113208 \times 10^{+1}$
B_1	$-0.1081432 \times 10^{-2}$	$-0.3001880 \times 10^{-3}$
B_2	0.5378218×10^{-6}	0.5367186×10^{-6}
B_3	0.6281060×10^{-4}	0.6410728×10^{-4}
B_4	0.2800354×10^{-3}	$-0.2461689 \times 10^{-3}$
B_5	-0.4471897	$-0.3109232 \times 10^{+1}$
B_6	0.3239203×10^{-4}	0.4965452×10^{-4}
B_7	0.1877559×10^{-5}	$-0.1906793 \times 10^{-3}$
B_8	$0.1180826 \times 10^{+1}$	$-0.1393259 \times 10^{+1}$

ACKNOWLEDGMENTS

The authors thank R. Byrne and G. Nair for countless discussions concerning the calibrations of the FPSS.

REFERENCES

1. Computer Sciences Corporation, CSC/TM-80/6159, Solar Maximum Mission (SMM) Attitude Analysis Postlaunch Report, G. Nair, R. H. Thompson, P. J. Gambardella, G. F. Neal, Y. R. Kwon, P. C. Kammeyer, and J. M. Buckley, August 1980

2. Private Communication with UVSP experimenters, September 17, 1980

3. H. M. Nautical Almanac Office, American Ephemeris and Nautical Almanac. London: Her Majesty's Stationery Office, 1980

MAGSAT ATTITUDE DYNAMICS AND CONTROL: SOME OBSERVATIONS AND EXPLANATIONS

Thomas H. Stengle

Goddard Space Flight Center

ABSTRACT

The Magsat spacecraft was placed into an elliptical sun synchronous orbit on October 30, 1979. Before its reentry 7 months later, Magsat had transmitted an abundance of valuable data for mapping the Earth's magnetic field. As an added benefit, a wealth of attitude data for study by spacecraft dynamicists was also collected. Because of its unique configuration, Magsat presented new control problems. With its aerodynamic trim boom, attitude control was given an added dimension. Minimization of attitude drift, which could be mapped in relative detail, became the goal. Momentum control, which was accomplished by pitching the spacecraft in order to balance aerodynamic and gravity gradient torques, was seldom difficult to achieve. However, several interesting phenomena were observed as part of this activity. This included occasional momentum wheel instability and a rough correlation between solar flux and the pitch angle required to maintain acceptable momentum.

This paper presents an overview of the attitude behavior of Magsat and some of the control problems encountered. Plausible explanations for some of this behavior are offered. Some of the control philosophy used during the mission is examined and aerodynamic trimming operations are summarized.

I. Introduction

Managed by NASA's Goddard Space Flight Center, the Magsat spacecraft was a 3-axis stabilized spacecraft placed into a sun synchronous elliptic orbit of 350 X 560 km on October 30, 1979. During its lifetime which ended with reentry on June 11, 1980, Magsat met its scientific goals and also provided valuable information regarding spacecraft attitude dynamics and control in the low altitude flight regime. Goddard's Attitude Determination and Control Section (ADCS) was charged with the responsibility of daily attitude control operations and monitoring the health and safety of Magsat's semiautonomous control system. As a fallout from this activity and definitive attitude processing by the ADCS, an abundance of attitude data was accumulated. Continued analysis of this data is providing practical insight into such items as aerodynamic drift characteristics, drift minimization, and momentum control. Another benefit from this mission was the operational experience gained from controlling a spacecraft which had a large amount of control autonomy, yet still required 24-hour monitoring and numerous ground supplied control system updates.

Built by the Applied Physics Laboratory (APL), the Magsat spacecraft pictured in figures 1 and 2 utilized a SAS-C type bus. In flight, the spacecraft's Z axis (pitch axis) was nominally pointed near negative orbit normal (NON). Angular momentum provided by the body and a momentum wheel was directed along the -Z axis. In contrast to SAS-C, Magsat was given additional attitude control autonomy due to anticipated high aerodynamic torques. An Attitude Signal Processor (ASP) performed the onboard control system functions and required occasional updates via ground command by the ADCS. The ASP will be discussed in more detail later. Ground commanding of the spacecraft's magnetic coils for roll/yaw or momentum control served as a backup mode which was never required following initial ASP acquisition.

Activation of the spacecraft's magnetic coils for roll/yaw control or momentum dumping by either the ASP or ground command was not desired for two reasons. First, this activity corrupted science data gathered by the experimenter's magnetometer. Second, nutation was increased which had the potential for impacting fine attitude determination required by the experimenter. In order to achieve the goal of minimizing magnetic coil activity, several control capabilities were available and were utilized by the ADCS. As an aid to balancing yaw torques and thus Z-axis drift, a variable length aerodynamic trim boom was built into the spacecraft. The length of this boom was controlled by ground command and was adjusted on several occasions during the mission. Also available for drift control was the capability to target the spacecraft's Z axis to some point off negative orbit normal where the spacecraft might be better trimmed aerodynamically. It was suggested in prelaunch analysis that the Magsat spacecraft might be trimmed with its Z axis at a point between 2 to 4° above NON. While actual experience presented later will show that this trim point varied considerably throughout the mission, the importance here is that control requirements were flexible enough (and, in fact, necessary) to allow placing of the

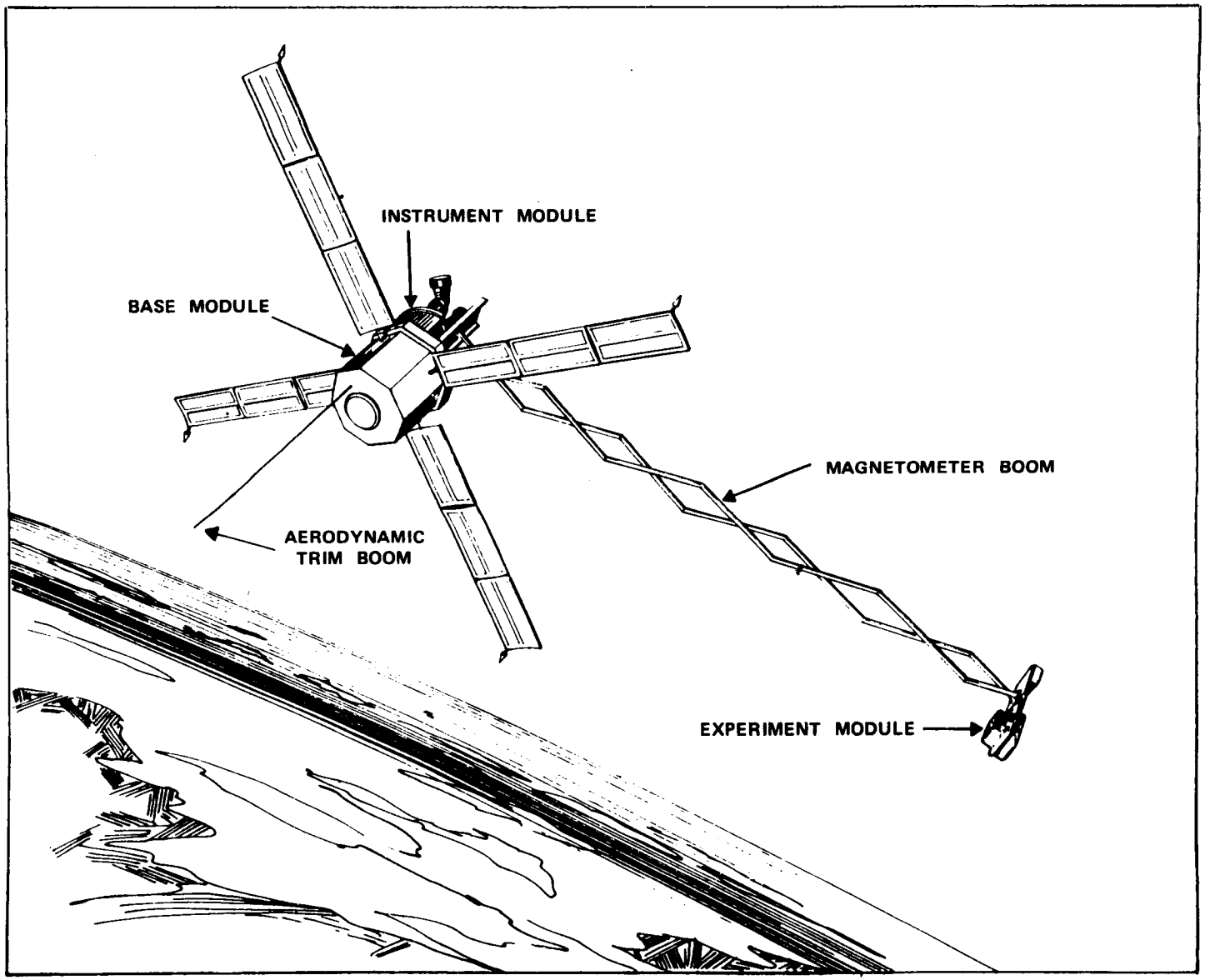

Figure 1. Artist's Conception of Magsat (reference 3)

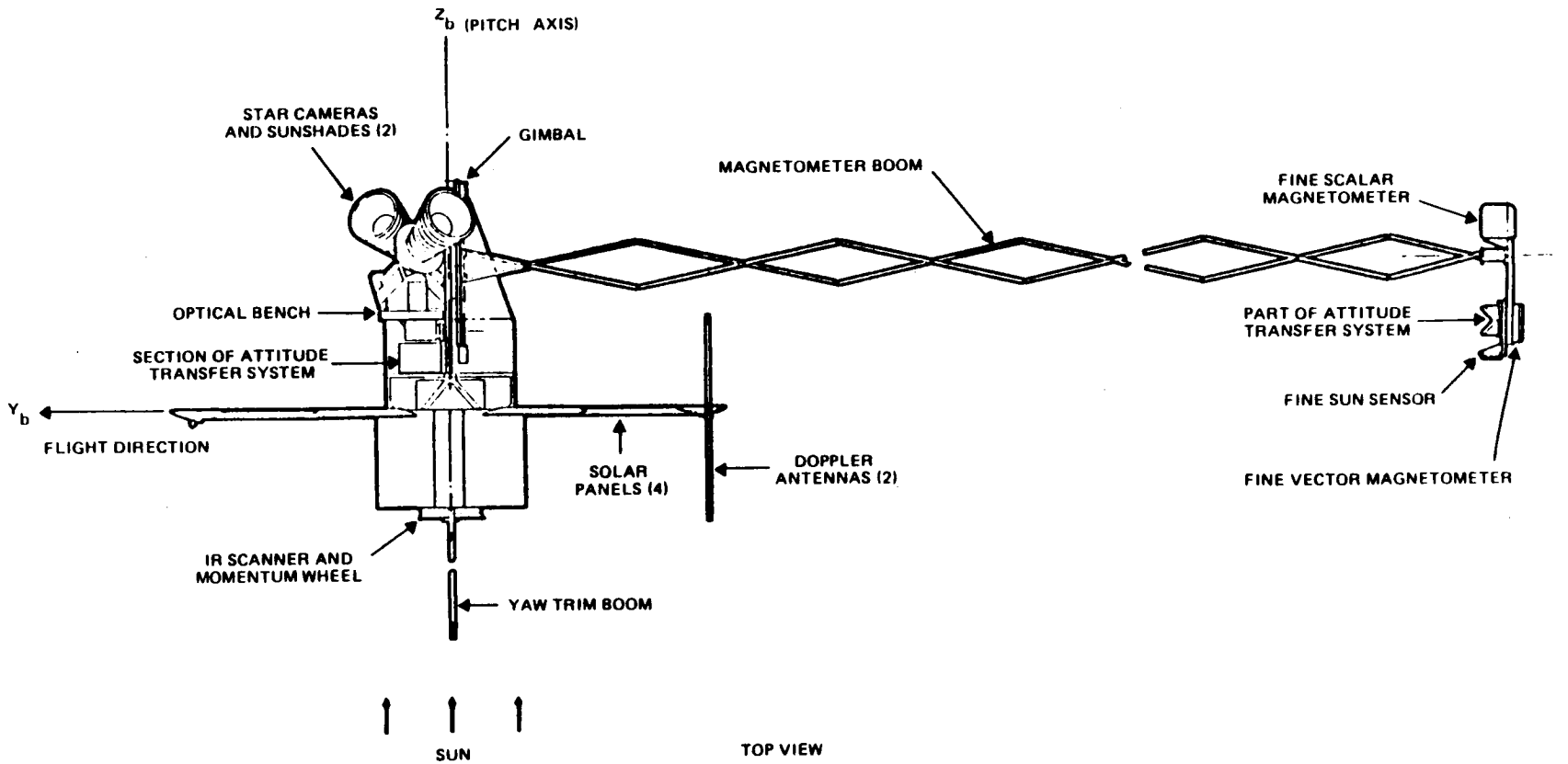

Figure 2. Magsat Orbital Configuration (reference 3)

spacecraft spin axis where roll/yaw control could be minimized. The amount of acceptable drift from the target attitude before ASP activation of control coils was also variable. By changing this control threshold, the drift could be highly restricted at the expense of control torques or given no tight bounds. Another major capability which aided in minimizing coil activity was associated with momentum control. On a near daily basis, the spacecraft's pitch was biased so as to alter the relative effects of the gravity gradient and aerodynamic torques on the spacecraft, thus affecting momentum build-up or loss.

From a control standpoint, Magsat's mission might be divided into three phases. First was an initial acquisition and trimming phase which took place the first 3 weeks of the mission. During this time, the spacecraft was placed into the ASP mode of operation, both the experiment and aerodynamic trim booms were deployed, and momentum control was established by biasing the spacecraft in pitch. This was also an active period of attempting to stabilize the spacecraft's drift with relatively frequent target changes and trim boom positioning.

Following this initial period was a time lasting roughly 4½ months which might be classified as the nominal operations phase. During this phase, control torques were kept to a minimum with active pitch biasing of the spacecraft and six trim boom operations. Magsat's target attitude remained nearly constant at a position 4° above NON.

The final 2 months of the mission were not nominal by any standard. Originally designed as a 5-month mission, orbit decay was less than predicted, thus giving the spacecraft an additional 2 months of life. This resulted in two complications. First, the orbit had time to precess enough so that the spacecraft encountered increasingly larger periods of darkness which had not been anticipated under the prelaunch mission plan. The second complication was that the Sun angle increased so as to create problems in fully charging the spacecraft's battery. These two factors necessitated a Project Office decision to move the spacecraft's target attitude roughly 10° to improve solar array position relative to the Sun. While the ASP successfully maintained the spacecraft Z axis at this off-nominal target roughly 6° below NON, the spacecraft drift and relative frequency of control torques increased drastically. Also as a result of the low power conditions that existed, a considerable amount of full orbit attitude data was lost due to tape recorder turn-offs. The off-nominal target was held until 2 weeks before reentry when it was decided that drift had to be reduced to insure successful attitude control during Magsat's final days. At that time the Z axis target attitude was returned to a point 4° above NON. Attitude drift and control activity benefited considerably. Approximately 27 hours before spacecraft reentry, the target attitude was changed due to Sun sensor calibration limitations to a point 2° above NON. The subsequent increase in drift could not be corrected by the ASP resulting in a nonrecoverable loss of attitude control 20 hours before reentry.

The primary intent of this paper is to summarize some of the dynamics and control phenomena observed by the ADCS during Magsat's 7-month mission. Specifically, items associated with roll/yaw control and momentum control are discussed. Where possible, flight data is presented and actual flight experience is compared to prelaunch expectations. Postmission analysis by the ADCS is continuing with emphasis being placed on obtaining a more thorough understanding of the nature of Magsat's aerodynamic trim point and in studying flexible boom dynamics.

II. The Attitude Signal Processor (ASP)

As mentioned before, the ASP performed the onboard control system functions and required periodic updates via ground command by Goddard's Attitude Determination and Control Section. While the ASP is not the subject of this paper, its general operation and capabilities should be summarized. For a detailed description, the reader is directed to references 2 and 3.

Pitch control was maintained with a momentum wheel tied into a control loop which included an Ithaco IR scanner, a filter, and a gyro. While pitch control was active throughout the spacecraft's orbit, activities associated with roll/yaw control and momentum dumping were keyed to 14 control points in the spacecraft's orbit referenced from the ascending node. These control points are depicted in figure 3. Of these 14 control points, four were roll sample checks, two were momentum checks and the remaining eight were points for possible magnetic coil commands by the ASP. Roll samples were taken by the IR scanner at the poles and nodes and indicated to the ASP any attitude error from a ground supplied target attitude. Note that a roll error at the poles represents a declination error from negative orbit normal. Likewise, a roll error at the nodes represents a right ascension error from negative orbit normal. If the ASP determined that the Z axis had precessed beyond some ground supplied threshold from the target attitude then the Z axis coil was commanded on at an appropriate torque zone. Right ascension torque zones were located around each node while declination torque zones were located between 22° and 40° in latitude. The duration of the Z coil on time was a ground supplied parameter but was typically 5 minutes. A similar procedure was followed for momentum control. If the speed of the momentum wheel exceeded the nominal speed of 1500 rpm by some ground supplied threshold (usually 200 rpm), spin/despin coils were commanded on. The duration of the coil on time for momentum dumping could be as high as 40 minutes. This outline of roll/yaw and momentum control represents the nominal operational ASP mode. Certain variations in roll/yaw, pitch and momentum control existed, but will not be covered here. One operational restriction which should be noted is that the spacecraft had to be maintained within 12° in roll in order to avoid an IR scanner failure due to calibration limitations. If this occurred, the pitch control loop was disabled and had to be reactivated by ground command.

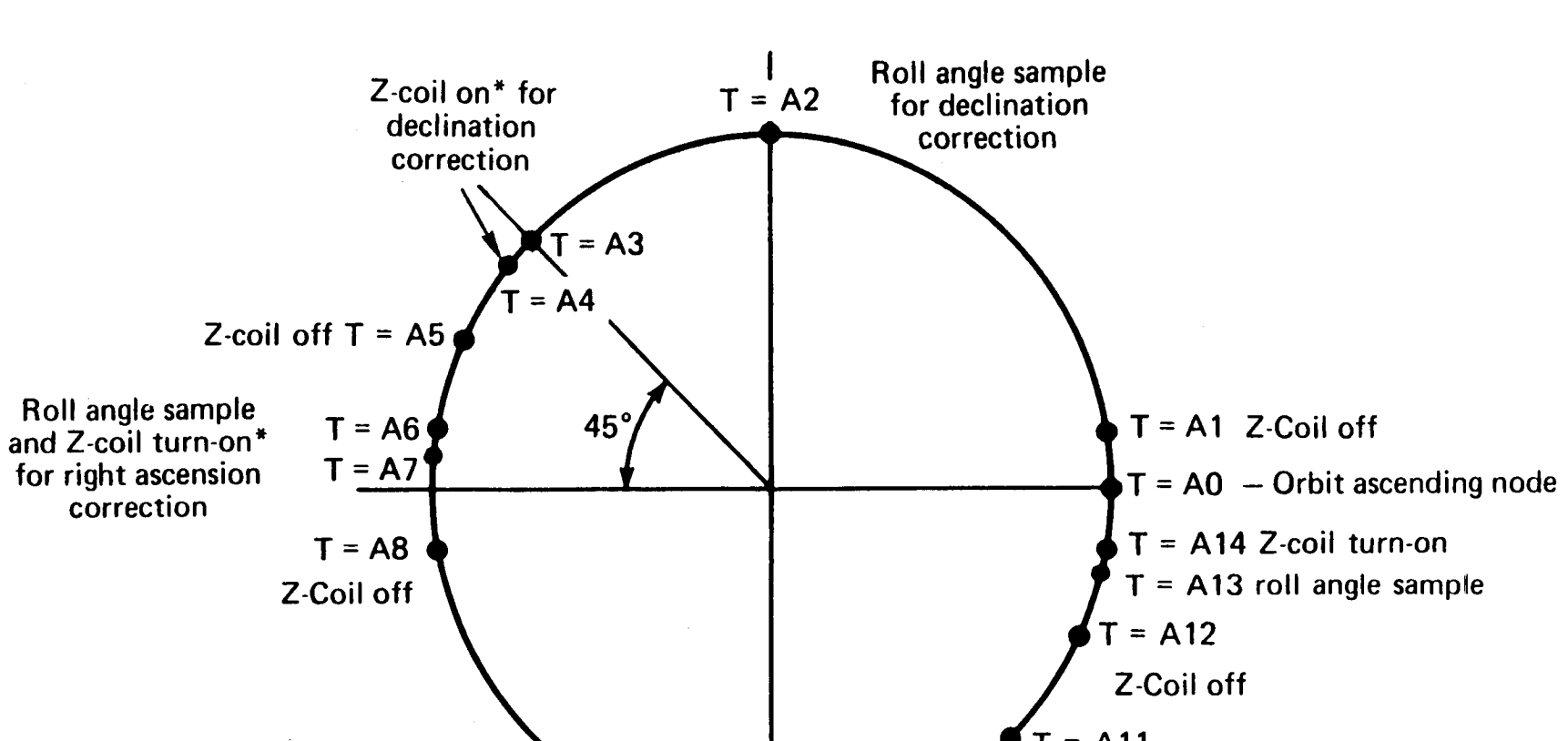

Figure 3.

Magsat Orbit Positions for ASP Observations and Control (reference 1)

Nineteen ASP parameters were uplinked to the spacecraft on a near daily basis. Most frequently changed were the spacecraft's orbital period, ASP clock correction, pitch bias, and percent Earth values used for roll determination. It should be pointed out that the spacecraft's target attitude was controlled with the percent Earth values. Other parameters which were changed, but with less frequency were the thresholds used by the ASP to determine the necessity for momentum dumping or roll control. Loads to the ASP were generated on tape and quality assured by the ADCS. These tapes were hand carried to Goddard's Multi-satellite Operations Control Center (MSOCC) for uplink to the spacecraft at a scheduled station pass. Although a minimum of one ASP load could usually be expected each day, updates to the pitch bias and orbit related parameters were not regularly scheduled events, but were the result of an attitude control analyst's decision to improve ASP performance. Changes in target or control threshold parameters, however, always followed consultation with the Magsat Project Office.

III. Momentum Control

Although conceptually easy to understand, momentum control activities often presented some perplexing problems operationally. Because automatic momentum dumping could result in coil activity for as long as 40 minutes, it was very desirous, and became a goal to eliminate the necessity for automatic dumping through proper biasing of the spacecraft in pitch. This approach to controlling momentum was advanced early in the mission planning by the APL and during most of the mission was handled with success by the ADCS. By pitching the spacecraft, the magnitude of the gravity gradient and aerodynamic torques could be altered so as to affect a wheel speed change advantageous to momentum control. An average of one pitch bias update was uplinked to the spacecraft each day. While this exceeded the APL's estimate of one every two days, there were periods of up to 4 days in which there were no pitch bias changes. As a measure of the success of this approach to momentum control, the spin/despin coils were inactive between November 10, 1979, and May 15, 1980. During much of the mission the primary control function was one of fine tuning the bias. Wheel speed changes were usually held to less than 5 rpm/orbit. Nominal changes in the pitch bias were on the order of .1-.2°.

The aerodynamic model of the Magsat spacecraft used in simulations and both prelaunch and postmission analysis decomposes the spacecraft into ten elements. While its accuracy is questionable, it is useful in showing general trends and in providing theoretical estimates of torque magnitude as shown in figure 4. Aerodynamic torques were addressed in several technical memos before launch and formed an integral part of the control philosophy. Intuitively, these torques can be expected to exhibit the largest daily variations due to the wide range of altitude dependent atmospheric variables. Successfully predicting these variations and their effect on the required pitch bias for momentum control does not appear practical. Plots of the pitch bias and averaged daily flux as given in figure 5 appeared to show some rough

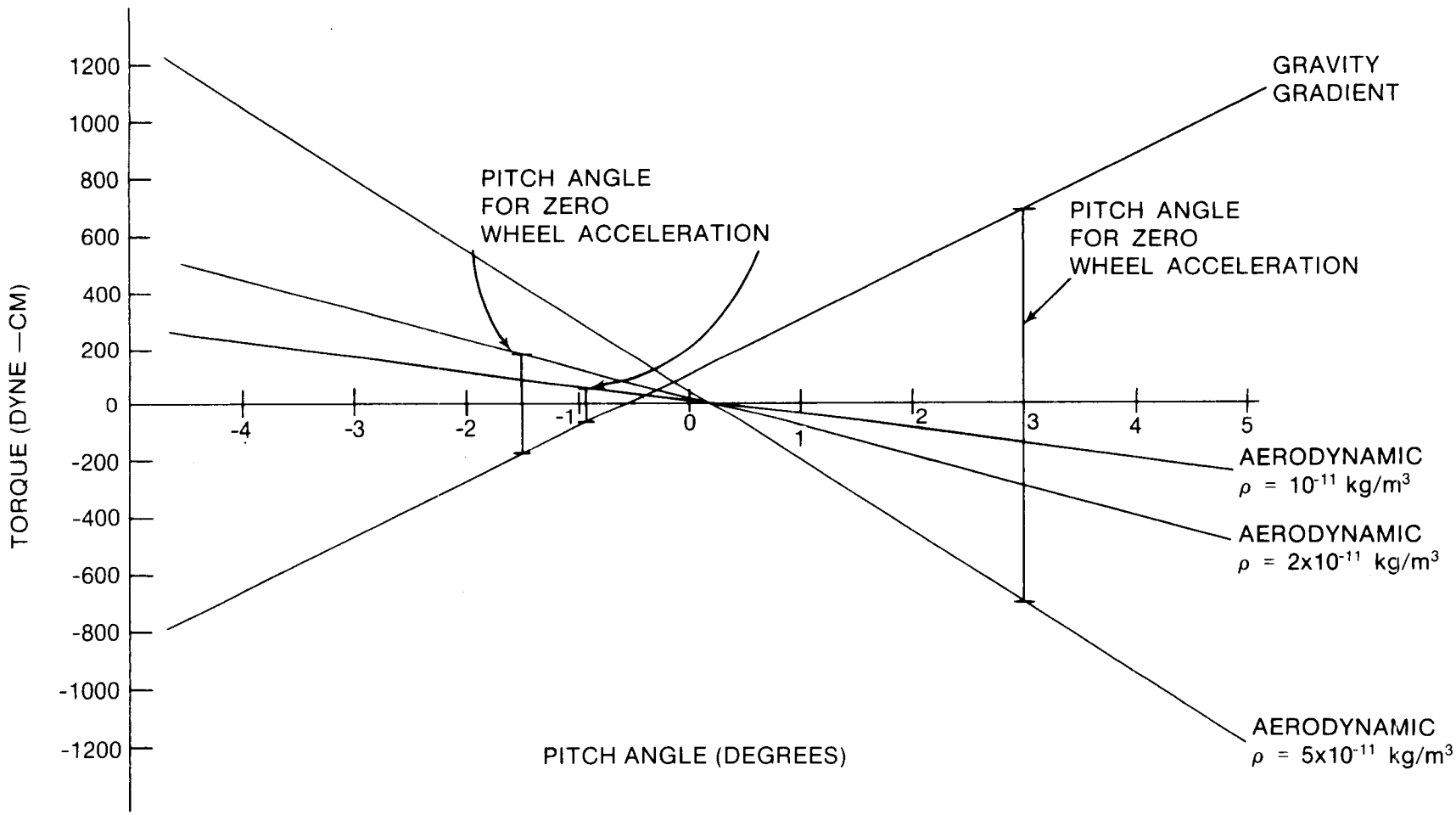

Figure 4.

Aerodynamic and Gravity Gradient

Torques Versus Pitch Angle

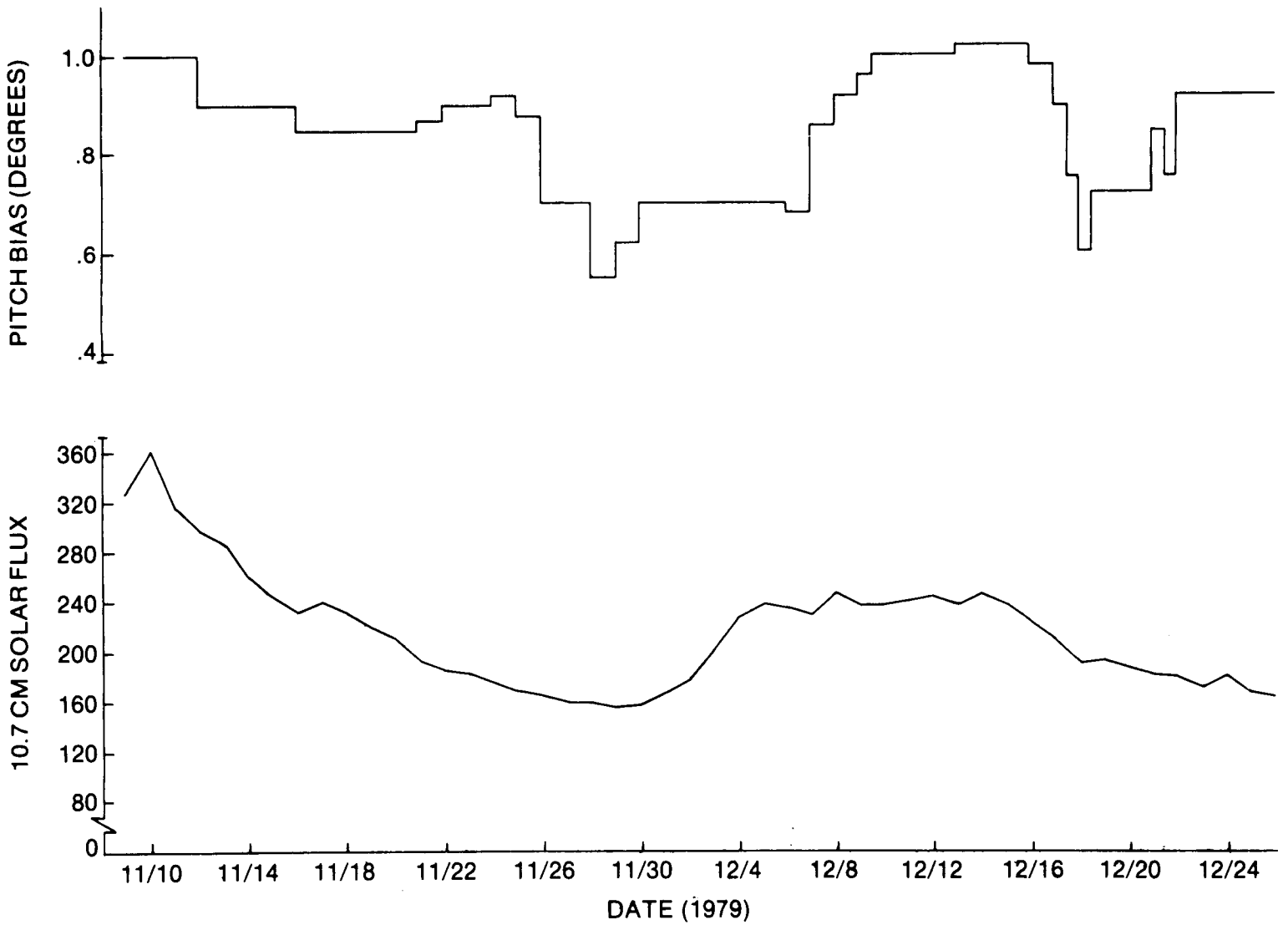

Figure 5. Pitch Bias and Solar Flux History

(November 8 - December 28, 1979)

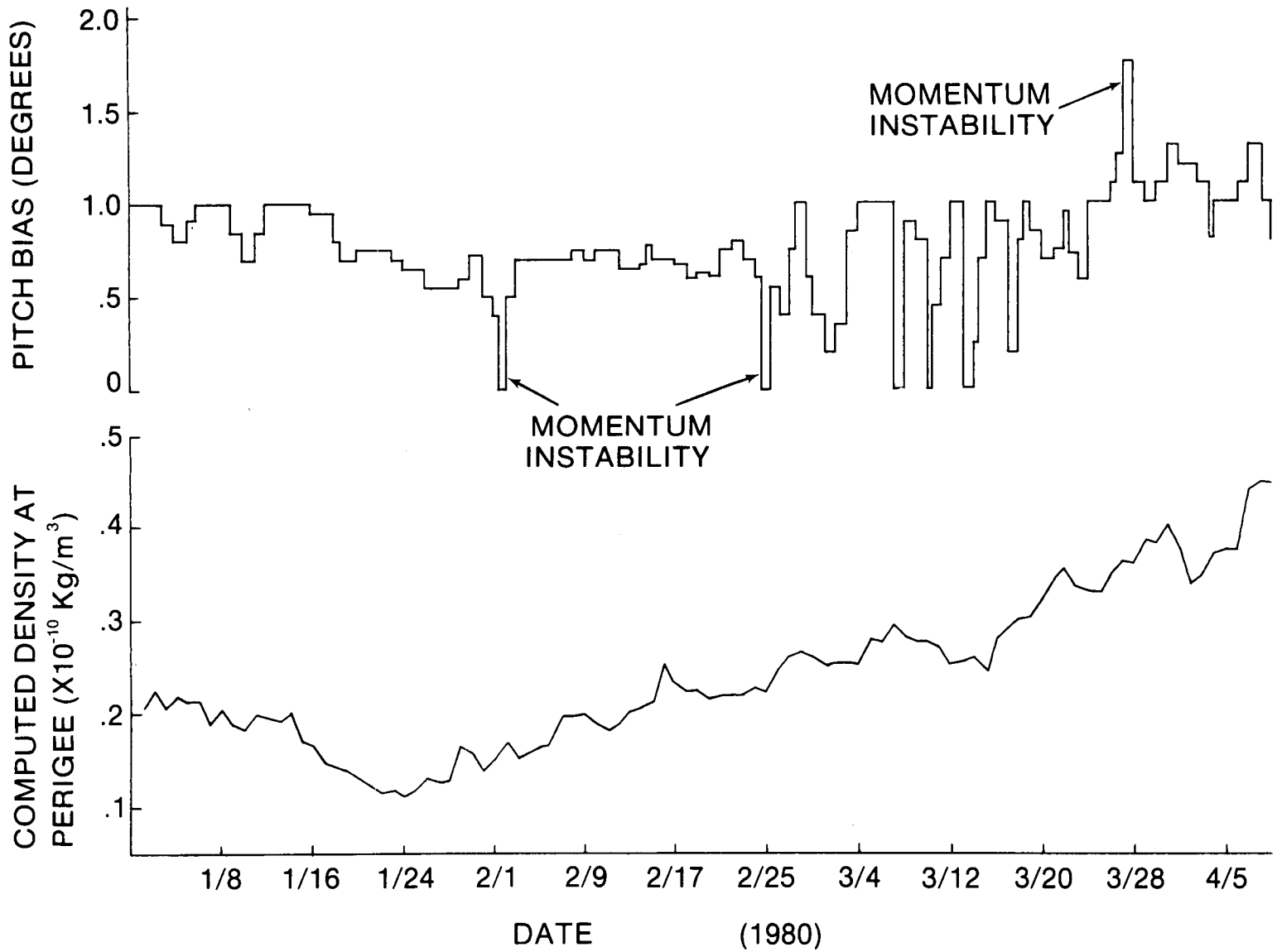

Figure 6. Pitch Bias and Computed Density History

(January 1 - April 15, 1980)

correlation early in the mission. A 28-day cycle associated with the pitch bias activity was evident and was phased similar to the Sun's 28-day cycle. However, this correlation did not hold true nor did the pitch bias history show any likeness to the nature of the atmospheric density at perigee computed using a flux dependent Jacchia model (figure 6).

Gravity gradient and aerodynamic torques act in opposite directions which makes possible the use of these torques for momentum control. It must be kept in mind that the purpose was to balance net orbital torques. Variations over the orbit in wheel speed could be expected due to the altitude dependent aerodynamic torques. (Altitude variations in gravity gradient torques were relatively small). The orbital variation in the wheel speed was nominally less than 15 rpm, but went higher than 100 rpm when the pitch bias was increased to 8° late in the mission. The magnitude and direction of the torques were such that to spin up the wheel the spacecraft was pitched in a negative sense when average orbital gravity gradient torques dominated during the first 6 months of the mission and a positive sense when average orbital aerodynamic torques dominated at the end of the mission. The transition period in which the relative roles of the gravity gradient and aerodynamic torques reversed was one of two noteworthy items observed as part of momentum control activities. This period occurred 6½ months into the mission with the spacecraft in a 270 km X 365 km orbit and lasted 2 weeks. During this time the momentum could not be controlled by biasing the spacecraft in pitch. The reason for this can be shown both theoretically and graphically. Tossman of the APL described the average orbital torque about the pitch axis as:

$$T = K_0 + K_{GG} P + K_{AERO} P$$

where K_0 = torque at zero pitch

$K_{GG} = \partial T_{GG} / \partial P$

$K_{AERO} = \partial T_{AERO} / \partial P$

P = pitch angle

T_{GG} = average orbital gravity gradient torques

T_{AERO} = average orbital aerodynamic torque

Theoretical results show that the coefficients K_{GG} and K_{AERO} are linear and of opposite sign over the range of pitch bias angles used operationally (figure 4). By defining K_{AERO} and K_0 as coefficients derived from average torques over an orbit, orbital variations in these coefficients are avoided. Solving for the pitch angle required to balance the two torques results in the following expression:

$$P = -K_0/(K_{GG} + K_{AERO})$$

As can be readily seen, when K_{GG} and K_{AERO} approach each other in magnitude (but still of opposite sign) torque control using pitch biasing becomes no longer effective. Also, depending on which torque dominates, the spacecraft must be pitched in opposite directions to achieve, for example, an increase in momentum.

Returning to the available wheel speed data during the mission and the pitch bias history, it is instructive to determine actual values for the coefficients K_{AERO} and K_{GG}. The sum of these two coefficients, $K_{GG} + K_{AERO}$ is plotted in figure 7 for the period between January 1 and May 1, 1980. The results do not clearly show what might intuitively be expected but do reflect the randomness and variability of the spacecraft's aerodynamics. A gradual decline in $K_{GG} + K_{AERO}$ would be expected as the aerodynamic torques gradually increase in importance. This, however, is not obvious from the flight data. Unfortunately, definitive values for $K_{GG} + K_{AERO}$ beyond May 1, 1980, cannot be easily determined. This is due to a scarcity of good data resulting from poor spacecraft health and the fact that with the higher pitch biases used, it is difficult to determine with some confidence the net wheel speed acceleration.

The transition period is depicted graphically in figure 4. Plotted are average gravity gradient torques and aerodynamic torques over an orbit versus pitch angle. Three theoretical curves are featured for the average aerodynamic torques corresponding to conditions found throughout the mission. As the mission progressed, the magnitude of these torques increased, thus effecting the magnitude of the slope of the aerodynamic torque curves given in figure 4. This plot shows graphically the proper pitch angle for zero torque about the pitch axis (and thus, no acceleration in the momentum wheel) and also the trend towards a more negative pitch as aerodynamic torques gain in relative importance. Figure 4 also shows the need for a positive pitch when this torque dominates the system.

One surprise associated with the transition period was how rapid the aerodynamics changed. In the 1-week period immediately preceding the loss of momentum control, the required pitch bias increased from 2° to its operational limit of 8°. Previous to that time momentum control activity had been relatively stable with pitch biases ranging between $.5^{\circ}$ and 2°.

Once it was concluded that wheel speed had been lost, the pitch bias was returned to zero. This was done to reduce orbital variations in the wheel speed caused by orbital variations in the aerodynamic torque. Without the momentum control capability with pitch biasing, automatic momentum dumping using electromagnetic coils occurred several times a day. Some degree of control over the momentum was achieved by biasing the spacecraft pitch following the 2-week transition period. It should be pointed out that this was approximately 1 week before spacecraft reentry and time did not permit the establishment of tight control over the momentum which was exhibited during the first 6½ months of the mission. Nevertheless, there was a reduction in momentum dumping activity the last week of the mission by biasing Magsat's pitch.

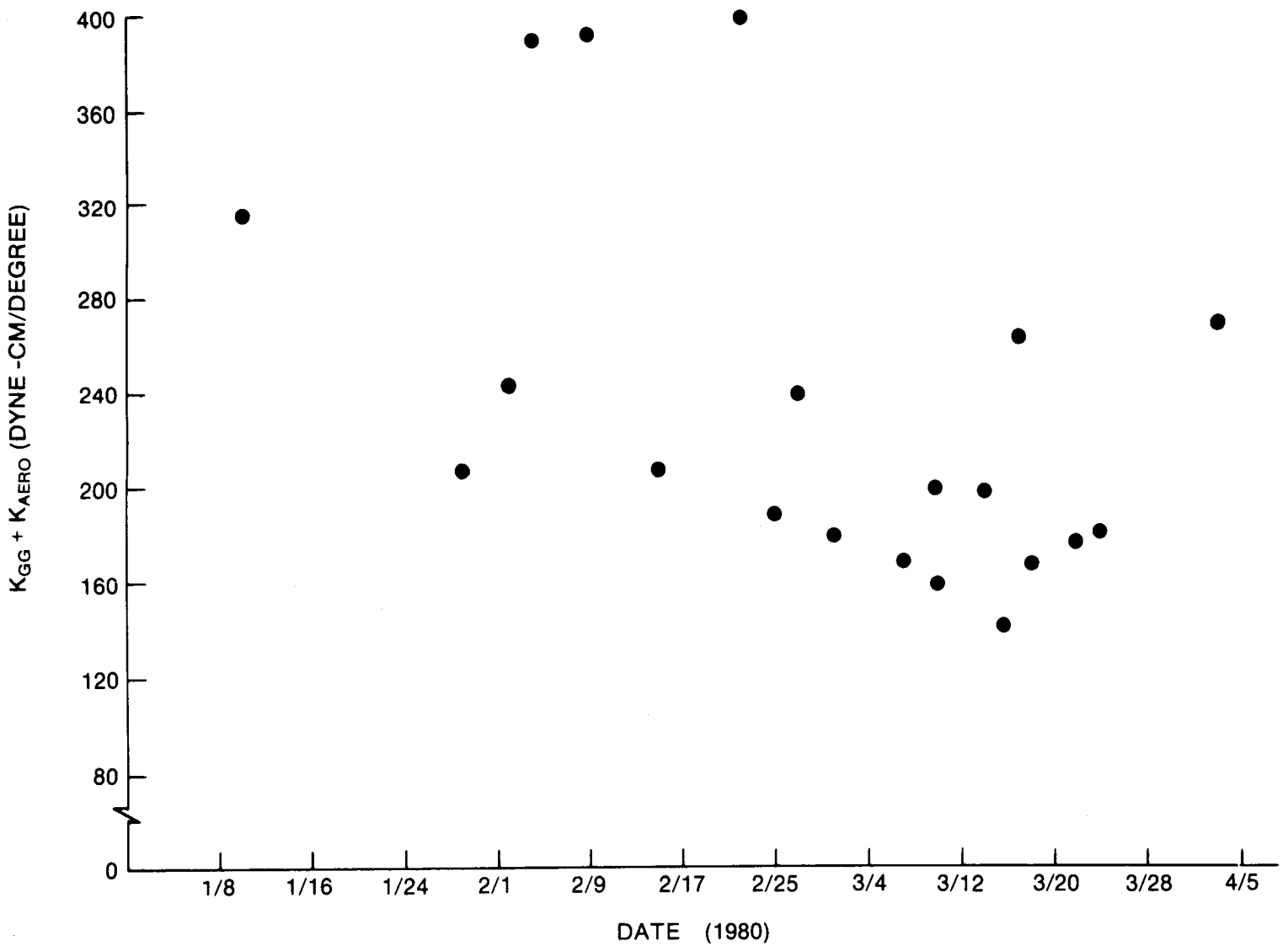

Figure 7. $K_{GG} + K_{AERO}$ Estimated from Wheel Speed and Pitch Bias History

A second noteworthy phenomenon associated with momentum control was occasional instability in the momentum. This required more active monitoring of the momentum wheel speed and numerous ASP loads with large pitch bias changes to bring the momentum back under control. At least three periods of wheel speed instability were encountered during the mission. These periods can be observed in figure 6 as sudden changes in the required pitch bias following a period of relatively small pitch bias changes. This feature was characterized by a rapid rise or fall in the wheel speed as high as 30 rpm per orbit requiring large, immediate changes to the pitch bias to avoid spin/despin coil activity. Thus far, there has been no confirmation that a sudden change in atmospheric conditions affecting aerodynamic torques caused these rapid changes in the wheel speed. This does, however, appear to be the only plausible explanation. There also has not been any consistent correlation found between these periods of wheel speed instability and significant changes in the spacecraft Z axis drift. This might be expected since Z axis drift should be affected by large changes in aerodynamics which might suddenly change spacecraft momentum. A rough correlation can be found for one case around March 25, 1980. On that day, the spacecraft drift suddenly increased from 2°/day to 8°/day. At that time, there was also a larger than nominal drop in wheel speed. The importance of the occasional momentum instability is that it illustrates the need for active monitoring of a spacecraft such as Magsat while in low altitude flight. Real time monitoring and near real time response was often necessary to avoid magnetic coil activity. This phenomenon also adds evidence to the extreme variability of atmospheric conditions.

IV. Spacecraft Drift

Drift minimization became the most challenging aspect of Magsat's control activities. The goal was to eliminate all attitude control torques by using the trim boom and by properly adjusting relevant ASP parameters for attitude target placement. Of course, this goal was not achieved. However, with the exception of the few weeks following launch when active trimming operations were underway and the final 9 weeks of the mission when the spacecraft had to be held at an off-nominal attitude, the number of control torques was below most prelaunch expectations. In fact, there were periods in excess of 2 weeks in which there were no control torques. These periods can be seen in a histogram of the attitude control torques given in figure 8. Part of this success must be attributed to the fact that a 6° control threshold was used during most of the mission rather than the 2° bounds suggested before launch. This allowed more overall drift, but did not jeopardize control or safety of the spacecraft. Prelaunch estimates of the control torque activity were as high as three torques per day with a control threshold of 2°.

The daily Attitude Determination and Control Section role in drift control was one of processing a minimum of one orbit of playback data to track the spacecraft Z axis drift in right ascension and declination coordinates. Decisions regarding trim boom operations and target changes were made by the Attitude Determination and Control Section following consultation with the Magsat Project Office and on occasion, the Applied Physics Laboratory. In general, there was considerable caution by all organizations involved during the early

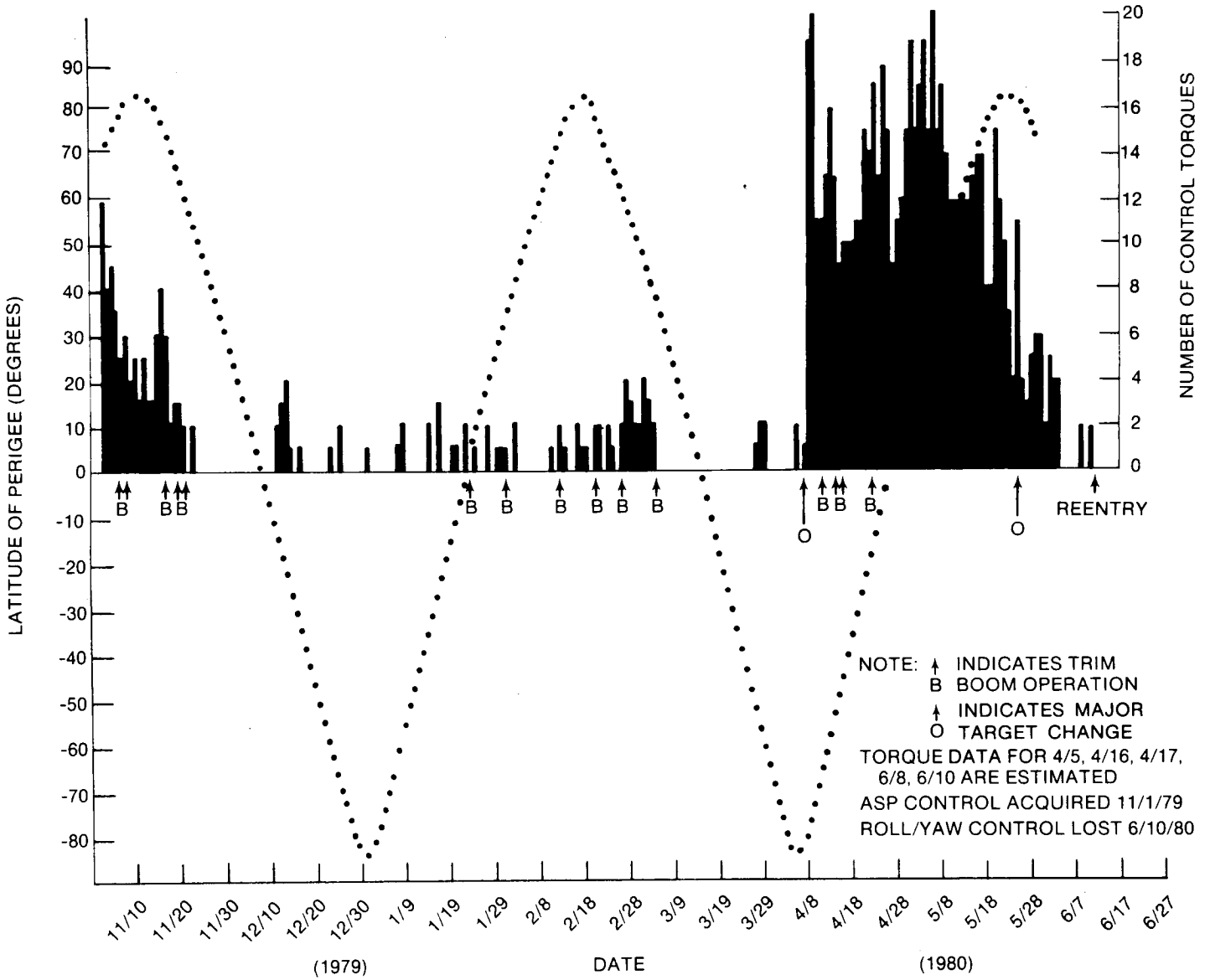

Figure 8. Roll/Yaw Control Torque Histogram and Perigee History for the Magsat Mission

months of the mission towards overuse of the aerodynamic trim boom and in actively changing the spacecraft target attitude. This initial conservatism was the result of several factors. First was the uncertainty in the physical reliability of the trim boom system following a large number of extensions and retractions. A second factor was the lack of experience in controlling a spacecraft such as Magsat with its unique configuration and control capabilities. Although the amount of prelaunch analysis by both the Applied Physics Laboratory and the Attitude Determination and Control Section was considerable, large uncertainties in modeling aerodynamic effects seemed to demand a certain degree of hesitancy in making changes to trim boom length or target location until more experience and confidence could be gained with these operations.

Use of definitive data can now give a more complete picture of Magsat's drift characteristics. As predicted by simulations conducted by the Applied Physics Laboratory, Magsat's drift track is characterized by two distinct circular motions as illustrated in figure 9. One circular track which is traced out over an orbit is of varying size, but typically around 1° in diameter. This orbital motion can be attributed primarily to variations in the aerodynamic torques as the spacecraft travels through its orbit. While gravity gradient torques were present and affected roll/yaw torques, their effect appears to be of lesser importance when compared to aerodynamic torques. If the spacecraft were properly trimmed such that total environmental torques averaged over the spacecraft's orbit were zero then the orbital drift circle was closed. If the net torque was nonzero, then in addition to the orbital drift track, the spacecraft's Z axis would also precess about a larger, secondary circle with a period ranging between 4-7 days. The size of this circle varied, but was typically observed to be between $2\text{-}6^{o}$ in diameter. Figure 10 is another example of this secondary Z axis precession. The orbital motion has been removed for clarity. In figure 10, not only can the circular drift track be observed, but also the consequence of drifting outside the control bounds as specified by the ground supplied target attitude and control threshold. Both a right ascension and declination control torque are shown.

The center of the secondary circle was referred to in prelaunch analysis and during the mission as the spacecraft trim point. While the location and uniqueness of this trim point is still being studied, the apparent trim point during the mission was not stationary, although it always remained above negative orbit normal in declination. The Applied Physics Laboratory predicted that net orbital Z axis motions would center about a preferred trim point. The desirability by the Z axis to remain above NON has been attributed to superrotation of the atmosphere. Dynamic analysis by Tossman (references 4 and 5) indicated that minimum attitude perturbations would exist if Magsat flew into the relative wind. Thus, Magsat wanted to fly at a biased declination angle, directed into the westerly wind caused by atmospheric superrotation. In effect, this superrotation of the atmosphere introduces a "side" component of wind which is variable in direction and magnitude as the spacecraft passes through its orbit. Figure 11 shows the X, Y, and Z components of the spacecraft wind vector in spacecraft body coordinates

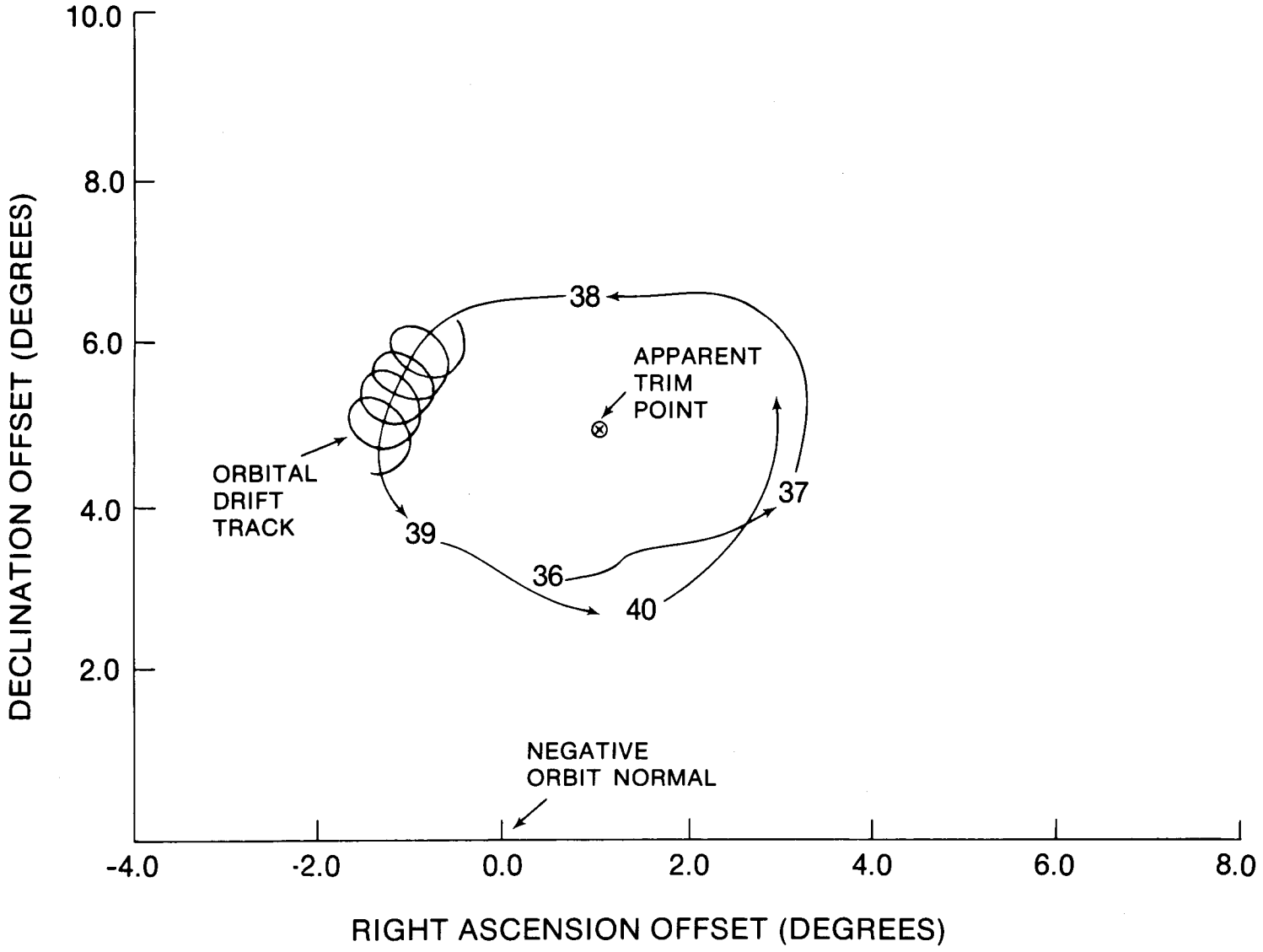

Figure 9. Z Axis Drift for Days 36-40 (February 5-9), 1980

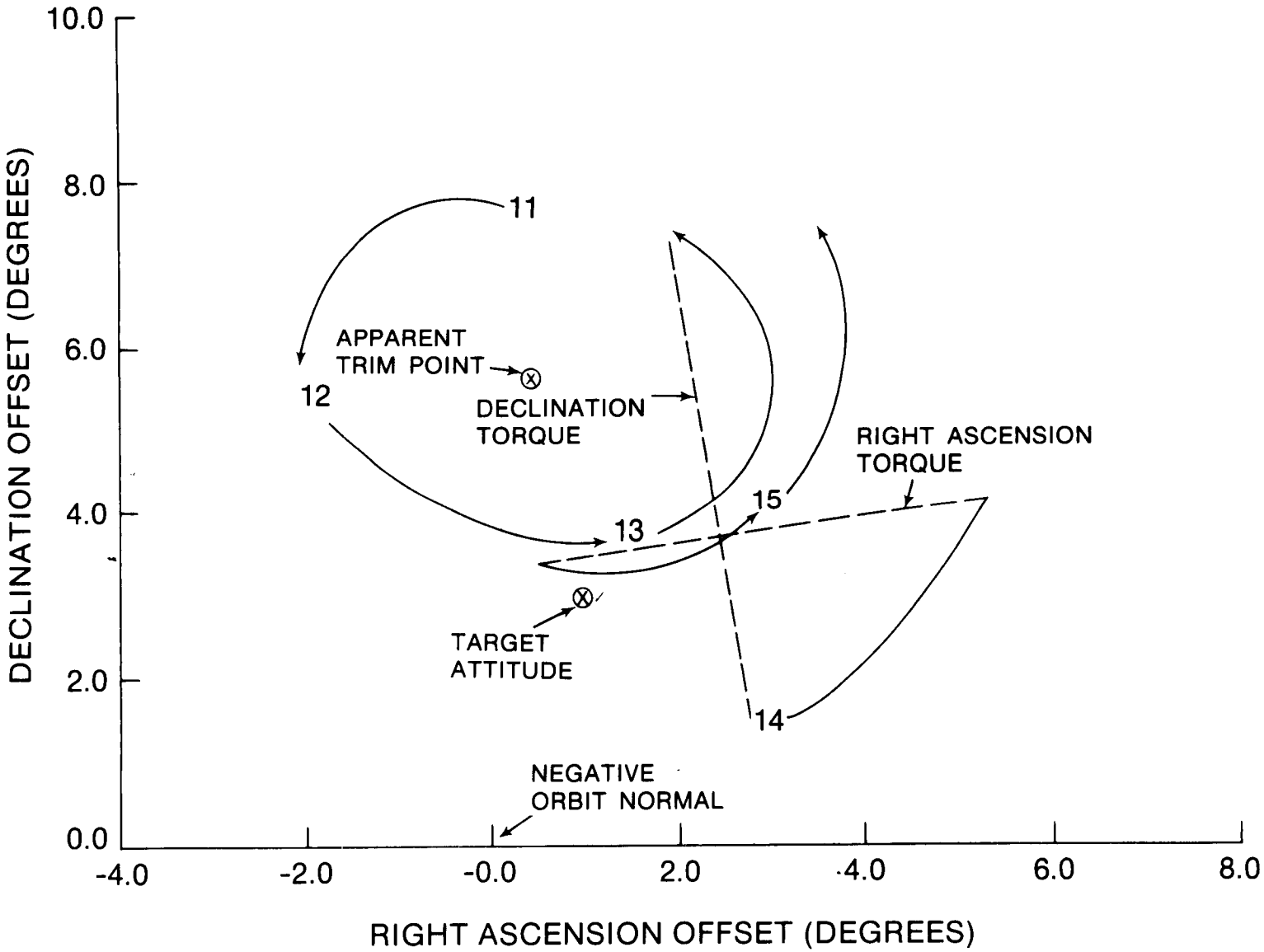

Figure 10. Net Orbital Drift for Days 11-15 (January 11-15), 1980

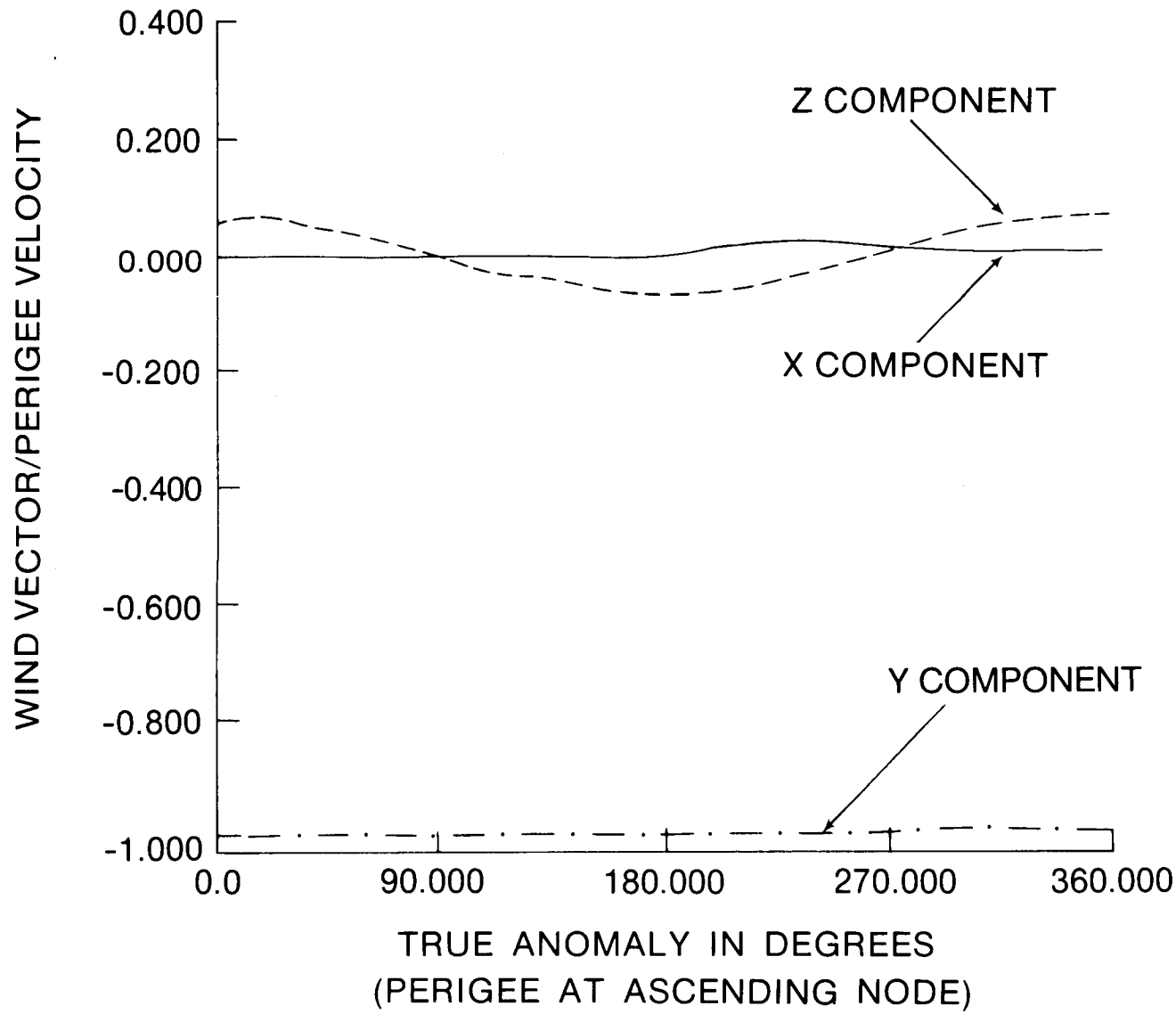

Figure 11.

Normalized Wind Vector for Magsat Targeted

At Negative Orbit Normal (Early Mission Orbit)

which were calculated for a Magsat orbit with the target attitude at NON. These components are normalized with respect to the spacecraft velocity at perigee. As can be seen, a considerable component of the wind vector is present in a direction parallel to the pitch axis. With Magsat's relatively large (.28 m) center of mass-center of pressure offset along the roll axis, density variations due to the orbit's eccentricity, and superrotation, significant variations in the yaw torque could be expected. Simulations show that the Z component of the wind vector is significantly reduced by targeting above NON. This results in yawing the spacecraft into the relative wind.

The significant point here is that no matter how far the spacecraft was placed from the trim point, the precession of the Z axis was always such that it circled a trim point located above negative orbit normal. Generally speaking, the larger the circle of precession, the higher the drift rate. The Applied Physics Laboratory believed that a viable control approach for reducing drift would be to determine the trim point by tracking the Z axis precession over a period of days and then maneuver the spacecraft to that target. Subsequently, the net orbital Z axis motion as predicted by the Applied Physics Laboratory's simulations would precess less than 1° from this point. Although this approach was tried, it was abandoned primarily because the drift bounds was increased to 6° and this significantly reduced control torques to a more tolerable level. When the Applied Physics Laboratory's suggested control approach was tried, two problems were evident. First, maneuvering the spacecraft to a specific target to within 1° was not a simple task. This type of maneuver was accomplished by closing the drift threshold to force the ASP to automatically torque the spacecraft to the desired target. The coarseness of the control system and coupling of right ascension motion with declination maneuvers and vice-versa did not permit accurate placement of the spacecraft's Z axis. This can be seen in figure 10. A second problem was that the desired target was dynamic. This was suspected in prelaunch analysis, but no estimates of the target's variability were made. Figure 12 shows the location of the apparent target attitude determined from the drift tracks during various periods of the mission. At one time it was postulated that the target location was a function of the latitude and altitude of perigee. This cannot yet be substantiated, although the target appears to want an offset in right ascension when perigee is at the poles. One period of operation does seem to validate the findings of the Applied Physics Laboratory's simulations. Between March 5-27, 1980, a very stable drift period existed. The net orbital drift track for 5 days during this period is given in figure 13. During this time the spacecraft remained close to its trim attitude, never precessing away from this point by more than 1°.

Concerning the size of the control threshold relative to control torque frequency, evidence certainly suggests that a further reduction in the number of control torques may have been achieved by using larger control threshold. An example of this can be seen in figure 10. The Z axis precession was following what appears to be a stable circular track about a trim point before

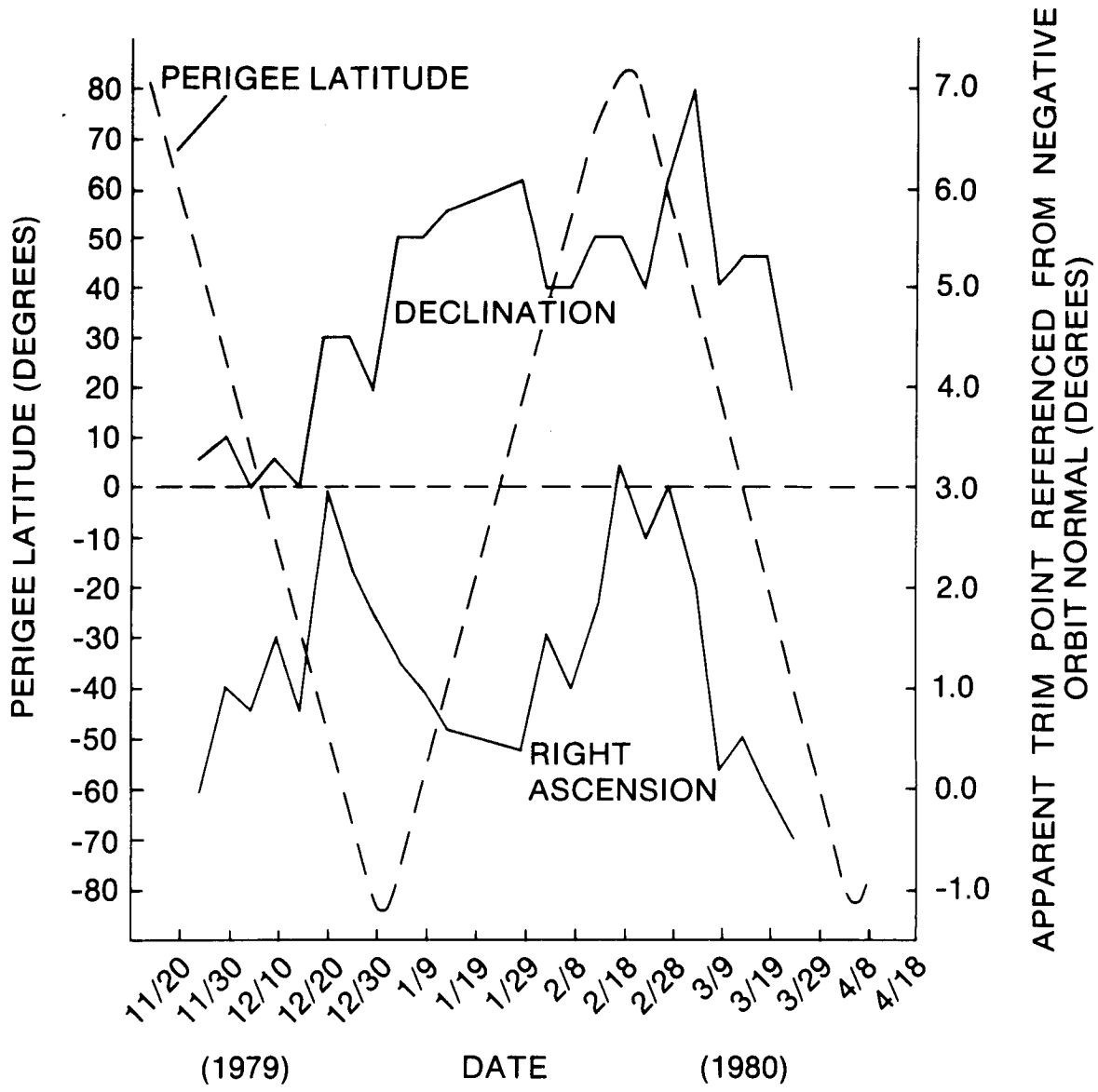

Figure 12.

Apparent Magsat Trim Point Determined From Definitive Data

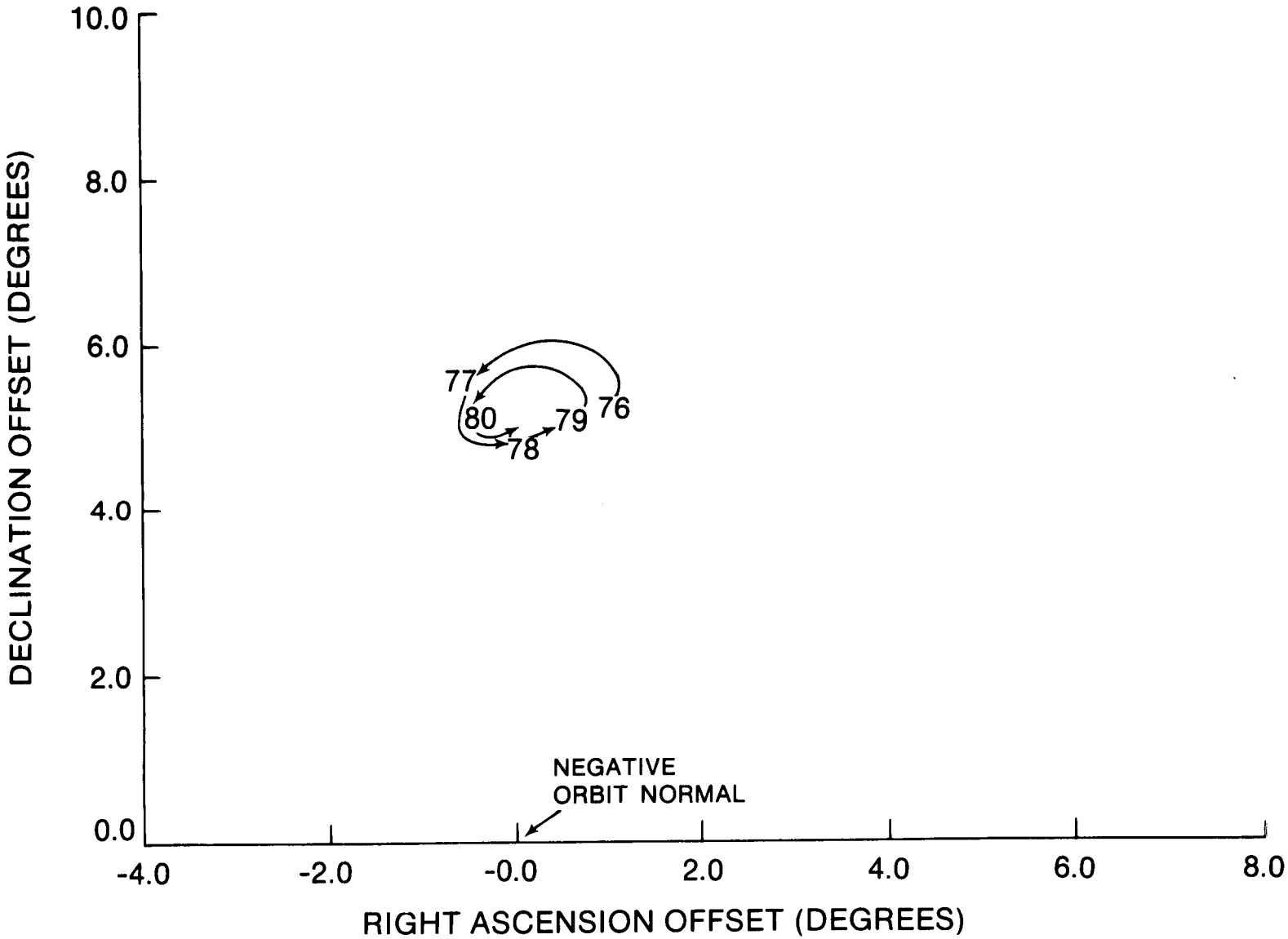

Figure 13.

Net Orbital Drift for Days 76-80 (March 16-20), 1980

it crossed the control threshold. Had the threshold been larger, the precession would have probably continued on the track pattern established. Figure 10 shows that two control torques would have been averted since coupling from the first (declination) torque necessitated a second (right ascension) torque. The main reason for not opening the threshold further was the 12° roll restriction with the IR horizon scanner had to be respected. It should also be kept in mind that real time data available during the mission could not supply analysts with the complete picture of the drift tracks which are now available from definitive data.

The importance of the aerodynamic trim boom cannot be minimized. In fact, the trim boom was a vital, if not essential tool for reducing drift. Sixteen boom operations were performed during the mission including 10 which took place following an initial 3-week period of trimming during Magsat's early mission phase. Boom operations have been marked on the histogram of control torques given in figure 8 so that the effectiveness of the trim boom can be clearly seen. Boom operations on November 20, 1979, and March 4, 1980, were followed by extended periods of nearly 3 weeks with low drift and no control coil activity. Perhaps the best example of what trim boom operations can accomplish can be seen in figure 14. Presented are drift tracks for 2 to 3 orbits on 4 days in late November 1979 with four different trim boom positions. Net orbital drift was significantly reduced.

Because of orbit eccentricity and variations in the spacecraft attitude, the yaw torque was always variable over the orbit regardless of the boom length. The general approach to trimming with the boom was to assume an imbalance in the yaw torque could be corrected only when the spacecraft was at perigee. Thus, when perigee was at either pole, boom extensions or retractions could be made to change yaw torque which would affect declination drift. Likewise, changes with perigee at the equator were made to reduce right ascension drift. While in practice the above approach proved adequate, the general lack of experience in working with a trim boom necessitated a certain degree of trial and error with this operation. Although a large degree of confidence was placed in the direction of boom change, the magnitude of these changes to affect an increase or decrease in yaw torque was always questionable. Typical changes in boom length were 25 cm. Some prelaunch analysis suggested that command sequences for extending or retracting the boom should be in 2 cm increments (reference 4).

Current postmission analysis is involved in a more detailed examination of the aerodynamic effects using definitive attitude data which is now available, and also critiquing drift control operations with the spacecraft's aerodynamic trim boom. Here, it is instructive to point out the nature of the drift patterns observed. Also, rather than take a theoretical approach to explaining how drift might be reduced, periods of relatively low drift can be examined with special attention to the trim boom configuration and target attitude which provided low drift. Two periods of low drift are summarized below. One period corresponds to a very stable drift period beginning around March 5 and lasting until March 27, 1980. During this period, perigee was located at or near the descending node. The second period covers the first week in January 1980 when perigee was at or near the

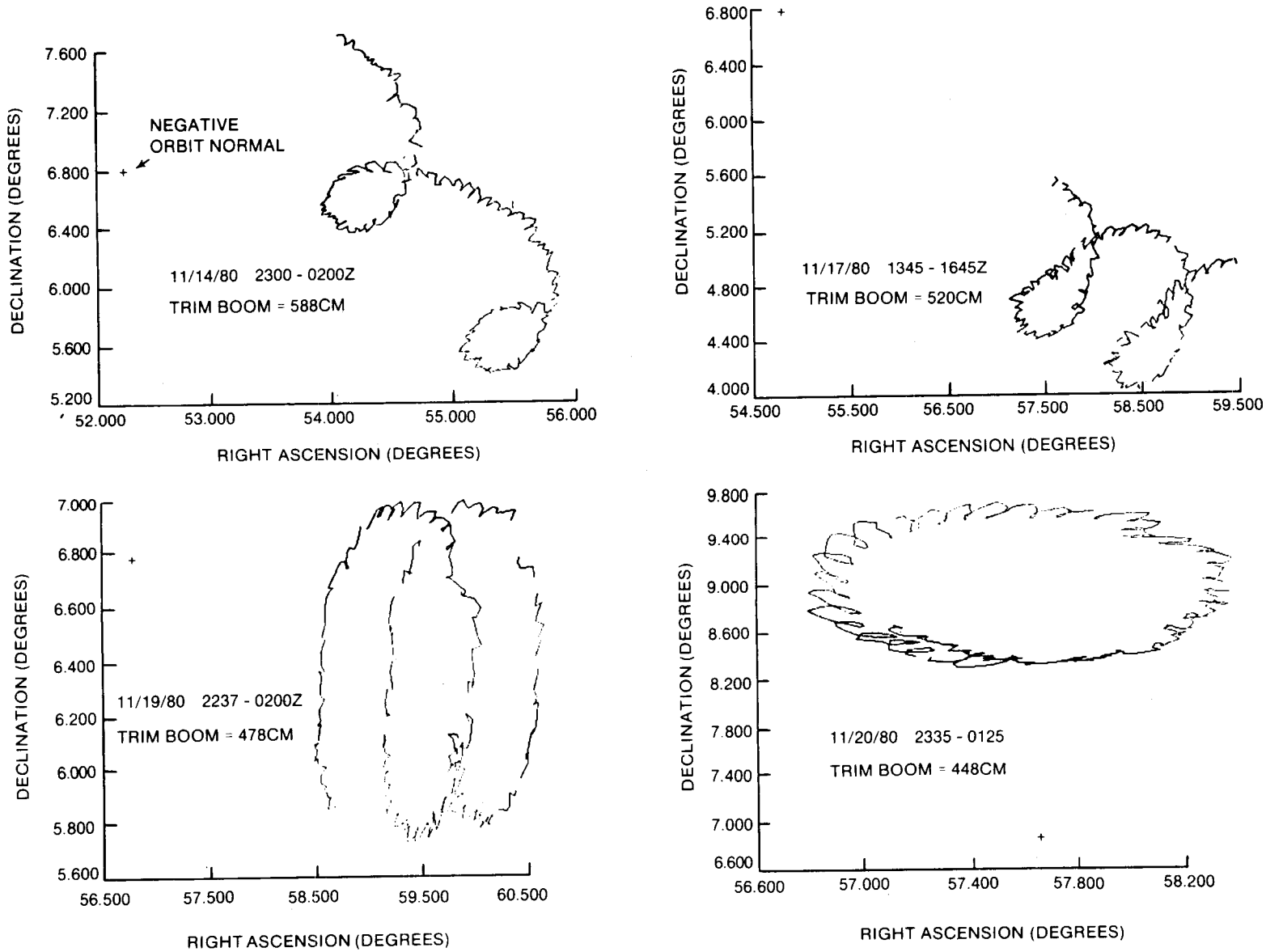

Figure 14.

Orbital Drift for Four Trim Boom Lengths in November 1979

South Pole. Examination reveals the existence of different conditions for minimal drift as perigee altitude and location change.

The March period is interesting because it was a time during the mission with very low drift (less than 2° net drift per day) and perigee located near the descending node. The trim boom was retracted 25 cm to 489 cm immediately preceding this period. Figure 15 shows right ascension, declination and yaw versus time for two Magsat orbits on March 17, 1980. Time of perigee crossing is also marked. Plots of these parameters for other orbits during this March period are nearly identical. The plots seem to contradict what was once advanced prelaunch as a possible drift control philosophy, namely to balance out yaw torques completely at perigee. Instead, as the right ascension plot in figure 15 shows, the spacecraft undergoes maximum drift due to yaw torque at perigee. Thus, what becomes important is not simply the balancing of drift at one point in the orbit, but to affect the drift at perigee in a way such that net orbital motion is reduced. Here, the high torques at perigee are adjusted to zero out the torque over the orbit. As can be seen in figure 15, the right ascension versus declination plot is a closed circle indicating little net orbital drift.

During this period, the Z axis precessed in a circle about a relatively stable trim point located 5° above negative orbit normal with little right ascension offset. The diameter of this circle was less than 2° and was traversed in approximately 4 days (figure 13). Note that since the trim point was located directly above negative orbit normal in declination that the maximum yaw angle was at perigee.

The second study case with representative plots given in figure 16 is taken from early January 1980. Although not as nice as the stable period in March, Magsat's drift during this January period was less than 3° per day and was relatively free of control torques. The Z axis precessed about a trim point 5.5^{o} above negative orbit normal in declination with a period of 5 days and traced out a circle with diameter of 4°. The trim boom length was 448 cm. Unlike the March period, perigee was near the South Pole during early January. With the trim point still above negative orbit normal in declination and only a small offset in right ascension, the yaw angle was not at its maximum value at perigee. Unlike the March period, there is drift in both right ascension and declination at perigee. Here, a balance in the yaw torque appears to occur near maximum yaw with both declination and right ascension drifts near minimum. The implication of this simple examination with perigee at the South Pole is that balancing the torque at maximum yaw is a valid, if not optimum control approach rather than balancing the torque at perigee. This perhaps shows the significance of torques due to high yaw angles near the nodes (where superrotation effects are largest) relative to torques at perigee when perigee is at a pole. Certainly this is a simplistic conclusion which will be examined in more detail. The eccentricity of the orbit, latitude of perigee, variation of aerodynamic effects with altitude and target placement (which will effect the phasing and magnitude of yaw) must be considered further.

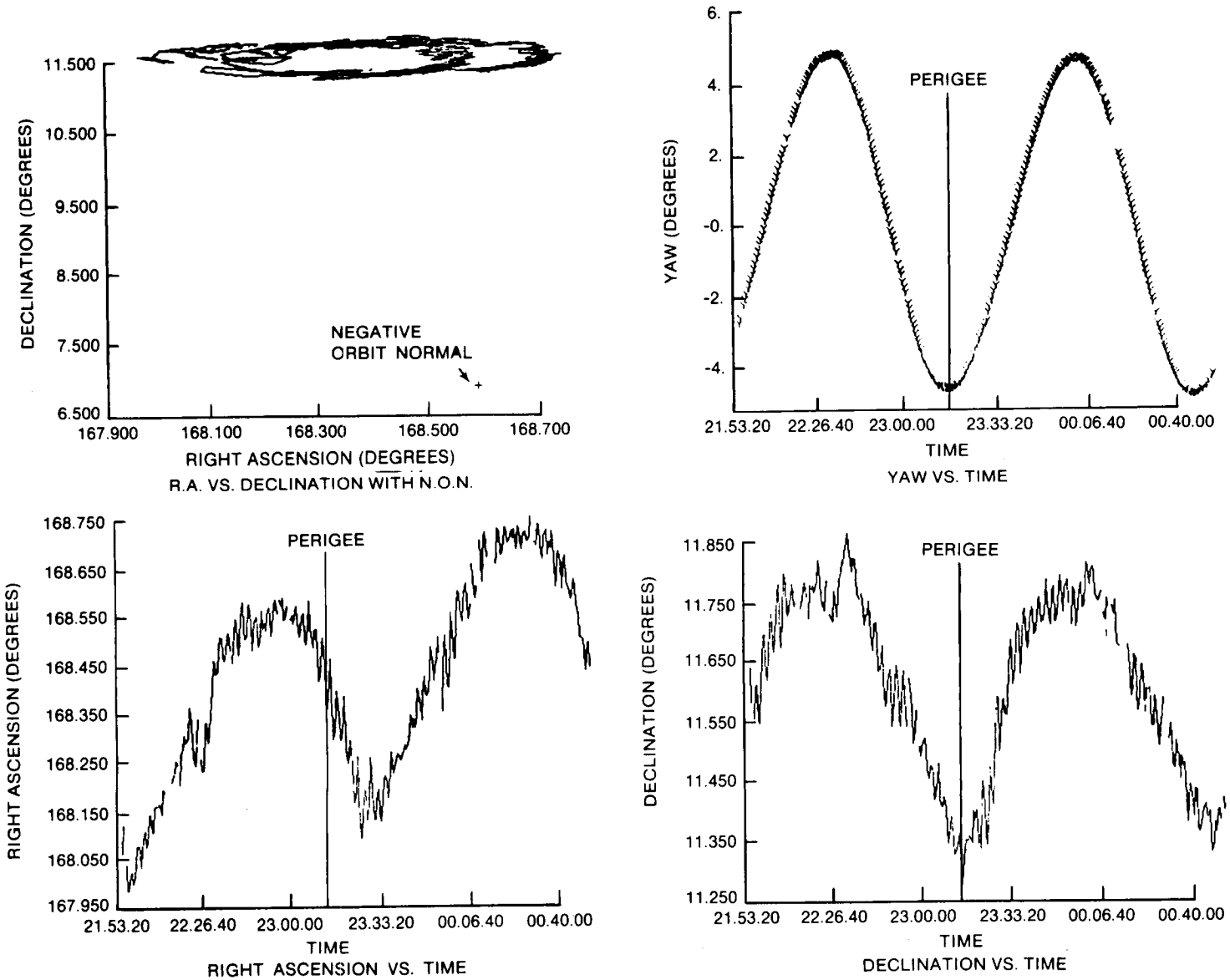

Figure 15.

Orbital Drift for Two Orbits on March 27, 1980

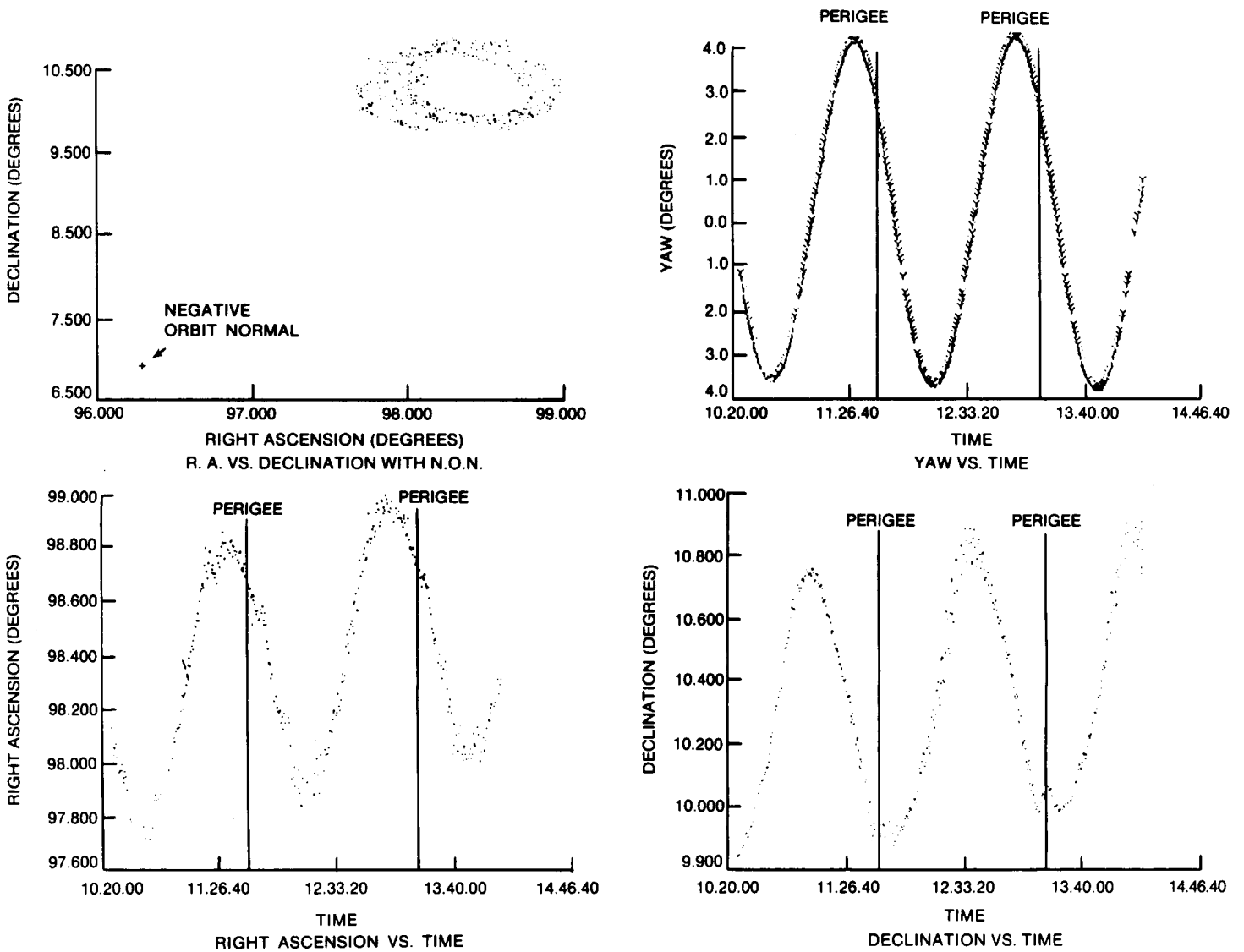

Figure 16.

Orbital Drift for Two Orbits on January 1, 1980

V. Closing Remarks

While analysis is continuing, some abstract conclusions can be drawn regarding the attitude control of Magsat. First, the ASP was essential for successful completion of the Magsat mission. Ground control, especially during the closing months of the mission, would have most likely been met with frustration and failure. Although drift was often low and manageable when the spacecraft was properly trimmed, this state was always achieved as a result of active adjustment of various ground supplied ASP parameters and the aerodynamic trim boom. In terms of performance, the ASP successfully satisfied all onboard control requirements. During times of high drift activity, the ASP displayed its effectiveness by maintaining Magsat within its prescribed control bounds. Ground control would not have been able to respond in time to violations of these control bounds. The importance of active ground monitoring of spacecraft attitude health and safety has been shown. The effectiveness of the ASP must be attributed, in part, to successful ground support.

Any optimum control philosophy for Magsat must be complex. The effects of boom length and perigee location on the spacecraft's trim point are not fully understood. At least two sets of conditions may exist for minimizing drift. Studies of the uniqueness and stability of the trim point are currently underway.

References

1. Applied Physics Laboratory, Johns Hopkins University, SDO 5146, "Magsat Spacecraft Description", March 1979.

2. Applied Physics Laboratory, Johns Hopkins University, BCE-T-0781, "Final Description of the Magsat Attitude Signal Processor Microcomputer Subsystem Command and Telemetry Words", T. Zaremba and D. Klein, revised September 1979.

3. Computer Sciences Corporation, CSC/SD-78/6077UD1, "MAPS/Magsat Attitude System Functional Specifications and Requirements Appendixes B and C - Attitude Signal Processor Ground Support Software (MAGSAP)", July 1979.

4. Applied Physics Laboratory, Johns Hopkins University, S4A-2-123, "Magsat Postlaunch Aerotrim Boom Length, Declination Bias and Pitch Bias Angle Selection Algorithms", B. Tossman, August 15, 1979.

5. Applied Physics Laboratory, Johns Hopkins University, S4A-2-060, "Magsat Z-Axis Stabilization in the Presence of Atmospheric Rotation", B. Tossman, March 23, 1975

THE RESPONSE OF THE SEASAT AND MAGSAT INFRARED HORIZON SCANNERS TO COLD CLOUDS

S. Bilanow and M. Phenneger

Computer Sciences Corporation, Silver Spring, Md.

ABSTRACT

Cold clouds over the Earth are shown to be the principal cause of pitch and roll measurement noise in flight data from the infrared horizon scanners onboard Seasat and Magsat. This paper discusses the observed effects of clouds on the fixed threshold horizon detection logic of the Magsat scanner and on the variable threshold detection logic of the Seasat scanner. National Oceanic and Atmospheric Administration (NOAA) Earth photographs marked with the scanner ground trace clearly confirm the relationship between measurement errors and Earth clouds. A one-to-one correspondence can be seen between excursions in the pitch and roll data and cloud crossings. The characteristics of the cloud-induced "noise" are discussed, and the response of the satellite control systems to the cloud errors is described. Changes to the horizon scanner designs that would reduce the effects of clouds are noted.

INTRODUCTION

The postlaunch evaluation of data from the Seasat and Magsat infrared (IR) horizon scanners has shown that cold clouds over the Earth are the principal cause of pitch and roll measurement noise[1]. This paper discusses the measurement

[1]Note that cold clouds are cited here as the principal cause of noise in IR scanner attitude data; this does not necessarily mean that they are the principal source of error in the attitudes.

errors that are caused by clouds. An understanding of IR scanner response to cold clouds is important for the determination of the attitude accuracy achievable using IR scanners. It is also important because control systems such as those of Seasat and Magsat use the IR scanner data as input to the control law. Most important, an accurate understanding of the scanner response to clouds can aid in the design of future scanners that will show less sensitivity to clouds.

The following sections of the paper will present a brief description of the Seasat and Magsat IR Earth sensor implementation and technology; a discussion of how cold clouds modify the Earth radiance profile in the infrared and how this affects the IR sensor Earth chord measurments; visual evidence for the cold cloud effects in the Seasat attitude data and confirmation of the coincidence of this effect in the Seasat and Magsat data with passage over clouds in the Earth IR photographs; visual evidence for cold clouds in the Magsat IR scanner data derived from comparisons with star camera attitudes; and a discussion of observations and conclusions concerning the technology of attitude sensing using IR scanners.

BACKGROUND

The Seasat IR attitude sensors were a pair of ITHACO Scanwheels[1] located on the left and right side of the spacecraft at 90 degrees to the nominal velocity vector and tilted 26 degrees below the horizontal, with 45-degree scan cones. This configuration is illustrated in Figure 1. The spacecraft flew in a nominal Earth-oriented attitude with a pitch

[1]Scanwheel is a registered trademark of ITHACO, Inc.

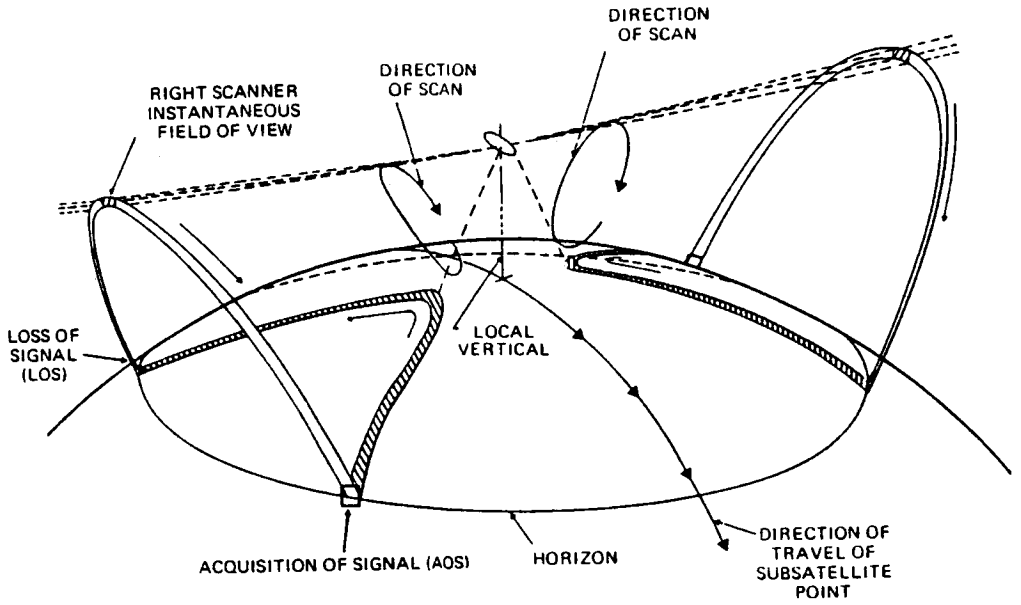

Figure 1. Seasat IR Scanner Configuration

rotation rate of 1 revolution per orbit. Although Seasat was designed to operate in a dual-IR-scanner mode, problems with Sun interference in the left scanner forced the use of a single-IR-scanner control mode. The pitch and roll[1] were derived in an onboard analog processor from the right IR scanner Earth chord measurement, according to the following equations:

$$\text{pitch} = K_p\left(\Omega^{LOS} - \Omega^{AOS}\right) \tag{1}$$

$$\text{roll} = K_r\left(\Omega^{AOS} + \Omega^{LOS} - \Omega_0\right) \tag{2}$$

[1]Pitch is a right-handed rotation about negative orbit normal; roll is a right-handed rotation about the spacecraft velocity vector for a circular orbit.

where Ω^{AOS} and Ω^{LOS} are the horizon-to-spacecraft-index dihedral angles for the sky/Earth and Earth/sky portions of the scan, respectively, and Ω_0, K_p, and K_r are constants based on the nominal Earth chord and the partials of pitch and roll with respect to Ω^{AOS} and Ω^{LOS}. The Earth horizon was detected using a normalized threshold method as illustrated in Figure 2. The horizon threshold was automatically adjusted to be 40 percent of the average of the Earth pulse amplitude between 5 and 11 scan degrees from the acquisition of signal (AOS) and loss of signal (LOS) horizons.

The Magsat Earth sensor was an ITHACO Scanwheel dual-flake IR sensor located 90 degrees to the nominal velocity vector in the horizontal plane on the left side of the spacecraft, with a 45-degree scan cone. The Earth horizon was sensed using a fixed-threshold locator logic, and the pitch and roll for Magsat were determined onboard. The ground processing

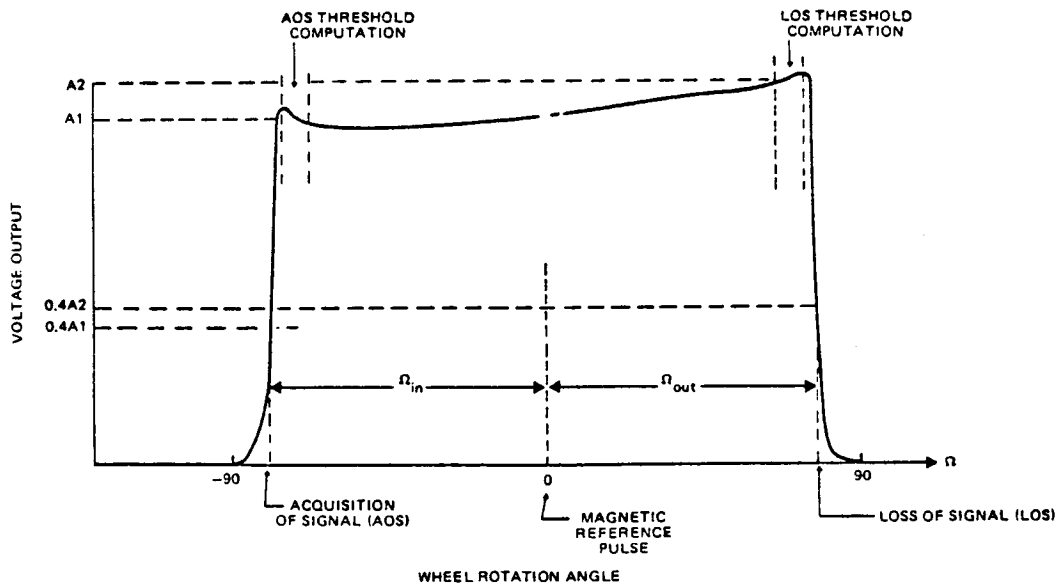

Figure 2. Seasat Horizon Locator Logic Applied to the Output from the Bolometer Signal Processing Electronics

software for both Seasat and Magsat refined the pitch and roll measurements to account for Earth oblateness, spacecraft altitude variations, and seasonal systematic Earth radiance variation effects.

EARTH RADIANCE VARIATION EFFECTS

The IR scanners operate in the 15-micron carbon dioxide (CO_2) absorption band to avoid large weather-dependent changes that occur in the Earth radiation above and below this wavelength. Figure 3 illustrates the spectrum of infrared radiation for a nadir view of the Earth for different geographical locations on April 10, 1970. It can be seen that the intensity in a narrow region centered on 15 microns (660 centimeters^{-1}) shows less dependence on the surface that is viewed.

The effect of clouds on the infrared Earth radiation spectrum was simulated by Keithly and Uplinger at Lockheed Missiles & Space Company (LMSC)(Reference 1). Results from their work are illustrated in Figure 4 for a nadir viewing angle at the Equator. The simulation was accomplished by computing the Earth infrared radiation spectrum using a standard atmosphere model and integrating the emitted and absorbed radiation from different starting altitudes to the top of the atmosphere to simulate total absorption of the IR Earth radiation by low, medium, and high cold clouds. An estimate of the effect of the clouds on the Earth radiation signal at the nadir viewing angle for the Seasat and Magsat IR sensors can be made by comparing the IR sensor frequency response functions illustrated in Figure 5 with the radiation spectra for different cloud heights in Figure 4. Integrating these cold cloud radiation spectra through the Seasat IR scanner bandpass showed that high cold clouds can lower the Earth pulse in the threshold computation regions of the scan

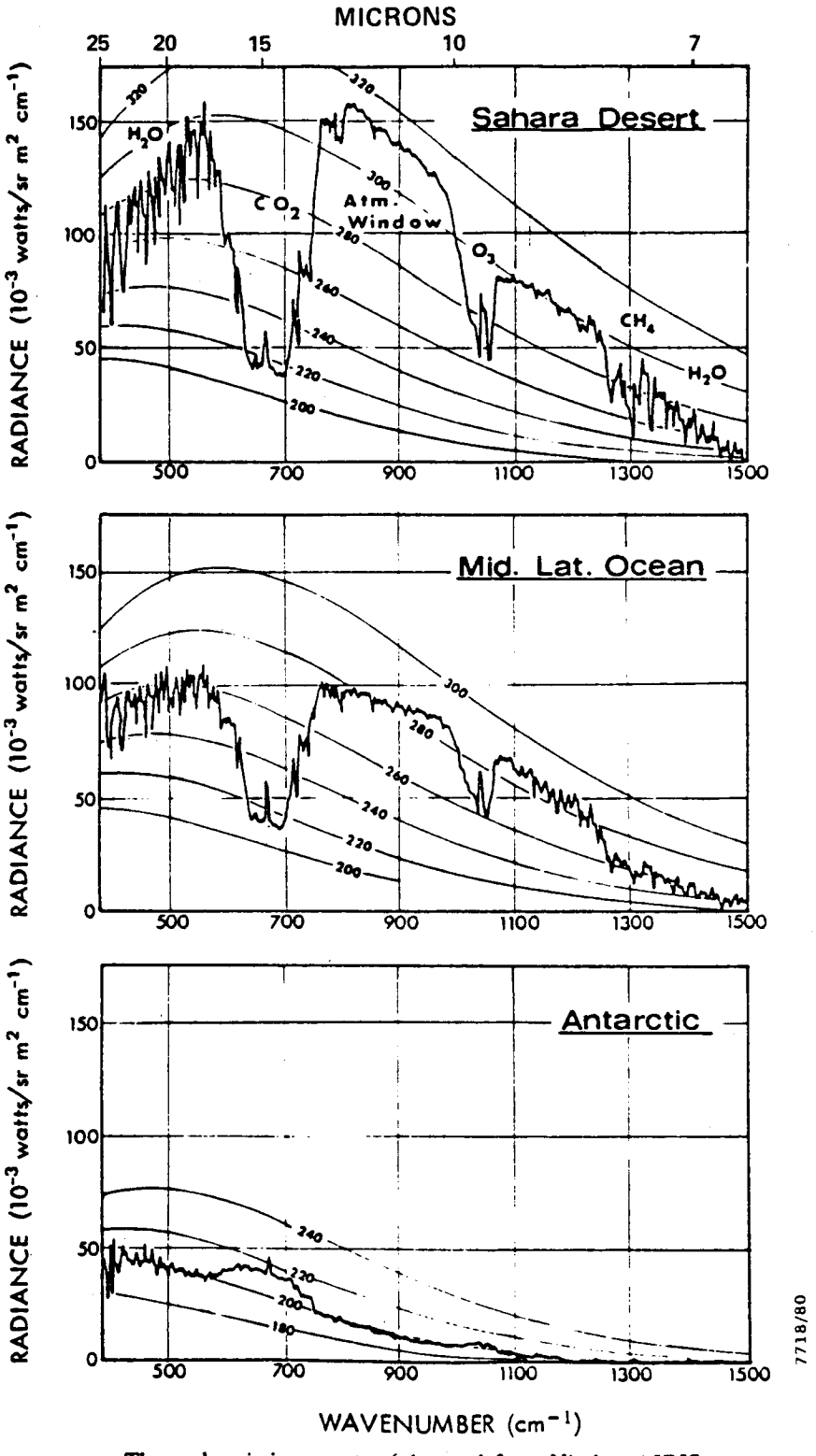

Thermal emission spectra (obtained from Nimbus 4 IRIS experiment during orbit 29, 10 April 1970) compared to curves of constant brightness temperatures (K).

Figure 3. Earth's Outgoing IR Radiation for Various Nadir Views

Figure 4. Radiance Variation in the Presence of Clouds of Various Altitudes According to LMSC

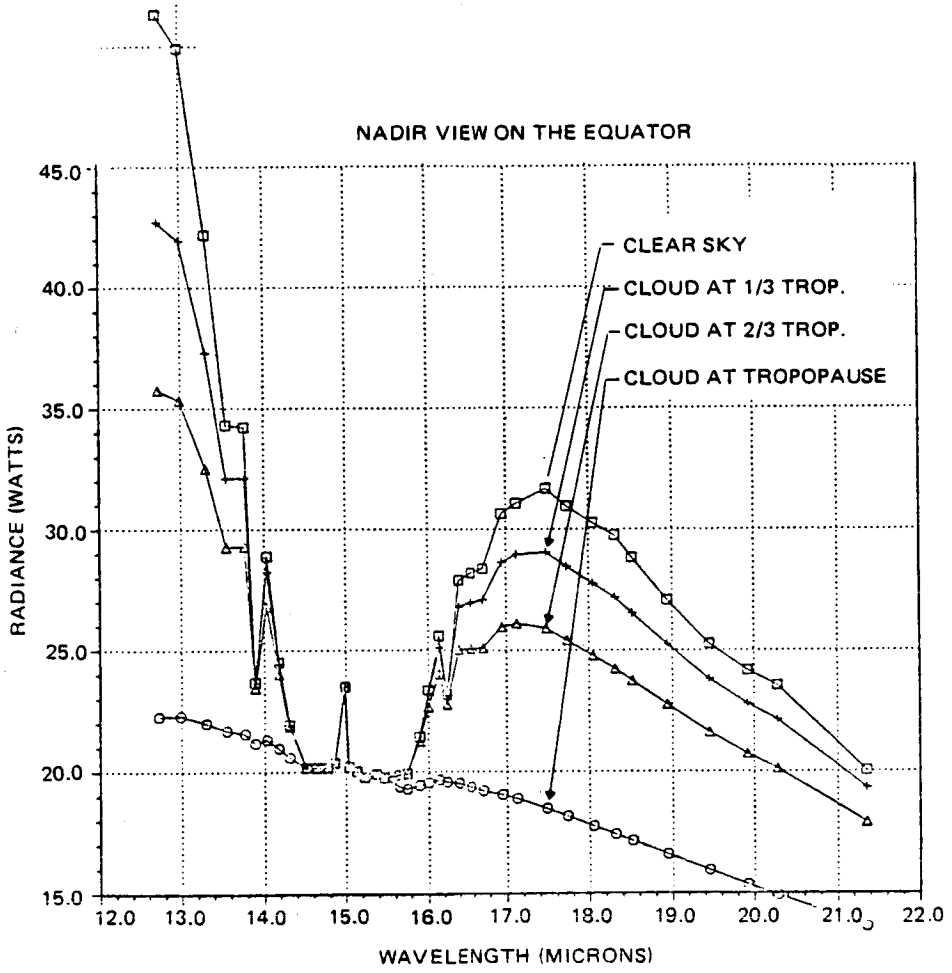

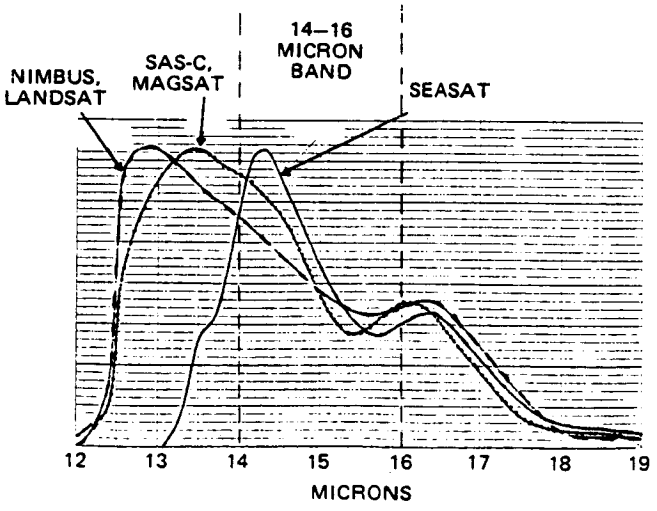

Figure 5. Spectral Response Functions of Several Spacecraft Horizon Scanners

by 30 percent (References 2 and 3). The effect of this is to lower the threshold voltage and increase the Earth chord at the AOS or LOS portion of the scan. The effect of this on the roll and pitch for Seasat, computed in Equations (1) and (2), is to increase the roll for clouds at both AOS and LOS horizons and to decrease the pitch at AOS and increase the pitch at LOS. The timing of cold-cloud-induced errors between AOS traversal and LOS traversal for the Seasat orbit is approximately 5 minutes. As the spacecraft moves along the orbit, the roll signal should show two positive pulses separated by 5 minutes, coincident with a negative and then a positive pulse in pitch, respectively. A schematic illustration of error signals from the Seasat IR sensors resulting from clouds of various sizes and locations is illustrated in Figure 6.

Seasat's Response to Clouds. Flight data from Seasat showed many striking examples of the isolated cold cloud signature. One example is shown in Figure 7, where a simultaneous negative excursion in pitch and a positive excursion in roll are followed 5 minutes later by simultaneous positive excursions in pitch and roll.

The Seasat pitch and roll values plotted in Figure 7 and the following figures were computed in the onboard analog processor and telemetered to the ground. The definitive pitch and roll, which were computed on the ground, used the data and added corrections for the effects of biases, Earth oblateness, satellite altitude variations, and seasonal systematic horizon radiance variations. These corrections are not required for the demonstration of the cold cloud effects. The observability of clouds in these data is dependent on the fact that the control system responds slowly to the pitch and roll error signals. The Seasat control system was designed to hold the spacecraft at zero pitch,

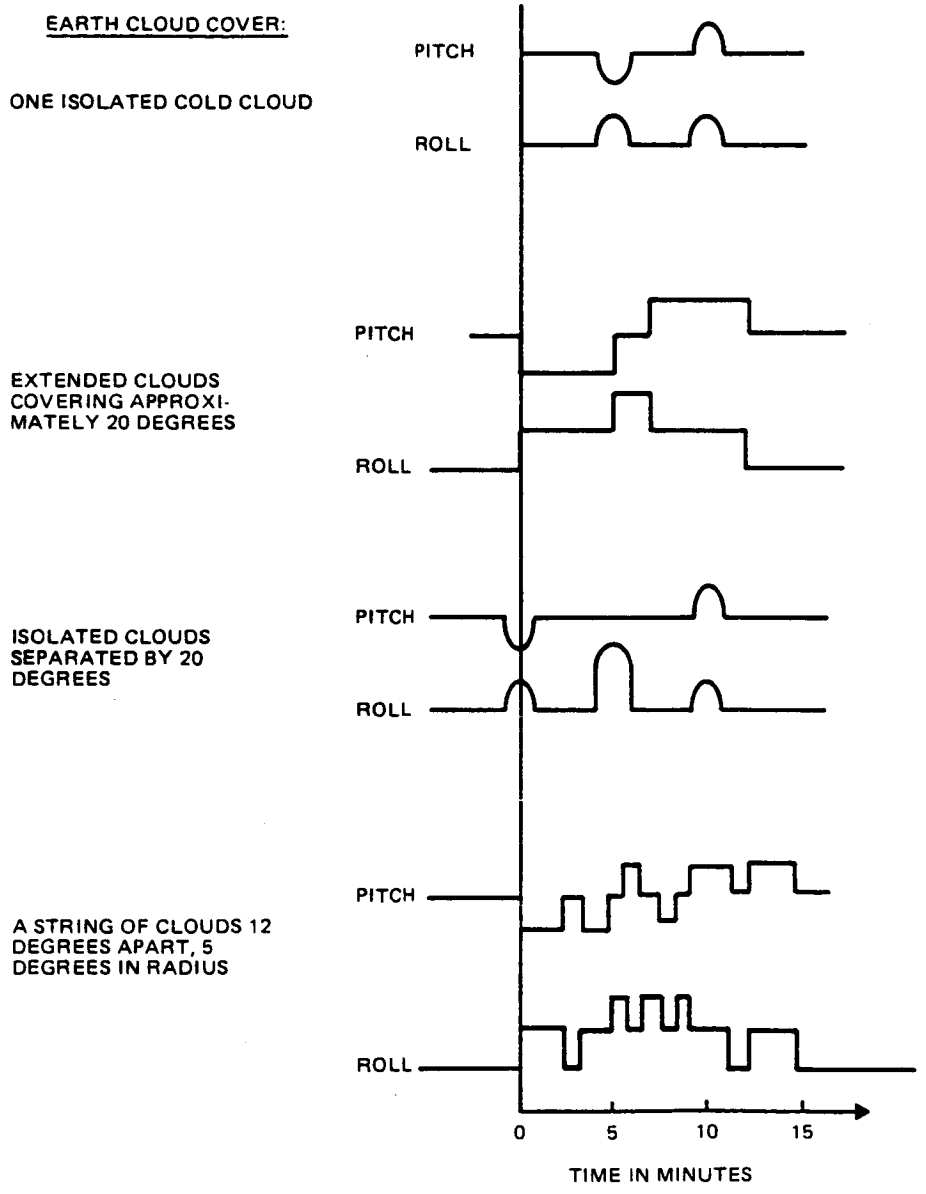

Figure 6. Schematic Illustration of Pitch and Roll Telemetry Patterns Generated by Four Specific Cloud Distributions on the Earth Surface

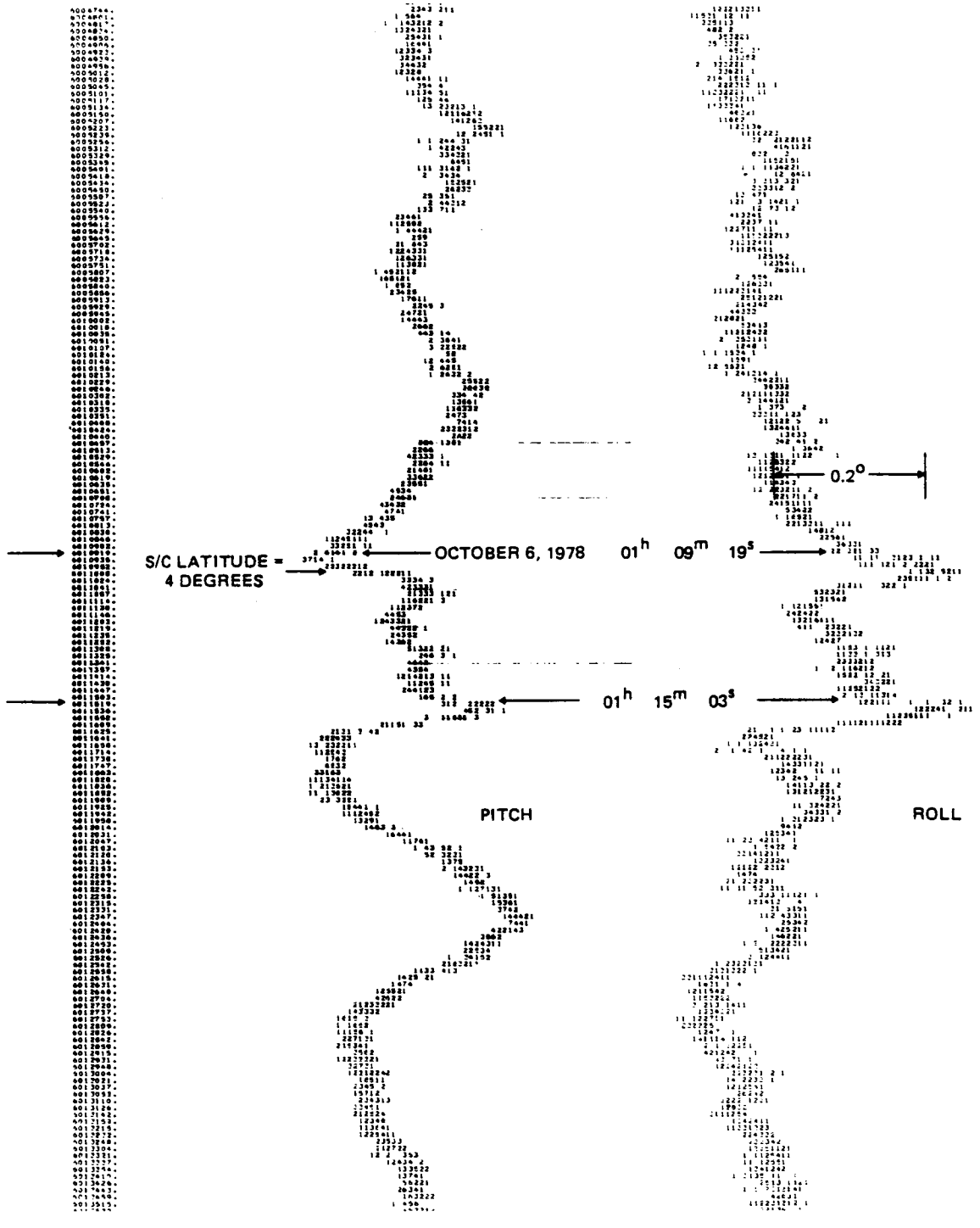

Figure 7. Seasat Fine Pitch and Roll Telemetry Data on October 6, 1978

roll, and yaw for a long time. If the spacecraft control system responded quickly to the errors from clouds, the pitch and roll voltages would be kept at zero while the spacecraft would rock back and forth in response to each cloud on the horizon. Because the roll control response is slower than the pitch response, the cloud effects are more clearly visible in the roll data.

Evidence of cold cloud signatures can be seen throughout the 12 orbits of pitch and roll data shown in Figures 8 and 9, respectively. The data was gathered from 12 consecutive orbits on October 2, 1978. Isolated clouds stand out as pairs of peaks in the roll data separated by 5 minutes. The cloud effects are harder to discern among the larger oscillations in the pitch data; nevertheless, the negative-positive signature in pitch can be picked out at the times when large clouds show their signatures in the roll data. Evidence exists in Figure 8 that the cold cloud anomalies helped induce some oscillations in the pitch.

To confirm that the cold cloud signatures in these data illustrated in Figures 8 and 9 correspond directly to features in the Earth IR image, photographs were obtained from NOAA of the Earth at the time of these data. Figure 10 shows an IR image of the Earth taken over the Pacific Ocean from the western Geosynchronous Operational Environmental Satellite (GOES) at 17:45 Greenwich mean time (GMT) on October 2, 1978. The IR scanner Earth scan is overlaid at two positions in the Seasat orbit, corresponding to 8:53 and 9:03 GMT. In each of these scans, the threshold computation regions from 5 to 11 scan degrees from the AOS and LOS horizon are marked. In Figure 11, the ground track of the middle of the threshold adjust regions is traced over four orbits, assuming a nominal attitude. The AOS threshold adjust track occurs to the west of the LOS threshold adjust

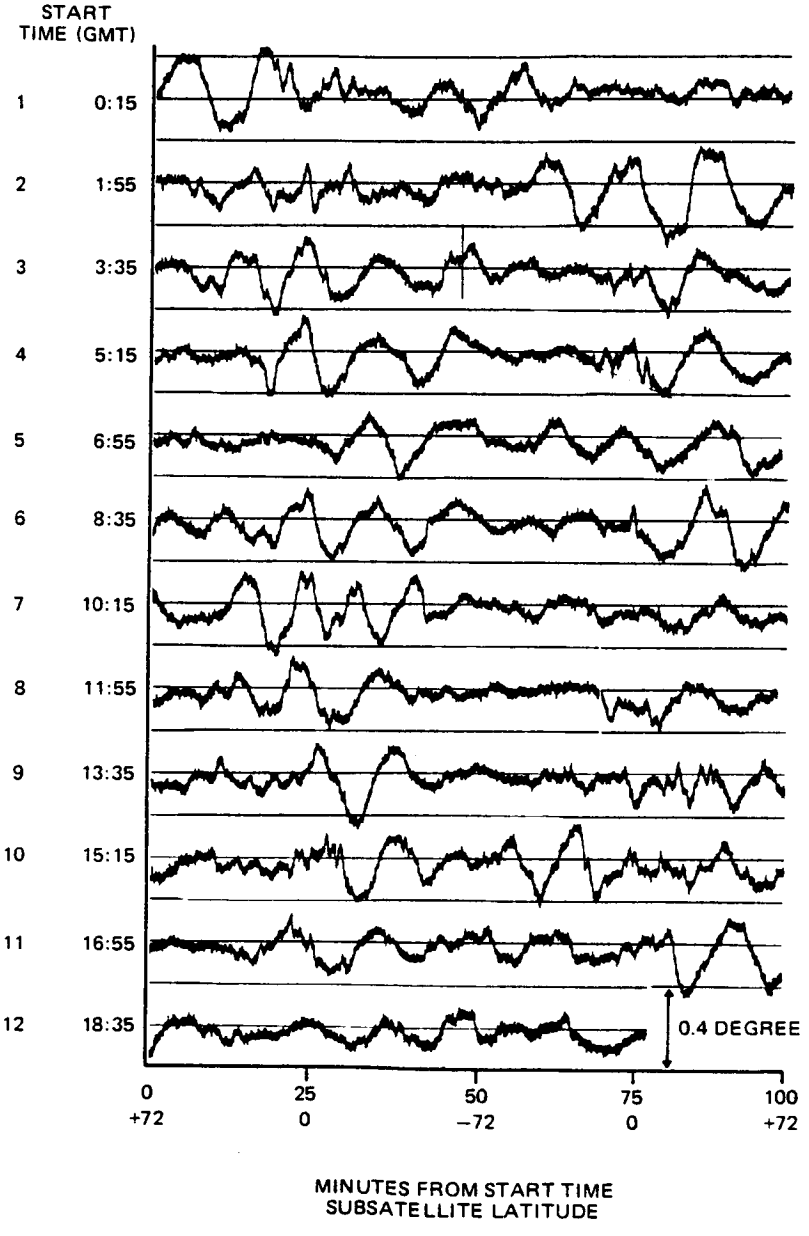

Figure 8. Seasat Pitch Telemetry for 12 Orbits on October 2, 1978

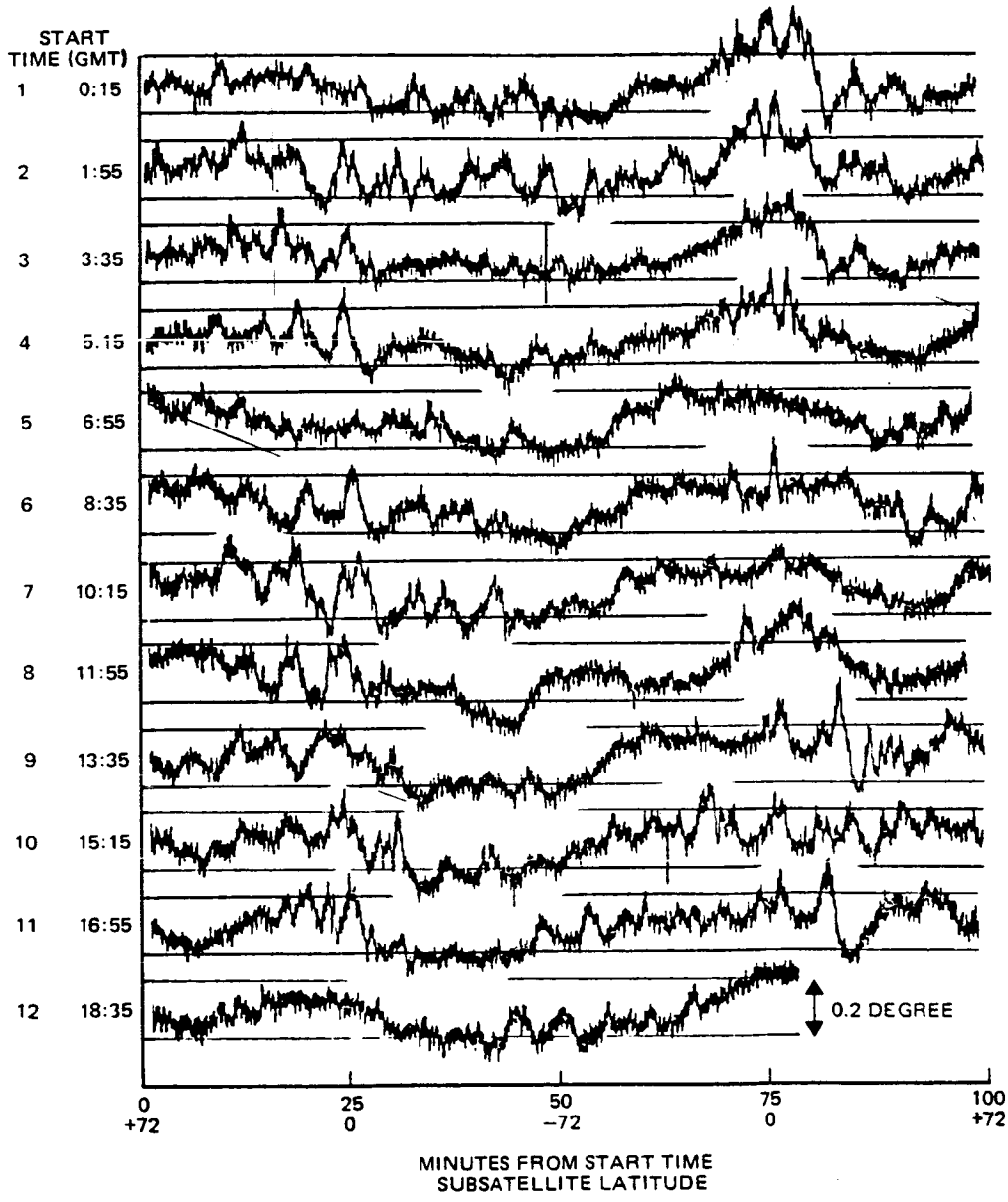

Figure 9. Seasat Roll Telemetry for 12 Orbits on October 2, 1978 Illustrating Cold Cloud Anomalies at the North and South Equator Crossings

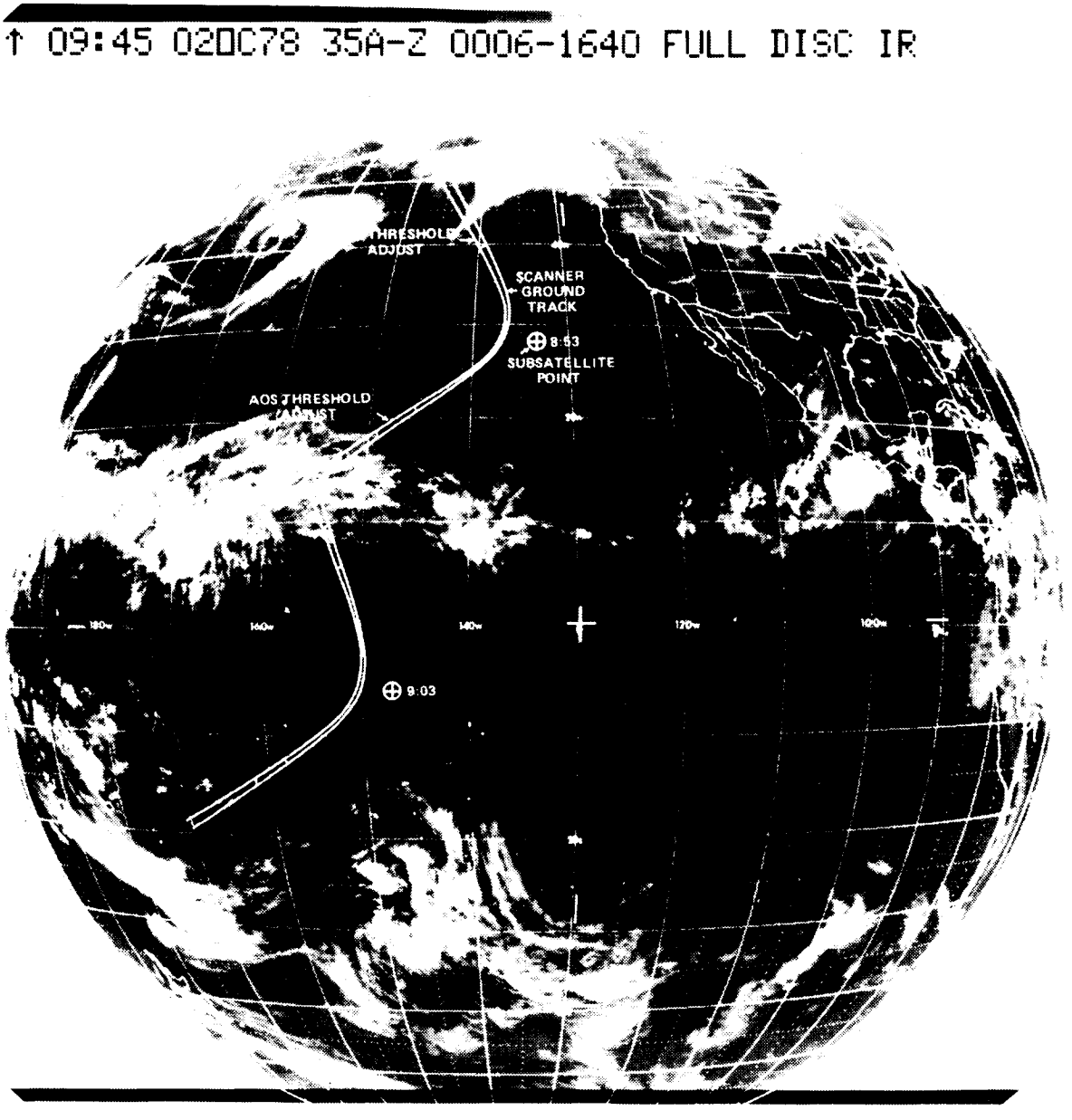

Figure 10. IR Scanner Path With Geographic Location of Horizons and Normalization Areas for a 790-kilometer Altitude (Photo from the Environmental Data Service of NOAA)

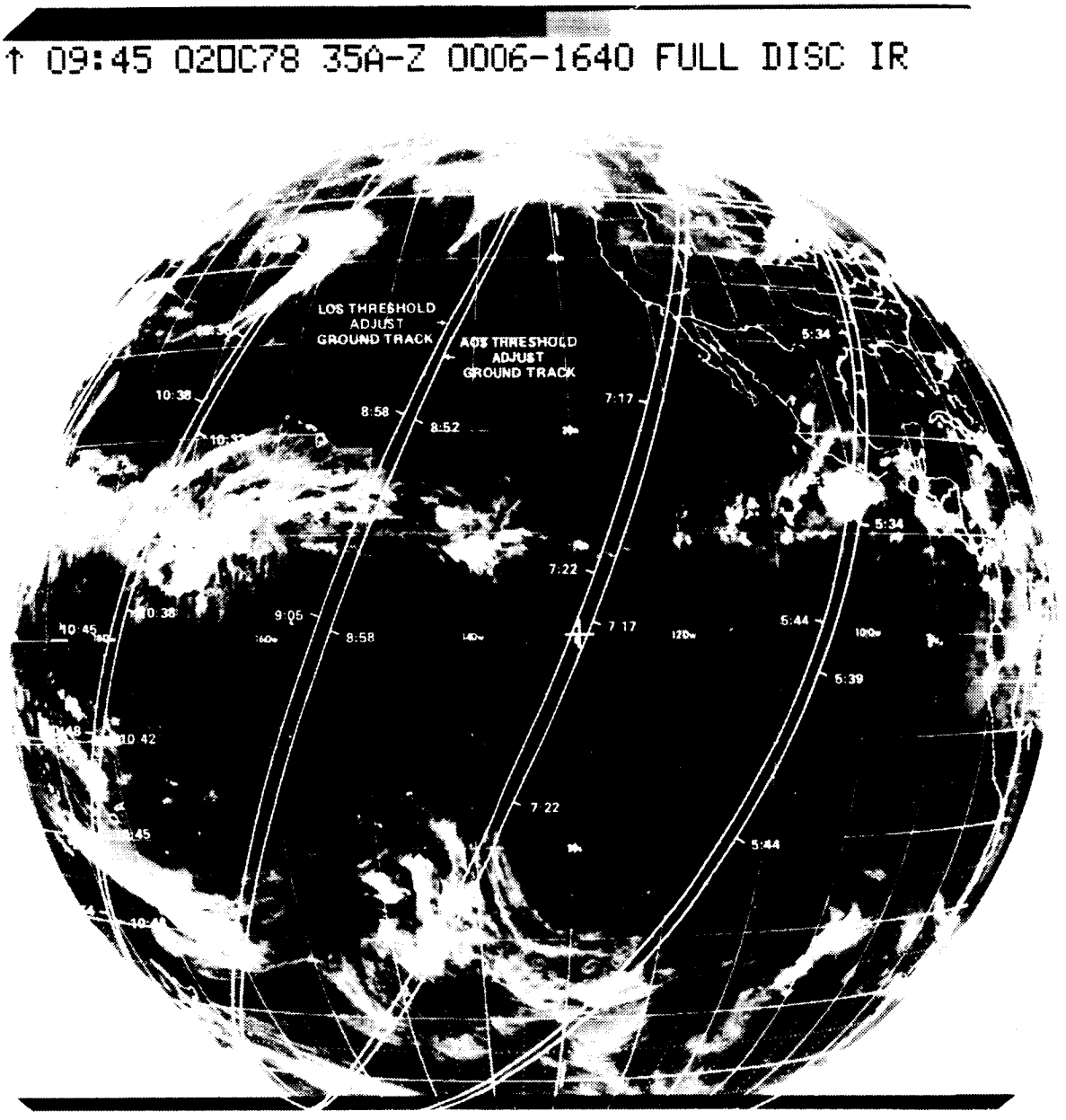

Figure 11. Synchronous Meteorological Satellite-2 Earth Photo with Scan Threshold Adjustment Region Ground Track Overlaid (Photo from the Environmental Data Service of NOAA)

track because of the Earth rotation effects. Since cloud patterns do not change greatly during the timespan of four orbits, these ground tracks can be used to predict the cloud effects that will be seen near the descending node in orbits 4, 5, 6 and 7 for the data in Figures 8 and 9. Comparison of Figure 11 with Figures 8 and 9 confirms that excursions in the pitch and roll data result from clouds visible in the IR photograph. In orbit 4, the threshold adjust region passes an isolated tropical storm, near 5:37 GMT; in orbit 5, no cloud is passed at the Equator; and in orbit 7, several large cloud systems are encountered simultaneously in the AOS and LOS. Numerous examples in the data can be correlated with the visual information in Figure 11 with a more detailed analysis.

Magsat's Response to Clouds. The procedures developed for Seasat cloud noise identification were applied to Magsat mission data analysis. The results of the cloud error analysis for Magsat are summarized below.

The signature of an isolated cloud in the Magsat data is a positive error followed by a negative error in pitch and two positive errors in roll. It differs from the Seasat signature because of differences in the horizon locator logic and the scanner mounting positions. The time separation between the AOS and LOS encounter of a cloud is approximately 4-1/2 minutes for the Magsat orbit and scan geometry.

Two Fixed-Head Star Trackers and a high-resolution Sun sensor provided an accurate attitude reference for evaluating the Magsat IR scanner data.

Figures 12 and 13 show the differences between the pitch and roll computed from the IR scanner and the pitch and roll computed from star camera data for 14 orbits on December 28, 1979. Numerous cold cloud signatures appear in these data. Orbital frequency systematic errors are also present,

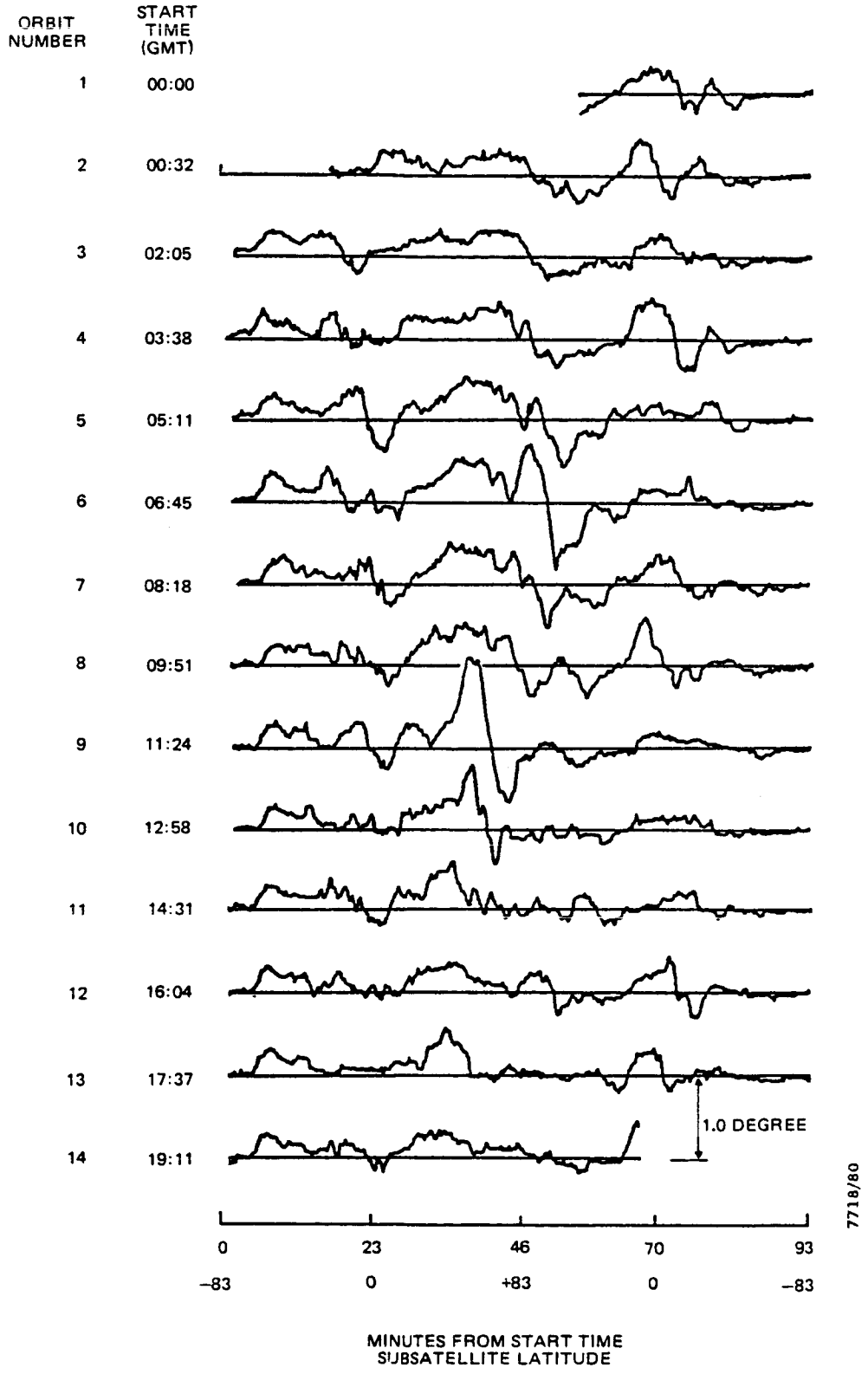

Figure 12. Difference Between Magsat IR-Scanner-Measured Pitch and Star-Camera-Measured Pitch on December 28, 1979

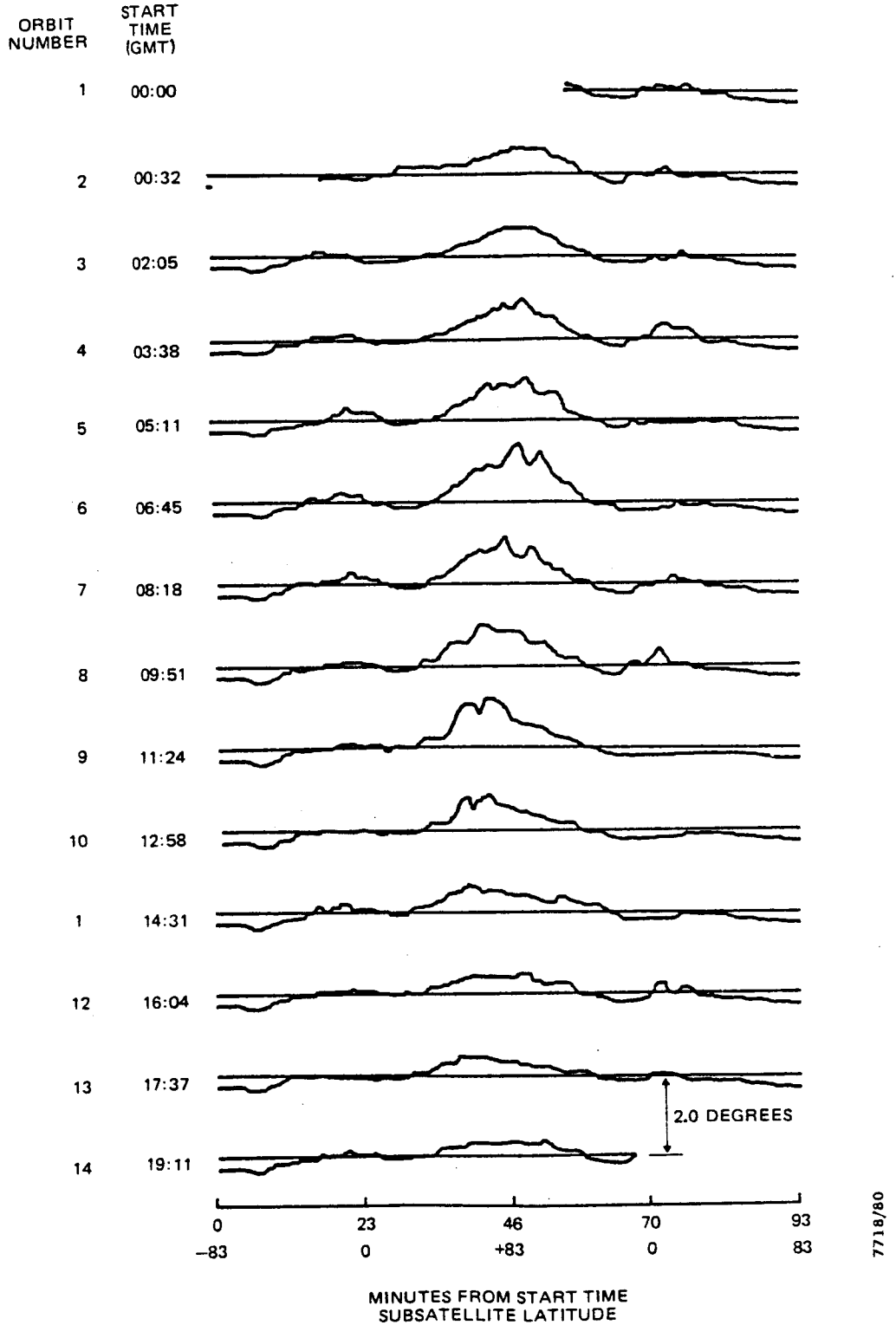

Figure 13. Difference Between Magsat IR-Scanner-Measured Roll and Star-Camera-Measured Roll on December 28, 1979

especially in the roll data. As of this writing, those systematic errors are not well understood. The large roll residuals may be due to systematic horizon radiance variations. The effects of satellite altitude variations and Earth oblateness were eliminated in the computation of IR scanner pitch and roll, but systematic horizon radiance variations were not. An anomaly in the data which regularly occurs just past the minimum subsatellite latitude crossing has been tentatively associated with the momentary shading of sunlight on the IR scanner by an aerodynamic trim boom on Magsat.

Detailed comparisons of the noise in the Magsat IR scanner data with Earth IR photographs were made, as was done for Seasat. These comparisons demonstrated that nearly every short-period excursion in the IR scanner data could be associated with cold cloud features on the Earth. The exception was the feature that was associated with the trim boom shading of the Sun. Figure 14 indicates specific cloud crossing events that were identified in 3 hours of pitch data. This figure also demonstrates that the high-frequency electronics noise in the pitch is effectively reduced with a simple 8-data-point average.

The response of the Magsat control system to a cold cloud crossing can be seen in Figure 15, where star camera pitch solutions are compared to the IR scanner pitch data. The control system responds to the pitch measurement error as if it is a true error in the pitch of the spacecraft. Thus, when the pitch measurement rises positive as the AOS portion of the Earth scan views the cloud, the control system moves the true pitch in the negative direction. When the LOS portion of the Earth scan views the cloud and the pitch measurement falls negative, the control system drives the pitch back in the positive direction.

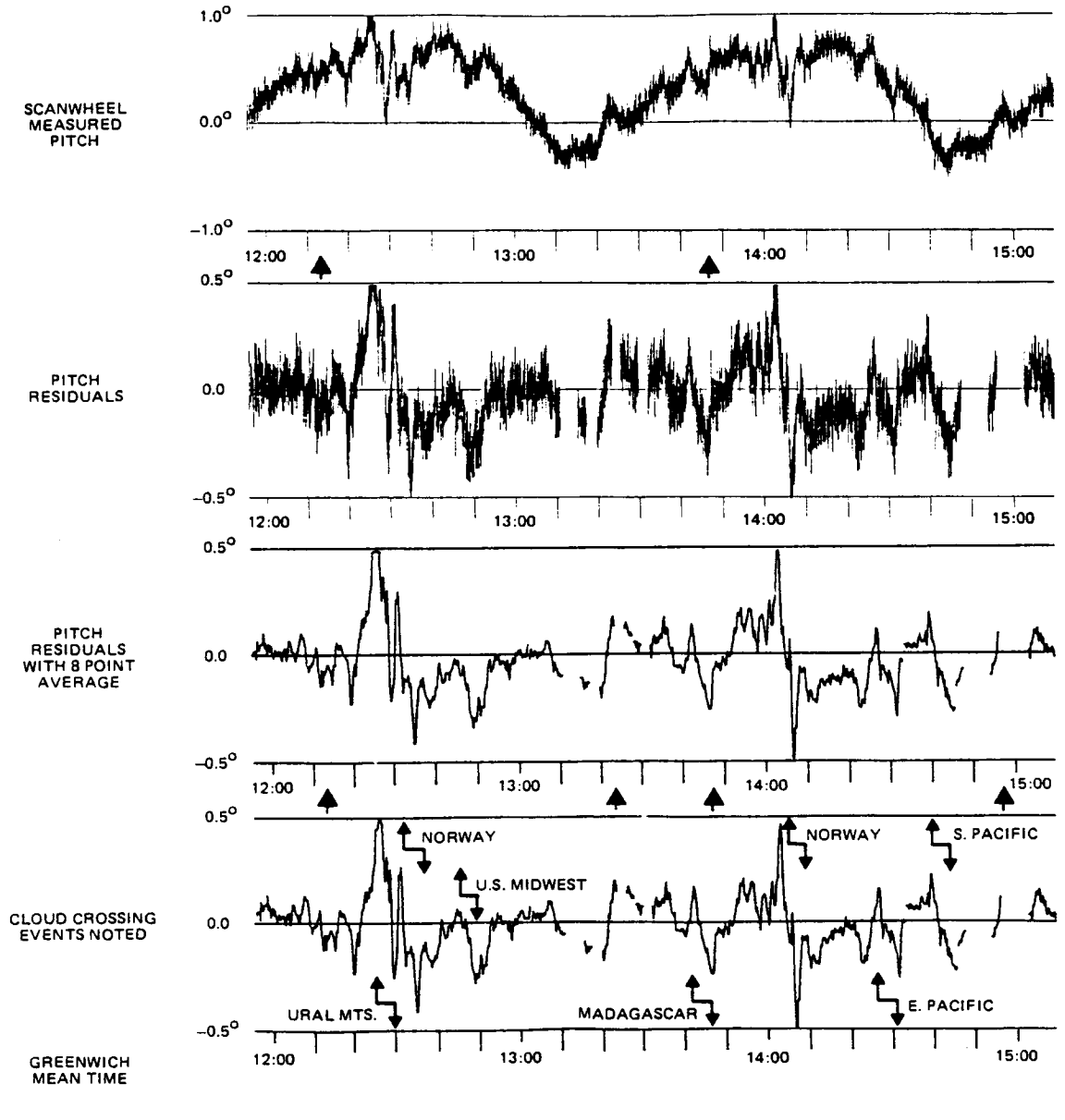

Figure 14. Magsat Scanwheel Pitch Measurement Errors with Errors Due to Cold Clouds Noted

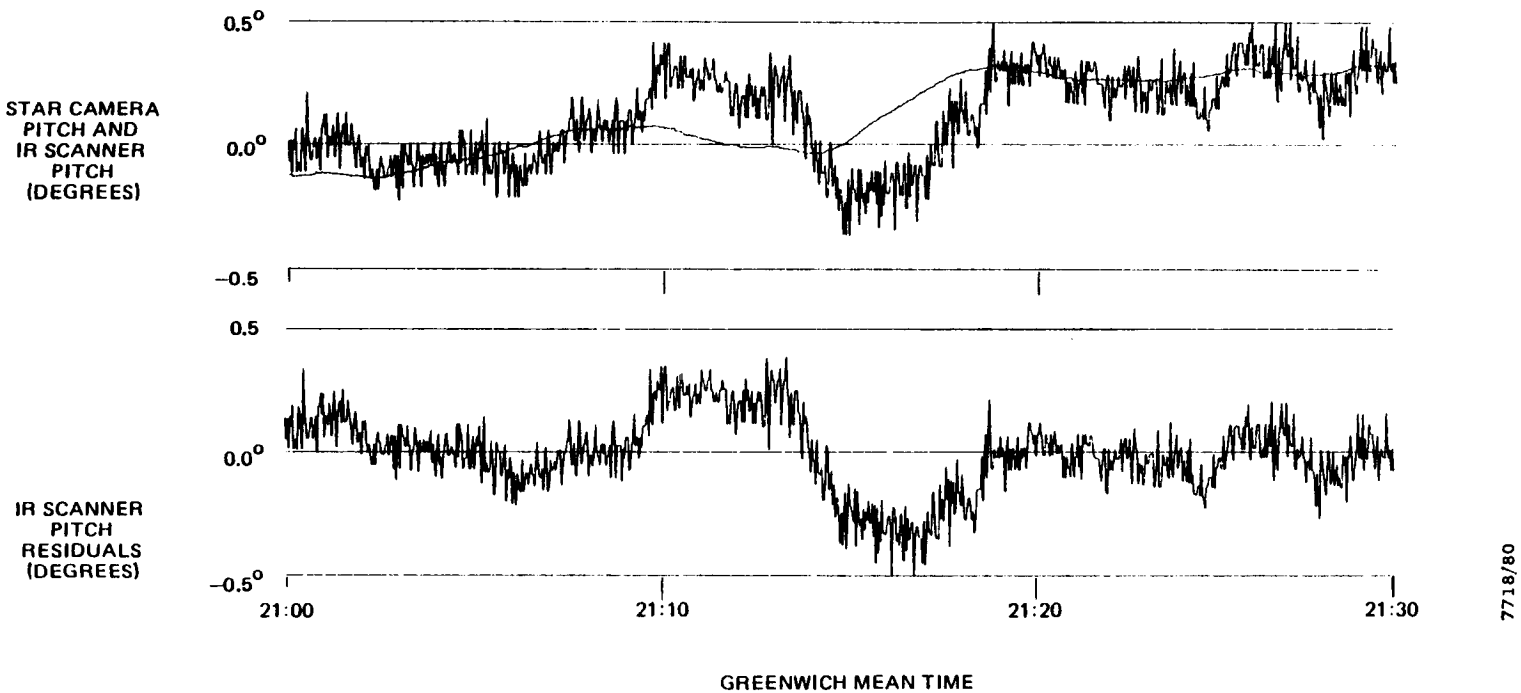

Figure 15. IR Sensor and Star Camera Pitch Data from Magsat on November 8, 1979

The clouds that show their signatures in Figures 12, 13, and 14 are much larger in the northern latitudes than in the southern latitudes. There are several possible explanations for the effect. First, the radiation from the CO_2 band is weaker in the winter hemisphere. Therefore, the radiation from outside the CO_2 band, which is influenced by clouds, may contribute a larger percentage of the total radiation incoming to the bolometer. Second, a fixed temperature difference between cloud top and ground means a greater percentage change in radiance for lower temperatures. A third explanation requires some understanding of the Magsat sensor signal processing electronics. In the electronics, the signal from the bolometer is passed through a preamplifier and a peaking amplifier, and then it is clipped at 1.2 volts, a level that is intended to correspond to a minimum Earth pulse height. If the signal level at this time is actually smaller than 1.2 volts, the response to this change in the noise filter that follows will cause the horizon detection error to be somewhat amplified. It is obvious that care should be taken to ensure that fixed-threshold horizon sensors do not trigger near the minimum Earth signal for the mission.

CONCLUSIONS AND RECOMMENDATIONS

Straightforward procedures have been developed for demonstrating that features in the IR scanner attitude data from the Seasat and Magsat missions correspond to meteorological features in the Earth's atmosphere. These procedures were made possible in part by NOAA's distribution of Earth imagery data from operational weather satellites.

From these procedures, it has been proved that cold cloud effects and other systematic Earth radiance variation effects dominate a large portion of the IR scanner attitude data for

the Seasat and Magsat missions. Proof of the origin of these noise features in the IR scanner data further justifies efforts to upgrade the IR sensor technology and the data processing software. Methods have been developed or are being developed at Computer Sciences Corporation that facilitate the study of changes in IR scanner technology in the area of spectral response function and signal processing and horizon triggering electronics. More work using the data analysis described above is needed to upgrade the ground processing software to reduce errors associated with random and systematic horizon radiance variations.

ACKNOWLEDGMENT

The authors thank Roger Werking and the other members of the Attitude Determination and Control Section at Goddard Spaceflight Center, Code 581.2, for their continuing support of this work.

REFERENCES

1. Lockheed Missiles & Space Company, Inc., Report No. GCS/4001/6211, Effects of Clouds on the Seasat-A Horizon Sensor, P. L. Keithley and W. G. Uplinger, July 13, 1977

2. National Aeronautics and Space Administration, NASA X-581-78-9, Seasat-A Attitude Analysis and Support Plan, W. T. Nutt, M. C. Phenneger, G. M. Lerner, C. F. Manders, F. E. Baginski, M. Rubinson, and G. F. Meyers, April 1978

3. Computer Sciences Corporation, CSC/TM-78/6064, Infrared Horizon Scanner Attitude Data Error Analysis for Seasat-A, M. C. Phenneger, C. F. Manders, and C. B. Spence, Jr., July 1977

SPACECRAFT MOMENTUM MANAGEMENT PROCEDURES*

Lily C. Chen
General Software Corporation, Silver Spring, Md.

Paul B. Davenport
NASA Goddard Space Flight Center, Greenbelt, Md.

Conrad R. Sturch
Computer Sciences Corporation, Silver Spring, Md.

ABSTRACT

This paper describes techniques appropriate for implementation onboard the Space Telescope and other spacecraft to manage the accumulation of momentum in reaction wheel control systems using magnetic torquing coils. Generalized analytical equations are derived for momentum control laws that command the magnetic torquers. These control laws naturally fall into two main categories according to the methods used for updating the magnetic dipole command: closed-loop, in which the update is based on current measurements to achieve a desired torque instantaneously, and open-loop, in which the update is based on predicted information to achieve a desired momentum at the end of a period of time. Each control law is further categorized by the physical quantities (e.g., energy, wheel speed, etc.) selected for minimization. Physical interpretations of control laws in general and of the Space Telescope cross product and minimum energy control laws in particular are presented, and their merits and drawbacks are discussed. A new technique is introduced to retain the advantages of

*Work supported by the Spacecraft Control Programs Branch, Goddard Space Flight Center, National Aeronautics and Space Administration, under Contract NAS 5-24300.

both the open-loop and the closed-loop control laws. Simulation results are presented to compare the performance of these control laws in the Space Telescope environment. The results discussed in the paper can be extended to the Multimission Modular Spacecraft (MMS) series and similar missions.

INTRODUCTION

The Space Telescope (ST) is an astronomical observatory to be launched in 1984 by the Space Shuttle into a nominal 500-kilometer circular orbit. The Pointing Control System provides the attitude reference and control stability for the ST. The most challenging requirement of the Pointing Control System is the pointing stability of 0.007 arc-second (one sigma). To achieve this stability required in the fine point mode, vibrations generated by the rotating reaction wheels must not excite significant ST bending modes.

Two momentum management control laws have been proposed by Lockheed Missiles & Space Company (LMSC) for desaturating the ST reaction wheels, namely, the cross product (CP) control law and the minimum energy (ME) control law. The CP law is a closed-loop control law that computes a control magnetic dipole based on current measurements to achieve a desired torque instantaneously. The ME law is an open-loop control law that generates the magnetic dipole commands based on predicted information to achieve a desired momentum at the end of a period of time, and at the same time minimizes the energy consumption by the magnetic coils. More detailed descriptions of ST momentum management procedures are given in Reference 1 and 2.

To further understand and compare these control laws, we have derived generalized analytical equations for spacecraft momentum management using magnetic torquers and have studied

their physical interpretations. As a result of this study, a new technique, referred to as the "mixed-mode" control law, has been introduced to retain the advantages of both closed-loop and open-loop control laws. The momentum management procedures during maneuvers were also investigated for the original technique and for the new technique. To support the current study, a simulator has been implemented to enable quantitative comparison of the performances of various control laws.

In this paper, the generalized analytical equations are presented first and interpreted. Then the merits and drawbacks of each type of control law are discussed and the basis for the new mixed-mode technique is introduced. The CP and ME laws currently implemented for ST are then described and discussed as special cases. Finally, the expected advantages of the mixed-mode control law over the current CP and ME laws for ST are summarized. The simulation results are not included in this paper because they have not been completely analyzed at this time. However, the simulation results are anticipated to be presented in the Symposium.

GENERALIZED ANALYTICAL EQUATIONS AND PHYSICAL INTERPRETATIONS

In general, a desaturation control law is a method of reducing the buildup of spacecraft momentum due to external environmental torques by generating a magnetic torque resulting from the interaction between the geomagnetic field and the commanded magnetic torquers situated on the spacecraft.

There are two fundamental distinctions that characterize a control law: the type of control and the minimization criterion. Each control law can in general be put into one

of the two main categories, depending on its type of control--closed loop or open loop. In a closed-loop control law, the magnetic dipole command is updated using instantaneous measurements with the intent to achieve a desired torque at each update time. In an open-loop control law, the magnetic dipole command is updated using predicted information with the intent to achieve a desired momentum at the end of each update period. In addition to these fundamental differences, the control laws can be further categorized by their minimization criteria. To achieve a desired torque or momentum, there is usually one degree of freedom in commanding the magnetic torquers. This degree of freedom can be used to select one quantity to minimize, such as the energy consumption or the reaction wheel speed.

The minimization criterion is completely independent of the control type. That is, every control law can be either closed loop or open loop regardless of which quantity is minimized. This categorization of control laws is illustrated in Figure 1. Thus, to specify a control law clearly, it is necessary to specify not only the minimization criterion but also the control type. In principle, a minimum energy law can be either a closed-loop law or an open-loop law depending on how the magnetic dipole command is generated. The ST tradition of using "CP law" to represent a closed-loop law and "ME law" to represent an open-loop law is confusing from a physical point of view. In the remainder of this paper, a control law is defined by specifying its control type followed by its minimizaton criterion, e.g., "closed-loop ME law" or "open-loop minimum wheel speed law." When a particular control law implemented for ST is referred to, the word"original" or "current" will be used to distinguish it from other control laws. For instance, the "current ME law" represents the ME law

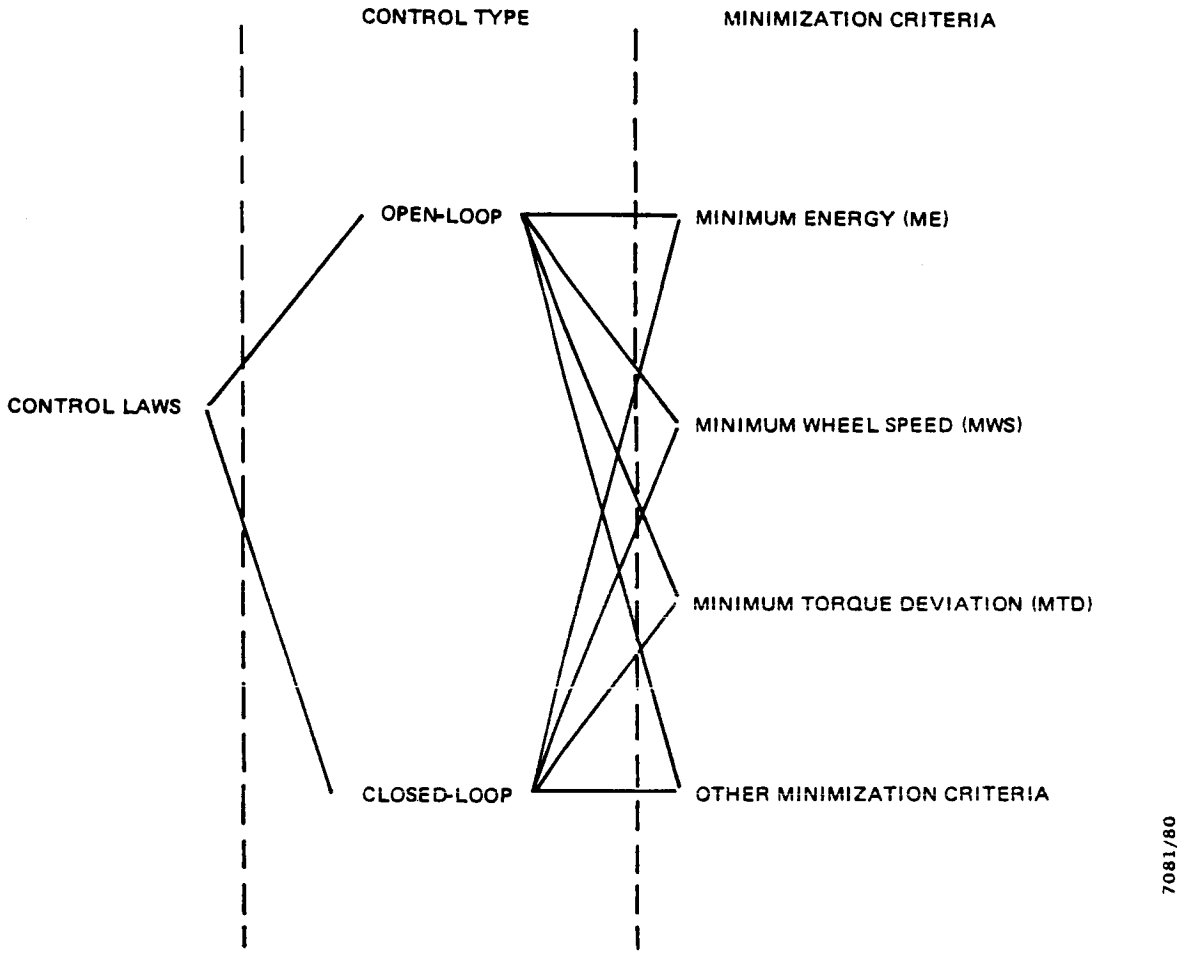

Figure 1. Categorization of Control Laws

implemented currently for ST, which actually is an open-loop ME law.

Table 1 presents the generalized analytical equations for all control laws using magnetic torquers. In the table, $\vec{T}_D$ is the desired torque, which is the torque a closed-loop control law is attempting to achieve momentarily through the interaction between the magnetic torquers and the geomagnetic field. Here $\vec{H}_D$, which is defined for open-loop control laws only, is the integration of the desired torque over a period of time (called the desaturation period). Physically, $\vec{H}_D$ is the desired momentum an open-loop control law attempts to achieve over the desaturation period through the interaction between the magnetic torquers and the geomagnetic field. Thus, the fundamental difference between the open-loop and the closed-loop control laws is that the former attempts to achieve $\vec{T}_D$ momentarily, whereas the latter attempts to achieve $\vec{H}_D$ over a desaturation period. The determination of $\vec{T}_D$ and $\vec{H}_D$ depends on the individual control law. However, good momentum management relies on proper determination of $\vec{T}_D$ and $\vec{H}_D$. One reasonable way of defining $\vec{T}_D$ and $\vec{H}_D$ is to assume that the gravity-gradient torque $\vec{T}_{GG}$ is the only significant environmental torque acting on the spacecraft. In this case,

$$\vec{T}_D = \dot{\vec{H}}_T - \vec{T}_{GG} \tag{1}$$

where $\vec{H}_T$ is the total system momentum which equals the reaction wheel momentum $\vec{H}_{RW}$ at inertial attitudes. For a closed-loop control law, $\vec{H}_T$ in Equation (1) is usually replaced by $-K_M(\vec{H}_T + \vec{H}_B)$, where K_M is a positive constant called the magnetic gain and $\vec{H}_B$ is a bias vector that is added to $\vec{H}_T$ to keep the reaction wheel speed center at zero. For an open-loop control law, Equation (1) is

Table 1. General Equations for All Control Laws

	CLOSED-LOOP LAW	OPEN-LOOP LAW
DESIRED TORQUE	$\vec{T}_D$	
DESIRED MOMENTUM	NOT APPLICABLE	$\vec{H}_D = \int_{t_i}^{t_f} \vec{T}_D dt$
WEIGHTING MATRIX	A	
COSTATE VECTOR	$\vec{P} = (\vec{B}^T A A^T \vec{B})^{-1} \vec{T}_D$	$\vec{P} = \left[\int_{t_i}^{t_f} \tilde{B}^T A A^T \tilde{B} dt\right]^{-1} \vec{H}_D$
SYSTEM MAGNETIC DIPOLE MOMENT	$\vec{\mu}_M = A A^T \tilde{B} \vec{P}$	
MAGNETIC TORQUE	$\vec{T}_M = \vec{\mu}_M \times \vec{B}$	
COMMANDED MAGNETIC DIPOLE MOMENT	$\vec{\mu}_T = M^T (MM^T)^{-1} \vec{\mu}_M$	

7081/80

integrated over the desaturation period to give the desired momentum $\vec{H}_D$. That is,

$$\vec{H}_D = \int_{t_i}^{t_f} \vec{T}_D \, dt$$

$$= \vec{H}_T(t_f) - \vec{H}_T(t_i) - \int_{t_i}^{t_f} \vec{T}_{GG} \, dt \tag{2}$$

where $\vec{H}_T(t_f)$ is the desired total momentum at the end of the desaturation period and $\vec{H}_T(t_i)$ is the measured total momentum at the start of the desaturation period. The length of the desaturation period controls the magnitude and direction of $\vec{H}_D$. Nominally, the desaturation period is set at half an orbital period to include the major variations in the geomagnetic field and to be compatible with the period of the gravity-gradient disturbances so that only the nonperiodic portion of the accumulated gravity-gradient momentum is dumped.

The weighting matrix A of Table 1 can be either an identity matrix or one of the mounting matrices, depending on the minimization criterion selected for the control law. For instance, A is the magnetic coil mounting matrix, M, for a minimum energy control law and is the reaction wheel mounting matrix, W, for a minimum wheel speed control law. For any orthogonal system, A is the identity matrix, and in the following discussion A is assumed to be the identity matrix.

The costate vector $\vec{P}$ is defined differently for the closed-loop and open-loop control laws. For a closed-loop control law, $\vec{P}$ is the desired torque weighted by $|\vec{B}|^{-2}$, where $\vec{B}$ is

the geomagnetic field. For an open-loop control law, $\vec{P}$ is the desired momentum weighted by both the magnitude and the direction of the geomagnetic field over the desaturation period. The physical meaning of $\vec{P}$ for an open-loop control law is illustrated in Figure 2 with the assumption that the magnitude of $\vec{B}$ is constant in time. As shown in Figure 2, $\vec{P}$ is a fictitious torque whose component along the direction normal to the instantaneous geomagnetic field is the instantaneous magnetic torque, $\vec{T}_M$, generated by the torquers. The integration of $\vec{T}_M$ over the desaturation period is equal to $\vec{H}_D$. The costate vector P in an open-loop control law is analogous to the desired torque $\vec{T}_D$ in a closed-loop control law after being properly weighted.

Figure 2 also illustrates the significance of the desaturation period for an open-loop control law. Three cases covering different desaturation periods are shown in Figure 2. When the desaturation period is very short, as illustrated in Figure 2(a), $\vec{P}$ approaches infinity due to the near-singular condition. In this case, the magnetic torquers are given poorly defined commands with the result that the magnetic torques generated may go through an undesirable path before the desired momentum is achieved. This is shown in Figure 2(a), where the magnetic torque $\vec{T}_{M_1}$ is along a direction almost opposite to the direction of the desired momentum $\vec{H}_D$. This can cause a very high reaction wheel speed at the end of t_1, which is undesirable. Thus, an open-loop control law operated under very short desaturation periods can sometimes lead to serious consequences. As the desaturation period increases as shown in Figure 2(b) and (c), the costate vector $\vec{P}$ becomes better defined and the path of the magnetic torques becomes closer to the desired momentum.

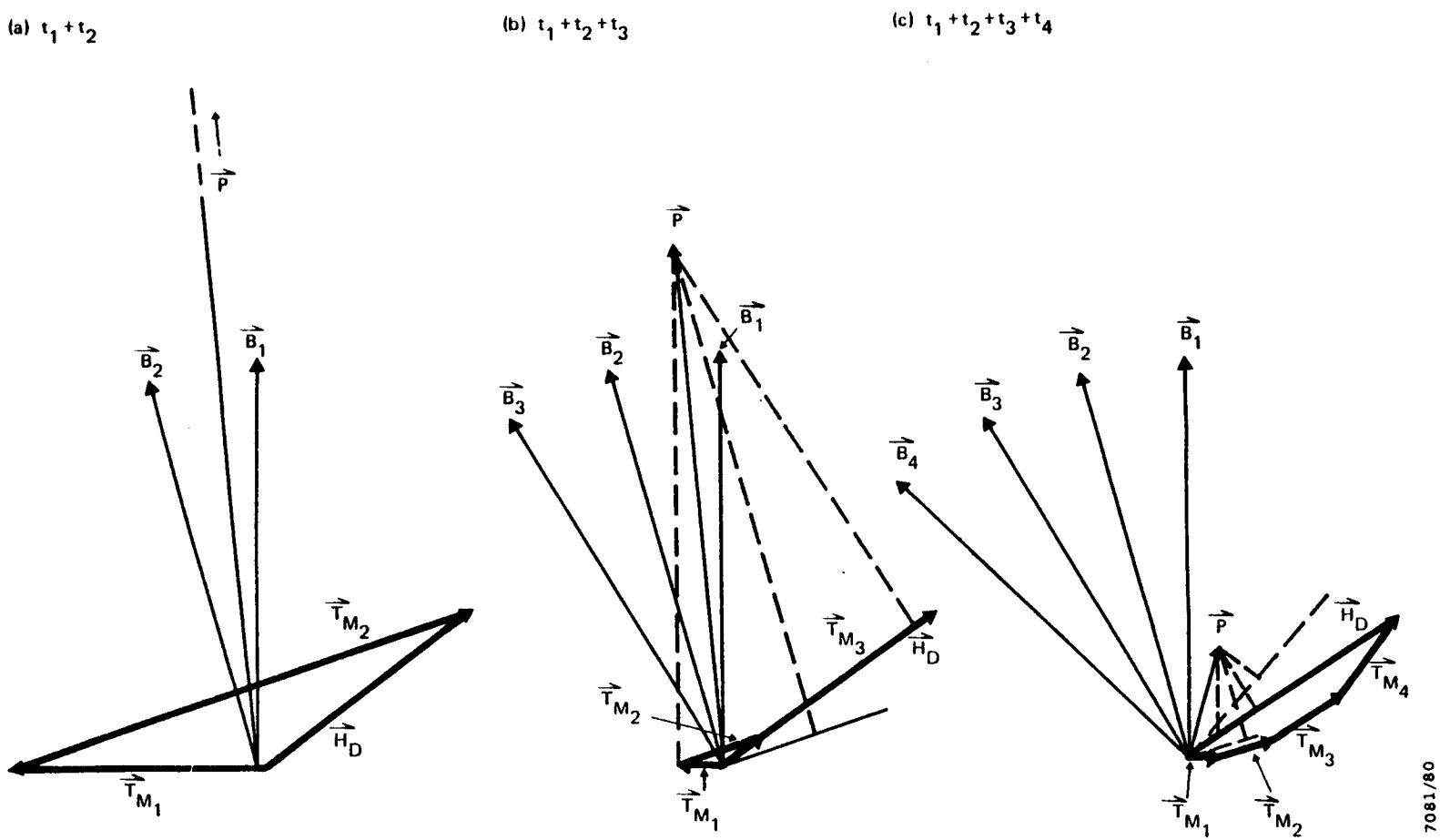

Figure 2. Physical Interpretation of the Costate Vector in an Open-Loop Control Law

Once the costate vector is determined, the remaining quantities of the control laws are computed through an identical set of equations for both the closed-loop and the open-loop control laws. The system magnetic dipole moment $\vec{\mu}_M$ is the magnetic dipole moment (defined in the spacecraft body coordinate system) that is required to generate the desired magnetic torques. The magnetic torque $\vec{T}_M$ is the actual instantaneous magnetic torque generated from the interaction between the magnetic torquers and the geomagnetic field. The magnitude and direction of $\vec{T}_M$ are as follows. For a closed-loop control law, $\vec{T}_M$ is the component of $\vec{T}_D$ that is normal to $\vec{B}$. This component is the best torque that can be achieved because $\vec{T}_M$ will be perpendicular to $\vec{B}$, although ideally it would be desirable to generate a $\vec{T}_M$ that equals $\vec{T}_D$. Depending on the minimization criterion, when the weighting matrix A is different from the identity, the magnitude and direction of $\vec{T}_M$ differ slightly from those described above. For an open-loop control law, $\vec{T}_M$ is also perpendicular to $\vec{B}$ at any moment. However, in this case $\vec{T}_m$ also satisfies the condition that its integrated effect over the desaturation period equals the desired momentum, $\vec{H}_D$. That is, $\vec{T}_M$ satisfies the condition that

$$\int_{t_i}^{t_f} \vec{T}_M \, dt = \vec{H}_D \tag{3}$$

This indicates that although the desired torques cannot always be generated momentarily, the desired momentum can usually be generated over a period of time, taking advantage of the variations in the geomagnetic field. This forms one major advantage of an open-loop control law over a closed-loop control law.

The last item in Table 1 is the commanded magnetic dipole moment $\vec{\mu}_T$. The components of $\vec{\mu}_T$ give the actual dipole moment required by each of the magnetic torquers to generate the magnetic torque $\vec{T}_M$, and $\vec{\mu}_T$ is the final output of a control law sent to the magnetic torquers.

COMPARISONS AND DISCUSSIONS

Both the closed-loop and the open-loop control laws have their merits and drawbacks. The greatest problem of a closed-loop control law is that it attempts to achieve a desired torque momentarily, which is impossible in general. The closed-loop control law produces a magnetic torque that is the component of $\vec{T}_D$ normal to the geomagnetic field. This effectively projects ther resultant torque into the direction of the geomagnetic field, which is an unfavorable direction for further reduction of the momentum. As a result, a great deal of energy is wasted in changing the direction rather than reducing the magnitude of the momentum. Furthermore, the closed-loop control law attempts to always reduce the same fraction of the total momentum as controlled by the magnetic gain K_M, regardless of the variation in geometry. This is not efficient, because the law should always attempt to dump more momentum when the geometry is favorable and less momentum at an unfavorable geometry. In addition, the closed-loop control laws attempt to dump both the periodic and the nonperiodic gravity-gradient momenta, while only the nonperiodic portion needs to be dumped in most applications. These problems associated with the closed-loop control laws are eliminated in the open-loop control laws, because the open-loop control laws always look at the situation ahead of time to take advantage of the variations in geometry to dump the proper amount of momentum at the proper time. Thus, at the end of the desaturation

period, the exact amount of desired momentum will be generated from the torquers.

The open-loop control laws are ideal if actual performance is exactly as predicted. However, in case of modeling errors or undetected failure conditions, reality can be very different from the prediction. This difference will not be known until the end of the desaturation periods, which may be too late for correction. To resolve this potential problem, LMSC modified the open-loop control for ST so that a half-orbit desaturation period is used in computing the nominal momentum profile $\vec{H}_{NOM}$ on the ground; then $\vec{H}_{NOM}$ is used as the targeting momentum ($\vec{H}_T(t_f)$ of Equation (2)) in computing $\vec{H}_D$ on board where a much shorter desaturation period is used. With this modification, the advantages of the open-loop control laws are kept by forcing the system momentum to follow the same time variation it would follow if a half-orbit desaturation period were used under nominal situations. At the same time, the disadvantage of the open-loop control laws is reduced by decreasing the duration of the desaturation period so that the actual system momentum can be measured at a much higher frequency, and the deviation between the reality and the prediction can be included in $\vec{H}_D$ and corrected for at this new frequency.

In principle, with a precomputed $\vec{H}_{NOM}$, the shorter the update period the better, if undetected failure conditions exist. However, as shown in Figure 2(a), making the desaturation period of an open-loop control law arbitrarily short may cause the costate vector P to be ill defined and result in very undesirable momentum before the desired momentum is achieved. For this reason, a 600-second desaturation period with a 200-second updating frequency was recommended in the current momentum management implementation for ST.

If instead of using an open-loop control law at a reduced desaturation period, a closed-loop control law is used with the precomputed H_{NOM}, the problem of determining $\vec{P}$ will no longer exist. In this technique, which we refer to as a mixed-mode control law, the updating frequency of $\vec{P}$ can be reduced to the frequency of the closed-loop control laws, which is approximately 50 seconds for ST. To accomplish this, the desired torque at any time t will be computed with the following equation, which is directly obtained from Equation (1):

$$\vec{T}_D = \frac{1}{\Delta t}[\vec{H}_{NOM}(t + \Delta t) - \vec{H}_T(t)] - \vec{T}_{GG}(t) \tag{4}$$

where Δt is the updating frequency for the closed-loop control law and $\vec{H}_{NOM}$ is the nominal momentum profile computed previously on the ground based upon an open-loop control law with a half-orbit desaturation period. The desired torque so determined is always nearly perpendicular to the instantaneous geomagnetic field because $\vec{H}_{NOM}$ is computed from the nominal magnetic torques, which are momentarily perpendicular to B. This mixed-mode control law, which is a closed-loop control law operated with an open-loop $\vec{H}_{NOM}$, seems to retain the advantages of both the open-loop and the closed-loop control laws and is believed to be the best technique for momentum management. This mixed-mode control law is further described later in this paper.

CURRENT ST IMPLEMENTATIONS

The current CP law implemented for ST is a closed-loop law that minimizes the reaction wheel speed. Thus, the desired torque $\vec{T}_D$ and weighting matrix A of Table 1 are given by

$$\vec{T}_D = -K_M \left(\vec{H}_T + \vec{H}_B\right) - \vec{T}_{GG} \tag{5}$$

$$A = W = \begin{bmatrix} a & -a & a & -a \\ -b & -b & b & b \\ -b & -b & -b & -b \end{bmatrix} \tag{6}$$

where a = sin 20 degrees and b = $1/\sqrt{2}$ cos 20 degrees. The current ME law implemented for ST is a modified open-loop control law that minimizes the coil energy consumption. In this control law, a nominal momentum profile $\vec{H}_{NOM}$ is computed on the ground for each of the inertial attitudes using a half-orbit as the desaturation period. This $\vec{H}_{NOM}$ is then used in the determination of $\vec{H}_D$ on board where a shorter desaturation period (600 seconds) and updating frequency (200 seconds) are used. As discussed earlier in the paper, the purpose of this modification is to reduce the error made in an open-loop control law in case undetected failure conditions exist. Thus, the desired momentum $\vec{H}_D$ and the weighting matrix A of Table 1 are given by the following equations for the current ME law:

$$\vec{H}_D = \vec{H}_{NOM}(t_f) - \vec{H}_{RW}(t_i) - \int_{t_i}^{t_f} \vec{T}_{GG} \tag{7}$$

where t_i is updated every 200 seconds and $t_f = t_i$ + 600 seconds.

$$A = M = \begin{bmatrix} s & s & s & s \\ c & -c & -c & c \\ c & c & -c & c \end{bmatrix} \tag{8}$$

where s = sin 35.26 degrees and $c = 1/\sqrt{2}$ cos 35.26 degrees.

Notice that in the determination of H_D for the current ME law, the total momentum $\vec{H}_T$ given in Equation (1) has been replaced by the reaction wheel momentum $\vec{H}_{RW}$. This is due to the special way in which the current ME law is implemented, which does not require the knowledge of the system momentum during maneuvers. In the case of maneuvers, the normal mode of operation of the current ME law with a 600-second desaturation period and 200-second updating frequency is terminated. It is replaced by a single maneuver desaturation period that includes a lead time before the start of the maneuver and a lag time after the end of the maneuver. Thus, the length of the maneuver desaturation period depends on the lengths of the maneuver and the lead and lag times. In the current onboard implementation, each maneuver has a single lead/lag time that will be determined on the ground and uplinked to the spacecraft with the maneuver commands. This requires some ground software support in addition to the $\vec{H}_{NOM}$ determination.

PROPOSED MIXED-MODE CONTROL LAW

As mentioned earlier in the paper, the mixed-mode control law, which retains the advantages of both closed-loop and

open-loop control laws, seems to be a good choice for momentum management using magnetic torquers. For the case of ST, the mixed-mode minimum wheel speed law, which is a closed-loop control law operated with an open-loop $\vec{H}_{NOM}$ using the minimum wheel speed minimization criterion, would be optimal. In this case, the desired torque $\vec{T}_D$ and the weighting matrix A of Table 1 are given by Equations (4) and (6), respectively. The advantages of this new technique over the current ST control laws are summarized below.

ADVANTAGES OVER THE CURRENT CP LAW

The mixed-mode minimum wheel speed law is better than the current CP law because it computes the desired torque based on the nominal momentum profile precomputed using an open-loop control law with a half-orbit desaturation period. The desired torque so determined has the following advantages:

1. It takes advantage of future geometrical variations so that the proper amount of momentum will be dumped at the proper time.

2. Only the nonperiodic portion of the gravity-gradient momentum will be dumped by the magnetic torquers.

3. The desired torque is always nearly perpendicular to the geomagnetic field so that very little energy will be wasted in changing the direction rather than reducing the magnitude of the momentum.

4. The reaction wheel center speed control loop is no longer needed because the targeting momentum $\vec{H}_{NOM}$ automatically keeps the reaction wheel center speed at zero. This greatly simplifies the onboard computation.

ADVANTAGES OVER THE CURRENT ME LAW

The mixed-mode minimum wheel speed control law has the following advantages over the current ME law:

1. It reduces the updating frequency of the costate vector P from 200 seconds to approximately 50 seconds. This will reduce the deviation between the actual and the predicted results when undetected failure conditions exist.

2. There is no need to define a desaturation period onboard. This eliminates the possibility of having a near-singularity condition in computing the costate vector P.

3. The required onboard computation is greatly simplified because it does not require the predicted geomagnetic field computation, and no integration is involved.

4. Minimization of wheel speeds reduces possible vibration in the spacecraft.

REFERENCES

1. Computer Sciences Corporation, CSC/TM-79/6313UD2, Space Telescope Momentum Management Procedure (Revision 2). L. Chen and C. Sturch, September 1980

2. A. Wernli, "Minimization of Reaction Wheel Momentum Storage With Magnetic Torquers," J. Astronautical Sciences, vol. 26, no. 3, p. 257, July-September 1978

BIBLIOGRAPHIC DATA SHEET

1. Report No. NASA CP-2152	2. Government Accession No.	3. Recipient's Catalog No.
4. Title and Subtitle FIFTH ANNUAL FLIGHT MECHANICS/ESTIMATION THEORY SYMPOSIUM - OCTOBER 1980		5. Report Date October 1980
		6. Performing Organization Code 582
7. Author(s) Jerome Teles, Editor		8. Performing Organization Report No.
9. Performing Organization Name and Address Goddard Space Flight Center Greenbelt, MD 20771		10. Work Unit No.
		11. Contract or Grant No.
12. Sponsoring Agency Name and Address National Aeronautics and Space Administration Washington, DC 20546		13. Type of Report and Period Covered Conference Publication
		14. Sponsoring Agency Code
15. Supplementary Notes		

16. Abstract

This document is a compilation of papers presented at the Fifth Annual Flight Mechanics/Estimation Theory Symposium held October 21-22, 1980, at the Goddard Space Flight Center.

17. Key Words (Selected by Author(s)) Astrodynamics		18. Distribution Statement STAR Category 13 Unclassified - Unlimited	
19. Security Classif. (of this report) Unclassified	20. Security Classif. (of this page) Unclassified	21. No. of Pages	22. Price* A12

*For sale by the National Technical Information Service, Springfield, Virginia 22151.

GSFC 25-44 (10/77)